Dissertation

zur Erlangung des Grades

Doktor der Naturwissenschaften im Promotionsfach Chemie

Am Fachbereich Chemie, Pharmazie und Geowissenschaften

der Johannes Gutenberg-Universität in Mainz

Dendronized Ions

vorgelegt von

David Türp

geboren in Berlin

Mainz, den 21.05.2012

Dekan: [redacted]

1. Berichterstatter: [redacted]

2. Berichterstatter: [redacted]

Tag der mündlichen Prüfung: [redacted]

Die vorliegende Dissertation wurde unter Betreuung durch [redacted] am Max Planck Institut für Polymerforschung in Mainz in der Zeit vom 08. Januar 2008 bis zum 27. April 2011 angefertigt.

Danksagung

[redacted]

Contents

List of Abbreviations

AcO	acetoxy
ATRP	atom transfer radical polymerization
CCDC	Cambridge Crystallographic Data Centre
d	day
DCM	dichloromethane (or: methylene chloride)
DFT	density functional theory
diglyme	diglycol methyl ether (or: bis(2-methoxyethyl) ether)
DLS	dynamic light scattering
DMSO	dimethylsulfoxide
DOSY	diffusion ordered spectroscopy
DSC	differential scanning calorimetry
ESP	electrostatic surface potential
EtO	ethoxy
FCS	fluorescence correlation spectroscopy
GPC	gel permeation chromatography
h	hour
HOMO	highest occupied molecular orbital
HOPG	highly oriented pyrolytic graphite
HPB	hexaphenylbenzene
HSQC	heteronuclear single quantum coherence
LUMO	lowest unoccupied molecular orbital
MAO	methylaluminoxane

MALDI-TOF	matrix assisted laser desorption ionization – time of flight
MAS	magic angle spinning
Me	methyl
MeCN	acetonitrile
MHz	megahertz
min	minute
MO	molecular orbital
NMR	nuclear magnetic resonance
PP	Polyphenylene
PPD	Polyphenylene Dendrimer
ppm	parts per million
PrO	propoxy
PSS	photostationary state
s	second
TBA^+	tetrabutylammonium
TBAF	tetrabutylammonium fluoride
TBTA	*Tris*-(benzyltriazolylmethyl)amine
*t*Bu	*tert*-butyl
*t*BuONO	*tert*-butyl nitrite
$TCNQ^-$	tetracyanoquinodimethane
THF	tetrahydrofuran
T*i*PS	triisopropylsilyl
TMS	trimethylsilyl

TGA	thermogravimetric analysis
VOC	volatile organic compound
WCA	weakly coordinating anion
XRD	X-ray diffraction

1 Introduction and Motivation

Nowadays, chemists can make use of an enormous amount of accumulated knowledge about the material world and the principles that guide its transformations. In addition to curiosity, this knowledge derives from the huge impact that the successful handling and utilization of various materials had and still has on human life. As a consequence, several materials are ubiquitous in the everyday environment of a modern person that did not even exist a generation earlier.

Already today, a growing number of materials derive their properties not only from their chemical constitution but also from their assembly into specific nano- or microscopically ordered structures. The most elaborated examples of property tuning via microstructure are provided by so called “metamaterials", which even enable creating seemingly "impossible" properties such as negative refractive indices. Composites also derive novel properties from the synergetic combination of different, often quite complementary types of materials. On yet smaller length scales, chemist have an ever increasing number of methods and tools at their disposal to specifically design, combine and fine-tune the properties of compounds via molecular structure. Among the many possible approaches, dendrimers probably provide the most versatile platform because they enable to combine and specifically place different functionalities within single, defined molecules.

Although it is impossible to provide accurate predictions, many of the compounds and materials in general use tomorrow will be better adapted for their specific purposes, and the degree of complexity regarding both their molecular and supramolecular structures will certainly increase. Such increase in complexity also means that a thorough understanding of structure-property relations requires consideration of ever more disciplines of science that were classically “separated”. Here again, dendrimers provide an excellent basis to bring together different concepts and create structures that are situated in between the classical realms of e.g. organic, inorganic and macromolecular chemistry.

1.1 Dendrimers

1.1.1 History and Methods

The term "dendrimer" is derived from the greek word δένδρον (dendron, meaning "tree"), and is used to denote macromolecules with a regularly branched and structurally perfect tree-like structure.[1,2] The invention of the term was necessary to discern dendrimers from other branched but structurally less defined macromolecules such as hyperbranched polymers.

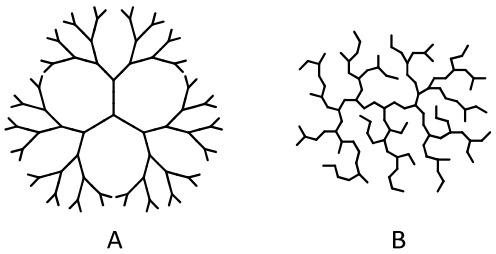

Figure 1: Comparison of the schematic structures of a dendrimer (A) and a hyperbranched polymer (B)

Originally, *F. Vögtle* used the term "cascade-molecules" in his first publication on tree-like poly(propyleneamine) molecules from 1978.[3] This term is useful to point out the cascade-like increase in the number of functions in subsequent stages of growth (called generations). After some additional neologisms for such molecules, including "arborols"[4] and "starburst-dendrimers"[5], *D. A. Tomalia* largely popularized the term "dendrimer" in his 1990 review on the topic.[1] This term is now most commonly used.

The reaction scheme for the synthesis of the first dendrimers, poly(propyleneamine) or POPAM dendrimers,[3] provides a good example to explain the general principle of dendrimer synthesis (see Figure 2).

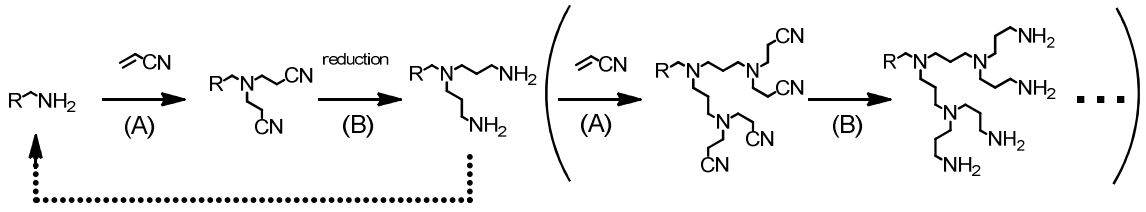

Figure 2: Synthesis of a POPAM dendrimer as described by *F. Vögtle*

In a first step (A) ("branching" step), an amine is functionalized with two nitrile functions via *Michael* addition of acrylonitrile. In a second step ("activation" step (B)), the resulting tertiary amine is activated for a subsequent repetition of branching step (A) via reduction

of its nitrile functions to primary amines. Continuous repetition of this cyclic synthetic protocol leads to a cascade-like growth of an ever more branched molecule.

The above described pattern, an alternating sequence of two orthogonal reactions (A) and (B), can be found in the synthetic protocols of all dendrimers and enables their structural perfection through controlled, stepwise synthesis. However, two general synthetic routes can be discerned regarding the "direction" of growth. The synthesis of a dendrimer starting from a central point and continuing outwards is called "divergent", while a synthesis starting from the periphery and growing inwards is called "convergent" (see Figure 3).

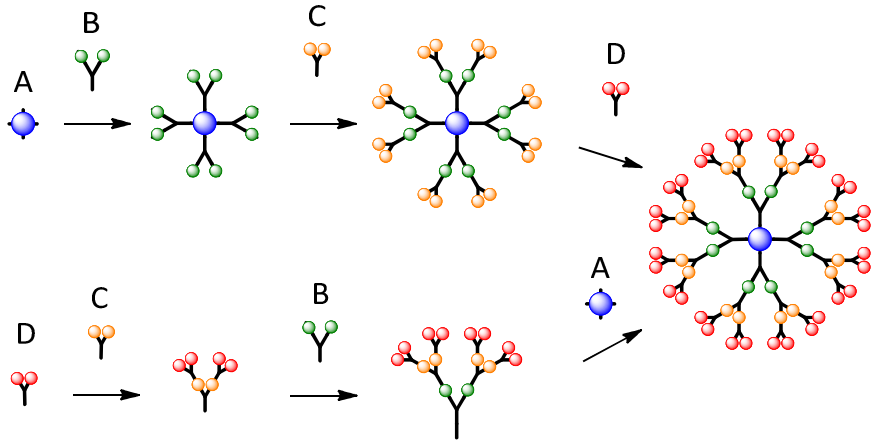

Figure 3: Schematic representation of dendrimer synthesis; upper route = divergent method (starting from the core A and successively reacting with building blocks B, C and D); lower route = convergent method (starting from the surface building block D and successively reacting with C, B and A)

Both the above mentioned POPAM dendrimers[3] of *F. Vögtle* and the poly(amidoamine) or PAMAM dendrimers[5] introduced by *D. A. Tomalia* in 1986 are classic examples of dendrimers synthesized by the divergent method.

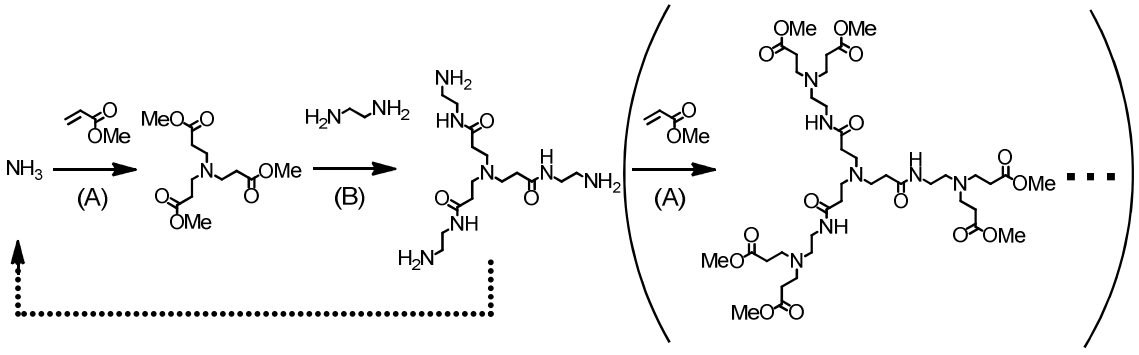

Figure 4: Synthesis of PAMAM dendrimers as described by *D. A. Tomalia*

For each generation, step (A) multiplies the number of growth-reactive functions of the dendrimer, which continually grows from its central core outwards. The exponentially growing number of functions increases the danger of incomplete conversion and thus the probability of structural defects in the so synthesized dendrimers.

In 1990, *J. M. J. Fréchet* and *C. Hawker* presented poly(aryl ether) dendrimers which were synthesized "from outside inwards", providing the first example of a convergent dendrimer synthesis.[6]

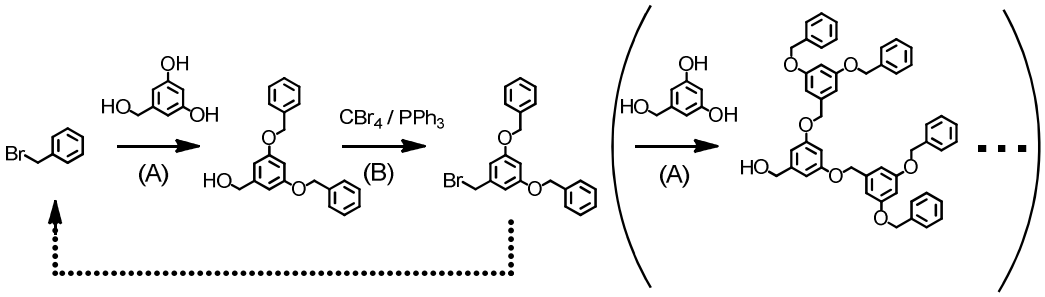

Figure 5: Synthesis of poly(aryl ether) dendrimers as described by *J. M. J. Fréchet* and *C. Hawker*

Convergent synthesis reduces the number of growth-reactive functions to constantly low numbers, regardless of the dendrimer generation. Thus, the danger of introducing structural defects via incomplete conversion is reduced. However, steric congestion between large-grown dendrons potentially prevents their convergent junction and thus often limits the applicability of the convergent method to lower generations as compared to the divergent method.

The convergent method was successfully applied for the synthesis of the first, fully arene-based dendrimers by *T. M. Miller* and *T. X. Neenan* in 1990.[7,8]

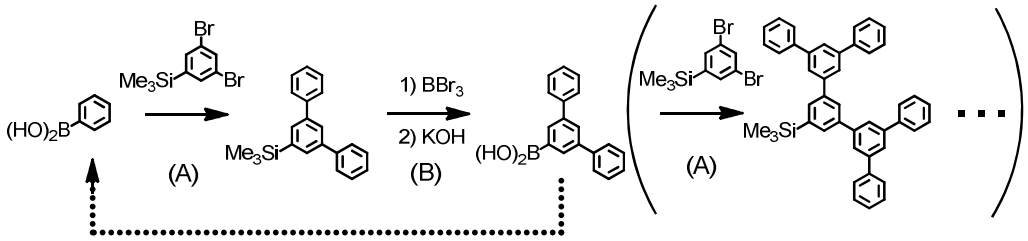

Figure 6: Synthesis of polyphenylene dendrimers as described by *T. M. Miller* and *T. X. Neenan*

A palladium catalyzed coupling of phenylboronic acids to phenylbromides yielded polyphenylene dendrimers with a 1,3,5-branching pattern. These dendrimers also provide the first example for a dendritic scaffolds build from relatively rigid moieties. Similarly,

the poly(phenylacetylene) dendrimers of *J. S. Moore* are build from rigid building blocks which are linked via palladium catalyzed coupling of phenyl acetylenes to aryl halides in a convergent way.[9,10]

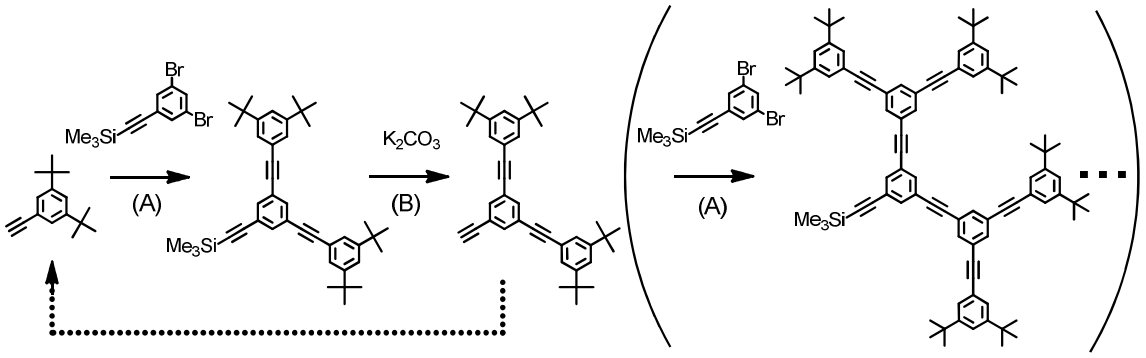

Figure 7: Synthesis of poly(phenylacetylene) dendrimers as described by *J. S. Moore*

In 1997, *K. Müllen* presented a new and very different approach for the synthesis of polyphenylene dendrimers (PPDs). Instead of utilizing metal catalyzed coupling reactions, the *Diels-Alder* cycloaddition of functionalized tetracyclones to ethynyl groups was used to generate new phenyl rings as branching points.[11]

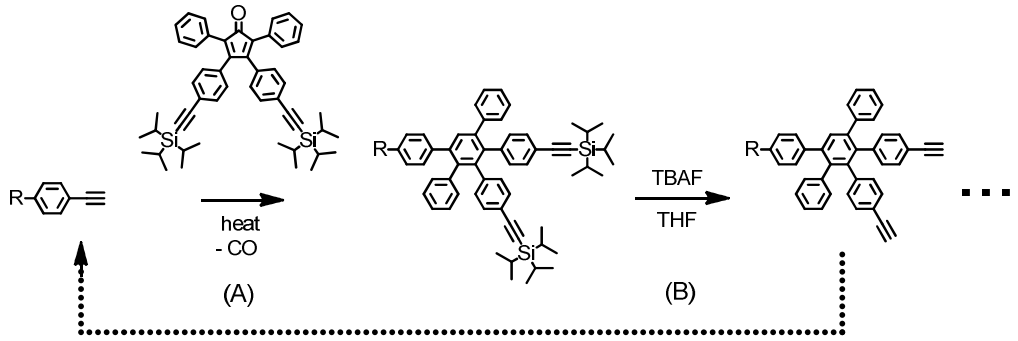

Figure 8: Synthesis of polyphenylene dendrimers as described by *K. Müllen*

Employment of thermal cycloaddition also enabled a divergent rather than only convergent build-up of PPDs whilst maintaining the structural perfection of the products. Especially with regard to stiff and bulky building blocks, divergent synthesis allows for much higher molecular weights and degrees of branching than convergent synthesis. The resulting polyphenylene dendrimers are very rigid and thus possess a shape persistent structure. Their rigidity is a result of their main structural motif: branching chains of stiff *para*-phenylenes (see 1.2.2). The inherent rigidity of PPDs leads to some unique characteristics, which have been exploited already for a variety of functional materials and applications. Some of these will be presented in 1.2.3.

1.1.2 Properties of Dendrimers

1.1.2.1 Fractal Structure and Limits of Growth

The structures of regularly branched dendrimers can be regarded as fractals. Fractals are geometric structures that are similar to themselves on different scales, so that a fragment can represent the whole. The self-similarity of many geometric fractals (*Koch* curve, *Sierpinski* triangle, *Heighway* dragon) can be produced by repeatedly transforming a simple geometric object (e.g. a point, a line, a triangle) in the ever same way and continuously feeding back an earlier transformation result as a new input (recursion).

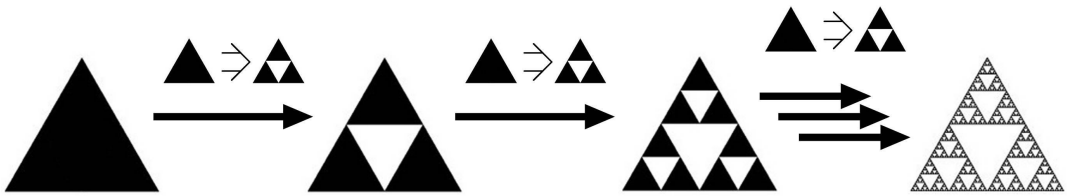

Figure 9: *Sierpinski* triangle as an example for the generation of self-similar fractals via cyclic application of a single transformation rule

The structures of dendrimers can be described and generated similarly (In the actual synthesis, the cyclic repetition of reaction steps (A) and (B) can be thought of as the analogue to a recursive algorithm of transformation). An appropriate (geometric) transformation for producing PPDs is displayed in Figure 10. The substitution of a blue "phenyl ring" of "tetraphenylmethane" by a "pentaphenylbenzene moiety" leads to a first generation PPD bearing four blue phenyl rings in each arm.

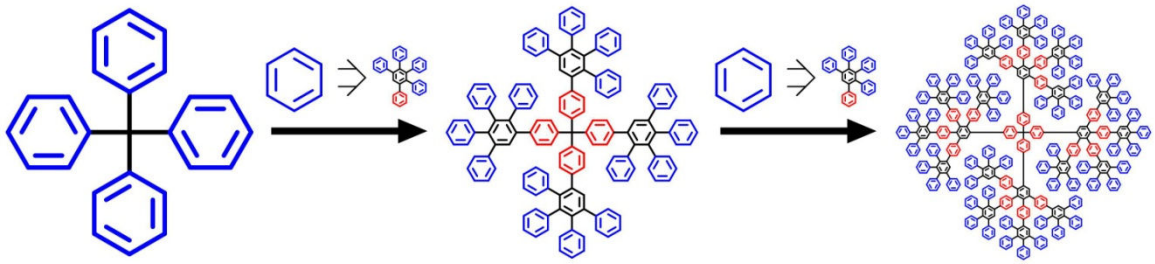

Figure 10: Example for the cyclic application of a transformation rule to generate the molecular structures of highly branched PPDs

Successive repetition of this transformation leads to highly branched PPD structures in the sequence of growing generations. In an idealized fractal, such transformations lead to ever finer, more and more detailed structures.

However, additional effects and constraints have to be considered for real existing dendrimers, in which constituting atoms have finite sizes and take up space. Such considerations led *P. G. de Gennes* and *H. Hervet* to conclude that a dendrimer should be more and more densely packed within its periphery upon growth (dense-shell model).[12] *R. S. Lescanec* and *M. Muthukumar* proposed a dense-core model instead, which also took into account the possibility of a "back-folding" of dendritic arms into the interior.[13] Refined models and small angle neutron scattering (SANS) experiments on dendrimer solutions by *M. Ballauff* and *C. N. Likos* generally confirmed the validity of the dense-core model for dendrimers with flexible scaffolds.[14,15] The rigid scaffold of PPDs should however preclude a back-folding of dendrons. Steric congestion between terminal groups should therefore increase the density of the peripheral shell with increasing generation, as predicted by the dense-shell model. SANS experiments on PPDs in solution did indeed support this expectation, making PPDs the only type of dendrimer so far which clearly exhibits denser shells instead of denser cores upon growth.[16]

Regardless of their rigidity or flexibility, all types of dendrimers exhibit an upper limit of growth. Above that limit, steric constraints hinder the quantitative and defect-free conversion to the next higher generation. In reference to *P. G. de Gennes*,[12] *D. A. Tomalia* concluded that defect-free poly(ethylenimine) dendrimers of 5th generation are "forbidden due to starburst dense packing", and defect levels already progressively increase from generations 3 to 4.[1] In rigid PPDs, the usually observed 4th generation limit of defect-free growth could be pushed further by way of extending the length between branching points and thus the space between terminal groups on the peripheral surface ("exploded" dendrimers).[17] The extra spacing enabled the synthesis of monodisperse and stiff dendrimers with diameters of up to 22 nm.[17]

1.1.2.2 Globular Shape and Multifunctionality

While the exact density profile of dendrimers depends on the rigidity/flexibility of their scaffold (see 1.1.2.1), all types of dendrimers generally exhibit an overall globular shape at sufficiently high generations and high degrees of branching. The globular shape of dendrimers decreases the probability of intermolecular entangling in solution and leads to lower viscosities and better solubilities as compared to polymers of the same constitution and molecular weight.[18] It is therefore not too surprising to find that polyphenylene dendrimers exhibit very good solubilities in organic solvents even despite being built from

stiff and rigid *para*-phenylene chains. Another consequence of the globular shape of dendrimers is that a distinction can be made between their interior (internal microenvironment) and the surrounding bulk solution, both of which may differ significantly from one another. Accordingly, dendrimers can be regarded as monodisperse "unimolecular micelles", and many research efforts are aimed at using dendrimers as "boxes" for the uptake, inclusion, transport and release of guest molecules.[19,20]

One of the most important advantages of dendrimers, however, is their unmatched potential to be specifically functionalized and to therefore yield defined macromolecules that can be adapted to various tasks. By utilization of suitably designed building blocks, large numbers of functionality can be accumulated within single molecules. Furthermore, the step-wise synthesis of dendrimers enables a combination of different kinds of functionality, as well as a specific placement of these functions into different parts of the final dendritic structure.

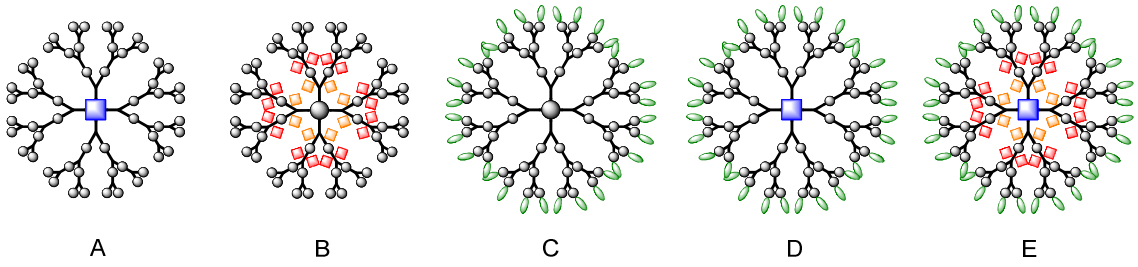

Figure 11: Schematic drawings of dendritic structures with additional functions in the core (A), the scaffold (B), on the surface (C), and combinations of these (D and E)

The schematic drawings in Figure 11 display some of the possible arrangements for functionalized dendrimers. Placement of a function into the dendritic core (see A, Figure 11) can be used to change the functions redox behavior,[21-23] its photo- and electroluminescence,[24-26] its reactivity[27] and its solubility.[28] Dendronization can further be used to screen a function from undesired intermolecular interactions and prevent aggregation,[29-31] or to increase enantio-, regio- and substrate selectivity of catalytically active species as well as facilitating their recovery after reaction.[32-34] Functionalization of the dendritic scaffold (see B, Figure 11) generally enables a multiplication of functionality and allows for changing and tailoring the properties of the dendritic microenvironment, including its hydrophobicity or hydrophilicity,[35,36] and the strength and specificity of host/guest interactions.[37,38] Modification of the dendritic surface (see C, Figure 11) can be used to significantly change solubility,[9,28] affect interactions with other molecules[39] or nanoparti-

cles,[40] increase biocompatibility[41,42] and enable biological targeting.[43,44] Finally, the degree of control over molecular properties and the behavior of dendrimers is multiplied by the possibility to combine different types of function and to place them into different parts of the scaffold (see D and E, Figure 11). Some very remarkable examples of this combinatory concept include the design of energy funnels,[45] dendritic light harvesting systems,[46-48] and dendrimers whose properties can be switched by external stimuli.[49-51] There are few limits to the imagination of ever new structures, and it is the responsibility of synthetic chemists to come up with preferably clever designs and solutions to the problems posed by material requirements.

Since major parts of this work are based on utilizing the advantages of polyphenylene dendrimers, a short review on this in many ways unique type of material will be given on the following pages. Most of these pages are an excerpt of a more complete review on polyphenylene dendrimers which has been published recently.[52]

1.2 Polyphenylene Dendrimers

1.2.1 Synthetic Concept

The synthesis of *Müllen*-type polyphenylene dendrimers (PPDs) is based on the generation of new arene rings from the *Diels-Alder* cycloaddition of tetraphenylcyclopentadienones (or short "tetracyclones") to ethynyl functions at high temperatures, as first described by *W. Dilthey* in 1933.[53-57]

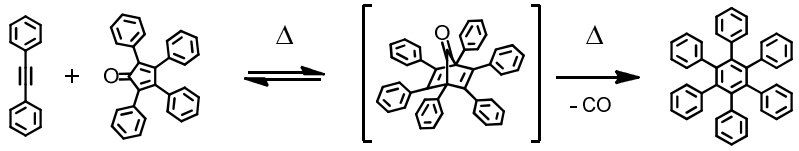

Figure 12: Reversible *Diels-Alder* cycloaddition of tolane and tetracyclone, which yields a norbornadien-7-one intermediate and, after cleavage of carbon monoxide, irreversibly yields hexaphenylbenzene

Reversible cycloaddition of a tolane (dienophile) to tetracyclone (diene) yields a norbornadien-7-one intermediate, which sometimes can even be isolated.[58] At high temperatures (>140 °C), the norbornadien-7-one intermediate irreversibly cleaves off carbon monoxide, whereupon a highly substituted benzene ring (here: hexaphenylbenzene or HPB) is formed. For the build-up of PPDs, the procedure most commonly applied today requires dissolution of the ethynyl functionalized component and the tetracyclone building block in *o*-xylene and heating the stirred mixture to about 150 –170 °C.

To allow for a continuation of growth after completed cycloaddition, further reactive ethynyl groups must be made available in the product. The key idea to satisfy this requirement was the synthesis of an ethynyl functionalized tetracyclone **1** (Figure 13).[11] Tetracyclone **1** comprises both a diene function for cycloaddition to a dienophile, and two protected ethynyl groups, which after deprotection can serve as new dienophiles. The reaction protocol therefore becomes cyclic (or recursive) and enables the continued synthesis of dendritic polyphenylene structures (see 1.1.1). In such synthesis, tetracyclone **1** serves as an AB_2 building block, because it introduces bifurcations or branching points into the structure and multiplies the number of available ethynyl groups by two.

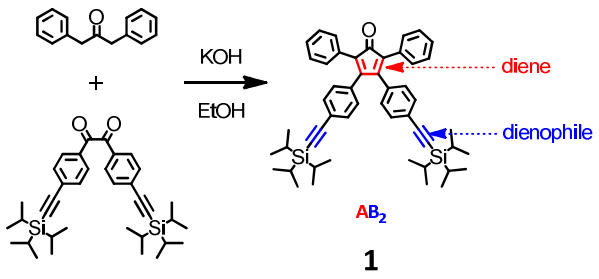

Figure 13: Synthesis and conceptual structure of the AB_2 building block **1**

As indicated in Figure 13, the AB_2 building block **1** can be generated by a *Knoevenagel* condensation of an ethynyl functionalized benzil to diphenylacetone.[11] Accordingly, an AB_4 building block **2** can be generated if an ethynyl functionalized diphenylacetone is used for the condensation instead (Figure 14).

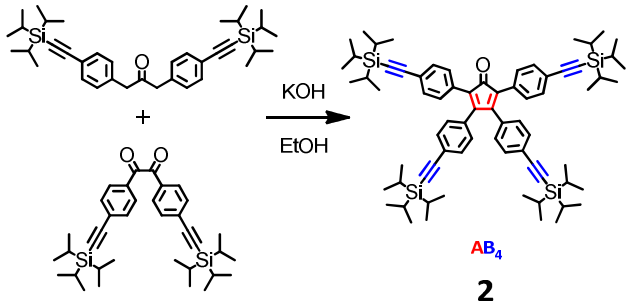

Figure 14: Synthesis of the AB_4 building block **2**

Tetracyclone **2** was the first example of an AB_4 building block in dendrimer chemistry.[59] It can be used to generate much higher degrees of branching in the resulting poly-phenylene structures.[59,60] Ethynyl functionalization of all required starting compounds is commonly achieved by *Sonogashira-Hagihara* coupling[61] of triisopropylsilyl acetylenes to the according aryl halides.

1.2.2 General Properties

The synthesis of PPDs via cycloaddition was initially introduced as an efficient means for rapidly arriving at large, three-dimensional and highly branched precursors for flat, defined and large polyaromatic hydrocarbons (PAHs).[11,62] Large PAHs can be regarded as cut-outs from graphene; a material, whose detailed description has rewarded *A. Geim* and *K. Novoselov* a recent Nobel prize.[63] So far, cyclodehydrogenation of PPD precursors is the only method that allows for the bottom-up synthesis of molecularly defined graphene molecules such as C_{96} (**3**)[64], C_{132} (**4**)[65] or the large hexagonal disk C_{222} (**5**)[64].

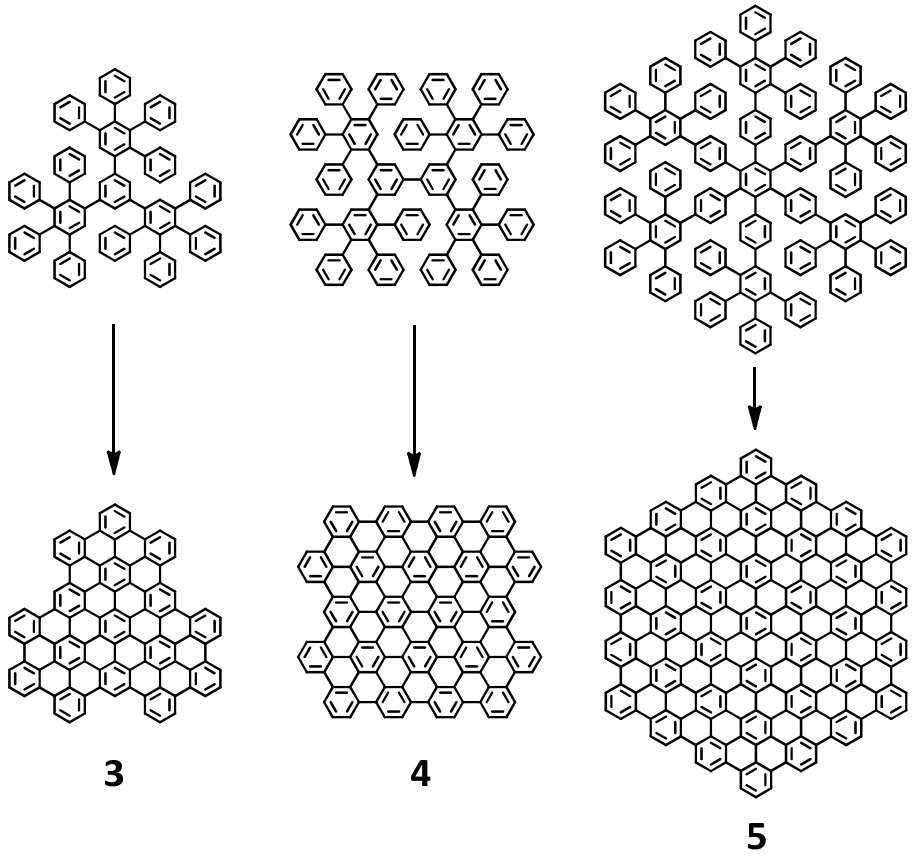

Figure 15: Synthesis of large PAHs from PPD precursors via cyclodehydrogenation

It was also realized very soon after *Müllen*-type PPDs were introduced as graphene precursors, that the unique properties of PPDs render them very exciting new materials in their very own right. Besides their outstanding thermal and chemical stability, PPDs differ from the large majority of other dendrimers in that they exhibit an inherently rigid and shape persistent structure.

As mentioned earlier (see 1.1.1), this rigidity is a result of their main structural motif: branching chains of *para*-connected benzene rings. While sufficiently long chains of poly-

para-phenylenes (and thus PPDs) can be bend to some extent,[66] a relatively short chain of about 3 to 9 benzene rings (such as in a typical PPDs) will not readily fold back onto itself. The persistence length of poly-*para*-phenylenes has been determined by a number of different experiments, which yielded variant values ranging from 13 to 28 nm.[67-70] A mean persistence length of 20 nm corresponds to a chain length of about 46 benzene rings.

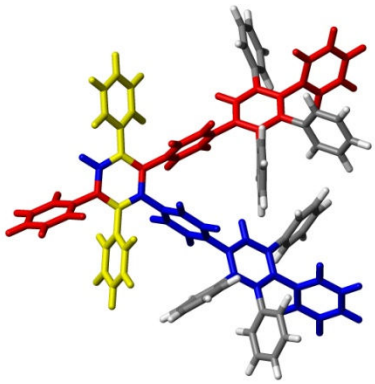

Figure 16: Model of a PP-dendron; different chains of stiff poly-*para*-phenylenes in different colors

Thus, in contrast to other types of dendrimers constituted from flexible building blocks, PPDs cannot collapse into a more compact form. Instead, PPDs possess a relatively rigid scaffold structure and thus a globally defined and persistent shape.

The rigidity and shape persistence has been demonstrated by small angle neutron scattering (SANS) experiments.[16] AFM studies revealed PPDs to be discrete nano-sized objects of certain heights which matched those calculated by molecular modeling.[71] Solid state NMR experiments further proved that molecular dynamics within PPDs are dominated by intramolecular steric constraints as a result of their rigid structure.[72,73]

The inherent stiffness of PPDs leads to four unique and important characteristics:

i) PPDs are bulky and sterically demanding (see 1.2.3.1)
ii) PPDs provide a spatially defined scaffold (see 1.2.3.2)
iii) PPDs possess an overall defined shape (see 1.2.3.3)
iv) PPDs possess inherent hydrophobic voids (see 1.2.3.4)

On the next few pages, it will be shown how the above mentioned unique characteristics of PPDs have been exploited in different ways for a variety of functional materials and applications.[52]

1.2.3 Functional Nano-Materials based on Polyphenylene Dendrimers

1.2.3.1 Bulkiness: Steric Screening and Isolation of Functionality

Many interactions between functional groups or molecules lead to undesirable effects with regard to their respective applications. Such effects include association, aggregation and emission quenching. The bulkiness of rigid PPDs can be utilized to very effectively screen different kinds of functionality from direct interactions by way of steric shielding. An often beneficial side effect of suppressed aggregation is an increased solubility as compared to non-dendronized analogues.

Functional groups or molecules must meet two general prerequisites in order to enable their encapsulation into a bulky PPD scaffold:

1) there must be a synthetic pathway to allow for a decoration of the functionality or its precursors with ethynyl groups,
2) the functionality must withstand the high temperature (at least 145 °C) during PP-dendron build-up via *Diels-Alder* cycloaddition.

While these prerequisites limit the number of potential candidates, the technique of dendronization with PPDs has already been successfully demonstrated with many very different materials.

For example, the aggregation of chromophores in the solid state often leads to red-shifted photoluminescence (PL) spectra or even emission quenching. Encapsulation of chromophores into a rigid and bulky PPD scaffold can be used to suppress chromophore aggregation and thus enhance their PL intensities.

Perylenetetracarboxydiimide (PDI) dyes, which exhibit exceptional chemical, thermal, photochemical and photophysical stabilities along with high extinction coefficients,[74] have been successfully dendronized with rigid polyphenylenes in both their bay[75,76] (**6**) and imide[77] (**7**) positions.

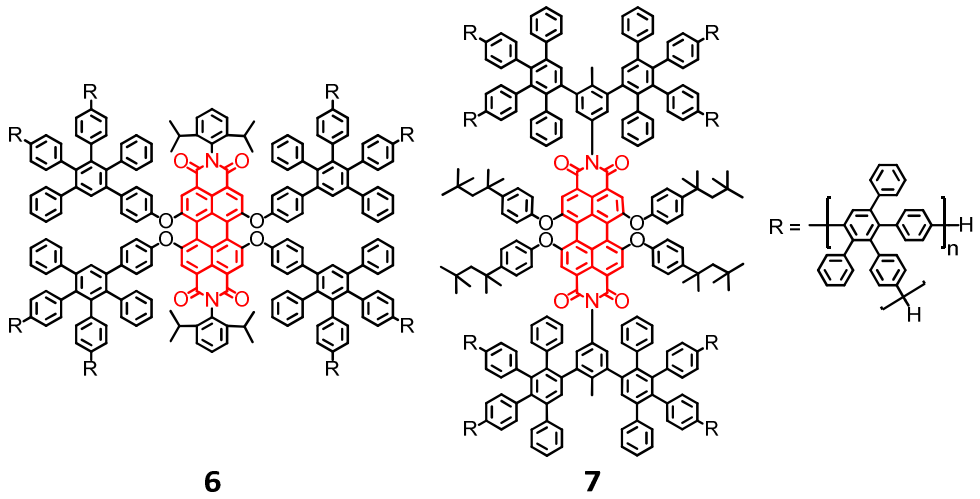

Figure 17: PDI chromophores dendronized with polyphenylenes in the bay (**6**) and the imide (**7**) positions

In contrast to their non-dendronized analogues, both dendronized PDIs exhibit no red shift of their solid state absorption and emission spectra as a result of their effective isolation from neighboring species. However, due to poor charge transport through their isolating PPD scaffold, electroluminescence (EL) efficiencies also decrease with increasing dendrimer generation.[76] EL efficiency can be improved by way of blending with polyfluorenes.[78]

Pyrene, another well studied chromophore, exhibits both long excited state lifetimes[79] and a pronounced solvatochromism[80] of its fluorescence emission. Normally, pyrene tends to form excimers in concentrated solution and in the solid state, resulting in a dramatic decrease in fluorescence intensity and spectral broadening.

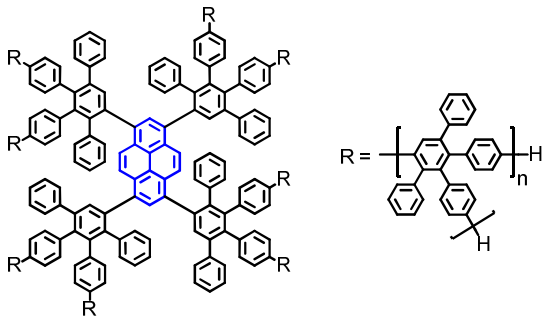

Figure 18: Pyrene dendronized with polyphenylenes

Such excimer formation can be effectively avoided by dendronization with second and higher generation PP-dendrons, as evidenced by fluorescence quenching studies and temperature-dependent fluorescence spectroscopy.[25]

Another example for an application of rigid dendronization is in the field of phosphorescent materials. In organic light emitting diodes (OLEDs), phosphorescent materials offer an advantage over fluorescent ones in that they exhibit both singlet and triplet emission, which increases their theoretical quantum efficiency from about 25% to 100%. However, triplet-triplet annihilation between neighboring chromophores markedly reduces that efficiency. It has been shown that triplet-triplet annihilation between phosphorescent iridium(III) complexes can be suppressed by way of dendronization with rigid polyphenylenes.[24]

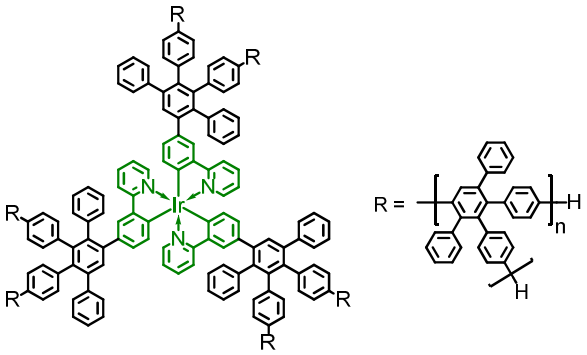

Figure 19: Green phosphorescent, rigidly dendronized iridium complex

In the solid state, photoluminescence quantum yields (PLQYs) of dendronized complexes increase up to four times compared to the non-dendronized species as a result of chromophore separation.[24]

Yet another example of application is provided by rigidly dendronized ligands for catalysts. Transition metal complexes are frequently utilized for the homogeneous catalysis of many useful and important reactions. However, catalyst decomposition via metal aggregation and precipitation often drastically reduces catalytic activity. It has been shown that the aggregation of palladium (Pd) catalysts (formation of Pd black) can be effectively suppressed by utilizing rigid, PP-dendronized pyridine ligands.[29,30]

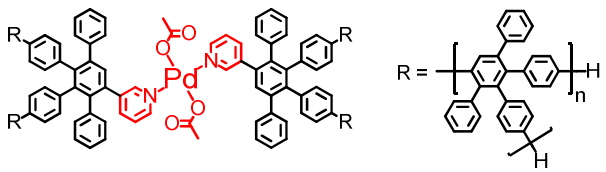

Figure 20: Catalytically active Pd complex bearing rigidly dendronized ligands

Rigid polyphenylene dendrons spatially extend from the Pd center and keep individual catalytic sites isolated from one another, which prevents Pd black formation.[31] At the

same time, rigid dendronization at the 3-position of pyridine does not affect the coordination sphere around the Pd center and thus does not sterically obstruct catalytic activity, as is the case when dendronized in the 2-position.[31] Palladium complexes were used as catalysts for the aerobic oxidation of alcohols. Rigidly dendronized Pd complexes did not precipitate and maintained their high catalytic activity under conditions where non-dendronized Pd complexes were rapidly deactivated by precipitation.[29]

Apart from the examples mentioned so far, many more functionalities have been dendronized with rigid PPDs. Besides their general function-isolating effect, PP-dendrons often affect reactivity and/or selectivity due to steric crowding. Cyclopentadienyl complexes of cobalt bearing different PP-dendronized cyclobutadiene ligands have been synthesized.[22]

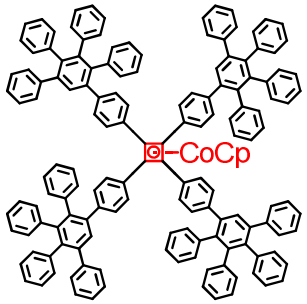

Figure 21: Rigidly dendronized sandwich complex of cobalt

As a result of rigid dendronization, oxidation of the electroactive cobalt complexes to their 17-electron cationic species is impaired, which is reflected in an increase of their oxidation potentials.[22]

A single benzophenone moiety has been dendronized with rigid PP-dendrons.[27]

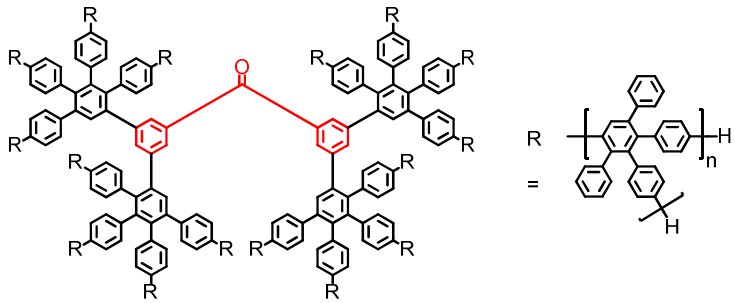

Figure 22: Benzophenone dendronized with polyphenylenes

Post-functionalization of the benzophenone core using aryl- and alkyllithium or *Grignard* reagents yielded the corresponding alcohols. However, if lithium reagents were too large

(e.g. biphenyl-lithium), steric shielding frustrated the reaction and only starting material was recovered. Reduction of PP-dendronized benzophenone on a potassium mirror under high vacuum produced radical anionic species. While first generation dendronized radical anions formed potassium-bridged dimers, second generation dendronized radical anions remained isolated.[27]

Dendronization of metallophthalocyanines with PPDs prevents their aggregation even in polar solvents such as ethanol, as evidenced by their UV-Vis spectra.[81]

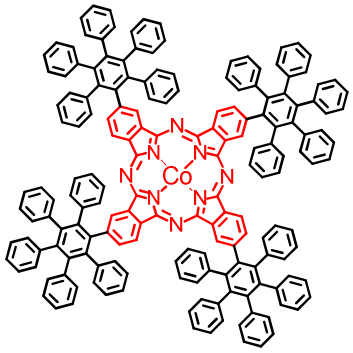

Figure 23: Dendronized phthalocyanine complex of cobalt

Furthermore, steric congestion of bulky groups in the phthalocyanine periphery affects the selectivity towards axial coordination of the cobalt center, as was demonstrated with a series of differently shaped pyridines.[81]

1.2.3.2 Site Specificity: Spatially Defined Placement of Function

The multivalency of dendritic systems allows for the incorporation of large numbers of functional groups into single molecules (see 1.1.2.2). Furthermore, different kinds of functionality can be combined to achieve advantageous synergistic effects. However, only with a rigid scaffold structure can functions also be placed in spatially defined positions relative to each other. In this regard, PPDs offer a great advantage over more flexible types of dendrimers.

For instance, the density of chromophores in a rigid dendrimer can be increased without running the risk of increased intramolecular aggregation, because each chromophore position is spatially fixed. A very striking example is the synthesis of blue-light-emitting dendrimers in which many triphenylene chromophores were incorporated by way of a minor change of the usual PPD structure: an extra C-C bond between two neighboring phenyl rings in each branching unit structurally transforms a non-functionalized PPD

into a triphenylene-rich multichromophore (the actual synthesis,[82,83] however, requires a suitably functionalized phencyclone AB_2 building block).

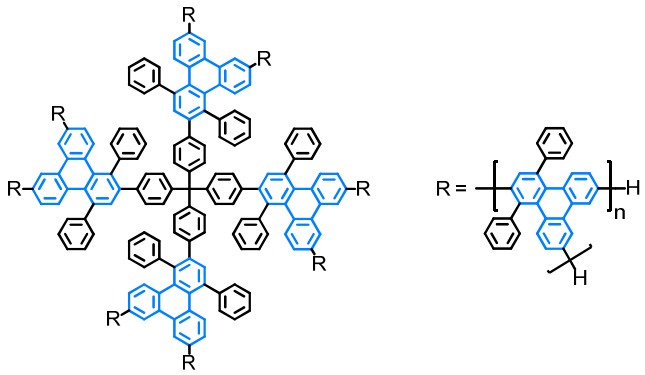

Figure 24: Blue emitting polytriphenylene dendrimer

Polytriphenylene dendrimers incorporating up to 28 triphenylene units have been synthesized.[82,83] Each triphenylene is electronically decoupled from neighboring triphenylenes due to their twisted alignment. Thus, inter- and intramolecular fluorescence quenching are effectively avoided. In fluorescence based blue-emitting LEDs, these dendrimers exhibit very reasonable device efficiencies and brightnesses as compared to small molecular or linear polymeric triphenylene derivatives.[82,83]

The performance could even be further enhanced by site specific optimization of the molecular structure.[84] The tetraphenylmethane core was replaced by pyrene, which enables resonant transfer of excitation energy from triphenylene to pyrene and thus boosts the quantum yield 4-fold. Triphenylamine groups were attached to the surface, which facilitate hole capturing and injection in LED devices.

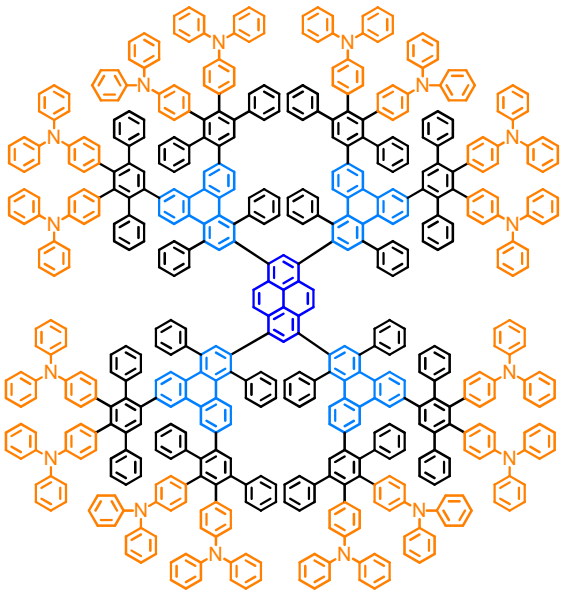

Figure 25: Multifunctional, blue emitting dendrimer

Saturated blue-emitting devices based on the so optimized dendrimer possess the highest brightness (1440 cd/m^2) and best stability values reported so far for fluorescence-based blue-emitting dendrimers.[84]

The concept of directed energy transfer between specifically placed chromophores in rigid PPD scaffolds has also been demonstrated with a number of diads and even triads.[74] A dendritic triad based on the chromophores naphthalenedicarboximide (NMI), perylene-dicarboximide (PMI) and terrylenetetracarboxdiimide (TDI) shows a stepwise vectorial energy transfer from NMI in the periphery over PMI towards TDI in the center.[46,48]

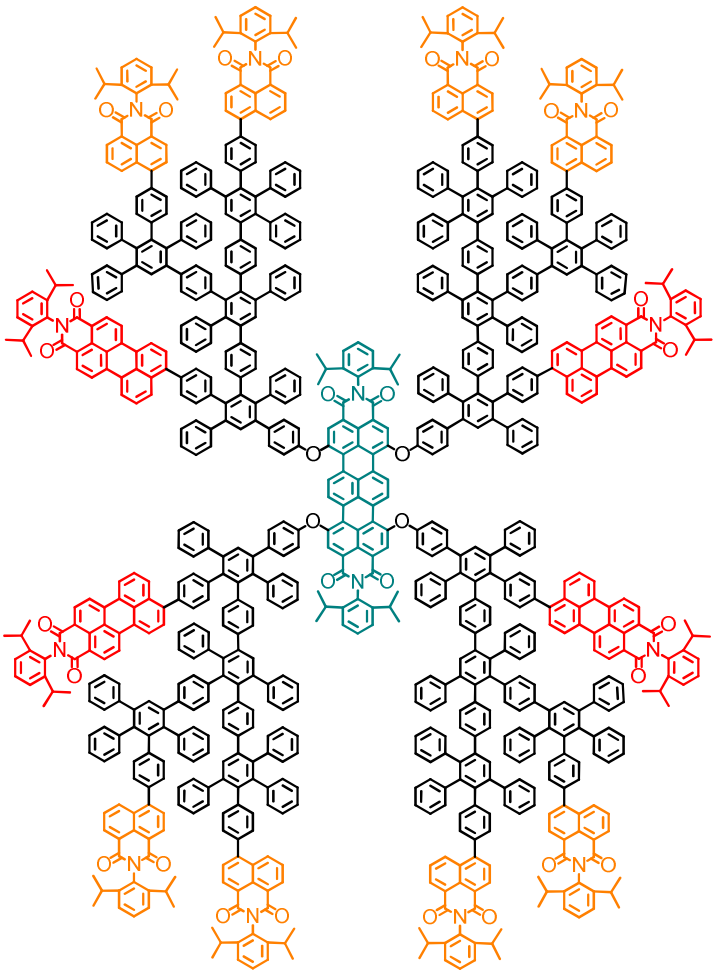

Figure 26: Light harvesting triad of three different chromophores

The site specific placement of these chromophores thus yields an efficient light harvesting system, which absorbs over the whole range of the visible spectrum.

1.2.3.3 Defined and Rigid Overall Shape: Precursors, Supramolecular Structures and Templates

Due to the inherent stiffness of the polyphenylene scaffold, PPDs adopt a defined overall shape. The appearance of this shape crucially depends on the geometry of the core which determines the spatial orientation of each major poly-*para*-phenylene branch in the final dendrimer.[85] These properties make PPDs very interesting for the use as precursors of defined, carbon-rich nanomaterials, for the formation of novel supramolecular nanostructures and as templates for different, nanostructured materials.

The use of PPDs as precursors for defined polycyclic aromatic hydrocarbons (PAHs) has already been mentioned (see **1.2.2**), because it was this particular application as PAH precursors that inspired the beginning of all (*Müllen*-type) PPD chemistry.[11] Indeed, cyclodehydrogenation of PPD precursors is one of the most elegant and powerful methods for the bottom-up synthesis of defined nanographenes.[64,11,65] Graphene nanostructures are of tremendous interest in many areas of research (e.g. organic electronics and optoelectronics).[86-91]

The extensive planarity of large aromatic PAHs leads to strong intermolecular π-π-stacking. The stacking markedly decreases the solubility of PAHs and thus makes both purification and characterization very difficult. However, by utilizing suitable PPD precursors, alkyl chains can be introduced into PAHs in defined positions to increase their solubility (Figure 27).

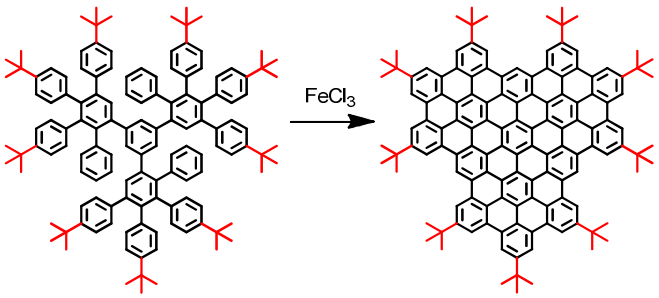

Figure 27: Synthesis of the *tert*-butyl functionalized PAH from a PPD precursor

Furthermore, the microphase separation between alkyl chains and the PAH cores favors the formation of columnar structures in discotic liquid crystals via π-π stacking. Varying the alkyl substitution in PPD precursors allows for a control over the self assembly behavior of PAHs in discotic mesophases.[92-95]

While complete cyclodehydrogenation of suitable PPD precursors leads to planar PAH discs, a partial or "incomplete" cyclodehydrogenation can be utilized for the formation of individual, planar and blade-shaped discs that are linked through a non-planar core.[96] Such molecules resemble the shape of propellers.

Another very exciting potential application is the use of PPDs as precursors for "cubic graphite". This hypothetical allotrope of the element carbon was first proposed in 1946.[97] Just like graphite (and graphene), its supposed structure can be constructed entirely from benzene rings, where each ring is connected to six other rings. In contrast to graphite,

however, bonds are not formed between benzene rings in a plane. Instead, the rings are connected in such a manner that a regular, three dimensional network with cubic symmetry is formed (Figure 28). In such network, the planes of the benzene rings are twisted relative to each other.

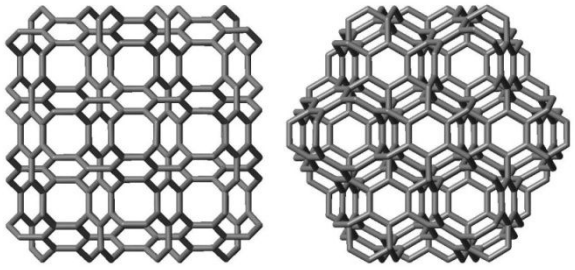

Figure 28: A subunit of the cubic graphite structure, projected along different directions

The structures of cubic graphite and of PPDs are closely related. In fact, cubic graphite can be considered the ultimate PPD structure at maximum degree of branching and maximum connectivity between benzene rings. PPDs might thus serve as suitable precursors for cubic graphite or subunits thereof.[98-101] Some efforts were made to synthesize "phenylogues" of cubic graphite structural motives. Hexaphenylbenzene units were linked to cycles that resemble the connection pattern of benzene rings in cubic graphite.[98] Another attempt was aimed at creating an actual subunit of cubic graphite from an extremely crowded PPD precursor.[100] So far, however, the oxidative bond formation towards the desired final cubic graphite structure remains a synthetic challenge.

The defined shape of rigid PPDs has also been exploited in their self-assembly to supramolecular stuctures. It has been demonstrated that PPDs self-assemble into micrometer long nanofibers when their solutions are drop-casted onto highly oriented pyrolytic graphite (HOPG)[102,103] or onto silicon substrates.[104] Since shape-persistent PPDs do not collapse, only a relatively small portion of phenyl rings is in contact with the substrate. The majority of phenyl rings is still available for π-π and van-der-Waals interactions between individual dendrimers. These dendrimer-dendrimer interactions lead to a directional growth of dendrimer aggregates into nanofibers. Fluorescent nanofibers can be produced via self-assembly of PPDs functionalized with a PDI chromophore either in the core or on the surface.[105] Some PPDs also self-assemble into rods instead of fibers. Nanorod formation on a HOPG surface was observed for a PPD functionalized with 16 C_{12} alkyl chains in its periphery.[106-108] Experiments with dendrimers of different alkyl

chain lengths indicated no change in the size of self-assembled nanorods. The alkyl chains are thus assumed to be oriented parallel to the direction of the nanorods.

The overall defined shape of PPDs has been utilized for templating mesoporous metallic oxide films. A suitable template was constructed from a second generation PPD bearing twelve 2-bromo-2-methylpropionic esters.[109-111] This compound was used as a macroinitiator to prepare a dendritic amphiphilic core–double-shell macromolecule via successive atom transfer radical polymerization (ATRP) with styrene and further extension with *tert*-butyl acrylate.[110,111]

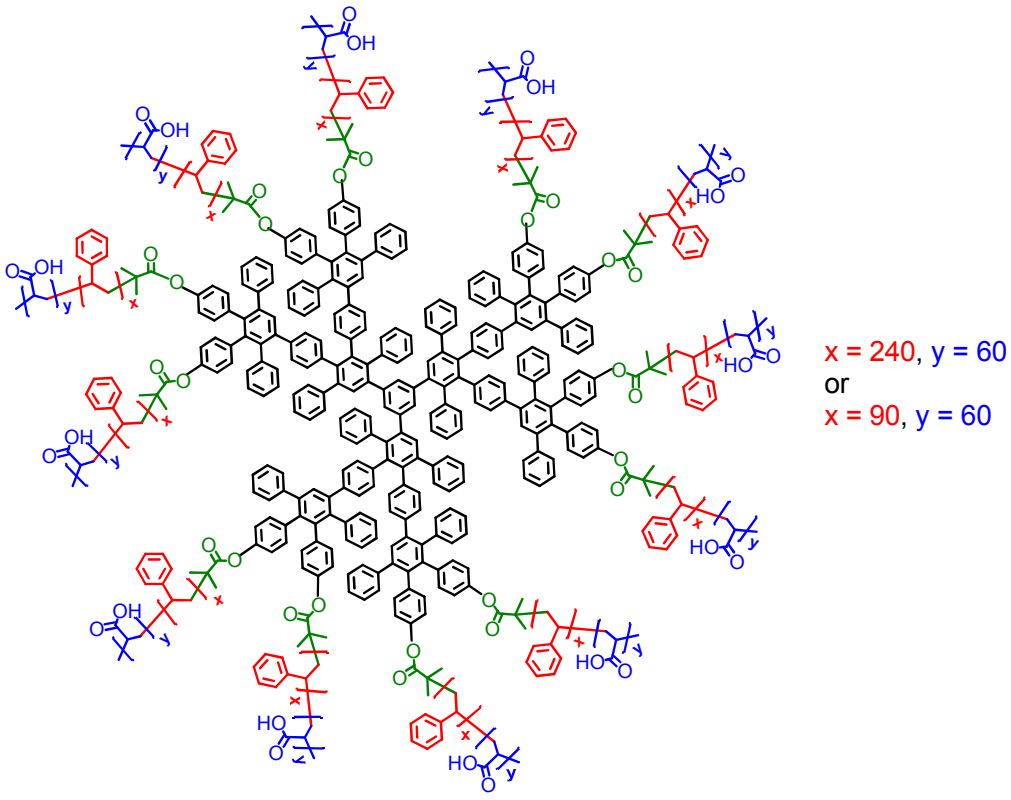

Figure 29: Structure of dendritic and amphiphilic core–double-shell macromolecules used as template for preparing mesoporous TiO_2 films

The resulting amphiphilic macromolecules consist of a central rigid PPD core and a flexible amphiphilic double-polymer shell consisting of twelve arms. The rigidity of the second-generation PPD core ensures the conformational stability of the template structure. In the flexible amphiphilic polymer shell, a polystyrene (PS) block serves as a hydrophobic segment, while poly(acrylic acid) (PA) forms a hydrophilic surface layer. The hydrophilic outer shell is used for the incorporation of metal alkoxides. Subsequent hydrolysis and condensation of the precursor and calcination of the organic template (dendrimer scaffold)

leaves hollow spheres or (after collapse) ring-shaped metal oxide structures. The amphiphilic template has been effectively used for the preparation of mesoporous TiO_2 films using titanium tetraisopropoxide (TTIP) as precursor.[110,111] The pore size could be controlled by modifying the length of the inner hydrophobic PS block of the core–double-shell macromolecule.

1.2.3.4 Hydrophobic Voids: Host-Guest Chemistry and Sensing Applications

An important consequence of the rigidity and shape persistence of branched PPD scaffolds is the inevitable occurrence of permanent intramolecular free volumes or voids. The existence of voids in PPDs has been confirmed by positron lifetime spectroscopy.[112] Crystal structures of different PPDs have revealed that solvent molecules are readily trapped within both intra- and intermolecular PPD cavities.[113,114] The existence of persisting hydrophobic voids are important to qualify PPDs as versatile host materials.[35,115,116]

Introduction of functionality within dendritic voids can be used to enhance the ability of dendrimers to take up guests. For example, internal pyridine moieties were found to enhance the uptake of specific guests.[117] A fourth generation PPD bearing 56 pyridyl functions within its interior (see Figure 30) shows surprisingly high affinity towards the explosive triacetone triperoxide (TATP).[118] TATP is a peroxidic compound with an explosive strength comparable to trinitrotoluene (TNT). However, it is extremely sensitive towards shock, heat, friction and electrical discharge. In terms of illegal uses, these drawbacks are compensated by the facile, large-scale preparation of TATP from common household chemicals. A continuous TATP surveillance at important public places is therefore highly desired.

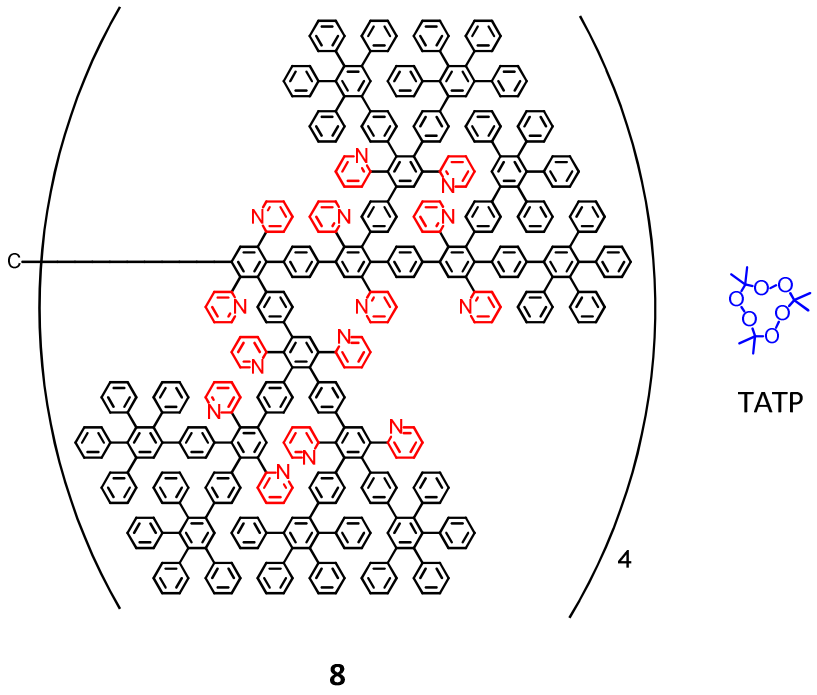

8

Figure 30: Fourth generation PPD with internal pyridine moieties; structure of the explosive TATP

The high affinity of PPD **8** to TATP could be utilized to build a highly sensitive TATP detector. In the presence of a layer of pyridine functionalized dendrimer **8** coated on a quartz crystal microbalance (QCM) detector, TATP can be detected with a sensitivity as low as 0.1 ppm.[37]

A number of other PPDs have been employed for the preparation of selective gravimetric sensors.[119] On QCM detectors, PPDs carrying electron withdrawing (CN or COOH) or electron donating ($N{=}CPh_2$) substituents in the periphery exhibit very selective response to polar volatile aromatic compounds. Carboxylic acid functionalized dendrimers possess a striking affinity towards guest molecules carrying amine substituents (e.g. NMP, diethylamine). Many different parameters such as electron densities of the host and the guests, as well as the dendrimer generation play an important role for the selectivity of such systems. Overall, the sensor responses are totally reversible and reproducible. Furthermore, a full measurement cycle including adsorption and desorption time takes only 4 minutes.

1.3 Ions, Salts and Electrolytes

A major objective of this thesis is the investigation of property changes in salts where the chemical structure and overall size of constituting ions has largely been modified. To facilitate the discussion in later chapters, the next pages shall provide an overview on the properties of ions, salts and electrolytes in general as well as introduce the concept of weakly coordinating anions in particular.

1.3.1 Definition

Ions are electrically charged atoms or molecules. Their net charge equals the difference between the total number of their electrons and their protons. If the number of negatively charged electrons exceeds the number of positively charged protons, the atom or molecule becomes negatively charged and is called an "anion". The opposite is true for a positively charged ion, which is called a "cation". A chemical compound solely composed of cations and anions is called a "salt".

Ions are ubiquitous in nature. They play key roles in the basic functioning of life. Even feelings and thoughts, the processing of the brain, are ultimately based on electrostatic potentials generated by concentration gradients of ions along nerve cell membranes. In terms of technical applications, the use of ions as electrolytes in batteries, fuel cells and accumulators is of central importance for a functioning of the modern world. Also, many catalytic processes and chemical transformations are based on the interaction of compounds with reactive ionic species.

1.3.2 Physical Properties

1.3.2.1 Coulomb Attraction

Oppositely charged ions attract each other via electrostatic interaction. The magnitude of electrostatic force between two point charges (e.g. two ions with charges q_a and q_b) is directly proportional to the product of their charges q, and inversely proportional to the squared distance r_ab between them. This inverse-square relation was first published in 1785[120] by *C. A. de Coulomb*:

$$F_\mathrm{c} = \frac{1}{4\pi\varepsilon_0}\frac{q_\mathrm{a}q_\mathrm{b}}{r_\mathrm{ab}^2} \tag{1}$$

where

F_c	*Coulomb* force
ε_0	permittivity of the vacuum

A negative value of F_c implies an attractive force, whereas a positive value (multiplication of charges of the same sign) implies a repulsive force. The electrostatic potential energy U_E describes the work that must be done in order to bring two point charges from "infinite" separation into a configuration where their distance is r_{ab}. For an ion pair with the charges $q_a = z^+e$ and $q_b = z^-e$, the electrostatic potential energy is thus given by:

$$U_E = \frac{1}{4\pi\varepsilon_0}\frac{z^+z^-e^2}{r_{ab}} \tag{2}$$

where

z^+, z^-	electrical valences of ions
e	elementary charge ($1.6022 \cdot 10^{-19}$ C)

Again, a negative value for the mutual potential energy U_E corresponds to an attraction between the charges and vice versa.

1.3.2.2 Lattice Energy

In an ionic compound, attractive *Coulomb* interactions between ions of opposite charge may lead to their regular packing into a crystal lattice. The driving force for crystal formation is their gain in lattice energy. A theoretical derivation for the lattice energy U_{lat} of ionic compounds was provided by *M. Born* and *A. Landé* in 1918.[121-123] Their model describes ions as elastic spheres which are compressed together by electrostatic attraction and balanced by short range repulsion from their electron shells. The according *Born-Landé* equation (equation (3)) is thus comprised of an attractive term for the electrostatic potential energy U_E (see equation (2)), and a term for a repulsive potential energy:

$$U_{lat} = -M\frac{z^+z^-e^2N_A}{4\pi\varepsilon_0 r_0}\left(1-\frac{1}{n}\right) \tag{3}$$

where

M	*Madelung* constant (depends on crystal geometry)
N_A	*Avogadro* constant ($6.0221 \cdot 10^{23}$ mol^{-1})
r_0	closest distance between ions of opposite charge, which corresponds to the sum of their radii ($r^+ + r^-$)
n	*Born* exponent (a measure of the compressibility of the solid)

However, the *Born-Landé* equation can only be applied if the exact crystal structure, the *Madelung* constant M and other parameters of the salt in question are already well known. In order to also enable an estimation of lattice energy when less information about a salt is available, *A. F. Kapustinskii* derived an equation which is solely based on "thermochemical" radii of ions.[124]

$$U_{\text{lat}} = -A\frac{\nu\,|z^+z^-|}{r^+ + r^-}\left(1 - \frac{d}{r^+ + r^-}\right) \tag{4}$$

where

A	numerical factor ($1.2025 \cdot 10^{-4}$ J·m·mol^{-1})
ν	numbers of ions per formula unit
r^+, r^-	ionic radii
d	empirical parameter ($3.45 \cdot 10^{-11}$ m)

The thermochemical radii r^+ and r^- can themselves be correlated with the molecular volume V_{m} of a salt (volume of one formula unit), as was demonstrated by *J. Passmore* and *H. D. B. Jenkins*.[125] Their equation allows a facile and relatively accurate estimation of lattice energy:

$$U_{\text{lat}} = \nu\,|z^+z^-|\left(\frac{\alpha}{\sqrt[3]{V_{\text{m}}}} + \beta\right)\ \text{kJ·mol}^{-1} \tag{5}$$

where

V_{m}	molecular volume of one formula unit in the crystal (in nm^3)
α	empirical parameter (117.3 kJ·mol^{-1} for 1:1 salts)
β	empirical parameter (51.9 kJ·mol^{-1} for 1:1 salts)

All equations (3), (4) and (5) reflect the reasonable expectation that the lattice energy of a crystal decreases with increasing ion size $r^+$and/or r^- (and thus with molecular volume V_m).

1.3.2.3 Solubility

The amount of lattice energy of a salt affects its solubility in different media. A salt can only be dissolved in a solvent if the solvation free energy ΔG^0_{solv} exceeds the lattice free energy ΔG^0_{lat} of the crystal (Since entropic contributions in a solid can be neglected, lattice free energy and lattice energy are practically identical[126]).

According to the *Born-Haber* cycle (see Figure 31), the free energy of dissolution ΔG_s^0 can be expressed as the sum of the (negative) lattice free energy ΔG_{lat}^0 and the solvation free energy ΔG_{solv}^0:[127]

$$\Delta G_{\text{s}}^0 = -\Delta G_{\text{lat}}^0 + \Delta G_{\text{solv}}^0 \tag{6}$$

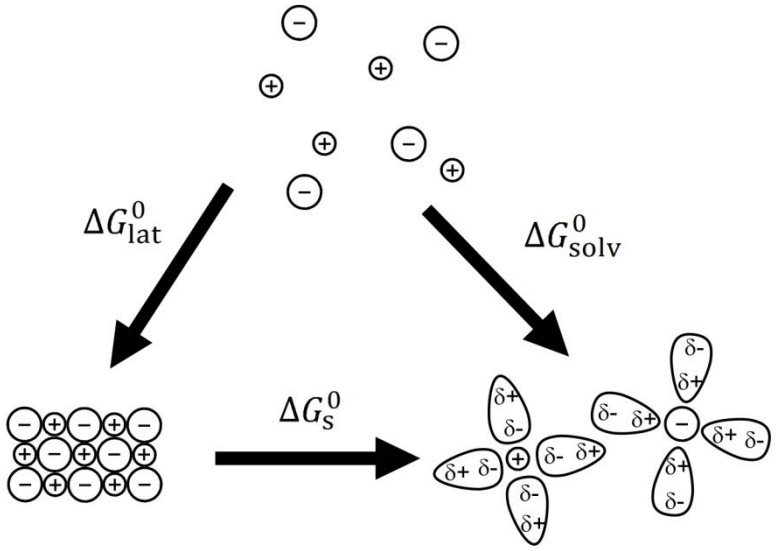

Figure 31: Derivation of the free energy ΔG_s^0 of salt dissolution via the *Born-Haber* cycle

The free energy of dissolution ΔG_{s}^0 is itself linked to the solubility product K_{sp} of a salt:

$$\Delta G_{\text{s}}^0 = -RT \ln K_{\text{sp}} \tag{7}$$

where

R ideal gas constant ($k_{\text{B}} N_{\text{A}} = 8.314472\ \text{J·mol}^{-1}\text{·K}^{-1}$)

In the case of a simple 1:1 salt A^+B^-, the solubility s is simply the square root of its solubility product:

$$K_{\text{sp}} = [\text{A}^+][\text{B}^-] = s^2 \tag{8}$$

where

[X] concentration of species X in mol·L^{-1}

It follows that the solubility s of a salt is largely affected by two parameters, lattice energy ΔG_{lat}^0 and solvation energy ΔG_{solv}^0. Lattice energy is itself mainly affected by ion size (see 1.3.2.2), whereas solvation energy is affected by the ability of a solvent to coordinate to ions and to screen their charges. Different physical properties of a solvent can serve as a

measure for its ability to solvate ions, including its dipole moment and the presence of electron donating or accepting groups. One of the most commonly used parameters, however, is the solvents relative permittivity ε_r.

An expression which relates the relative permittivity ε_r of a solvent to the solvation energy $\Delta G^0_{solv,i}$ of an ion of charge $q_i = z_i e$ and radius r_i was proposed by *M. Born* in 1920:[127]

$$\Delta G^0_{solv,\,i} = -\frac{1}{2} \cdot \frac{N_A z_i^2 e^2}{4\pi\varepsilon_0 r_i}\left(1 - \frac{1}{\varepsilon_r}\right) \tag{9}$$

Although this expression has been further refined with additional parameters to better fit experimental data (most importantly the "mean spherical approximation" or MSA[127]), the original expression can still be used for a reasonable approximation of solvation energy[126] and provides a good qualitative description of dissolution phenomena.

In Figure 32, the solvation energy ΔG^0_{solv} of an ion of radius r = 0.1 nm is plotted as a function of relative permittivity ε_r of the solvent using the *Born* equation (9).

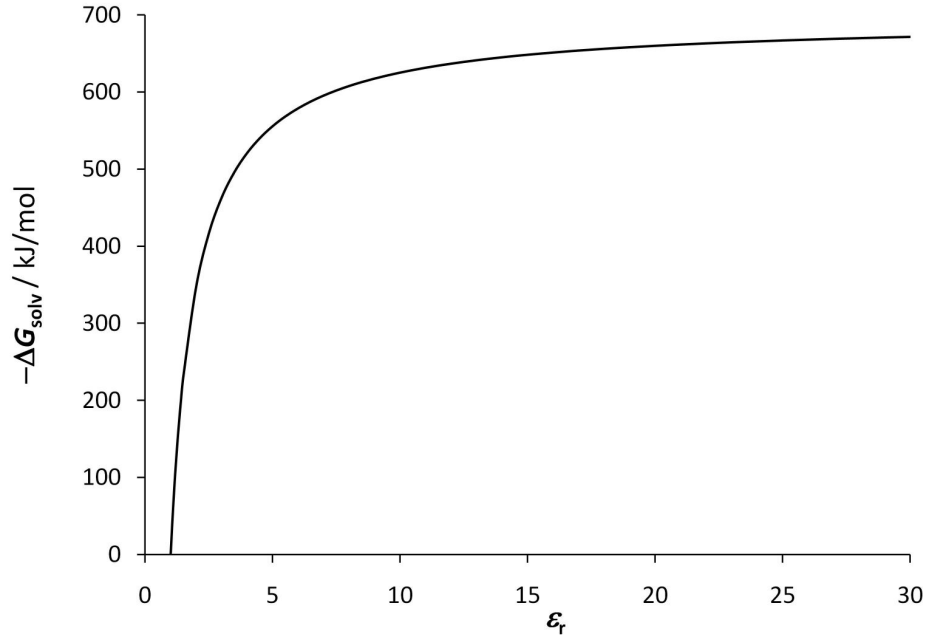

Figure 32: Plot of the solvation energy ΔG^0_{solv} of an ion (r = 0.1 nm) as a function of relative permittivity ε_r of the solvent

Figure 32 illustrates that the solvation energy ΔG^0_{solv} of ions rapidly decreases in media of low permittivity ε_r and, naturally, becomes 0 in vacuum (at $\varepsilon_r = 1$). As a consequence, many salts composed of relatively small ions do not gain sufficient solvation energy in low

permittivity media to overcome their lattice energy and become dissolved. They are insoluble in media such as methylene chloride ($\varepsilon_r = 8.9$), tetrahydrofuran ($\varepsilon_r = 7.6$) or chloroform ($\varepsilon_r = 4.8$). Only salts composed of relatively large ions exhibit low enough lattice energies so that their also low solvation energies are still sufficient to drive the dissolution of the salt (see also paragraph 6.4).

1.3.2.4 Conductivity and Ion Association

The conductivity σ of an electrolyte solution is determined by *i*) the number of available charge carriers n_i, *ii*) their electrical charges q_i and *iii*) their mobility μ_i.

$$\sigma = n^+ q^+ \mu^+ + n^- q^- \mu^- \tag{10}$$

In an idealized situation where electrostatic interactions to all other ions are neglected, the electrical mobility μ_i of an ion of charge $q_i = z_i e$ can be expressed as:

$$\mu_i = \frac{z_i e}{6\pi\eta r_i} \tag{11}$$

where

η	viscositiy of the solvent
r_i	ionic radius

The absolute number n_i of charge carriers i in a certain volume is given by the molar concentration c of the electrolyte, multiplied by the number ν_i of ions of type i per formula unit and by the *Avogadro* constant N_A ($n_i = c\nu_i N_A$). Together with $q_i = z_i e$, equation (10) can thus be expressed as:

$$\sigma = c\nu^+ N_A z^+ e\mu^+ + c\nu^- N_A z^- e\mu^- \tag{12}$$

and then simplified to:

$$\sigma = cF(\nu^+ z^+ \mu^+ + \nu^- z^- \mu^-) \tag{13}$$

with

F	*Faraday* constant ($N_A e$ = 96485.3399 C·mol^{-1})

In high-permittivity solvents (ε_r > 40) and at low concentration, strong electrolytes dissolve and dissociate completely into "free" solvated ions.[127] If such "free" ions behaved ideally (movement independent from other ions, such as assumed in equation (11)), then the conductivity σ of the electrolyte solution would be directly proportional to its concentration c (see equation (13)), and the ratio $\Lambda = \frac{\sigma}{c}$ (called molar conductivity) would be an electrolyte specific constant. However, *F. W. G. Kohlrausch* found empirically that the

molar conductivity Λ is not a constant but decreases linearly with the square root of concentration c even in very dilute solutions of strong electrolytes.

$$\Lambda = \Lambda_0 - S\sqrt{c} \tag{14}$$

where

Λ_0	molar conductivity at infinite dilution ($c \to 0$)
S	*Onsager* slope

If an association of ions (and thus an effective decrease in the number n_i of available charge carriers; see equation (10)) were responsible for the decrease in molar conductivity Λ, then a strong dependence of the slope S on the chemical nature and size of the ions would be expected. However, the declination of S is almost independent of chemical structure, while it depends crucially on the electrical valences z_i (e.g. +1 or +2) of the ions involved.[128] Thus, it is not ion association but long-range electrostatic interactions (deceleration of ions i by their counter-ion cloud and thus decrease of their mobility μ_i) that lead to the observed linear decrease of Λ with $\sqrt{c}$. An agreement of Λ with *Kohlrausch´*s square root law (equation (14)) can thus be used to confirm complete ion dissociation in an electrolyte.[127]

In a low permittivity solvent, the electrostatic attraction between two oppositely charged ions is stronger (if a fixed distance r_ab is considered) or has a longer range (if a fixed force F_c is considered) as compared to high permittivity solvents (see *Coulomb´*s law, equation (1), and write F_c or r_ab as a function of $\varepsilon = \varepsilon_0\varepsilon_\mathrm{r}$). Consequently, it is more likely that oppositely charged ions A^+ and B^- form ion pairs $\mathsf{A}^+\mathsf{B}^-$ which are stable enough to persist against the energy of thermal agitation. The probability of ion-pair formation is also increased by higher electrolyte concentrations c due to the consequential increase in probability of ions randomly approaching each other closely. Ion pair formation leads to deviations from the above mentioned linear Λ vs. $\sqrt{c}$ dependence: The effective charge of an $\mathsf{A}^+\mathsf{B}^-$ ion pair is zero. Thus, paired ions do not contribute to the overall conductivity. This situation corresponds to an effective decrease in the number of available charge carriers n_i in equation (10).

Ion pair formation can be expressed in the terms of the law of mass action:

$$\mathsf{A}^+ + \mathsf{B}^- \rightleftharpoons \mathsf{A}^+\mathsf{B}^- \tag{15}$$

$$K_a = \frac{1}{K_d} = \frac{[A^+B^-]}{[A^+][B^-]} \tag{16}$$

where K_a is the association constant, and its inverse the according dissociation constant K_d. The ratio of completely dissociated ions to the total concentration of electrolyte is called the degree of dissociation α:

$$\alpha = \frac{[A^+]}{c} = \frac{[B^-]}{c}; \quad [A^+] = [B^-] = \alpha c \tag{17}$$

where

c total concentration of A^+B^- ($c = [A^+] + [A^+B^-]$)

Using the definition of α (equation (17)), the dissociation constant K_d (equation (16)) can be expressed as:

$$K_d = \frac{[A^+][B^-]}{[A^+B^-]} = \frac{\alpha^2 c^2}{c(1-\alpha)} = \frac{\alpha^2 c}{(1-\alpha)} \tag{17}$$

This definition will be used later on for the determination of both the degrees of dissociation α and the dissociation constants K_d of different electrolytes in different media via conductivity measurements (see paragraph 6.5.2).

N. J. Bjerrum was the first to introduce the concept of ion association, and he also provided useful definitions to study it theoretically.[128] He defined a critical distance l (*Bjerrum* length) between two oppositely charged ions, below which the work necessary to separate them exceeds their mean kinetic energy by four times per degree of freedom $\left(4\frac{k_B T}{2}\right)$.[129] At the exact *Bjerrum* distance $r_{ab} = l$, electrostatic attraction and thermal agitation are just balanced:

$$\frac{|z^+z^-|e^2}{4\pi\varepsilon_0\varepsilon_r l} = 2k_B T \tag{18}$$

which provides the *Bjerrum* length l as:

$$l = \frac{|z^+z^-|e^2}{8\pi\varepsilon_0\varepsilon_r k_B T} \tag{19}$$

Ions that are closer to one another than the *Bjerrum* length ($r_{ab} < l$; thermal energy too weak to separate the ion pair) are considered associated. Accordingly, ions that are further separated than the *Bjerrum* length ($r_{ab} > l$; electrostatic energy too weak to keep ions bound together) are considered dissociated. As *N. J. Bjerrum* pointed out,[129] this distinc-

tion is merely a mathematical device which enables an approximate theoretical description under conditions where complete electrolyte dissociation is not satisfied.[128]

N. J. Bjerrum used the above definition of l to derive a theoretical expression for the association constant K_a:

$$K_a = \frac{4\pi N_A}{1000} \int_{r_0}^{l} r^2 \exp\left(\frac{2l}{r}\right) dr \tag{20}$$

where

r_0 closest distance between ions $(r^+ + r^-)$

An empirical access to electrolyte properties such as their association constant K_a in different media is instead provided by conductivity measurements. The conductivity of an electrolyte solution has been expressed earlier in terms of concentration c, charge numbers z_i and mobilities μ_i (see equation (13)). In weak electrolytes, the major deviation from the so described conductivity comes from non-dissociated ions, which cause a decrease in the number of available charge carriers. This partial association of ions can be accounted for by introducing the degree of dissociation α into equation (13):

$$\sigma = \alpha c F(\nu^+ z^+ \mu^+ + \nu^- z^- \mu^-) \tag{21}$$

and accordingly

$$\Lambda = \frac{\sigma}{c} = \alpha F(\nu^+ z^+ \mu^+ + \nu^- z^- \mu^-) \tag{22}$$

Of course, this description of molar conductivity Λ is still idealized because it does not take into account long-range electrostatic effects on ion mobility μ_i. For weak electrolytes and dilute solutions, however, the above description is still reasonable because *i*) the effect of ion association on conductivity decrease is far greater than the effect resulting from mobility decrease, and *ii*) since ion pairs are effectively "neutral", they cannot contribute to exerting electrostatic effects on the mobility of other ions.

At infinite dilution ($c \to 0$), all ions should be completely dissociated ($\alpha = 1$) even in very weak electrolytes. The according limit of molar conductivity Λ_0 is thus given by:

$$\Lambda_0 = F(\nu^+ z^+ \mu^+ + \nu^- z^- \mu^-) \tag{23}$$

and the ratio Λ/Λ_0 can serve as a good approximation for the degree of dissociation α at non infinitely diluted concentrations:

$$\frac{\Lambda}{\Lambda_0} = \alpha \tag{24}$$

F. W. Ostwald used the above definition of the degree of dissociation α and applied it to the before derived description of the dissociation constant K_d in equation (17), which yields the *Ostwald* law of dilution:

$$K_\mathrm{d} = \frac{\alpha^2 c}{(1-\alpha)} = \frac{\Lambda^2 c}{\Lambda_0(\Lambda_0 - \Lambda)} \tag{25}$$

Rearrangement of equation (25) and considering $\sigma = \Lambda c$ gives:

$$\frac{1}{\Lambda} = \frac{1}{K_\mathrm{d}\Lambda_0^2}\sigma + \frac{1}{\Lambda_0} \tag{26}$$

Now, the inverse molar conductivity $1/\Lambda$ is expressed as a linear function of the conductivity σ, both of which can be determined by conductivity measurement. A plot of $1/\Lambda$ vs. σ thus provides the limiting molar conductivity Λ_0 from the line´s $1/\Lambda$ axis intercept, and the dissociation constant K_d from the linear slope $1/K_\mathrm{d}\Lambda_0^2$. The according degrees of dissociation are simply given by the ratio of measured molar conductivity Λ to limiting molar conductivity Λ_0 at infinite dilution: $\alpha = \Lambda/\Lambda_0$ (equation (24)).

1.3.3 Weakly Coordinating Anions

1.3.3.1 History

For a long time, chemists referred to complex anions such as $[BF_4]^-$, $[ClO_4]^-$, $[PF_6]^-$ or $[CF_3SO_3]^-$ as "non-coordinating".[130] Indeed, these anions are considerably less coordinating than smaller, structurally more simple anions such as halides $[X]^-$, as evidenced by their comparatively better solubilities, higher degrees of dissociation and better conductivities of their salts in less polar solvents (see paragraph 1.3.2 for a description of the physical background). However, studies by means of IR- and NMR spectroscopy as well as crystal structure analysis proved that even "non-coordinating" anions are clearly coordinating to cationic species.[131,132] *S. Strauss* thus recommended to change the term "non-coordinating" anion to the more precise and less dogmatic term "weakly coordinating" anion.[130] Today, the term "non-coordinating" anion may still be used in an intentionally provocative sense, but the expression "weakly coordinating anion" (WCA) has been generally accepted.[126]

1.3.3.2 Relevance and Applications

The unaltered interest in WCAs derives from a number of different motivations. Weak coordination between ions creates very unusual conditions for condensed phases. *I. Krossing* frequently uses the term "pseudo gas-phase" conditions[133] to express the fact that, when WCAs are utilized, even highly electrophilic and thus considerably labile cationic complexes can be stabilized that otherwise could only be observed in the gaseous phase.[134-138] Many important applications of WCAs are derived from their electrophile stabilizing properties. One of the most thoroughly investigated of these applications is the utilization of WCAs as cocatalysts in the polymerization of olefins by electrophilic group IV metallocene catalysts (homogeneous *Kaminsky* type catalysts).[139-144]

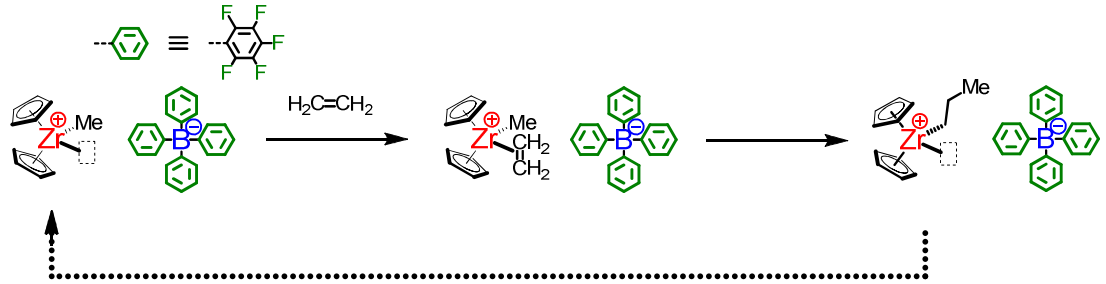

Figure 33: Polymerization of ethylene by a Zirconocene catalyst using $[B(C_6F_5)_4]^-$ as WCA

Therein, WCAs serve as exact stoichiometric substitutes for the otherwise utilized methylaluminoxane (MAO), which is typically employed in very large excess (up to 1000-fold). Further examples include the use of WCA salts for *Lewis* acid catalyzed organic transformations such as pericyclic rearrangements,[145] carbon-carbon bond formation,[146] hydroamination and –arylation,[147] and hetero-*Diels-Alder* reactions.[148] Due to their good solubilities and weak interaction even in low polarity media, WCA salts are used as electrolytes in electrochemistry[149-157] and battery technology.[158-161] Also, the weak coordination of WCAs can be used to lower the viscosity of ionic liquids.[162-165]

1.3.3.3 Structural Guidelines and Examples

Although a truly "non-coordinating" anion has been recognized as a merely fictitious entity,[131] several new WCAs have been developed which allow approaching this ideal ever closer.[126] The general guidelines that have been applied for producing better WCA can be summarized as follows:

1) Anions should be **singly charged**: As demonstrated in 1.3.2.1 (equation (1)), the magnitude of electrostatic attraction crucially depends on the charges q_i of the interacting ions. Going from a singly to a doubly charged anion would also immediately double electrostatic attraction to its counterion.
2) Anions should **not contain basic sites**: Any nucleophilic site in an anion structure will strongly increase the anions tendency to coordinate to cations via donating electron pairs.
3) Anions should be **built from chemically stable moieties**: The energetically unfavored but structurally enforced separation of charges can only be maintained if there are no simple decomposition pathways (e.g. via electrophilic attack, rearrangement, fragmentation) for the enforcing chemical structures.
4) Anions should posses an **inert, hydrophobic surface**: Temporarily induced dipoles (dispersive interactions) can add to the overall tendency of an ion to coordinate to other ions. Such forces can be minimized by employing highly fluorinated surfaces, which are inert, hydrophobic and exhibit very limited polarizability.[126]
5) Anions should be **as large as possible**: As demonstrated in 1.3.2, the most obvious and direct way to effectively reduce the ability of ions to coordinate to other ions is to increase their overall size.[126,133] An increase in molecular size is generally

achieved by surrounding the native ion with preferably large, bulky and rigid substituents.

It is exactly along these guidelines that important improvements in the design of more weakly coordinating anions have been achieved. Three important milestones will be presented here:

1.3.3.3.1 Carborates

A number of very weakly coordinating anions have been developed based on the monocarba-*closo*-dodecaborate or $[CB_{11}H_{12}]^-$ anion (see Figure 34 (A)). The structure of this anion is closely related to the B_{12} icosahedron, which is a common motif in many allotropes of the element boron.

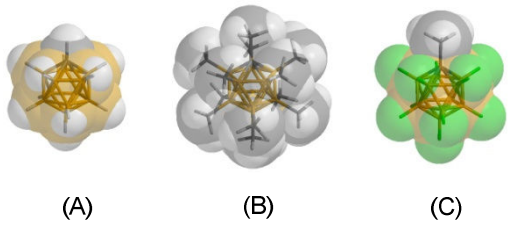

Figure 34: Models of carborate based anions $[CB_{11}H_{12}]^-$ (A), $[CB_{11}Me_{12}]^-$ (B) and $[Me\text{-}CB_{11}F_{11}]^-$ (C)

While the native carborate $[CB_{11}H_{12}]^-$ is already relatively large and thus coordinates comparatively weakly, it is also quite sensitive towards oxidation.[126] A partial ($[CB_{11}H_6X_6]^-$; X = Cl, Br)[166,167] or almost complete ($[H\text{-}CB_{11}X_6Y_5]^-$ and $[Me\text{-}CB_{11}X_6Y_5]^-$; X,Y = Cl, Br, I)[168,169] halogenation of its periphery significantly improves its oxidation stability. *J. Michl et al.* introduced the yet larger, fully methylated carborate ($[CB_{11}Me_{12}]^-$, see Figure 34 (B))[170] and the explosive, fully trifluoromethylated carborate ($[CB_{11}(CF_3)_{12}]^-$),[171] while highly fluorinated carborates ($[R\text{-}CB_{11}F_{11}]^-$; R = Me, Et; see Figure 34 (C))[172,173] were developed by *S. Strauss et al.*. The latter two are regarded the most weakly coordinating carborate-based anions to date.[126]

1.3.3.3.2 Alkoxy- and Aryloxymetallates

Highly *Lewis*-acidic and oxophile metal atoms such as B^{III}, Al^{III}, Nb^{V}, Ta^{V}, Y^{III} and La^{III} have been used for the generation of WCAs via introduction of poly- or perfluorinated alkoxy- or aryloxy substituents.[126] The introduction of such substituents yields alkoxy- or aryloxymetallates of the type $[M(OR^F)_n]^-$. Of course, the presence of basic oxygen sites increases the danger of both undesired coordination as well as anion decomposition (see

the above guidelines regarding the design of WCAs). Accordingly, anions of the type $[M(OC_6F_5)_6]^-$ with M = Nb or Ta (see Figure 35 (A)) have been found to be sensitive towards OC_6F_5 abstraction by highly electrophilic zirconocene catalysts such as $[Cp_2ZrMe]^+$.[174,175] The undesired effects from the presence of oxygen sites can however be compensated by using sufficiently bulky substituents. *I. Krossing* presented WCAs based on alkoxyaluminates which are highly shielded by bulky $OC(CF_3)_3$ substituents.[176]

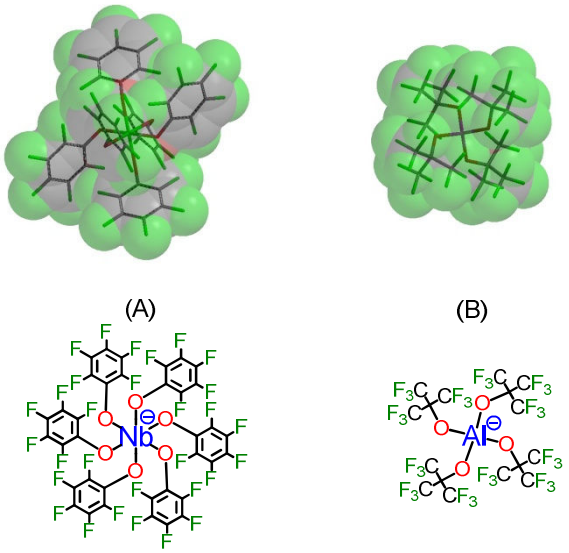

Figure 35: Models and structures of alkoxy based WCAs $[Nb(OC_6F_5)_6]^-$ (A) and $[Al(OC(CF_3)_3)_4]^-$ (B)

In the resulting aluminates, oxygen atoms are sufficiently screened from coordinative interactions by steric screening from the $C(CF_3)_3$ moiety, which stabilizes the $[Al(OC(CF_3)_3)_4]^-$ anion against hydrolysis even in nitric acid. Another advantage of the $[Al(OC(CF_3)_3)_4]^-$ anion is its facile, large scale preparation from relatively simple starting compounds.[176]

1.3.3.3.3 Tetraphenylborates

Due to their large size and their weakly coordinating properties, tetraphenylborate and its derivatives have frequently been used as WCAs.[130,177] Both fluorine and CF_3-groups have been introduced into tetraphenylborates (see Figure 36), initially to increase their hydrophobicity and to yield more efficient phase transfer catalysts for electrophilic and acid mediated reactions.[178-180] However, substitution with fluorine also helped to largely improve the stability of tetraphenylborates against protic acids and oxidants.[181]

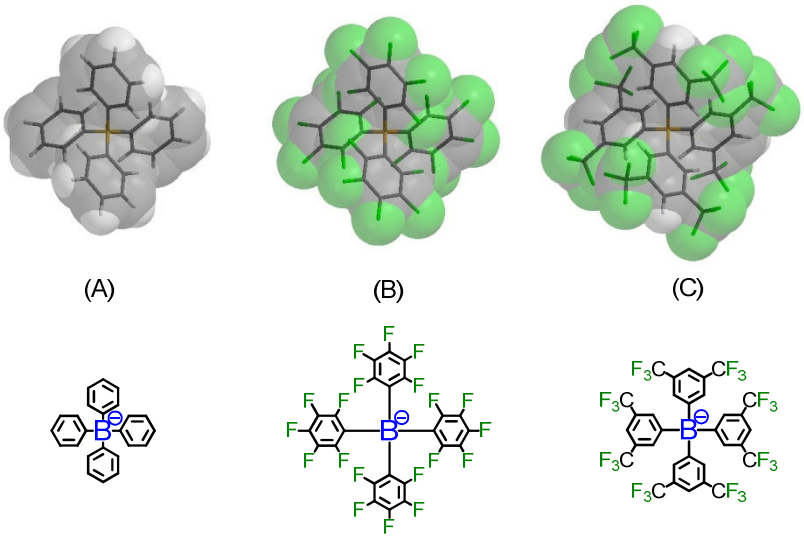

Figure 36: Models and structures of tetraphenylborate $[BPh_4]^-$ (A), perfluoro-tetraphenylborate $[B(C_6F_5)_4]^-$ (B) and *meta*-CF_3 functionalized tetraphenylborate $[B(C_6H_3(CF_3)_2)_4]^-$ (C)

In order to further reduce the coordination strength of tetraphenylborates, yet larger and bulkier ligands have been introduced. Examples for substitution include phenyl rings with longer perfluoroalkyl chains or in the *meta* position,[182,183] modification of the *para* position with either F_3C-,[184] *i*Pr_3Si-, Me_2*t*BuSi-,[185,186] or $(C_6F_5)_2FC$-moieties,[187] and the use of fluorinated biphenyl or naphthalene substituents.[141] Yet larger tetraphenylborates could not be achieved thus far due to steric congestions between individual ligands. Nevertheless, the family of tetraphenylborate anions represents a structural starting point for the herein aspired synthesis of potentially much larger anions.

1.4 Motivation

The structural requirements to design less coordinating anions are well known and understood (see paragraph 1.3.3.3). Nevertheless, the extent to which these structural requirements can be implemented into actual chemical structures crucially depends on the constraints and limits of the synthetic methods applied.

As mentioned earlier, the single most obvious structural tweak to obtain less coordinating anions would be a drastic increase of their overall sizes: Since the power of electrostatic attraction between oppositely charged ions is inversely proportional to the square of their distance r (see paragraph 1.3.2.1), an increase in anion size would result in a reduction of coordination power and lead to a decrease of mutual attraction between anion and cation (see Figure 37).

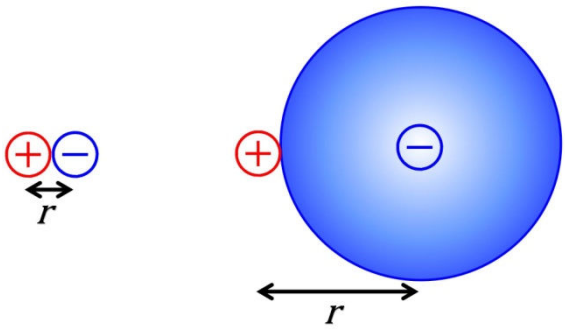

Figure 37: Schematic drawing of ion pairs constituted of differently sized ions, resulting in different anion-cation distances r (with increasing ion size, mutual electrostatic attraction F_c between ions decreases with $1/r^2$; see paragraph 1.3.2.1, equation (1))

Although WCA syntheses generally aimed at achieving larger anion sizes, a really drastic increase in anion size has thus far eluded feasible synthetic methods.

For example, tetraphenylborates with increased overall sizes were produced by utilizing larger and bulkier ligands, such as perfluoroalkyl-substituted phenyl rings (see Figure 38 (A)),[182,183] or phenyl rings bearing even more bulky $(C_6F_5)_2FC$- moieties in their *para*-position (see Figure 38 (B)).[187]

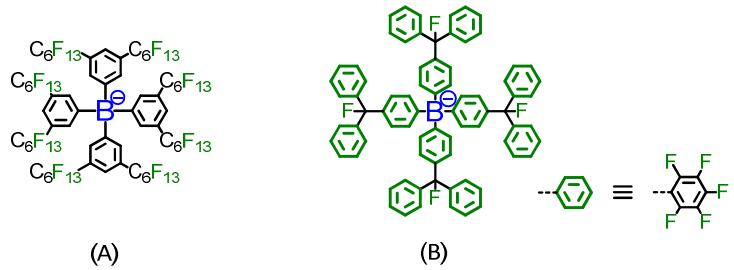

Figure 38: Examples of tetraphenylborates bearing larger substituents

While the so obtained borate species certainly exhibited somewhat larger overall anion sizes than previous borate derivatives, the applied synthetic strategy could not be driven to yet larger sizes: If the ligands were too large and bulky, their steric demand hindered other large ligands and mutually blocked their (fourfold) introduction to a single central boron atom (see Figure 39 (B)).

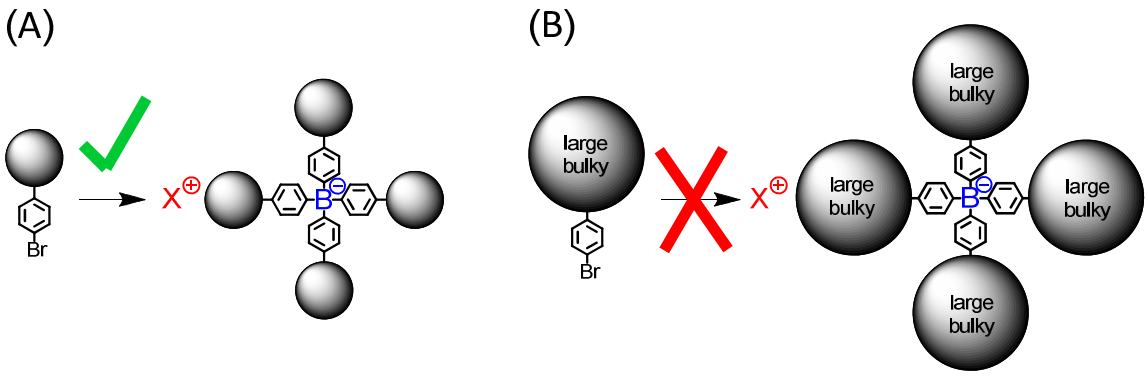

Figure 39: Schemes for the synthesis of tetraphenylborate from aryl halides; (A): With sufficiently small ligands, the synthesis can be performed, (B): Steric repulsion between large and bulky substituents prevents borate formation

The steric repulsion between different ligands thus marked an upper limit for the size and bulkiness of borate anions that could be synthesized directly (introduction of ready-made ligands). In terms of dendrimer chemistry, all of the above efforts could be summarized as "convergent" synthetic approaches.

In polyphenylene dendrimer synthesis, by contrast, divergent synthetic approaches have already proven as a suitable means to build up very large and bulky rigid scaffolds around central functions. As mentioned in paragraph 1.2.3.1, this concept has been used to sterically screen and isolate different functionalities and thus prevent their aggregation or enhance their intrinsic properties.

We wondered whether this concept, namely the divergent dendritic growth of large, rigid and bulky scaffolds around single functions, could also be applied to intrinsically charged species such as anions in a salt. In contrast to introducing large "ready-grown" ligands in a single step ("convergent" approach), sufficiently small ligands might be introduced to the boron atom firstly. These small ligands might be functionalized in such a way as to enable their growth and extension in one or more subsequent reaction steps (see Figure 40).

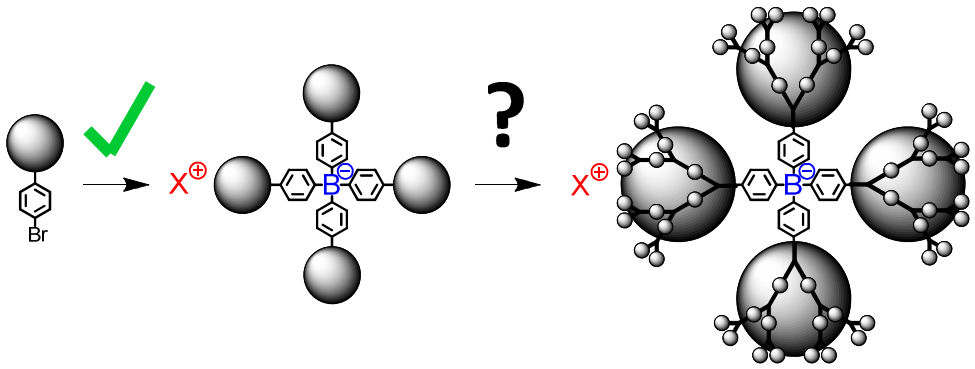

Figure 40: Scheme for the synthesis of a very large and highly screened borate anion by means of divergent dendritic growth

If applicable, this concept might enable the synthesis of significantly larger and much more bulky anions than all anions reported previously.

Moreover, in contrast to virtually all other types of dendrons, polyphenylene dendrimers readily fulfill all the important requirements for the structural design of efficient WCAs (see paragraph 1.3.3.3): Highly branched polyphenylenes are *i*) entirely built from chemically stable moieties, *ii*) are considerably hydrophobic, *iii*) lack any basic oxygen or nitrogen sites in their scaffold and *iv*) are stiff and rigid and may thus provide anions with a shape persistent, non collapsible shell. Steric screening of the central charge by dense dendritic polyphenylene shells might render the resulting, highly screened anions very weakly coordinating.

Due to the modular nature of divergent dendrimer synthesis, dendronized anions might also represent a versatile structural platform for a systematic investigation of the relationship between chemical structure, weak coordination and electrolyte properties. Important structural parameters of the anion, such as anion size (dendrimer generation), density of the anion shell (degree of branching) or the chemical nature of the anion surface (choice of building blocks) might be modified and tested with regard to their individual impact on coordination/dissociation properties of the resulting electrolyte.

Hence, the most central task of this work is to test whether the here outlined strategy, the divergent growth of anions, represents a feasible solution for anion size increase in novel WCA synthesis and may thus help to answer some of the following questions:

“Is the divergent dendronization with rigid polyphenylenes generally applicable to individual ions in a salt?”

“If so, could rigid dendronization be used as a means to substantially increase the size of anions, possibly far above the level of all molecular anions known to date?”

“Would the potential increase in anion size also reduce the coordination strength of these anions through sterically enforcing larger distances between anion and cation?”

"What would be the effects of nanoscopically enlarged ions on the overall properties of their salts and the behaviour of these salts as electrolytes?"

Due to numerous observations made and insights gained in the process of addressing the above questions, several new objectives appeared in due course and led to further branches of explorative work. All of these will be described in the following chapters.

2 Synthesis of Rigidly Dendronized Anions

2.1 Introduction

Increasing the size and bulkiness of molecular anions is a major task for the preparation of more **w**eakly **c**oordinating **a**nions (WCAs, see 1.3.3),[126] which have attracted remarkable interest due to their importance in catalysis,[145-148,188,189] polymerization,[139,141-144,190] electrochemistry,[149-157] stabilization of electrophilic cationic species,[134-138] ionic liquids[162-165] and battery technology.[158-161] Among the many different WCAs reported, tetraphenylborate and its derivatives are some of the most frequently applied.[130] The advantageous properties of tetraphenylborates originate from their relatively large size as compared to more classical WCAs such as BF_4^- and PF_6^-. As mentioned earlier (see 1.3.3.3.3), fluorine and CF_3-groups have been introduced to tetraphenylborates, which helped to increase their hydrophobicity,[178-180] but also largely improved their stability against protic acids and oxidants.[181] While synthetic routes have been proposed to further reduce the coordination strength of tetraphenylborates by way of introducing larger and bulkier ligands,[141,182-187] these efforts were strongly limited in achievable anion sizes due to steric constraints.

In the motivation to this work (see paragraph 1.4), the central synthetic strategy has been introduced which shall enable the synthesis of significantly larger and much more bulky anions: The divergent dendritic growth of rigid, highly branched polyphenylenes was put forward as a potential means to circumvent the steric constraints of direct synthesis and possibly push the limits of achievable anion sizes. The many synthetic approaches that have been tested and improved within this work to achieve a rigid dendronization of tetraphenylborate anions will be described on the following pages. Therein, borates based on non-fluorinated or based on fluorinated tetraphenylborate will be presented within subsequent but separate paragraphs (2.2 and 2.3) due to their different structural families and the large number of compounds related to either one.

2.2 Dendronized Anions based on Tetraphenylborate

Ethynyl functionalized tetraphenylmethane has been used frequently as a core for the build-up of PPDs. The tetraphenylborate anion resembles the geometry and structure of tetraphenylmethane very closely. Despite their superficial structural resemblance however, the inherent anionic nature of the borate anion inevitably requires the presence of a cationic counterion (see Figure 41).

(A) (B)

Figure 41: Comparison of tetraphenylmethane (A) and tetraphenylborate salt (B)

In contrast to tetraphenylmethane (A), the properties of tetraphenylborate salts (B) are determined by the chemical building blocks (phenyl rings, alkyl chains etc.) and properties of the anion and its counter-cation as well as the types and strengths of their interactions with one another. Accordingly, the ionic nature of all dendronized salts presented herein has to be considered in the elaboration of their synthesis and work up.

2.2.1 Ethynyl-Functionalization of Tetraphenylborate

The first task to enable the rigid dendronization of a tetraphenylborate with PP dendrons was a functionalization of the anion with ethynyl groups. A suitable procedure has been developed by [redacted] during her time as a postdoctoral fellow in the group of [redacted]. The procedure utilizes the facile generation of tetraphenylborates from the lithiation of aryl halides and their subsequent conversion with boron trichloride in diethyl ether. The required ethinyl functionalized ligand **10** was synthesized via selective *Sonogashira* coupling[61] of T*i*PS-acetylene to 1-bromo-4-iodobenzene **9** at 0 °C. The obtained ligand **10** was then converted to the according T*i*PS-protected borate salt **11**. After removal of T*i*PS groups with tetrabutylammonium fluoride (TBAF) in THF, the desired ethynyl functionalized tetraphenylborate **12** was obtained.

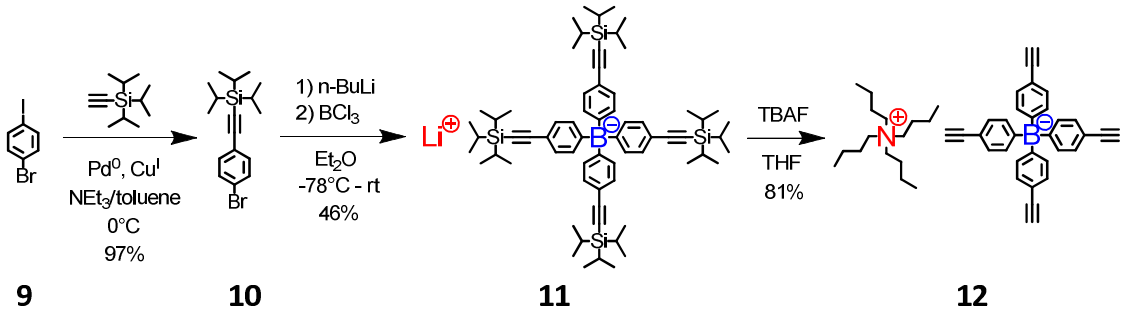

Figure 42: Synthesis of ethynyl functionalized tetraphenylborate **12**

It is noteworthy that during deprotection with TBAF, the lithium cation Li^+ of salt **11** is inevitably exchanged to tetrabutylammonium TBA^+ in salt **12**.

Complete cation exchange of lithium to tetrabutylammonium was confirmed by means of proton NMR, where the ratio between anion and cation can be checked conveniently via relative integration of ^{1}H-NMR signal intensity (see Figure 43).

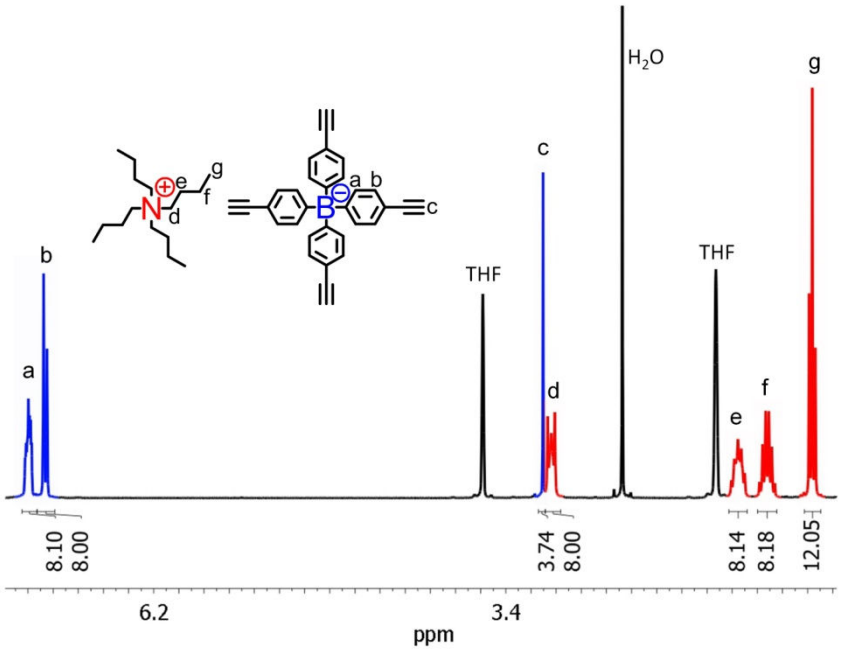

Figure 43: ^{1}H-NMR spectrum of borate salt **12** in THF-d8 (300 MHz); anion signals in blue, cation signals in red

An interesting feature of the above spectrum of borate **12** (Figure 43), and more generally of many NMR spectra of organic borate salts, is the emergence of characteristic signal patterns due to the magnetic coupling of boron to other nuclei: The element boron exists in the form of two isotopes, ^{11}B and ^{10}B, with natural abundances of 80.1 % and 19.9 %, respectively. The more abundant ^{11}B nucleus has a spin of $I = 3/2$. If one ($n = 1$) ^{11}B nu-

cleus couples to neighboring proton-, carbon- or other nuclei, the signals of these nuclei will split into multiplets M (here quartets, since $M = 4$) according to the formula of multiplicity (equation (26)).

$$M = 2nI + 1 \tag{26}$$

Hence, the signal of proton H^a in borate **12** appears as a doublet (HH coupling; $^3J_{HH}$ = 7.9 Hz) of quartets (BH coupling; $^3J_{BH}$ = 2.7 Hz) in the ^{1}H-NMR spectrum (see Figure 44).

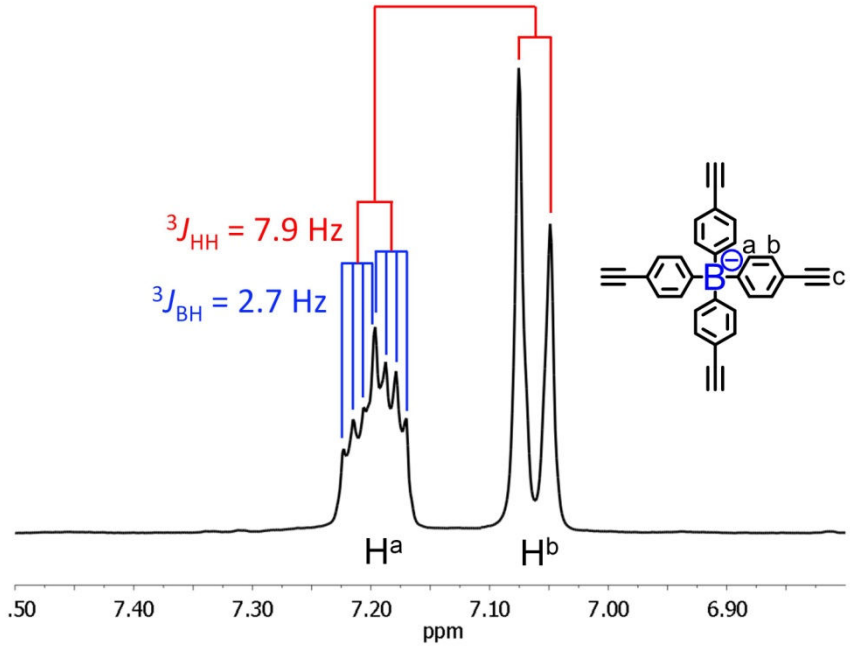

Figure 44: Characteristic splitting of proton signals in ^{1}H-NMR spectra caused by the coupling of protons with an ^{11}B nucleus; here for the proton H^a of borate salt **12** in THF-d8 (300 MHz)

At the same time, about 20% of all borate ions should contain ^{10}B ($I = 3$) instead of ^{11}B nuclei and give rise to a splitting of the H^a proton signal into septets ($M = 7$) instead of quartets. For the borate salts investigated in this work, however, these couplings remained hidden beneath the signal measured for the ^{11}B species: Not only is the abundance of the ^{10}B species comparatively low, but the associated coupling constant is expected to be smaller and thus more difficult to resolve. Furthermore, the already low signal intensity of proton H^a in the 20% ^{10}B species of salt **12** is distributed to as many as 14 peaks due to coupling, which makes its detection even more difficult.

However, the coupling of ^{10}B nuclei with directly bound carbon atoms could be observed in long time accumulated ^{13}C-NMR spectra of borate salts **11** and **12**, even despite the low abundance of ^{13}C nuclei and thus low signal-to-noise ratios (see Figure 45).

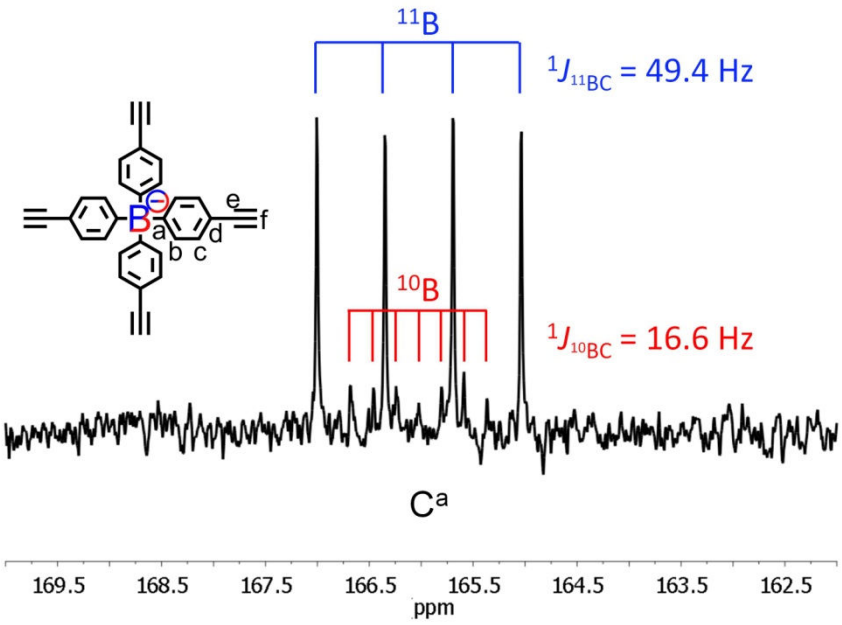

Figure 45: ^{13}C-NMR signal (300 MHz) of the carbon atom C^a directly attached to boron in salt **12**; the measurement time is just sufficient to also resolve the coupling of C^a to the ^{10}B nucleus

The carbon atom C^a, which is directly attached to the boron atom in borate **12**, experiences a strong enough coupling with boron to give rise to a relatively large coupling constant, which facilitates the distinction of individual peaks in the spectrum and allowed to resolve both the ^{11}B and ^{10}B coupling with carbon C^a at the same time.

A coupling of ^{11}B to the even more distant carbon atoms C^b and C^c could also be detected. Surprisingly, the coupling of ^{11}B to the more distant carbon C^c is stronger (^3J = 2.8 Hz) than the coupling to the closer carbon C^b ($^2J_{BC}$ not resolved, but apparent due to signal broadening).

Further proof for the exact 1:1 composition of borate salt **12** was provided by a single crystal structural analysis of the compound. Borate salt **12** could easily be grown into large and transparent crystal needles of up to 2 cm length, which were suitable for structure determination by means of X-ray diffraction (see Figure 46).

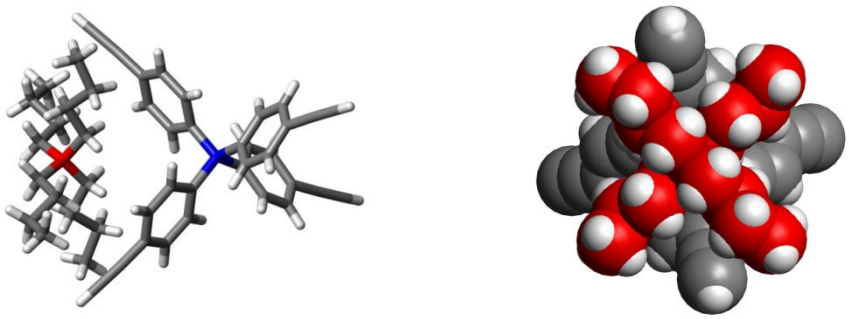

Figure 46: Single crystal structure of borate salt **12**; left: side view of a stick model; right: frontal view of a space filling model (TBA^+ carbon atoms in red for better contrast)

A more thorough discussion of the above structure and a comparison with other crystal structures will be provided in upcoming paragraph 6.3.1 of this work.

2.2.2 Increase of Anion Size via Divergent Dendritic Growth

With the ethynyl functionalized tetraphenylborate **12** at hand, its applicability for a divergent dendronization with polyphenylenes could be tested. An immediate objective therefore was the synthesis of the first generation PP-dendronized borate **14** (Figure 47), which already represents a larger borate species than any borate reported previously.

Build-up of PPDs via *Diels-Alder* cycloaddition is usually performed in *o*-xylene at high temperature (150–170 °C, see 1.2.1). Due to the ionic nature of salt **12** and its low solubility in *o*-xylene, the cycloaddition reaction was initially performed in relatively polar solvents such as DMSO or diglyme at 160 °C for 12 hours (see Figure 47).

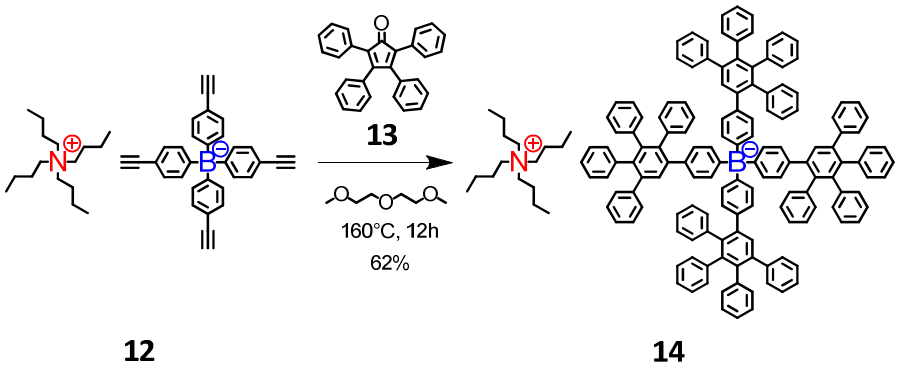

Figure 47: Divergent synthesis of a first generation polyphenylene dendronized borate **14** via cycloaddition of tetracyclone **13** to ethynyl functionalized borate **12**

Nevertheless, later experiments confirmed that the reaction can also be performed in *o*-xylene due to the consecutively increasing solubility of intermediates and the product in *o*-

xylene, causing a continuous dissolution of non-reacted starting compound **12** with progressing reaction. Xylene even has an advantage over diglyme in that it can be separated from the product more easily via column chromatography.

The reaction (Figure 47) was monitored by means of MALDI-TOF mass spectrometry. Since borate anions are already negatively charged, irradiation with a UV laser (337 nm) was not necessary for their ionization but was used to evaporate borate ions from a dithranol matrix. Moreover, the polarity of the electrical field applied in the mass spectrometer had to be reversed in order to enable detection of negatively charged species. MALDI-TOF measurements confirmed that divergent dendritic growth could indeed be used to successfully synthesize the large and rigid PP-dendronized borate **14** (Figure 48).

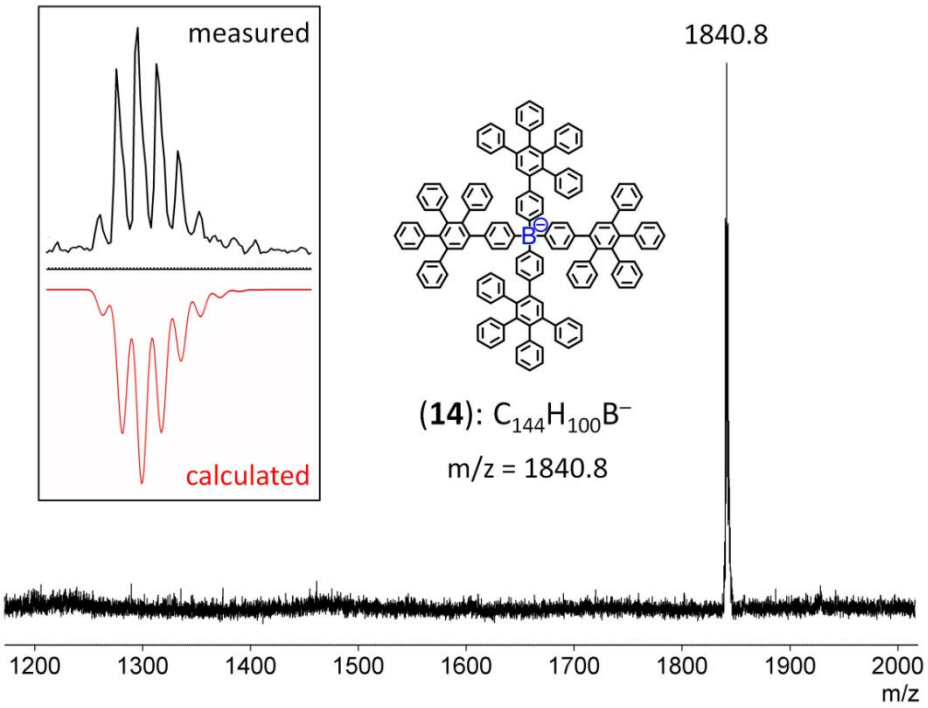

Figure 48: MALDI-TOF of dendronized borate **14**; inset: comparison of measured and calculated isotope distribution pattern of the peak

It should be emphasized here that while the synthesis of **14** via the above described divergent route was possible, the same borate anion could not be synthesized in a convergent manner: Ready-made PP dendrons **16** have been synthesized via cycloaddition of tetracyclone **13** to 1-bromo-4-ethynylbenzene **15** (Figure 49). However, introduction of readily dendronized ligands **16** to boron (Figure 49) did not yield the desired dendronized product **17** (Li^+ salt analogue of salt **14**) but a mixture of non-identified lower molecular weight species.

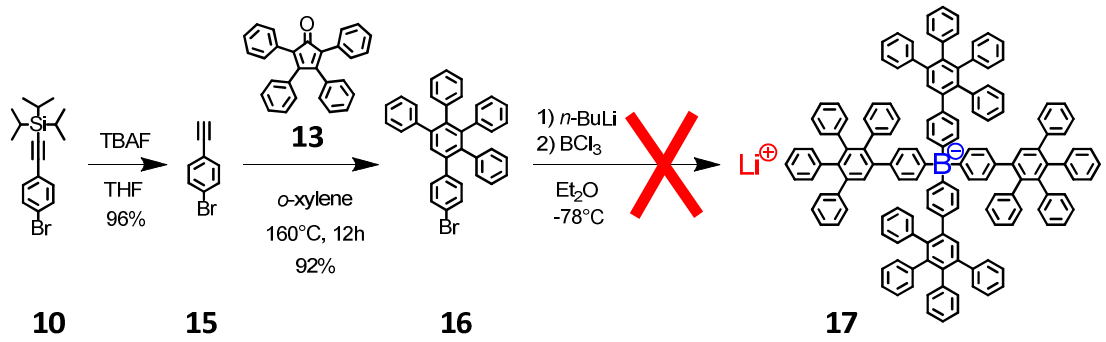

Figure 49: Convergent synthesis of a first generation polyphenylene dendronized borate via direct introduction of the ready-made PP-dendron **16** to boron (failed!)

Most probably, the steric demand of PP-dendron **16** precluded its fourfold introduction to boron and thus hindered the formation of the borate. The method of divergent dendritic growth (see movitation in paragraph 1.4, Figure 40) hence provides a significant advantage over direct (or "convergent") synthetic methods for the preparation of large and sterically encumbered borates such as borate **14**.

Since the structures of both the anion and the cation of borate salt **14** possess a large number of protons, ^{1}H-NMR spectroscopy is a very suitable as well as informative method of characterization here and for dendronized borates in general (Figure 50).

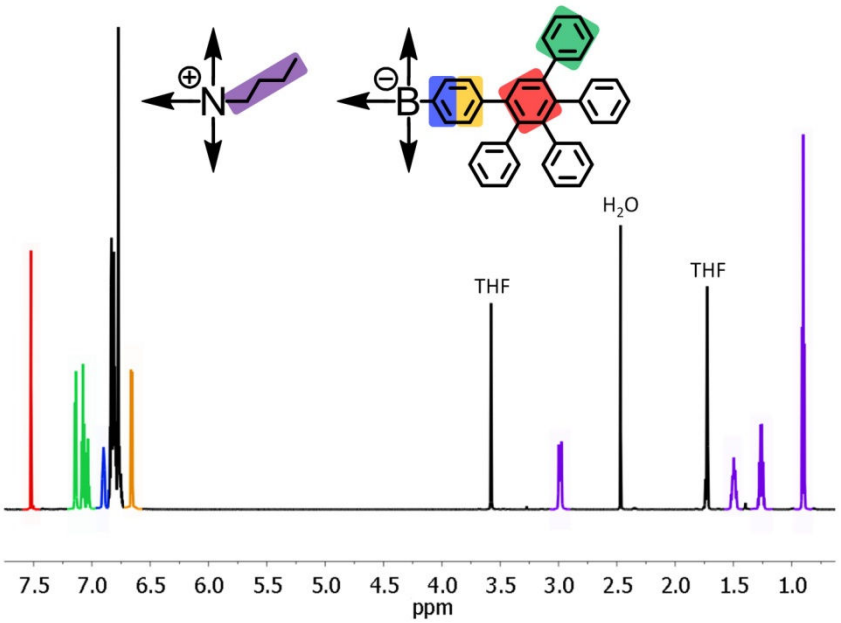

Figure 50: ^{1}H-NMR spectrum of **14** in THF-d8 (700 MHz); color code for assigned proton signals

A closer look at the low field region (high chemical shifts) of the above ^{1}H-NMR spectrum (Figure 50) reveals specific signals which are typical for ^{1}H-spectra of polyphenylene

dendrimers (Figure 51). The sharp singlet which appears shifted farthest towards low field is attributed to the proton H^c at the central "branching" phenyl ring (colored red in Figure 51) and will be called "generation proton" from here on.

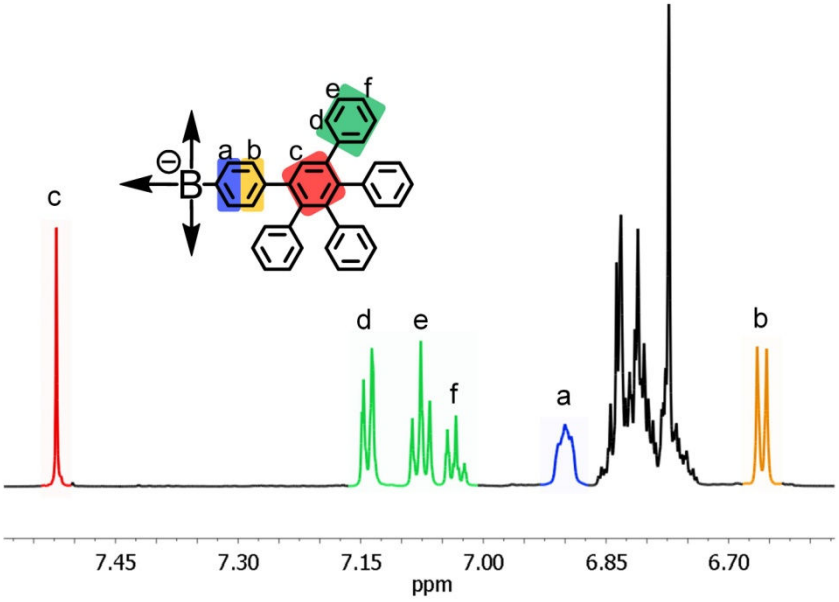

Figure 51: Detail of the low field region of the ^1H-NMR spectrum of **14** in THF-d8 (700 MHz)

Higher generation PPDs possess larger numbers of generation protons and thus larger numbers of low field shifted singlets in their ^1H-NMR spectra. The signals of protons H^d, H^e and H^f of the phenyl ring next to the generation proton outwards (marked green in Figure 51) also appear at relatively high chemical shifts. The according phenyl ring is less shielded from the magnetic field by neighboring aromatic rings (only one direct phenyl neighbor) as compared to all other rings. Each of the other rings either has two direct phenyl neighbors (those not marked with any overlay color in Figure 51), or is shielded by phenyl rings of the core (protons H^a and H^b in Figure 51). While the effect of coupling of the ^{11}B nucleus with proton H^a is still visible in the above spectrum of **14**, the quartet coupling pattern could not be resolved anymore.

The dendronized salt $TBA^+[B\text{-}G1]^-$ **14** was crystallized in the form of transparent needles and analyzed by X-ray diffraction. Its single crystal structure confirms that the polyphenylene dendrons form a large, rigid and bulky extension of the inner tetraphenylborate core (Figure 52).

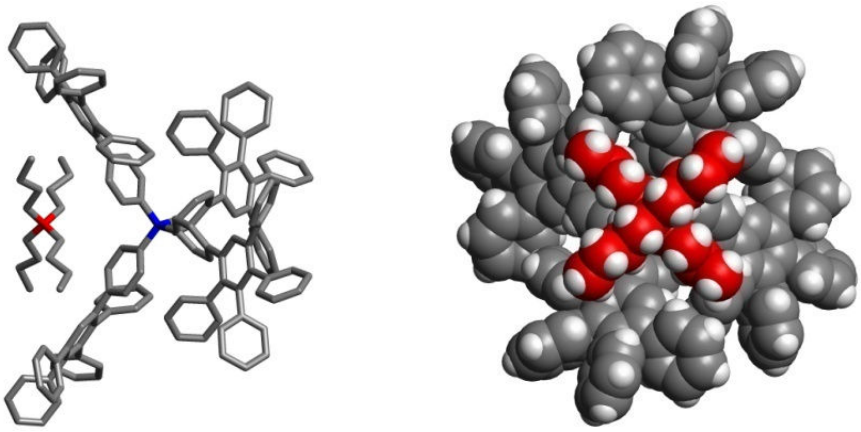

Figure 52: Single crystal structure of borate salt **14** (solvent molecules omitted for clarity); left: side view of a stick model (hydrogen atoms omitted for clarity); right: frontal view of a space filling model (TBA^+ carbon atoms in red for better contrast)

The achieved increase of steric shielding by polyphenylene dendrons should make dendronized borate **14** less coordinating than a non-dendronized tetraphenylborate. Weaker coordination should be reflected in a promotion of ion dissociation, especially in low polarity media. These effects will be tested and compared in paragraph 6.5 of this work.

After successful synthesis of **14**, the next task was to test whether divergent growth also enables the synthesis of even larger and more bulky borate species of higher (>1) PPD generations. Therefore, borate core **12** was reacted with both AB_2 (**1**) and AB_4 (**2**) building blocks, respectively, to yield the dendronized and ethynyl functionalized borate species **18** and **19** (see Figure 53).

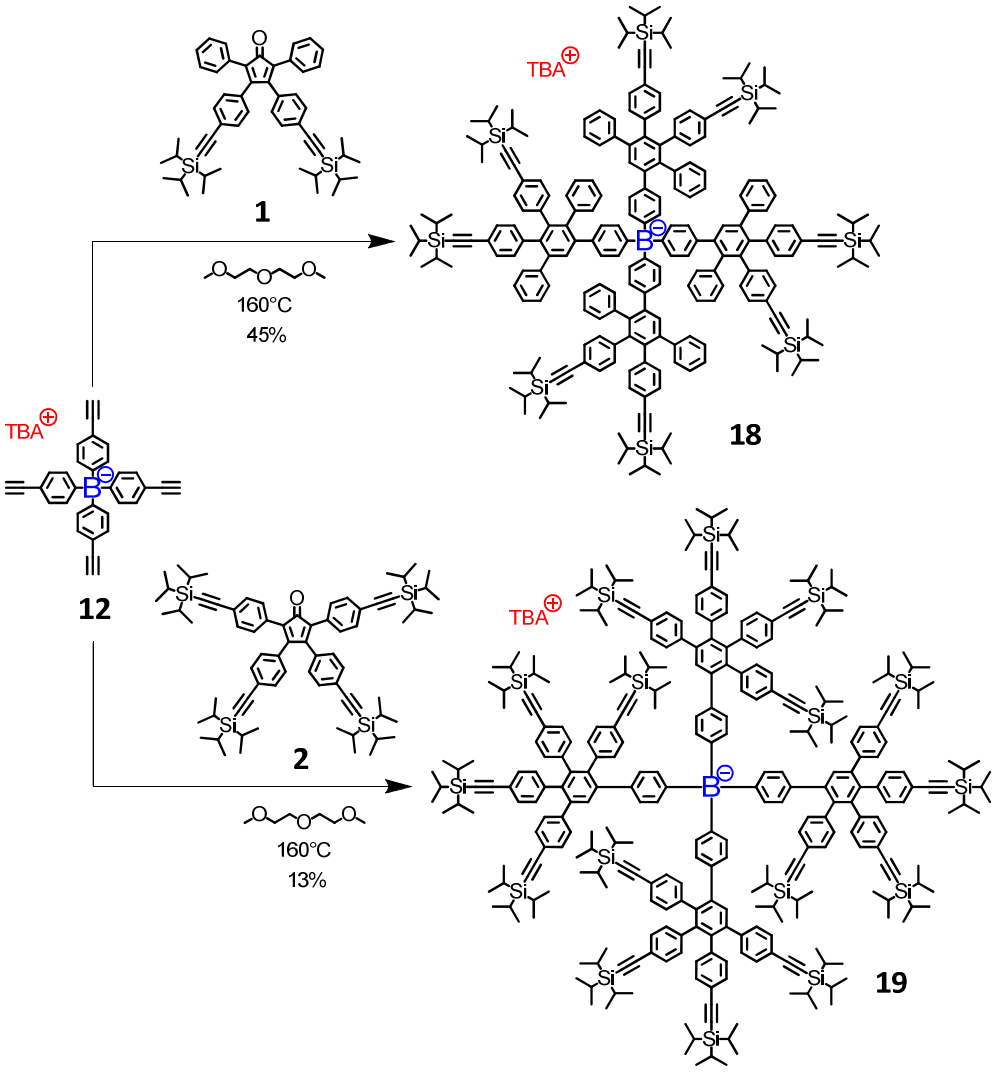

Figure 53: Synthesis of ethynyl functionalized first generation dendronized borates **18** and **19**

Despite the large steric demand of tetracyclone building blocks AB_2 (**1**) and especially AB_4 (**2**), the cycloaddition reactions towards both borates **18** and **19** were successful. Their yields, however, decreased drastically with increasing steric demand of the building blocks (from 62% for non-functionalized tetracyclone **13** to 45% for tetracyclone **1** and to 13% for tetracyclone **2**). Major side products in all performed cycloaddition reactions were the according single PP-dendrons generated by a cleavage of the boron-carbon bond at high temperatures. Steric repulsion between dendrons thus accelerates thermal decomposition reactions and leads to decreasing yields.

To activate both species **18** and **19** for the next step of dendritic growth, their T*i*PS groups were removed with TBAF in THF solution, yielding the ethynyl functionalized borates **20** and **21**, respectively (see Figure 54).

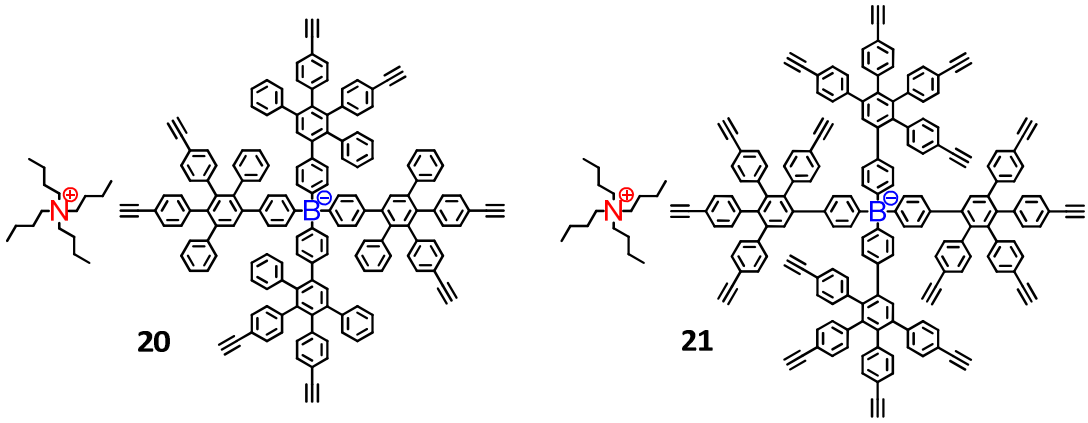

Figure 54: Structures of ethynyl functionalized first generation PP-dendronized borates **20** and **21**

In addition to the full assignment of all proton signals of borate **20**, the combination of different NMR methods (HSQC, NOESY) also enabled the specific assignment of all of the thirty carbon signals to each of the anion´s thirty chemically distinct carbon atoms (see 0).

However, conversion of both activated borates **20** and **21** to the according second generation dendronized borates failed (see Figure 55).

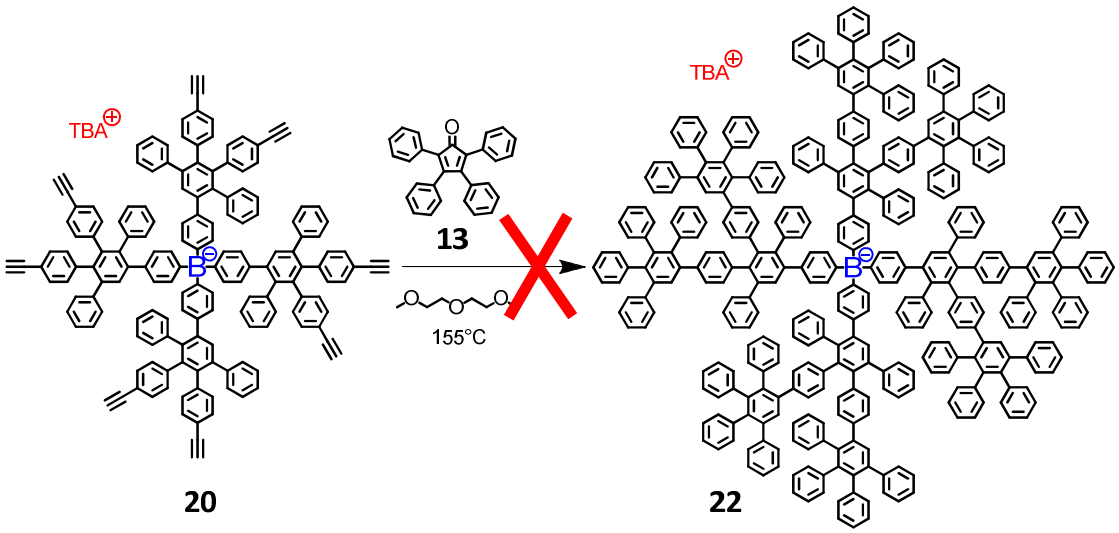

Figure 55: Divergent synthesis of a normally branched second generation dendronized borate **22** starting from **20** (failed!)

At the high temperature (> 150 °C) required for cycloaddition, starting compounds and intermediates decomposed, mainly via cleavage of the B-C bond. The cleavage generated singular dendrons but also species of two dendrons fused together. A further heating of not fully converted intermediates resulted in their complete decomposition before the

reaction was finished. While an 8-fold cycloaddition at **20** is necessary for its complete conversion to **22**, the maximum number of cycloadditions that could be detected by means MALDI-TOF was only 7-fold (with peaks of highest intensity still around 4 to 5-fold). No product **22** could be detected by means of MALDI-TOF at any time.

In order to enable a further dendritic growth despite the thermal instability of borate species built upon borate **12**, two alternative strategies of dendritic growth were tested (see 2.2.3).

2.2.3 Alternatives to Divergent Dendritic Growth of Polyphenylenes

The above described divergent approach of dendritic growth at high temperature failed to yield any second or higher generation PP dendronized borate due to insufficient temperature stability of the core **12** (2.2.2). Conceivable alternatives involving the same starting compound **12** might aim to either shorten the total time of exposure of borates to high temperature (see 2.2.3.1), or to switch to a type of dendritic growth that can be performed at low temperature (see 2.2.3.2).

2.2.3.1 Semi-Convergent Dendritic Growth

The total time of exposure of borates to high temperatures might be shortened by switching over from a fully divergent to a partly convergent or "semi-convergent" type of PP growth. While the fully convergent approach requires the introduction of ready-made dendrons to the central boron atom in a final step (not applicable due to steric congestion, see 2.1), the semi-convergent approach merely requires introduction of a dendronized tetracyclone building block **23** to readily "pre-formed" borate **12**. These prerequisites render the semi-convergent approach a balanced solution between divergent and convergent synthesis, which both have proven unsuited. The utilization of dendronized tetracyclone[191] building block **23** reduces the number of high temperature reaction steps towards second generation borate **22** from two steps to only one (4-fold cycloaddition of **23** to **12**; see Figure 56).

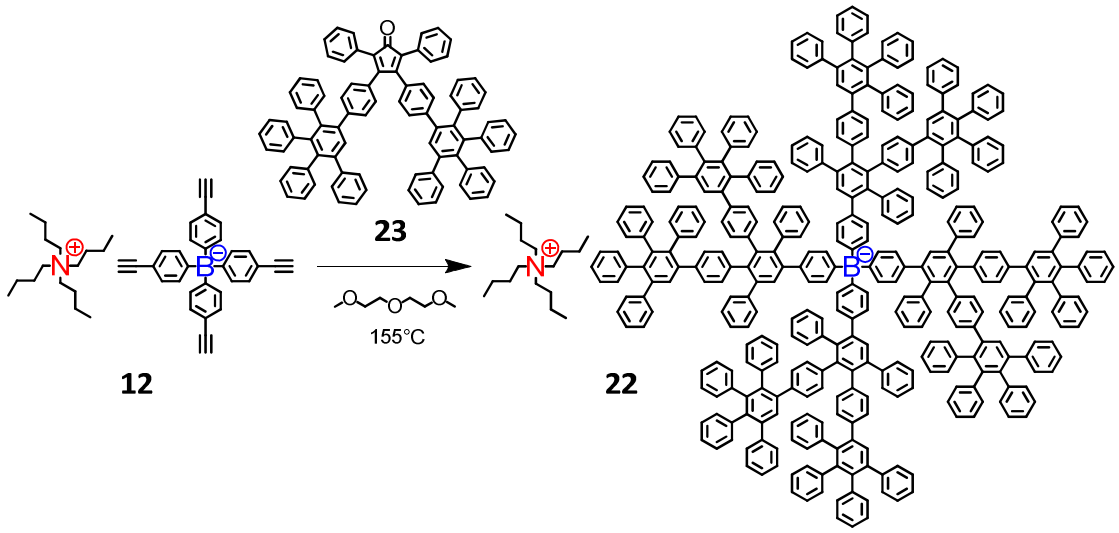

Figure 56: Semi-convergent synthesis of a second generation PP dendronized borate in one reaction step (fourfold cycloaddition) starting from **12**

Admittedly, the steric demand of dendronized building block **23** is considerably larger than that of a non-dendronized tetracyclone **13**, making its cycloaddition more difficult. Nevertheless, upon monitoring the semi-convergent synthesis of **22** by means of MALDI-TOF mass spectrometry, the formation of second generation dendronized borate **22** could indeed be observed (see Figure 57).

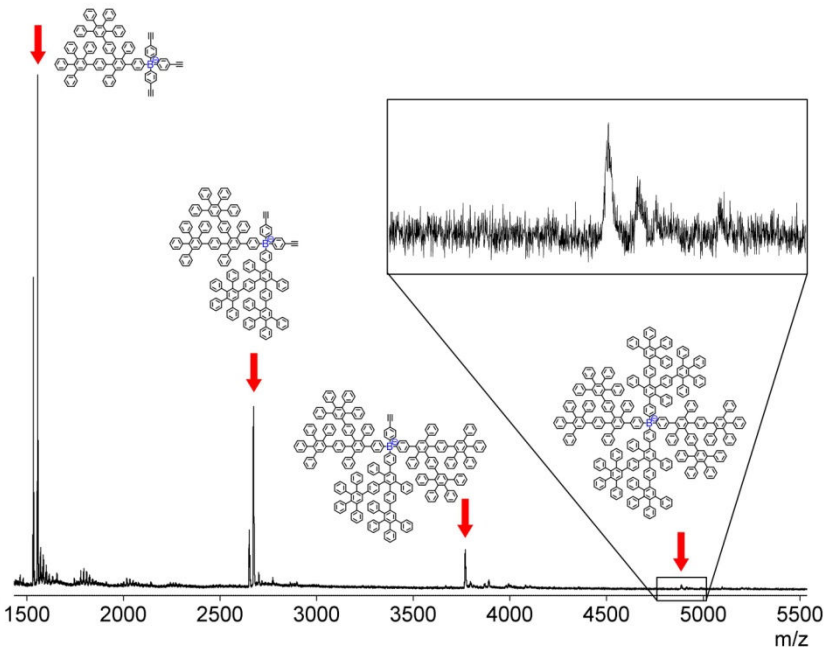

Figure 57: MALDI-TOF of reaction mixture for the semi-convergent synthesis of second generation dendronized borate **22**; inset: detail for the signal of borate **22**

However, similar to the divergent approach, the semi-convergent synthesis could not be completed before all intermediates and the product were fully decomposed. Furthermore, the salt character of all intermediates and the product also excluded a subsequent separation and isolation of the trace amounts of product **22** that had already been formed. Complete conversion of starting material in the cycloaddition reactions thus is an imperative for the successful synthesis of any dendronized borates. Apparently, ethynyl functionalized borate **12** cannot be used for the synthesis of higher than first generation polyphenylene dendronized borates.

2.2.3.2 Dendritic Growth via 1,3-Dipolar Cycloaddition

While dendronization of borate **12** via *Diels-Alder* cycloaddition at high temperature is limited to first generation borate species, higher dendrimer generations might be achieved by methods of growth which require less to no extra heating. The ethynyl functions of borates could be used for a 1,3-dipolar cycloaddition of azides (*Huisgen* cycloaddition).[192] The *Husigen* reaction can be catalyzed by Cu^{1+} ions and thus be performed at room temperature, where it regioselectively yields 1,4-disubstituted 1,2,3-triazoles (see Figure 58).[193] Following *K. B. Sharpless*, the Cu^{1+} catalyzed procedure for the azide-alkyne cycloaddition is a prominent example of so called "click chemistry" (which as a whole includes many different types of reactions). The reaction enables "clicking" together different (suitably functionalized) components very easily.

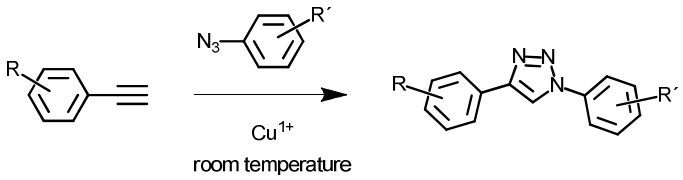

Figure 58: General scheme for the click reaction between an ethynyl- and an azide functionalized aryl component, resulting in the formation of a 1,4-disubstituted 1,2,3-triazol linkage

Since room temperature is already sufficient for the above reaction, it might be advantageous for generating larger borate species with a tetraphenylborate core despite the thermal lability of its B-C bond.

In order to provide an effective steric screening of the resulting borate, sufficiently large, bulky and rigid azides are required, which closely resemble the structure of polyphenylenes. Thus, only aryl azides were considered as suitable building blocks. They can be generated from the according anilines under mild conditions using *tert*-butyl nitrite

(*t*BuONO) and trimethylsilyl azide ($TMSN_3$) as a secure azide source.[194] Aniline **24** is a very large and bulky aryl amine that somewhat resembles the structure of polyphenylenes (Figure 59). It was converted to the according azide **25** using the above mentioned and mild method.

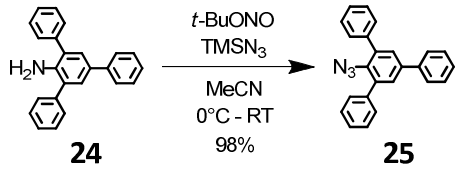

Figure 59: Synthesis of the bulky and rigid aryl azide **25** from the according aniline **24**

To enable "clicking" of bulky azide **25** to borate anions, a catalytically active Cu^{1+} species is required. Cu^{1+} is usually generated *in situ*, either from the comproportionation of Cu^{2+} and Cu^0 (e.g. from $Cu(OAc)_2$ and Cu metal), via reduction of Cu^{2+} (from $CuSO_4 \cdot 5H_2O$) using sodium ascorbate, or by directly using Cu^{1+} salts (such as CuBr or $Cu(MeCN)_4PF_6$). To be efficient as a click catalyst, the Cu^{1+} species should be well solubilized in the reaction medium.

Mixtures of water and *tert*-butanol are frequently used as solvents in click chemistry. These solvent mixtures are however much too hydrophilic for the hydrophobic borate salts **12** or **20**, while THF has proven to be an excellent solvent for both. However, to provide a sufficient solubilization of Cu^{1+} in THF, a suitable Cu^{1+} ligand is required. In the group of *V. V. Fokin*, a very effective Cu^{1+} ligand has been developed.[195] This ligand, *Tris*-(**b**enzyltriazolylmethyl)**a**mine or "TBTA" **28**, is itself synthesized by a click reaction (threefold 1,3-dipolar cycloaddition of benzyl azide **27** to tripropargylamine **26**).

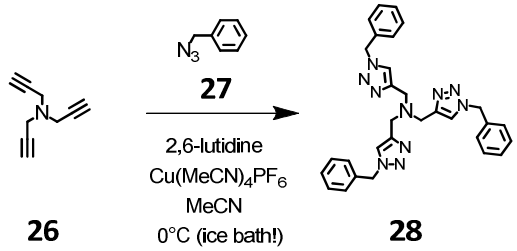

Figure 60: Synthesis of the Cu^{1+} stabilizing ligand TBTA as described by *V. V. Fokin et al.*[195]

During the large scale synthesis of TBTA (ca. 17 g) for this work, it was realized that the reaction does generate considerable amounts of heat. Precautions should be taken to cool down the reaction mixture sufficiently and in due time! The ligand forms very stable

complexes with Cu^{1+} and Cu^{2+} ions. Both complexes have already been analyzed by single crystal X-ray diffraction.[196] The complex formed with Cu^{1+} is displayed in Figure 61.

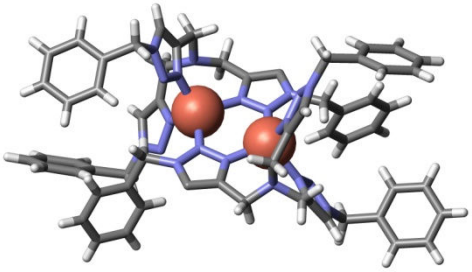

Figure 61: Single crystal sturcture of a dimer of the TBTA-Cu^{1+} complex (TBTA: stick model; copper ions: cpk model)[196]

As evidenced by the crystal structure, the triazole rings are able to coordinate to the cationic Cu^{1+} species. In the dimers displayed above (Figure 61), the two Cu^{1+} ions are both coordinated tetrahedrally. One of the three triazole rings of each TBTA molecule bridges two copper ions by binding to both of them at the same time.

The stability of the TBTA-Cu^{1+} complex is also evidenced by MALDI-TOF spectra of the compound. It seems that during the synthesis of TBTA (see Figure 60), newly formed TBTA ligands retain Cu^{1+} ions so relentlessly that the complex is the major species that can be detected (see Figure 62).

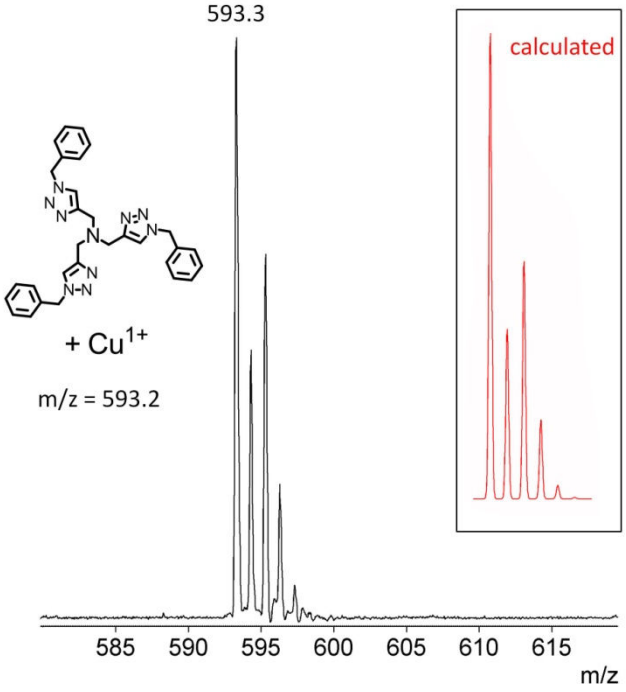

Figure 62: MALDI-TOF of TBTA **28** retaining Cu^{1+} form synthesis; inset: calculated isotope pattern

The ligand TBTA was used to enable clicking the large and bulky azide **25** onto ethynyl functionalized borate **12** at room temperature, using THF as the reaction medium (see Figure 63).

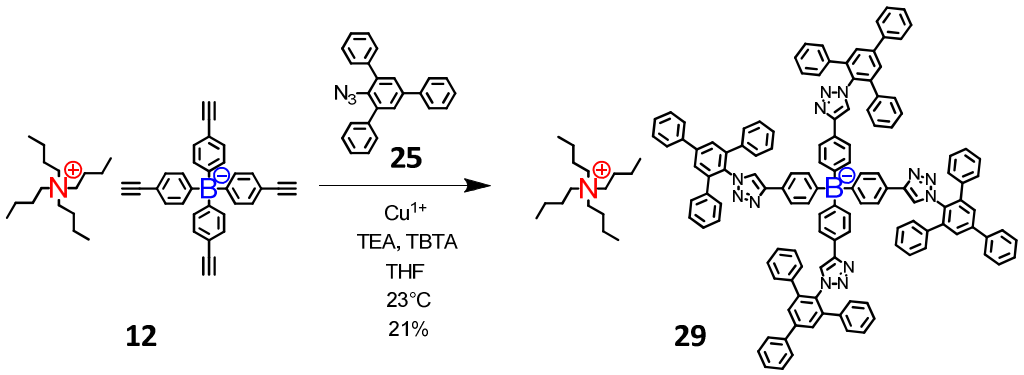

Figure 63: Synthesis of dendronized borate **29** via 1,3-dipolar cycloaddition at room temperature

The Cu^{1+} catalyzed 4-fold click reaction of bulky azide **25** to borate **12** was successful despite the ionic nature of substrate **12** (and thus potentially disruptive electrostatic interactions between the copper ion and the borate). It is noteworthy that the resulting borate **29** showed a pronounced tendency to form aggregates, which made its purification difficult. As evidenced by a slightly blue-greenish color cast of its solutions, a certain amount of copper ions was retained in **29**. In contrast to polyphenylene dendronized borate **14**, click-dendronized borate **29** could be eluted only partially after adsorption onto silica: Aggregation as well as strong adhesion to silica caused a significant reduction of the yield.

Nevertheless, with the positive proof of principle for the general applicability of click chemistry for borate dendronization, the next task was the synthesis of a second generation dendronized borate via the click method. Hence, first generation PP dendronized and ethynyl functionalized borate **20** was used as the substrate for the 8-fold dipolar cycloaddition of bulky azide **25** (see Figure 64).

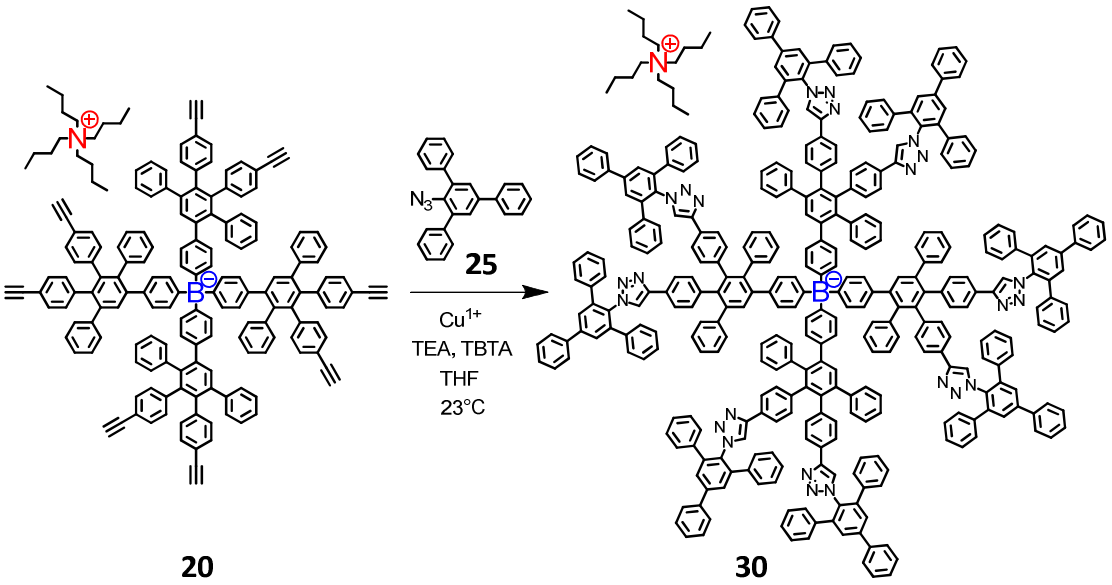

Figure 64: Synthesis of a second generation dendronized borate **30** via 1,3-dipolar cycloaddition at room temperature

The supposed product **30** was purified several times by means of column chromatography and precipitation. ^{1}H-NMR spectra of the product confirmed complete conversion of all eight ethynyl groups of the starting compound **20**, but not all of the measured signals could be assigned to the desired structure **30**. Moreover, instead of the expected 1:1 ratio of TBA^{+} cation to borate anion, a ratio of about 3:1 was found. Due to lack of a mass spectrometric proof (see also chapter 3) and apparently insufficient purification, it could not be decided conclusively whether the reaction towards borate **30** was successful.

Overall, the applicability of click chemistry for the generation of weakly coordinating anions seems fairly limited. In addition to the difficult purification of the products, there are also inherent structural drawbacks of click-dendronized borates as compared to purely polyphenylene dendronized ones:

Although the azide building block **25** has been chosen as to ensure a maximum of rigidity in the resulting anion structures, the introduction of five-membered triazole rings certainly reduces the overall rigidity of the anion due to an accompanied angulation of the otherwise rectilinear polyphenylene backbone.

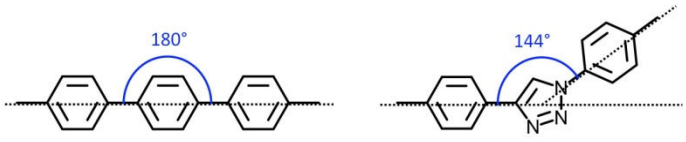

Figure 65: Comparison of a rigid *para*-phenylene and an angulated triazole-phenylene backbone

Furthermore, the nitrogen atoms of triazole possess free electron pairs and will thus serve as considerably strong coordination sites (see for example the effective coordination of Cu^{1+} by triazole groups in the ligand TBTA; Figure 61 and Figure 62). As mentioned earlier (see the guidelines for the design of WCA; paragraph 1.3.3.3), the presence of nucleophilic sites will drastically reduce the ability of any anion to serve as a weakly coordinating anion and should thus be avoided.

From a more general perspective, however, the above described methodology could be used for the synthesis of relatively rigid, largely extended and nitrogen rich dendritic architectures at room temperature (see chapter 3).

2.2.4 Increase of Anion Shell Density via Modification of the Core

As described in the sections above (paragraphs 2.2.2 and 2.2.3), dendritic growth of functionalized borate **12** to larger than first generation species was not successful. Despite the apparent limitation in size, the weakly coordinating properties of **14** (compare paragraph 6.5.1.1) might be further enhanced by an increase of the polyphenylene density of its shell. A more densely packed shell should lead to more efficient steric screening of the central charge and thus help to reduce the anions tendency to coordinate.

Two ways to achieve a higher polyphenylene density in a first generation dendronized borate have been conceived (see paragraphs 2.2.4.1 and 2.2.4.2).

2.2.4.1 Synthesis of a Highly Ethynyl Functionalized Tetraphenylborate

A way of potentially doubling the polyphenylene density around a first generation dendronized borate is the synthesis of tetraphenylborate **34** (Figure 66) functionalized with eight instead of just four ethynyl functions. The required ligand **33** was synthesized from 1,3,5-bromobenzene **31** via selective iodination and subsequent selective *Sonogashira* coupling of T*i*PS-acetylene to the resulting 1-bromo-3,5-diiodobenzene **32** (Figure 66).

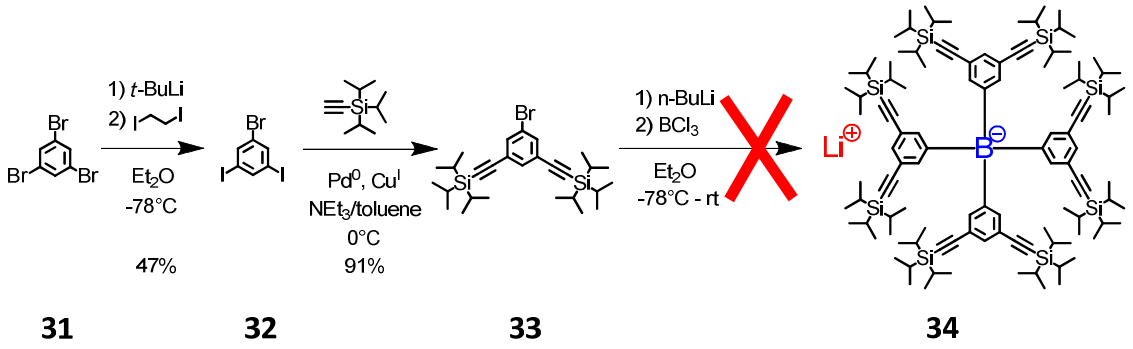

Figure 66: Synthesis of a highly ethynyl functionalized borate core **34** (failed!)

However, introduction of ligand **33** to boron failed due to its considerably large steric demand (see also paragraph 2.1). Without an additional spacer to disencumber the borate and prevent steric overcrowding, the number of ethynyl groups might not be increased (see paragraph 2.2.1).

2.2.4.2 Synthesis of an Ethynyl-Phenyl Functionalized Tetraphenylborate

The total number of phenyl rings in the shell of a first generation dendronized borate could also be increased by substituting each of the generation protons of borate **14** with a phenyl ring. Substitution could be achieved by using the ethynyl-phenyl functionalized borate **36** (Figure 67) instead of solely ethynyl functionalized borate **12** as the core. The synthesis of a non-charged tetraphenylmethane analogue of **36** and its conversion to a more densely packed first generation PPD has already been reported by *U. Wiesler*.[113,114] For the synthesis of the salt analogue **36**, tolane ligand **35** was synthesized via selective *Sonogashira* coupling and treated with butyl lithium and boron trichloride in diethyl ether (Figure 67).

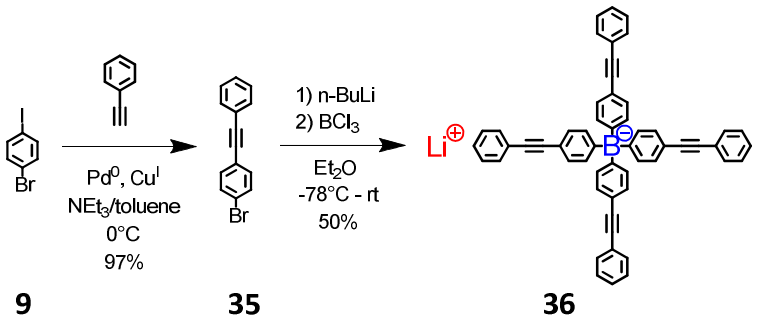

Figure 67: Synthesis of ethynyl-phenyl functionalized borate **36**

The hygroscopic nature of borate **36** made its general handling difficult. After deliberate cation exchange to the according TBA^+ salt **37**, the borate could be handled and weighted without complication (Figure 68).

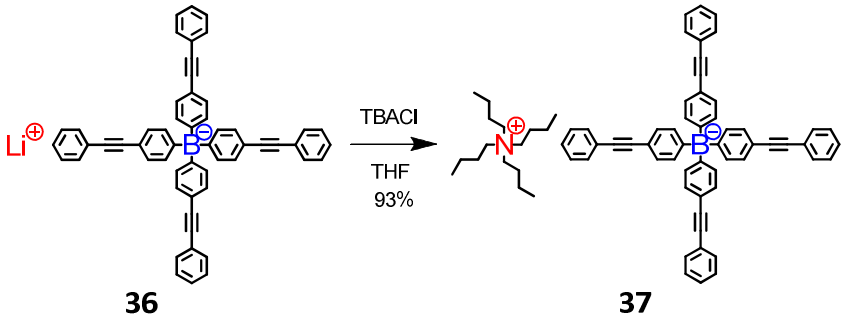

Figure 68: Cation exchange towards TBA^+ salt **37**

In addition to facilitated handling, borate **37** could now also be crystallized into transparent needles of up to 3 mm length. Its crystal structure reveals a significant bending of some of the otherwise linear phenyl-ethynyl-phenyl arms due to packing effects in the crystal lattice (Figure 69).

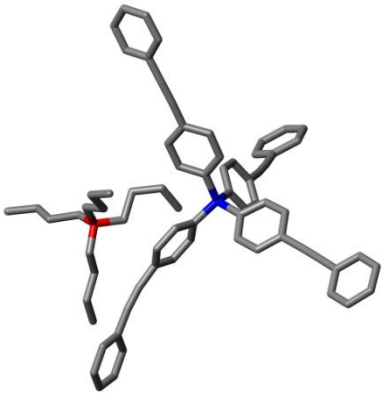

Figure 69: Single crystal structure of borate salt **37** (stick model; hydrogen atoms and solvent molecules omitted for clarity)

Unfortunately, however, the synthesis of more highly shielded borate **38** via dendronization of borate **37** with polyphenylenes was not successful (see Figure 70).

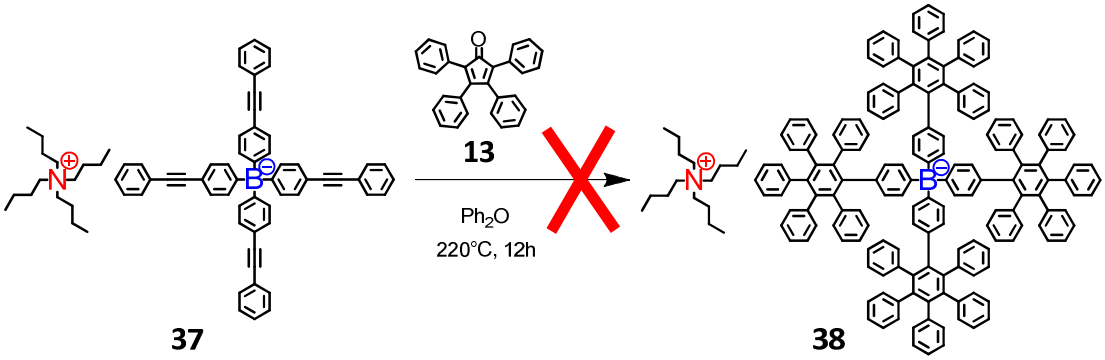

Figure 70: Synthesis of first generation dendronized borate **38** with a more dense PP shell as compared to borate **14** (failed!)

Most probably, the even higher temperature (>220 °C as compared to only 150 °C) required for the cycloaddition of **13** to internal (in contrast to terminal) ethynyl functions accelerates premature decomposition of borate core **37** and potential intermediates towards **38**. In addition, the resulting dendrons of **38** bear a larger steric pressure as compared to the dendrons of "normally" dendronized borate **14**. Consequentially, the only intermediate that could be detected by means of MALDI-TOF was the species resulting from a one-fold cycloaddition of tetracyclone **13** to borate **37**. The core **37** can thus not be used to generate more highly shielded dendronized borates.

2.2.5 Fluorination of the Anion Surface

Attempts of generating more weakly coordinating borates (as compared to **14**) by either increasing borate size or borate shell density did not succeed thus far due to synthetic constraints (see 2.2.3 and 2.2.4). However, an extremely efficient means of further decreasing an anions tendency to coordinate is the fluorination of its surface. Most weakly coordinating anions possess highly fluorinated surfaces (see 1.3.3). A fluorinated surface is both hydrophobic and lipophobic at the same time, in addition to being chemically robust and inert. More importantly, however, fluorine atoms can hardly be polarized due to their unmatched electronegativity. The low polarizability of fluorine causes a suppression of even tiny and temporary attractive forces (dispersive interactions) towards other molecules. Thus, fluorinated anions are considerably less coordinating as compared to their non-fluorinated analogues. As a consequence, the two borate species most commonly used as WCAs are the either fully perfluorinated or the *meta*-CF_3-functionalized tetraphenylborate (see paragraph 1.3.3.3, Figure 36, species (B) and (C)). An analogous

surface fluorination of dendronized borate **14** might be achieved by using highly fluorinated tetracyclone building blocks.

2.2.5.1 Surface Fluorination with Perfluorinated Phenyl Moieties

The synthesis of a fully surface fluorinated analogue of dendronized borate **14** requires a fully perfluorinated tetracyclone **40** (Figure 71). Such building block has already been described[197,198] and has been used for the synthesis of asymmetric, partly perfluorinated PPDs.[39] In contrast to the original synthetic strategy, which starts from acetylene,[39] the required perfluorinated tolane **39** was generated from 1,2-bis(tributylstannyl)ethyne), which gives better yields (75% as compared to 45%) and reduces the number of required reaction steps to only one. The synthesis utilizes a recently developed *Stille* coupling protocol which enables the coupling even of electron poor compounds.[199] Perfluorinated tolane **39** could then be converted to the desired perfluorinated tetracyclone building block **40** according to the literature procedure[39] (see Figure 71).

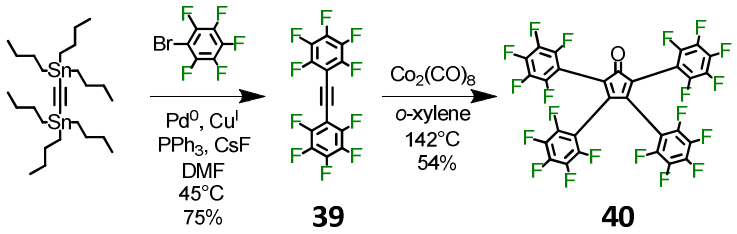

Figure 71: Improved synthesis of perfluorinated tetracyclone building block **40**

Perfluorinated tetracyclone **40** has a distinctly orange-red color in the solid state as compared to the dark violet to almost black color of other non-fluorinated tetracyclones. It was crystallized in the form of triclinic red plates, which were used for crystal structure determination by means of X-ray diffraction (Figure 72).

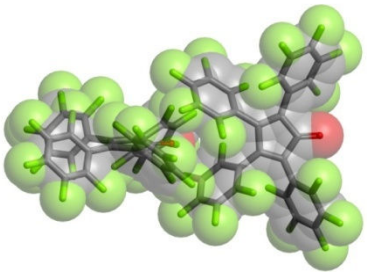

Figure 72: Single crystal structure of perfluorinated tetracyclone **40** (two molecules displayed to show stacking; overlay of cpk and stick model)

In the crystal, tetracyclone **40** forms parallel rows (alternately oriented in opposite directions) of molecules stacked behind one another. Density functional calculations (B3LYP, 6-31G*; based on geometric parameters obtained by crystal structure analysis) indicate a decrease of molecular orbital energy levels of perfluorinated tetracyclone **40** (HOMO: -6.83 eV; LUMO: -3.78 eV) as compared to non-fluorinated tetracyclone **13** (HOMO: -5.41 eV; LUMO: -2.70 eV). The decrease of molecular orbital energy levels does not affect the mechanism of *Diels-Alder* cycloaddition, since reactions with either tetracyclone **13** or **40** are both with an inverse demand of electrons.

For the generation of a surface fluorinated first generation dendronized borate **41**, perfluorinated tetracyclone **40** was cycloadded to ethynyl functionalized borate salt **12**.

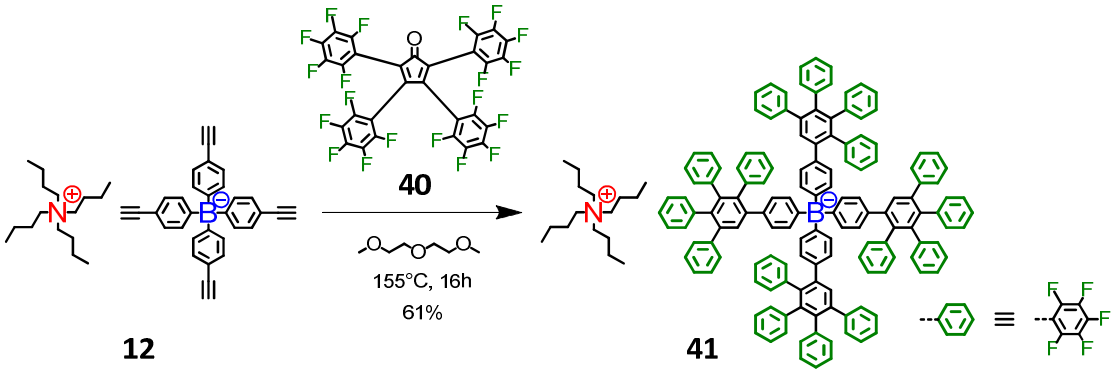

Figure 73: Divergent synthesis of a surface fluorinated, first generation polyphenylene dendronized borate **41** via cycloaddition of perfluorinated tetracyclone **40** to ethynyl functionalized borate **12**

The synthesis of surface fluorinated borate **41** via *Diels-Alder* cycloaddition could be performed successfully as evidenced by MALDI-TOF mass spectrometry (Figure 74).

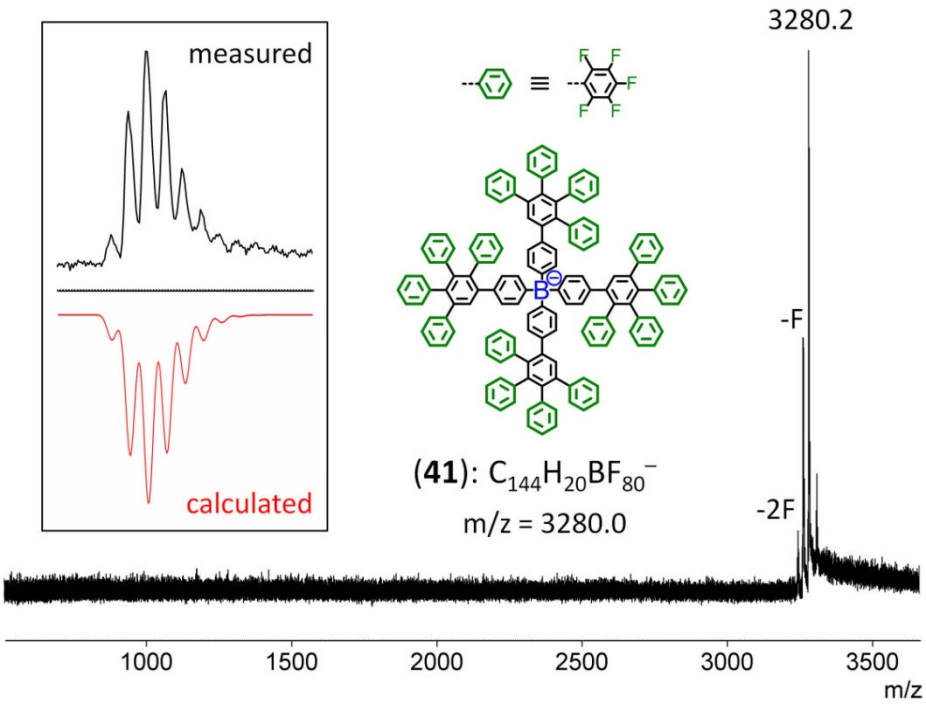

Figure 74: MALDI-TOF of dendronized and surface fluorinated borate **41**; inset: comparison of measured and calculated pattern of isotope distribution

In addition to the compound signal at $m/z = 3280$, two signals at lower m/z ratios (each with a Δm of 19) were detected. These can be assigned to species of borate **41** where one or two of the surface fluorine atoms have been cleaved off, respectively. The partial loss of fluorine occurs during MALDI-TOF measurement, which requires irradiation of the compound with a strong UV laser.

The tetrabutylammonium salt of borate **41** could even be crystallized in the form of transparent yellow needles. These needles were used for a determination of the salts crystal structure by means of X-ray diffraction (see crystal structure in Figure 75).

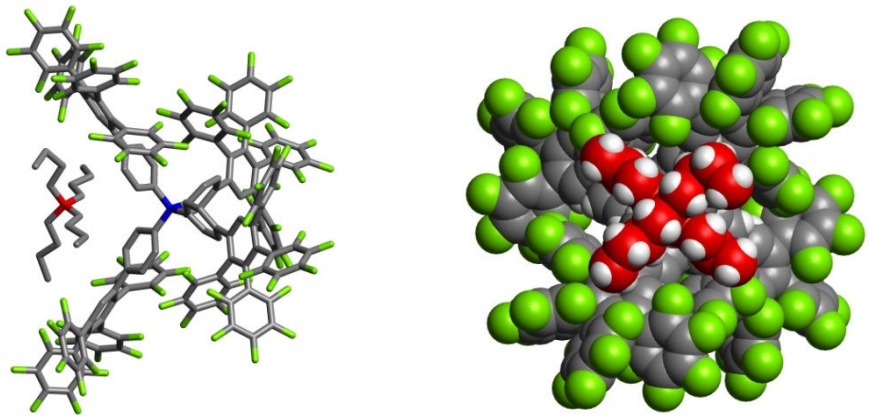

Figure 75: Single crystal structure of borate salt **41**; left: stick model (hydrogen atoms and solvent molecules omitted for clarity); right: frontal view of a space filling model (TBA^+ carbon atoms in red for better contrast)

Surface fluorinated borate **41** should be even less coordinating than borate **14** due to the dispersion forces suppressing effect of its highly fluorinated surface, which acts in addition to the steric shielding provided by the polyphenylene shell.

In a PPD scaffold, the twisted alignment of individual phenyl rings relative to each other should disrupt their electronic conjugation. Despite that twisted alignment, however, the fluorinated phenyl rings of borate **41** seem to have a significant electronic effect on neighboring phenyl rings, which is evidenced by a considerable shift of proton signals in the ^1H-NMR spectrum of borate **41** ((A) in Figure 76) as compared to its non-fluorinated analogue borate **14** ((B) in Figure 76).

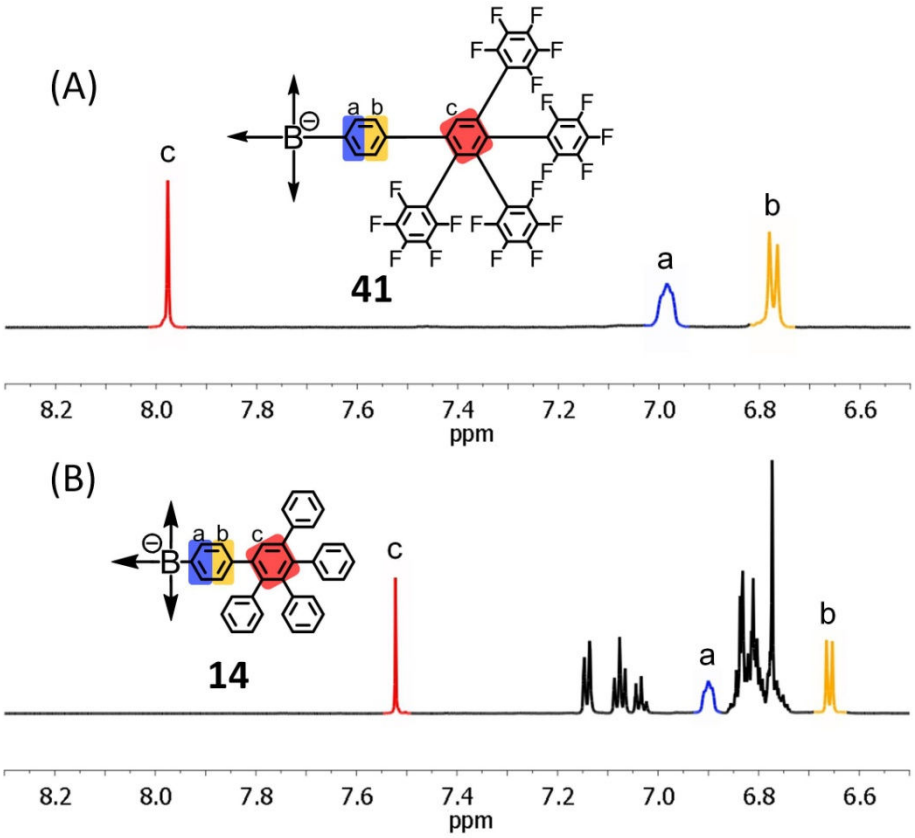

Figure 76: Comparison of ^{1}H-NMR spectra of surface fluorinated dendronized borate **41** (top (A); 500 MHz) and non-fluorinated dendronized borate **14** (bottom (B); 700 MHz) in THF-d8

The characteristic sharp singlet attributed to the generation proton H^c (marked red in Figure 76) is strongly shifted towards lower field from 7.52 ppm in non-fluorinated borate **14** to 7.98 ppm in surface fluorinated borate **41**, probably due to a withdrawal of electron density by fluorine. Moreover, even the innermost aryl rings of the borate core (bearing both protons H^a and H^b) are affected by surface fluorination, despite the fact that these rings are not even directly connected to fluorinated phenyl rings themselves. While the low field shift of their proton signals H^a and H^b is less pronounced than that of H^c, a shift can clearly be observed nevertheless. The observed low field shifts are probably caused by the electron withdrawing effect of the fluorinated phenyl rings at the borate surface. In contrast, the singlet observed in the ^{11}B-NMR spectrum shifts high field in surface fluorinated borate **41** (δ = -4.91 ppm) as compared to non-fluorinated borate **14** (δ = -6.95 ppm).

Geometric parameters of the crystal structures were used to calculate and compare the electrostatic surface potentials (ESPs) of first generation dendronized borates **14** (no

fluorinated surface) and **41** (fluorinated surface, see Figure 77) using semi-empirical methods (AM1).

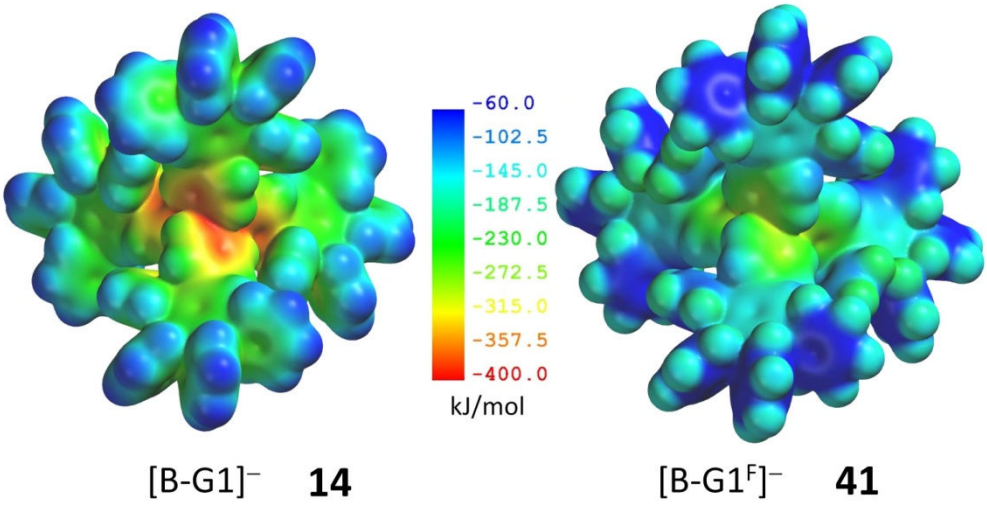

Figure 77: Electrostatic surface potentials of first generation dendronized borates **14** (left, without fluorinated surface) and **41** (right, with fluorinated surface) based on semi-empirical AM1 calculations

In the above illustration of the ESPs of borates **14** and **41**, colors at the red end of the spectrum indicate the most negative electrostatic potential. Red to yellow colors therefore highlight parts of a molecule that attract positive charges most strongly. As expected, the negatively charged boron core possesses the most negative ESP in both borates. However, despite the twisted alignment of fluorinated and non-fluorinated phenyl rings, fluorinated rings at the surface clearly reduce the negative potential at the core of borate **41** as compared to borate **14**. Differences in the ESPs of both borates also reflect the observed differences in proton chemical shifts in the NMR spectra (see Figure 76).

Another striking difference of surface fluorinated borate **41** to other PP dendronized borates is its strong orange-red (as compared to otherwise typically weak blue) fluorescence under UV light. The fluorescence of solutions of borate **41** precluded their analysis by means of dynamic light scattering (DLS). Figure 78 shows the normalized absorption (maximum at 420 nm) and emission (maximum at 571 nm) spectra of surface fluorinated borate **41** in THF. The origin of the borates fluorescence is not yet fully understood, but it is clear that the electron-withdrawing fluorinated surface and the central negative charge of the anion both are crucial factors.

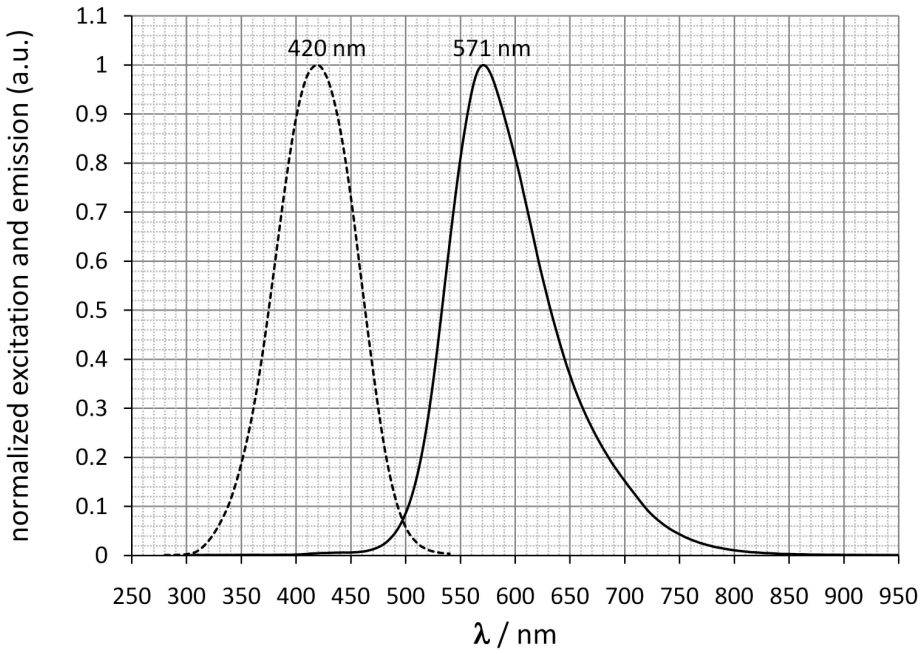

Figure 78: Absorption and emission spectra of surface fluorinated borate **41** in THF

Without the central negative charge, this type of fluorescence is not observed: A first generation PPD with the same chemical structure and perfluorinated surface but a neutral tetraphenylmethane core shows only weak blue fluorescence (absorption at about 342 nm; emission at about 416 nm).

Interestingly, permanent irradiation of borate **41** with UV light (254 nm) leads to an irreversible change of the absorption and emission spectra (compare 2D plots of absorption vs. emission before and after UV irradiation in Figure 79). UV irradiation apparently drives the cleavage of single dendrons from the borate core. The cleaved-off fluorinated dendrons show an absorption maximum at about 330 nm. In a previously UV irradiated mixture containing both cleaved-off dendrons and intact borate **41**, an excitation at about 330 nm leads to a cascade-like transfer of energy via fluorescence of the dendron at 403 nm, re-absorption by the borate and fluorescence of the borate at 555 nm (see 2D absorption vs. emission plot (B) in Figure 79).

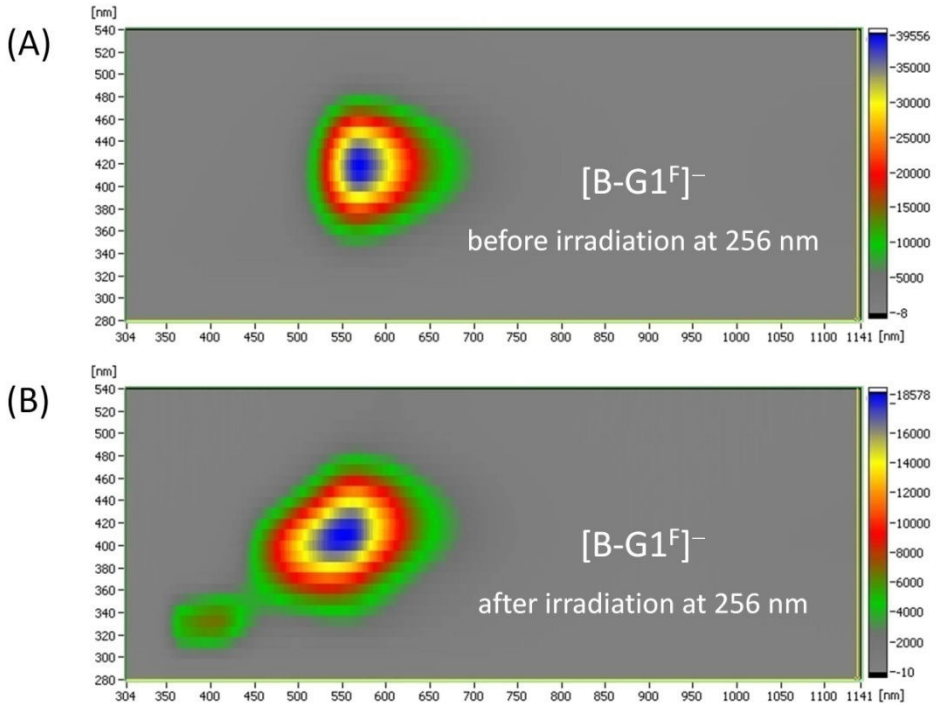

Figure 79: 2D plot of absorption and emission spectra of surface fluorinated borate **41** in THF before and after exposure to UV irradiation (254 nm); colors indicate counts of the photodetector

2.2.5.2 Surface Fluorination with CF_3-functionalized Phenyl Moieties

In the previous part 2.2.5.1, the successful surface fluorination of a dendronized borate has been presented. Alongside full perfluorination, the introduction of perfluorinated methyl groups CF_3 has also proven a very effective measure to enhance the weakly coordinating properties of tetraphenylborates[178-181,184] and other anions.[176] The bulkiness and larger spatial demand of the CF_3 group (as compared to fluorine alone) also increases steric shielding in addition to the general suppression of dispersive interactions provided by fluorine.

Consequently, attempts were made to synthesize a highly CF_3 functionalized analogue **44** (Figure 81) of tetracyclone **13** by the procedure already described for perfluorinated tetracyclone **40** (Figure 71, part 2.2.5.1). The required CF_3 functionalized tolane **42** was obtained via *Stille* coupling of *meta*-CF_3-functionalized bromobenzene to bis(tributylstannyl)acetylene (Figure 80).

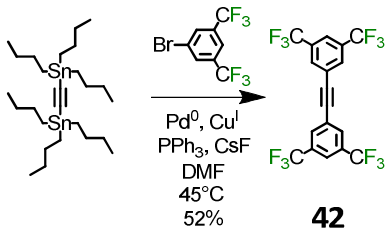

Figure 80: Synthesis of CF_3-functionalized tolane **42** via *Stille* coupling

Tolane **42** could however not be converted to the desired CF_3 functionalized tetracyclone **44**. Instead, only the intermediate cobalt carbonyl complex **43** was isolated (Figure 81).

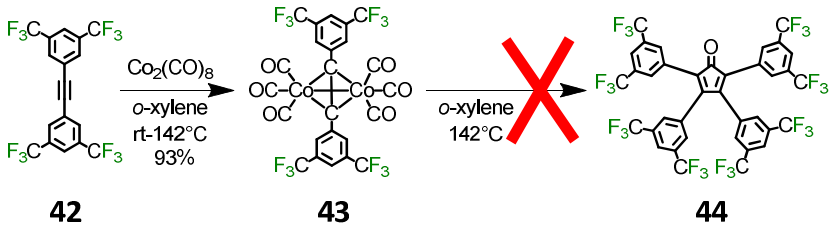

Figure 81: Synthesis of CF_3 functionalized tetracyclone **44** (failed!)

Increasing the reaction temperature from 142 °C to about 165 °C merely resulted in a decomposition of the cobalt carbonyl complex **43**, yielding a mixture of non identified products. As an alternative, tetracyclone **44** may be generated via the classic route of a *Knoevenagel* condensation of diphenylacetone and benzil (both CF_3 functionalized). The required benzil could be generated from tolane **42** via catalytic *Wacker* oxidation with O_2.[200] However, an even better solution is the synthesis of a tetracyclone with an extra phenyl spacer, yielding a bulkier, presumably more stable and yet highly CF_3 functionalized tetracyclone building block **47**. My colleague [redacted], who is also interested in the creation of fluorinated building blocks for PPD synthesis, successfully synthesized tetracyclone **47** via *Suzuki* coupling of *meta*-CF_3-functionalized bromobenzene to tetracyclone **46**. He also kindly supplied me with large amounts of the product **47** for my experiments.

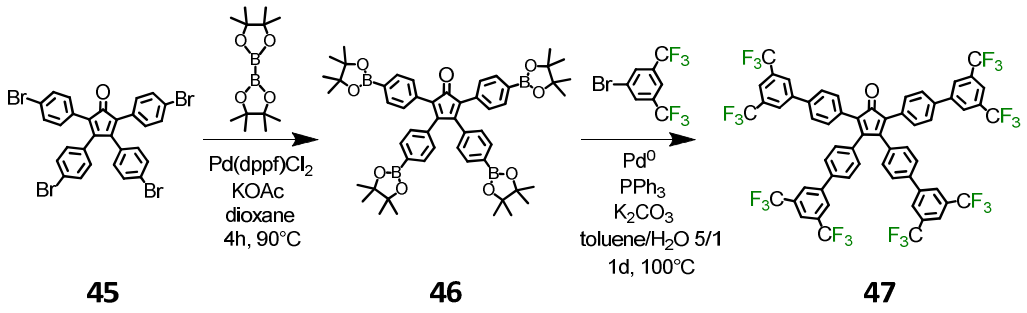

Figure 82: Synthesis of highly CF_3 functionalized tetracyclone **47** as developed and performed by [redacted]

In addition to being highly fluorinated, tetracyclone **47** might prove of value for generating more effective WCAs due to its even larger steric demand as compared to fluorinated tetracyclone **44**. The synthesis of highly CF_3 functionalized and bulky borate **48** was performed in *o*-xylene at 160 °C (see Figure 83).

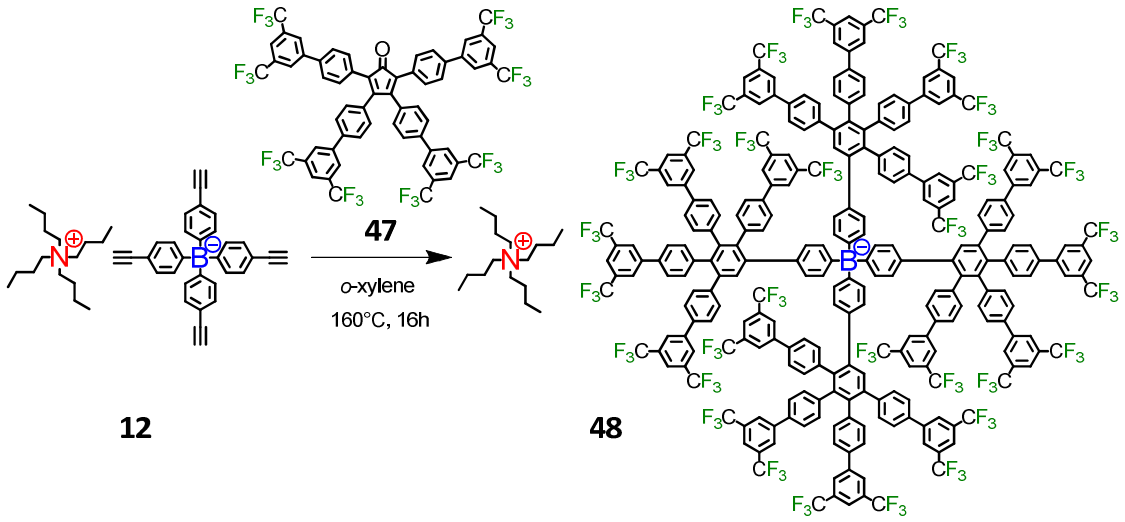

Figure 83: Divergent synthesis of highly CF_3 functionalized, first generation polyphenylene dendronized borate **48** via cycloaddition of CF_3 functionalized tetracyclone **47** to ethynyl functionalized borate **12**

After heating for several hours, the according product peak could indeed be detected by means of MALDI-TOF. However, mass spectrometry and ^{11}B-NMR spectroscopy also indicated that a number of side products had been formed during the reaction. While the obtained product mixture was thus not used for further tests, the experiments still clearly confirmed that a cycloaddition of bulky tetracyclone **47** to a borate core is possible in principle. Utilization of the CF_3 functionalized building block **47** was thus picked up again later on, when a more stabilized borate core was available (see paragraph 2.3.5.2).

2.3 Dendronized Anions based on Perfluorinated Tetraphenylborate

2.3.1 Introduction

In the above paragraph 2.2 of this chapter, the successful syntheses of different first generation dendronized borate salts based on ethynyl functionalized tetraphenylborate **12** have been described. All of these first generation dendronized borates represent larger and bulkier molecular anions than ever synthesized previously. However, attempts to further increase their density (see 2.2.4) or their overall size (see 2.2.2 and 2.2.3) by means of divergent dendritic growth were not successful: The insufficient thermal stability of the borate core imposed an upper limit as to how far the divergent dendritic growth of borates could be pushed in terms of size and density.

A potentially effective means of surpassing the size limit set by the thermal lability of borate **12** is its direct fluorination. Fluorination has already been used to successfully reduce the tendency of regular tetraphenylborates for B-C bond cleavage: The electron withdrawing effect of fluorine decreases the amount of negative charge at the ipso carbon atoms and thus helps stabilizing the B-C bond.[130] Such bond strengthening in fluorinated tetraphenylborates is evidenced by their immensely increased stability against *Brønsted* and *Lewis* acids[201,202] as well as oxidants.[181] Therefore, the synthesis of yet larger dendronized borates might be enabled by the synthesis of a perfluorinated analogue of ethynyl functionalized borate **12**.

2.3.2 Ethynyl-Functionalization of Perfluorotetraphenylborate

For the synthesis of a perfluorinated analogue of ethynyl functionalized borate **12**, a suitably functionalized ligand is required. The direct analogue of ligand **10**, which has been used for the synthesis of borate **12** (Figure 42, part 2.2.1), would be a fluorinated, ethynyl functionalized and singly brominated ligand **48** (Figure 84). In contrast to the non-fluorinated case (paragraph 2.2.1) however, a both bromo- and iodo functionalized tetrafluorobenzene is not commercially available. Therefore, ethynyl functionalization of commercially available fluorinated 1,4-dibromobenzene (Figure 84) requires a regulation of mono-functionality via stoichiometry.

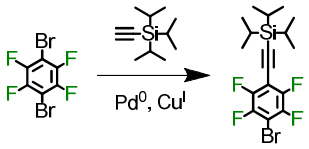

48

Figure 84: Stoichiometry regulated synthesis of fluorinated, ethynyl functionalized ligand **48** (not performed!)

Due to the significantly reduced reactivity of fluorinated aryl halides for coupling reactions, large amounts of homo-coupled T*i*PS-acetylene are generated as side product in addition to the desired coupling product. Thus, adjusting the stoichiometry as to achieve mono-functionalization towards **48** is a very intricate task. A conceivably better solution to obtain a suitable, mono-ethynyl functionalized ligand is the use of commercially available mono-brominated tetrafluorobenzene **49** instead (Figure 85). Now an excess of T*i*PS-acetylene can be employed to push the *Sonogashira* coupling towards complete conversion. Moreover, no separation of differently functionalized products is required.

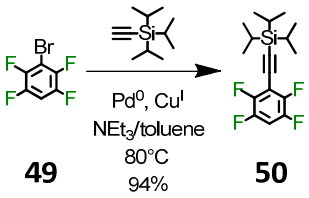

49 **50**

Figure 85: Synthesis of fluorinated, ethynyl functionalized ligand **50** for borate synthesis

The remaining aryl proton of ligand **50** possesses the highest C-H acidity of the molecule and hence defines the location where exchange to lithium occurs if the ligand is treated with a strong base such as *n*-butyl lithium (in direct analogy to the lithium-halogen exchange of brominated ligand **10**). Hence, no bromine function is required in ligand **50**.

Spin coupling of the fluorine nuclei of **50** to both the aryl proton and the aryl carbon atoms leads to very characteristic signal patterns in the NMR spectra, some of which are displayed in Figure 86.

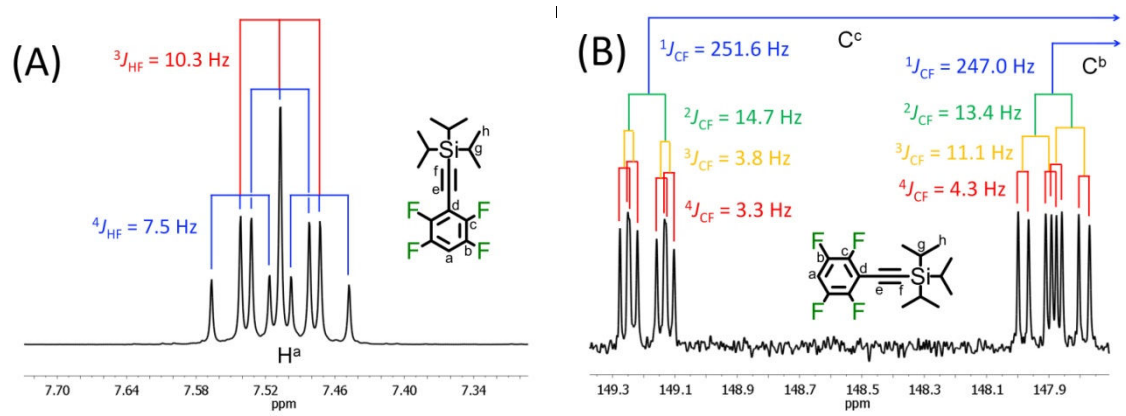

Figure 86: Details of NMR spectra of ligand **50** in THF-d8; (A): ^{1}H-NMR signal of the aryl proton H^a; (B): low field part of the ^{13}C-NMR doublet signals of aryl carbons C^b and C^c

In the case of aryl carbon atoms C^b and C^c, couplings to all of the four fluorine atoms of ligand **50** can be observed, giving rise to a doublet of doublets of doublets of doublets for for both nuclei (dddd, see Figure 86 (B)).

Ligand **50** was converted to the according T*i*PS-protected and fluorinated borate salt **51** (Figure 87). As mentioned earlier, fluorination of all but one position of aryl ligand **50** makes presence of a bromine function obsolete. After removal of the T*i*PS groups of salt **51** with tetrabutylammonium fluoride in THF, the desired ethynyl functionalized and fully fluorinated tetraphenylborate **52** was obtained.

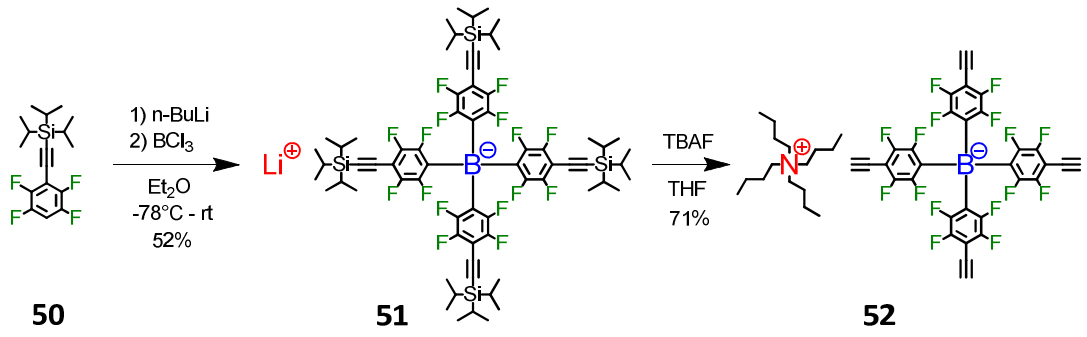

Figure 87: Synthesis of ethynyl functionalized and fully fluorinated tetraphenylborate **52**

Fluorination of the core has a significant effect on the ^{11}B-NMR signal of the central boron atom, which shifts towards high field from –6.50 ppm in non-fluorinated borate **12** to –15.95 ppm in fluorinated borate **52**. The high field shift indicates a better shielding of the central boron from the outer magnetic field in fluorinated borate **52** as compared to borate **12**, probably due to the generally increased number of electrons in proximity to the center.

In contrast to non-fluorinated borate **12**, fluorinated borate **52** may retain an excess of tetrabutylammonium cations (in the form of its chloride salt) even after filtration of its THF solution over silica. The presence of a mixed salt constituted of both **52** and TBA^+Cl^- does not affect its applicability for divergent growth, because excessive TBA^+Cl^- can easily and cleanly be removed from the borate salt after dendronization. Alternatively, borate salt **52** can be purified directly via precipitation in hexane and subsequent filtration of its methylene chloride solution over silica.

A salt of the defined, mixed composition $(TBA^+)_2[B(Ph^F\text{-}in)_4]^-Cl^-$ was used for producing crystals for a structure determination by means of X-ray analysis (Figure 88).

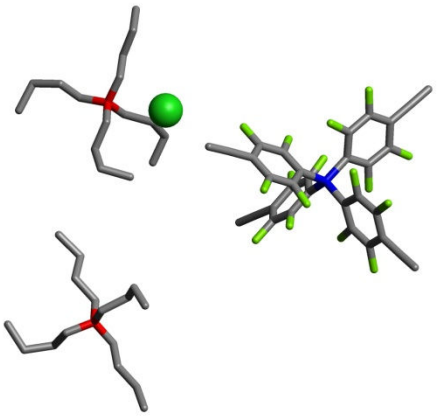

Figure 88: Single crystal structure of a salt constituted of both TBA^+Cl^- and borate salt **52**; (stick model; hydrogen atoms omitted for clarity)

The geometric parameters of the borate anion obtained from its crystal structure were then used to calculate the HOMO and LUMO energy levels of borate **52** using density functional methods (B3LYP, 6-31G*). These calculations indicate a decrease of the MO energy levels of perfluorinated borate **52**. Due to the comparatively low energy levels of the tetracyclone building blocks **13** and **40**, the decrease of the LUMO in fluorinated borate **52** is negligible with regard to the expected demand of electrons in the *Diels-Alder* cycloaddition. For all combinations of either fluorinated or non-fluorinated dienes (tetracyclones) and dienophiles (borates), cycloadditions with a reverse demand of electrons are expected (reaction of a diene´s LUMO with a dienophile´s HOMO).

2.3.3 Increase of Anion Size via Divergent Dendritic Growth

Fluorinated and ethynyl functionalized borate salt **52** was used for the synthesis of a first generation PP dendronized borate **53**, possessing a fluorinated core and thus a supposedly better thermal stability.

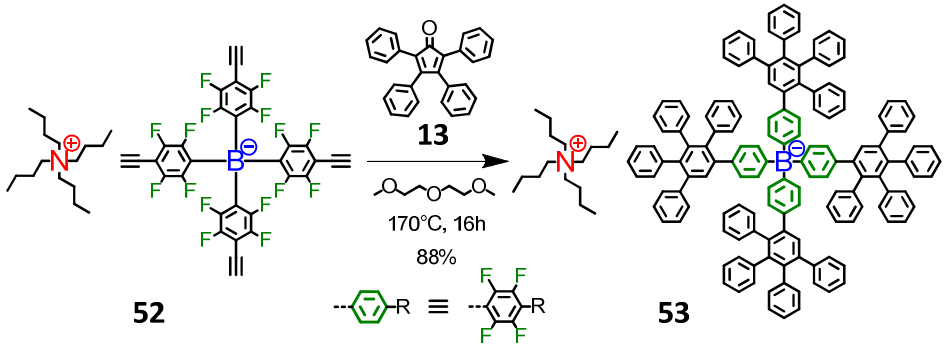

Figure 89: Divergent synthesis of first generation polyphenylene dendronized borate **53** with a fluorinated core via cycloaddition of tetracyclone **13** to fluorinated, ethynyl functionalized borate **52**

Despite the even slightly increased reaction temperature (170 °C instead of 160 °C), the amount of side products formed by thermal decomposition decreased significantly as compared to the cycloaddition reactions of borates based on the non-fluorinated core **12**. The reaction was monitored by means of MALDI-TOF mass spectrometry. These measurements confirmed complete conversion of borate **52** to rigidly dendronized borate **53** (Figure 90).

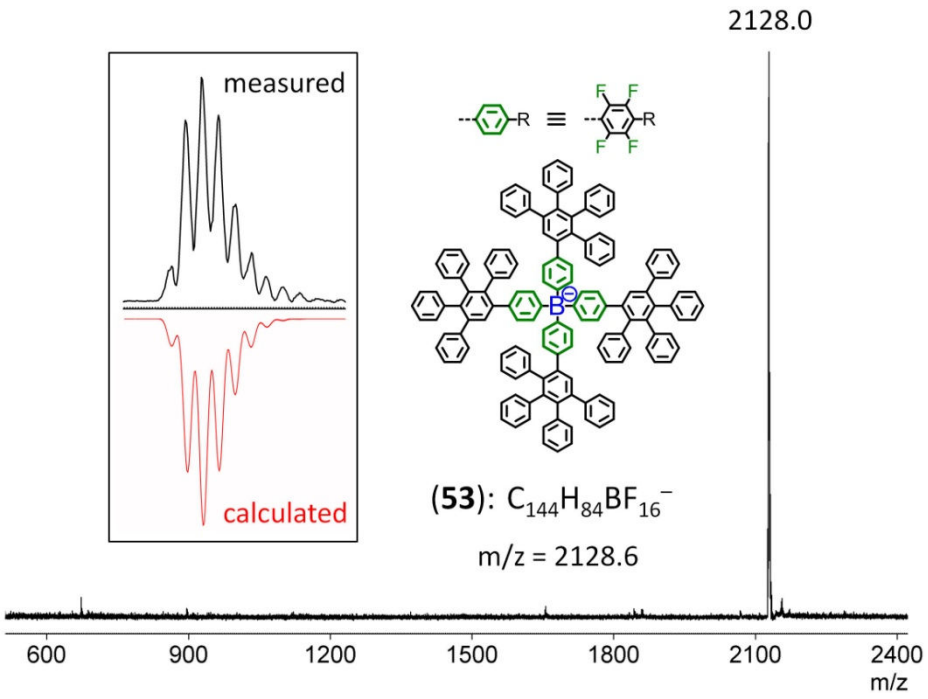

Figure 90: MALDI-TOF of dendronized borate **53**; inset: comparison of measured and calculated isotope distribution pattern of the peak

It was thus confirmed that the method of divergent dendritic growth can also be applied to borates featuring fluorinated cores. Due to its better thermal stability, fluorinated core **52** was expected to enable the synthesis of larger than first generation dendronized borates.

However, while MALDI-TOF mass spectrometry clearly confirmed a complete conversion of fluorinated core **52** to dendronized borate **53**, the ^{1}H-NMR spectrum of the product exhibited many surprising features (Figure 91). Instead of the expected sharp singlet of the generation proton H^c, which is typically observed in PPDs (see red marked signal of borate **14**, bottom (B) in Figure 91), more than 12 distinct singlets with different intensities and shifts were detected in the case of borate **53** (see red marked signal, top (A) in Figure 91). Other protons, such as H^d, H^e and H^f of the blue marked phenyl ring in Figure 91, also gave rise to a larger number of signals than expected.

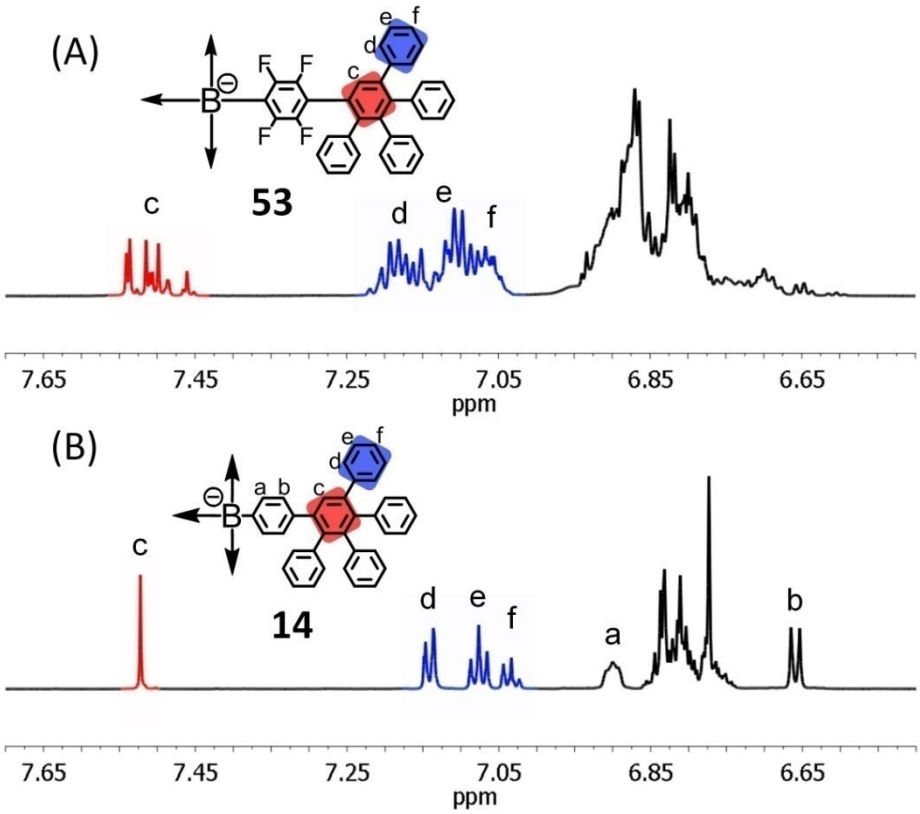

Figure 91: Comparison of ^{1}H-NMR spectra of dendronized borate **53** with a fluorinated core (top (A); 700 MHz) and dendronized borate **14** with a non-fluorinated core (bottom (B); 700 MHz) in THF-d8

The observed multiplication of NMR signals can be explained by the fact that different atropisomers of borate **53** exist. Fluorine atoms have a considerably larger covalent radius as compared to hydrogen atoms. The database of the Cambridge Crystallographic Data Centre (CCDC) specifies a value of 0.23 Å for the covalent radius of hydrogen, and 0.64 Å (nearly three times as large) for the covalent radius of fluorine. Comparison of the bond lengths obtained from the crystal structures of both borate cores **12** and **52** point to the same fact: The aryl C-H bond of borate **12** has a consistent length of 0.951 Å, while the aryl C-F bonds of borate **52** have significantly larger lengths ranging from 1.344 to 1.356 Å. In borate **53**, this increase in atomic size and steric demand leads to a hindrance of the rotation of dendrons about the core-dendron bond (see Figure 92), which eventually leads to the appearance of several atropisomers.

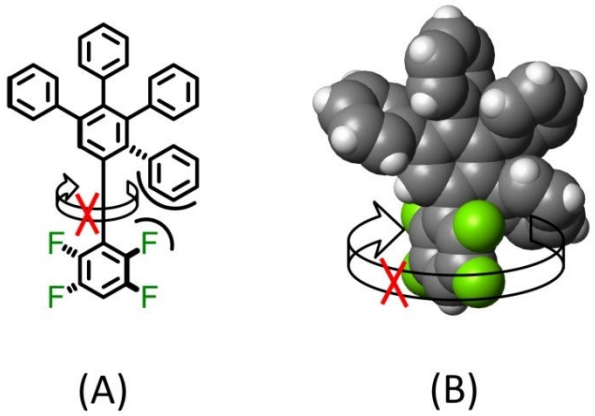

Figure 92: Hindrance of rotation of a single dendron about a fluorinated phenyl ring; (A): illustration with a *Lewis* structural formula; (B): illustration with a space filling model

At room temperature, thermal energy does not suffice to cause a fast enough equilibration between different isomers with regard to the NMR time scale. Hence, different signals are detected for chemically identical protons residing within different isomers or even within different dendrons of a single isomer.

Atropisomerism was observed for all borates based on the fluorinated core **52**. Its causes and effects will be discussed in much greater detail in chapter 5. For this chapter, it is sufficient to note that atropisomers occur, but that divergent dendronization of fluorinated tetraphenylborates can be successfully performed nevertheless.

The next task after successful synthesis of first generation dendronized borate **53** was utilization of the fluorinated core for the synthesis of a larger, second generation PP dendronized borate **56**. Therefore, the fluorinated core **52** was reacted with AB_2 building block **1** in diglyme at 170 °C (see Figure 93). The yield of T*i*PS-protected ethynyl functionalized borate **54** increased significantly (91%) as compared to the non-fluorinated analogue borate **18** (45%). Borate **54** was then activated for a subsequent growth step via deprotection of its ethynyl groups with TBAF in THF (Figure 93).

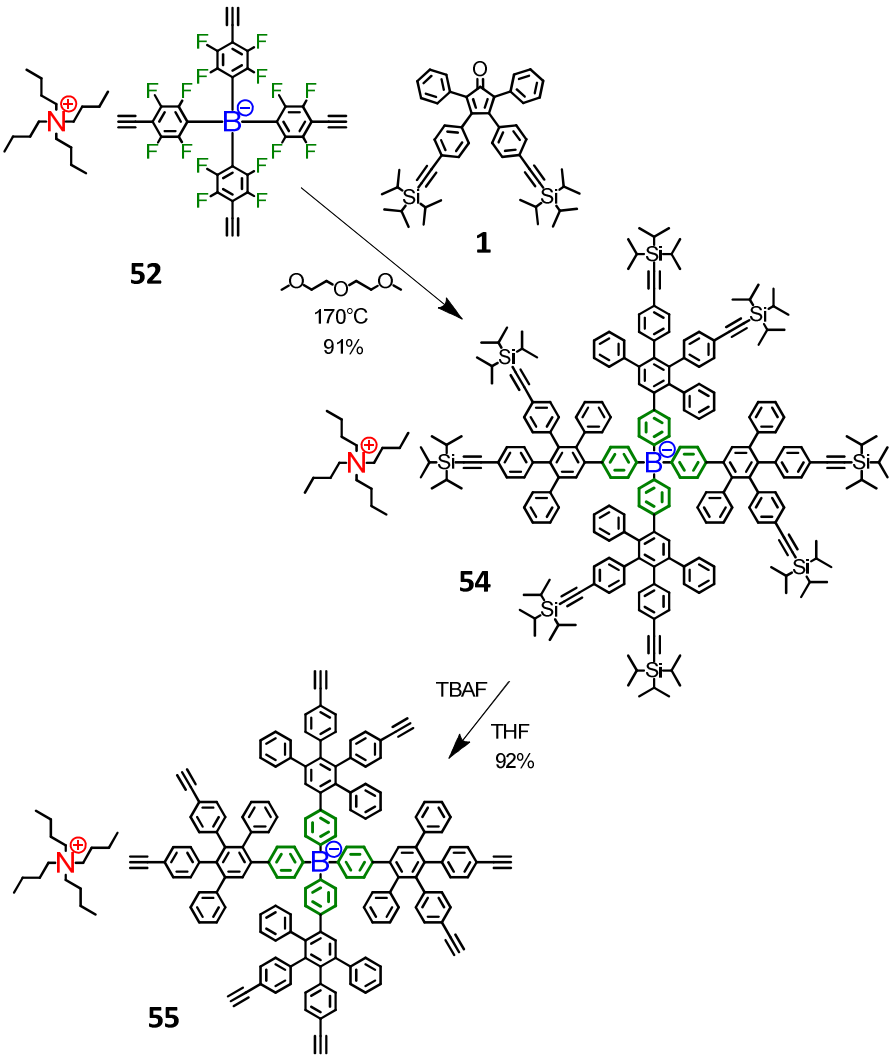

Figure 93: Synthesis of ethynyl functionalized first generation dendronized borate **55** with a fluorinated core

The obtained dendronized borate **55** was used for the second dendronization step with tetracyclone **13** in diglyme at 170 °C (Figure 94).

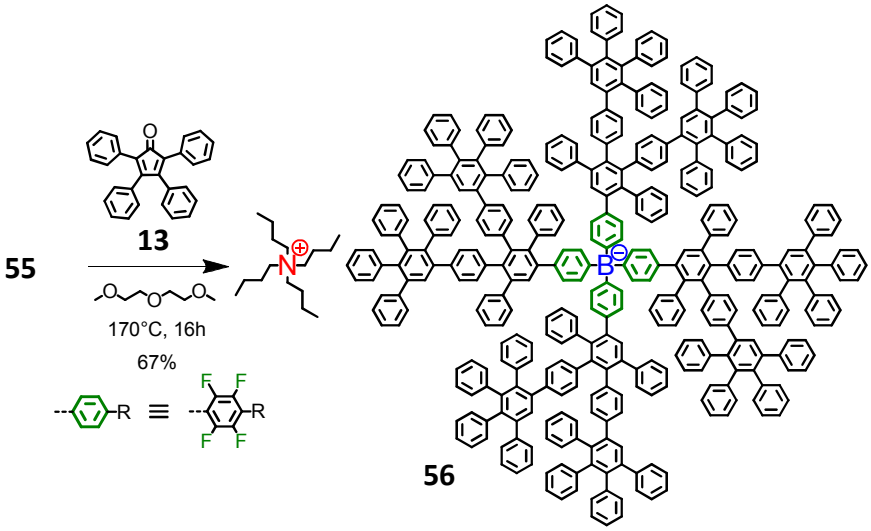

Figure 94: Divergent synthesis of a second generation polyphenylene dendronized borate **56** via cycloaddition of tetracyclone **13** to ethynyl functionalized first generation dendronized borate **55**

The reaction was monitored by means of MALDI-TOF mass spectrometry (see Figure 95). As evidenced by these measurements, the strategy of divergent dendronization could successfully be used to synthesize borate **56**, which represents the first example of a rigidly dendronized borate of second generation.

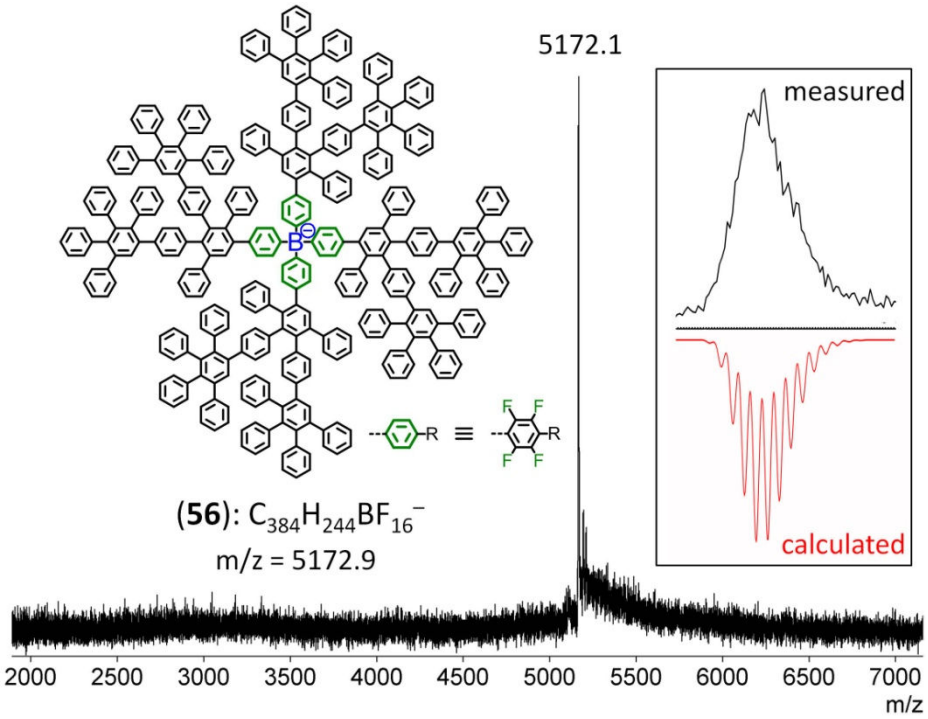

Figure 95: MALDI-TOF of second generation dendronized borate **56**; inset: isotope distribution pattern of the measured peak (not resolved!)

While the measured MALDI-TOF peak could clearly be assigned to the fully converted product, the isotope distribution pattern of the peak was not resolved anymore (see inset in Figure 95). Consequentially, isotope distribution patterns will only be displayed for first generation dendronized borates, where resolution is still sufficient.

Fluorination of the borate core has clearly proven to be an effective means for enhancing thermal stability and thus enable the synthesis of larger borates. Better steric screening by the enlarged PP shell of borate **56** as compared to first generation dendronized borate **53** should be reflected in a further reduction of the anion´s ability to coordinate to counterions (see paragraph 6.5.1.1).

In order to push divergent growth towards an even larger, third generation dendronized borate, ethynyl functionalized borate **55** was reacted with AB_2 building block **1**. The resulting second generation borate **57** was then deprotected with TBAF in THF, yielding ethynyl functionalized second generation borate **58** (Figure 96).

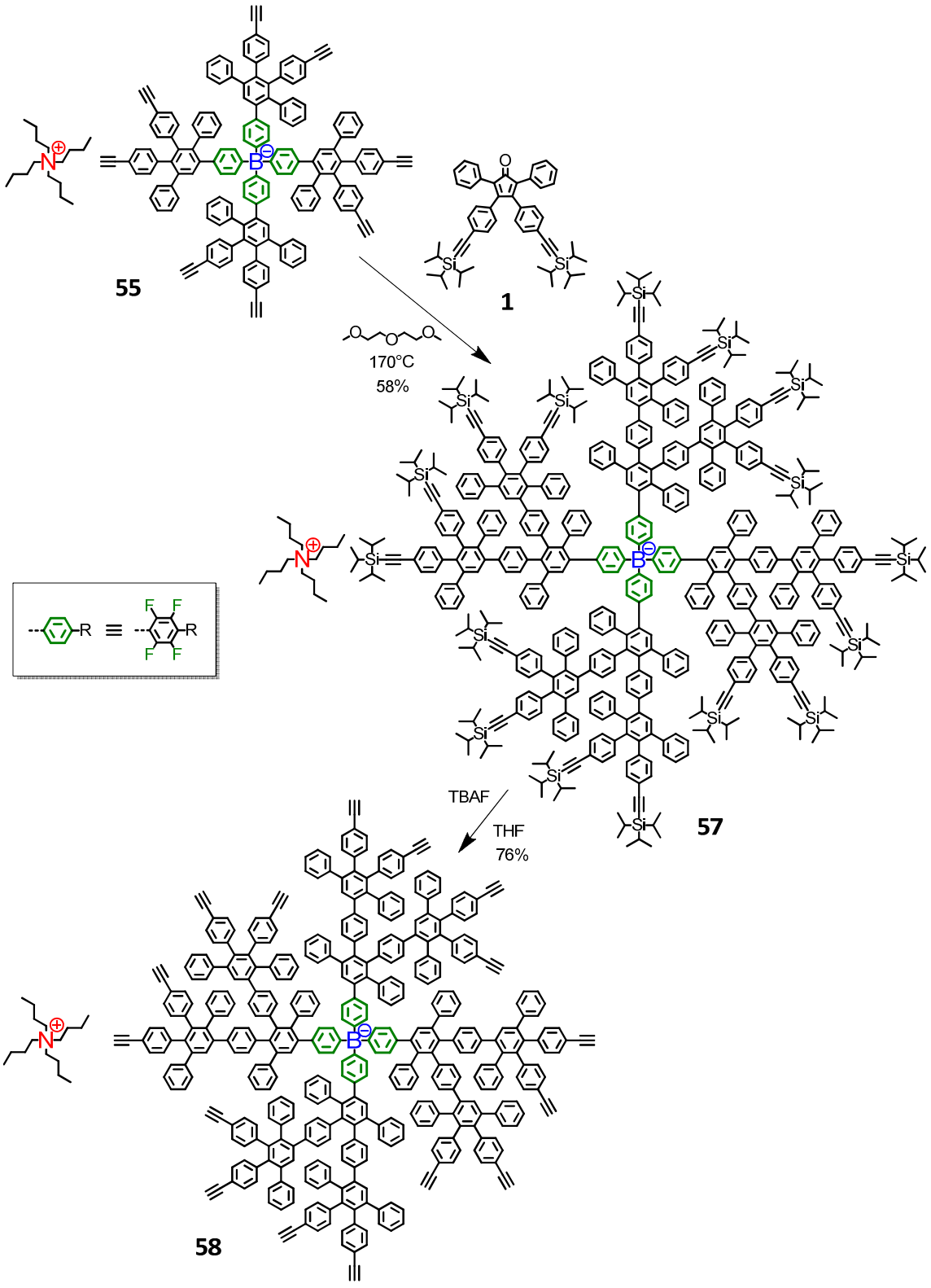

Figure 96: Divergent synthesis of ethynyl functionalized second generation dendronized borate **58** with a fluorinated core

The obtained second generation dendronized borate **58** was used for a third dendronization step with tetracyclone **13** in diglyme at 170 °C (Figure 97).

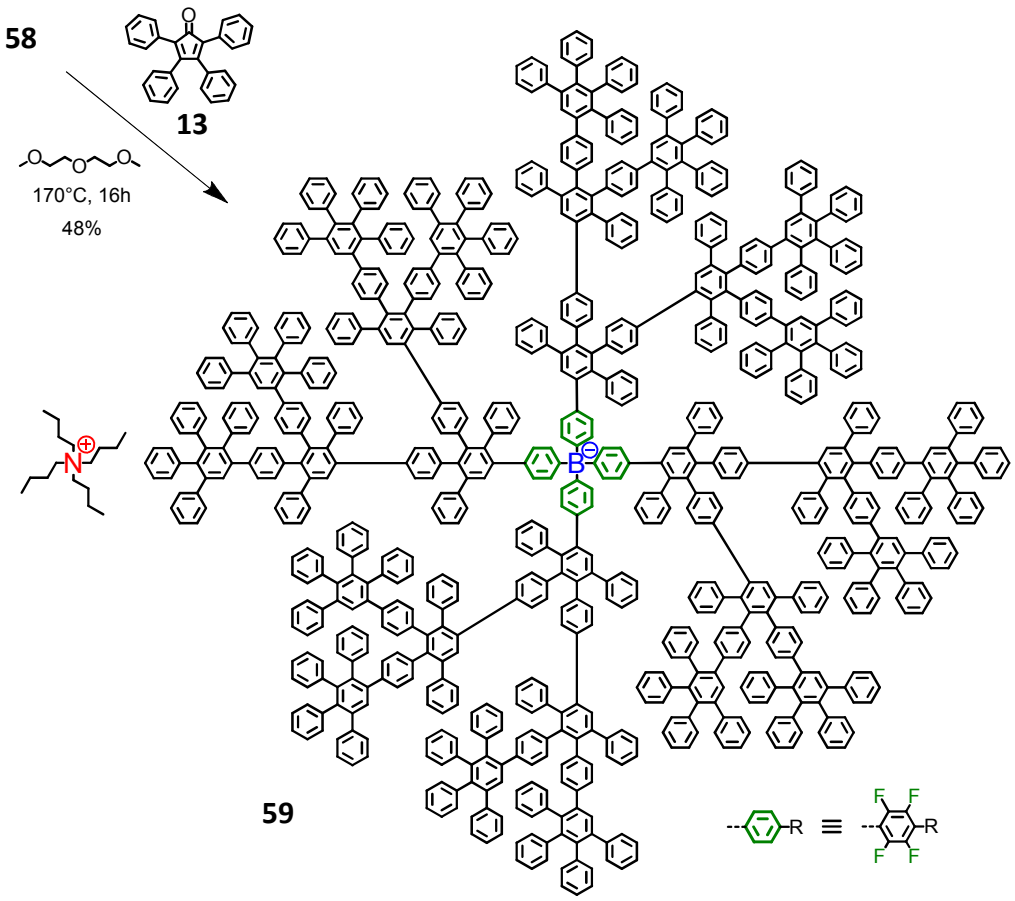

Figure 97: Divergent synthesis of a third generation polyphenylene dendronized borate **59** via cycloaddition of tetracyclone **13** to ethynyl functionalized second generation dendronized borate **58**

The reaction was monitored by means of MALDI-TOF mass spectrometry (see Figure 98). As evidenced by these measurements, the increased overall stability of the fluorinated borate core **52** is sufficient for enabling the synthesis of a third generation rigidly dendronized borate **59**. Thus, alternative methods of dendronization, such as the semi-convergent approach (paragraph 2.2.3.1) or the copper catalyzed addition of azides (paragraph 2.2.3.2), were not taken into consideration here.

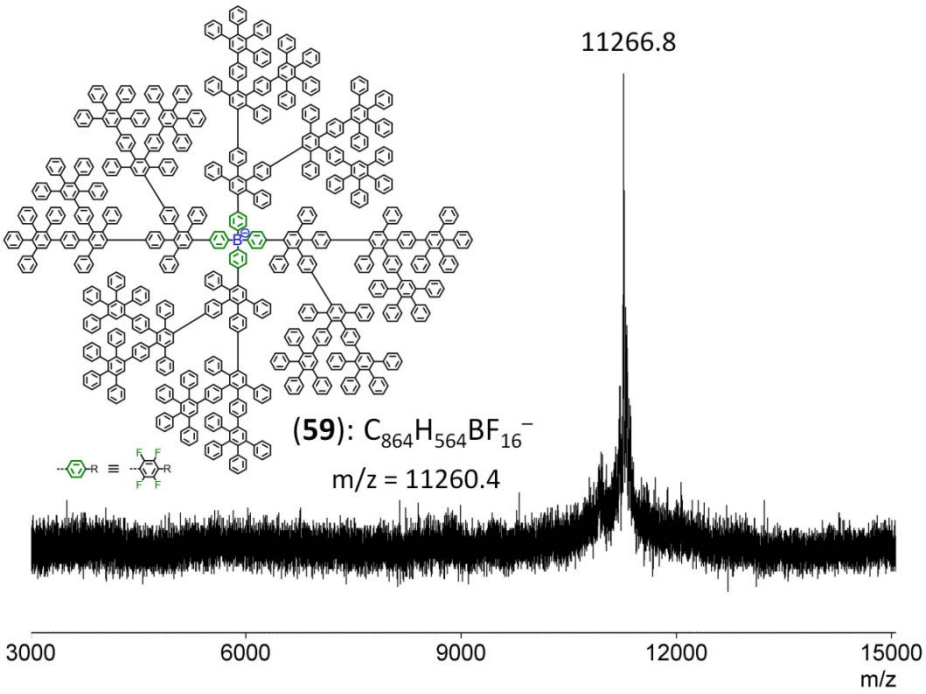

Figure 98: MALDI-TOF of third generation rigidly dendronized borate **59**

The further enlarged PP shell of borate **59** as compared to second generation dendronized borate **56** should be reflected in an even weaker coordination of **59** to its counterion (see paragraph 6.5.1.1).

2.3.4 Increase of Anion Shell Density via Degree of Branching

As demonstrated in 2.3.3, dendronization with PP-dendrons yields anions with larger overall sizes than ever synthesized before. However, a shell constituted from polyphenylenes cannot be regarded as a completely filled, "solid" shell. Instead, PP scaffolds only take up a certain fraction of space and thus inevitably contain voids. Thermally driven rapid rotation of phenyl rings or dendron subunits (or even whole dendrons) will of course increase the virtual space taken up by polyphenylenes. Nevertheless, the size of existing voids should be kept at a minimum in order to maximize the sterically screening effect of the PP shell and effectively prevent even small counterions to approach the central negative charge closely. Thus, instead of solely pushing overall anion size ever further, attempts were made to drastically increase overall polyphenylene density at a given dendrimer generation.

The density of a polyphenylene scaffold can be increased by maximizing its degree of branching. Earlier attempts to increase the degree of branching by way of modifying the functionality of the borate core have proven inefficient (see 2.2.4). Due to the enhanced thermal stability of the fluorinated borate core, however, attempts are not limited to first generation dendronized borates anymore. For the synthesis of an extremely branched, second generation PP dendronized borate **62**, the fluorinated borate core **52** was reacted with highly ethynyl functionalized AB_4 building block **2** instead of AB_2 in the first dendronization step. The resulting borate **60** was then deprotected with TBAF in THF to yield highly ethynyl functionalized first generation borate **61** (Figure 99).

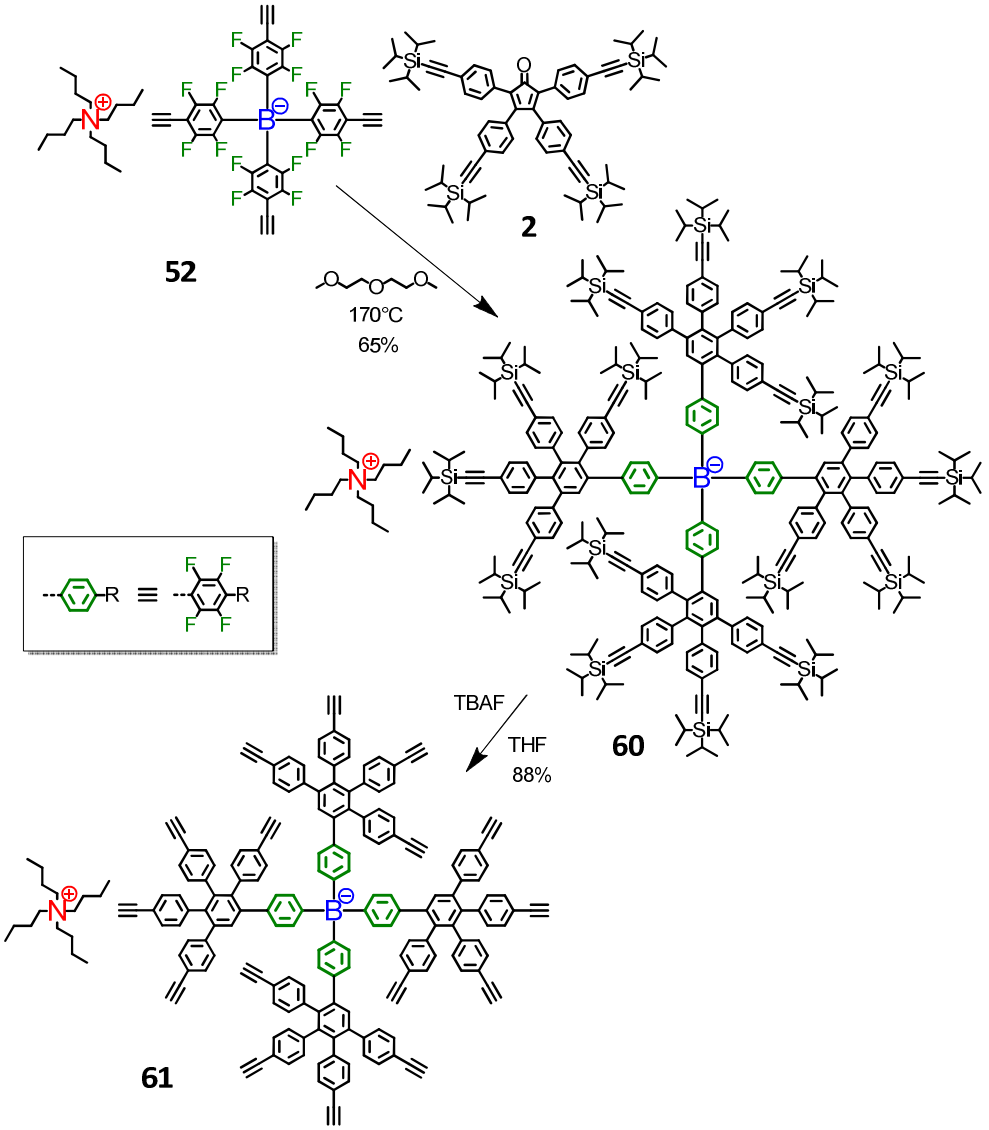

Figure 99: Divergent synthesis of highly ethynyl functionalized first generation dendronized borate **61** with a fluorinated core

The obtained highly ethynyl functionalized first generation dendronized borate **61** was used for a second dendronization step with tetracyclone **13** in diglyme at 170 °C.

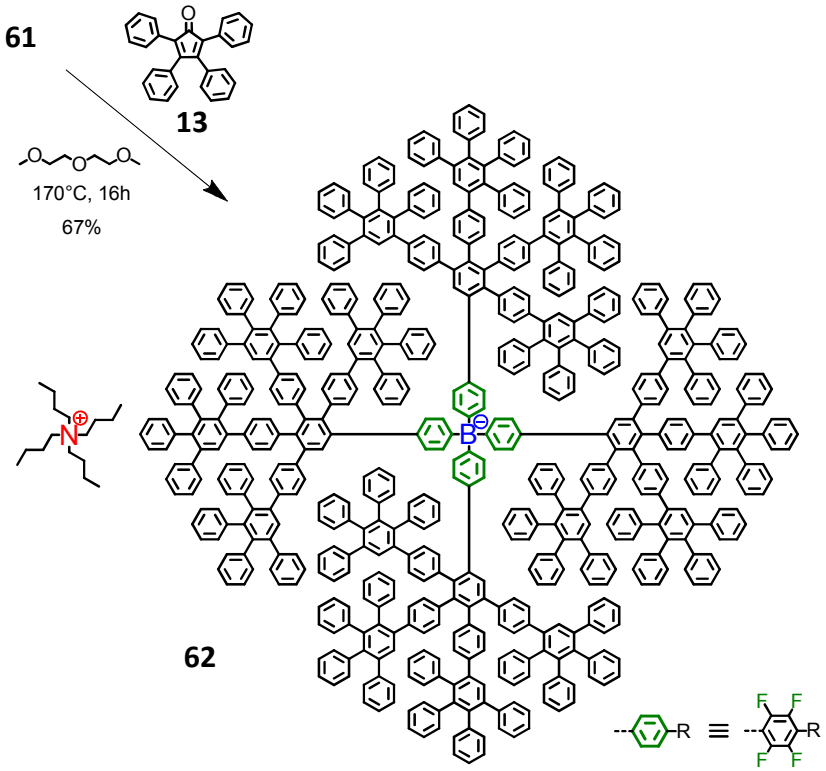

Figure 100: Divergent synthesis of highly branched second generation polyphenylene dendronized borate **62** via cycloaddition of tetracyclone **13** to highly ethynyl functionalized first generation dendronized borate **61**

The reaction was monitored by means of MALDI-TOF mass spectrometry (see Figure 101). Despite a considerably reduced accessibility of ethynyl groups for cycloaddition reactions in borate **61** and the increased steric repulsion from an ever denser polyphenylene shell in the resulting product, highly branched second generation dendronized borate **62** could successfully be synthesized.

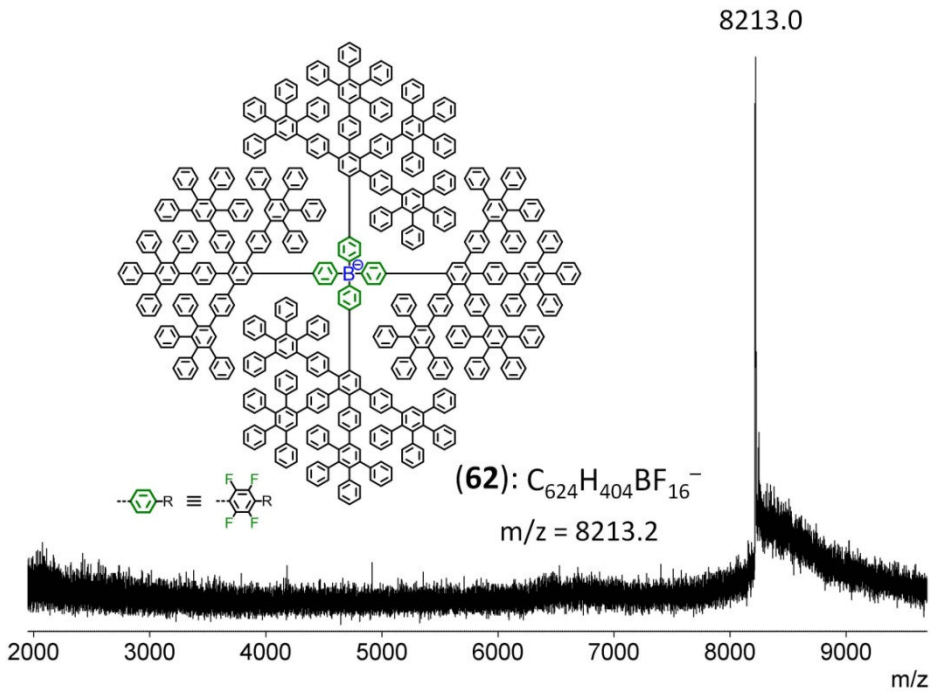

Figure 101: MALDI-TOF of highly branched second generation dendronized borate **62**

The example of borate **62** again clearly emphasizes the huge advantage of divergent dendritic growth for the synthesis of highly shielded anions. It is clear that the synthesis of any borate as sterically encumbered as borate **62** would have never been possible if direct synthetic methods had been used. The largely increased polyphenylene density of its shell should make borate **62** noticeably less coordinating as compared to its normally branched second generation analogue, borate **56** (see paragraph 6.5.1.2).

Molecular models of borate **62** indicate that the steric demand of its highly branched dendrons is in fact so huge that individual dendrons of one molecule exclude intramolecular volume from one another. As a consequence, only a few concerted overall orientations of dendrons are possible for a given borate molecule. The steric restriction of spatial orientations of dendrons should be reflected in a reduced number of atropisomers. This effect can indeed be observed and is reflected in a reduced number of signals in the NMR spectra of borate **62** as compared to other, less branched PP dendronized borates with a fluorinated core (see paragraph 5.4.1). The modeled structure of borate **62** also indicates that continuing dendritic growth towards the third generation is highly unlikely due to steric overcrowding.

A highly branched third generation dendronized borate may however be generated by postponing the step of increased branching to the second generation. Thus, “normally”

functionalized first generation dendronized borate **55** was reacted with AB_4 building block **2** to yield second generation borate **63**.

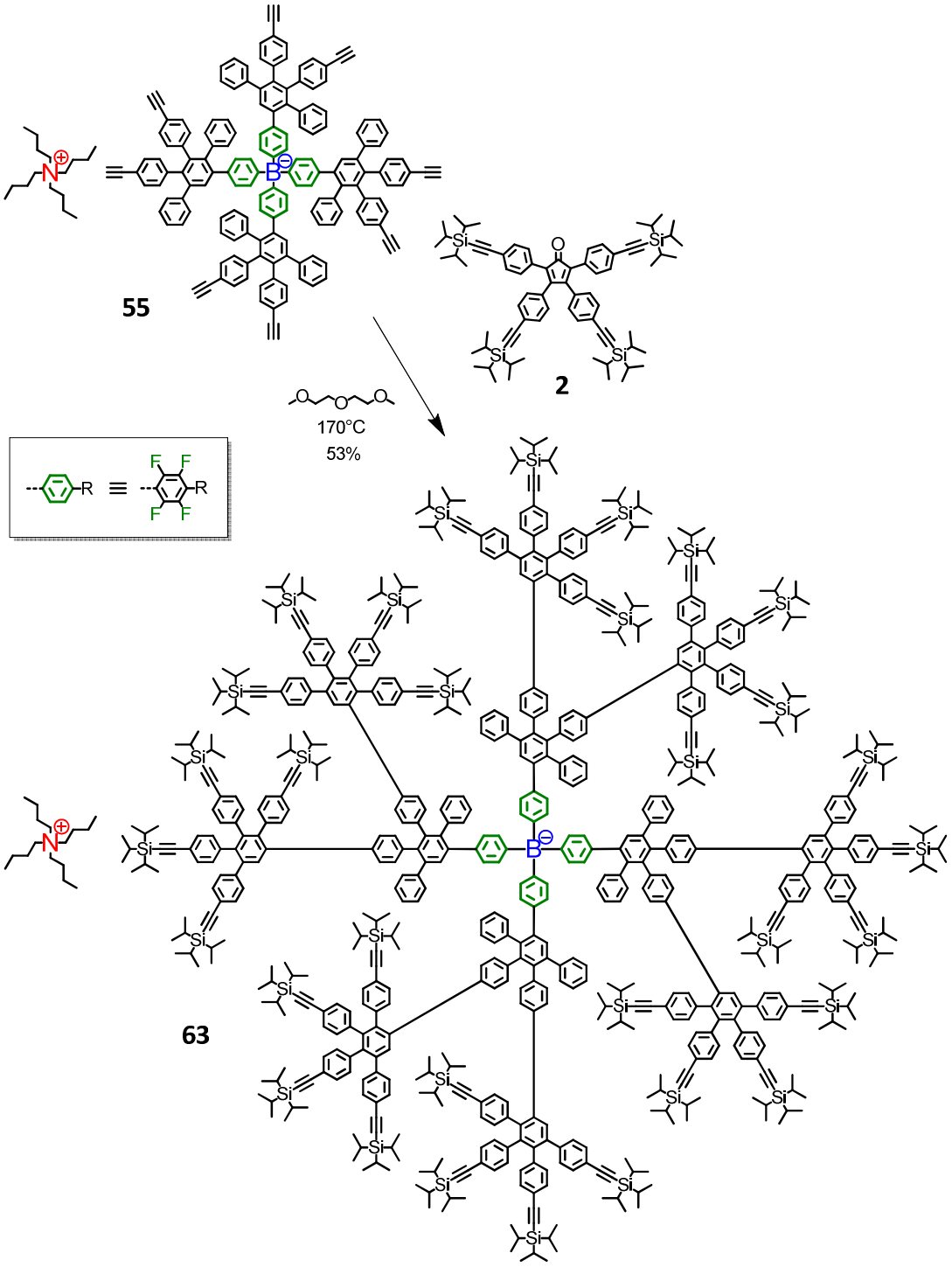

Figure 102: Divergent synthesis of highly ethynyl functionalized second generation dendronized borate **63**

After removal of T*i*PS-groups of borate **63** with TBAF in THF, the according highly ethynyl functionalized borate **64** was obtained (83%). Borate **64** was then used for a third dendronization step with tetracyclone **13** in diglyme at 170 °C, yielding the highly

branched third generation PP dendronized borate **65**. The reaction was monitored by means of MALDI-TOF mass spectrometry (see Figure 103).

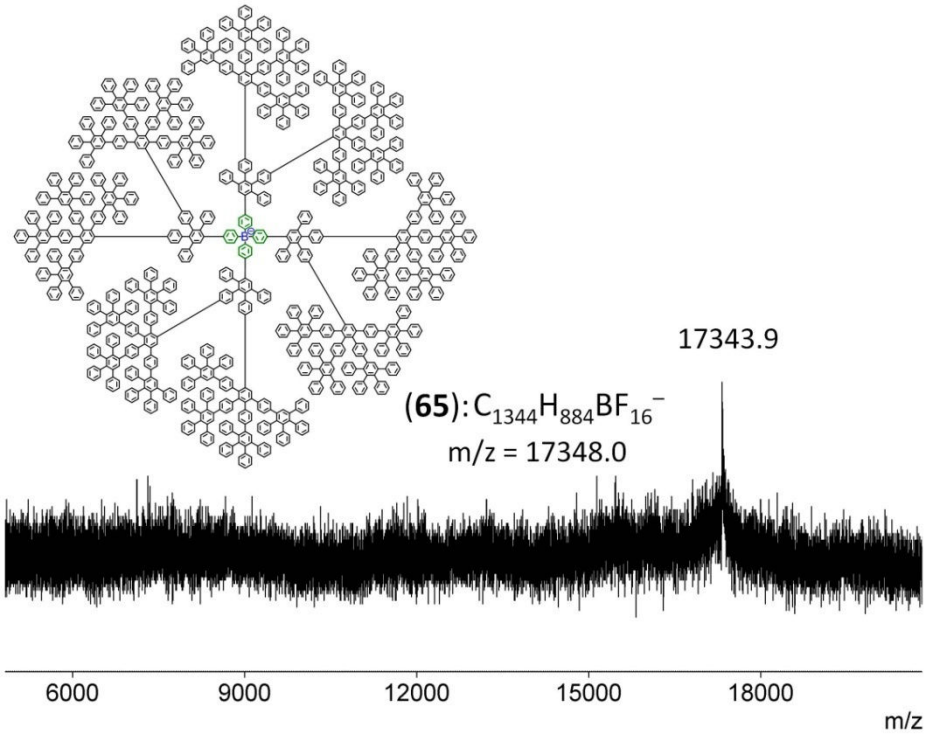

Figure 103: MALDI-TOF of highly branched third generation dendronized borate **65**

Apparently, the signal-to-noise ratio in MALDI-TOF decreases with increasing borate size, making the detection of larger borates more difficult. Nevertheless, the achieved signal-to-noise ratio is sufficient to confirm complete conversion and thus successful synthesis of highly branched third generation PP dendronized borate **65**. If defect structures were present, they would be visible as peaks with local displacements of the base line underneath.

In addition to being well shielded by its highly branched and rigid polyphenylene shell, this borate anion is much larger than all tetraphenylborates known previously. With a diameter of about six nanometers (as confirmed by DOSY-NMR; see paragraph 6.2), this anion well reaches into the size range of typical nanoscopic objects such as nanoparticles. Nevertheless, borate **65** is an atomically precise molecular anion with a fully defined chemical structure.

In order to visualize the increase in anion size and density enabled by divergent dendronization, the modeled structure of borate **65** was contrasted with the structures of a

number other WCAs, most of which are already considered very large anionic species (see Figure 104).

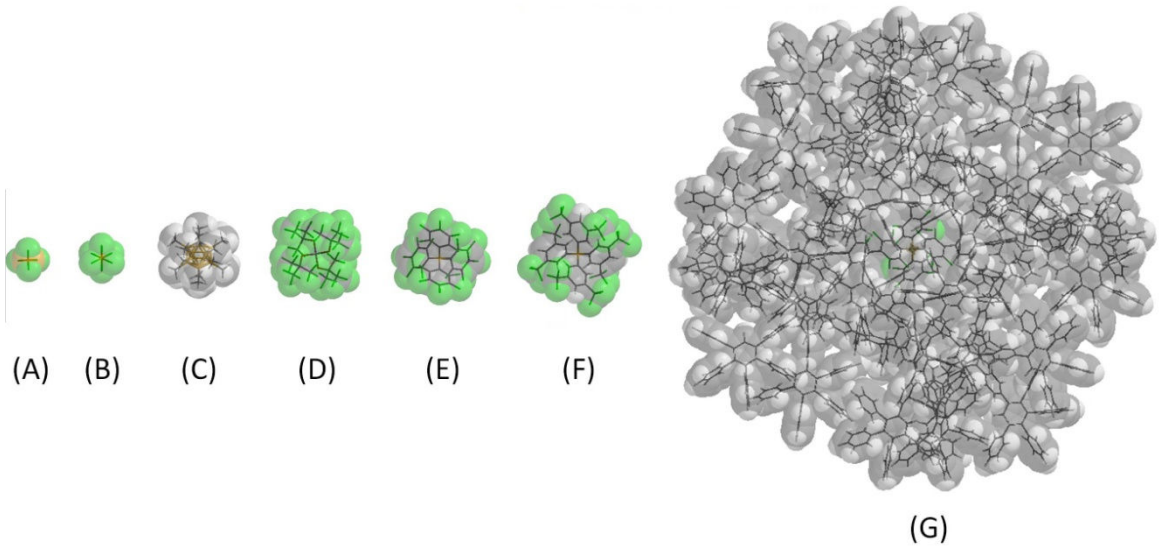

Figure 104: Comparison of the dimensions of some weakly coordinating anions: (A): $[BF_4]^-$; (B): $[PF_6]^-$; (C): $[CB_{11}Me_{12}]^-$; (D): $[Al(OC(CF_3)_3)_4]^-$; (E): $[B(C_6F_5)_4]^-$; (F): $[B(C_6H_3(CF_3)_2)_4]^-$; (G): highly branched third generation dendronized borate $[B^F\text{-}G3^{24}]^-$ (**65**)

Both size and density of borate **65** should make it a very weakly coordinating anion. An investigation and comparison of the weakly coordinating properties of all anions presented herein will be provided in chapter 6.

2.3.5 Fluorination of the Anion Surface

As already mentioned under 2.2.5, the weakly coordinating properties of anions can be improved significantly by a fluorination of their surfaces. While fluorinated borate core **52** has already enabled an increase in borate size (2.3.3) and polyphenylene density (2.3.4), the use of fluorinated tetracyclone building blocks for surface fluorination might provide an additional weakening of the coordination strength of dendronized borates.

2.3.5.1 Surface Fluorination with Perfluorinated Phenyl Moieties

For the synthesis of first generation dendronized borate **66** with both a fluorinated core and a fluorinated surface, borate **52** was reacted with perfluorinated tetracyclone **40** in diglyme at 170 °C (see Figure 105).

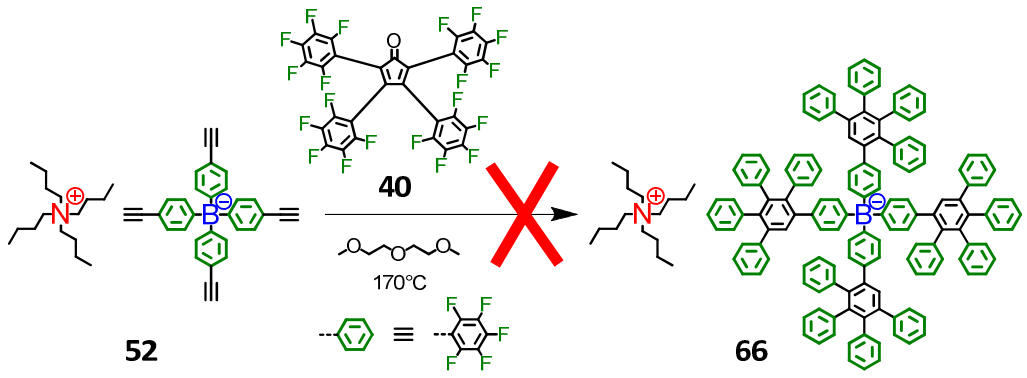

Figure 105: Synthesis of first generation dendronized borate **66** with both a fluorinated core and a fluorinated surface (failed!)

In contrast to the reaction of tetracyclone **40** with non-fluorinated borate **12**, the reaction with fluorinated borate **52** was not successful. In MALDI-TOF, several peaks with m/z values in the range of 1350 to 1650 were detected, but could not be assigned to specific intermediates or products. With regard to molecular orbital energy levels, there is no direct argument against the cycloaddition of fluorinated tetracyclone **40** to borate **52** (inverse demand of electrons; $\Delta E = 2.61$ eV). Maybe the larger steric demand of fluorinated phenyl rings, which are directly attached to both the diene and the dienophile functionality, preclude both functions from approaching one another sufficiently closely. In any case, the desired product **66** could not be obtained.

For the synthesis of a second generation dendronized borate **67** with a fluorinated surface, the presence of fluorinated phenyl rings was only required in direct neighborhood to the diene functionality and was thus assumed to be possible. Therefore, ethynyl functionalized borate **55** was reacted with tetracyclone **40** in diglyme at 170 °C (see Figure 106).

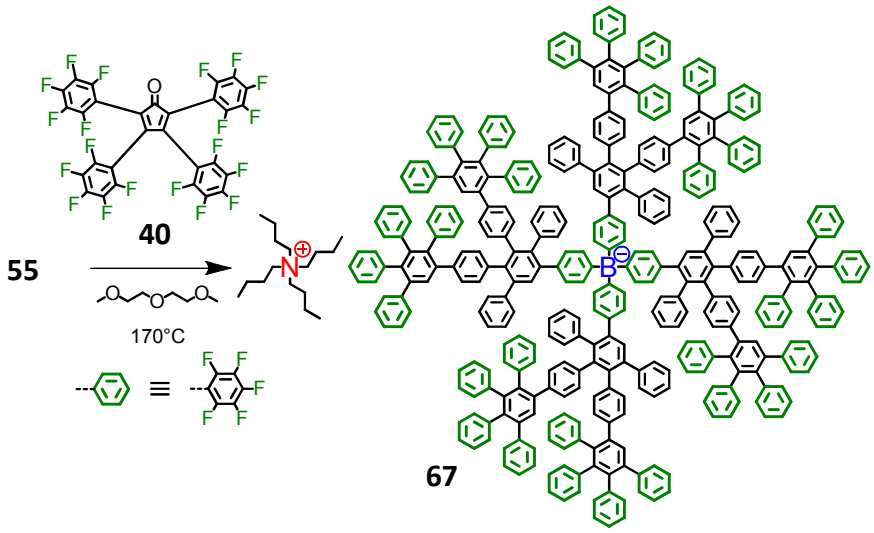

Figure 106: Divergent synthesis of surface fluorinated second generation polyphenylene dendronized borate **67** via cycloaddition of fluorinated tetracyclone **40** to ethynyl functionalized first generation dendronized borate **55**

The reaction was monitored by MALDI-TOF mass spectrometry. As indicated in Figure 107 (A), the reaction towards borate **67** was still very incomplete even after 16 h at 170 °C. Under identical conditions, a conversion to a second generation dendronized borate **56** without a fluorinated surface is typically completed (see 2.3.3). Here, by contrast, even non-reacted starting compound **55** could still be detected (Figure 107 (A)). After doubling the reaction time to 32 h, first signals resulting from 7-fold cycloaddition species were found (Figure 107 (B)). Only after quadrupling the reaction time to 64 h, a first signal of the desired product **67** (8-fold cycloaddition) could clearly be detected by MALDI-TOF (Figure 107 (C)). Nevertheless, the reaction remained very incomplete. A further increase of reaction time had a negligible effect on further reaction progress. Thus, the obtained mixture of intermediates and product was purified and used as starting compound for another cycloaddition reaction under more drastic conditions. The solvent was changed to diphenyl ether, the temperature was increased to up to 240 °C, and the reaction was assisted by irradiation with microwaves. While these means clearly pushed reaction progress further towards the desired product, the reaction still remained incomplete (see Figure 107 (D)).

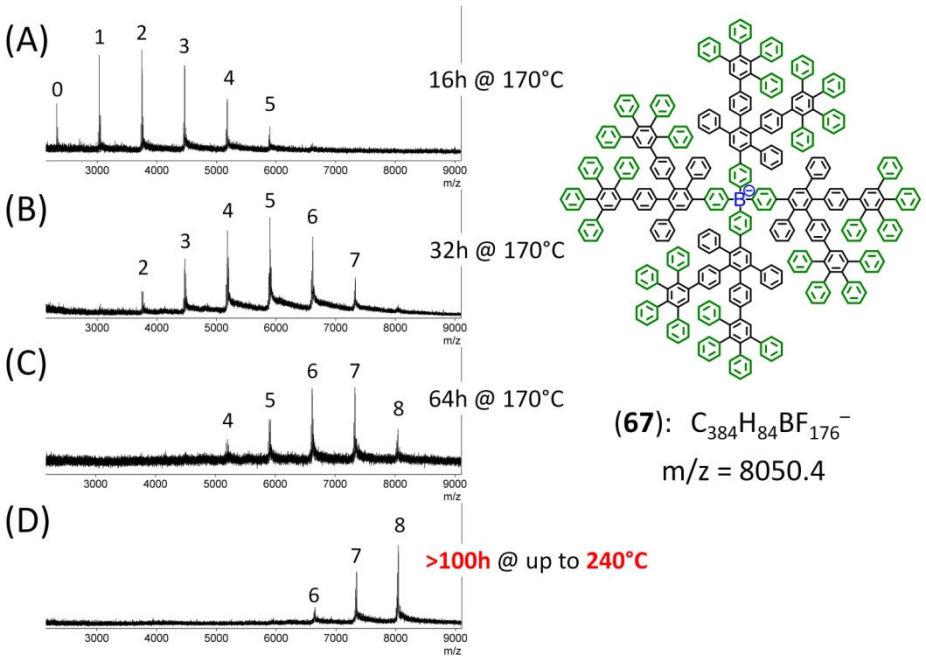

Figure 107: MALDI-TOF of reaction mixtures towards surface fluorinated second generation dendronized borate **67** (The numbers on top of the peaks indicate the number of cycloadditions. For a complete conversion to borate **55**, an 8-fold cycloaddition is required.)

Unfortunately, a further extension of reaction time did not have a significant effect on reaction progress. Instead, cleavage of single dendrons led to a gradual decomposition of intermediates and the product. Therefore, surface fluorinated second generation dendronized borate **67** could not be isolated. The reason for the largely decreased reaction rate towards borate **67** as compared to second generation borate **56** is not yet fully understood. It is however clear that a complete conversion to even larger or more highly branched borates with fluorinated surfaces using fluorinated tetracyclone **40** appears just the more unlikely.

2.3.5.2 Surface Fluorination with CF_3-functionalized Phenyl Moieties

Another tetracyclone building block which is suitable for surface fluorination is the CF_3-functionalized tetracyclone **47** developed by [redacted] (see 2.2.5.2). As mentioned earlier, tetracyclone **47** might prove of value for generating more effective WCAs due to its increased steric demand as compared to fluorinated tetracyclone **44**.

Borate core **52** was reacted with CF_3-functionalized tetracyclone **47** in *o*-xylene at 160 °C to yield first generation dendronized borate **68** with both a fluorinated core and a fluorinated surface.

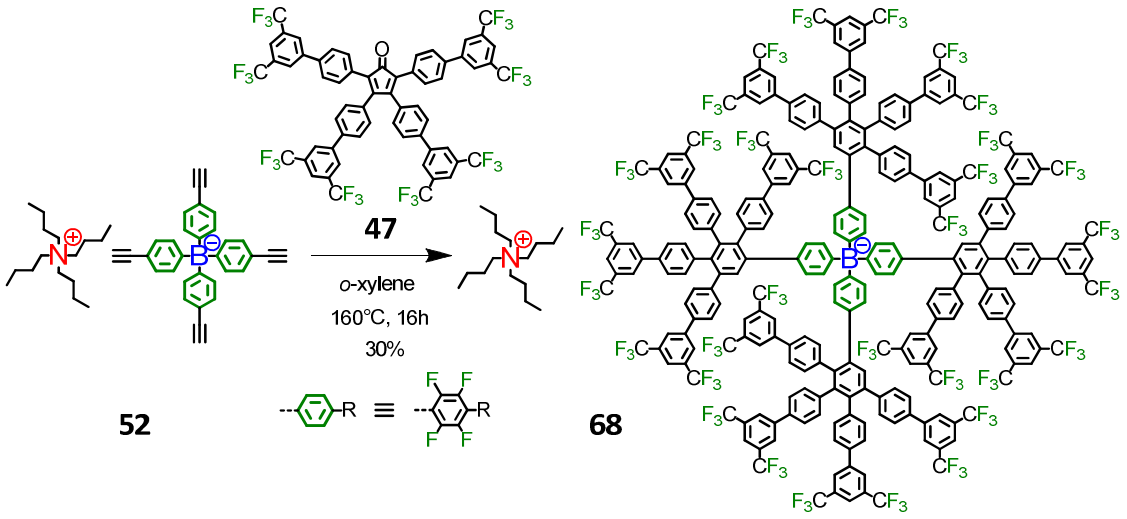

Figure 108: Synthesis of first generation dendronized borate **68** with both a fluorinated core and a fluorinated surface

Despite the large steric demand of tetracyclone **47**, the synthesis of borate **68** could be performed successfully. The according MALDI-TOF mass spectrum of the product is displayed in Figure 109. Borate **68** was the first example of a borate with a stabilized, fluorinated core and a fluorinated surface at the same time.

As a whole, CF_3-functionalized tetracyclone building block **47** is considerably larger and more spatially expansive than perfluorinated tetracyclone **40**. However, the immediate vicinity of the reactive diene function is actually less congested and more easily accessible in tetracyclone **47** as compared to **40**. Moreover, the electron withdrawing effect of fluorine has a smaller effect on the diene function in **47** due to its intermediary aryl spacer. Such differences between both fluorinated tetracyclone building blocks **40** and **47** might explain why the synthesis of borate **66** failed, while borate **68** could be synthesized.

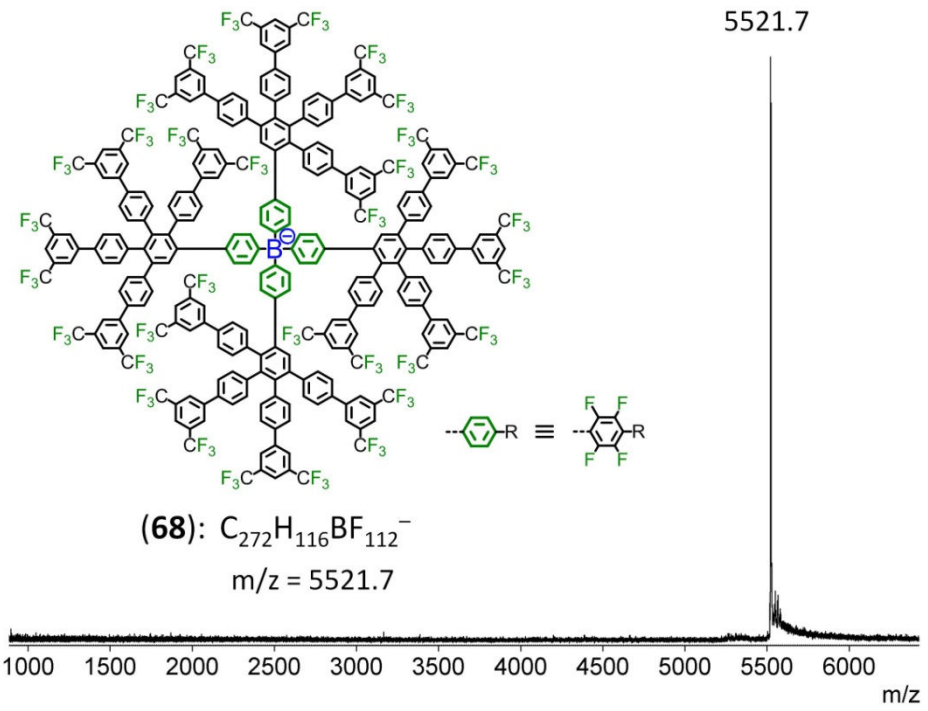

Figure 109: MALDI-TOF of highly CF_3-functionalized first generation dendronized borate **68** with a fluorinated core

The effect of CF_3-functionalized tetracyclone building block **47** on the overall size of the resulting first generation dendronized borate **68** is illustrated in Figure 110, where its space filling model is contrasted with the model of first generation dendronized borate **53**. Moreover, Figure 110 demonstrates the resulting distribution of CF_3 groups on the anion surface in **68**.

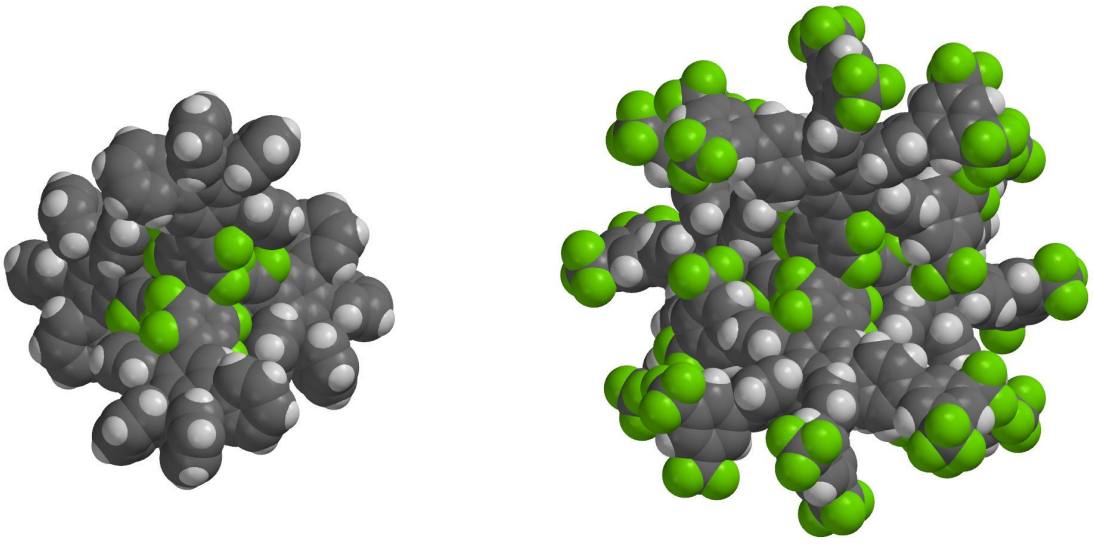

Figure 110: Effect of surface functionalization on anion size and fluorine distribution; left: borate anion **53** without surface functionalization; right: borate anion **68** with $Ph(CF_3)_2$-functionalized surface

Its larger size and the presence of 32 CF_3 groups on its surface should make borate **68** a much less coordinating anion than borate **53** (see paragraph 6.5.2).

For the synthesis of a second generation dendronized borate **69** with a fluorinated surface, ethynyl functionalized borate **55** was reacted with tetracyclone **47** in *o*-xylene at 160°C for 16 h. The reaction was monitored by means of MALDI-TOF mass spectrometry (see Figure 111).

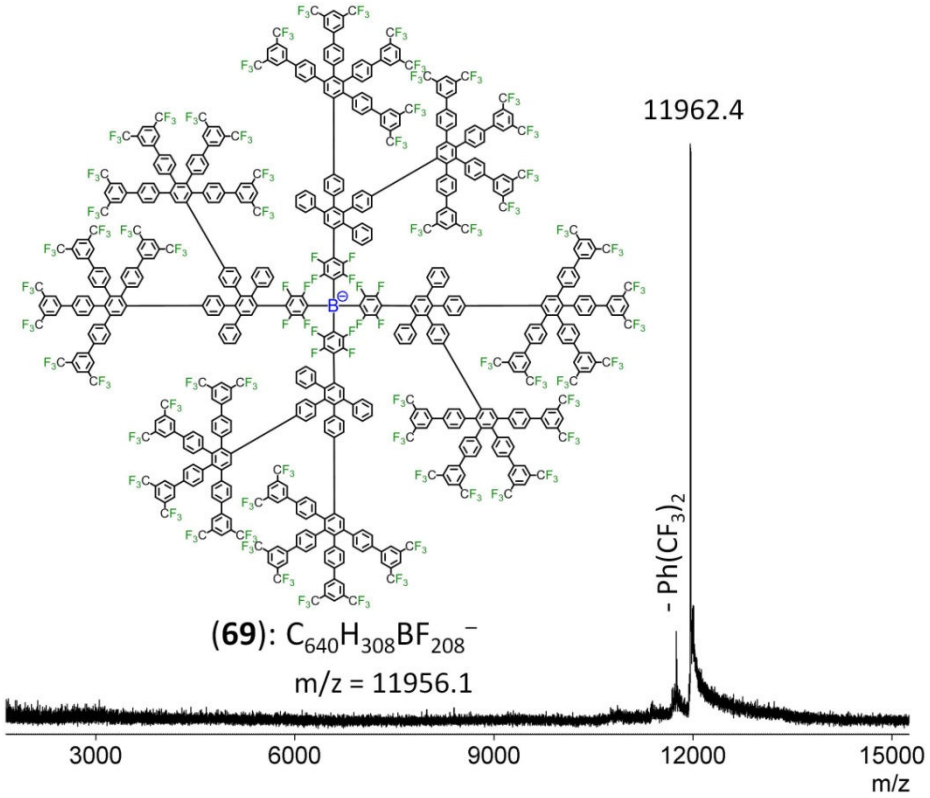

Figure 111: MALDI-TOF of highly CF_3-functionalized second generation dendronized borate **69**

The MALDI-TOF measurement confirmed successful conversion of borate **55** to highly CF_3-functionalized second generation dendronized borate **69**. In addition to the product peak, another peak at lower m/z ratio (with a Δm of 213) was detected, which could be assigned to a species of **69** where one CF_3-functionalized phenyl ring ($Ph(CF_3)_2$) had been cleaved off due to UV laser irradiation. Additionally, a signal at the very high m/z ratio of about 23968 (roughly two times the mass of the product) was detected, indicating the presence of anion dimers.

Synthesis of CF_3-functionalized borates was pushed further to even higher generations. Mass spectrometric detection of the normally branched third generation dendronized borate **70** with a CF_3-functionalized surface was more difficult and only possible in linear

detection mode of MALDI-TOF. The obtained signals were significantly broadened as compared to signals of lower generation borates. Moreover, a larger amount of dimers and even trimers was observed at high m/z-ratios (see Figure 112).

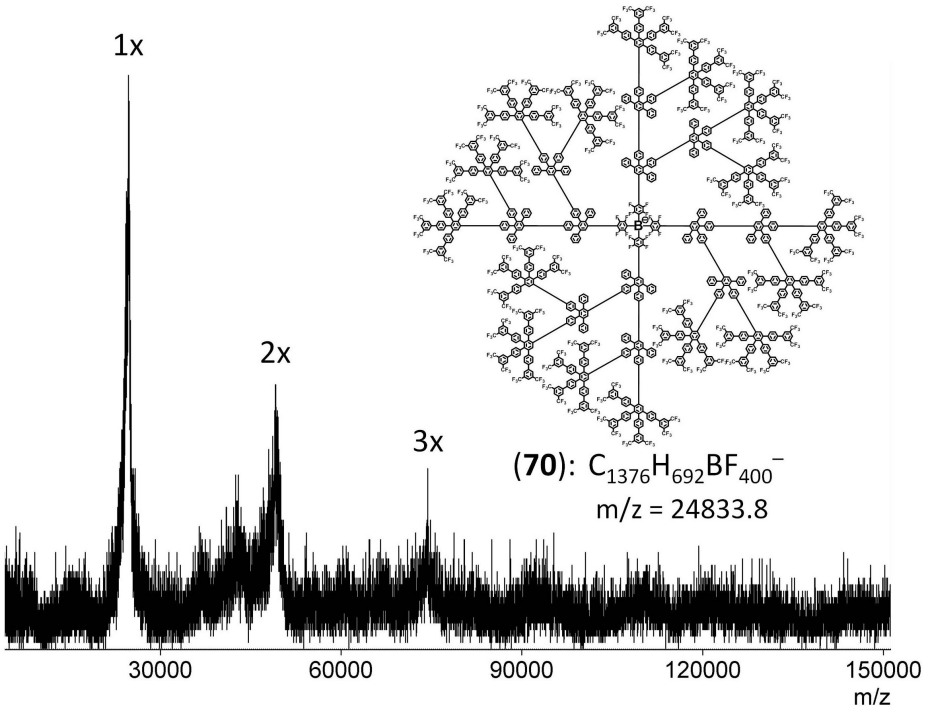

Figure 112: MALDI-TOF of highly CF_3-functionalized third generation dendronized borate **70** (extended to very high m/z-ratios, where peaks at double and triple mass of the product were observed)

Here, complete conversion to the desired product **70** was possible within the frame of standard *Diels-Alder* cycloaddition reaction conditions (heating to 160 °C for 16 h in *o*-xylene). By contrast, cycloaddition to the highly branched third generation analogue **71** was much more difficult, and the reaction was still very incomplete after 16 h at 170 °C (see Figure 113 (A)). Due to its high degree of branching, borate **71** exhibits a much higher density of surface functional groups. The higher density leads to an increased congestion and steric repulsion between tetracyclone building blocks and the borate surface. Remaining non-reacted ethynyl functions at the surface are thus less and less accessible with increasing reaction progress. Consequentially, reaction time was continuously extended to up to two weeks, resulting in a gradual shift of intermediate species towards the desired, high molecular weight product (see Figure 113 (B)). While the reaction remained incomplete, the signal of the desired product **71** could be detected nevertheless, confirming that a highly branched and highly surface fluorinated third generation dendronized borate can exist. However, these results also show that highly branched borate **71** repre-

sents the upper limit in terms of anion size and bulkiness that can be achieved synthetically with the herein presented methods.

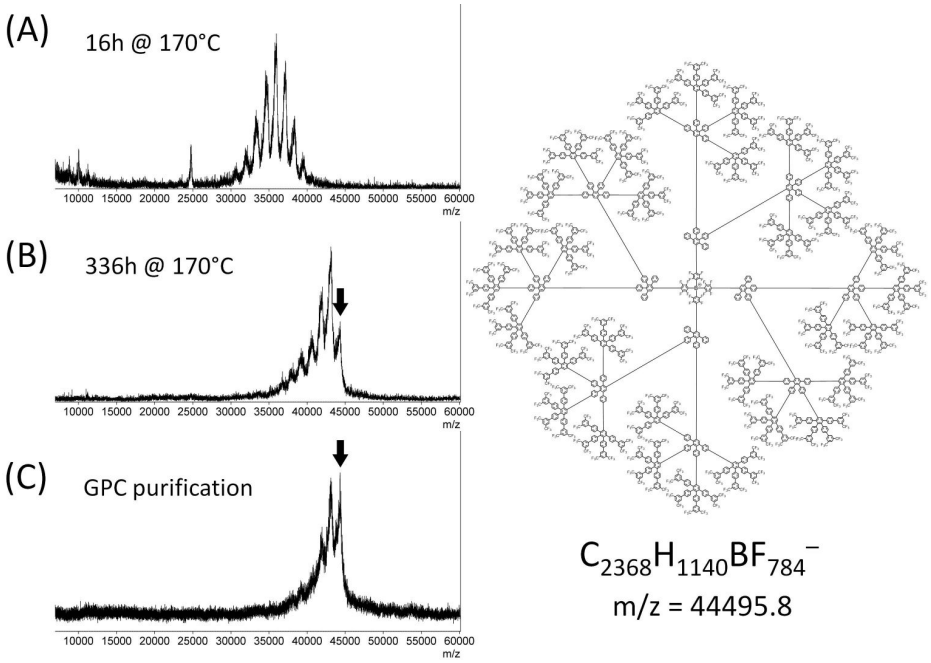

Figure 113: MALDI-TOF spectra of reaction mixtures towards highly branched and surface fluorinated third generation dendronized borate **71** (The arrow on top of the rightmost peak indicates the signal of the desired product **71**, resulting from a 32-fold cycloaddition)

A further increase in reaction time or temperature as well as additional irradiation with microwaves did not improve overall reaction progress but rather led to a gradual decomposition of the product and intermediates. Thus, attempts were made to isolate the desired product **71** from not fully converted borate species physically via gel permeation chromatography. While the ratio of borate **71** to borate intermediates could indeed be improved by GPC, borate **71** could not be isolated completely (see Figure 113 (C)). Due to its enormous molecular size and weight, its densely packed polyphenylene shell and its highly fluorinated surface, the obtained product was nevertheless tested with regard to its weakly coordinating properties (see paragraph 6.5.1.5).

2.4 Summary and Outlook

In this chapter, a new strategy for the synthesis of extremely large, rigid and bulky anions has been presented. The strategy is based on well established synthetic methods, which have been combined and transferred from neutral molecules to inherently charged ions.

It has been demonstrated that molecular ions, if suitably functionalized, can be grown larger and larger in successive steps. Tetraphenylborate anions (both non-fluorinated and fluorinated) have successfully been functionalized with ethynyl groups. These functionalized tetraphenylborates have then been decorated with highly branched, rigid and shape persistent polyphenylene shells. Regarding overall anion size and bulkiness, the method of divergent dendritic growth has proven to surpass the limits of direct synthesis by far: Atomically precise and monodisperse anions with diameters of up to six nanometers have been achieved. Since anions of nano-sized dimensions were hitherto unknown, the salts of these ions constitute a whole new class of materials.

It has also been demonstrated that by choice of different building blocks, each of the structural parameters of dendronized anions (their overall size, the density of their dendritic shells and the chemical nature of their surfaces) could be modified and adjusted individually. In prospect of the potential application of dendronized anions as novel weakly coordinating anions, their structure could thus be ever more optimized for their specific task.

In direct consequence to the thus achieved, a number of new challenges arise. Due to the synthetic protocols followed in this chapter, dendronized borates were always obtained in the form of their tetrabutylammonium salts. In order to broaden the range of potential applications of dendronized salts, a reliable method for a clean exchange of tetrabutylammonium to other counter-cations should be developed (see chapter 0). Also, a better understanding of the origin and effects of atropisomerism in dendronized borates with a fluorinated core should be provided (see chapter 5). More generally, the effects of anion size, shell density and surface functionalization on the physical properties of the salt should be investigated (see chapter 6). Finally, it should be tested whether the method of divergent dendritic growth might also enable the synthesis of functionalized salts, in which the properties of the electrolyte could be switched reversibly by an external stimulus (see chapter 7).

3 Synthesis of Aryl-Triazole Dendrimers

3.1 Introduction

Dendrimers can be build by a variety of different synthetic methods (see 1.1). Among these methods, "spring-loaded" (exothermic) reactions are especially useful since they enable joining together small modular units quickly and reliably with high yields and selectivity. Reactions that fulfill such requirements are now collectively recognized as examples of "click chemistry", a term coined by *K. B. Sharpless* in 2001.[193]

Click reactions have been used for the functionalization of dendrimer surfaces[203,204] and for building dendrimers by linking together several ready-made dendrons to a single core.[205,206] A combination of both surface functionalization and dendron linkage has been used to synthesize unsymmetrical functional dendrimers, containing both mannose binding units and fluorescent coumarin moieties.[207] However, click reactions have also been utilized for the synthesis of dendritic scaffolds themselves. In the group of *C. J. Hawker*, triazole-rich and flexible dendrimers have been synthesized by a convergent approach using the copper catalyzed *Huisgen* cycloaddition of azides to alkynes (see Figure 114).[208]

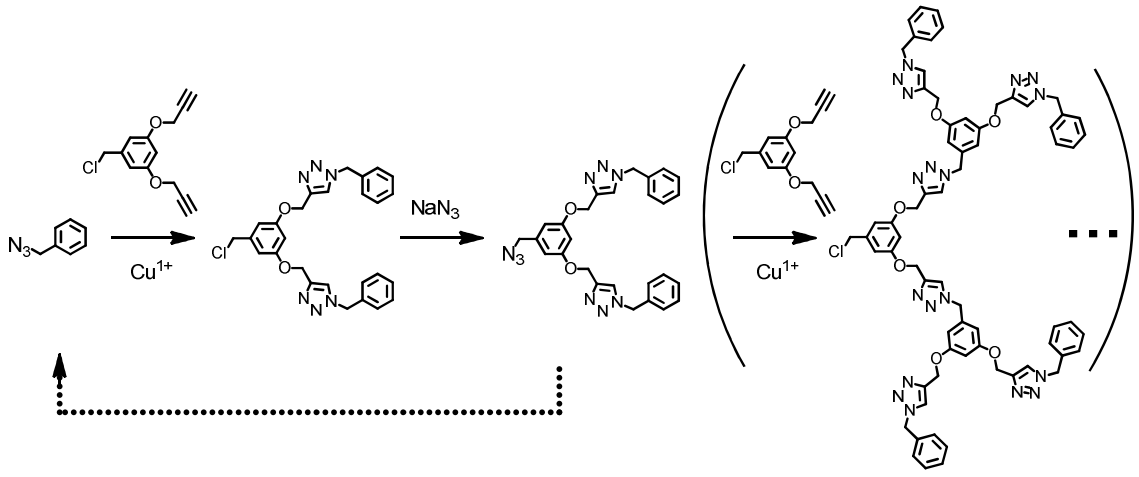

Figure 114: Convergent synthesis of a dendrimer via copper catalyzed azide-alkyne *Huisgen* cycloaddition[208]

In combination with esterification and etherification, click reactions have been used to synthesize fourth generation dendrimers in just four steps by eliminating the reaction steps required for activation.[209] With regard to dendrimer synthesis, the copper catalyzed *Huisgen* cycloaddition between azides and alkynes is not the only type of click reaction that has been utilized. As a means to abolish the use of metal catalysts, the click reaction

between thiols and alkenes has been employed.[210] This type of click reaction only requires trace amounts of a photoinitiator (2,2-dimethoxy-2-phenylacetophenone) and irradiation with UV light ($\lambda_{ex} = 365$ nm) to proceed. In addition to the construction of the dendritic scaffold, the surface of such dendrimers can be functionalized by employing functional thiols for endcapping. A further example is the synthesis of dendrimers based on thio-bromo click reactions.[211] Indeed, more and more click reaction procedures are now being developed which do not require metal catalysis.[212,213] In this regard, the modular synthesis of functional polyphenylene dendrimers via *Diels-Alder* cycloaddition could be considered an example of applied, catalyst free click chemistry, which had been realized as early as 1997.[11]

In paragraph 2.2.3.2, the concept of copper catalyzed azide-alkyne *Huisgen* cycloaddition (presumably the most popular type of click-reaction) has been taken into consideration as a low temperature alternative to *Diels-Alder* cycloaddition for the synthesis of large borate anions. However, the presence of triazole rings in the resulting dendritic scaffolds leads to several disadvantages regarding the anion´s applicability as weakly coordinating anion: In addition to lowering the rigidity of the dendritic shell, each five-membered triazole ring also serves as a nucleophilic, strongly coordinating site.

Nevertheless, during the development of suitable building blocks for the construction of relatively rigid, aryl rich dendrimers via azide-alkyne *Huisgen* cycloaddition, it became clear that the concept may be exploited for different purposes altogether. The concept may enable generating stiff dendritic architectures solely based on arene and triazole rings at room temperature. Moreover, the requirement of ethynyl functions for both PPD chemistry[52] and azide-alkyne click chemistry[214] readily invites for a combination of both concepts: Dendrimer hybrids may be designed, or the catalyzed click chemistry may be exploited for the functionalization of PPDs with temperature sensitive moieties.

Within this work, initial experiments have been made regarding the applicability of click chemistry for the synthesis of relatively stiff dendrimers at room temperature, whose scaffolds are solely based on interconnected aryl and triazole rings. The design and synthesis of these dendrimers will be presented on the following pages.

3.2 Design and Synthesis of Building Blocks

To enable the synthesis of dendritically branched aryl-triazole scaffolds, an ethynyl functionalized aryl azide is required that can serve as the branching building block. As mentioned earlier, aryl azides can easily be obtained via conversion of the according aryl amines.[194] Commercially available 3,5-dibromo-4-methylaniline **72** was selected as the starting compound, which after functionalization with T*i*PS-acetylene via *Sonogashira* coupling yielded aniline **73**. Functionalized aniline **73** was then converted to azide **74**, which represented an AB_2 building block that was suitable for dendritic growth (Figure 115).

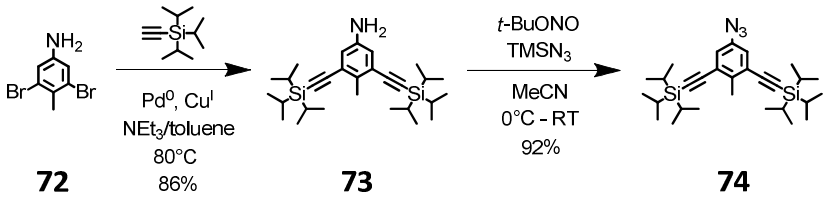

Figure 115: Synthesis of AB_2 building block **74** for the build-up of dendritic aryl triazole scaffolds

AB_2 building block **74** was obtained in the form of a yellow, viscous oil. Although it could be stored for several weeks at 3 °C, building block **74** was usually used up immediately after preparation, and only its amine precursor **73** was stored for longer periods of time. Hence, for every growth step during aryl-triazole dendrimer synthesis, **74** was prepared freshly.

A comparison of the building blocks, reaction temperatures and resulting scaffold structures of polyphenylene dendrimers (right) and aryl-triazole dendrimers (left) is given in Figure 116.

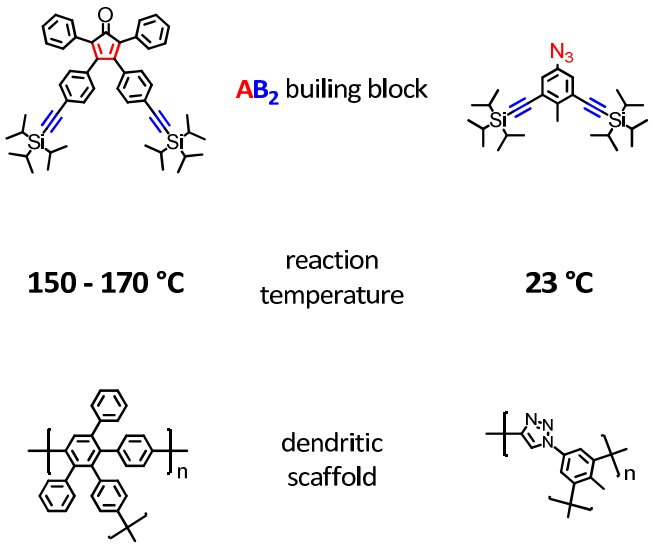

Figure 116: Comparison of building blocks, reaction temperatures and resulting scaffold structures of polyphenylene dendrimers (left) and aryl-triazole dendrimers (right)

Although the dendritic scaffold resulting from AB_2 building block **74** is not as rigid as a PPD scaffold, it should be considerably stiffer than the dendritic scaffolds based on click reactions that have been reported thus far: A stiff chain segment (dotted lines in Figure 117) in the scaffold built from **74** has a fixed length of about 4.00 Å (see Figure 117 (A)). By contrast, dendritic scaffolds containing aliphatic bridges or single, sp^3 hybridized atoms along the backbone possess much smaller chain segments down to only 1.42 Å (see Figure 117 (B)).

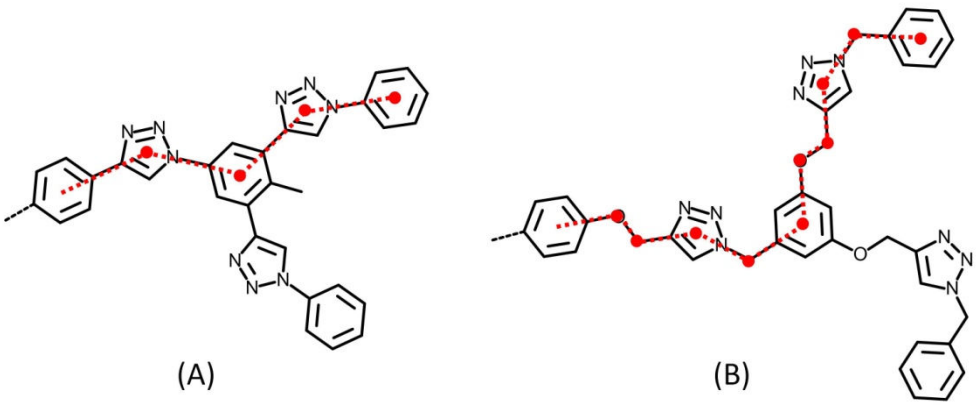

Figure 117: Angulation of the backbone in aryl-triazole dendrimers (A) and in a typical click dendrimer (**B**)

Furthermore, at any given generation the number of angulation points (red dots in Figure 117) is higher in typical dendrimer backbones such as (B) than in aryl-triazole dendrimer (A). Finally, density functional calculations (B3LYP, 6-31G*, see (A) in Figure 118) and

crystal structures[215] (see (B) in Figure 118) both indicate a strong preference for a coplanar alignment of triazole and neighboring aryl rings due to electronic conjugation.

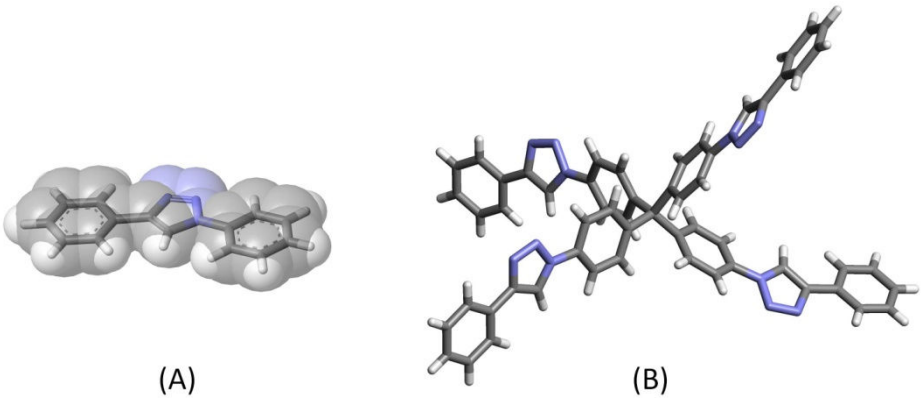

Figure 118: Coplanar alignment of neighboring triazole and phenyl rings; (A): model of two phenyl rings linked by a triazole after energy minimization using DFT calculations; (B): crystal structure of a triazole-phenyl functionalized tetraphenylmethane (as described by *Stefan Bräse et al.*[215]) which exhibits nearly co-planar alignment of neighboring triazole and phenyl rings

Due to their energetically favored coplanar alignment, an extra expense of activation energy is required for rotating neighboring rings out of their common plane. An increase in activation energy of rotation corresponds to a kinetic stiffening of the backbone. Such stiffening can only occur in a dendritic scaffold such as (A) in Figure 117, where each triazole ring is directly neighbored to aryl rings and vice versa.

For the endcapping of aryl-triazole dendrimers, both azidobenzene **75** and the bulky aryl azide **25** (as presented earlier in paragraph 2.2.3.2) have been tested.

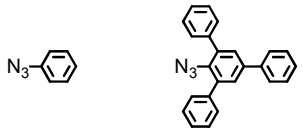

75 **25**

Figure 119: Aryl azides considered for endcapping of aryl-triazole dendrimers

Due to the largely increased solubility and reduced aggregation of dendrimers endcapped with bulky azide **25** as compared to small azidobenzene **75**, the larger azide **25** was preferentially used as the endcapping reagent.

3.3 Divergent Build-up of Aryl-Triazole Dendrimers

As already described in chapter 2 (paragraph 2.2.3.2), the build-up of dendritic scaffolds from aryl rich and fairly hydrophobic building blocks makes the use of non-aqueous reaction media inevitable. THF has been recognized as an adequate medium for dissolution of educts and products. To also ensure a good solubilization of the catalytically active Cu^{1+} in THF, the ligand TBTA **28** was synthesized (see 2.2.3.2 for details) and employed in each of the *Huisgen* cycloadditions described below. Moreover, to ensure pushing the performed cycloaddition reactions towards completion, a large excess of the azide component (about 2 to 3 equivalents per alkyne function) was generally used.

3.3.1 Aryl-Triazole Dendrimers with a Trigonal Planar Core

For the growth of aryl-triazole dendrimers from a trigonal planar core **78**, 1,3,5-tribromobenzene **76** was functionalized with T*i*PS-protected ethynyl groups and activated for cycloaddition via deprotection with TBAF in THF (see Figure 120).

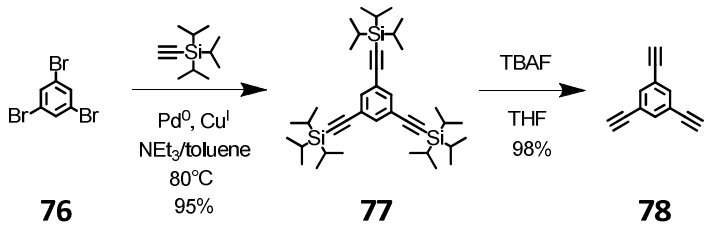

Figure 120: Synthesis of trigonal planar dendrimer core **78**

First generation aryl-triazole dendrimer **79** was synthesized from the core **78** via copper catalyzed azide-alkyne *Huisgen* cycloaddition of bulky azide **25** (Figure 121).

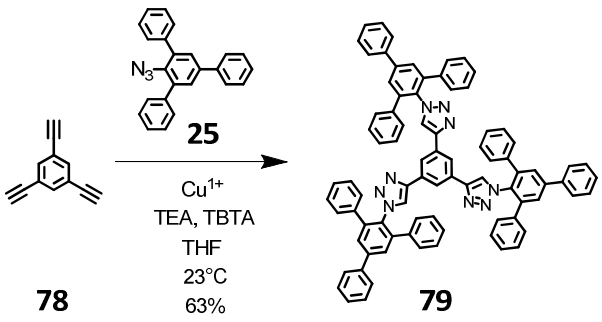

Figure 121: Synthesis of first generation aryl-triazole dendrimer **79** via copper catalyzed *Huisgen* cycloaddition at room temperature

The mixture was purified twice by column chromatography and precipitation in hexane, but this procedure did not suffice to yield a really pure product. Instead, purification by

means of recycling gel permeation chromatography (GPC) was mandatory to enable isolation of dendrimer **79**.

While the ^{1}H- and ^{13}C-signals in the NMR spectra of **79** could readily be assigned and were used to confirm complete conversion as well as purity, a MALDI-TOF mass spectrum of the compound could not be obtained. Indeed, most aryl-triazole dendrimers and intermediates synthesized herein could not be detected by means of MALDI-TOF. In the few exceptions where a product signal could be detected, there were also a number of signals at lower m/z ratios, which resulted from a decomposition of the laser irradiated product (see also Figure 134). Despite recurrent signal patterns, the detected signals could not always be identified and assigned to specific molecular fragments. Dendrimer **79** could however be crystallized in the form of colorless triclinic needles. These needles were used for a determination of the compounds single crystal structure by means of X-ray diffraction (Figure 122).

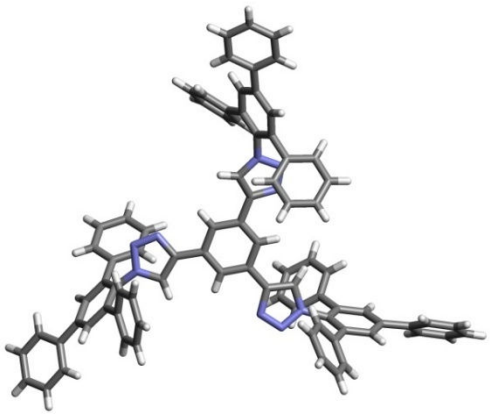

Figure 122: Single crystal structure of first generation aryl-triazole dendrimer **79** with a trigonal planar core

As evidenced by the crystal structure (Figure 122), the steric demand of *ortho*-phenyl rings of each 2,4,6-triphenylbenzene moiety enforces a twisting of aryl rings out of their common plane with neighboring triazole rings, while all triazole rings retain their almost coplanar alignment with the central aryl ring of the core (and thus with each other). The alignment is only slightly disturbed due to packing effects in the crystal lattice.

The geometric parameters of the crystal structure were used as input for an approximation of the electrostatic surface potential (ESP) of **79** by semi-empirical AM1 calculations. A mapping of the ESP onto the electron density map of **79** is displayed in Figure 123.

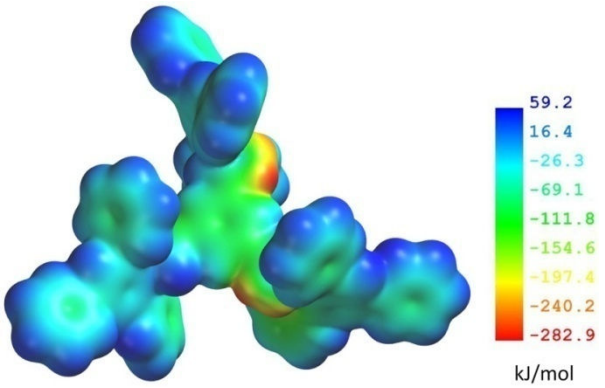

Figure 123: Electrostatic surface potential of aryl-triazole dendrimer **79**

The nitrogen atoms of each triazole ring possess a pronounced negative electrostatic potential (up to –283 kJ/mol; indicated by a red color in Figure 123), which correlates to their tendency to coordinate to positively charged species such as cations or positively polarized atoms of other molecules. However, the stiffness of the scaffold and the screening effect of neighboring phenyl rings make dendrimer **79** less coordinating than triazole containing compounds with more flexible scaffolds (such as the frequently used ligand TBTA, see 2.2.3.2).

To enable the synthesis of a second generation aryl-triazole dendrimer, azide AB_2 building block **74** was cycloadded to the trigonal planar core **78**, followed by an activation of the resulting species **79** for another growth step via removal of its T*i*PS-groups with TBAF in THF (see Figure 124).

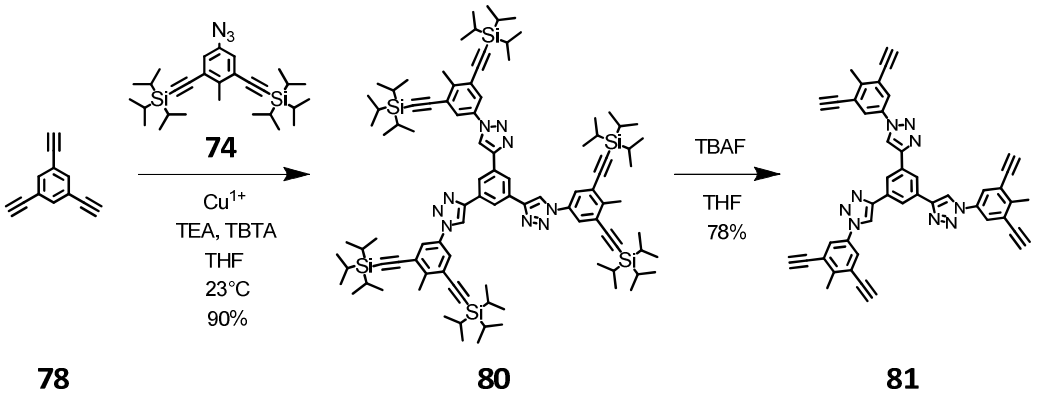

Figure 124: Synthesis of ethynyl functionalized aryl-triazole dendrimer **81** with a trigonal planar core

It is noteworthy that ethynyl functionalized species **80** and (even more so) deprotected species **81** both easily form aggregates. Aggregate formation was evidenced by the appearance of white, solid precipitate in their solutions even at moderate concentrations (approx.

10 mg/mL) in comparatively good solvents such as THF. Moreover, aggregation caused a very slow elution of both **80** and **81** from silica, which made the use of large amounts of elution solvent necessary. Surprisingly, the solubility of **81** in methylene chloride was so little that this solvent could be used to purify **81** by way of extraction of impurities from the non dissolved and solid raw product.

Ethynyl functionalized compound **81** was converted to second generation aryl-triazole dendrimer **82** in THF at room temperature using bulky azide **25** for endcapping (Figure 125). Due to the low solubility of the starting material **81** in THF (aggregation), a relatively diluted solution (50 mg of **81** dissolved in 150 mL THF) was used for the reaction. After addition of azide **25** and stirring the reaction mixture at room temperature over night, an olive-green precipitate had formed, which was separated from the otherwise clear, orange-brown solution.

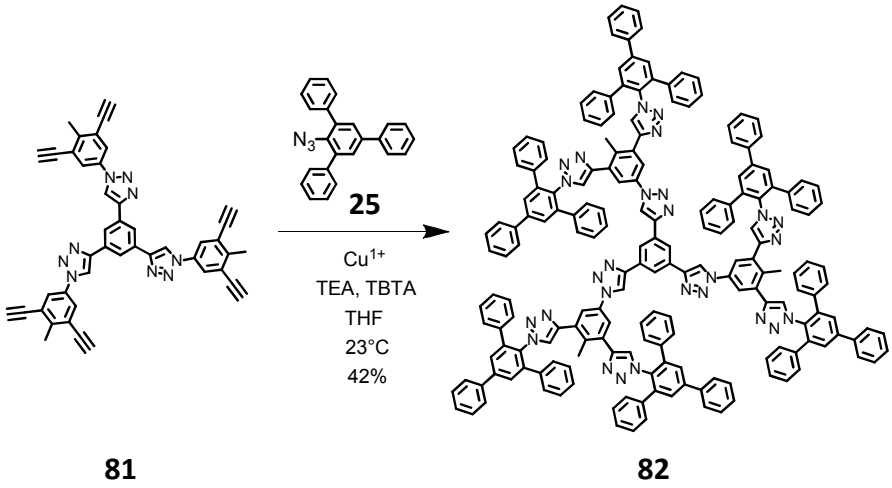

Figure 125: Synthesis of second generation aryl-triazole dendrimer **82** with a trigonal planar core

This solution was purified by column chromatography and the therein contained dendrimer **82** was precipitated in hexane. However, just as in the case of first generation dendrimer **79**, an additional purification of by means of recycling GPC was mandatory to enable pure isolation of aryl-triazole dendrimer **82**.

The low field region of the ^{1}H-NMR spectrum of dendrimer **82** comprises all of its proton signals (see Figure 126) except for the singlet of the methyl group ($\delta = 1.87$ ppm) located at the branching phenyl ring.

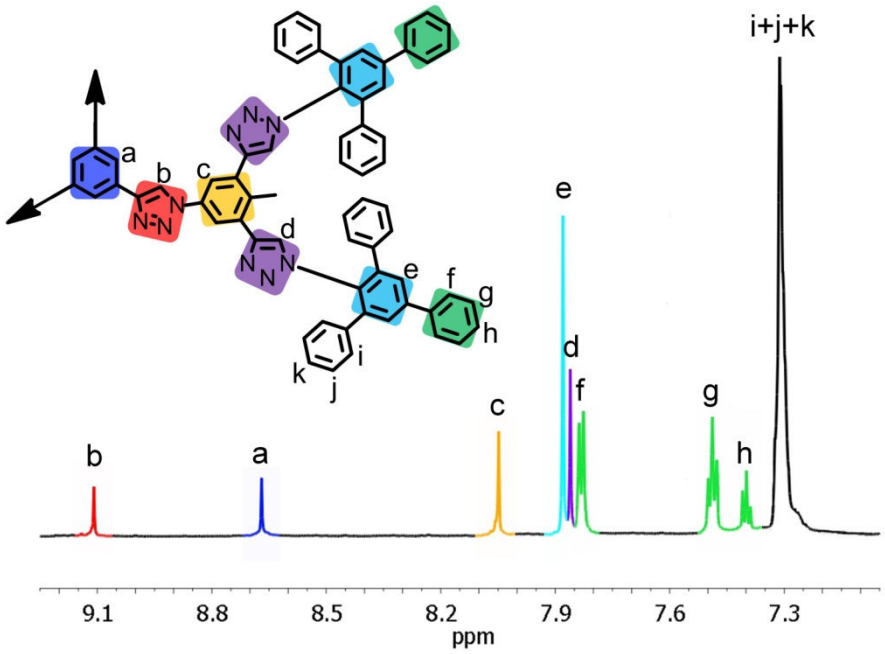

Figure 126: Low field region of the ^{1}H-NMR spectrum of **82** in THF-d8 (700 MHz)

Due to their bulky 2,4,6-triphenylbenzene neighbors, the protons H^{d} of the outer triazole rings of dendrimer **82** (δ = 7.86 ppm, marked violett in Figure 126) are significantly better shielded from the outer magnetic field than the protons H^{b} of the inner triazole rings (δ = 9.11 ppm, marked red in Figure 126).

The geometry optimized structure of dendrimer **82** (semi-empirical AM1 calculation) suggests a relatively flat overall orientation of dendrons, caused by the preference for a coplanar alignment of triazole and neighboring phenyl rings. The stick model representation of the optimized structure of **82** is displayed in Figure 127.

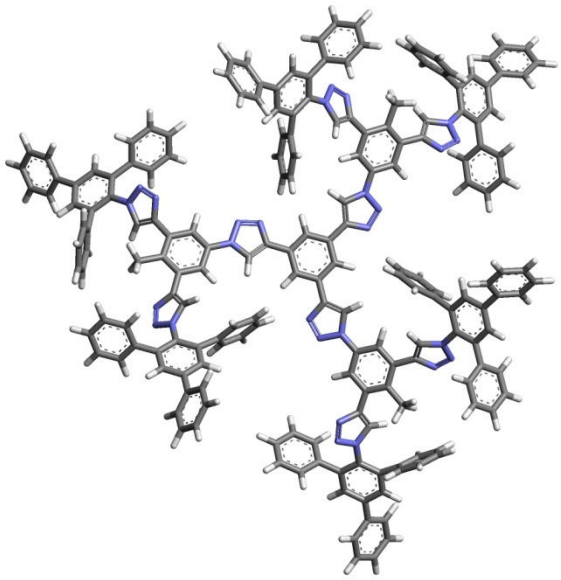

Figure 127: Modeled structure of second generation aryl-triazole dendrimer **82** with a trigonal planar core (stick model, geometry optimized by semi-empirical AM1 calculation)

The bulky 2,4,6-triphenylbenzene moieties at the surface cause a twisting as well as provide a screening of the outer triazole rings of **82**, which might explain the largely increased solubility of the dendrimer **82** in THF and DCM as compared to its starting material **81**.

3.3.2 Aryl-Triazole Dendrimers with a Tetrahedral Core

Ethynyl functionalized tetraphenylmethane **83** has frequently been utilized as a core for the build-up of polyphenylene dendrimers. Due to its tetrahedral geometry, tetraphenylmethane orients growing dendrons into all three spatial dimensions, and the dendrimer adopts an overall globular shape at comparatively low generations and low degrees of branching.[52] In order to achieve a more globular overall shape and thus potentially better solubilities in organic solvents, ethynyl functionalized tetraphenylmethane **83** was also utilized here. Copper catalyzed cycloaddition of bulky azide **25** gave the first generation aryl-triazole dendrimer **84** with a tetrahedral core (see Figure 128).

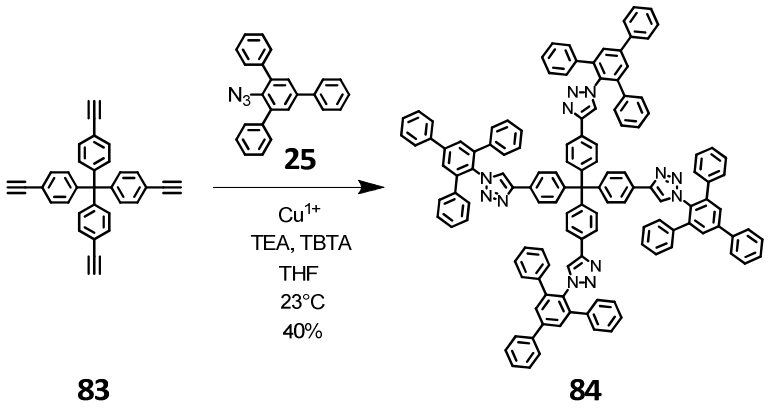

Figure 128: Synthesis of first generation aryl-triazole dendrimer **84** with a tetrahedral core

Dendrimer **84** can be regarded as a related structure to the triazole-phenyl functionalized tetraphenylmethane described by *Stefan Bräse et al.* (see crystal structure in Figure 118 (B)[215]). Despite the tetrahedral geometry of its core, however, dendrimer **84** still showed a considerable tendency to aggregate. The ^{1}H-NMR spectrum of **84** was recorded in methylene chloride at a concentration where the dendrimer had already partly precipitated. The recorded signals of the dissolved species (which were in equilibrium with the white precipitate) and the assignment to the according protons of **84** are displayed in Figure 129.

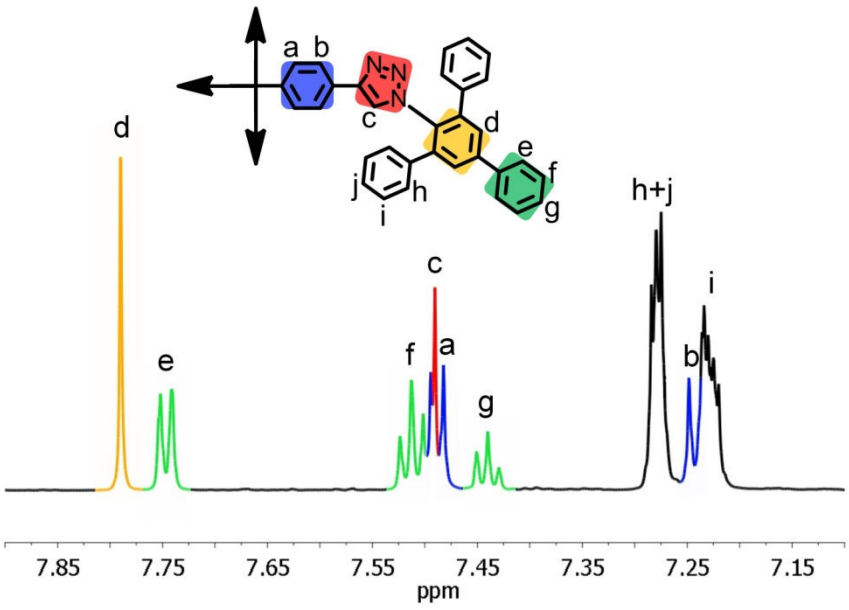

Figure 129: ^{1}H-NMR spectrum of **84** in CD_2Cl_2 (700 MHz)

Due to the screening effect of its neighboring phenyl rings, the signal of the triazole proton H^c appears significantly shifted towards high field.

The geometry optimized structure of dendrimer **84** (semi-empirical AM1 calculation), which is displayed in Figure 130, demonstrates the spatial orientation of dendrons resulting from the tetrahedral geometry of the core.

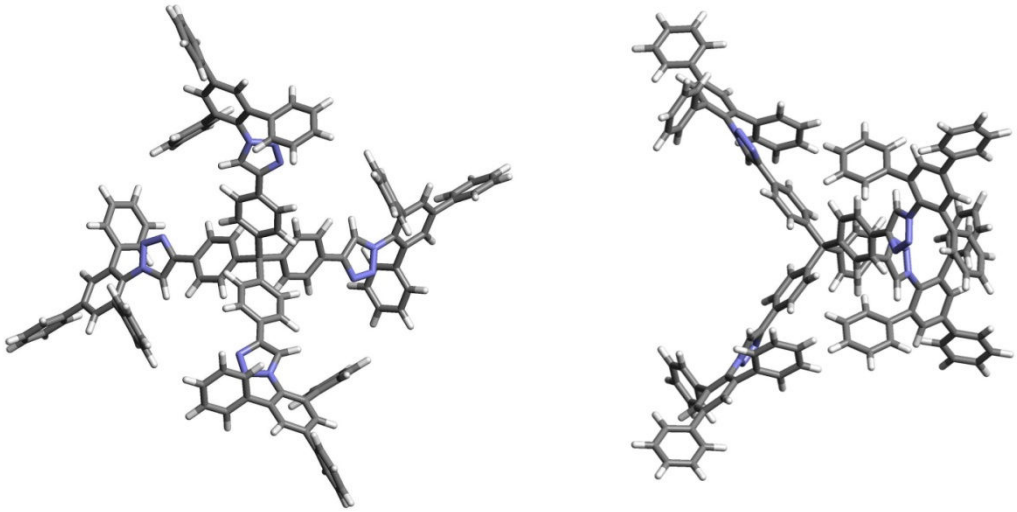

Figure 130: Front (left) and side view (right) of the spatial structure of first generation aryl-triazole dendrimer **84** with a tetrahedral core (stick model, geometry optimized by AM1 semi-empirical calculation)

The structure of **84** is very similar to the expected structure of click-dendronized borate **29** (see paragraph 2.2.3.2). Taking into account the fairly globular structures of **84** and **29** (as compared to aryl-triazole dendrimers with a trigonal planar core) and the comparatively better steric screening of coordinating triazole moieties (see ESP of **84** in Figure 131), the observed tendency of dendrimer **84** and similarly of borate **29** to aggregate is somewhat surprising.

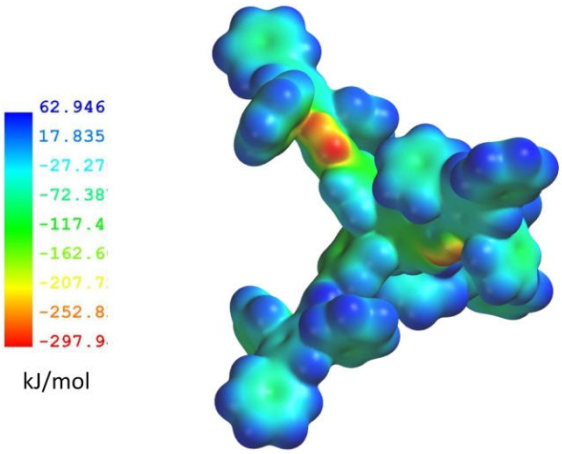

Figure 131: Electrostatic surface potential of aryl-triazole dendrimer **84** (based on semi-empirical AM1 calculation)

To enable the synthesis of a second generation aryl-triazole dendrimer with a tetrahedral core, AB_2 building block **74** was cycloadded to the tetraphenylmethane core **83** and the resulting species **85** was activated for a second growth step via removal of its T*i*PS-groups with TBAF in THF (see Figure 132).

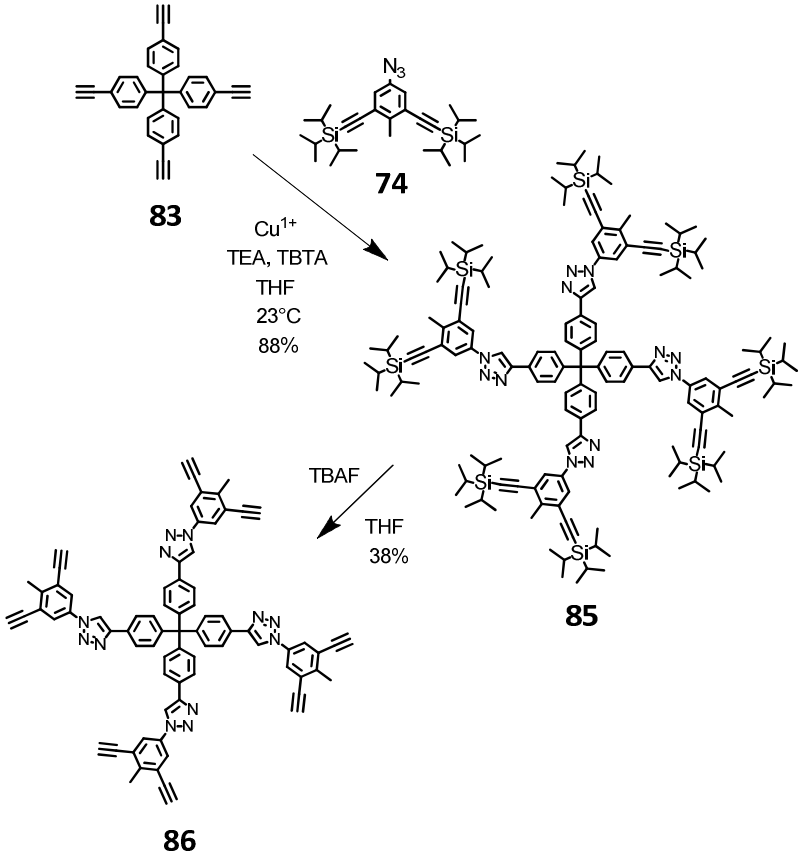

Figure 132: Synthesis of ethynyl functionalized aryl-triazole dendrimer **86** with a tetrahedral core

T*i*PS-protected compound **85** was one of very few aryl-triazole species that could be detected by means of MALDI-TOF mass spectrometry (see Figure 133). Besides the very weak signal of the product, three additional signals at lower m/z ratios (each with a $\Delta m/z$-steps of roughly 25) were observed.

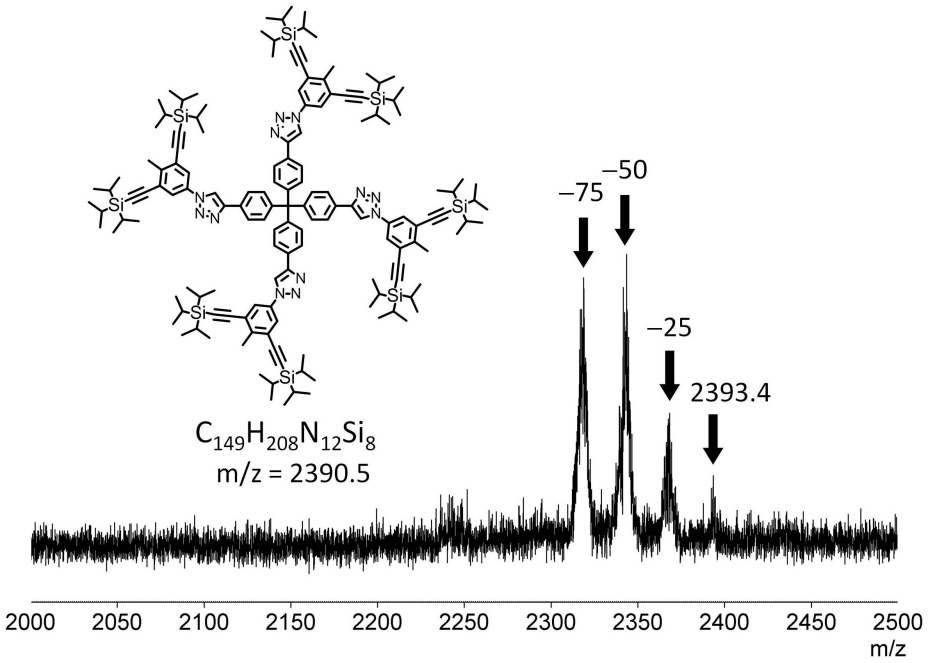

Figure 133: MALDI-TOF of aryl-triazole compound **85**

Most probably, the three additional signals at lower m/z ratios result from a UV laser induced decomposition of the triazole rings in **85**. Upon cleavage of N_2 from triazole, either enamine/imine (top) or an aziridine (bottom) moieties are obtained, corresponding to a loss in mass of 26 units (Figure 134).

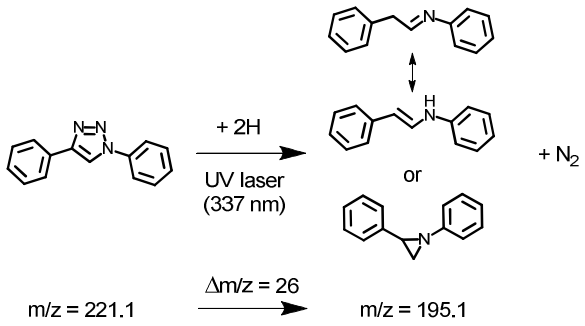

Figure 134: UV laser induced loss of nitrogen N_2 from triazole rings in aryl-triazole compounds

It is however surprising that cleavage of nitrogen from compound **85** only occurs up to three times, although four triazole rings are present in the structure. Along with other pathways of UV laser induced decomposition, the above described loss of nitrogen from triazole might be responsible for the frequent failure to detect aryl-triazole dendrimer species by means of MALDI-TOF.

The yield of activated, ethynyl functionalized species **86** (Figure 132) was relatively low due to aggregation and incomplete elution during purification by column chromatography.

After isolation, **86** was endcapped to form a second generation dendrimer by using two different reagents: Azidobenzene **75** was used to synthesize second generation aryl-triazole dendrimer **87**, while bulky azide **25** was used for the synthesis of 2,4,6-triphenylbenzene endcapped aryl-triazole dendrimer **88** (Figure 135).

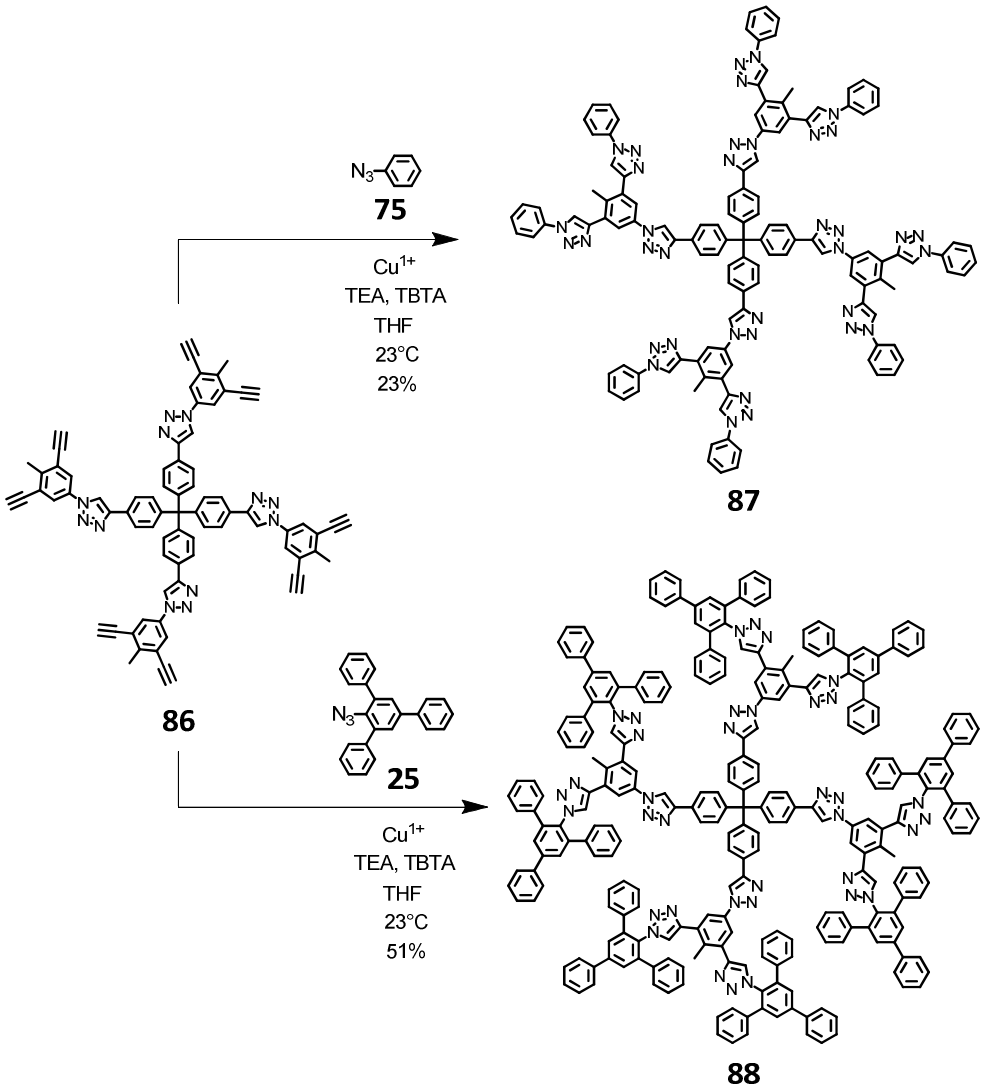

Figure 135: Synthesis of second generation aryl-triazole dendrimers **87** and **88** with a tetrahedral core

The more highly shielded second generation dendrimer **88** exhibited much better solubility in THF and a reduced tendency to aggregate as compared to dendrimer **87**. Nevertheless, purification by means of recycling GPC was necessary to obtain a pure product. A comparison of the modeled structures of both dendrimers (Figure 136) indicates that the energetically favored coplanar alignment of phenyl and triazole rings is not only disturbed by the large spatial demand of bulky 2,4,6-triphenylbenzene moieties in **88**, but also by the methyl group of each branching phenyl ring in both dendrimers **87** an **88**.

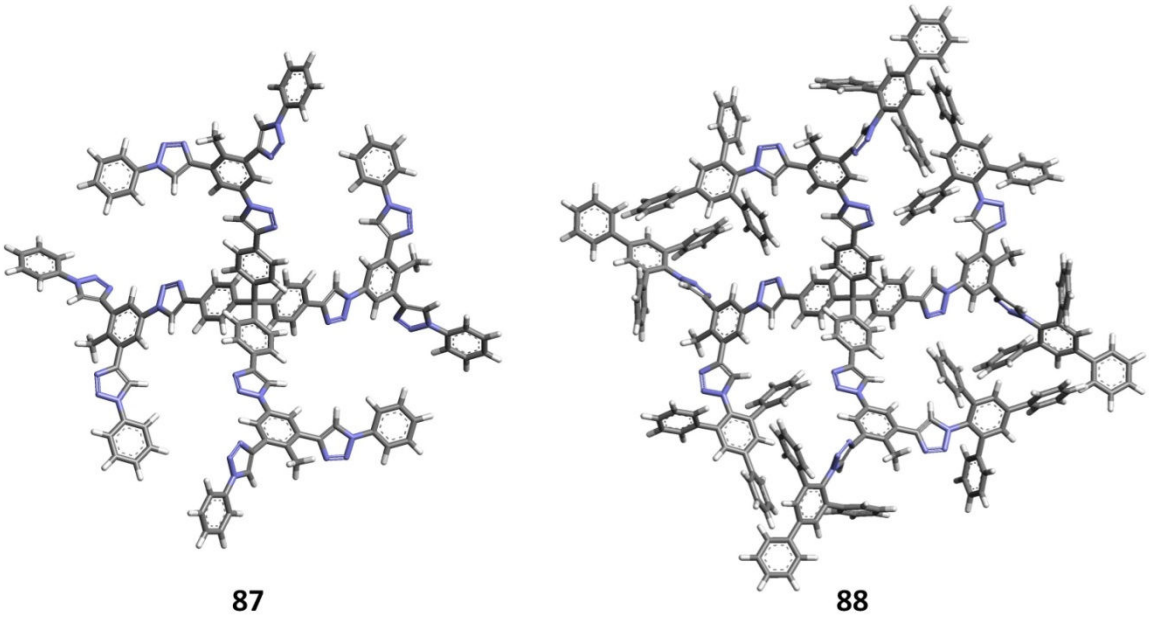

Figure 136: Modeled structures of second generation aryl-triazole dendrimers **87** and **88** with a tetrahedral core (stick model, geometry optimized by semi-empirical AM1 calculations)

The proton signals of dendrimer **88** are displayed in Figure 137 (except for the singlet of the methyl group at δ = 1.71 ppm). As compared to the spectrum of first generation aryl-triazole dendrimer **84** (see Figure 129), proton signals attributed to the dendritic core (such as H^a, H^b and inner triazole proton H^c) appear at significantly higher chemical shifts in **88**.

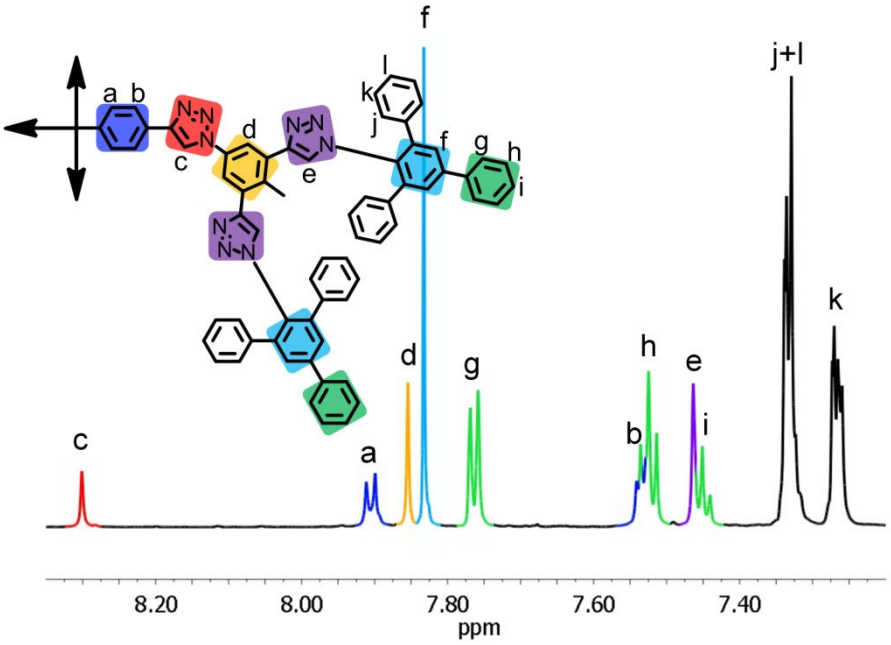

Figure 137: Low field region of the ^{1}H-NMR spectrum of **88** in THF-d8 (700 MHz)

Nevertheless, the inner triazole protons are still more strongly shielded from the outer magnetic field in the case of a tetrahedral core (see Figure 137, dendrimer **88**, H^c, δ = 8.30 ppm) than a trigonal planar core (see Figure 126, dendrimer **82**, H^b, δ = 9.11 ppm). This observation agrees with the overall more globular shape of aryl-triazole dendrimers with a tetrahedral core.

For the synthesis of a third generation aryl-triazole dendrimer, AB_2 building block **74** was cycloadded to first generation ethynyl functionalized dendrimer **86**, whereupon the resulting second generation dendrimer **89** was activated for a third growth step (Figure 138).

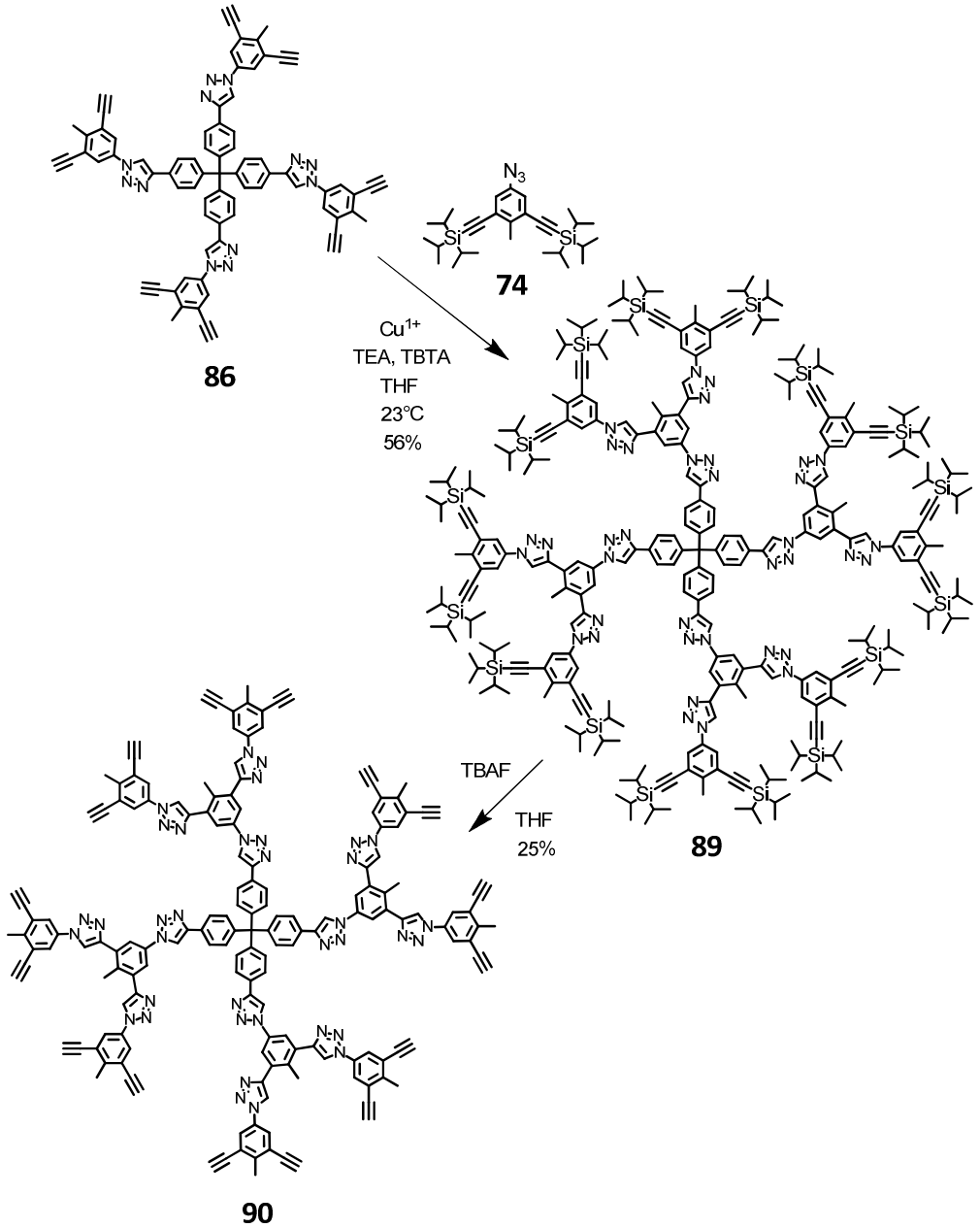

Figure 138: Synthesis of ethynyl functionalized aryl-triazole dendrimer **90** with a tetrahedral core

Intermediate **89** was purified by means of recycling GPC. Upon treatment of **89** with TBAF in THF (Figure 138), the resulting deprotected species **90** started aggregating spontaneously. After dilution and filtration over silica, compound **90** was purified via extraction of the solid raw product with methylene chloride. For the synthesis of third generation aryl-triazole dendrimer **91**, compound **90** was then reacted with bulky azide **25** in THF (Figure 139).

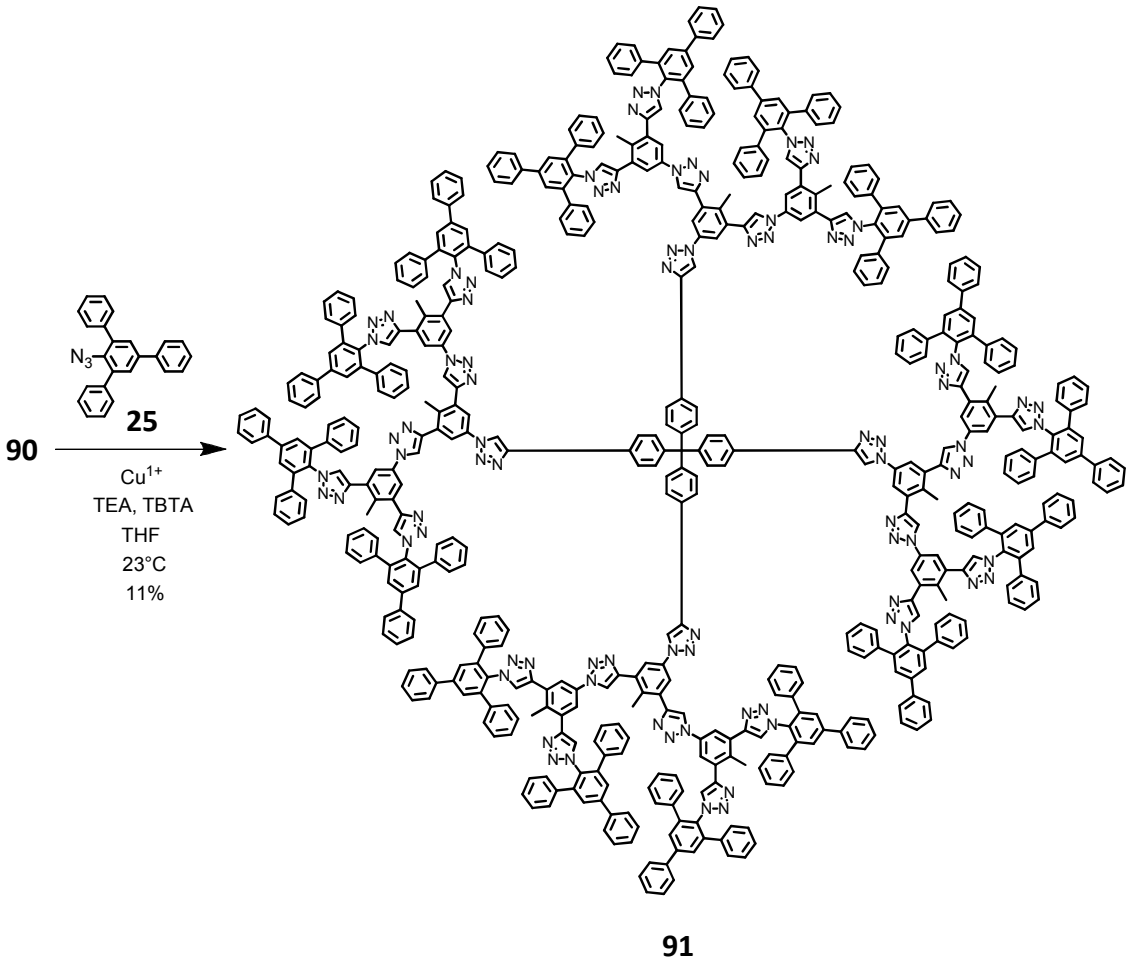

Figure 139: Synthesis of third generation aryl-triazole dendrimer **91** with a tetrahedral core

Several attempts to synthesize dendrimer **91** failed, presumably due to the relatively low solubility of starting compound **90** in the reaction medium THF as well as the loss of potentially formed product during purification. Even after a successful synthetic attempt and purification of the mixture via filtration and recycling GPC, only trace amounts (about 0.8 mg) of third generation aryl-triazole dendrimer **91** could be isolated. The obtained amount was just sufficient for a characterization of **91** by means of ^{1}H-NMR spectroscopy.

A stick representation of the modeled structure of aryl-triazole dendrimer **91** is displayed in Figure 140.

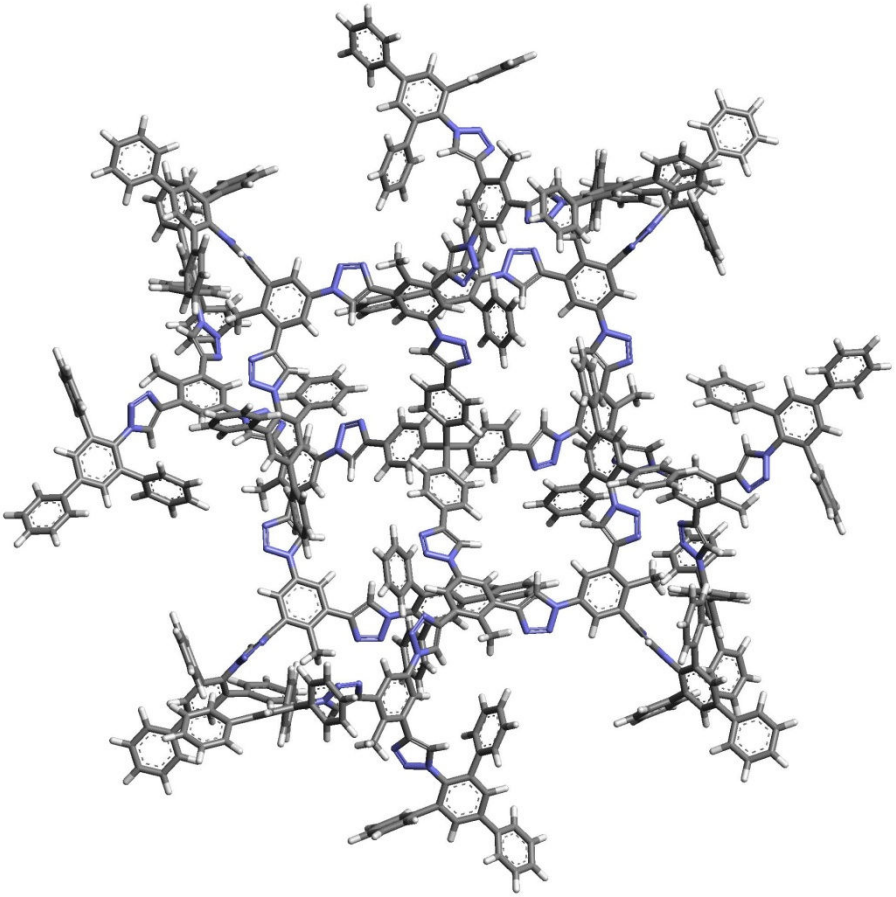

Figure 140: Modeled structure of third generation aryl-triazole dendrimer **91** with a tetrahedral core (stick model, geometry optimized by semi-empirical AM1 calculations)

The modeled structure of aryl-triazole dendrimer **91** illustrates that its scaffold contains relatively large voids, similar to the inherent voids present in rigid PPD scaffolds. Here, however, the void boundaries are formed not only by aryl moieties, but also by a large number of nitrogen containing triazole rings. Due to the pronounced negative electrostatic surface potential of triazole moieties (compare Figure 123 and Figure 131) and the inherent porosity of the scaffold, materials based on aryl-triazole dendrimers might be suitable for sensing applications.

3.3.3 Hybrid Dendrimers composed of Aryl-Triazole and PPD scaffolds

As mentioned earlier, the common requirement of ethynyl functions in both polyphenylene and aryl-triazole dendrimer synthesis readily invites for a combination of both concepts and the design of dendrimer hybrids. A copper catalyzed cycloaddition of azides to alkynes can certainly be used to further functionalize PPD surfaces. This concept would be especially advantageous with respect to the functionalization of PPDs with temperature sensitive moieties.

However, are aryl-triazole scaffolds also stable enough to endure the high temperatures that are required for the growth of PPDs? From a thermodynamic point of view, triazole rings should be sufficiently stable. Thermal degradation of 1,2,3-triazole occurs between 218 °C and 338 °C.[216] Nevertheless, measurements by means of MALDI-TOF mass spectrometry also demonstrated that aryl-triazole compounds decompose easily upon appropriate irradiation.

In order to test the applicability of an aryl-triazole scaffold with regard to a further functionalization with polyphenylenes, ethynyl functionalized species **81** was dispersed in *o*-xylene and reacted with tetracyclone **13** at 160 °C.

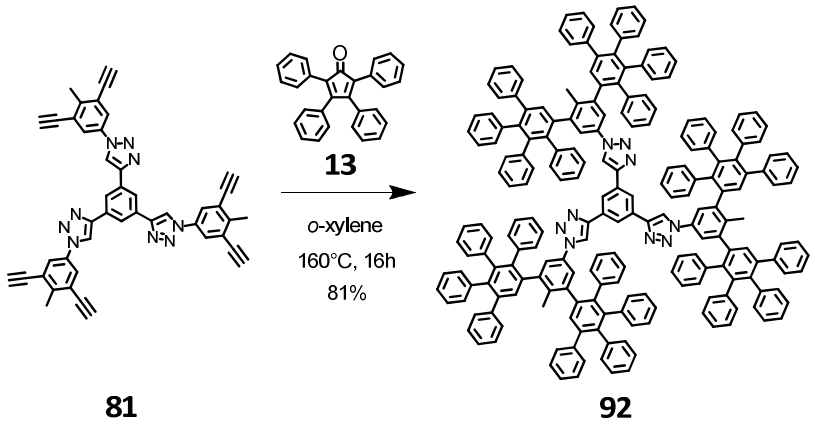

Figure 141: Synthesis of second generation aryl-triazole/polyphenylene hybrid dendrimer **92**

The synthesis of hybrid dendrimer **92** was successful, which thus confirmed a sufficient stability of the triazole moiety for the functionalization with polyphenylenes. The product was one of the few aryl-triazole species that could be detected by means of MALDI-TOF mass spectrometry (see Figure 142). As described earlier in the case of aryl-triazole compound **85**, the signal of dendrimer hybrid **92** is accompanied by three additional signals at

lower m/z ratios as a result of UV laser induced decomposition, which leads to a release of nitrogen from triazole moieties (see also Figure 134).

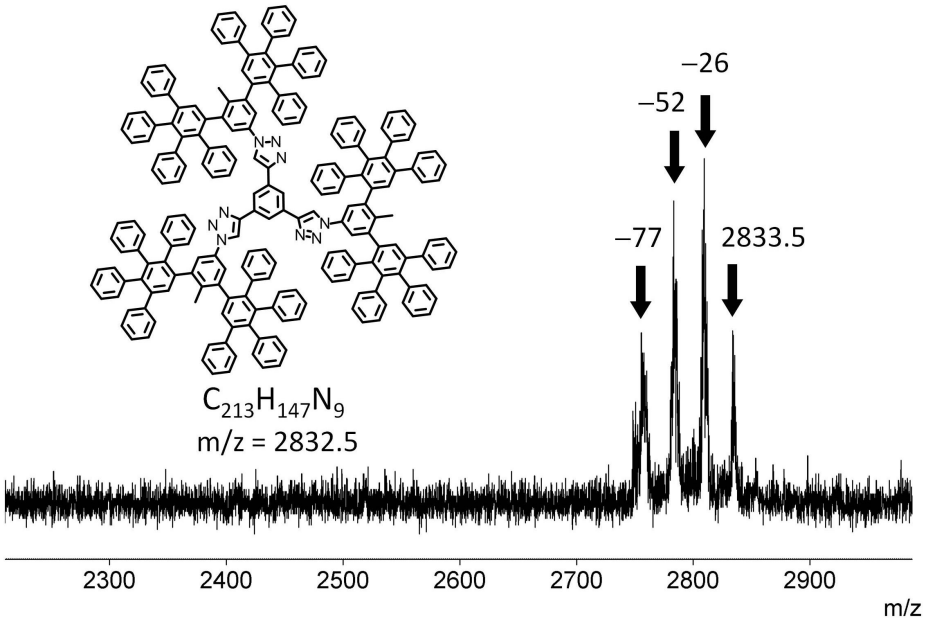

Figure 142: MALDI-TOF of aryl-triazole compound **92**

Hybrid dendrimer **92** exhibits much better solubility in THF than its precursor compound **81** or first generation aryl-triazole dendrimer **79**. The increased solubility is probably caused by the sterically screening effect of the PPD surface (see modeled structure of **92** in Figure 143).

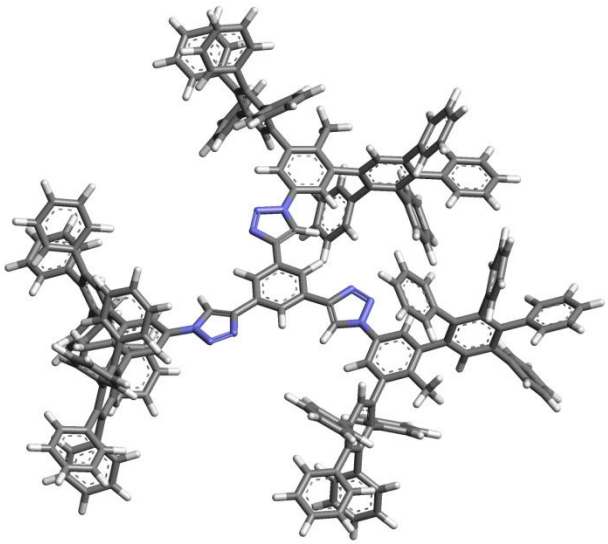

Figure 143: Modeled structure of aryl-triazole/polyphenylene hybrid dendrimer **92** with a trigonal planar core (stick model, geometry optimized by semi-empirical AM1 calculations)

Surprisingly, the ^{1}H-NMR spectrum of hybrid dendrimer **92** in THF was highly complex (see Figure 144). Two clearly distinct singlets of comparable intensity (instead of the expected one singlet) were detected for the methyl groups (H^d) of **92** (compare Figure 145). It followed that at least two isomers A and B of hybrid dendrimer **92** were present in the solution, which most probably were the result of sterically blocked rotations in the molecule. By convention, the isomer of **92** in which the signal H^d of the methyl group was recorded at a chemical shift of $\delta = 2.23$ ppm was called isomer A, whereas the isomer with a methyl group signal at $\delta = 1.92$ ppm was called isomer B. General distinction of proton signals and assignment to the two major isomers A and B of **92** was enabled by a combination of different NMR spectroscopic methods, most importantly by NOESY. The low field region of the ^{1}H-NMR spectrum of **92** and the according assignment of recorded signals to both isomers A and B is shown in Figure 144.

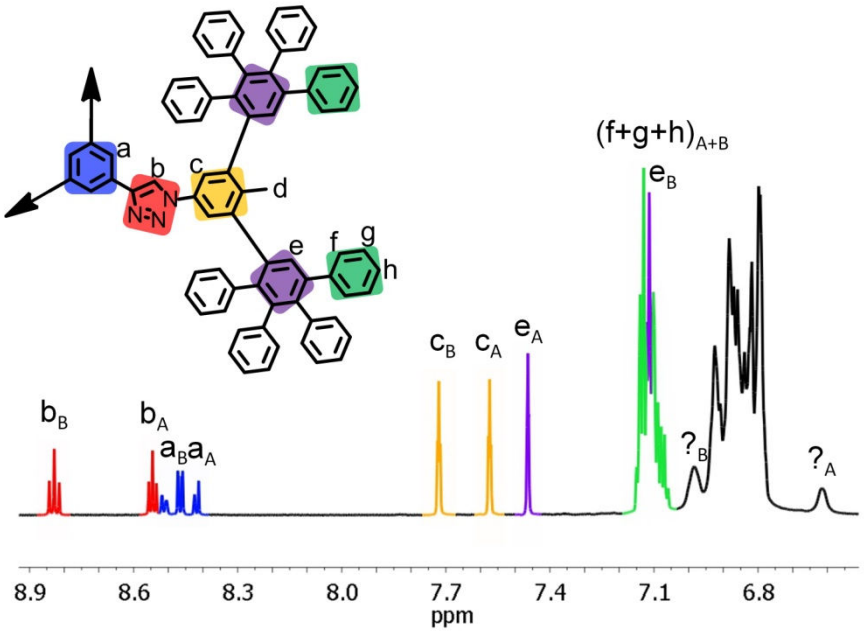

Figure 144: Low field region of the ^{1}H-NMR spectrum of **92** in THF-d8 (700 MHz) and assignment of proton signals to the two major atropisomers A and B of **92**

In addition to the distribution of proton signal intensity to the two major isomers A and B, an even finer distribution to yet more numerous "sub-isomers" could be observed. Although some of the detected signals closely resembled coupling patterns from spin-spin coupling (such as the triplet-like signals of the triazole proton H^b, marked red in Figure 144), the recorded signals were actually solely composed of several distinct singlets and were not the result of any coupling.

The most apparent differences in chemical shifts between isomers A and B were observed for the PPD generation protons H^e ($\Delta\delta_{AB} = 0.35$ ppm), the protons H^d of the methyl groups ($\Delta\delta_{AB} = 0.31$ ppm), the triazole protons H^b ($\Delta\delta_{AB} = 0.28$ ppm) and the protons H^c of the branching phenyl ring ($\Delta\delta_{AB} = 0.15$ ppm). The regions of the molecule **92** attributed to these protons were most strongly affected by the difference in molecular environments between isomers A and B. It is therefore highly probable that the appearance of isomers A and B is caused by a blocked rotation within exactly that region of the molecule, namely the rotation of a PP-dendron about the methylated phenyl ring (see also Figure 146).

Signals of the methyl group protons H^d of dendrimer **92** have been measured as a function of temperature in deuterated tetrachloroethane (see Figure 145) in order to check whether a coalescence of both signals could be induced.

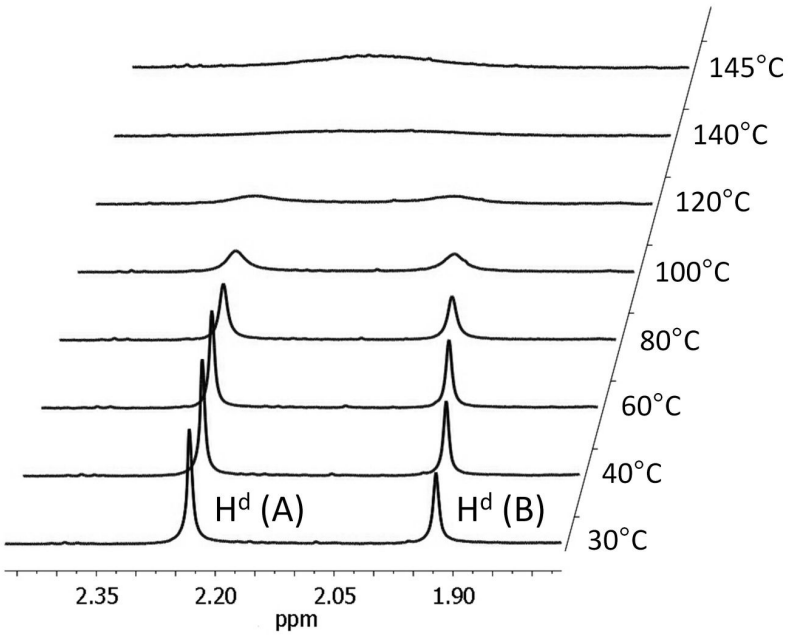

Figure 145: ^{1}H-NMR signals of the methyl groups of dendrimer **92** as a function of temperature; measured in deuterated tetrachloroethane (500 MHz)

Figure 145 demonstrates that coalescence of the methyl group signals merely begins at about 140 °C, indicating a considerably high energy barrier for dendron rotation. With the rotation of PP-dendrons blocked, two distinct "local" conformation in each dendron of **92** can be discerned (see Figure 146):

Local conformation A: The generation protons H^e of both PP-dendrons occupy the same side relative to the plane of the methylated phenyl ring (left illustration in Figure 146).

Local conformation B: The generation protons H^e of the PP-dendrons occupy opposite sides relative to the plane of the methylated phenyl ring (right illustration in Figure 146). This second conformation most probably corresponds to the before mentioned isomer B, because here the generation protons H^e are mutually shielded by their neighboring PP-dendron and should thus exhibit an NMR signal at a lower chemical shift as compared to the same protons H^e in local conformation A (compare signals of H^e of both isomers in Figure 144).

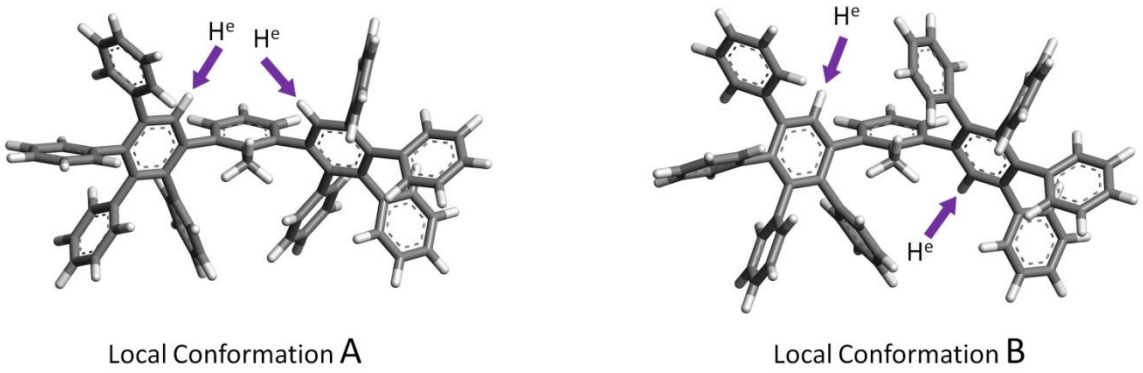

Figure 146: Illustration of the two distinct conformations for the relative orientation of polyphenylene dendrons in a singular aryl-triazole dendron of **92**

As already mentioned, the difference between isomers A and B is solely caused by a distinct local conformation of polyphenylenes in single dendrons of **92**. If however the orientation of the whole aryl-triazole dendron relative to the two remaining dendrons is considered, then again two distinct overall conformations can be discerned. These overall conformations were termed M and N in order to distinguish them from the above mentioned local conformations A and B.

Overall conformation M: all triazole protons H^b head towards the same (circular) direction (left illustration in Figure 147), and

Overall conformation N: one triazole proton heads in an opposite direction from the other two (right illustration in Figure 147).

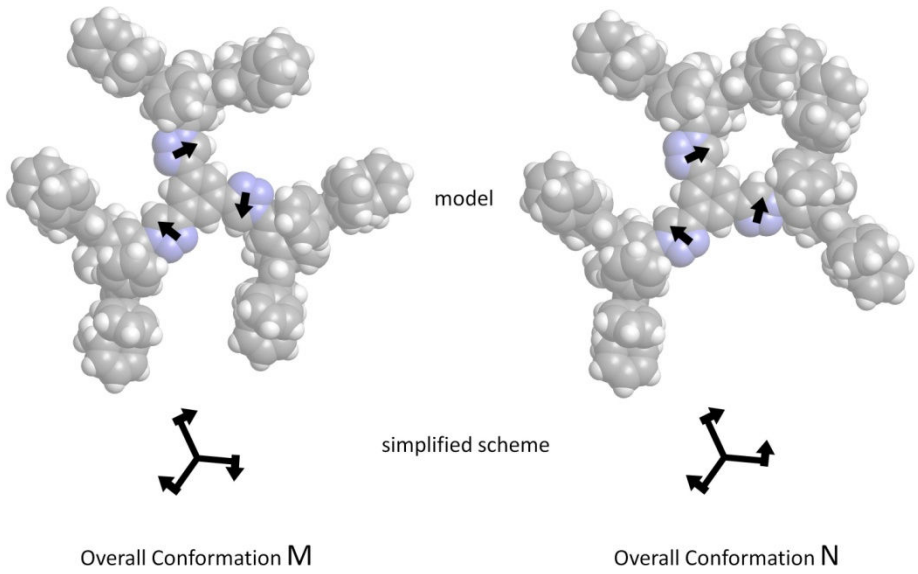

Figure 147: Illustration of the two distinct relative orientation of whole aryl-triazole dendrons in hybrid dendrimer **92**

Considering all possible orientations of dendrons (see Figure 148), each specific conformation can be transformed into one of the two above described conformation M or N via rotation of the dendrimer **92** in space. This is illustrated in Figure 148, where the letters *r* (for "right") and *l* (for "left") underneath each schematic drawing of **92** indicate the directions of the arrows (triazole protons) as viewed from top (starting with the lower left arrow and counting clockwise). Obviously, the conformations *rrr* and *lll* can be transformed into one another by flipping the whole molecule over in space and are therefore identical (conformation M). Accordingly, all remaining c conformations can be transformed into one another via rotation and/or flipping in space and are therefore identical, too.

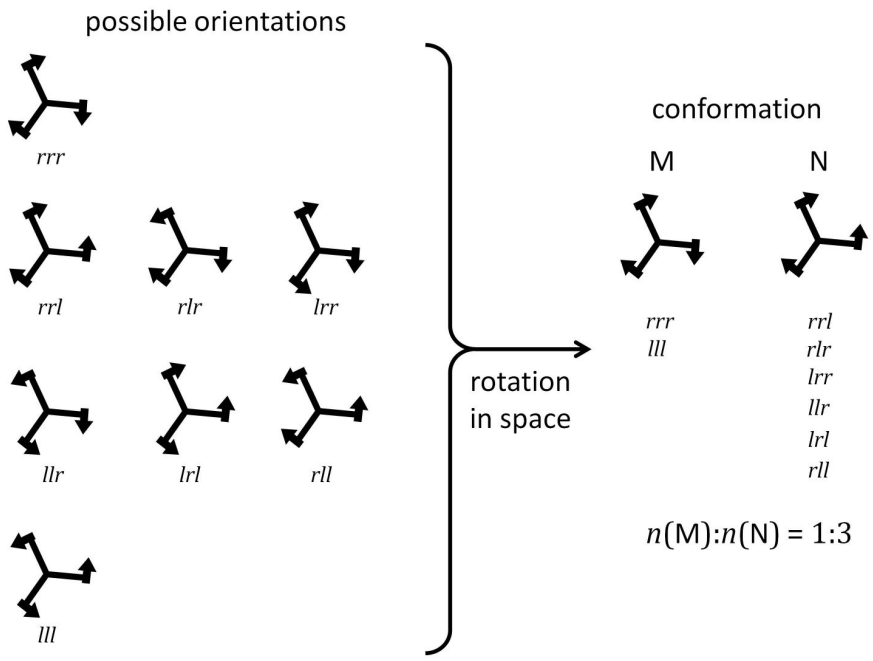

Figure 148: All possible overall orientations of dendrons in **92**, which after rotation in space can be summerized as two distinct overall conformations M and N

If the orientation of each aryl-triazole dendron is random and independent of the orientation of the other two, then overall conformation N is three times as likely as conformation M. Comparison of the molecular structure, however, suggests that conformation M could be favored over N due to reduced steric congestion between individual dendrons (see Figure 147).

Now that the overall conformations M and N have been described, the total number of possible atropisomers of **92** can be obtained by generating all possible combinations of local (A and B) and global (M and N) conformations via permutation. In Figure 149, the arrows used for the schematic drawings of dendrimer **92** have been color coded as to indicate either a local conformation of A (blue) or B (red). In total, 12 different atropisomers of **92** can be generated. It is important to bear in mind, however, that the most drastic effect of atropisomerism on proton chemical shifts results from the two distinct local conformations A and B within different overall isomers, representing the afore mentioned major two "isomers" of **92**. In agreement with the NMR data (Figure 144), the ratio A:B of these local conformations remains 1:1 when summed up over all possible atropisomers.

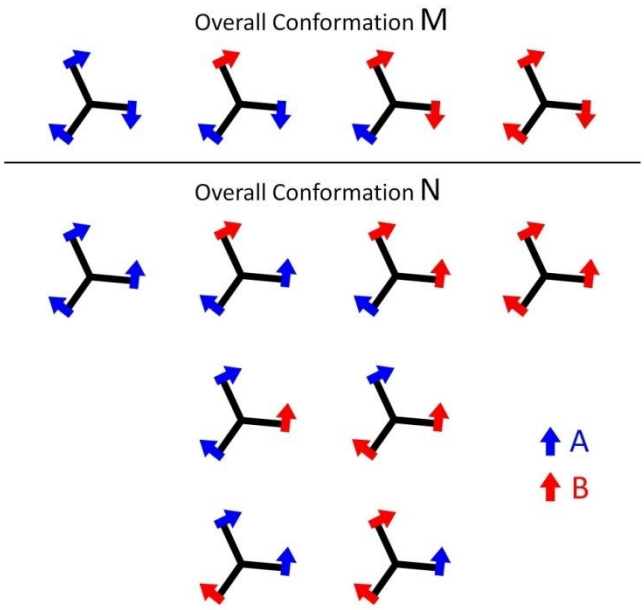

Figure 149: All 12 possible atropisomers of dendrimer **92**

Smaller differences in chemical environment caused by the different relative orientation of whole dendrons is then responsible for an additional distribution of signal intensity to even more numerous but more finely spaced signals in the NMR spectra of **92**.

Despite the occurrence of atropisomerism, the synthesis of hybrid dendrimer **92** generally confirms that a further functionalization of aryl-triazole scaffolds by means of *Diels-Alder* cycloaddition at 160 °C can indeed be performed. Functionalization of dendritic poly-phenylene and aryl-triazole scaffolds therefore works in any desired sequence and can readily be varied in each subsequent reaction step.

3.4 Summary and Outlook

In this chapter, the synthesis of a new type of dendrimer scaffold has been presented. Utilization of the copper catalyzed azide-alkyne *Huisgen* cycloaddition has enabled the synthesis of a number of different dendrimers at room temperature, solely constituted from aryl and triazole rings. Due to the comparatively large size of their backbone chain segments (Figure 117) and the energetic preference for a coplanar alignment of neighboring triazole and aryl rings (Figure 118), the resulting dendritic scaffolds were relatively stiff. Many of the intermediate aryl-triazole species as well as some of the final aryl-triazole dendrimers showed a pronounced tendency to form aggregates. Employment of bulky surface groups helped to reduce their tendency to aggregate and increased their solubility in THF and DCM. A detection of aryl-triazole dendrimers by means of MALDI-TOF mass spectrometry was often precluded by a fast decomposition of the compounds under irradiation with a UV laser (e.g. via cleavage of nitrogen from triazole).

Two distinct cores with different geometries (trigonal planar and tetrahedral) have been used to generate aryl-triazole dendrimers with either preferentially flat or globular overall shapes. The large number of triazole rings in aryl-triazole dendrimers led to a considerably high nitrogen content in the according dendritic scaffolds (see Figure 150).

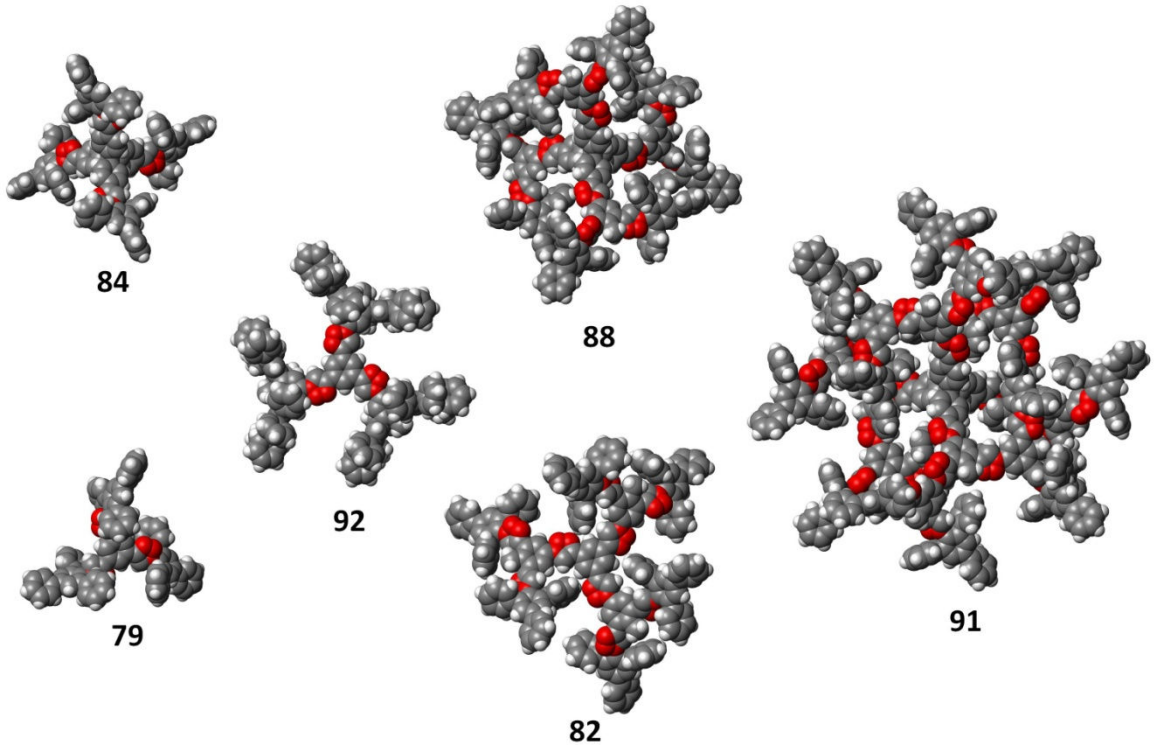

Figure 150: Dendrimers with aryl-triazole scaffolds (nitrogen atoms in red for better contrast)

Triazole rings might serve as coordination sites that enhance the interaction of the dendritic scaffold with potential guest molecules or cations.

In addition to aryl-triazole dendrimer synthesis, the potential for a combination with polyphenylene dendrimer chemistry was tested. It was found that the thermal stability of the triazole linkage is sufficient to allow for a functionalization of dendritic aryl-triazole scaffolds with rigid polyphenylenes. However, steric demand of the methyl group in the here presented AB_2 building block **74** also caused a blocking of rotation of PPD dendrons and led to the formation of 12 distinct atropisomers for the here presented hybrid dendrimer **92**.

In the future, aryl-triazole dendrimers of higher generations as well as dendrimers with different core geometries might be synthesized. Molecular modeling indicates that a fourth generation aryl-triazole dendrimer with a tetraphenylmethane core might still be accessible.

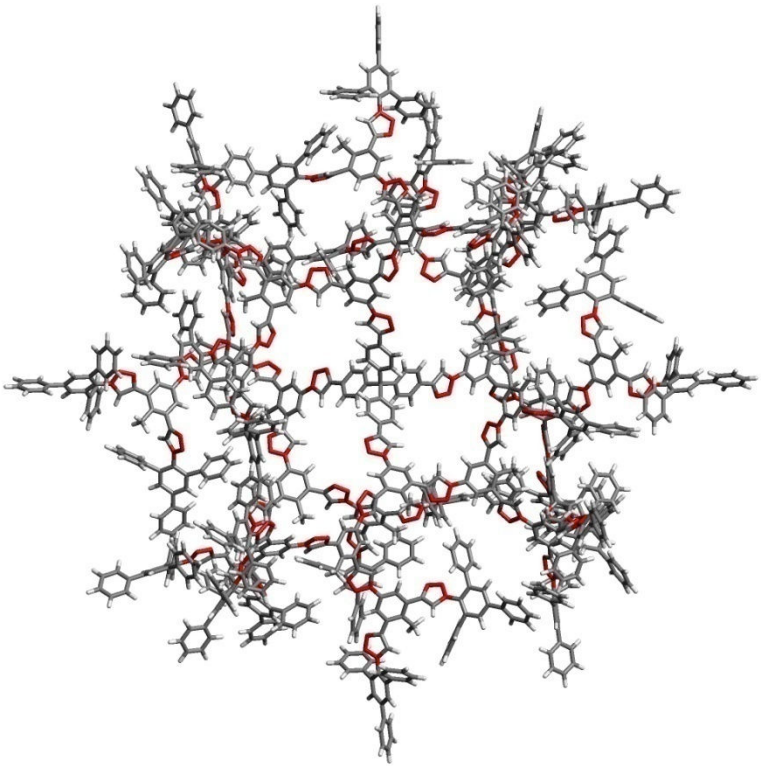

Figure 151: Potential fourth generation aryl-triazole dendrimer with a tetrahedral core

The applicability of these nitrogen rich, stiff and porous materials as sensing layers for the detection of specific guest molecules could be tested. More generally, the concept of reacting ethynyl groups at room temperature might be exploited to functionalize poly-

phenylene dendrimers with temperature sensitive surface moieties. Finally, the design of alternative AB_2 building blocks (e.g. with a larger spacing between the two ethynyl functions as compared to building block **74**) might help to avoid the formation of atropisomers in novel aryl-triazole/polyphenylene dendrimer hybrids.

4 Cation Exchange in Salts of Dendronized Anions

4.1 Introduction

The properties of a salt are governed by the intrinsic properties of their constituting cations and anions as well as by the interactions between the two (see 1.3). As a result of the synthetic protocol described in chapter 2, all rigidly dendronized borates were exclusively obtained in the form of their tetrabutylammonium (TBA^+) salts: During the step of deprotection towards borate cores **12** and **52** with tetrabutylammonium fluoride (removal of T*i*PS-groups, see Figure 152), lithium cations were inevitably and completely exchanged to tetrabutylammonium cations.

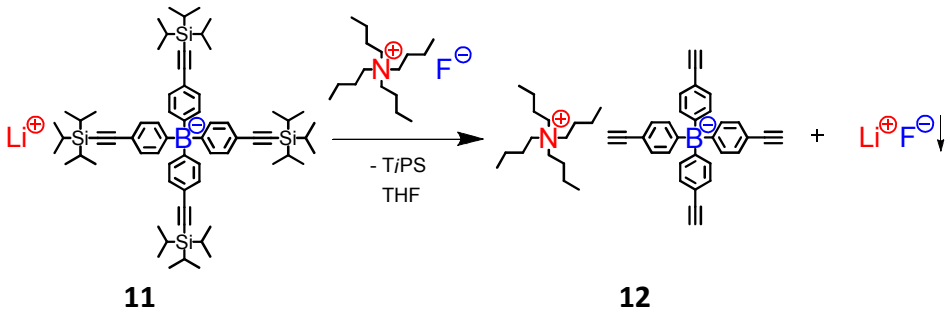

Figure 152: Deprotection of borate salt **11** and accompanied exchange of cations from Li^+ to TBA^+

As a consequence, all subsequent salts built upon the so obtained borate cores also retained TBA^+ as their counterion. Many interesting applications of weakly coordinating anions, however, require the presence of cations that are different from TBA^+. Obviously, lithium salts are required if the WCA salt shall serve as an electrolyte in lithium ion batteries. Tritylium or dimethylanilinium salts are required if the WCA salt shall yield an efficient activator for the polymerization of olefines by transition metal catalysts.

Yet tetrabutylammonium could not be exchanged to other cations by means of classical cation metathesis: Solvents of comparatively low polarity had to be used in order to dissolve the considerably hydrophobic borate salts. In such low polarity solvents, however, the TBA^+ salts of dendronized borates generally exhibited much greater solubilities than any conceivable combination of alternative cations and anions. Therefore, no salt X^+Y^- was available which, when added to a solution of TBA^+ borate, could induce a shift of the dis-

solution equilibrium towards the desired exchange of TBA^+ by another cation X^+ (Figure 153).

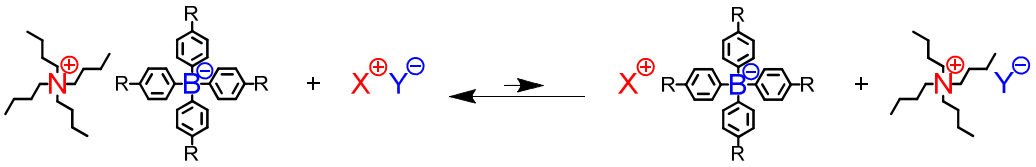

Figure 153: Scheme for the attempted cation exchange in TBA^+ salts of dendronized borates via cation metathesis (not successful!)

Physical methods to remove and exchange TBA^+, including the use of dialysis membranes, exchange resins or GPC column chromatography, were neither successful thus far.

In contrast to tetrabutylammonium, small cationic species such as Li^+ and Na^+ can easily be exchanged to other cations due to the vast number of potential salts with which these cations readily precipitate from low polarity media. This has already been demonstrated with the deliberate exchange of Li^+ to TBA^+ in the case of borate **36** (see paragraph 2.2.4.2), yielding the non-hygroscopic and thus better to handle borate salt **37**. Furthermore, the exchange of small cations has been used to obtain a number of tetrabutylammonium and tetraphenylphosphonium salts as reference compounds for the herein presented salts of dendronized anions (see Figure 154).

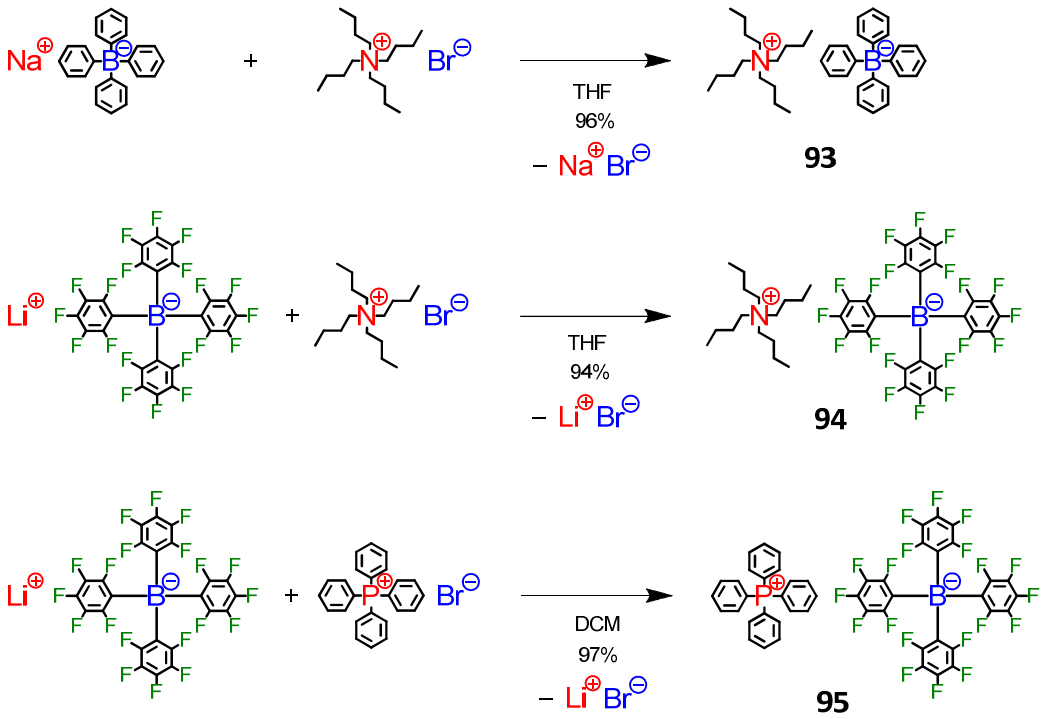

Figure 154: Cation exchange of Na^+ and Li^+ to TBA^+ and PPh_4^+ to produce suitable references for dendronized borates

It was therefore a key task to find a suitable method for generating the lithium salts of dendronized borates (or salt of other, similarly small cations) and therewith enable a deliberate exchange of cations. Ideally, the method of generating lithium salts should be applicable to TBA^+ salts during any stage of dendritic growth and should not depend on retaining e.g. Li^+ all throughout dendrimer build-up. Otherwise, any (frequently required) deprotection step involving TBAF would again lead to an exchange towards the undesired TBA^+ salt.

A suitable method for obtaining the lithium salts of dendronized borates of any generation will be presented on the following pages. Moreover, the subsequent exchange of lithium to other cations such as tetraphenylphosphonium and the newly developed diphosphonium dication will be demonstrated.

4.2 Generation of Lithium Salts of Dendronized Borates

As mentioned in the introduction to this chapter, a method for generating the lithium salts of dendronized borates is a key task to enable a facile exchange towards other cations.

When starting from the according TBA^+ salt, direct cation metathesis has proven unsuited for the task. I am therefore grateful to [redacted] who suggested using the *Hofman* elimination of amines as a completely different means to remove the tetrabutylammonium counterion via decomposition.

As its name implies, the *Hofman* elimination can be used to eliminate amine moieties in diverse molecules. For this purpose, the amine is initially quarternized to ammonium using methyl iodide, followed by treatment with silver oxide, which generates hydroxide or alkoxide ions in aqueous or alcoholic solution. For the reaction to proceed, a proton in *β*-position to the nitrogen atom is required. The proton can be abstracted by the base generated from Ag_2O. The mixture is heated to between 100 °C and 200 °C under reduced pressure, affording an olefin and the eliminated amine (see Figure 155).[217]

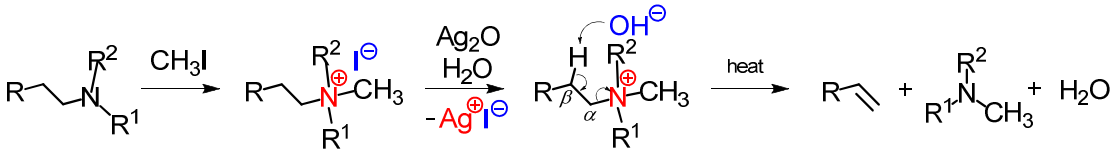

Figure 155: Scheme for the *Hofmann* elimination of amines

An important variation of the *Hofman* elimination is the *Wittig* modification, which employs very strong bases such as alkyllithium reagents or alkali metal amides instead of silver oxide.[218] By means of this modification, the *Hofman* elimination can also be carried out in THF instead of aqueous or alcoholic solutions.[219] Due to the exceptional solubility of dendronized borate salts in THF, this modified elimination method was chosen for the attempted selective decomposition of tetrabutylammonium. The use of *n*–butyl lithium as the strong base is an ideal choice, because decomposition of the TBA^+ cation to amine would be accompanied by its substitution with lithium cations in the resulting salt (see Figure 156).

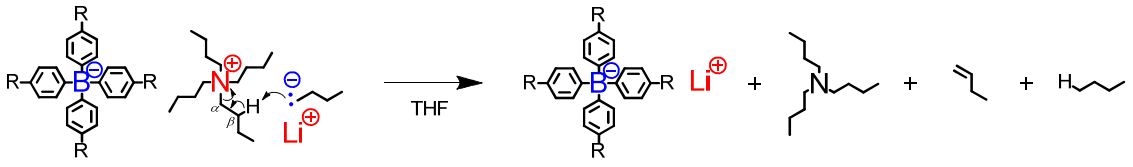

Figure 156: Scheme for the attempted exchange of TBA^+ with Li^+ in borate salts via *Wittig* modified *Hofman* elimination (selective decomposition of TBA^+)

The above described decomposition of tetrabutylammonium via *Wittig* modified *Hofmann* elimination was tested for first generation dendronized borates **14** and **53**. Figure

157 illustrates the reaction as performed for borate **53**, which can serve as a general example.

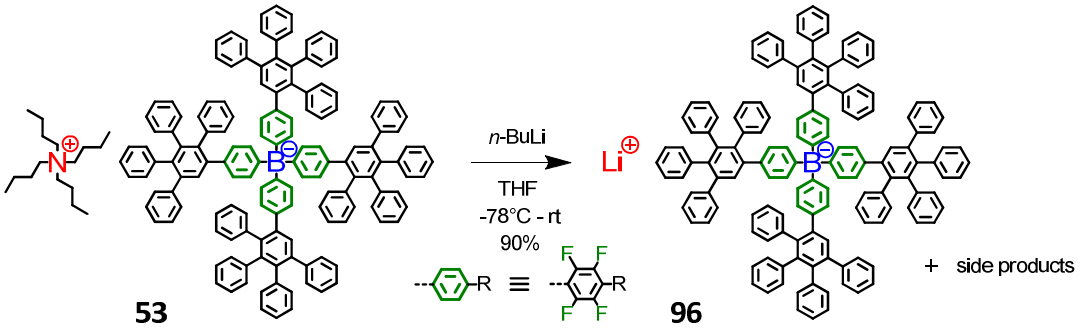

Figure 157: Decomposition of TBA^+ via Hofman elimination and substitution with Li^+ in first generation dendronized borate **53**

This method of cation exchange (decomposition of TBA^+ and simultaneous generation of the lithium salt) was indeed successful and applicable to dendronized borates with fluorinated as well as non-fluorinated cores. The strong base *n*-butyl lithium did not harm the structural integrity of the non-fluorinated tetraphenylborate core.

While tetrabutylammonium cations could successfully be decomposed, a thorough purification and isolation of the resulting lithium salts was generally difficult. In addition to the above described, regularly formed side products, further side reactions may have led to the formation of additional side products that so far could not completely be removed by means of column chromatography, extraction or precipitation. Nevertheless, even the raw produced lithium salts of dendronized borates could be utilized for a subsequent cation exchange. After exchange of their lithium cations, the newly generated salts could be obtained in very high purity using column chromatography.

4.3 Exchange to Tetraphenylphosphonium Cations

The tetraphenylphosphonium cation can be regarded as a direct structural analogue to tetraphenylborate. Due to its rigidity, salts of tetraphenylphosphonium usually crystallize more easily than the according tetraalkylammonium salts. Indeed, the tetraphenylphosphonium salt of perfluorinated tetraphenylborate **95** (produced as a reference compound; see Figure 154) was the by far most rapidly crystallizing salt that was observed within this work. In addition to facile ion packing, structure guiding attractive interac-

tions between electron rich and electron poor aryl rings apparently boosted crystallization in salt **95** rather drastically (see also paragraph 6.3.1).

For the fabrication of tetraphenylphosphonium salts of dendronized anions, the lithium salt of first generation dendronized borate **14** was dissolved in a mixture of methylene chloride and THF and treated with an excess of tetraphenylphosphonium bromide. The mixture was then filtered over silica (removal of Li^+Br^- and excess $PPh_4^+Br^-$) and precipitated in hexane. Filtration of the precipitate afforded phosphonium borate **97** in high purity (see Figure 158).

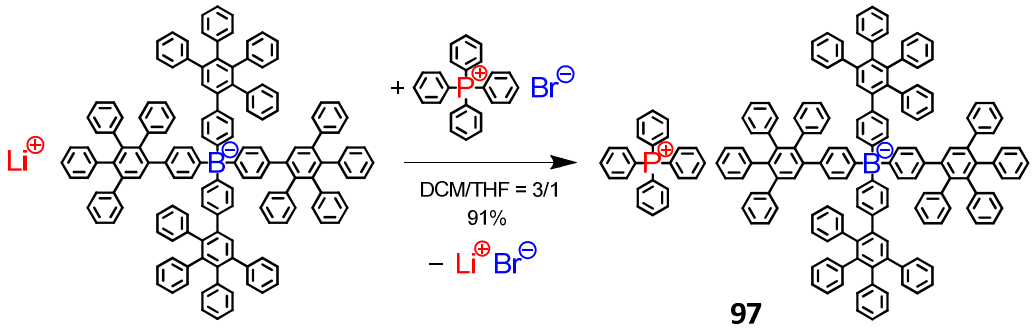

Figure 158: Cation exchange towards tetraphenylphosphonium salt **97** of first generation dendronized borate $[B\text{-}G1]^-$ with a non-fluorinated core

Relative integration of signal intensity in the NMR spectra of **97** confirmed a complete exchange of lithium to the phosphonium cation. Figure 159 displays a detail of the ^1H-NMR spectra of the PPh_4^+ and the TBA^+ salts of a first generation dendronized borate in CD_2Cl_2. In the latter case (Figure 159 (B)), signals of the cation TBA^+ are not included since they appear at much lower chemical shifts.

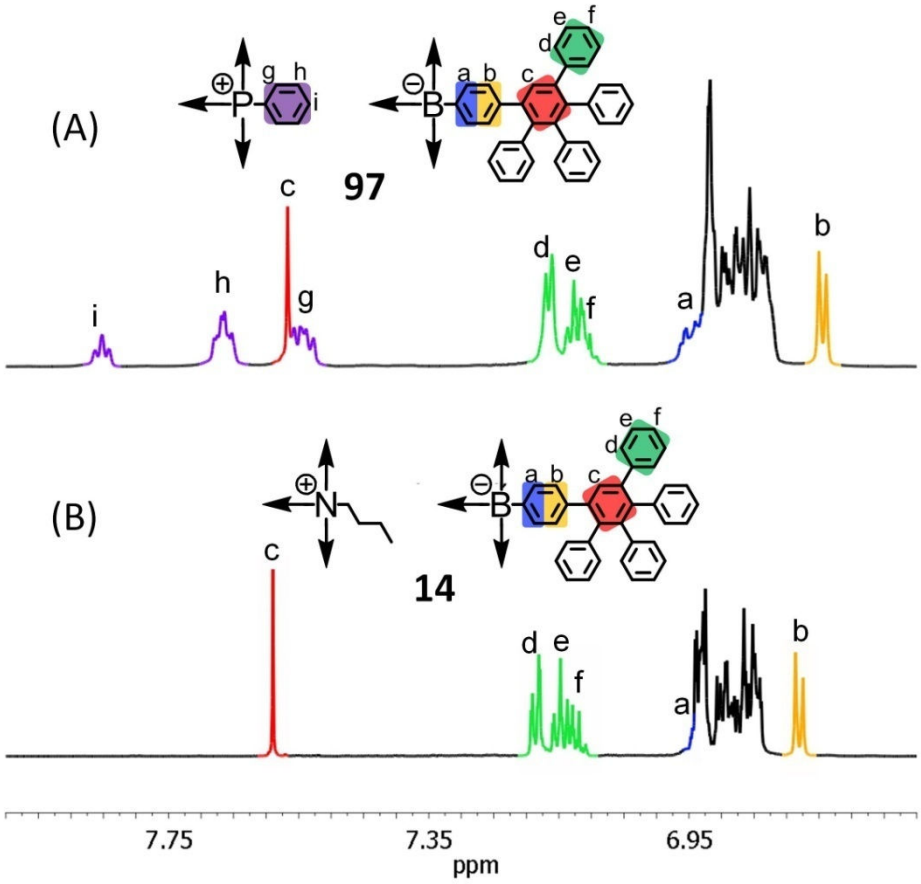

Figure 159: Comparison of ^{1}H-NMR spectra (700 MHz, CD_2Cl_2) of the PPh_4^+ salt **97** (top (A)) and the TBA^+ salt **14** (bottom (B)) of first generation dendronized borate $[B\text{-}G1]^-$

Some ^{1}H signals of dendronized borate $[B\text{-}G1]^-$ are shifted towards lower chemical shifts as a result of the exchange of TBA^+ to PPh_4^+. The phosphonium cation thus seems to provide a slightly better screening of protons (such as H^b and H^c) from the outer magnetic field. The better screening does not necessarily reflect a stronger coordination of PPh_4^+ to the borate as compared to TBA^+ but could rather be the result of the phosphonium ion´s different chemical structure. At a given state of coordination, currents in aryl rings of PPh_4^+ will certainly modify the local magnetic field in a different manner than the aliphatic chains of TBA^+.

The above NMR spectrum also exhibits a typical feature of compounds containing a ^{31}P nucleus (100 % natural abundance). According to the formula of multiplicity (formula (26) in paragraph 2.2.1), the coupling of ^{31}P (spin $I = 1/2$) with a neighboring nucleus causes a splitting of NMR signals into doublets (multiplicity $M = 2$). The coupling with phosphorus is quite noticeable for protons H^g and H^h (see Figure 159 (A)), but even more ap-

parent in the according ^{13}C-NMR spectrum of the salt (see signals of carbon atoms C^g and C^h in Figure 160).

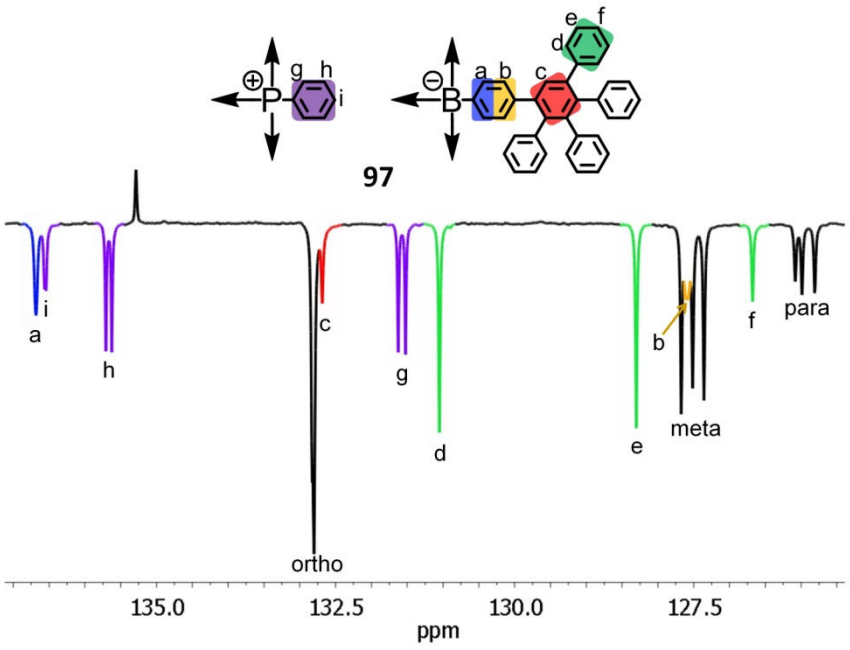

Figure 160: Detail of the spin-echo ^{13}C-NMR spectrum of phosphonium borate **97** in THF-d8 (700 MHz)

Moreover, the positive charge at the center of tetraphenylphosphonium is reflected in the order of its aryl chemical shifts from *ortho*- to *meta*- to *para*-position (H^g/C^g to H^h/C^h to H^i/C^i from lower to higher shifts), which is the reverse order of the according shifts in negatively charged tetraphenylborate (see Figure 160, also compare with Figure 169).

The tetraphenylphosphonium salt **98** of borate $[B^F\text{-}G1]^-$ with a fluorinated core was also prepared via exchange of lithium to phosphonium cations (see Figure 161).

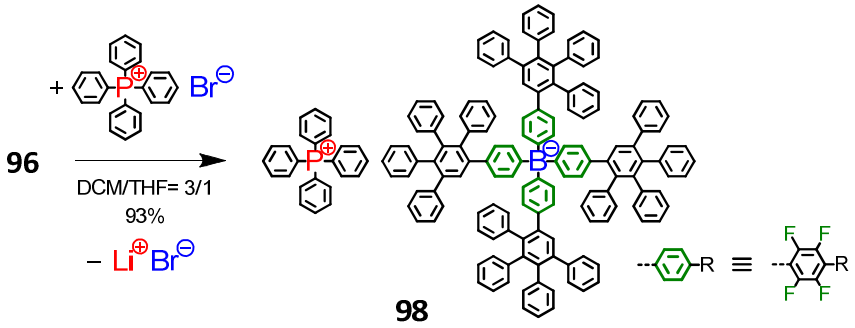

Figure 161: Cation exchange towards tetraphenylphosphonium salt **98** of first generation dendronized borate $[B^F\text{-}G1]^-$ with a fluorinated core

As mentioned earlier (see paragraph 2.3.3), dendronized borates with a fluorinated core exhibit atropisomerism due to blocked rotation of dendrons. The occurrence of atropisomers has been evidenced by several methods, such as the temperature induced coalescence of NMR signals of chemically equivalent nuclei. Remarkably, an exchange of the cation from TBA^+ to PPh_4^+ also has a pronounced effect on the atropisomer related pattern and distribution of NMR signals. Due to their higher chemical shift as compared to other borate signals, the signals of the generation proton H^c (marked red in Figure 162) can serve as a convenient probe which allows to easily monitor changes in signal patterns. In addition to a general change of the overall pattern, some of the H^c signals in borate **98** also appear at lower chemical shifts (Figure 162 (A)). Their low chemical shift might indicate a closer approach of the counterion PPh_4^+ to generation protons in the according atropisomers. Similar observations were made for ^1H-NMR spectra of borate **98** recorded in THF-d8. In contrast to the TBA^+ salts, however, atropisomerism of the borate did not lead to a multiplication of phosphonium cation signals.

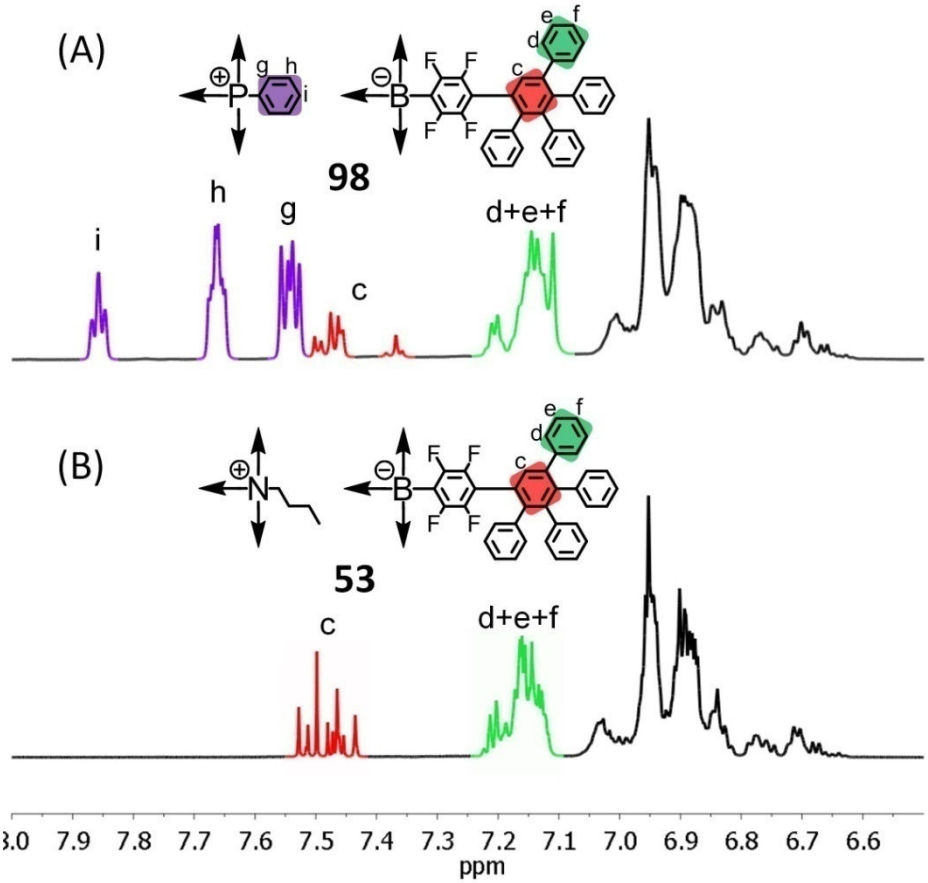

Figure 162: Comparison of ^{1}H-NMR spectra (700 MHz, CD_2Cl_2) of the PPh_4^+ salt **98** (top (A)) and the TBA^+ salt **53** (bottom (B)) of first generation dendronized borate $[B^F\text{-}G1]^-$ with a fluorinated core

Although the actual changes in atropisomer signal patterns due to cation exchange are not fully understood, the above measurements clearly demonstrate that tetrabutylammonium cations could indeed be exchanged to tetraphenylphosphonium cations in dendronized borate salts. The here presented method of cation exchange has thus proven to be applicable.

4.4 Synthesis and Exchange to Bis-Tetraphenylphosphonium Dications

An interesting potential application of dendronized anions is their employment as counterions of linear polyelectrolytes such as polyvinylpyridinium polymers. The very large size and rigid structure of dendronized anions should have a pronounced effect on several polyelectrolyte properties. It can be expected that electrostatic as well as steric interactions will enforce different conformations of the polycationic chain in solution as compared to small counter-anions, eventually resulting in different supramolecular structures as a function of anion size.

A dication may be regarded a first and simple step towards a multi-cationic polyelectrolyte. Nevertheless, going from a single cation to a dicationic species will already have a significant effect on the properties of the resulting salt.

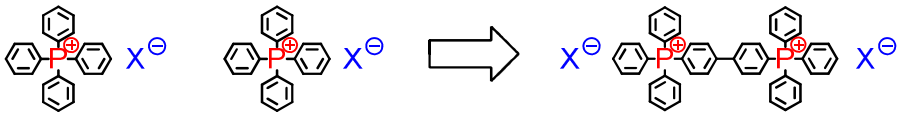

Figure 163: Structural transition from two mono-cations to a dicationic analogue

While the diphosphonium dication would be almost identical to the mono-cationic species with regard to its building blocks, the chemically enforced proximity between two positive charges will nevertheless affect *i*) the way in which ions are able to pack into a crystal lattice, *ii*) the solubility of the resulting salt and *iii*) the dissociation equilibrium of the salt in solution. Here, a dication of tetraphenylphosphonium was chosen as the synthetic objective in order to keep all other structural parameters constant. Differences between mono- and dicationic salts should thus directly reflect differences caused by the cation linkage.

For the synthesis of the desired tetraphenylphosphonium dication, mono-bromo functionalized phosphonium **99** was synthesized according to a literature procedure.[220]

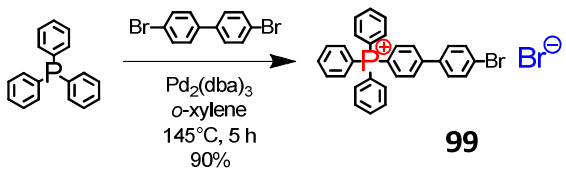

Figure 164: Synthesis of a mono-bromo functionalized tetraphenylphosphonium derivative **99** (following the procedure of *D. Marcoux et al*)[220]

The obtained salt **99** could be crystallized into transparent triclinic needles, which were used for a determination of the crystal structure by means of X-ray diffraction (see Figure 165).

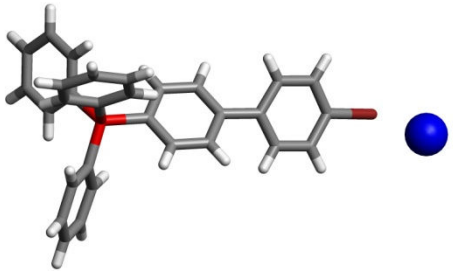

Figure 165: Single crystal structure of mono-bromo functionalized tetraphenylphosphonium salt **99**

Quaternization towards the desired dicationic salt **100** was performed in analogy to a method described by *L. Horner* ("Quaternisierung nach der Komplexsalzmethode").[221] Instead of the therein recommended beer bottle, a Teflon® container sealed within an autoclave was used as a pressure vessel for the reaction. In the container, mono-bromo functionalized phosphonium salt **99** was mixed with an excess of triphenylphosphine and nickel bromide and heated to 200 °C for 15 hours, yielding novel dicationic phosphonium bromide **100**.

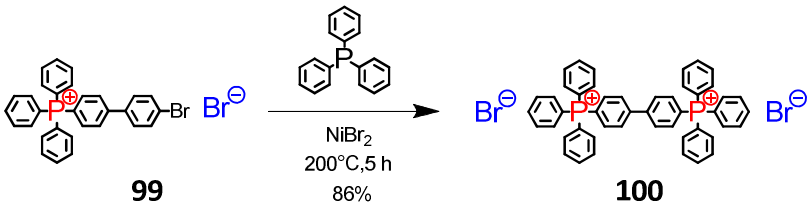

99 **100**

Figure 166: Synthesis of dicationic phosphonium salt **100**

The reaction towards phosphonium salt **100** might also be performed in one step, starting from 4,4´-dibromo-biphenyl and tetraphenylphosphine instead of mono-functionalized salt **99**. However, this direct route may require longer reaction times, and the probability of obtaining a mono-cationic salt as a side product would be increased.

The obtained novel dicationic phosphonium salt **100** was crystallized into transparent triclinic needles, which were used for a determination of the crystal structure by means of X-ray diffraction (see Figure 167).

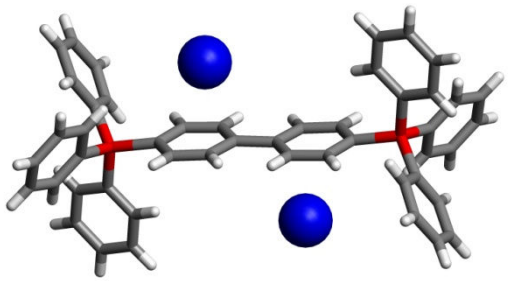

Figure 167: Single crystal structure of dicationic tetraphenylphosphonium salt **100** (solvent molecules omitted for clarity)

The observed coplanarity of the biphenylene bridge does not necessarily indicate a conjugation and thus delocalization of positive charge between both positively charged phosphorus atoms. It may merely reflect the fact that the center of the bridge occupies a symmetry center in the crystal structure. The distance between both cationic centers in salt **100** is structurally fixed to about 10.7 Å and may differ only slightly due to bending of the otherwise rigid biphenylene bridge.

Bromide anions of salt **100** were exchanged to tetraphenylborate anions via anion metathesis in a mixture of THF and methylene chloride (see Figure 168).

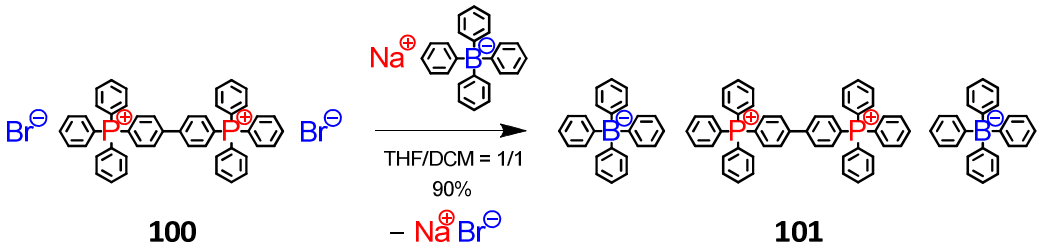

Figure 168: Metathesis towards diphosphonium tetraphenylborate salt **101**

In the ^{1}H-NMR spectrum of the so obtained borate salt **101**, signals of the phosphonium dication (red in Figure 169) and the tetraphenylborate anion (blue in Figure 169) appear well separated and, due to their opposite central charge, in reverse order of chemical shifts when going from the *ortho*- to the *meta*- to the *para*-position.

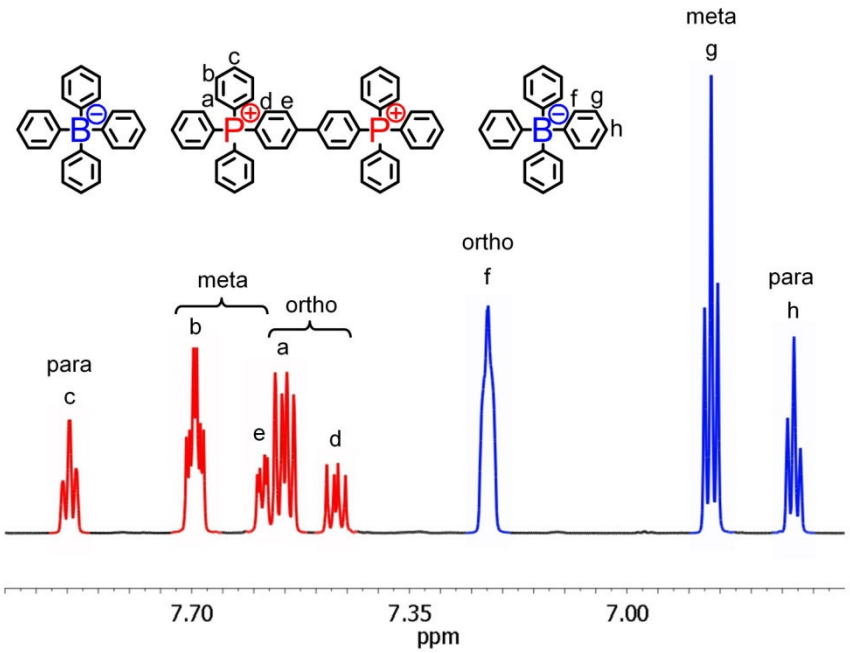

Figure 169: ^{1}H-NMR spectrum of diphosphonium tetraphenylborate salt **101** in CD_2Cl_2 (700 MHz; cation signals in red, anion signals in blue)

The coupling of phosphorus with protons in *ortho*- and *meta*-position is well resolved, whereas the coupling of boron to *ortho*-protons (where a doublet of quartets is expected; compare Figure 51 in paragraph 2.2.1) is merely apparent in a modification of the doublet signals line shape.

The obtained dicationic tetraphenylborate salt **101** was also crystallized into transparent needles, which were used for a determination of the crystal structure by means of X-ray diffraction (see Figure 170).

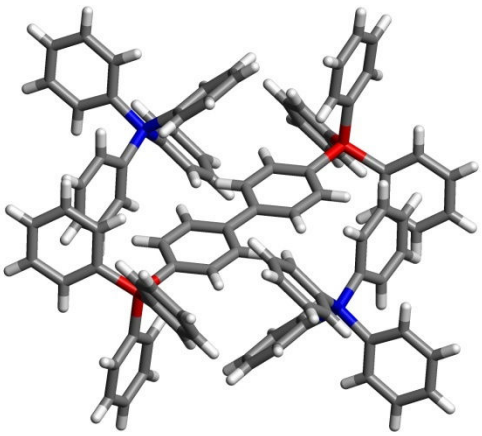

Figure 170: Single crystal structure of dicationic tetraphenylphosphonium tetraphenylborate salt **101** (solvent molecules omitted for clarity)

Again, the rings of the biphenylene bridge were found to be coplanar. Moreover, the biphenylene bridge appears to be approached "sideways" by two tetraphenylborate counter-anions. This configuration may help to minimize the summed-up distances between the two anions and both positively charged centers of the dication (see also paragraph 6.3.1).

A tetrakis(perfluorophenyl)borate salt **102** of the dication was also prepared from dicationic bromide salt **100** via anion metathesis in methylene chloride (see Figure 171).

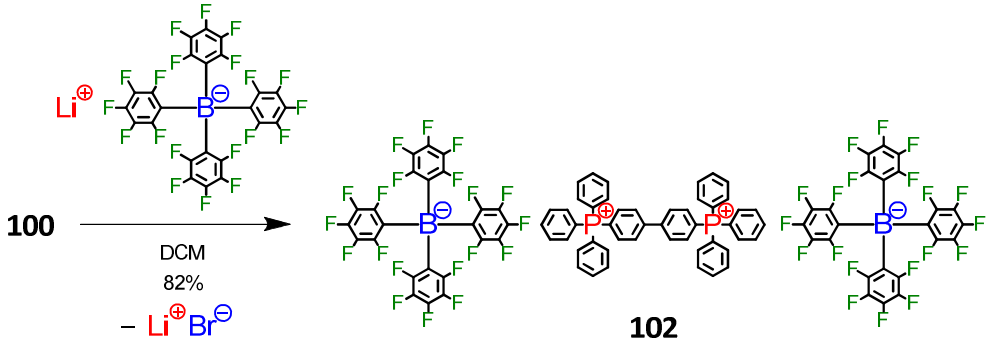

Figure 171: Metathesis towards diphosphonium tetrakis(perfluorophenyl)borate salt **102**

In contrast to the analog mono-cationic salt **95**, this dicationic salt **102** did not crystallize as rapidly upon precipitation in hexane. Despite reduced crystalizability as compared to the mono-cationic salt, the dicationic salt could also be crystallized into transparent crystal needles, which were analyzed by means of X-ray diffraction (see Figure 172).

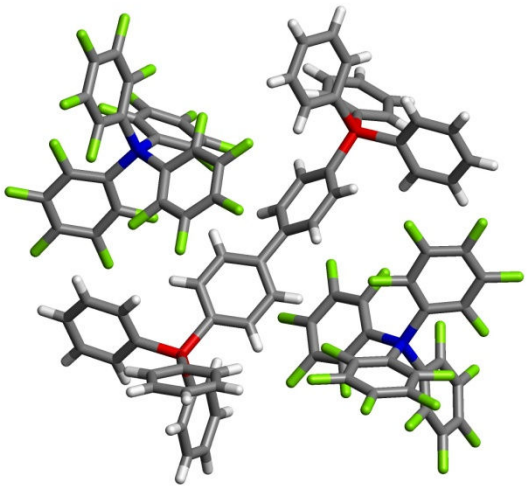

Figure 172: Single crystal structure of dicationic tetraphenylphosphonium perfluorotetraphenylborate salt **102** (solvent molecules omitted for clarity)

Again, borate anions minimize their distance to both cationic centers by adopting positions close to the biphenylene bridge. In contrast to both former dicationic crystal structures, however, the crystal structure of borate **102** provided a first example where the rings of the biphenylene bridge were not coplanar but twisted relative to each other.

^{1}H-NMR spectra of dicationic phosphonium salts **100** (bromide), **101** (tetraphenylborate) and **102** (perfluorotetraphenylborate) in deuterated methylene chloride show that the aryl protons of the dication´s biphenylene bridge are shielded by their counter-anions to very different extents (see Figure 173).

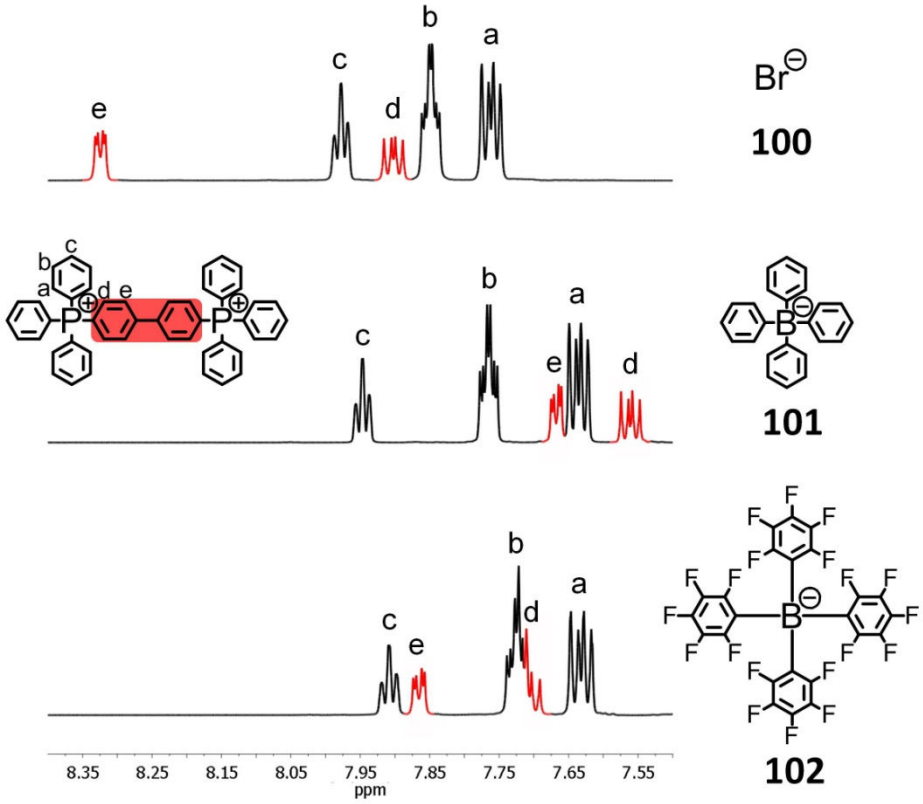

Figure 173: Comparison of ^{1}H-NMR spectra (700 MHz, in CD_2Cl_2) of the diphosphonium dication as a function of the counterion (proton signals H^d and H^e of the biphenyl bridge in red; signals of tetraphenylborate anion in salt **101** appear at lower chemical shifts and are not shown here)

The bromide anions in salt **100** have the smallest shielding effect on the biphenylene signals H^d and H^e, probably due to their lack of aryl moieties. Both biphenylene protons H^d and H^e are however considerably shielded in the according tetraphenylborate salt **101**. The shielding of the bridge protons provides evidence for the existence of ion pairs in solution, and the structure of such ion pairs may resemble the paired structure observed in crystals of tetraphenylborate salt **101** (see Figure 170), where borate anions reside in close

proximity to the biphenylene bridge. The same line of argument may be used for dicationic salt **102** with perfluorinated tetraphenylborate anions. The fluorinated anions of salt **102**, however, seem to have a smaller shielding effect than the non-fluorinated anions of salt **101**. This weaker shielding of bridge protons might correspond to the generally expected weaker interaction and coordination of cations with perfluorinated anions (see 1.3.3.3).

The bromide anions of dicationic salt **100** were also exchanged to large, rigidly dendronized borates with a fluorinated core (see Figure 174).

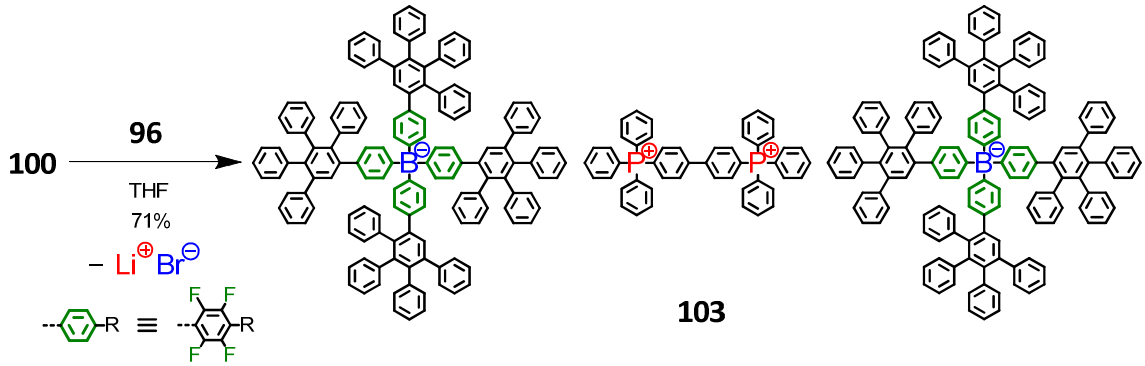

Figure 174: Metathesis towards diphosphonium salt **103** of PP-dendronized borate $[B^F\text{-}G1]^-$ with a fluorinated core

Due to the occurrence of atropisomerism, however, analysis of the obtained NMR spectra of salt **103** was ambiguous. Moreover, the extended polyphenylene shell of the borate might enable an interaction between the dication and the polyphenylene shell even despite comparatively large cation-anion distances, further complicating the analysis of the here recorded overlapping NMR signals. In order to reduce complexity and enable a comparison of NMR spectra with the spectra of other salts, the according dicationic salt of a first generation dendronized borate without a fluorinated core (such as based on borates **14** and **41**) should be prepared and investigated in the future.

4.5 Summary and Outlook

In this chapter, a method was presented which enables the exchange of tetrabutylammonium to different cations in salts of dendronized borates. The method is based on the decomposition of tetrabutylammonium ions via *Wittig* modified *Hofmann* elimination and provides an elegant solution to the otherwise difficult exchange of cations in salts of dendronized borates. Due to the choice of *n*-butyl lithium as the reactant base for elimination, lithium salts of dendronized borates (with fluorinated as well as non-fluorinated cores) could be generated. These lithium cations could then easily be exchanged to other cations by way of classical metathesis procedures. Tetraphenylphosphonium salts of dendronized borates were obtained in high purity. In the case of borate **98**, a strong influence of the counter-cation (TBA^+ vs. PPh_4^+) on the atropisomer signal pattern was observed in ^1H-NMR.

In addition to cation exchange, a novel tetraphenylphosphonium dication was synthesized. Anions of the dicationic salts were varied from bromide to tetraphenylborate to perfluorotetraphenylborate. All of these dicationic salts were crystallized and analyzed by means of X-ray diffraction.

In the future, the exchange towards different cations in salts of dendronized anions should be extended and further investigated. An exchange towards ever larger cations (e.g. (A) in Figure 175) might enable a further reduction of electrostatic attraction between ions and help to generate nanoscopic salts with unusual, thus far unknown electrolyte properties. Also, the conceptual idea of the here presented dication $[Ph_3P(Ph\text{-}Ph)PPh_3]^{2+}$ could be extended to even larger, multi-cationic species with defined spatial geometries.

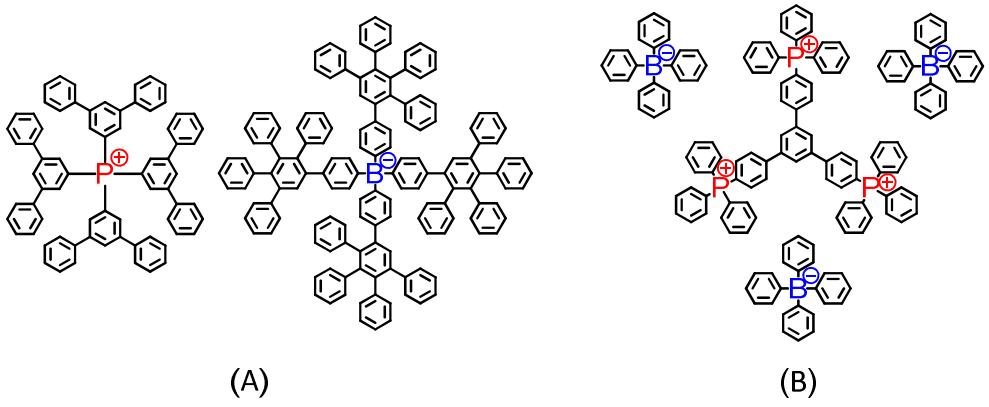

Figure 175: (A) Example of a dendronized salts based on a very large anion *and* a very large counter-cation; (B) novel multi-cations with different, well-defined geometries

More specifically, the method of cation exchange presented in this chapter offers new options in the field of catalysis. Dendronized borates with trityl or dimethylanilinium cations might be prepared and used to generate much more efficient metallocene catalysts, e.g. for the homogeneous polymerisation of olefines.

Finally, the anions of poly-cationic polyelectrolytes might be exchanged to the herein presented, large dendronized anions in order to investigate the effect of size and coordination on chain conformation and supramolecular structuring.

5 Atropisomerism in Dendronized Borates with a Fluorinated Core

5.1 Introduction

All rigidly dendronized borates with a fluorinated core exhibit a significantly larger number of signals in their NMR spectra than expected from their chemical structures. In every case, these additional signals are not the result of impurities or side products, but are caused by the simultaneous existence of several conformational isomers (atropisomers) of the same particular chemical structure. Evidence for the existence of just one chemical constitution was provided by MALDI-TOF mass spectrometry (see 2.3.3) and by the coalescence of NMR signals at sufficiently high temperature (see also 5.4.4).

Since atropisomerism certainly affects the properties of the according salts, its origin and effects should be discussed in greater detail. A structural basis for the here observed atropisomerism will be provided in 5.2, followed in 0 by a detailed investigation of the interdependence between atropisomerism and dendron size, type of solvent, concentration and temperature. Moreover, partly deuterated analogues of first generation dendronized borates will be introduced in 5.3 as a means to enable investigation of atropisomerism by advanced solid state NMR techniques.

5.2 Structural Considerations

It was already mentioned in 2.3.3 that atropisomerism is caused by the blocking of rotations of polyphenylene dendrons about fluorinated phenyl rings of the borate core. If the blocking is caused by the increased steric demand of fluorine as compared to hydrogen, then why do borates with a fluorinated core (such as borate **53**, Figure 176) exhibit atropisomerism, while borates with a fluorinated surface (such as borate **41**, Figure 176) do not?

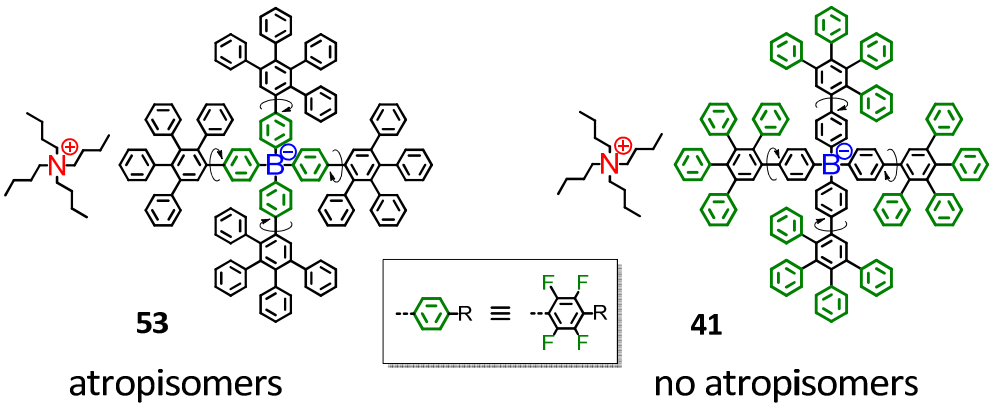

Figure 176: Two types of dendronized borates with fluorinated aryl moieties (borate **53** shows atropisomerism, whereas borate **41** does not!)

The answer is connected to the distinction between those rotations that, if impeded, are able to cause atropisomerism and those rotations that are irrelevant for overall isomer formation: Only a blocking of dendron rotation about the borate core (core-dendron bon indicated by circular arrows in Figure 176) will lead to overall distinguishable borate isomers. In borates with a fluorinated core (see **53** in Figure 176), this core-dendron bond is directly linked to a fluorinated phenyl ring. By contrast, the same bond is not linked to a fluorinated phenyl ring in surface fluorinated borate **41**. As a consequence, the energy barrier for a rotation about the core-dendron bond is comparatively smaller in borate **41**: Here, the fluorinated phenyl ring of the surface may simply tilt sideways and slide over the non-fluorinated phenyl ring at the core (Figure 177 (B)). In borate **53**, by contrast, the phenyl ring of the surface may also tilt sideways, but its tilt will not reduce the steric demand of the fluorinated phenyl ring with respect to the considered rotation about the core-dendron bond (Figure 177 (A)). It is therefore more likely to expect atropisomerism in borates with fluorinated cores.

Figure 177: Modeled structures of fluorinated dendrons of borate **53** (A) and **41** (B)

To determine the number of possible atropisomers in dendronized borates, the before obtained crystal structures of PP-dendronized borates **14** and **41** were used as a structural starting point. It was assumed that the arrangement of phenyl rings around the core remains fixed. In contrast to a true tetrahedron, which possesses three two-fold symmetry axes, a maximum of only one remaining two-fold axis is observed in tetraphenylborates, irrespective of the actual conformation of phenyl rings around the sp^3 hybridized central atom (see Figure 178).

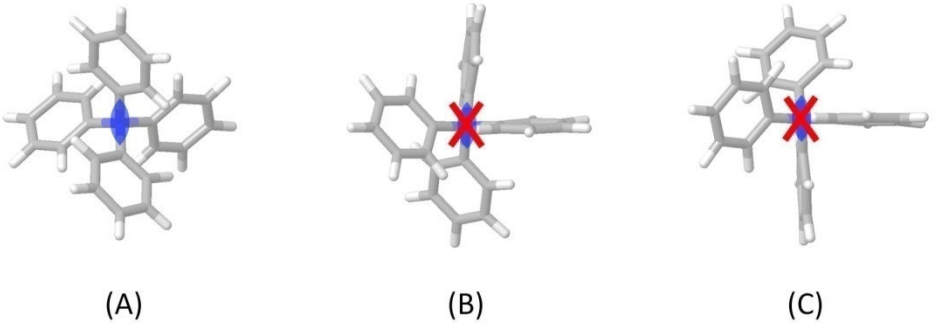

Figure 178: Three different projections of the same phenyl substituted molecule with an sp^3 hybridized central atom; only for the projection along (A) a 2-fold symmetry axis can be observed

The crystal structure of fully dendronized anion **14** was then modified by consecutively rotating single dendrons about the extended B-C bond of the "fixed" core. The geometry of the core allows to distinguish two "sides" for each of its four phenyl rings: one side of each core phenyl ring is facing towards the two-fold axis of the core (and towards one phenyl ring in opposition), whereas the other side of the phenyl ring is facing away from the two-fold axis (and towards the gap between the two remaining phenyl rings). Since rotation of a polyphenylene dendron about the core shall be blocked, two relative orientations of each polyphenylene dendron can be distinguished. Taking into consideration all combinations of dendron orientations gives rise to six overall different isomers A to F in total. In Figure 179, these isomers are displayed schematically, with the two-fold symmetry axis indicated by a blue line. Therein, the specific orientation of each dendron is indicated by the orientation of its generation proton relative to the side of its core phenyl ring. The orientation of the generation proton is described by arrows: Red arrows in Figure 179 indicate generation protons oriented towards the two-fold axis, whereas green arrows indicate generation protons oriented away from the two-fold axis.

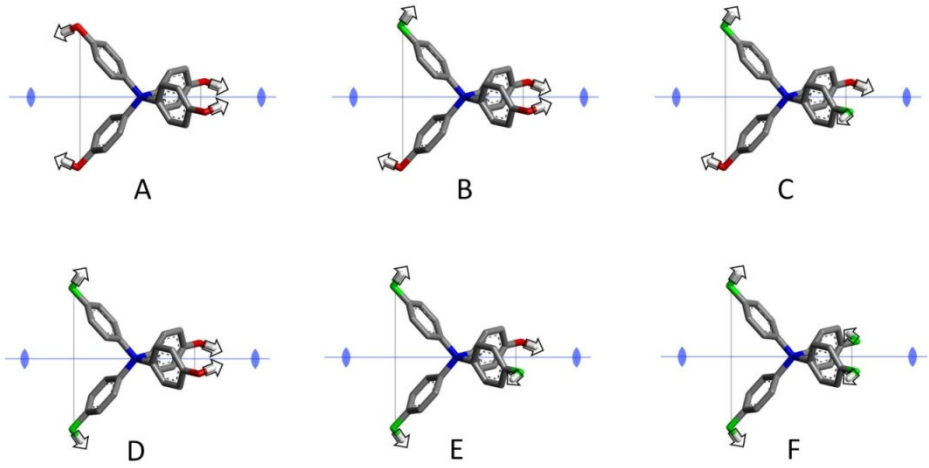

Figure 179: Potential atropisomers A to F of dendronized borates with a fluorinated core

It is noteworthy that atropisomer C is chiral (axial chirality) and thus exists in the form of two mirror-image enantiomers. If the orientation of each dendron is random and independent of the orientations of all other dendrons, then permutation of all possible orientations of dendrons gives the following possible isomers (see Figure 180).

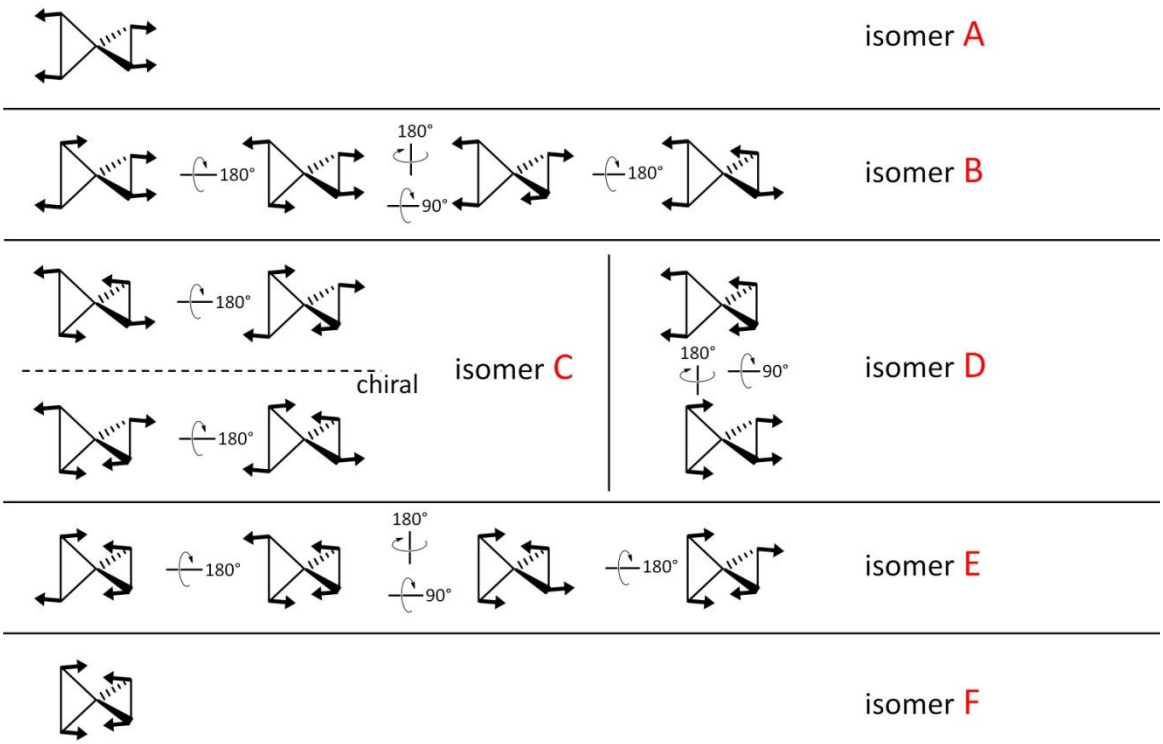

Figure 180: Scheme to determine the number ratio of atropisomers via permutation of dendron orientations

According to the number of ways in which individual isomers can be obtained by random orientation of dendrons (see Figure 180), the probability of obtaining isomer B should be

four times as high as the probability of obtaining isomer A. It is however plausible to assume that isomer A is in fact energetically favored because dendronized borates **14** and **41** both crystallize in the form of this particular isomer. Isomer F, by contrast, might not be favored energetically because of potentially increased steric interactions between its dendrons. The energetic preference for specific isomers will of course lead to other number ratios between different isomers than expected from probability considerations alone.

Within isomers A to F, up to 12 different environments for generation protons can be distinguished. If the number of generation proton signals was solely determined by different magnetic environments within the different borate isomers A to F, then up to 12 distinct generation proton singlets would be expected. In some ^{1}H-NMR spectra, the number of observed generation proton singlets was however even slightly larger than 12. In these cases, the presence of the counterion may have led to an even larger number of distinct magnetic environments.

5.3 Synthesis of Partly Deuterated Dendronized Anions

To enable the investigation of rotational dynamics by advanced solid state NMR techniques, a number of partially deuterated dendronized borates were synthesized. The synthesis of fully surface deuterated dendronized borates requires the employment of a fully deuterated tetracyclone building block **105**. This deuterated building block was synthesized via *Knoevenagel* condensation of deuterated benzil (commercially available) and deuterated diphenylacetone **104**, which was previously synthesized from deuterated benzyl bromide using iron pentacarbonyl (see Figure 181).

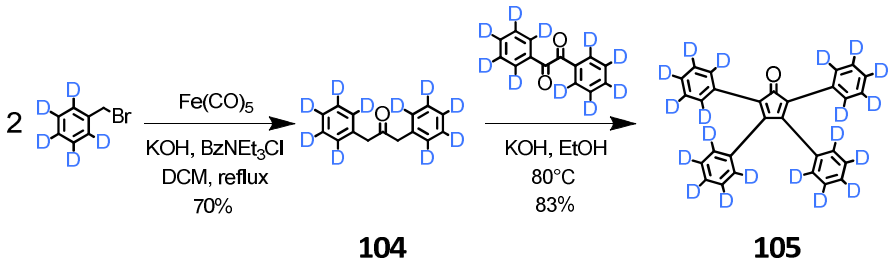

Figure 181: Synthesis of fully deuterated tetracyclone **105**

Deuterated tetracyclone **105** was then used for the synthesis of surface deuterated analogue **106** of dendronized borate **14** via *Diels-Alder* cycloaddition (see Figure 182).

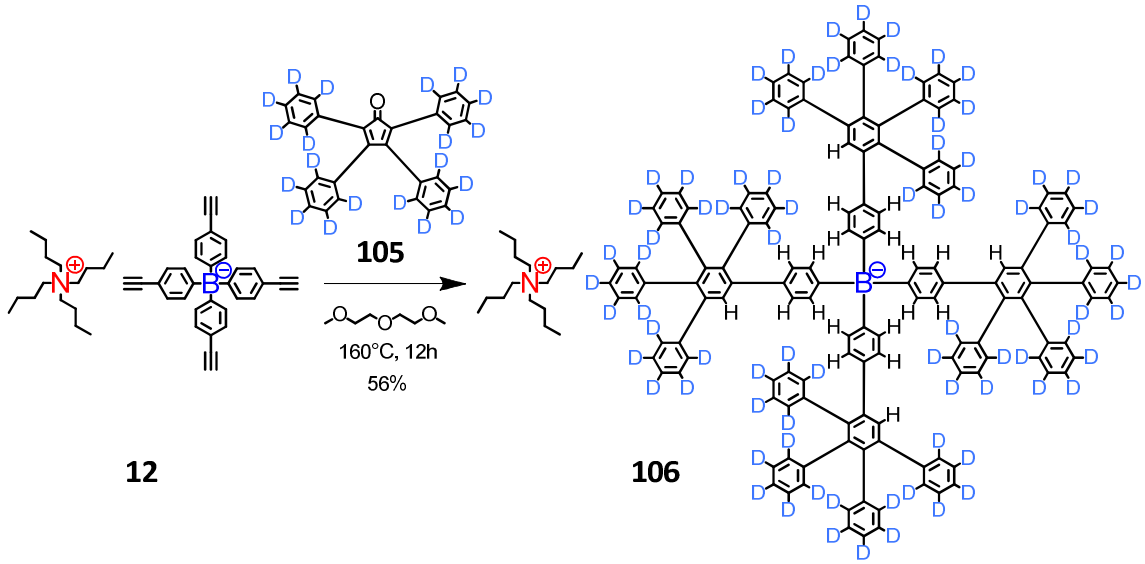

Figure 182: Synthesis of surface deuterated first generation dendronized borate **106**

The reaction was monitored by means of MALDI-TOF mass spectrometry. Figure 183 shows a comparison of the MALDI-TOF spectra of non-deuterated first generation dendronized borate $[B\text{-}G1]^-$ (**14**) and its surface deuterated analogue $[B\text{-}G1^D]^-$ (**106**). The exchange of 80 surface protons in borate **14** to 80 deuterons in borate **106** markedly increases the borates molecular weight while largely retaining its chemical reactivity as well as molecular size.

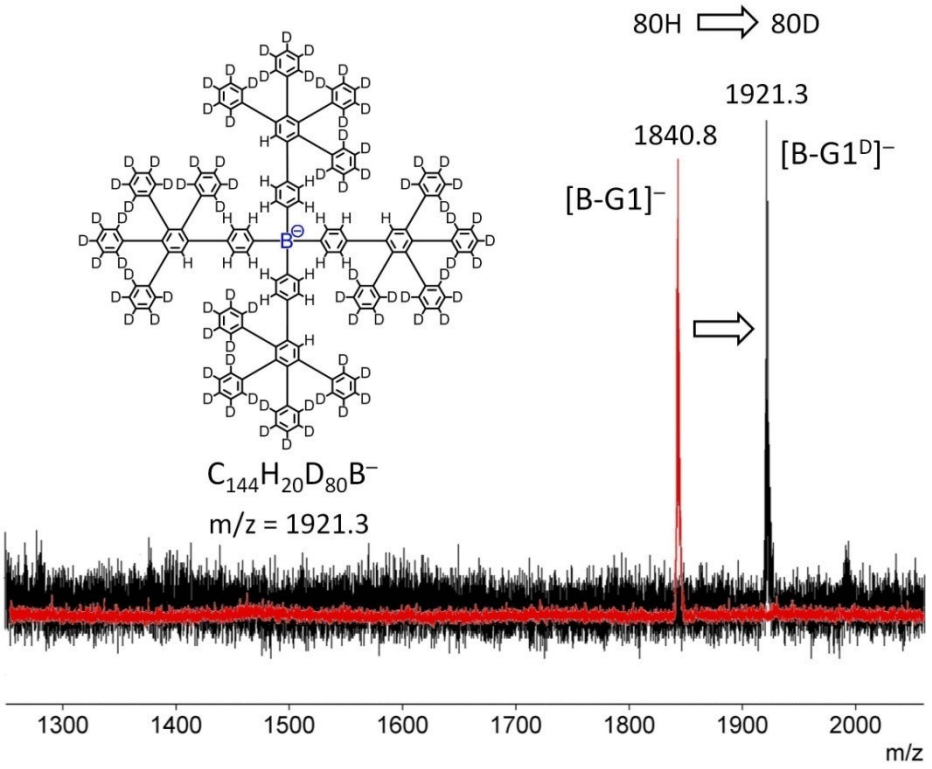

Figure 183: Comparison of the MALDI-TOF mass spectra of dendronized borate

Similar to borate **106**, a surface deuterated borate $[B^F\text{-}G1^D]^-$ with a fluorinated core was synthesized via *Diels-Alder* cycloaddition of deuterated tetracyclone **105** to fluorinated borate core **52** (see Figure 184).

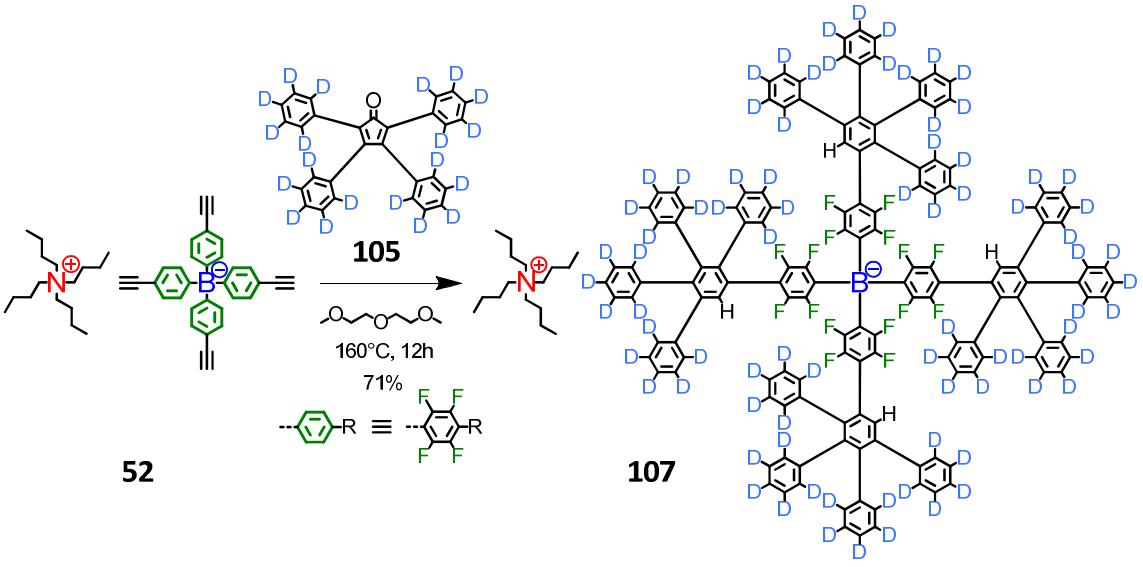

Figure 184: Synthesis of surface deuterated first generation dendronized borate **107** with a fluorinated core

In the resulting dendrimer **107**, the generation proton is the only remaining proton within the anions chemical structure. As a consequence, the carbon atom attached to the gen-

eration proton can easily be identified in a spin-echo ^{13}C-NMR experiment. The spin-echo ^{13}C-NMR spectrum of **107** demonstrates that atropisomerism is also causing a multiplication of carbon signals (see Figure 185).

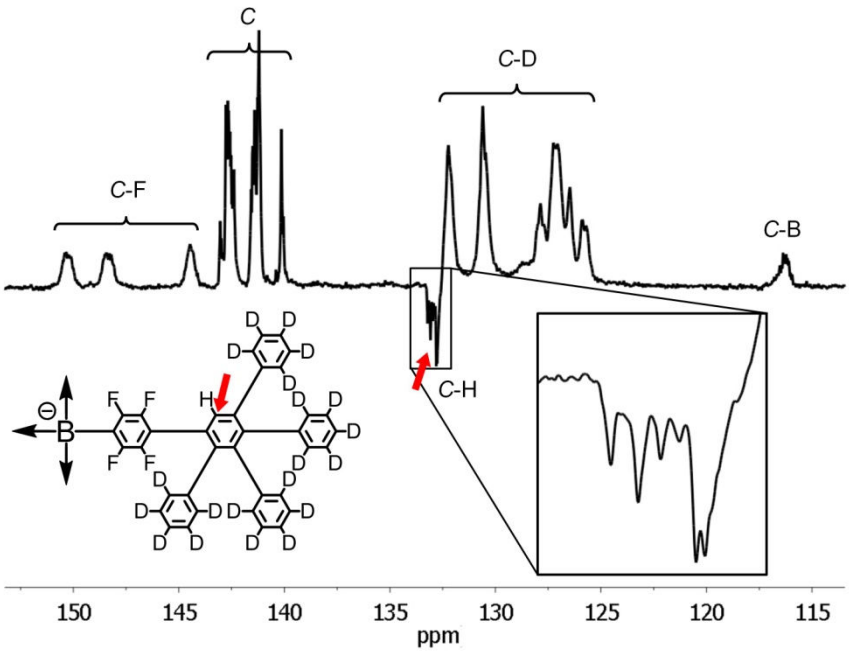

Figure 185: Detail of the spin-echo ^{13}C-NMR spectrum (THF-d8, 126 MHz) of surface deuterated dendronized borate **107**, exhibiting several distinct signals for the carbon atom attached to the generation proton as a result of atropisomerism

In dendronized borate **107**, many different NMR active nuclei (^{1}H, ^{2}H, ^{11}B, ^{13}C, ^{19}F) are combined within a single, defined molecule. Due to their close proximity and the defined structure of dendronized borates, a broad variety of NMR techniques can be applied to investigate their rotational dynamics and the interactions of nuclei in such molecules.

In order to enable the specific investigation of a single chemical site within different atropisomers by means of solid state NMR, attempts were made to also synthesize dendronized borates in which only the generation protons were deuterated. Therefore, T*i*PS-protected and fluorinated borate core **51** was deprotected with a solution of water-free TBAF in a mixture of dry THF and deuterium oxide (Figure 186).

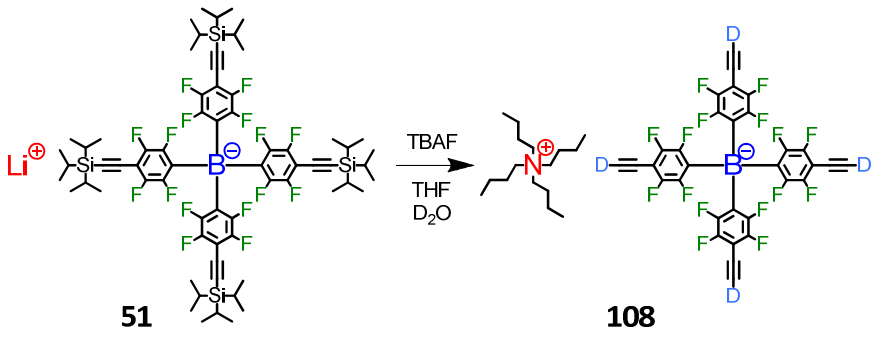

Figure 186: Deprotection of the fluorinated borate core **51** in a mixture of dry THF and D_2O

Since the ethynyl deuterons of deprotected salt **108** are considerably acidic, a gradual exchange of deuterium to hydrogen is inevitable, even if a large excess of deuterium oxide is used as a co-solvent during deprotection. Measurements by means of MALDI-TOF mass spectrometry indicate that after removal of T*i*PS-groups, about 80% of the ethynyl functions were substituted with deuterium instead of hydrogen (see Figure 187).

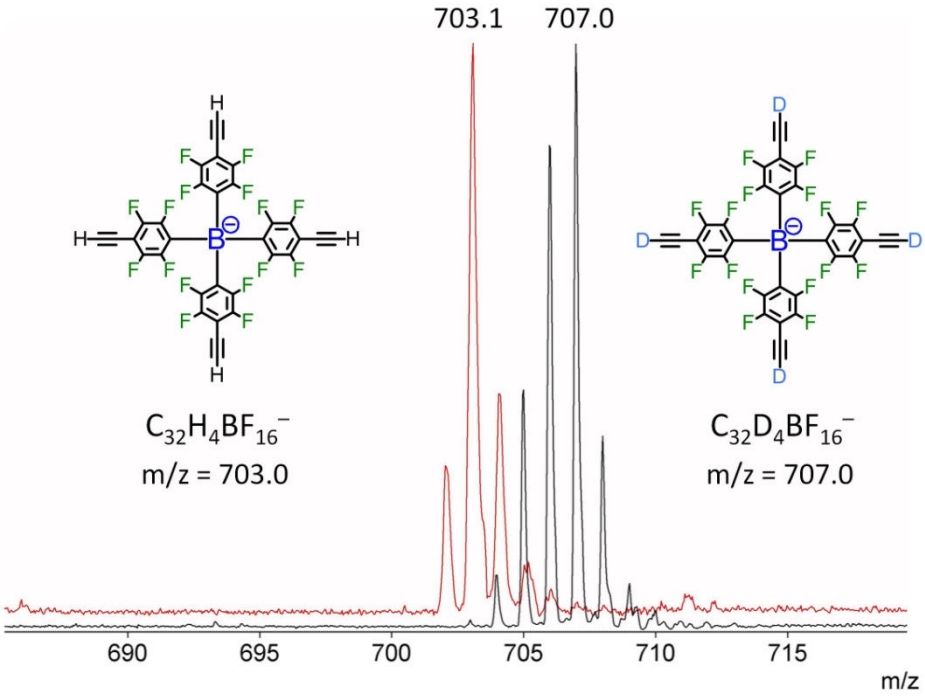

Figure 187: Comparison of MALDI-TOF mass spectra of fluorinated borate core **52** (right) and deuterated borate core **108** (left); signal intensities of **108** (left) indicate the presence of about 20% hydrogen instead of deuterium, generated by exchange of deuterium with protons from the environment

Due to the fairly rapid exchange of deuterium to hydrogen, the obtained deuterated borate core **108** was used immediately for the synthesis of dendronized borate **109**, containing several "generation deuterons" instead of generation protons.

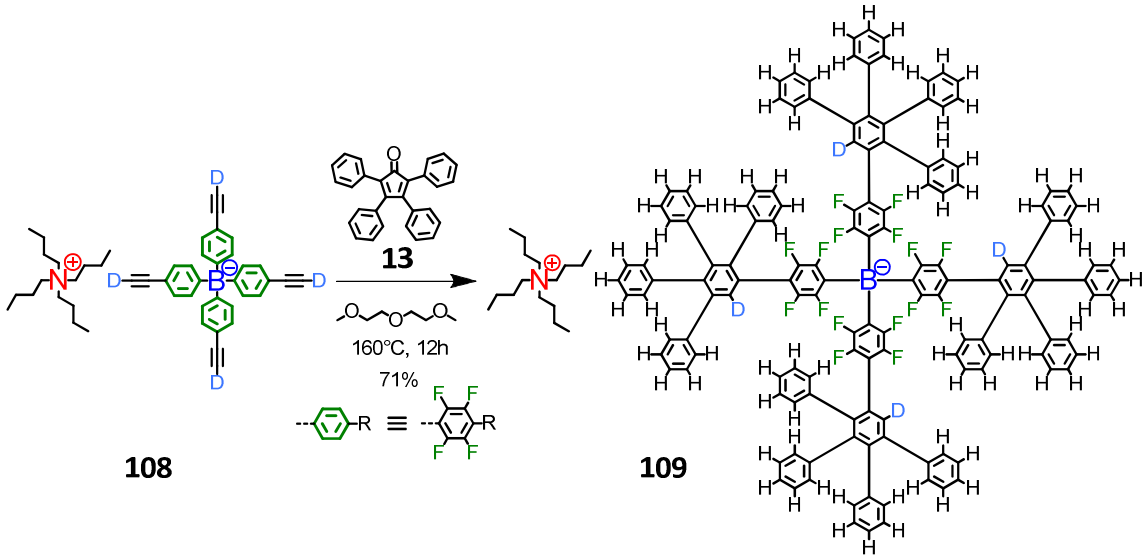

Figure 188: Synthesis of first generation dendronized borate **109** with a fluorinated core and (partly) deuterated generation proton sites

The ^{1}H-NMR spectrum of so obtained borate **109** indicated the presence of about 50% hydrogen instead of the desired deuterium at the generation proton positions. Despite incomplete substitution of protons with deuterium, borate **109** could be utilized for an investigation of rotational dynamics via ^{2}D-NMR spectroscopy in the solid state.

On the following pages, however, the observed effects of atropisomerism on solution NMR spectra will be presented firstly.

5.4 Investigation of Atropisomerism via NMR in Solution

The atropisomerism of dendronized borates with fluorinated cores is reflected in a multiplication of their resonance signals in NMR spectroscopy. The effects on ^{1}H- and ^{13}C-NMR signals have already been discussed. The following pages shall provide a completive description of the many observed effects of atropisomerism on solution NMR signals.

For example, ^{19}F-NMR signals are strongly affected by atropisomerism. While fluorinated borate core **52** only shows two relatively sharp signals for its two types of fluorine atoms in the *ortho*- and the *meta*-position ((B) in Figure 189), polyphenylene dendronized borates built upon that core **52** (such as dendronized borate **53**) show two clusters of many distinct signals ((A) in Figure 189).

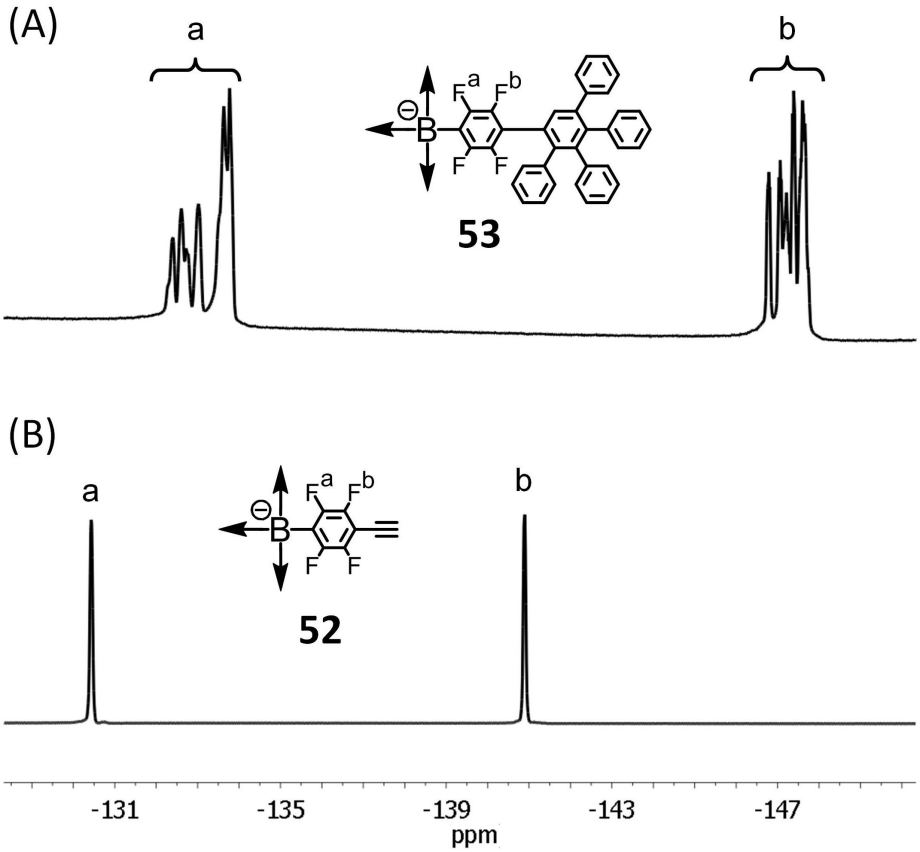

Figure 189: Comparison of ^{19}F-NMR spectra (THF-d8, 471 MHz) of dendronized borate **53** (A) and fluorinated borate core **52** (B)

These clustered fluorine signals are also shifted towards lower field due to the presence of the polyphenylene shell. Interestingly, the magnetic equivalency between fluorine atoms in the *ortho*- as well as the *meta*-position is lost within dendronized borate **53**. Due to their lack in magnetic equivalence, some *ortho* fluorine atoms (F^a) even show a coupling to

other *ortho* fluorine atoms. Moreover, a pronounced coupling between fluorine atoms in *ortho* position (F^a) and fluorine atoms in the *meta* position (F^b) can be observed. Figure 190 shows the cross-peaks of the *ortho* cluster of F^a signals with the *meta* cluster of F^b signals of dendronized borate **53** as recorded in a ^{19}F-^{19}F COSY-NMR experiment.

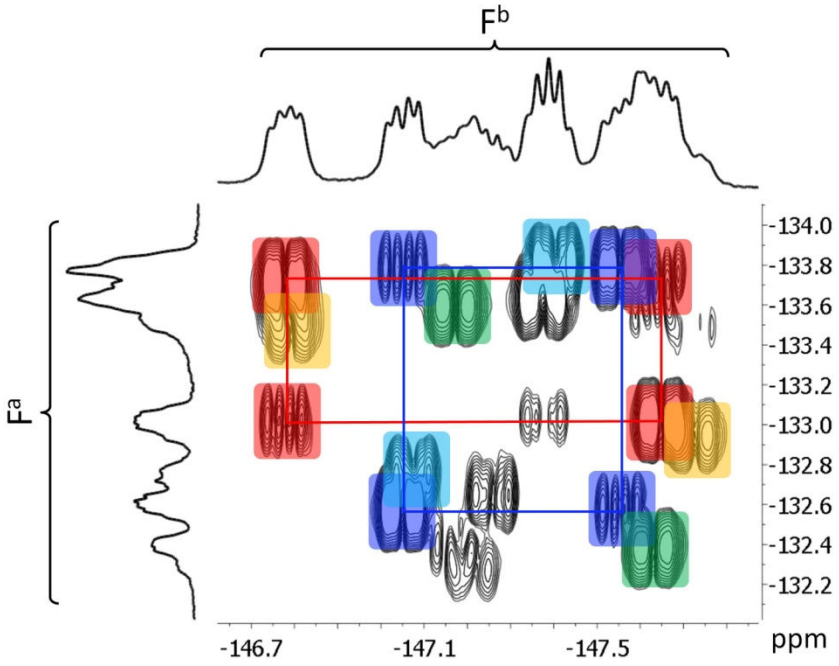

Figure 190: F^a-F^b cross peaks in a ^{19}F-^{19}F COSY-NMR spectrum (THF-d8, 471 MHz) of dendronized borate **53** with a fluorinated core (cross peak patterns marked with different colors)

Among the many recorded cross peaks, some regular patterns can be identified. For example, blue lines in Figure 190 connect the blue marked cross peak signals of two distinct *ortho*-fluorine atoms with two distinct *meta*-fluorine atoms. These fluorine atoms apparently interact with one another via coupling and should thus belong to the same phenyl ring. A similar pattern was observed for the red marked cross peak signals. For the occurrence of the observed type of coupling, all of the four fluorine atoms of a phenyl ring must have lost their magnetic equivalence. The according ring is thus best described as an ABCD-system, in contrast to the before observed AB-system of the non-dendronized core.

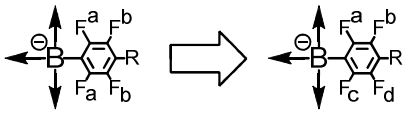

It follows that in Figure 190, vertical lines connect the cross peaks of one *meta*-fluorine atom with two distinct *ortho*-fluorine atoms F^a and F^c, whereas horizontal lines connect

the cross peaks of one *ortho*-fluorine atom with two distinct *meta*-fluorine atoms F^b and F^d. Additional colors (yellow, green, turquoise) in Figure 190 merely indicate similar cross peaks that might also be related to one another.

The atropisomerism of dendronized borate **53** also has an effect on the number of signals of the TBA^+ counterion. For example, the methyl protons H^d of TBA^+ show two or even more distinct triplet signals in ^1H-NMR spectra of borate salt **53** (see Figure 191).

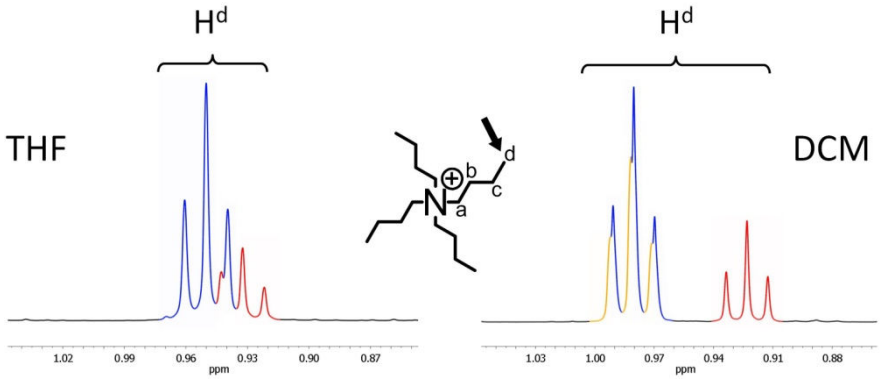

Figure 191: Effect of atropisomerism of borate **53** on the ^1H-NMR signals of protons H^d of TBA^+ in THF-d8 and in CD_2Cl_2

Apparently, the counterion TBA^+ experiences different magnetic environments when interacting with different isomers of the borate. Within certain isomers of borate **53**, a closer approach of TBA^+ to the borate center may be possible as compared to other isomers, resulting in the observed differences in chemical shifts. The largest differences were found for the protons H^d and H^a of TBA^+.

5.4.1 Influence of the Degree of Branching

Dendronized borates with different degrees of branching have been synthesized (see 2.3.4). An increase in the degree of branching corresponds to an increase in density of the polyphenylene shell, which was assumed to result in a better steric screening of the central charge.

Interestingly, the increase in polyphenylene scaffold density also led to a reduction in the number and complexity of ^1H-NMR signals caused by atropisomerism (see for example the more complex generation proton signals of normally branched borate **56** as compared to highly branched borate **62** in Figure 192). This observation of decreasing signal com-

plexity was made even despite the fact that the actual number of generation protons increases from **53** over **56** to **62**. The reduced number in observed signals in borate **62** is most probably caused by a reduced number of possible atropisomers for this particular borate: Steric exclusion between highly branched dendrons in borate **62** may largely limit the number of potential dendron orientations.

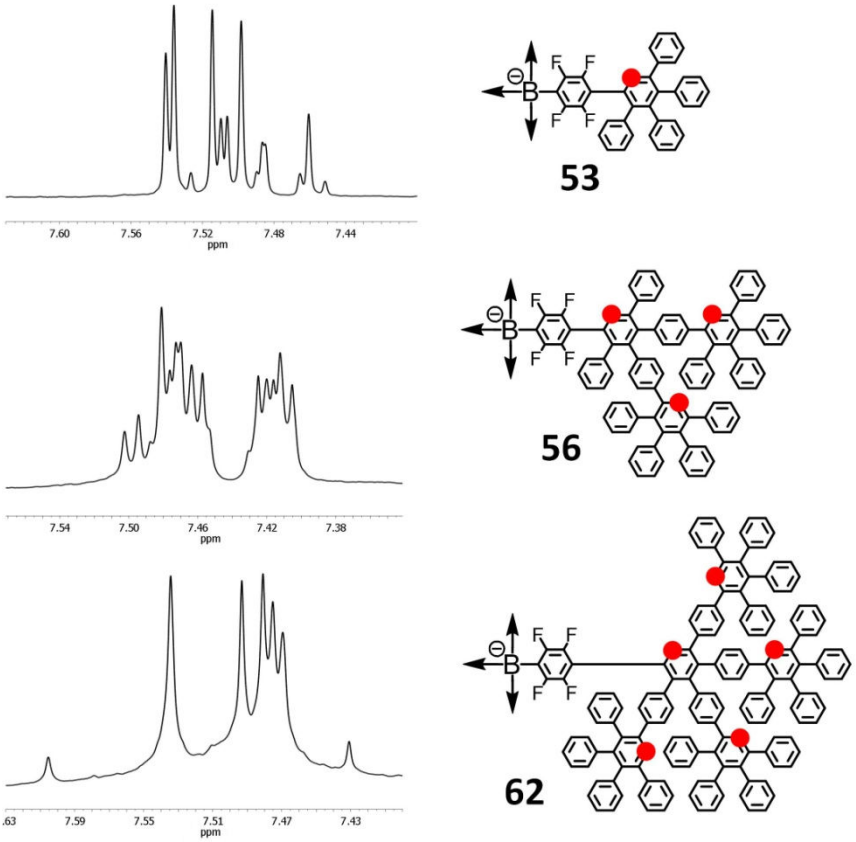

Figure 192: Generation proton signals of dendronized borates $[B^F\text{-}G1]^-$ (**53**), $[B^F\text{-}G2^2]^-$ (**56**) and highly branched $[B^F\text{-}G2^4]^-$ (**62**) with a fluorinated core (red dots mark the positions of individual generation protons in a single dendron of each borate)

Similarly, the ^{19}F-NMR spectrum of highly branched borate **62** was found to be considerably less complex than the according ^{19}F-spectra of borates **56** and **53** (see Figure 193). In fact, the ^{19}F-NMR spectrum of borate **62** almost resembled the simplicity of non-atropisomer compounds (such as fluorinated borate core **52**; compare (B) in Figure 189). Only two comparatively weak signals indicate the existence of additional atropisomers in highly branched borate **62**.

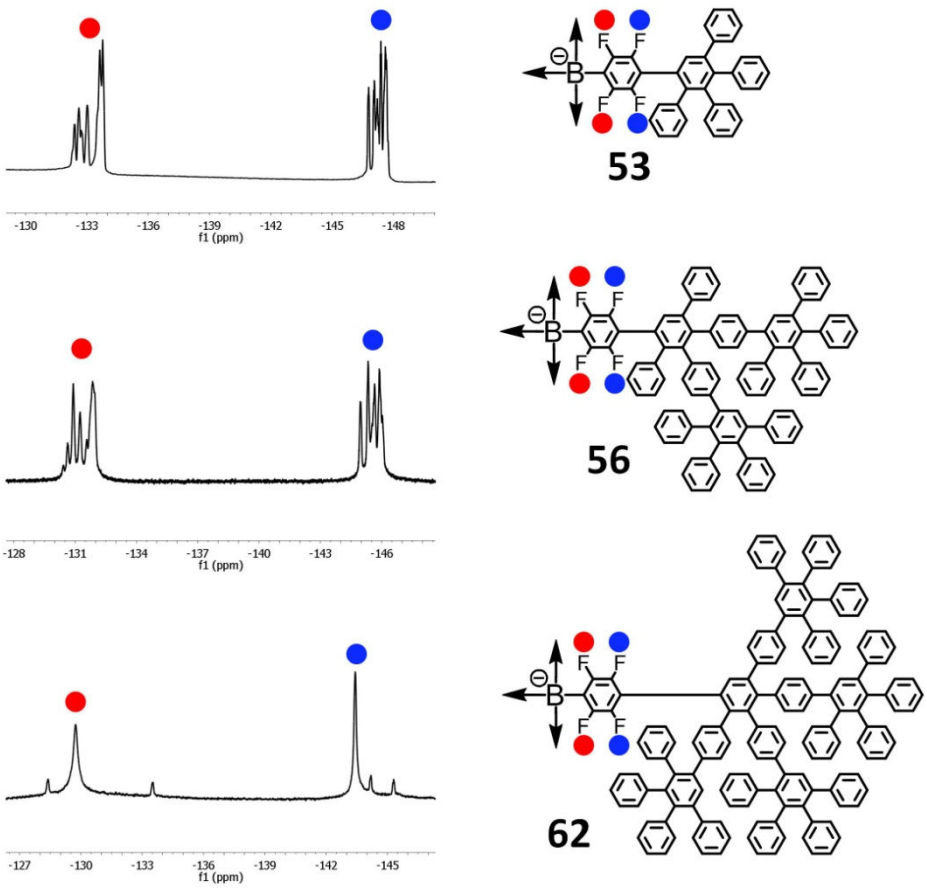

Figure 193: ^{19}F-NMR signals of dendronized borates $[B^F\text{-}G1]^-$ (**53**), $[B^F\text{-}G2^2]^-$ (**56**) and highly branched $[B^F\text{-}G2^4]^-$ (**62**) with a fluorinated core in THF-d8

This observation confirms that the number of atropisomers in borate **62** is probably reduced due to mutual steric exclusion between highly branched polyphenylene dendrons.

5.4.2 Influence of the Solvent

Solvents also have a pronounced effect on the signal patterns observed in NMR spectroscopy. Of course, the interaction of a solvent with a given solute is dependent on the solvents polarity, its dielectric constant, the existence of certain functional groups that may interact with the solute and so on. As a consequence, the nuclei of a given compound naturally give rise to different chemical shifts when measured in different media. Here, however, the nature of the solvent may additionally influence the strength of interaction between differently solvated anions and cations. Also, the screening of nuclei may depend on the accessibility of different atropisomers for solvent molecules. To observe these differences, ^{1}H-NMR spectra of borate salt **53** were recorded in a number of different sol-

vents that cover a wide range of polarities (tetrachloroethane, methylene chloride, tetrahydrofuran, toluene, dimethyl sulfoxide). The obtained spectra are displayed in Figure 194.

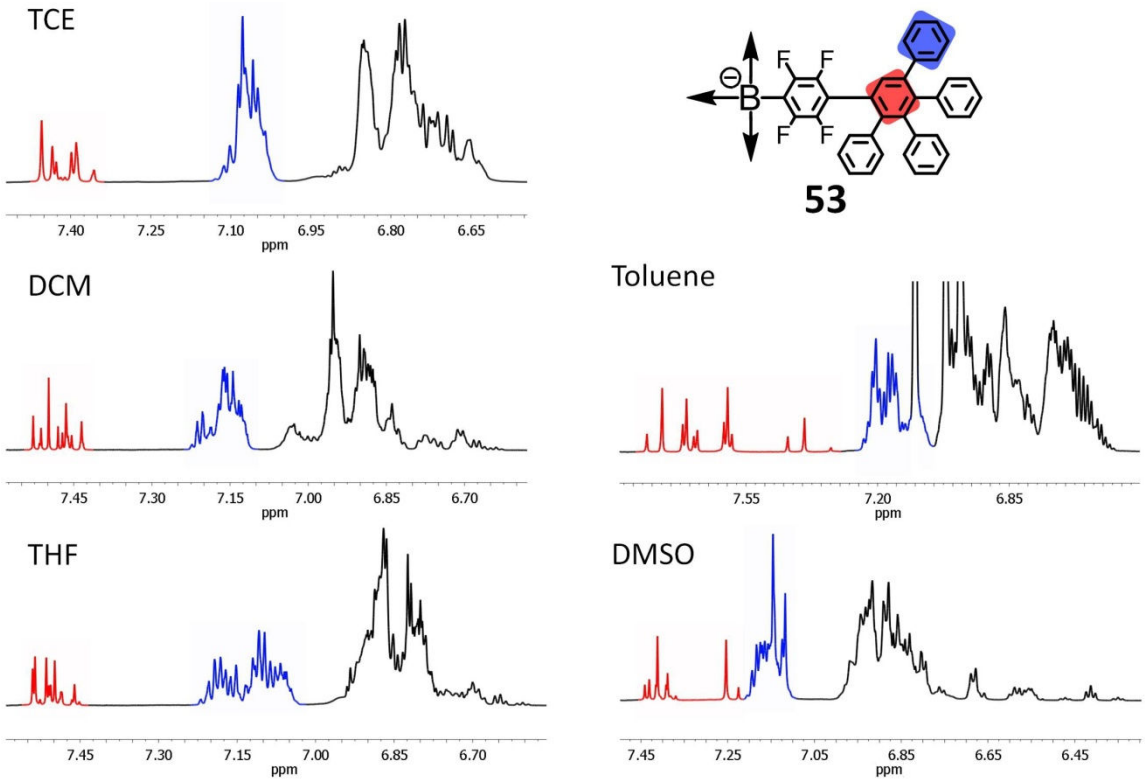

Figure 194: Comparison of ^{1}H-NMR spectra of dendronized borate **53** in different solvents

In mildly polar solvents such as tetrachloroethane (TCE, $\varepsilon_r = 8.4$), methylene chloride (DCM, $\varepsilon_r = 8.9$) or tetrahydrofuran (THF, $\varepsilon_r = 7.6$), the signals of the generation proton (red in Figure 194) appear more or less clustered. In non-polar solvents such as toluene ($\varepsilon_r = 2.4$), the generation proton signals are distributed over a much wider window of chemical shifts, ranging from 7.82 to 7.32 ppm. In fairly polar dimethyl sulfoxide (DMSO, $\varepsilon_r = 48$), just two of the signals attributed to generation protons of borate **53** are separated from the remaining signals by a low field shift. Moreover, some well separated triplet signals (most probably attributed to *para*-protons of phenyl rings of the outer shell) can be identified due to their considerable low field shift towards around 6.45 ppm. Apparently, some nuclei experience very different magnetic environments within different atropisomers when dissolved in a given solvent. The biggest differences in magnetic environments were clearly observed in solvents of either very low or fairly high polarity.

To obtain information about the relative spatial orientation of dendrons in certain atropisomers, the spatial coupling of proton nuclei was recorded by means of **n**uclear **O**verhauser **e**ffect **s**pectroscop**y** (NOESY). Due to the excellent separation of generation proton as well as surface-aryl proton signals in the solvent dimethyl sulfoxide, this medium was chosen for the ^{1}H-NOESY experiments on borate **53** (see Figure 195).

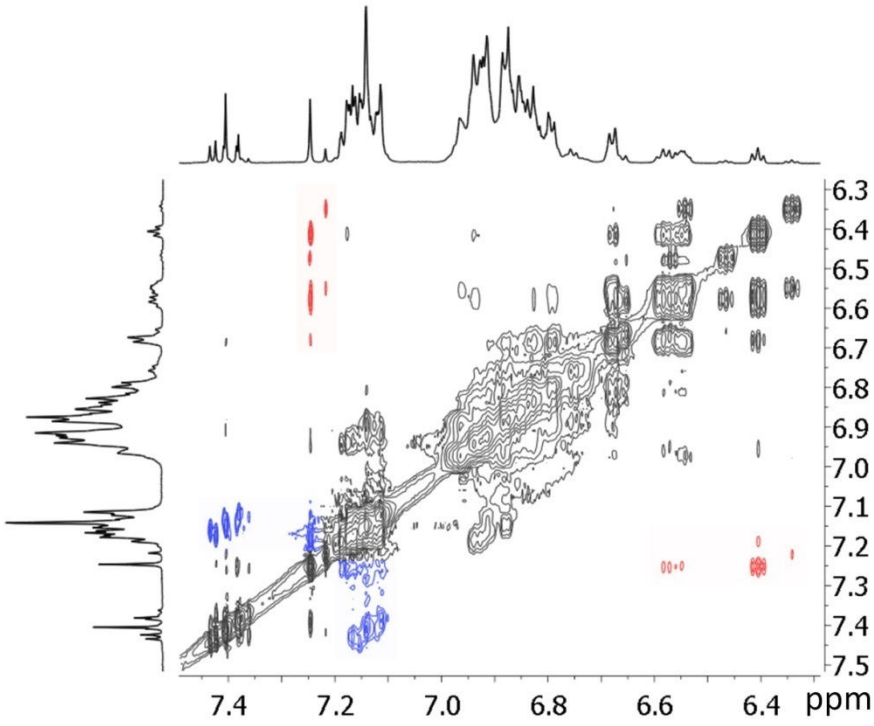

Figure 195: ^{1}H-NOESY-NMR spectrum of dendronized borate **53** in DMSO-d6 (700 MHz)

As expected, coupling interactions can be observed between generation protons and the protons of the first neighboring phenyl ring outwards (marked blue in Figure 195).

More interestingly, however, coupling interactions can also be observed between low field shifted generation protons and the *para*-protons of surface phenyl rings (marked red in Figure 195). For these couplings to occur, protons from different dendrons have to be involved. Dendrons have to be oriented in such a way as to allow for a close spatial approach between both types of protons (see Figure 196).

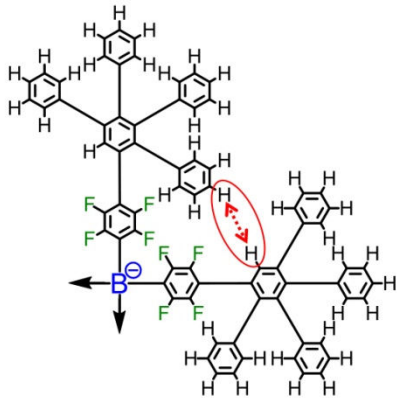

Figure 196: Selected coupling interactions between protons in borate **53** as observed in ^{1}H-NOESY NMR

These coupling interactions can also be observed in other solvents such as tetrachloroethane. Usually, only about two of the several generation proton signals show the here described kind of coupling over space from one dendron to another.

5.4.3 Influence of Concentration

It was already demonstrated that the signal patterns caused by atropisomerism are dependent on the chemical nature of the counter-cation (see 4.3). Since the strength of interaction between cation and anion is proportional to the degree of dissociation, the signal patterns should also be dependent on concentration (see 1.3.2.4). In going to ever more diluted solutions, the impact of the counterion on the observed signal pattern should continually decrease. In order to investigate the impact of the concentration on signal patterns and distribution, concentration dependant measurements on the ^{1}H-signal of the generation proton of borate salt **53** were performed in THF-d8 (ranging from concentrated $1 \cdot 10^{-3}$ mol/L to very dilute $1.56 \cdot 10^{-5}$ mol/L solutions; see Figure 197).

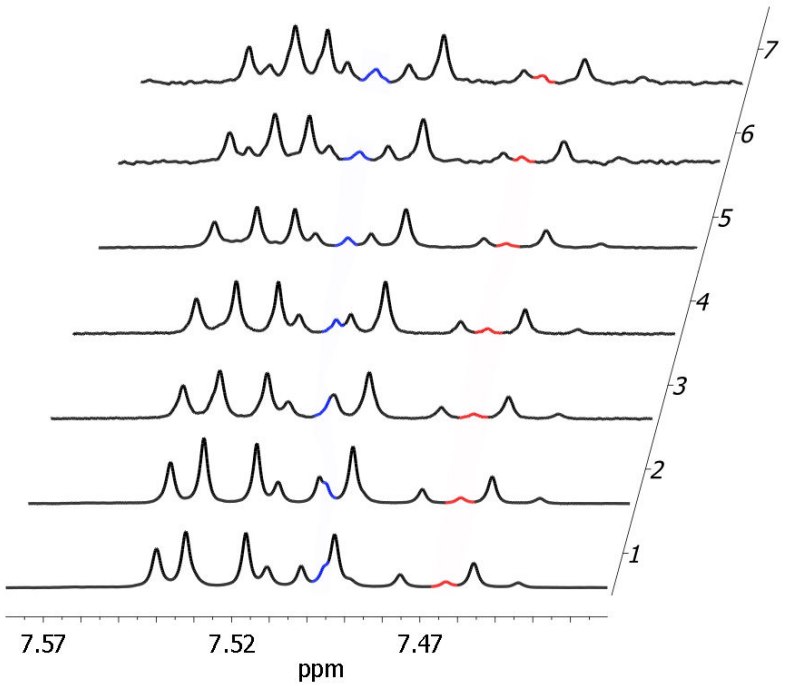

Figure 197: Signal pattern of the generation proton of borate **53** as a function of concentration in THF-d8 (700 MHz); ***1***: $1 \cdot 10^{-3}$ mol/L, ***2***: $5 \cdot 10^{-4}$ mol/L, ***3***: $2.5 \cdot 10^{-4}$ mol/L, ***4***: $1.25 \cdot 10^{-4}$ mol/L, ***5***: $6.25 \cdot 10^{-5}$ mol/L, ***6***: $3.13 \cdot 10^{-5}$ mol/L, ***7***: $1.56 \cdot 10^{-5}$ mol/L

Due to the decreasing signal-to-noise ratio with decreasing concentration, proton spectra recorded at very low borate concentrations were comparatively noisy. Figure 197 shows that several proton signals changed their chemical shift as well as their relative position to other signals upon dilution. The observed changes in the overall signal pattern were however less pronounced than expected. Nevertheless, these measurements demonstrate that the strength of interaction between anion and cation clearly influences the magnetic environment within different borate atropisomers. Some of these atropisomers may be more susceptible to changes in the strength of interaction with cations than others.

5.4.4 Influence of Temperature

Temperature generally determines the rate with which isomerization between different atropisomers occurs. A temperature dependant measurement of NMR spectra therefore provides a direct insight into the kinetics of dendron rotation. At sufficiently high temperatures, isomerization should be fast enough to lead to a coalescence of before separated NMR signals. In order to induce the coalescence of distinct isomer signals, ^{1}H-NMR spectra of dendronized borate **53** were recorded at increasingly higher temperatures (see

details of these spectra in Figure 198, which displays the signal(s) of the generation proton). The solvent, deuterated tetrachloroethane, was chosen because of its fairly high boiling point of about 147 °C.

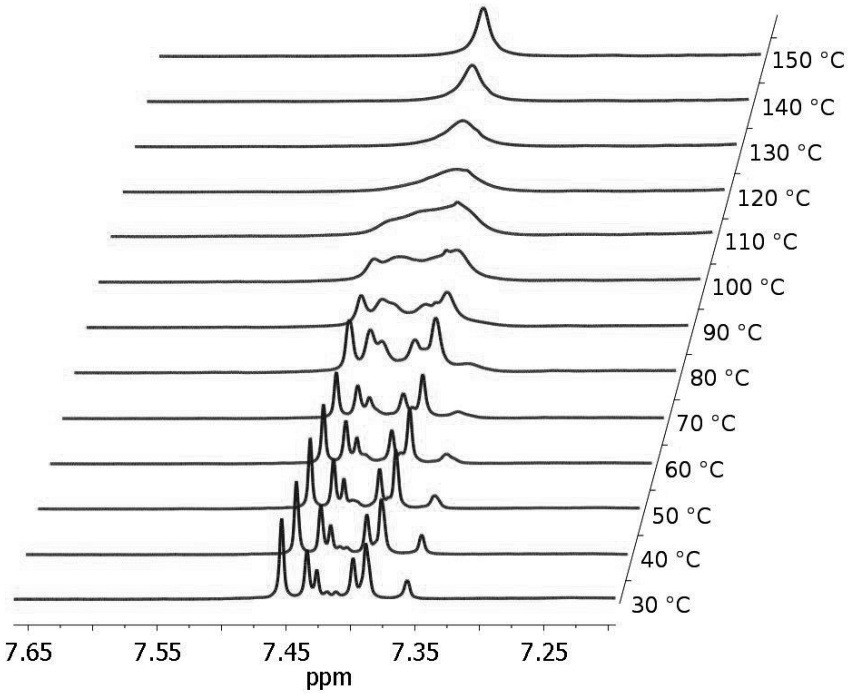

Figure 198: ^{1}H-NMR signal of the generation proton (500 MHz) of dendronized borate **53** in $C_2D_2Cl_4$ as a function of temperature

Figure 198 clearly shows that at a temperature of about 135 °C, the many signals of the generation proton eventually collapse into the single singlet signal, which is typically expected for dendronized borates that do not exhibit atropisomers. The complete spectrum of borate **53** at high temperature shows all the typical features and signal patterns that are expected for a typical first generation dendronized borate structure such as borate **14** at room temperature. A further increase of temperature above the point of signal coalescence leads to a further gradual narrowing of signal line-widths and hence a continuously better definition of signals. Upon cooling to room temperature, the initial and complex pattern of multiple proton signals reappears.

In the case of less complex signal patterns, an analysis of all line shapes (**c**omplete **l**ineshape **a**nalysis, CLA) might be used to estimate the rate constants k of exchange at each temperature T, and a plot of their natural logarithm $\ln(k)$ against $1/T$ might be used to determine the activation energy E_A of rotation according to the law of

Arrhenius.[222] However, due to the complexity of the pattern observed in borate **53**, the activation energy E_A of rotation could not be estimated here.

5.5 Investigation of Atropisomerism via NMR in the Solid State

As mentioned above (see paragraph 5.3), several specifically deuterated borate anions have been synthesized to allow for an analysis of atropisomerism by advanced solid state NMR techniques that would also allow for a determination of the activation energy of dendron rotation. At the time of writing of this thesis, the investigations of deuterated (**106**, **107**, **109**) as well as non-deuterated dendronized borates (**14**, **41**, **53**, **56**, **62**) were still ongoing and being performed by [redacted] (associated to the research group of [redacted] in our institute). His investigations of dendronized borates make use of all of their NMR active nuclei (^{1}H, ^{2}H, ^{11}B, ^{13}C, ^{19}F) using a broad range of NMR spectroscopic techniques (e.g. conventional single-pulse experiments, ^{1}H-^{1}H correlation spectra, ^{2}H solid echo experiments, ^{13}C cross-polarization spectra). [redacted] kindly provided me with initial results of his measurements, one of which will be presented here.

The ^{2}H-ssNMR spectra of surface deuterated borates **106** and **107** were recorded at room temperature and at 430 K and 470 K, respectively (see Figure 199).

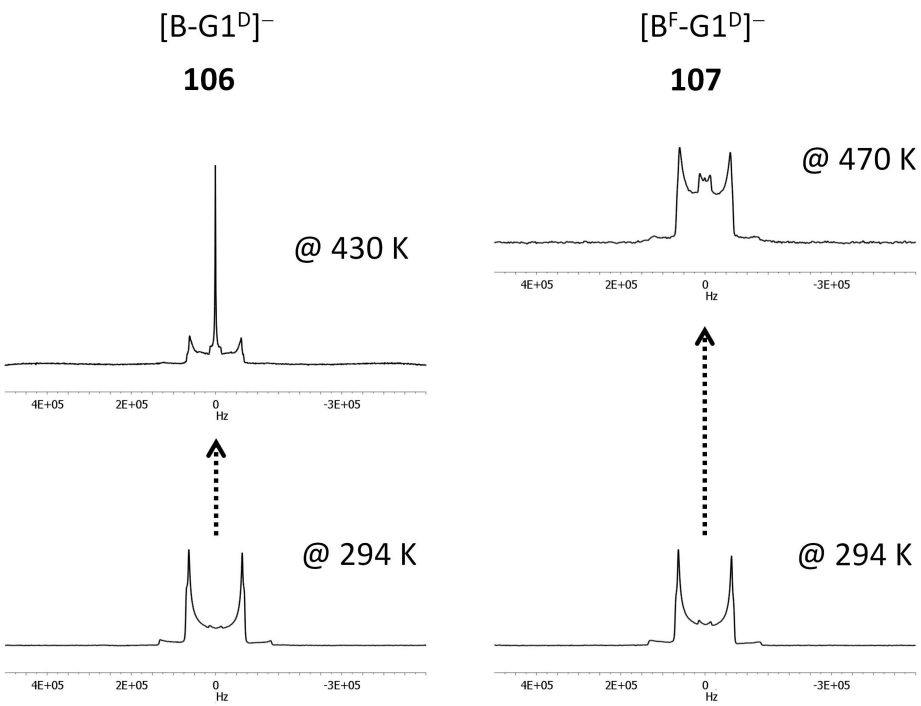

Figure 199: ^{2}H-ssNMR spectra of surface deuterated borates **106** and **107** at different temperatures

At room temperature (294 K), both surface deuterated borates **106** and **107** show a *Pake* pattern in their respective ^{2}H-ssNMR spectra. The observed pattern indicates that rotation of deuterated phenyl rings is blocked within both types of dendronized borates in the solid state. The *Pake* pattern collapses at about 430 K in the case of borate **106** with a non-fluorinated core, whereas it is largely retained at even higher temperatures (470 K) in the case of core-fluorinated borate **107**. In agreement with NMR measurements in solution, the hindrance of rotation of dendrons caused by fluorination of the borate core can also be detected in the solid state. In addition to earlier results in solution, however, a complete analysis of the (more simple) line shapes should be possible here, so that rate constants and the activation energies of rotation could be extracted and compared. Analysis of the recorded spectra still has to be finalized in the research group of [redacted].

5.6 Summary and Outlook

In this chapter, the origin and effects of atropisomerism in dendronized borates with fluorinated cores were investigated. Geometric considerations allowed to determine the total number of possible atropisomers as well as estimating the number of signals expected for the generation proton in ^{1}H-NMR spectroscopy.

Atropisomerism was investigated in depth by different NMR techniques (spin echo, NOESY, ^{19}F-^{19}F COSY) in solution. The impact of atropisomerism on ^{19}F-NMR signals of the core (loss of magnetic equivalence; transition from AB- to ABCD-system) and ^{1}H-NMR signals of the counterion were described. It was shown that with increasing degree of branching (and thus with increasing steric demand of dendrons) the number of potential atropisomers does in fact decrease because of effects of mutual steric exclusion. Moreover, NMR signal patterns were shown to largely differ within different solvents, but differ only slightly at different concentrations (different degrees of dissociation). ^{1}H-NOESY experiments identified a spatial coupling of protons between different dendrons within specific borate isomers. High temperature ^{1}H-NMR spectra of borate **53** in tetrachloroethane confirmed that coalescence of before separated signals occurs at about 130 °C. Unfortunately, determination of the activation energy of rotation by means of a complete line shape analysis was not possible due to the complexity of the signal pattern.

In order to also enable a thorough investigation of atropisomerism by means of solid state NMR spectroscopy, a number of partially deuterated dendronized borates have been synthesized. Surface deuterated borate **107** provided a first unambiguous example for a multiplication of ^{13}C-NMR signals due to atropisomerism. The obtained temperature dependent ^{2}H-NMR spectra in the solid state will be analyzed by complete line shape analyses in the group of [redacted] and will enable determination of the activation energy of dendron rotation. The ongoing investigation of dendronized borates by means of solid state NMR ([redacted]) further include ^{1}H-^{1}H correlation experiments applying the BaBa pulse sequence to investigate the location of the counter-cation in the solid state.

6 Physical Properties of Dendronized Salts

6.1 Introduction

In previous chapters, the synthesis of large dendronized anions and their various salts had been presented. A central motivation for the increase in anion size was the rational and specific change of classical anion properties, most importantly the reduction of their coordination strength. The properties of salts of dendronized anions may however differ in many more ways from the properties of traditional salts. An examination of the changes of physical properties caused by rigid dendronization shall be provided in this chapter.

Of course, a larger anion size should be reflected in a decrease of anion mobility, which should in turn reduce the conductivity of solutions of its salts. In paragraph 6.2, the impact of anion size and scaffold density (degree of branching) on ion mobility will be examined, where spatial size and extension will be contrasted with molecular weight. The size of ions and their surface functionalization may also affect the way in which ions are able to pack into regular crystal lattices. Interesting features and aspects of some of the crystal structures obtained within this work will be discussed in paragraph 6.3. The cell constants of those crystals were also used to approximate and compare lattice enthalpies. The impact of both lattice enthalpy and chemical functionalization on salt solubility will be described in paragraph 6.4. Finally, the impact of rigid dendronization on the coordination strength of anions, as examined by means of concentration dependant measurements of conductivity, will be described in paragraph 6.5.

6.2 Mobility and Hydrodynamic Radii (DOSY-NMR)

Diffusion ordered spectroscopy (DOSY) NMR provides a means to directly measure and compare the mobility of different molecular species in solution. The measurement yields a two-dimensional plot in which the classical NMR signals are spread along an extra dimension. This dimension represents the logarithm of the diffusion coefficient $D = \mu\, k_B T$ in solution. Signals of different nuclei that exhibit the same translational mobility in solution appear at the same relative height of the $\lg D$ axis, whereas signals of slower (or faster) nuclei appear at higher (or lower) relative positions. In some cases, DOSY-NMR can

thus be used as a spectroscopic analogue of "chromatographic separation methods" such as thin-layer chromatography to identify different components in complex mixtures. In the case of salts of dendronized borates, ^{1}H-NMR signals of the anion, the cation and the solvent are already well separated and can easily be attributed to the according nuclei without the use of DOSY-NMR. However, the measurement provides a direct insight into the dependence between mobility and molecular size. In the case of dendronized anions, mobility can also be determined as a function of their scaffold density and surface functionalization. In order to serve as a general example, the DOSY-NMR of first generation dendronized borate **14** in THF is displayed in Figure 200.

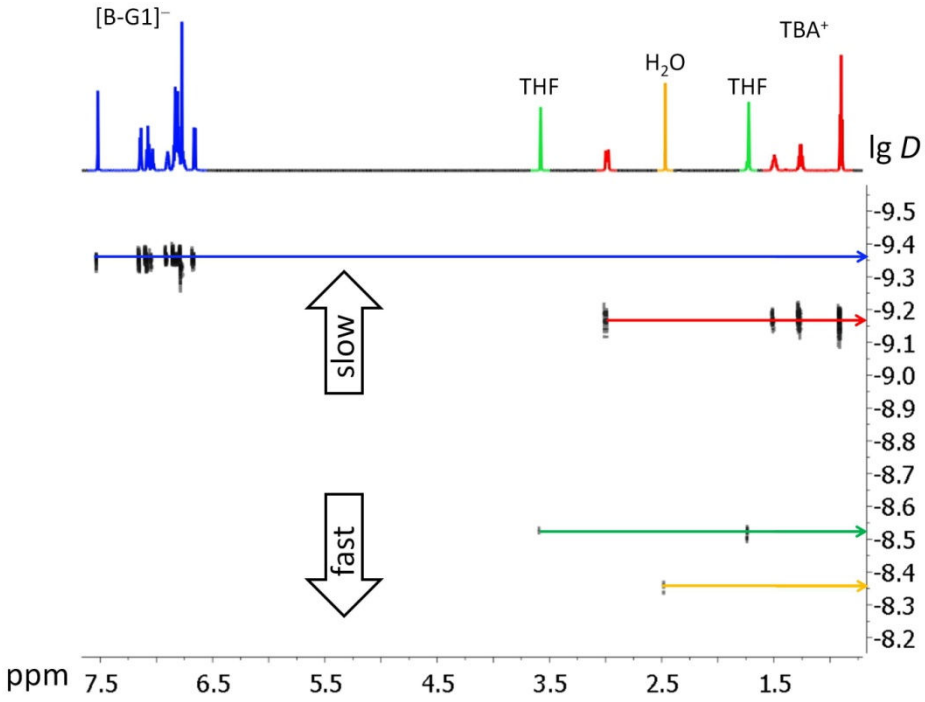

Figure 200: DOSY-NMR spectrum (700 MHz) of first generation dendronized borate **14** in THF-d8

Figure 200 clearly demonstrates that the anion [B-G1]$^-$ (blue), the cation TBA$^+$ (red) and solvent molecules (green and yellow) exhibit very different mobilities in THF. While small and mobile water molecules (yellow) diffuse most rapidly, large dendronized [B-G1]$^-$ anions (blue) diffuse most slowly. It is important to bear in mind the logarithmic scale of the diffusion axis. TBA$^+$ cations are indeed considerably faster than the larger borate anions. The measured mobility $\mu = D/k_BT$ can be correlated to spatial molecular dimensions through the *Stokes-Einstein* equation (27), which describes the equivalent mobility μ of an ideal sphere of radius r_H (hydrodynamic radius) in a medium of a given viscosity η.

$$\mu = \frac{1}{6\pi\eta r_{\mathrm{H}}} \tag{27}$$

The relation between mobility and hydrodynamic radius is frequently used to extract information about the size and conformation of polymers in solution, as e.g. in dynamic light scattering experiments.

Comparative DOSY-NMR measurements on dendronized borates indicate that the mobility of a molecular species is not directly related to its molecular weight: While first generation dendronized borates **14** and **41** differ significantly from one another with respect to molecular weight (1840 versus 3280 g/mol), their mobilities and thus hydrodynamic radii in THF are in fact relatively similar (1.0 nm versus 1.1 nm). The observed similarity in hydrodynamic radii and mobilities of both molecules can be explained by their very similar shape, size and spatial extension. Apparently, geometric parameters have a far greater impact on ion mobility than molecular weight alone. DOSY-NMR measurements may thus be used to directly correlate the mobility of dendronized anions with their individual sizes, geometries and shapes.

The maximum radius r_{max} of each borate, which describes its maximum spatial extension, can also be derived geometrically (instead of measured) due to the defined and rigid chemical structure of the polyphenylene scaffold. From the center to its farthest extension, a first generation dendronized borate has a maximum radius of $r_{max} = 1.40$ nm, a second generation dendronized borate a maximum radius of $r_{max} = 2.28$ nm, and a third generation dendronized borate a maximum radius of $r_{max} = 3.15$ nm. The value of r_{max} is of course identical for normally and highly branched borates of the same dendrimer generation.

However, it was already mentioned earlier (see 1.2) that rigid polyphenylene dendrimers do not fill space entirely. Instead, inherent intramolecular voids are always present, and lower hydrodynamic radii r_{H} are measured than those expected from the borates maximum extensions r_{max}.

As a means to decrease the free volume within polyphenylene scaffolds, highly branched analogues of second as well as third generation dendronized borates had been synthesized (see 2.3.4). In highly branched borates, the total volume circumscribed by the maximum extension r_{max} is "filled" with polyphenylenes to a much larger extent. The hydrodynamic radius r_{H} measured for a highly branched borate should thus approach the theoretical ra-

dius r_{max} of an ideal, completely filled sphere more closely. To test this hypothesis, hydrodynamic radii of differently sized and branched borates were measured by means of DOSY-NMR spectroscopy (see results in Figure 201).

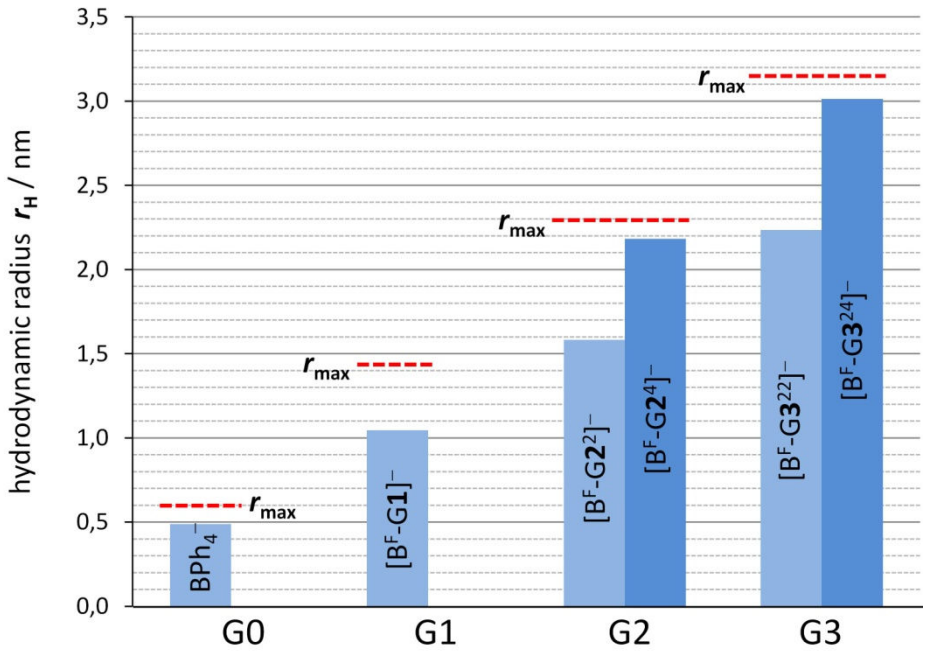

Figure 201: Comparison of hydrodynamic radii as determined by DOSY-NMR

The measurements confirmed that hydrodynamic radii r_H of dendronized anions generally increase with increasing dendrimer generation (G0 to G3). Moreover, an increase in the degree of branching is indeed reflected in a closer approach of the hydrodynamic radius r_H towards the radius of maximum extension r_{max} (compare both G2 as well as both G3 dendronized borates with the same maximum radii r_{max}, respectively). At a given maximum size, the extent to which the measured radius r_H agrees with theoretical value r_{max} can thus be used as a rough measure for the overall globularity of a dendronized ion (corresponding to its congruence with a full sphere). The ratio r_H/r_{max} might then be correlated to the screening efficiency of the ion´s polyphenylene shell.

6.3 Crystal Structures

6.3.1 Packing

In classical crystals build from mono-atomic ions, the charges as well as size ratios of anions and cations largely dominate the way in which ions may pack into ordered crystal

lattices. Molecular ions are however built from several to up to hundreds of atoms and typically lack a perfectly spherical geometry. Hence, attraction of oppositely charged ions is not completely symmetric in every spatial direction, and the final packing of ions into regular lattices is constrained and strongly influenced by molecular shape and geometry.

Generally, electrostatic attraction and the potential gain in lattice enthalpy both lead to a preferably close packing of oppositely charged ions. In the case of non-spherical ions such as borate **12**, the counter-cation may minimize its distance from the boron center (6.09 Å) by approaching the borate along its (single remaining) two-fold axis. Along all other directions, the anion-cation distance would be greater. Consequentially, TBA^+ cations and borate anions stack into closely packed, alternating strings along the direction of the two-fold symmetry axis of the borate anion (see Figure 202 (A)).

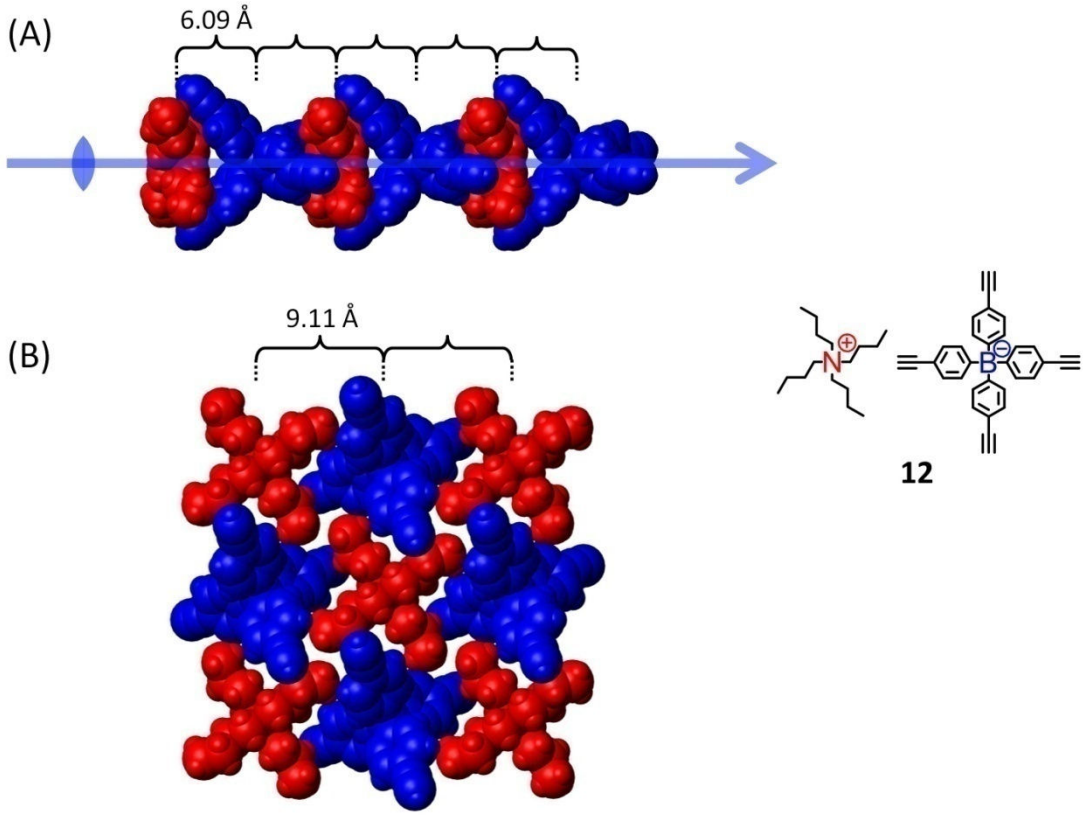

Figure 202: Single crystal structure of ethynyl functionalized borate **12** (cations in red, anions in blue; brackets indicate distances between anion and cation central atoms); (A): strings of alternating, closely stacked anions and cations; (B): view along two-fold axis

When viewed along the direction of the borates two-fold axis (Figure 202 (B)), a secondary alternating pattern of ions can be recognized, in which the distance between the op-

positely charged centers is 9.11 Å. Macroscopically, the crystal structure appears as colorless, orthorhombic needles.

In contrast to non-fluorinated borate **12**, the fluorinated borate core **52** has thus far only been crystallized in the form of a 1:1 mixed salt together with tetrabutylammonium chloride. Due to their considerable positive polarization, the ethynyl protons of the borate anion are able to coordinate to negatively charged chloride anions. Through this coordinative interaction, both types of anions (borate and chloride) are able to form three-dimensional anion networks (see Figure 203). Two equivalent anion networks are formed in parallel, and both networks interpenetrate one another throughout the crystal structure.

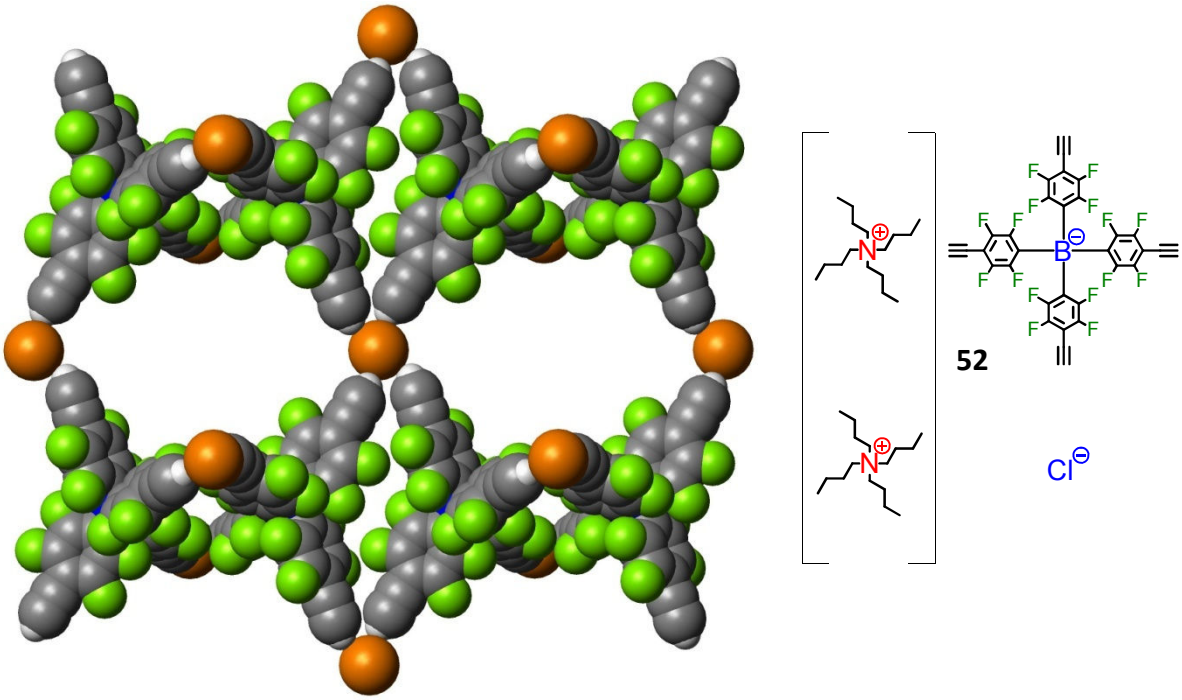

Figure 203: Detail of one of the two interpenetrating anion networks, build through coordination of chloride anions (orange) by positively polarized ethynyl protons of borate **52**

Remaining voids within these interpenetrating anion networks are orderly filled with tetrabutylammonium counterions. The resulting overall crystal structure is monoclinic. In addition to molecular geometry, local polarization of functional groups apparently also influences ion packing and thus the resulting crystal structures of molecular ions.

An alternating sequence of anions and cations stacked along the two-fold axis of tetraphenylborate, as observed in TBA^+ borate salt **12** (Figure 202), can also be observed in the structurally related tetraphenylphosphonium salt (see Figure 204).[223]

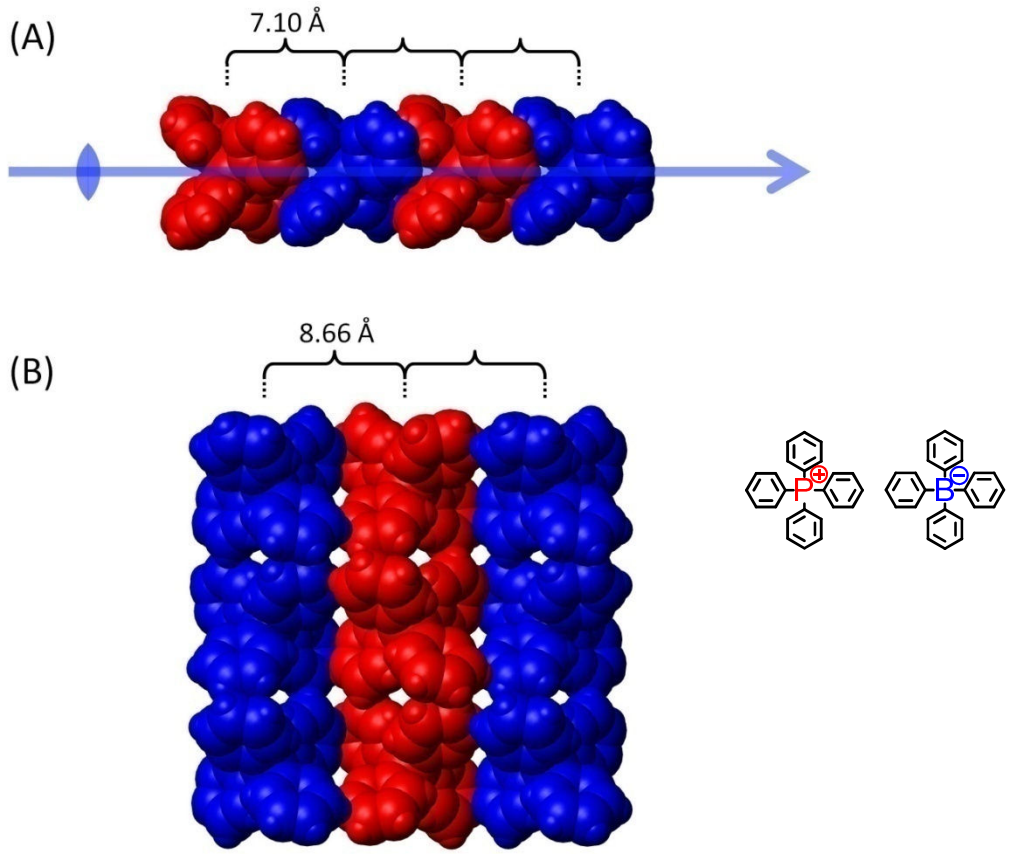

Figure 204: Single crystal structure of tetraphenylphosphonium tetraphenylborate (cations in red, anions in blue; brackets indicate distances between anion and cation central atoms); (A): strings of alternating, closely stacked anions and cations; (B): view along two-fold axis[223]

Due to the larger size of the phosphonium cation as compared to tetrabutylammonium, the minimum distance between the cationic and the anionic center increases from 6.09 Å to 7.10 Å. However, the distance to the next neighbor "sideways" decreases from 9.11 Å in borate **12** to 8.66 Å, probably due to the overall smaller size of the borate anion, which is not functionalized with ethynyl groups here.

Despite their similar geometry and comparable size, the tetraphenylphosphonium salts of tetraphenylborate (Figure 204) and perfluorinated tetraphenylborate (Figure 205) exhibit very different patterns of ion packing within their crystals. As mentioned earlier, an alternating stacking of anions and cations along the two-fold axis can frequently be observed due to the minimized distance between oppositely charged centers. Here however, ions of the same instead of opposite signs are packed closest along that two-fold axis (see Figure 205 (A)).

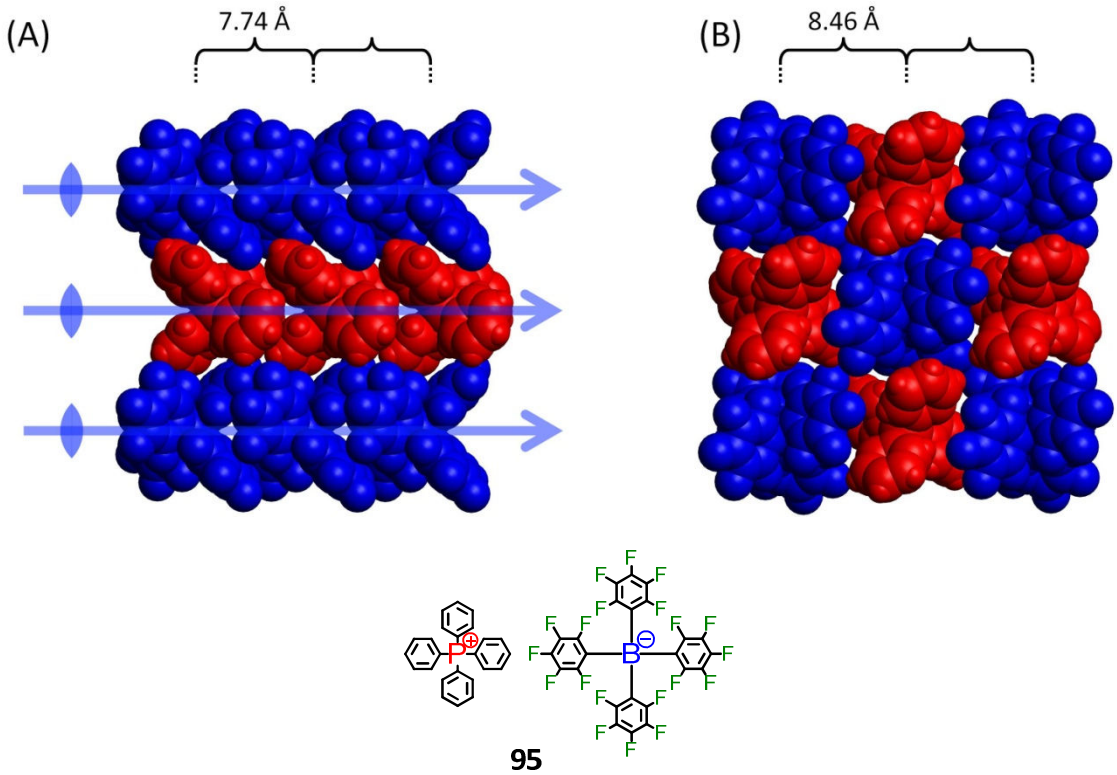

Figure 205: Single crystal structure of borate **95**, which exhibits strings of closely packed ions of the same sign (cations in red, anions in blue; brackets indicate distances between anion and cation central atoms); (A): strings of **non**-alternating, closely stacked anions or cations; (B): view along two-fold axis

Moreover, crystal formation of borate **95** was found to be extremely rapid: Upon addition of hexane to a concentrated solution of borate **95** in methylene chloride, large transparent crystal needles formed within a matter of only a few seconds!

Both the rapid formation of crystals and the surprising packing pattern of ions in borate **95** might be explained by taking into account perfluoroarene-arene interactions. Benzene and perfluorobenzene are known to form 1:1 co-crystals with a significantly higher melting point (about 24 °C) than the crystals of either one of both components (each at about 5 °C). Moreover, the crystal structure of the mixture differs significantly from those of both components. Whereas edge to face orientations of rings are prevalent in structures of the individual compounds, alternating stacks of coplanar oriented rings are observed in the mixture.[224]

Figure 206: Comparison of the electrostatic surface potentials of benzene (left) and perfluoro-benzene (right) based on quantum chemical calculations (B3LYP, 6-31G)

Figure 206 shows the electrostatic surface potentials (ESPs) of benzene (left) and perfluorobenzene (right). The figure provides a graphic illustration for the origin of alternate stacking in mixtures of arenes and perfluoroarenes: Those parts of a given molecule that have a negative surface potential (orange to red in Figure 206) readily interact with those parts of other molecules that have a positive surface potential (cyan to blue in Figure 206). In 1:1 mixtures of both compounds, the alternate stacking of benzene and perfluorobenzene maximizes this type of interaction.

Now, if perfluorinated tetraphenylborates and tetraphenylphosphonium cations of salt **95** were stacked closely along their two-fold axis in an alternating sequence (as might be expected from considering *Coulomb* attraction and molecular geometry only), then a coplanar alignment of phenyl rings of the cation and perfluorophenyl rings of the anion would be impossible. Instead, the exact opposite of coplanarity (almost edge-to-face) would be the result. However, if ions of the same sign are stacked closely along the two-fold axis and the resulting columns of either anions or cations are arranged next to one another, then an almost coplanar alignment of each phenyl rings with another perfluorinated phenyl ring can be obtained.

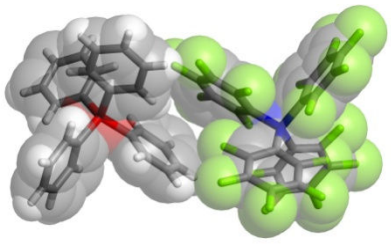

Figure 207: Arene-perfluoroarene interaction in borate salt **95**

The typical strengths of arene-perfluoroarene interactions are in the range between –3.7 and –5.6 kcal/mol.[225,226] Here, the summed up effect of many such interactions between arene substituted cations and perfluoroarene substituted anions leads to the initially sur-

prising overall packing in the crystal as well as rapid crystal formation in borate **95**. Due to their impact on structure formation, perfluoroarenes and arenes have already been recognized as supramolecular synthons for crystal engineering.[227-232]

When going to the dicationic tetraphenylphosphonium salt analogues **101** and **102**, yet different types of packing can be observed. Tetraphenylphosphonium dications do not possess a two-fold symmetry axis that runs through one or both phosphorus centers. Consequentially, no close alternating packing of anions and cations along such axis is possible. Tetraphenylborate anions do however possess a two-fold symmetry axis, and this axis is oriented differently relative to the phosphonium dication depending on whether the borate is fluorinated or not (see Figure 208).

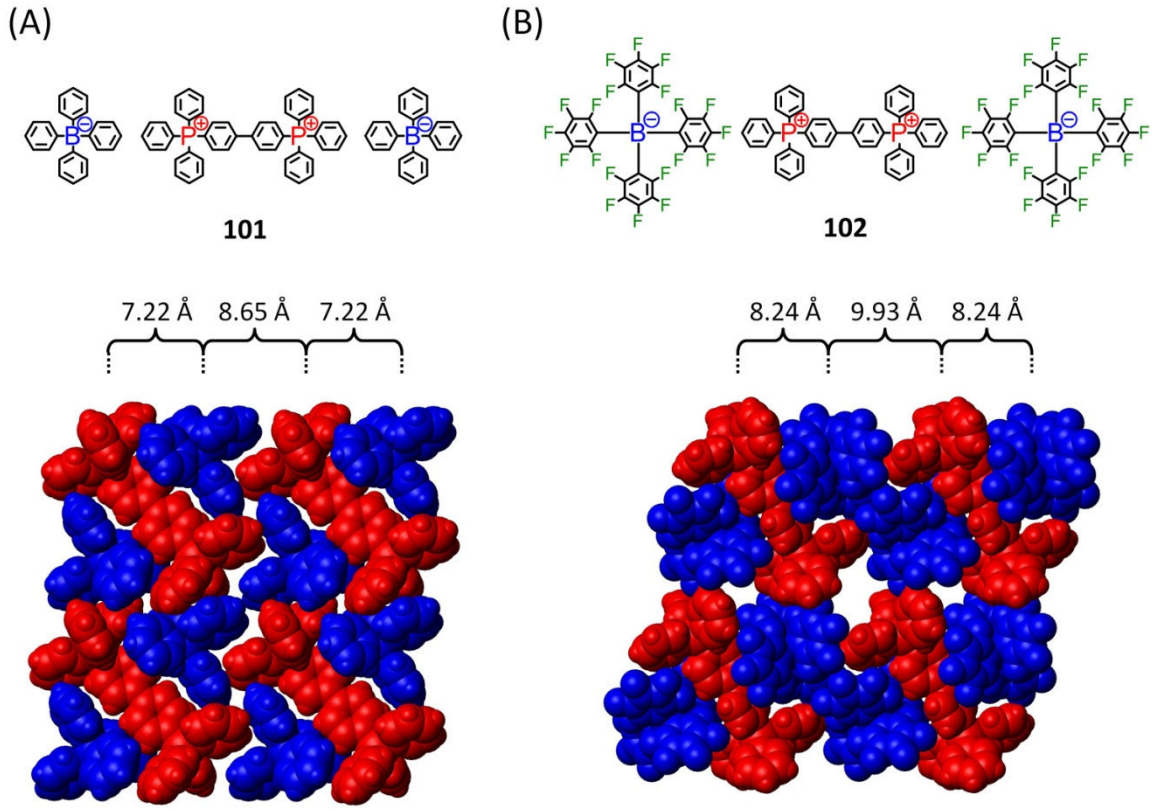

Figure 208: Single crystal structures of dicationic salts **101** and **102** (cations in red, anions in blue; brackets indicate distances between anion and cation central atoms)

In the tetraphenylborate salt **101**, the borate´s two-fold axis roughly points towards the phosphonium centers, whereas the same axis points in an orthogonal direction in perfluoro-tetraphenylborate **102**. In contrast to the monocationic salt **95**, arene-perfluoroarene interactions are not immediately apparent here. However, at least two of

the four perfluorinated phenyl rings of the anion in salt **102** appear to interact with phenyl rings of the dication´s biphenyl bridge.

Large borates such as first generation dendronized borate **14** or its surface fluorinated analogue **41** both show the typical close packing of anions and cations along the borates two-fold axis (see Figure 209 and Figure 210). Despite the significantly increased overall sizes of these borates as compared to their borate core **12** (Figure 202), the closest anion-cation contact remains at only 6.09 Å in borate **14** or at 6.16 Å in borate **41**, respectively. However, the polyphenylene shells largely increase ion distances towards secondary counterion neighbors.

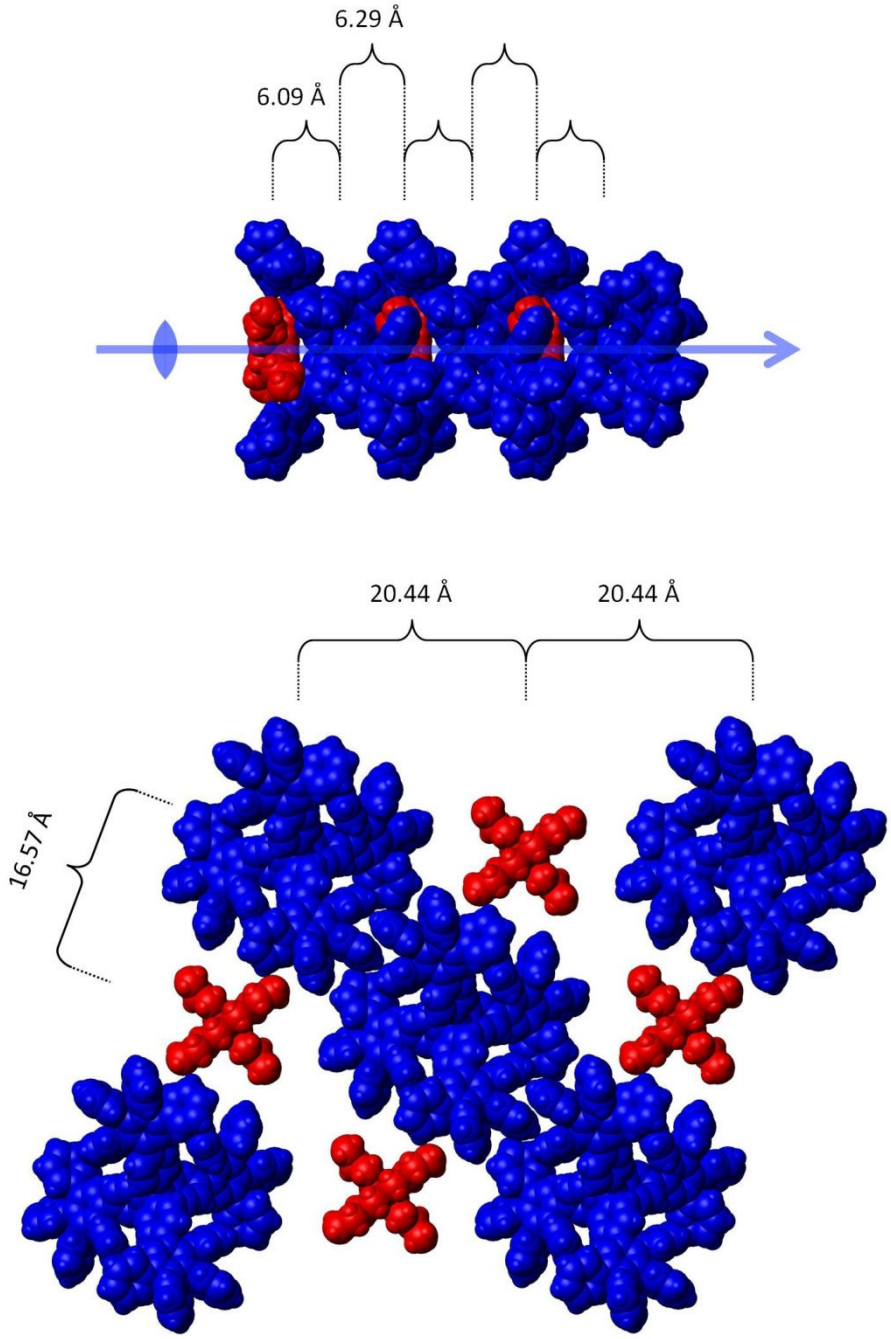

Figure 209: Single crystal structure of first generation PP dendronized borate **14** (cations in red, anions in blue; brackets indicate distances between anion and cation centers)

While secondary counterion neighbors are separated by only 9.11 Å in non-dendronized borate core **12** (Figure 202), the closest secondary counterion neighbors are already at a 16.57 Å or even 20.44 Å distance in first generation dendronized borate **14** (Figure 209). Similarly, the distance to secondary counterion neighbors is also increased in surface fluorinated dendronized borate **41** (Figure 210).

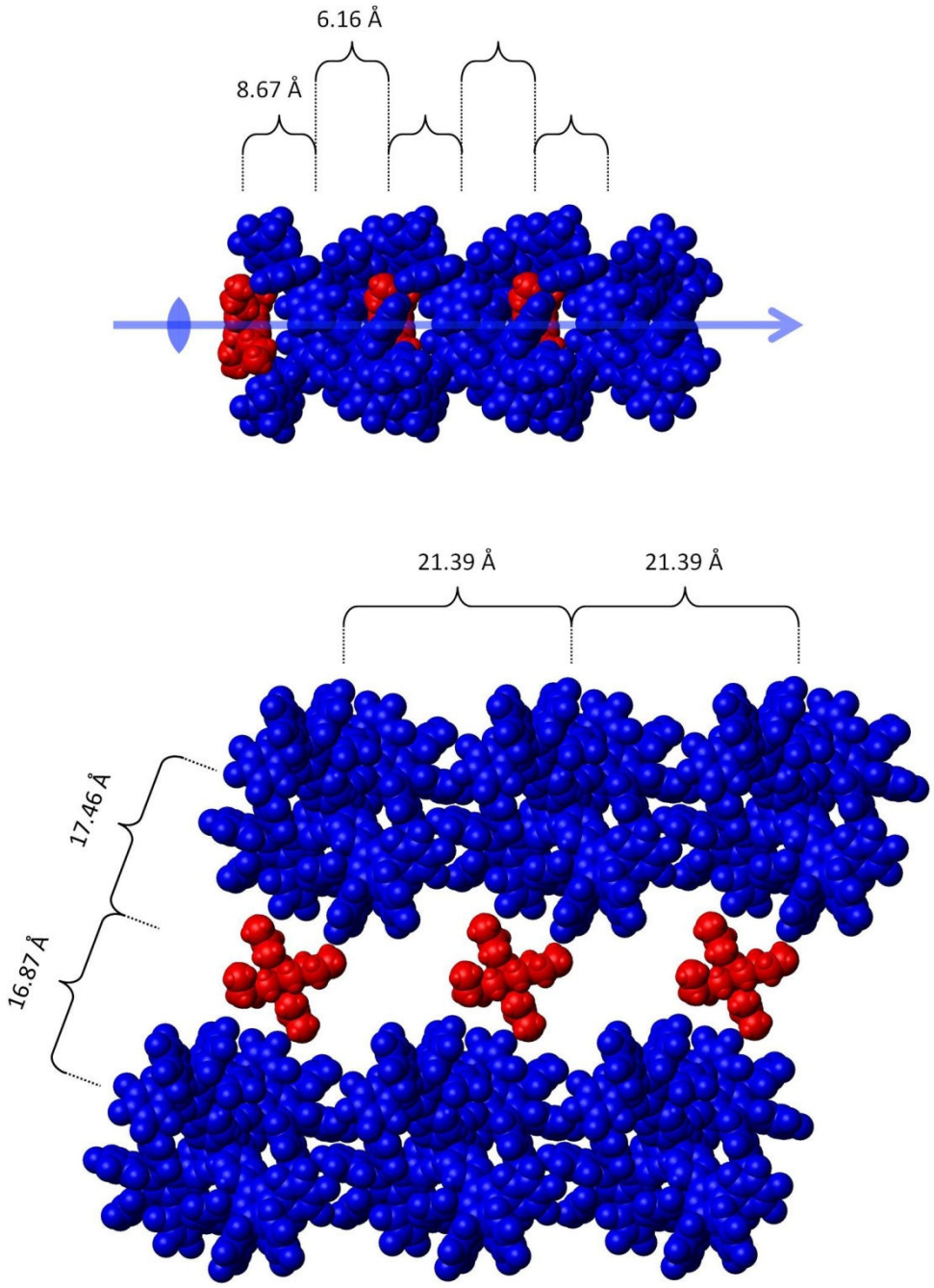

Figure 210: Single crystal structure of surface fluorinated dendronized borate **41** (cations in red, anions in blue)

As a consequence, the resulting lattice enthalpies of dendronized borates **14** and **41** can be expected to be significantly lower than those of non-dendronized salts (see also paragraph 6.3.3 of this chapter).

6.3.2 Cavities and Solvate Molecules

Due to the inevitable presence of inter- and intramolecular voids within polyphenylene scaffolds, PPDs do readily take up guest molecules (see introduction, paragraph 1.2.3.4). The ability of PPDs to interact with guests has been exploited by using them as sensitive layers in detectors for explosives[37,118] or volatile organic compounds[119] (VOCs). Furthermore, the crystal structures of several different PPDs[114,115] revealed that solvent molecules are often trapped within inter- and intramolecular voids of PP scaffolds.

Within the crystal structures of first generation dendronized borates **14** and **41**, solvent molecules have been detected as well. Both salts have been crystallized from mixtures of methylene chloride and hexane. In borate **14**, two hexane and six methylene chloride molecules have been found within each formula unit of the salt. In surface fluorinated borate **41**, no hexane molecules were detected, but each formula unit of the salt contained eight methylene chloride molecules.

An apparent difference between the crystal needles of borate **14** (colorless) and surface fluorinated borate **41** (intense yellow) besides their color was the speed of their gradual degradation. While crystal needles of borate **41** could be stored for several months under ambient conditions, the crystal needles of borate **14** slowly turned turbid within a few days. Upon examination of the crystals by means of X-ray diffraction, internal channels could be identified within both structures (see Figure 211).

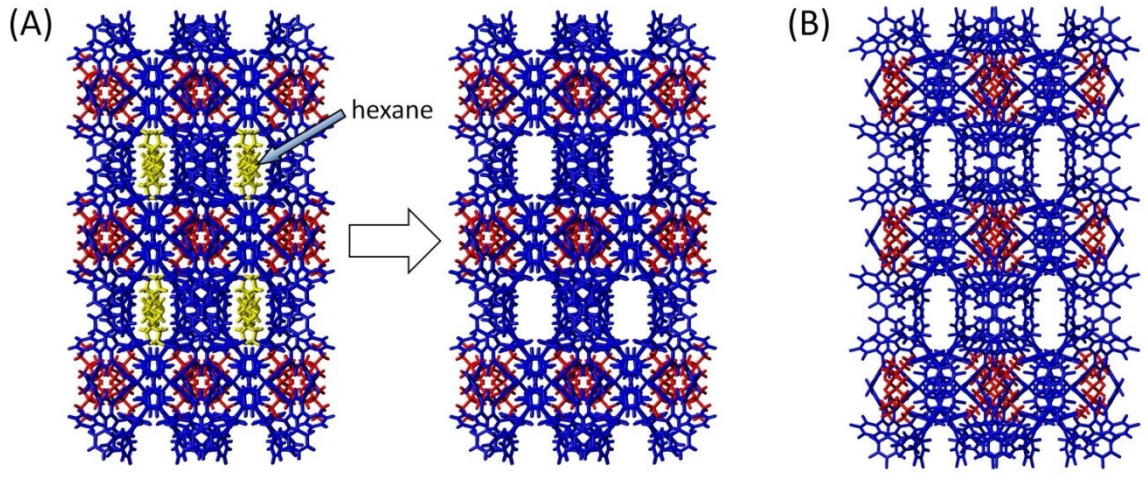

Figure 211: Channels within the crystal structures of first generation dendronized borates **14** (A) and **41** (B); stick model representation of anions in blue, cations in red and hexane molecules in yellow

In first generation dendronized borate **14** (Figure 211 (A)), channels in the crystal are mainly filled with hexane molecules. Since the channels continue throughout the entire crystal, hexane molecules might be able to continually escape internal parts of the crystal structure, which eventually leads to the observed degradation of the crystal (Figure 211 (A)). While similar channels do also exist in crystals of surface fluorinated borate **41** (Figure 211 (B)), no fast degradation of the crystal structure was observed here. Probably, the more flattened cross-section of its channels results in a decreased tendency of solvent loss from the internal structure.

6.3.3 Lattice Enthalpies

Crystal structure data of salts can be used to approximate their lattice enthalpies (see introduction, paragraph 1.3.2.2). Of course, lattice enthalpy decreases with decreasing number of ions packed into a given volume. Larger ions result in less dense packing of charges and hence in smaller lattice enthalpies. For very accurate estimations of lattice enthalpy, a large number of (often unknown) geometric parameters would have to be considered. By contrast, the *Passmore-Jenkins* equation[125] only requires knowledge of the molecular volume of a salt, which can easily be derived from the cell constants of the crystal.

It should however be mentioned that the theoretical derivation of lattice enthalpy as described in 1.3.2.2 does not account for the many secondary interactions between molecules that may contribute significantly to overall lattice enthalpy. In addition to electrostatic attraction, these secondary interactions are of increasing relevance in the case of more complex molecules such as molecular ions (see for example the arene-perfluoroarene interactions in borate **95**, paragraph **6.3.1**, Figure 207). Nevertheless, the *Passmore-Jenkins* equation generally provides good approximations for the lattice enthalpies.

In order to determine the impact of anion size, the lattice enthalpies of a number of different tetrabutylammonium salts (including those of iodide and of some other established weakly coordinating anions) were approximated following the procedure described in paragraph 1.3.2.2, equation (5)).

tetrabutylammonium salt	**formula**	**lattice enthalpy**
iodide	$TBA^+ I^-$	407 kJ/mol
hexafluorophosphate	$TBA^+ PF_6^-$	398 kJ/mol

tetraphenylborate **93**	$TBA^+ BPh_4^-$	349 kJ/mol
perfluoro-tetraphenylborate **94**	$TBA^+ BPh^F_4{}^-$	337 kJ/mol
dendronized borate **14**	TBA^+ B-G1$^-$	254 kJ/mol
perfluoro-dendronized borate **41**	TBA^+ B-G1^{F-}	241 kJ/mol

Table 1: Lattice enthalpies of different tetrabutylammonium salts as estimated theoretically from their single crystal cell constants using the *Passmore-Jenkins* equation[125]

Apparently, the tetraphenylborate salt **93** of tetrabutylammonium already exhibits a 12% lower lattice enthalpy than the according hexafluorophosphate or iodide salts as a result of the tetraphenylborates larger ion size. In perfluorinated tetraphenylborate salt **94**, the anion size increases only slightly, leading to a slight further decrease in lattice enthalpy. Decoration of both tetraphenylborate anions **93** as well as **94** with first generation rigid polyphenylene dendrons (dendronized borates **14** and **41**) reduces the lattice enthalpies of TBA^+ salts drastically by another 30%.

Due to a lack of crystalline material for cell constant determination, lattice enthalpies of even larger dendronized borates could not be approximated. It is however reasonable to expect even lower lattice enthalpies for their salts.

6.4 Solubility

In the introduction of this thesis (paragraph 1.3.2.3) it was mentioned that the solubility of salts is largely governed by the size of their constituting ions: Large ion sizes result in a decrease of electrostatic attraction between ions of opposite charge and consequentially lead to a decrease of the lattice energy of the salt. Hence, at a given solvation energy (depending on parameters such as the polarity of the solvent), salts of large ions should generally dissolve more easily than salts of small ions.

However, treatment of dendronized ions as point charges surrounded by smooth rigid shells only takes into account the impact of direct electrostatic attraction on solubility. This view is too oversimplified to describe the solubility of more complex molecular ions satisfactorily. In dendronized ions, the surrounding dendritic scaffold makes up a tremendously large ratio of the overall chemical structure. Therefore, the chemical nature of the scaffold also markedly influences overall solubility of the molecular ion. Neutral polyphenylene dendrimers, for example, show extremely low solubility in hexane. Conse-

quentially, the salts of ions that are solely dendronized with polyphenylene scaffolds should also exhibit very low solubilities in hexane. A low solubility would even be observed if electrostatic interactions between anions and cations could be screened perfectly by means of rigid dendronization. The negligible solubility of dendronized borate salts in hexane therefore does not provide any information as to how effective electrostatic interactions are suppressed.

The same line of argument can be applied to very polar solvents such as water: non-functionalized and neutral PPDs are insoluble in water and, consequentially, so are salts consisting of ions dendronized with polyphenylenes. If designing electrolytes for specific high or low polarity solvents (such as water or hexane) were the task, then suitably surface functionalized (e.g. highly PEGylated or alkylated) PP-dendronized ions would have to be synthesized. Within this work, the negligible solubility of PPDs in hexane was instead utilized as a means to purify salts of PP-dendronized anions via precipitation.

Some incompatibilities with solvents arise from the general sensitivity of tetraphenylborate against protic acids. For example, it was observed that the C-H acidity of chloroform led to a partial decomposition of tetraphenylborate in solution. Fluorinated tetraphenylborates, by contrast, are much less sensitive against *Brønsted* acidic media. Thus, only those borates were tested as electrolytes in chloroform that were equipped with a fluorinated core (see paragraph 6.5.1.5).

Dendronized borate salts could easily be dissolved in polar solvents such as acetonitrile ($\varepsilon_r = 38$) or dimethyl sulfoxide ($\varepsilon_r = 48$). Solvents of relatively low polarity such as methylene chloride ($\varepsilon_r = 8.9$) and tetrahydrofuran ($\varepsilon_r = 7.6$) have also proven to be excellent solvents for all dendronized borate salts. In fact, the solubility product of these salts was too high to be determined. Upon increasing the salt concentration further and further, no precipitate formation and hence no solubility limit could be observed. Instead, the viscosity of all salt solutions gradually increased with increasing solids content (>400 mg/mL). A correct description of the solution behavior therefore would require treating dendronized borates as both classical salts (to account for electrostatic interactions, solvation energies etc.) and as large macromolecules (to account for dispersive interactions, potential entanglement etc.) at the same time.

In solvents of very low polarity such as toluene ($\varepsilon_r = 2.4$), all dendronized borates with fluorinated cores readily dissolved completely at any given concentration. Salts of first generation dendronized borates **14** and **41** with non-fluorinated cores also dissolved in toluene, but did so considerably more slowly and only in low concentration. The differences in toluene solubility between both classes of dendronized borates may be related to inherent differences in crystallinity: Due to the existence of many different atropisomers in borates with fluorinated cores (see chapter 5), these borates seem unable to form regular crystalline lattices. Instead, they most probably remain amorphous even on the nanoscopic level. As a consequence, a comparatively smaller amount of solvation energy may be required to transfer individual ions from their amorphous bulk solid environment into solution as compared to borates **14** and **41** with potentially crystalline solid environments.

In the case of borate **52**, up to 450 mg of salt have been dissolved in just 1 mL of toluene, resulting in an apparently much more viscous liquid than the pure solvent toluene alone. It should be emphasized again that the here mentioned 450 mg of borate salt **52** did not indicate any solubility limit and that toluene solutions with even higher solid contents could be possible.

6.5 Conductivity and Coordination Strength

In the introduction (paragraph 1.3.2.4), it was mentioned that concentration dependent measurements of conductivity can be used to roughly estimate the degrees of dissociation α of electrolytes in solution. A comparison of α values of different electrolytes under the same conditions (solvent, temperature, concentration, counter-cation) shall herein be used as a relative measure for the coordination strength of different anions.

It should however be mentioned that the accuracy of the obtained α values is also dependant on the accuracy of the before derived limiting molar conductivities Λ_0. Limiting molar conductivities have been derived via linear extrapolation of measured molar conductivities Λ to $c = 0$ according to the *Ostwald* law of dilution (see paragraph 1.3.2.4, and paragraph 9.1 in the experimental part). Especially in the low concentration regime, errors in measured conductivity values Λ can have a non negligible effect on the resulting Λ_0 values. However, since all measurements were performed under the same conditions, us-

ing the same equipment, the same solvents and the same procedures, all experiments should also exhibit the same systematic errors. A comparison of the degrees of dissociation α of different salts should therefore reflect qualitatively correct relations. The relative error in conductivity measurement was 0.5% of the measured value, as specified by Metler-Toledo.

6.5.1 Degrees of Dissociation

Ideally, the degree of dissociation of a dendronized electrolyte should depend on several different parameters, such as ion size, density of the dendritic scaffold, surface functionalization, type of the counterion and of course the polarity of the solvent. In the following paragraphs, the impact of all these parameters will be analyzed individually.

6.5.1.1 Effect of Anion Size

To test the effect of anion size on electrolyte dissociation, the conductivities of a number of tetrabutylammonium salts with anions of different sizes (ranging from non-dendronized tetraphenylborate **93** to third generation highly branched borate **65**) were measured in THF at room temperature. The according degrees of dissociation α derived via *Ostwald*'s law of dilution (paragraph 1.3.2.4) are displayed in Figure 212.

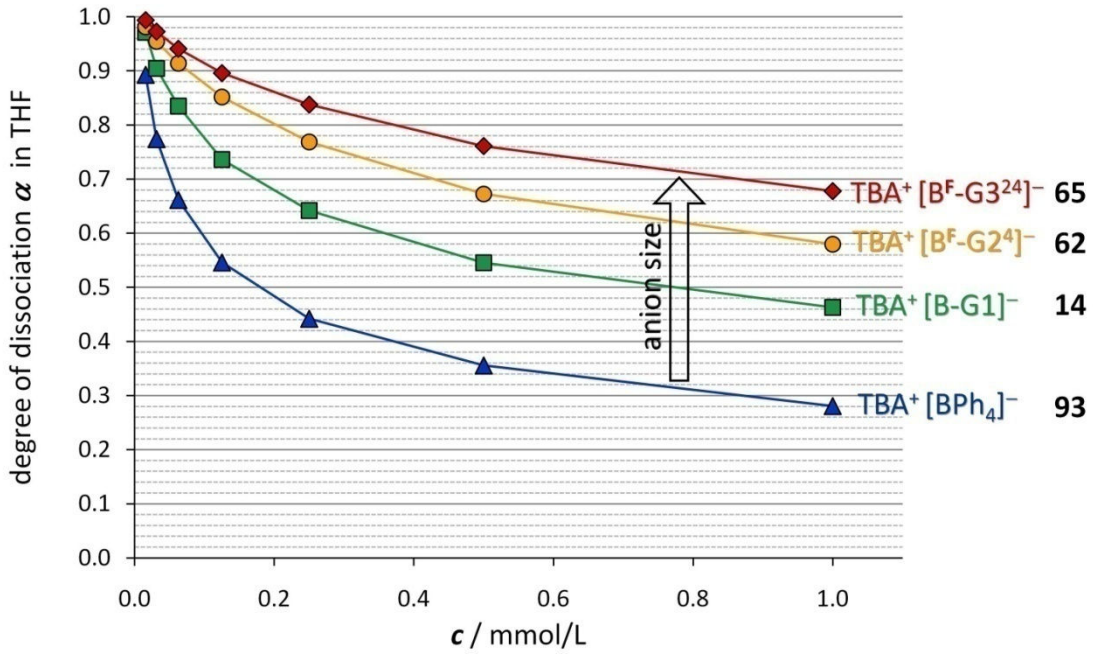

Figure 212: Degree of dissociation α in THF as a function of anion size

As expected, the degree of dissociation α of all salts generally increases at lower salt concentrations. In very dilute THF solutions, all dendronized borates are almost completely

dissociated (α almost 1) and even non-dendronized tetraphenylborate is largely dissociated from tetrabutylammonium (α about 0.89). The degree of dissociation drops significantly at higher salt concentrations. However, it was found that with increasing anion size, the effect of concentration on ion association decreased. While non-dendronized tetraphenylborate shows a comparatively strong association to tetrabutylammonium (α only about 0.28) at a concentration of $c = 1$ mmol/L, third generation dendronized borate **65** still remains largely dissociated (α still about 0.68) at the same concentration.

It is noteworthy that the degree of dissociation does not increase proportionally to increasing anion size. Instead, each further increase of ion dissociation requires ever greater increases in ion size (compare also Figure 213, where the α values of normally branched second and third generation borates **56** and **59** are displayed).

6.5.1.2 Effect of Anion Shell Density (Degree of Branching)

To investigate the impact of anion shell density on ion dissociation, the conductivities of differently branched borates of second as well as third generation were measured and compared. Degrees of dissociation α derived from concentration dependant measurements of conductivity are displayed in Figure 213.

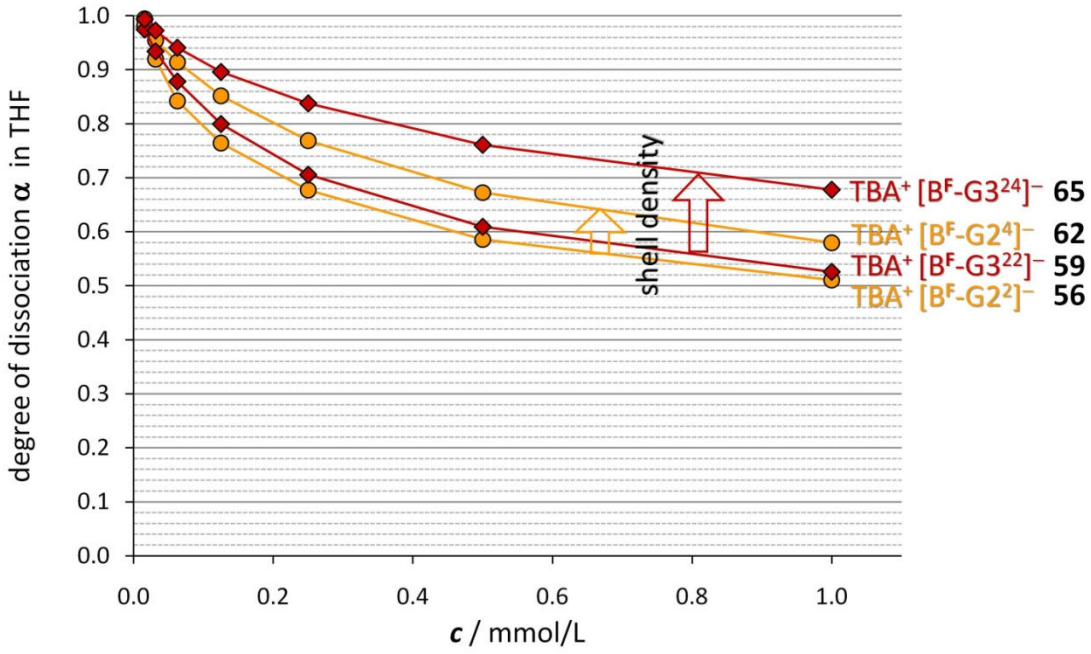

Figure 213: Degree of dissociation α in THF as a function of degree of branching

Apparently, the density of the dendritic shell (degree of branching) has a marked effect on ion dissociation in dendronized salts. By contrast, an increase in the maximum exten-

sion r_{max} of a dendronized anion does not suffice to ensure a significant increase in ion dissociation. For example, normally branched third generation dendronized borate **59** exhibits almost identical degrees of dissociation as its second generation analogue **56**, even despite the significant difference between their maximum sizes (r_{max}(**59**) = 3.15 nm; r_{max}(**56**) = 2.28 nm). By contrast, highly branched second generation dendronized borate **62** exhibits even higher degrees of dissociation than the overall larger but normally branched borate **59** of third generation. An increase in overall anion size via dendronization therefore is only effective if the density of the dendritic scaffold is also sufficiently high. Normally branched borate anions **56** and **59** may contain too large inter-dendritic voids to effectively prevent tetrabutylammonium counterions from approaching these anions central negative charge. To generally ensure an effective steric screening and suppression of ion association, the degree of branching in dendronized ions should thus always be maximized.

6.5.1.3 Effect of Surface Fluorination

Surface fluorination has generally proven an effective means to lower the coordinative power of molecular anions. Most of the anions commonly used as weakly coordinating anions feature highly or fully fluorinated surfaces. To investigate the effect of surface fluorination, the degree of dissociation α of several tetrabutylammonium salts with non-fluorinated (**93**, **14** and **56**) as well as analogous, surface fluorinated anions (**94**, **41** and **69**) were measured and compared (see Figure 213).

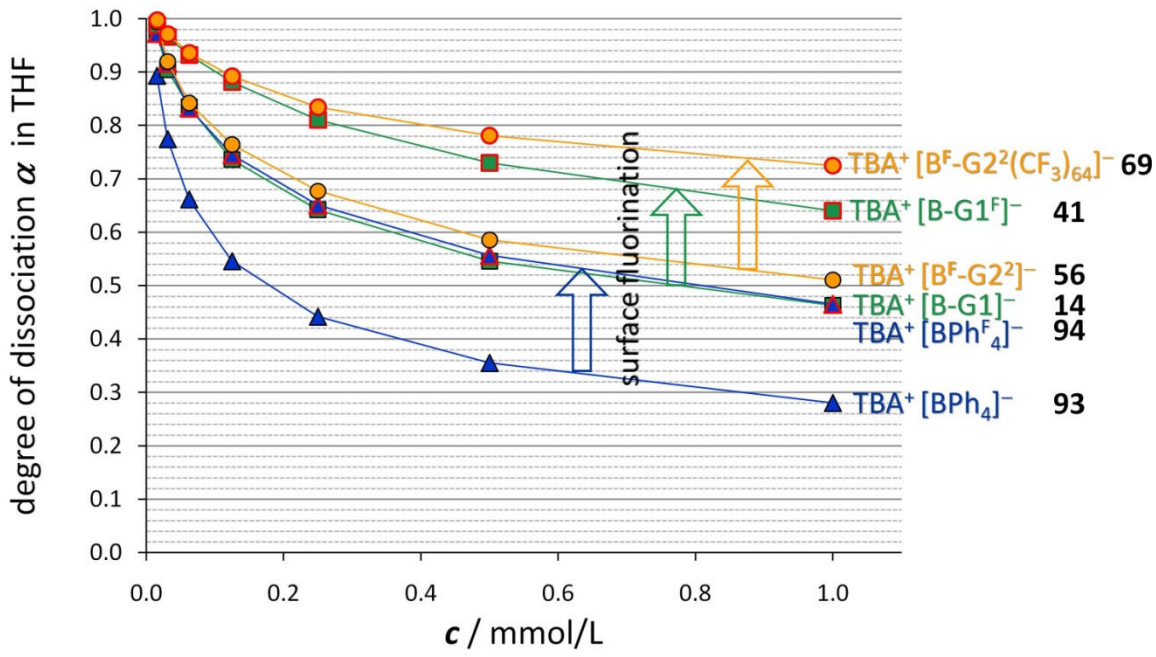

Figure 214: Degree of dissociation α in THF as a function of surface functionalization

In non-dendronized salt **93**, surface fluorination of the tetraphenylborate anion (resulting in borate **94**) was found to significantly weaken attractive interactions between anions and cations. At a concentration of 1 mmol/L in THF, the degree of dissociation α increased from 28% (borate **93**) to 47% (borate **94**) due to surface fluorination. Interestingly, the mere dendronization of tetraphenylborate **93** with polyphenylene dendrons (giving rise to first generation dendronized borate **14**) was found to be similarly effective for promoting ion dissociation in THF. An additional fluorination of its surface (giving rise to first generation dendronized as well as surface fluorinated borate **41**) consequentially led to even higher degrees of dissociation. The observed increase in α from 47% (borate **14**) to 64% (borate **41**) at $c = 1$ mmol/L can be explained by the combined effects of increased steric screening by the polyphenylene shell and suppression of dispersive interactions due to surface fluorination.

It was mentioned already (see paragraph 2.3.5) that the synthesis of surface fluorinated analogues of higher generation dendronized borates (such as borate **56**) could not be driven towards completion if fluorinated tetracyclone **40** was employed. Utilization of CF_3-functionalized tetracylcone **47** however also enabled the synthesis of higher than first generation dendronized borates with highly fluorinated surfaces, such as borates **69** and **70**. It should be noted though that the resulting borates do not represent direct structural analogues of the non-fluorinated structures due to their larger sized dendrons and additional

CF_3-groups (see for example Figure 110 in paragraph 2.2.5.2). It was also demonstrated already that an increase in anion size does not suffice to ensure better steric screening and higher degrees of dissociation (see paragraph 6.5.1.2 above). Normally branched second generation dendronized borate **56** therefore exhibits only slightly increased degrees of dissociation (51% at 1 mM) than first generation dendronized borate **14** (47% at 1 mM). Nevertheless, fluorination of the surface of **56** via CF_3-functionalization towards borate **69** was found to again drastically boost ion dissociation by up to 72% in THF.

A highly branched analogue of borate **69** with a highly CF_3-functionalized surface might be even less coordinating than the normally branched second generation borate, but has not been synthesized yet.

6.5.1.4 Effect of Counter-Cation

Of course, the type and nature of the counter-cation generally has as much influence on overall ion dissociation as the type and nature of the anion. In terms of ion sizes, much greater differences have been achieved with anionic than with cationic species. Nevertheless, the herein presented method for the exchange of counterions in salts of dendronized borates (see chapter 0) also enables an investigation of the impact of counterion type on ion dissociation. Therefore, the degree of dissociation of tetrabutylammonium salts were compared to those of the according tetraphenylphosphonium salts in both tetrahydrofuran and methylene chloride (see Figure 215).

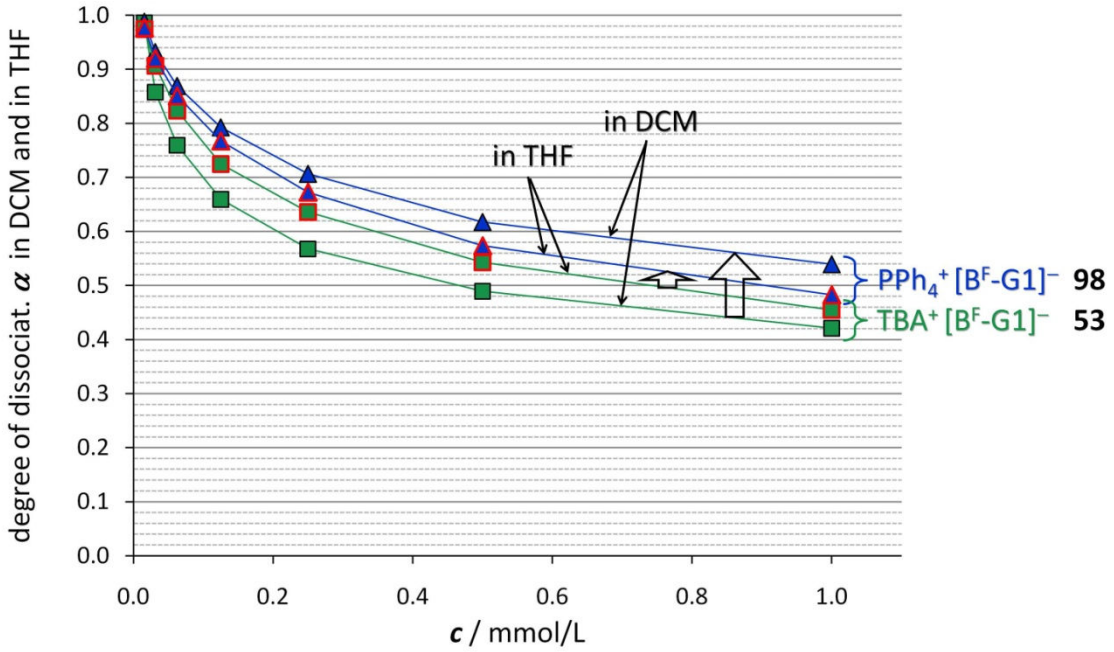

Figure 215: Degree of dissociation α in THF as a function of the type of counterion

In both tetrahydrofuran and methylene chloride, a change of the counter-cation from TBA^+ (**53**) to PPh_4^+ (**98**) resulted in an increase of the degree of dissociation. The increase in ion dissociation was much more pronounced in methylene chloride than in THF. Moreover, in the case of first generation dendronized borate without a fluorinated core (not displayed in Figure 213, see paragraph 9.1), the tetraphenylphosphonium salt **97** was found to be even less dissociated in THF than the according tetrabutylammonium salt **14**. Furthermore, non-dendronized tetraphenylphosphonium tetraphenylborate ($PPh_4^+BPh_4^-$) had such a low solubility in THF that (in contrast to the according tetrabutylammonium salt $TBA^+BPh_4^-$) its degree of dissociation in THF could not even be measured. These observations may be related to poor solvation energies ΔG^0_{solv} of tetraphenylphosphonium in THF. Observed differences in salt solubilities and ion dissociation might also be related to the type of packing and crystallinity of salts on the microscopic level. While tetraphenylphosphonium salts may easily form well ordered aggregates or even crystalline domains with counterions such as tetraphenylborate or dendronized borate, the existence of many atropisomers of borate **98** surely precludes any formation of ordered aggregates. In any case, it becomes clear that a large number of different parameters (occurrence or absence of atropisomerism, solvation energies of respective ions) have an impact on electrolyte dissociation. In the future, it will be interesting to see how ion dissociation is influenced by going to even larger cationic species, such as *m*-terphenyl functionalized tetraphenylphosphonium or even PP dendronized cations.

6.5.1.5 Effect of Solvent Polarity

The polarity of a solvent crucially affects the degree of dissociation of electrolytes dissolved therein (see introduction, paragraphs 1.3.2.2 and 1.3.2.4). The lower the polarity and the dielectric constant ε of the dissolving medium, the less electrostatic interactions between positive and negative charges can be screened after electrolyte dissolution. Consequentially, salts generally dissolve and dissociate less in low polarity media. In order to investigate the effect of solvent polarity on ion-pair dissociation, concentration dependent measurements of conductivity of different electrolytes (borates **94**, **53** and **62**) were performed in both THF ($\varepsilon_r = 7.6$) and chloroform ($\varepsilon_r = 4.8$). The obtained degrees of dissociation are displayed in Figure 216.

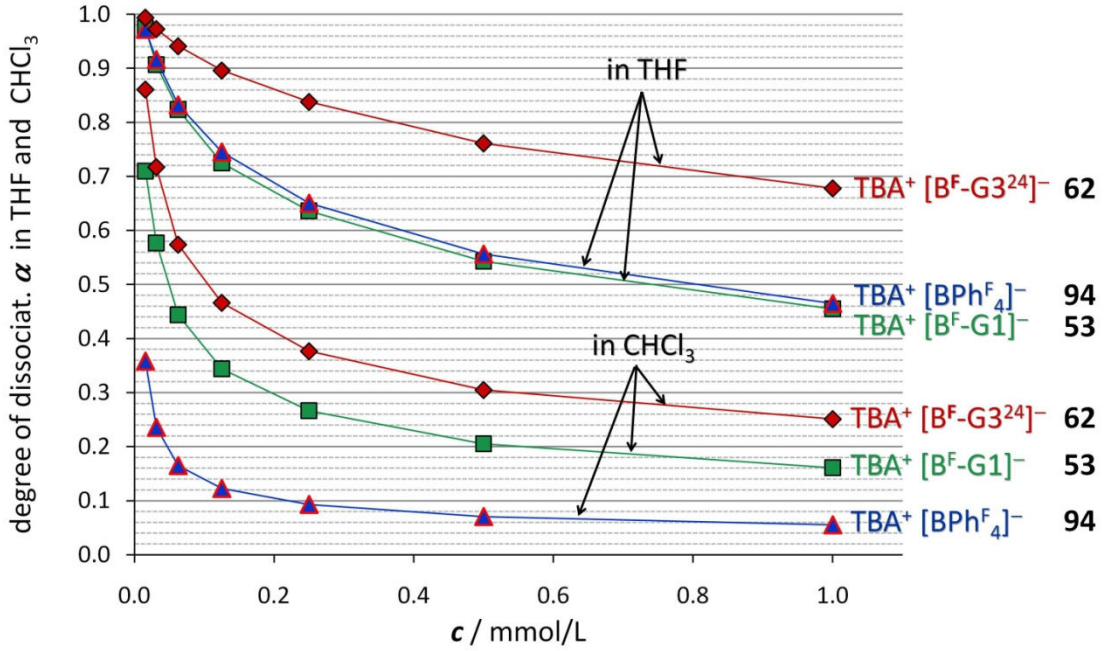

Figure 216: Degree of dissociation α as a function of anion size and polarity of the solvent

As expected, a generally lower degree of dissociation was observed for all electrolytes in chloroform as compared to tetrahydrofuran. However, while non-dendronized tetraphenylborate **94** with a fluorinated surface exhibited comparable degrees of dissociation as first generation dendronized borate **53** in THF, the non-dendronized salt **94** was found to be considerably less dissociated in chloroform than borate **53**. Apparently, the larger anion size of dendronized borate **53** is more advantageous with regard to ion dissociation in low polarity media than the fluorinated surface of borate **94**. Nevertheless, even highly branched third generation dendronized borate **62** merely exhibits a degree of dissociation of about 25% at $c = 1$ mmol/L in chloroform.

Interesting results were also found for CF_3-functionalized analogues of dendronized borates. In chloroform, first generation dendronized and CF_3-functionalized borate **68** was found to be even less coordinating than third generation dendronized borate **62** or the normally branched and CF_3-functionalized analogues **69** and **70**, respectively (see paragraph 9.1). These larger sized borates **69** and **70** may have a stronger tendency to aggregate under low polarity conditions, or the counter-cation may have a stronger tendency to remain within intra- and interdendritic voids.

A drastic boost of ion dissociation was observed in extremely dense and highly branched third generation dendronized borate **71**, decorated with 256 surface CF_3 groups (see Figure 217).

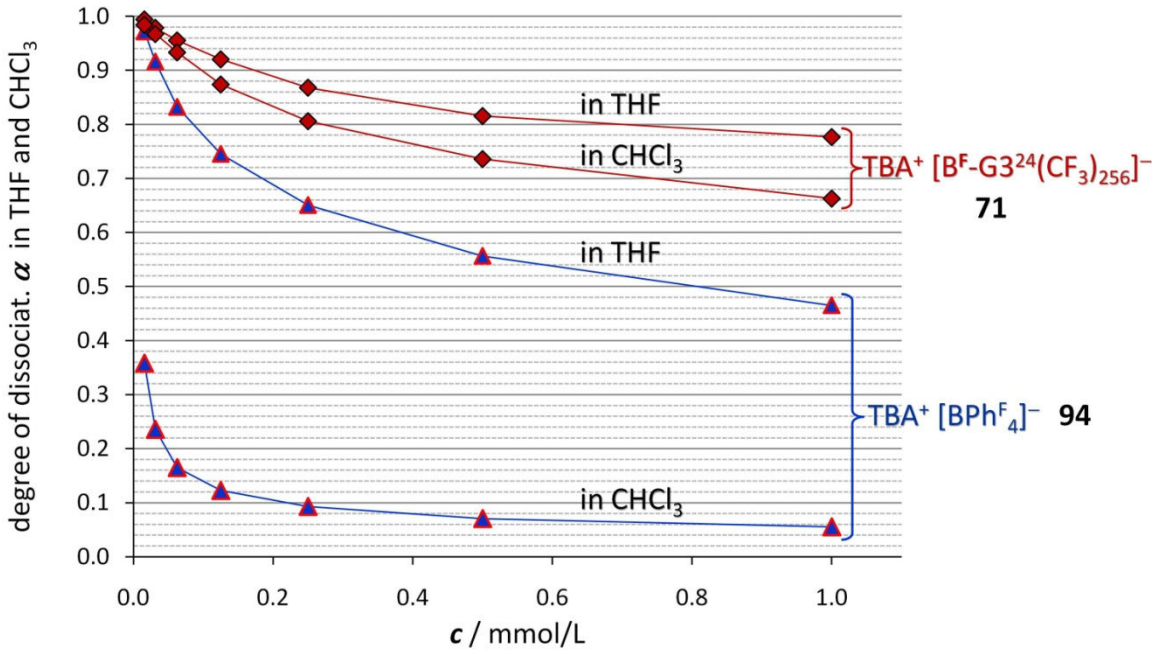

Figure 217: Degree of dissociation α as a function of anion size and polarity of the solvent

It should be mentioned again that the synthesis of borate **71** could not be driven to entire completion (32-fold cycloaddition), so that the product measured here also contained a fraction of borate anions resulting from an incomplete (29- to 31-fold) cycloaddition (see paragraph 2.3.5.2, Figure 112). Nevertheless, the already achieved large size, high scaffold density and high degree of surface fluorination led to very high degrees of dissociation of the obtained salt even in chloroform. At a concentration of $c = 1$ mmol/L, the degree of dissociation of borate **71** was still at about 66% as compared to merely 6% for benchmark weakly coordinating borate **94**.

In toluene, which has an even lower dielectric constant than chloroform (toluene $\varepsilon_r = 2.4$; chloroform $\varepsilon_r = 4.8$), a very surprising and unusual dependence of molar conductivity Λ on concentration of dendronized salt **53** was observed. At the typically low concentrations (≤ 1 mmol/L) used for all conductivity measurements presented above, hardly any conductivity in toluene could be detected. However, molar conductivity apparently increased instead of decreased with increasing concentration in toluene (see Figure 218)! This conductivity behavior is in sharp contrast to all previously studied solvents (methylene chloride, tetrahydrofuran, chloroform) and salt samples. The increase in molar conductivity Λ with increasing concentration continued to up to about $c = 60$ mmol/L, whereupon a further increase in salt concentration led to a decrease of molar conductivity.

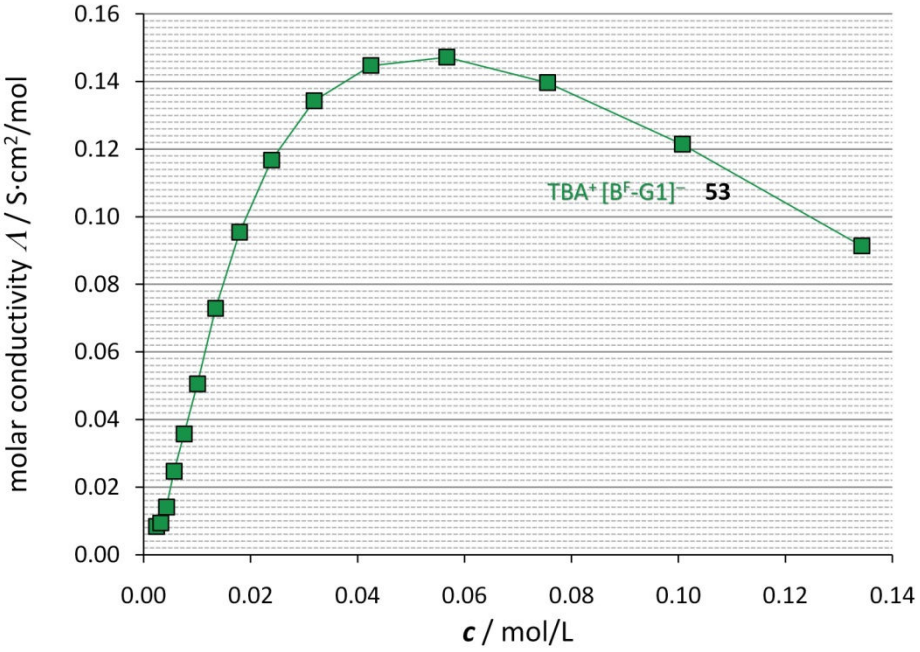

Figure 218: Interdependence between molar conductivity Λ and concentration c of borate **53** in toluene

These surprising results (Figure 218) demonstrate that the laws and models used previously to describe the behavior of electrolytes in solution (including *Kohlrausch´s* square root law and *Ostwald´s* law of dilution, see paragraph 1.3.2.4) cannot be applied in the case of dendronized salts in toluene. Also, due to the lack of an appropriate theoretical description, no meaningful limiting molar conductivity Λ_0 or degrees of dissociation α can be derived here.

How can this unusual electrolyte behavior be understood on the molecular level? Maybe the poor electrostatic screening provided by toluene is too little to enable an "escape" of individual ions from their counterions, even despite temporary dissociation at very low

concentration (see Figure 219 (A)). To serve as a rough point of orientation, the *Bjerrum* length (as described in paragraph 1.3.2.4, equation (19)), has a fairly large value of $l = 11.7$ nm in toluene ($\varepsilon_r = 2.4$) at room temperature ($T = 298$ K). So despite temporary separation, anions and cations might be unable to escape the electrostatic potential of their respective counterion (exceed the *Bjerrum* length in separation). The solution at low concentration could hence be described as containing effectively "large" but isolated and overall neutral ion pairs, which cannot contribute to overall charge transport. With increasing concentration, then, some electrostatic potential isosurfaces of neighboring pairs may overlap and allow for a transition of cations (or anions) from one ion pair to another (Figure 219 (B)). The process might be envisioned as a "hopping" of ions between before isolated "islands" of ion pairs. At higher concentration, the probability of "ion hopping" would naturally increase and lead to an increased number of temporary pathways that enable moving charge carriers throughout the solution and give rise to macroscopically detectable conductivity.

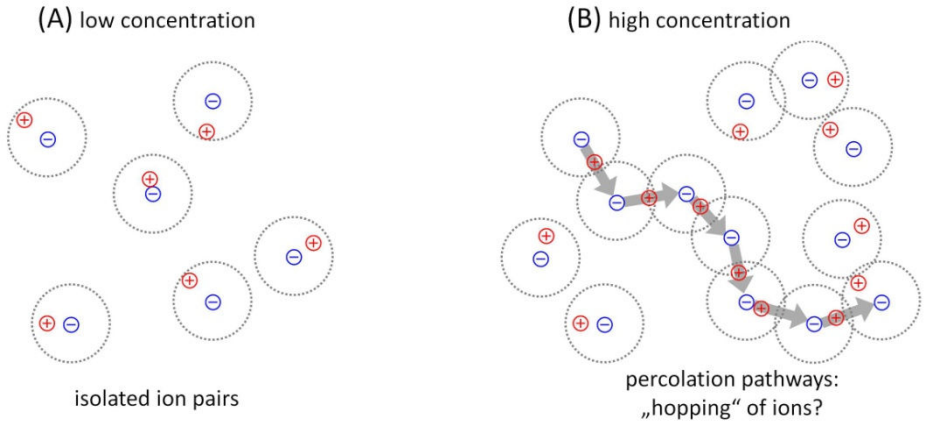

Figure 219: (A) At low concentration, cations may not completely escape their counter-anion despite partial dissociation due to weak screening by toluene; (B) at higher concentration, the probability of ions transitioning from one pair to another might increase, which may give rise to charge mobility along percolation pathways

Only at yet higher concentrations of borate **53** than $c \geq 60$ mmol/L, a decrease of molar conductivity in toluene can be observed. This decrease may be caused by either *i*) the continued increase of the solution´s viscosity with salt concentration or by *ii*) a transition towards a more classical electrolyte behavior due to better electrostatic screening, which could be provided by counterion clouds.

6.5.2 Dissociation Constants

In the introduction (paragraph 1.3.2.4), it was described how concentration dependent measurements of conductivity can be used to determine the degree of dissociation α as well as the according dissociation constant K_d of an electrolyte in a given medium. In Figure 220, the estimated dissociation constants K_d of several tetrabutylammonium salts in THF are displayed in dependence of their type of borate counter-anion. In order to facilitate their comparison, the obtained constant values were visualized in a histogram.

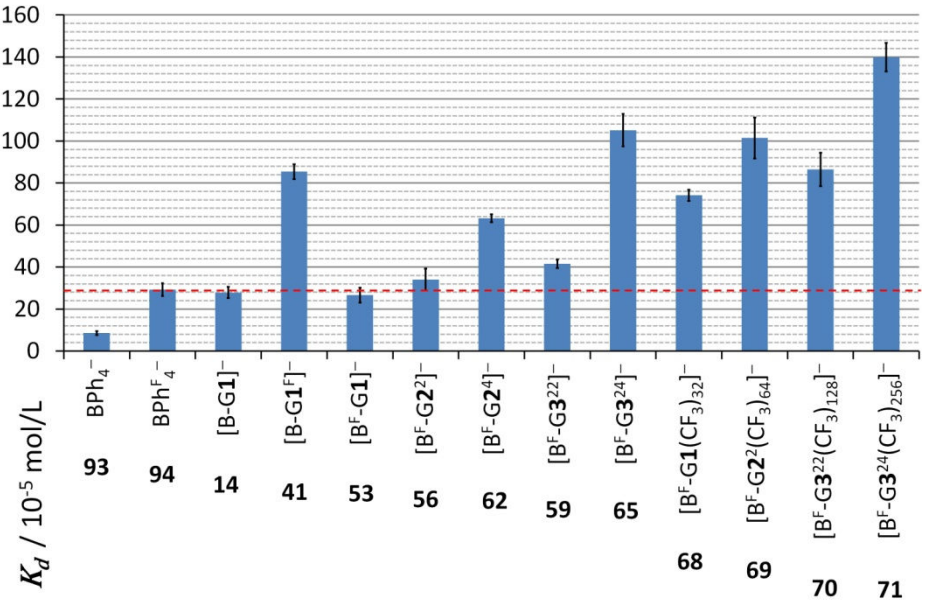

Figure 220: Comparison of dissociation constants K_d of different TBA^+ borates in THF

The red dotted horizontal line in Figure 220 marks the dissociation constant of the tetrabutylammonium salt of perfluorinated tetraphenylborate **94**, which can serve as a benchmark, representing a well established and widely used weakly coordinating anion. In agreement with the results discussed above (paragraphs 6.5.1.1 to 6.5.1.5), the derived dissociation constants show that ion dissociation can be improved far above the level of classical weakly coordinating anions (such as "BARF" borate **94**) by means of anion dendronization with rigid and highly branched polyphenylenes. The highest dissociation constants were reached within salts where the anion *i*) featured a highly fluorinated surface and *ii*) was highly branched at the same time. The values of the dissociation constants K_d can of course be used to in turn calculate the degrees of dissociation α as a function of salt concentration c, according to the rearranged *Ostwald* law of dilution (equation (25), paragraph 1.3.2.4).

$$\alpha = -\frac{K_d}{2c} + \sqrt{\frac{K_d^2 + 4cK_d}{4c^2}}$$

In Figure 221, the degrees of dissociation α as determined via conductivity measurement (solid lines) and as calculated from the obtained dissociation constants K_d (dotted lines) are compared with one another.

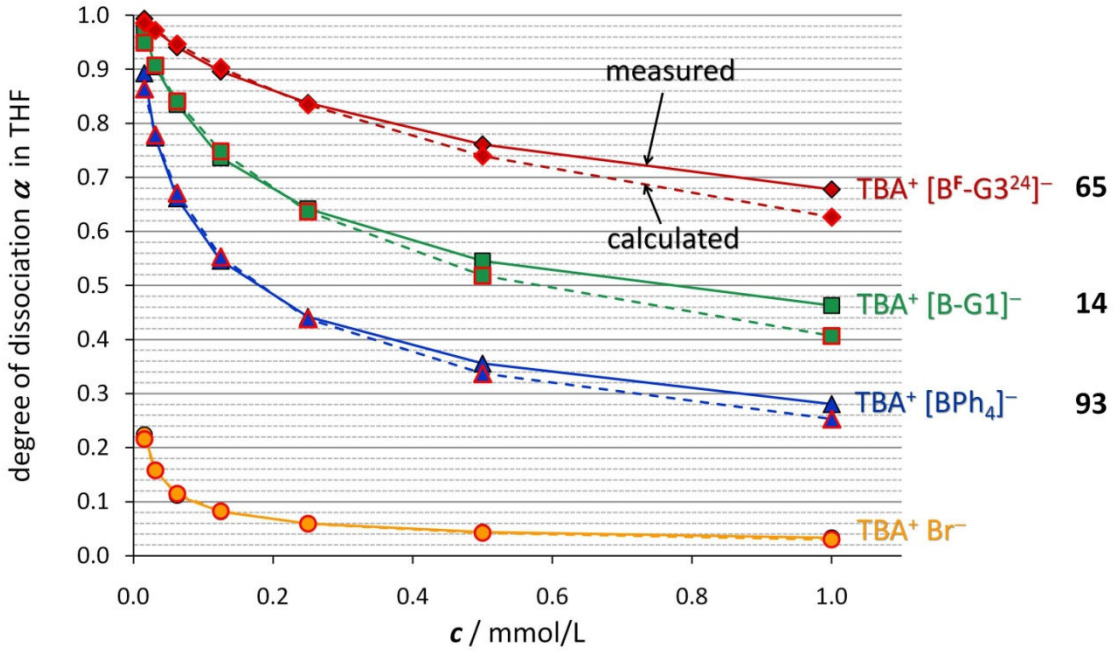

Figure 221: Comparison of measured (solid lines) and calculated (dotted lines) degrees of dissociation

With increasing concentration, the K_d-derived degrees of dissociation α (dotted lines) show slight deviations from the measured values (solid lines). For all salts, slightly higher degrees of dissociation are observed than calculated. Of course, electrolyte solutions naturally approach the behavior of ideal solutions better at low concentrations, where long range electrostatic interactions can be neglected. In the case of tetrabutylammonium bromide (yellow lines in Figure 221), calculated and measured values match almost perfectly. The level of agreement indicates that the *Ostwald* law of dilution provides an adequate description for solutions of weak electrolytes with ions of fairly simple chemical structures. In the case of more complex molecular ions, additional effects and interactions might have to be considered in order to obtain a more satisfactory description. Nevertheless, calculated and measured values based on *Ostwald*'s law of dilution still show a reasonable overall agreement even for large dendronized ions.

6.6 Summary and Outlook

In this chapter, the effect of dendronization on a number of characteristic salt properties has been investigated. It was shown by means of DOSY-NMR that ion mobility correlates with overall ion shape and size (molecular geometry), but not necessarily with molecular weight. The extent of agreement between measured hydrodynamic radius and theoretical radius of maximum extension was found to represent a good measure for the globularity of a dendronized ion. The globularity was in turn shown later to correlate with the effectiveness of the polyphenylene shell to sterically screen a dendronized ions central charge.

Examination of several single crystal structures of molecular salts revealed that in addition to electrostatic attraction and repulsion, the patterns of ion packing in a crystal are largely dominated by *i*) molecular shape and geometry as well as *ii*) secondary interactions (coordination of ions through polarized groups; arene-perfluoroarene interactions). Measured lattice constants were used to approximate the lattice enthalpies of different tetrabutylammonium salts. Solubilities of dendronized salts were found to be generally high within a wide range of solvents of very low ($\varepsilon_r = 2.4$) to moderately high ($\varepsilon_r = 48$) polarities. Moreover, it was found that atropisomerism in dendronized borates apparently enhances solubility in very low polarity solvents such as toluene, probably via frustrating the formation of crystalline domains.

Conductivity measurements on solutions of dendronized salts were performed to investigate the effect of ion dendronization on electrostatic interaction between ions and ion-pair dissociation. Three main structural parameters (namely ion size, scaffold density and surface functionalization) were varied and tested individually with regard to their impact on the coordinative power of anions. It was shown that an increase in anion size only reduced coordination strength significantly if the density of the dendritic scaffold was sufficiently high at the same time. Nevertheless, even comparatively small dendronized borates of only first generation and without fluorinated surfaces were found to already coordinate as weakly in THF as highly fluorinated WCA borate **94**. When going to less polar solvents such as chloroform, dendronization was found to be even more advantageous for weaker coordination. A further increase in either anion size, scaffold density or surface fluorination led to much less coordinating anions than benchmark WCA borate **94**.

Decoration of ions with rigid, branched and functionalized dendrons has thus proven an effective means to reduce electrostatic attraction between oppositely charged ions and boost ion dissociation in low polarity media. In the future, it will be interesting to investigate the electrolyte behavior of dendronized borates in more detail, with a strong focus on their behavior in very low polarity solvents such as toluene, which is not yet fully understood (see 6.5.1.5). Moreover, the weakly coordinating properties of dendronized ions should be utilized in WCA applications such as the metallocene catalyzed polymerization of olefins.

7 Anions with Photo-Switchable Control of Size and Coordination

7.1 Introduction

The previous chapters have demonstrated the applicability of dendrimer synthesis for the preparation of rigid, bulky and specifically functionalized macromolecular salts. Physical properties of the salts could be varied and tuned by adjusting their dendritic structure, *i.e.* size, density and surface functionality. This chapter will demonstrate how PPD chemistry offers an even broader scope for structural adaptation and property tuning. Among the many possible types of modification, the introduction of stimulus responsive functionalities deserves particular attention.

Macromolecules that are responsive to an external stimulus in a controlled and reproducible manner have many potential applications.[233-246] They enable a reversible manipulation of molecular properties such as shape, conformation or polarity whenever desired.[245] Especially the *cis-trans* photoisomerization of azobenzene continues to attract considerable attention since its discovery in the late 1930s.[247] Owing to its photostability and the substantial change of geometry accompanying *cis-trans* isomerization, azobenzene has enabled the development of a variety of photoresponsive functional materials and devices, including smart polymers,[239,241] molecular machines[242] and molecular switches.[240] There have been attempts to combine the switchability of conformation in azobenzene with the structural perfectness and multivalency of dendrimers.[50,248-256] *Vögtle et al.* reported that peripheral decoration of a polypropyleneamine dendrimer with 32 azobenzene moieties enabled changing the permeability of the dendritic shell towards guest molecules.[50] However, due to the flexibility of most types of dendrons, the conformational change of azobenzene could only affect its direct and most immediate molecular environment.

As mentioned earlier (see paragraph 1.2), polyphenylene dendrimers are unique in that they are rigid and shape-persistent.[11,257,258] Due to that rigidity, local changes of conformation do not only affect the immediate molecular environment but translate throughout the entire stiff scaffold and affect the dendritic structure as a whole. Consequently, azobenzene has been tested as a PPD core with switchable geometry in previous work of our group.[259] The resulting PP dendrimer exhibited a significant change of its overall

shape upon *cis-trans* photoisomerization of its core. More recently, my colleague [redacted] designed an azobenzene as well as pyridine functionalized AB_2 building block and used it for the synthesis of a fluorescent PP dendritic host with photoswitchable properties.[51] Studies on the obtained dendrimer confirmed that the introduction of eight azobenzene moieties as "hinges" into specific sites of the rigid PPD scaffold significantly enhanced the impact of azobenzene conformation on the overall size and shape of the dendrimer (see Figure 222). The resulting species exhibited a drastic decrease in hydrodynamic volume (-66%) upon light-induced *trans*-to-*cis* isomerization of its azobenzene moieties, as confirmed by means of fluorescence correlation spectroscopy (FCS).

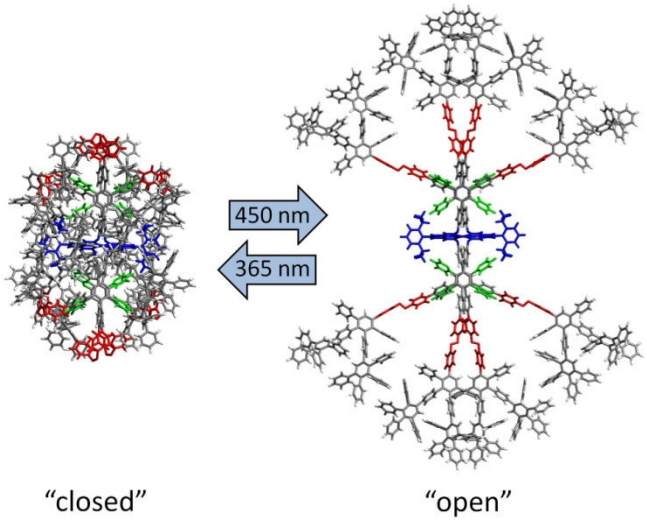

Figure 222: Fluorescent dendritic host (blue: PDI core; green: pyridine; red: azobenzene)[51]

The change in overall conformation was utilized to physically encapsulate guest molecules within the dendritic host´s interior (retarded leakage) by way of switching from a wide and "open" to a much more compact "closed" form (see Figure 222).

Within the context of this thesis, the introduction of azobenzene functions into the scaffold of rigidly dendronized anions could be used to generate anions with photoswitchable sizes. As explained earlier (see equation (20) in 1.3.2), the conductivity σ of a solution is dependent on the degree of dissociation α of the electrolyte and the mobility μ of its charge carriers. Ions with smaller radii exhibit higher mobilities than those with larger radii (see results in 6.2). In addition, it has been shown that dendronized ions with denser shells are less coordinating than ions with more open dendritic shells of lower density (as reflected in the according degrees of dissociation of their salts; see 6.5.1.2).

Switching the conformation of several azobenzene moieties in the shell of a dendronized anion from *trans* to *cis* should decrease the overall size of the anion and thus increase its mobility. Moreover, a higher density of polyphenylene branches should also enhance the shielding effect of the dendritic shell and hence increase the degree of dissociation between anion and cation (see schematic illustration in Figure 223).

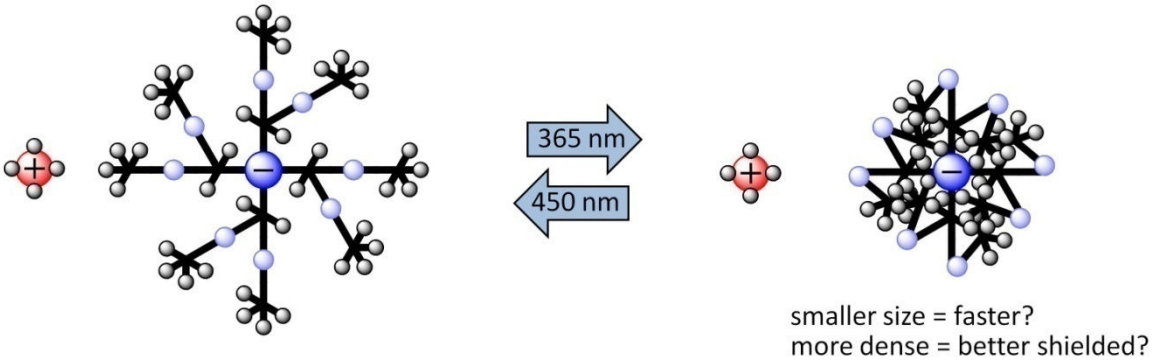

Figure 223: Scheme for switching the size and density of a rigidly dendronized anion via azobenzene photoisomerization

Both effects should be reflected in an increase of conductivity upon azobenzene switching from *trans* to *cis* via irradiation of the electrolyte solution with UV light. Changing the conductivity of an electrolyte by switching the size, mobility and coordination strength of one of the charge carriers (here: the anion) has never been attempted yet. Only recently, all of the necessary synthetic avenues (rigid dendronization of ions, introduction of azobenzene into PP scaffolds) have been developed and described,[51,260] which allows testing the above hypotheses.

The central tasks described in this chapter therefore are the synthesis of a salt containing a large anion with photo-switchable size and coordination strength, as well as a first investigation of the behavior of the resulting salt as an electrolyte.

7.2 Synthesis of a Photo-Responsive Anion

For the synthesis of a rigidly dendronized anion containing several photo-switchable azobenzene moieties within its scaffold, the suitably functionalized AB_2 building block **111** was required. The building block was synthesized via *Knoevenagel* condensation of azobenzene-ethynyl-T*i*PS functionalized benzil **110**, which had previously been developed and synthesized by [redacted],[51] to 1,3-diphenylpropan-2-one in ethanol (see Figure 224). The reaction also produced considerable amounts (about 40%) of 4-hydroxytetraphenylcyclopent-2-enone **112** in addition to the desired tetracyclone **111**.

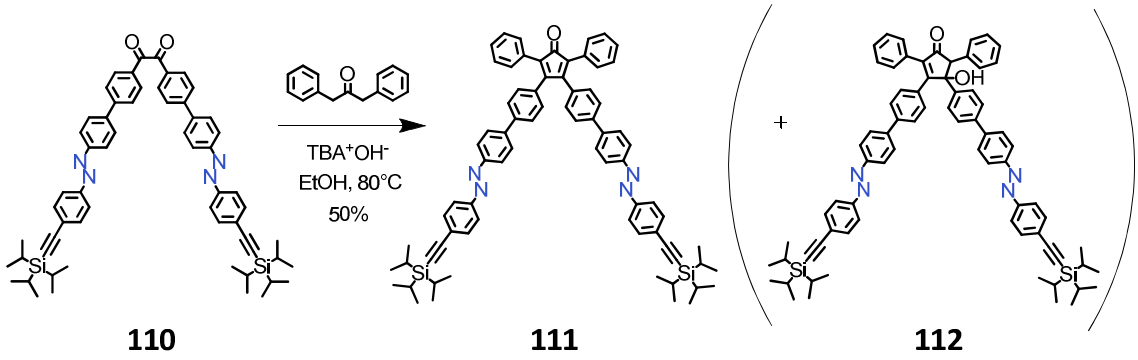

Figure 224: *Knoevenagel* condensation towards azobenzene functionalized AB_2 building block **111**

The dark violet product mixture was purified by means of filtration over silica as well as gel permeation chromatography. Although 4-hydroxycyclopent-2-enone **112** could not be removed completely, the thus purified mixture of building block **111** and side product **112** could still be used for the successful conversion of fluorinated borate core **52** to azobenzene functionalized borate **113** (see Figure 225). This may be attributed to the fact that a further dehydration of **112** to **111** takes place during *Diels-Alder* cycloaddition at 155 °C.

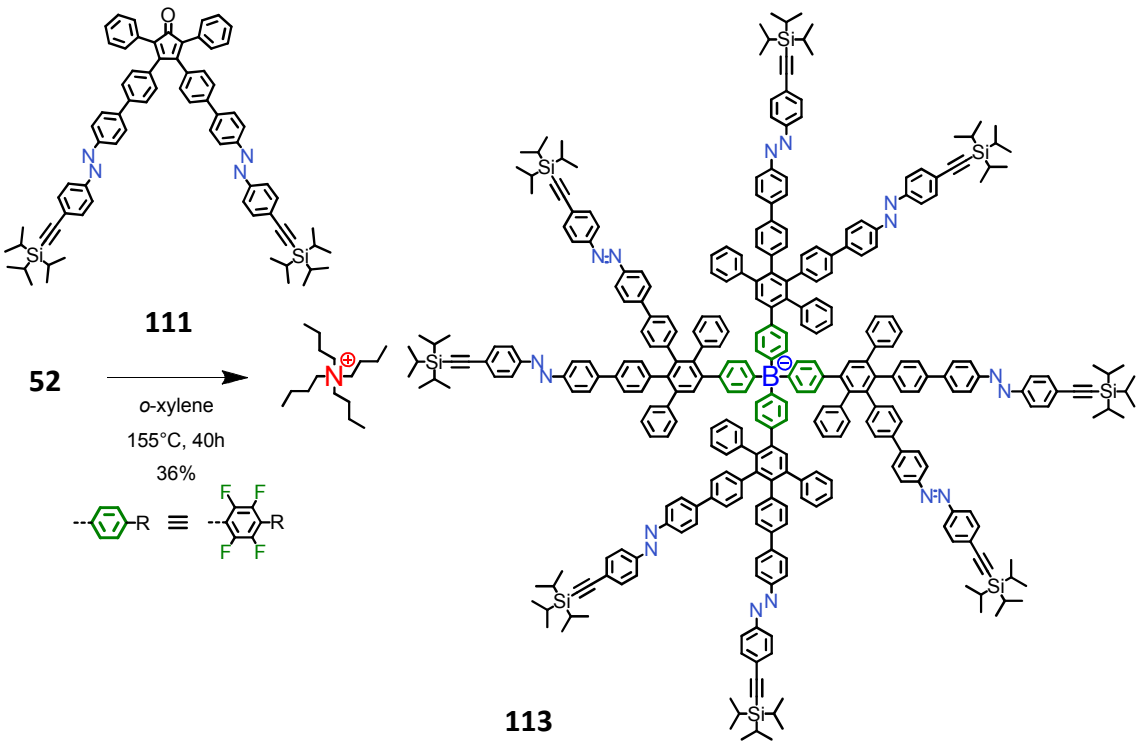

Figure 225: Synthesis of azobenzene functionalized borate anion **113**

Due to the presence of azobenzene, borate **113** exhibited an intense orange-red color in the solid state and a yellow color in solution. In order to activate borate **113** for a second dendronization step, its ethynyl functions were deprotected with tetrabutylammonium fluoride in THF at room temperature. The obtained borate **114** was then converted to second generation PP-dendronized borate **115** via *Diels-Alder* cycloaddition of tetracyclone **13** in *o*-xylene (see Figure 226).

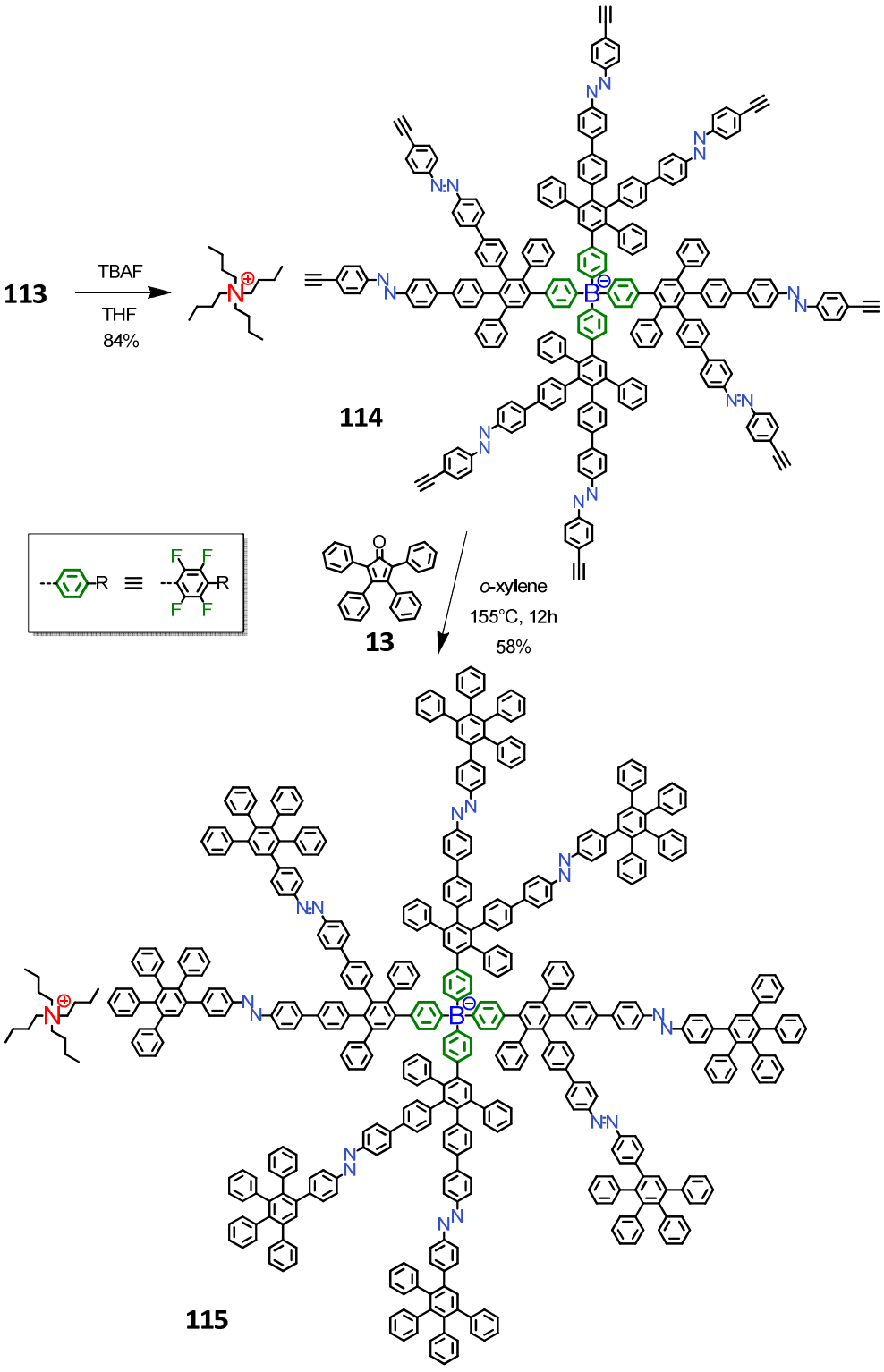

Figure 226: Synthesis of second generation dendronized borate **115** with eight photo-switchable azobenzene hinges within its polyphenylene scaffold

The reaction progress was monitored by means of MALDI-TOF mass spectrometry. After completion of the reaction, conventional column chromatography was sufficient to

isolate borate **115** as an orange powder of high purity, as evidenced by both MALDI-TOF (see Figure 227) and NMR spectroscopy.

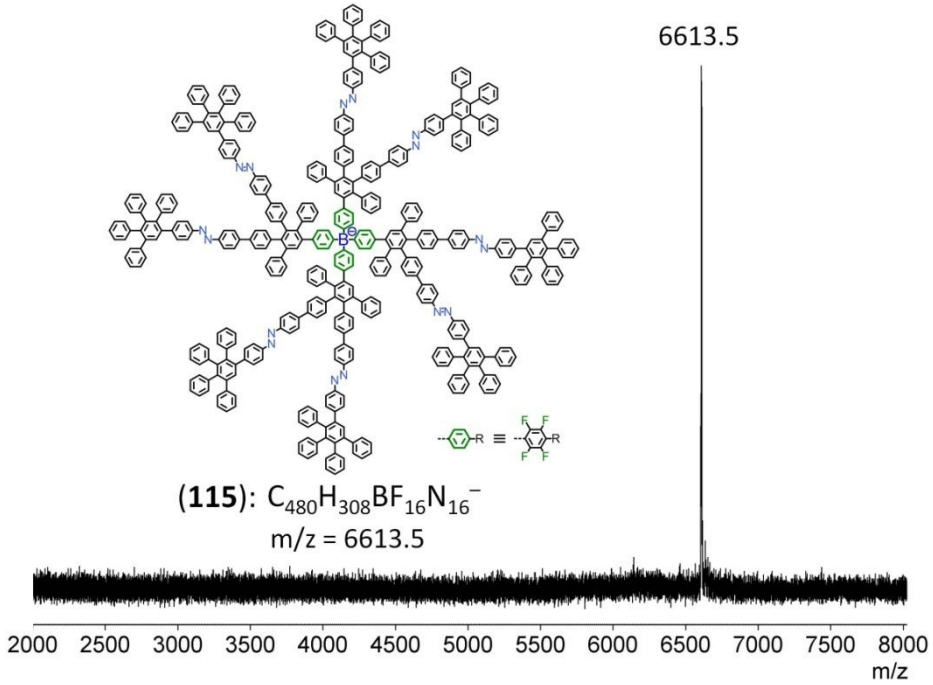

Figure 227: MALDI-TOF of second generation dendronized and azobenzene functionalized borate **115**

To summarize, the combination of several synthetic strategies (borate core fluorination, rigid dendronization of ions, introduction of azobenzene moieties into PP-dendritic scaffolds) enabled the preparation of a salt containing a huge and photo-switchable borate anion **115**, bearing eight azobenzene moieties within its rigid scaffold.

With the successful synthesis of this functional anion, several questions could now be addressed: Can the azobenzene moieties within anion **115** be switched from *trans* to *cis* using UV light of 365 nm wavelength, or are these changes in azobenzene conformation precluded due to steric constraints? If the switching of azobenzene conformation is possible, does the anion structurally survive the procedure? And finally, if the switching is possible and the anion remains structurally intact, does the switching also have a measurable effect on the macroscopic properties of the electrolyte?

7.3 Investigation of the Photo-Switchability of Electrolyte Properties

In order to visualize the effect of conformational changes of azobenzene, space filling models of anion **115** were generated via force field energy minimization methods. The obtained models provide a simplified and static illustration of the impact of azobenzene conformation on anion size, shape and density (see Figure 228).

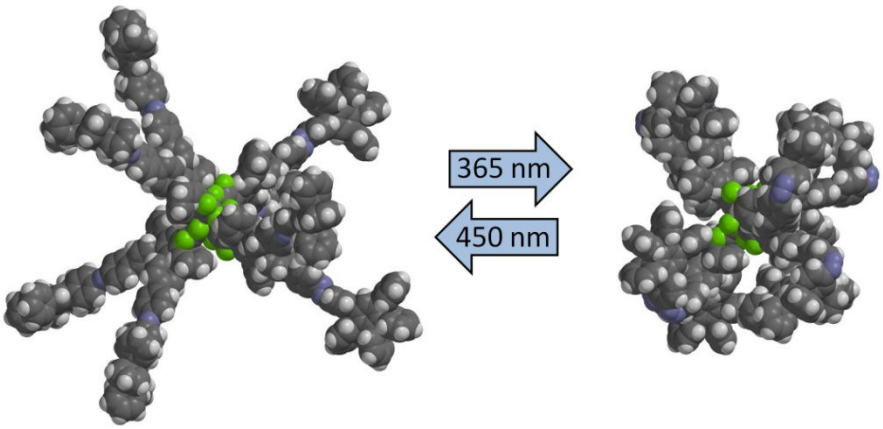

Figure 228: Comparison of space filling models of anion **115** with different azobenzene conformations; left: all azobenzene moieties in *trans*-conformation; right: all azobenzene moieties in *cis*-conformation

The above space filling models generally confirm that a switching of all azobenzene moieties from *trans* to *cis* should be possible with regard to steric interactions within single anions. The model structures also suggest a noticeable change in anion size as well as polyphenylene density upon azobenzene switching.

To convey a more realistic view, borate **115** should though be imagined as tumbling wildly due to thermal agitation, while its dendrons rotate rapidly. Moreover, even if borate **115** was irradiated continuously, a photostationary state (PSS) would be reached where the ratio of azobenzene moieties in either the *cis* or the *trans* conformation is dynamically constant within the given equilibrium conditions. Thus, only a certain fraction of borate anions will be in the desired overall conformation (all-*trans* or all-*cis*), whereas several borates will also contain one, two or more azobenzene moieties with an opposite conformation.

Experimental proof for the ability of azobenzene moieties to change their conformation within the rigid scaffold of borate **115** was provided by UV/Vis absorption (see Figure 229). Azobenzene moieties within borate **115** could be switched from *trans* to *cis* and vice

versa by irradiating its THF solution with light of either 365 nm (*trans* to *cis*) or 450 nm (*cis* to *trans*) wavelength, respectively. Due to differences in the extinction coefficients of *trans*- and *cis*-azobenzene, a change of conformation of azobenzene within borate **115** is reflected in a change of intensity of the according absorption band of the anion.

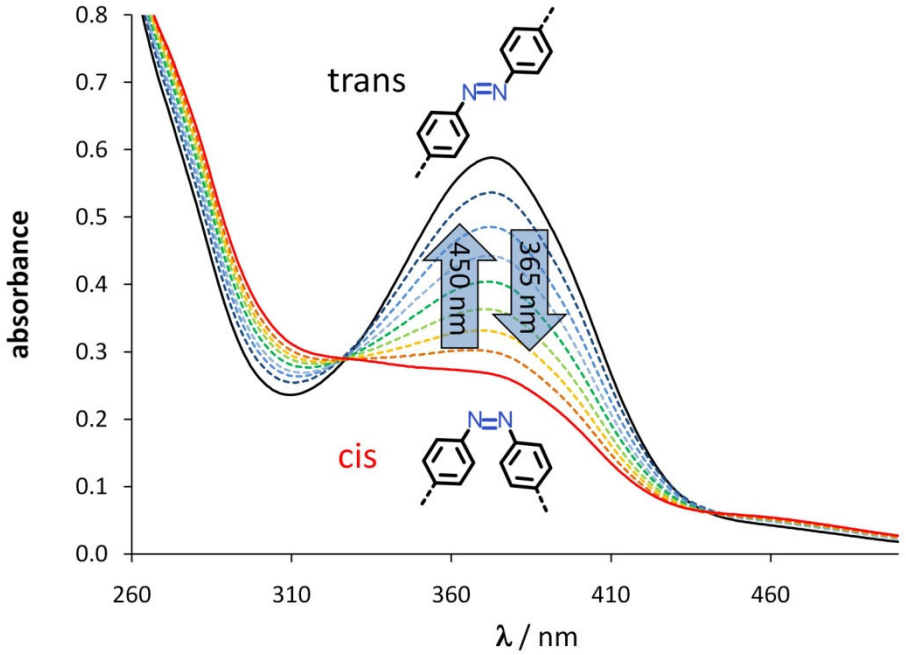

Figure 229: Change of UV/Vis absorption spectra of borate **115** (absorption band of azobenzene) in THF upon exposure to light of either 365 nm (*trans* to *cis*) or 450 nm (*cis* to *trans*) wavelength

Unfortunately, independent methods for the detection of size changes in borate **115** such as dynamic light scattering (borate at the lower size limit of detection), size exclusion chromatography (interaction of electrolyte with SEC gel) or fluorescence correlation spectroscopy (no fluorophore present) could not be performed. However, conductivity measurements could be performed in order to test whether the changes in azobenzene conformation had an impact on the macroscopic properties of the salt.

Therefore, the conductivity of borate **115** (0.5 mmol/L in dry THF) before and after UV-irradiation was measured. The non-irradiated THF solution of borate **115** had a molar conductivity Λ of 22.5 ± 0.1 S·cm^2/mol at room temperature. After irradiation of the solution at 365 nm (*trans* to *cis*), the molar conductivity Λ increased to 28.0 ± 0.1 S·cm^2/mol (+24%; see Figure 230).

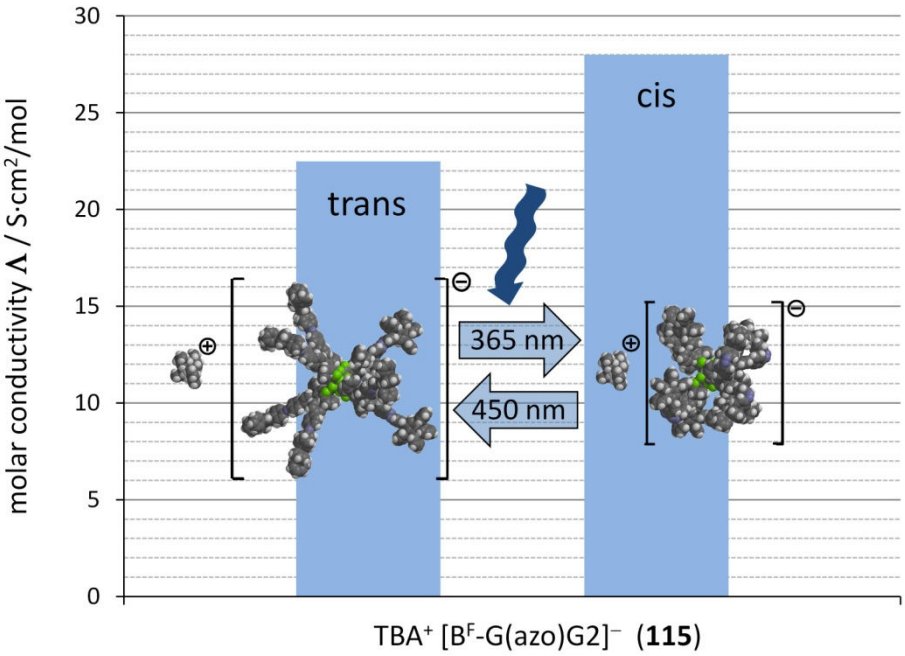

Figure 230: Effect of irradiation at different wavelengths (365 nm and 450 nm) on the molar conductivity Λ of a $5 \cdot 10^{-4}$ mol/L solution of **115** in THF

The conductivity Λ could then be reduced back to about 23 S·cm²/mol by irradiating the solution at 450 nm (*cis* to *trans*). Alternatively, the conductivity also decreased without further irradiation within several hours due to thermal equilibration of azobenzene within borate **115** towards its thermodynamically more stable *trans* conformation.

As hypothesized earlier, the observed increase in solution conductivity upon azobenzene switching from *trans* to *cis* (irradiation of the salt solution at 365 nm) may be attributed to two effects:

1) Impact of azobenzene conformation on polyphenylene density and thus on the degree of dissociation α of the electrolyte: If the azobenzene moieties in borate **115** are in *cis* conformation, the negatively charged core should be screened more efficiently due to more densely packed polyphenylenes as compared to the *trans* conformation (see the respective models in Figure 228). It is therefore reasonable to expect higher degrees of dissociation α if the azobenzene moieties within borate **115** predominantly adapt the *cis* conformation.
2) Effect of azobenzene conformation on anion size and thus on anion mobility μ^-: Along with increased density, the overall size and extension of borate anion **115** decreases if its azobenzene moieties are switched from *trans* to *cis*. This decrease in anion size should be accompanied by a general increase in overall anion mobility.

Equation (21) (see below; derivation shown in the introduction, paragraph 1.3.2.4) demonstrates that the contribution of anion mobility μ^- to molar conductivity Λ is scaled by the actual degree of dissociation α: Only at relatively high degrees of dissociation ($\alpha \to 1$) can a potential increase in anion mobility μ^- substantially contribute to overall molar conductivity Λ.

$$\Lambda = \alpha F(\nu^+ z^+ \mu^+ + \nu^- z^- \mu^-) \tag{21}$$

While both variables α and μ that govern changes in conductivity were known in principle, the extent of their individual contribution to conductivity increase/decrease was still unknown. In order to obtain information about both the degree of dissociation α and the mobility μ, concentration dependant measurements of conductivity before and after irradiation were made. In addition, DOSY-NMR was used as an independent method to determine molecular mobilities μ.

Concentration dependant conductivity measurements of salt **115** in THF before and after UV-irradiation (see Table 2; and paragraph 9.1) indicate an increase in the degree of dissociation α by about 7% at a concentration of $5 \cdot 10^{-4}$ mol/L (which was the maximum concentration measured due to the amount of borate salt **115** available). The difference in α between irradiated and non-irradiated solution decreases with decreasing concentration as α converges to 1 in both solutions, irrespective of their irradiation history.

	non-irradiated			**irradiated** at 365 nm		
c / mol/L	σ / µS/cm	Λ / S·cm^2/mol	α	σ / µS/cm	Λ / S·cm^2/mol	α
$1.56 \cdot 10^{-5}$	0.56	35.84	0.996	0.65	41.60	0.995
$3.13 \cdot 10^{-5}$	1.05	33.60	0.934	1.24	39.68	0.949
$6.25 \cdot 10^{-5}$	1.97	31.52	0.876	2.36	37.76	0.903
$1.25 \cdot 10^{-4}$	3.61	28.88	0.803	4.40	35.20	0.842
$2.50 \cdot 10^{-4}$	6.49	25.96	0.722	8.00	32.00	0.766
$5.00 \cdot 10^{-4}$	11.25	22.50	0.625	14.00	28.00	0.670

Table 2: Concentration dependant measurement of conductivities of borate salt **115** in THF before and after irradiation at 365 nm

The conductivity measurements also provide an insight into the relative change of molecular mobility μ: As mentioned earlier, a limiting molar conductivity Λ_0 at infinite dilution can be determined via linear extrapolation of the inverse molar conductivity $1/\Lambda$ to a concentration of $c = 0$ mol/L (see the rearranged *Ostwald* law of dilution in paragraph

1.3.2.4, equation (25)). Since the degree of dissociation α is 1 for every electrolyte at infinite dilution, a change in limiting molar conductivity Λ_0 due to irradiation reflects an intrinsic property change for an electrolyte. An increase in Λ_0 can solely be attributed to an increase in ion mobility μ (see equation (21)). In the case of borate **115**, the limiting molar conductivity Λ_0 (and thus in direct proportion the mobility μ of the anion) increases by about 16% (from 36.0 ± 0.7 to 41.8 ± 0.5 S·cm²/mol) as a result of azobenzene switching from *trans* to *cis*.

In order to confirm the relative increase in ion mobility by an independent method, DOSY-NMR spectra of **115** before and after UV-irradiation at 365 nm were recorded in THF-d8. However, the obtained 2D NMR signals were smeared along the $-\lg D$ dimension, which largely limited the accuracy of the estimated mobility values. Moreover, while DOSY-NMR spectroscopy enables measuring molecular mobilities directly, the method is also naturally limited to non-infinitely diluted solutions. The mobility values observed by means of DOSY-NMR are therefore averaged over associated as well as non-associated ions, while intrinsic ion mobilities "without association" cannot be obtained directly.[261] Nevertheless, a general increase in average ion mobility could be detected as a consequence of azobenzene switching from *trans* to *cis* within borate **115**. At a concentration of about $5 \cdot 10^{-4}$ mol/L, the average mobility of the anion increased by about 10% from $5.1 \cdot 10^{10}$ s/kg to $5.6 \cdot 10^{10}$ s/kg, while the average mobility of the cation also increased by 5% from $17.6 \cdot 10^{10}$ s/kg to $18.4 \cdot 10^{10}$ s/kg.

7.4 Summary and Outlook

In this chapter, the first example of a 1:1 salt (borate **115**) was presented in which intrinsic salt properties could be switched by reversibly changing the overall size and shape of one of the constituting ions. The synthesis of the according nanometer-sized and specifically functionalized borate anion has been enabled by a combination of several synthetic strategies, some of which have been developed only recently in our group.[51,260]

Investigation of the obtained macromolecular salt **115** by UV/Vis spectroscopy confirmed that the azobenzene moieties within the dendritic scaffold of the anion could be switched from *trans* to *cis* and vice versa. It was further shown that this conformational switch had a marked effect on the overall conductivity of solutions of the salt. Concentration dependent conductivity measurements allowed estimating the individual contribution of ion mobility as well as coordination strength to conductivity increase/decrease.

Overall, this chapter provides another example for the broad potential of dendrimer chemistry with regard to designing defined macromolecules with tailored and even switchable material properties. As mentioned earlier, PPDs are especially useful for highly specific designs due to their rigid scaffold, which enables a precise site definition and a translation of local to global changes in conformation.

In the future, the impact of azobenzene conformation on electrolyte properties could be further enhanced by utilizing more bulky as well as highly fluorinated building blocks such as tetracyclone **47** for end-capping (see Figure 231).

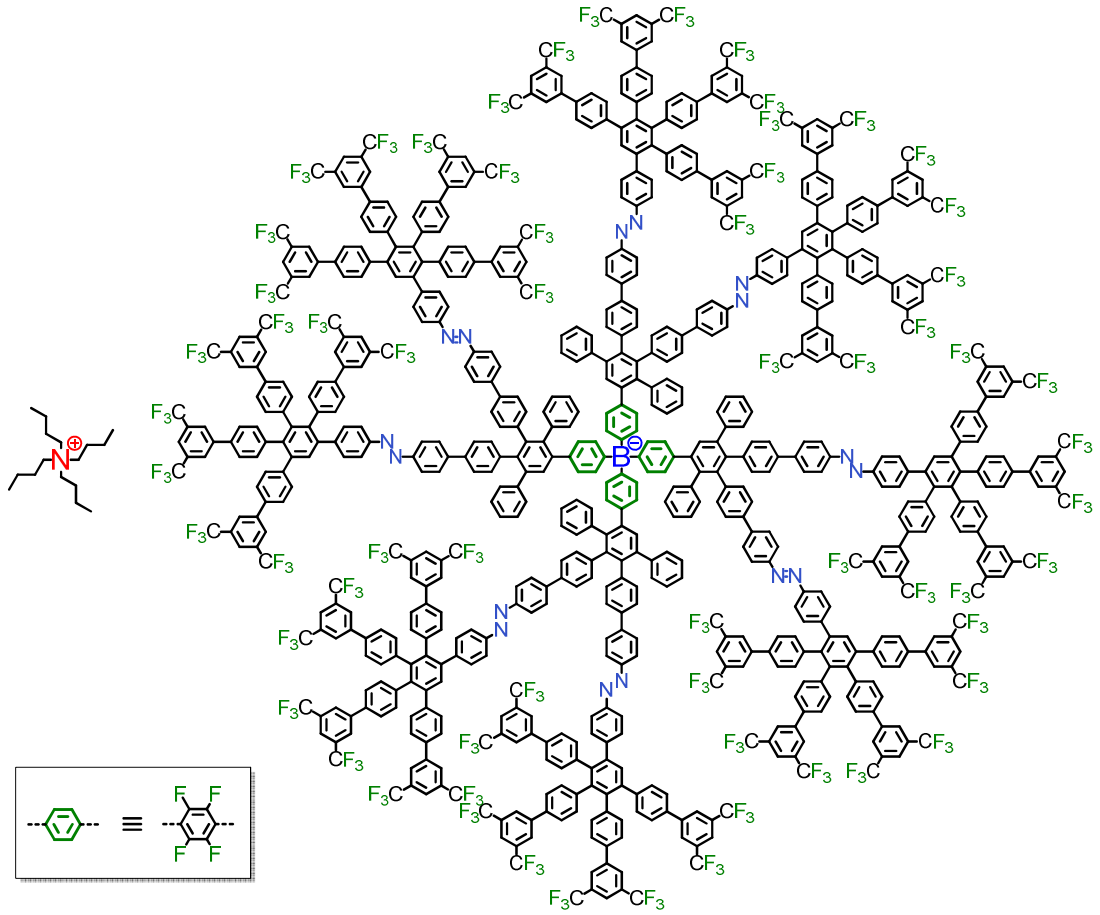

Figure 231: Potential candidate of a rigidly dendronized, azobenzene and CF_3-functionalized borate anion with a presumably strong dependence of electrolyte properties on azobenzene conformation

Moreover, macromolecular salts might be synthesized in which both the anion and the cation are rigidly dendronized and functionalized with photo-switchable moieties. Therein, conformational changes would affect the coordination strength and mobility of both anionic and cationic species. The resulting effect of azobenzene switching on electrolyte conductivity should be even more pronounced.

8 Summary and Outlook

The central objective of this work was to generate significantly larger, denser and hence presumably less coordinating anions than the weakly coordinating anions already described in literature. It was hypothesized that the divergent growth of highly branched and rigid polyphenylenes might be a feasible technique to circumvent earlier synthetic limits and enable a drastic push in anion sizes.

This initial hypothesis could clearly be verified: Divergent dendritic growth indeed enabled for the first time the synthesis of gigantic, yet atomically precise anions with truly nanoscopic dimensions (see Figure 232 and chapter 2). Moreover, many structural parameters of these nano-sized anions could be varied and tuned as desired. Due to the steric screening provided by their large, hydrophobic and non-collapsible polyphenylene shells, rigidly dendronized anions also proved very weakly coordinating (see chapter 6).

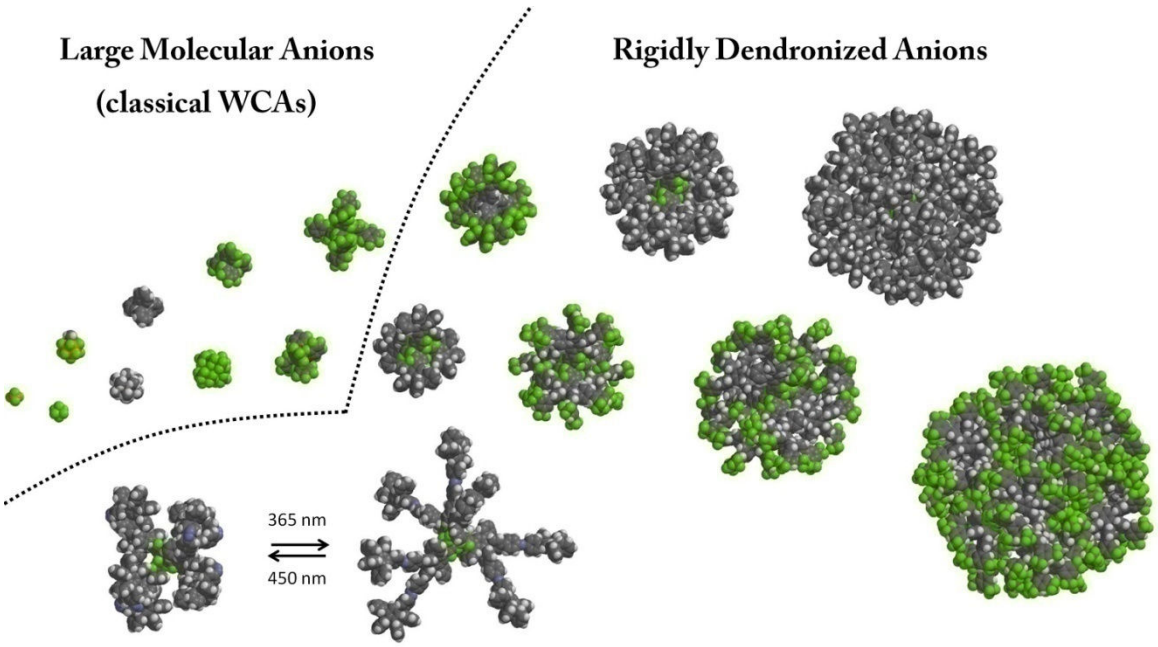

Figure 232: Comparison of the structures of some classical WCAs and some of the herein developed rigidly dendronized anions

Conductivity measurements confirmed that rigidly dendronized borates were much less coordinating than their non-dendronized analogues (see 6.5). Weak coordination was further reflected in the very low lattice enthalpies (see 6.3.3) and excellent solubilities of their salts in low polarity solvents such as THF, chloroform or even toluene (see 6.4). To

extend the scope of their potential applications, a method was developed that enabled a facile exchange of their tetrabutylammonium counterions to other cationic species (see chapter 4). Moreover, a novel phosphonium-based dication was presented.

Earlier efforts to generate comparatively stiff dendritic scaffolds at room temperature led to another side branch of this work: A novel class of dendrimers has been developed which entirely consist of interconnected aryl and triazole rings (see chapter 3). It was also demonstrated that the concepts of aryl-triazole and polyphenylene dendrimers could readily be combined with one another.

The origin and effects of atropisomerism, as observed for borates with fluorinated cores, were studied by a broad range of NMR spectroscopic techniques and analyzed in considerable detail (see chapter 5). Partially deuterated dendronized borates were synthesized which enabled detailed experiments by means of solid state NMR. Analyses of the recorded spectra are still ongoing and might allow for a comparison of the energy barriers of dendron rotation in borates with and without fluorinated cores, which could then be correlated to their efficiency in steric screening.

Many of the properties of dendronized salts (ion packing in crystals, mobility, solubility, conductivity) have been investigated and discussed (see chapter 6). Thanks to the modular and stepwise nature of dendronized anion synthesis, it was even possible to generate salts with light-switchable properties. By incorporating light-responsive building blocks into their dendritic shell, anions with light-switchable size, mobility and coordination strength could be synthesized (see chapter 7). The switchability of anion properties was evidenced by a reversible switching of the conductivity of their salt solutions.

In summary, this work demonstrates how the principles of dendrimer chemistry can be used in unprecedented ways to modify and specifically tailor the properties of salts. The many rigidly dendronized ions shown herein represent a new link between the realms of organic, macromolecular and inorganic chemistry, but also illustrate the versatility and broad applicability of polyphenylene dendrimers. The diversity of questions related to either electrolyte behavior, organic synthesis or suitable analytic methods render this work quite interdisciplinary.

Although most properties of the salts presented herein could be explained, some observations still require further investigations in the future. For example, the origin of the in-

tense orange-red fluorescence of surface fluorinated borate **41** (see paragraph 2.2.5.1) is not yet fully understood. Also, the dependence between molar conductivity of borate **53** and its salt concentration in toluene is very unusual (see paragraph 6.5.1.5). The explanations brought forward here will need to be further verified.

One of the most important tasks for the future will be a testing of here presented anions in typical WCA applications. Dimethylanilinium or trityl salts of dendronized borates should be generated and tested with regard to their performance in metallocene catalyzed polymerization reactions. Lithium salts of dendronized anions might be tested as electrolytes in lithium ion batteries that utilize very low polarity solvents.

Another interesting task for the future is the transfer of the concept of divergent dendritic growth to cationic species such as tetraphenylphosphonium cations. If applicable, salts entirely constituted of both nanometer-sized anions as well as cations could be generated. Such salts should exhibit even more unusual properties than WCA salts. Furthermore, the potential to guide supramolecular structuring by means of electrostatic, dispersive or steric interactions (see 6.3.1) could be explored and in a highly systematic manner to build up nanoscopically structured materials. In order to identify potential dangers but also recognize potential opportunities, future efforts might also aim at investigating the effects of dendronized salts on biological systems. With regard to interactions with living tissue, dendronized salts could again be suitably functionalized for various highly specific tasks.

9 Experimental Part

9.1 Materials and Methods

All starting materials were purchased from Sigma-Aldrich, Acros, ABCR, Alfa Aesar and used as received without further purification. AB_2 and AB_4 cyclopentadienone building blocks were synthesized according to literature procedures.[11,191] All syntheses were carried out under argon atmosphere using anhydrous solvents. Given reaction temperatures refer to the temperature of the oil bath used for heating. Thin layer chromatography was performed on silica coated aluminum sheets from Machery-Nagel. Column chromatography was done with silica gel (particle size 0.063-0.200 mm) from Merck.

All ^{1}H, ^{11}B, ^{13}C, ^{19}F and ^{31}P NMR spectra were recorded in different solvents like THF-d_8, $C_2D_2Cl_4$, CD_2Cl_2, $CDCl_3$, DMSO-d_6 and toluene-d_8 at different temperatures. The spectra were obtained with $\pi/2$-pulse lengths of 10 µs (^{1}H), 27 µs (^{11}B) and 11 µs (^{19}F) and a sweep width of 20 ppm for ^{1}H, 200 ppm for ^{11}B and 80 ppm for ^{19}F. Proton spectra were referenced using the remaining solvents signals as an internal standard, ^{11}B spectra with $BF_3{\cdot}OEt_2$ at 0 ppm and ^{19}F spectra with fluorobenzene at -103 ppm. Diffusion Ordered Spectroscopy (DOSY) NMR experiments were done with a 5 mm BBI ^{1}H/X z-gradient probe and a gradient strength of 5.516 [G/mm] on the 700 MHz spectrometer and with a 5 mm BBFO z-gradient probe and a gradient strength of 5.350 [G/mm] on the 500 MHz system. For the calibration of the gradient strength, a sample of $^{2}H_2O/^{1}H_2O$ was measured at a defined temperature and compared with the literature diffusion coefficient of $^{2}H_2O/^{1}H_2O$. The temperature was kept at 298.3 K and regulated by a standard ^{1}H methanol NMR sample using the topspin 2.1 software (Bruker). In this work, the gradient strength was varied in 32 steps or 64 steps from 2 % to 100 %. The diffusion time d20 was optimized between 100 ms up to 800 ms and the gradient length p30 between 0.6 ms up to 1.2 ms, depending on the investigated dendrimers. Denoted mobilities μ equal measured diffusion coefficients D divided by $k_B T$ with T = 298 K. Hydrodynamic radii r_H were calculated from measured diffusion coefficients D via the *Einstein-Stokes* relation.[262]

Conductivities of solutions of borate salts were measured at 298 K with a Mettler Toledo SevenEasy™ S30 conductivity meter using a Mettler Toledo InLab® 741 conductivity sensor with a cell constant of 0.102826 cm^{-1}. Prior to each measurement, the equipment was calibrated with a certified standard solution of a conductivity of 84 $\mu S{\cdot}cm^{-1}$ (KCl in water). Measured values have a relative accuracy of ±0.5%. For the determination of the dissociation constants K_d and the degrees of dissociation α, conductivities were measured at different salt concentrations ranging from $1{\cdot}10^{-3}$ mol/L to $1.56{\cdot}10^{-5}$ mol/L. In Figure 233, the according values for borate **41** in THF is displayed as an example.

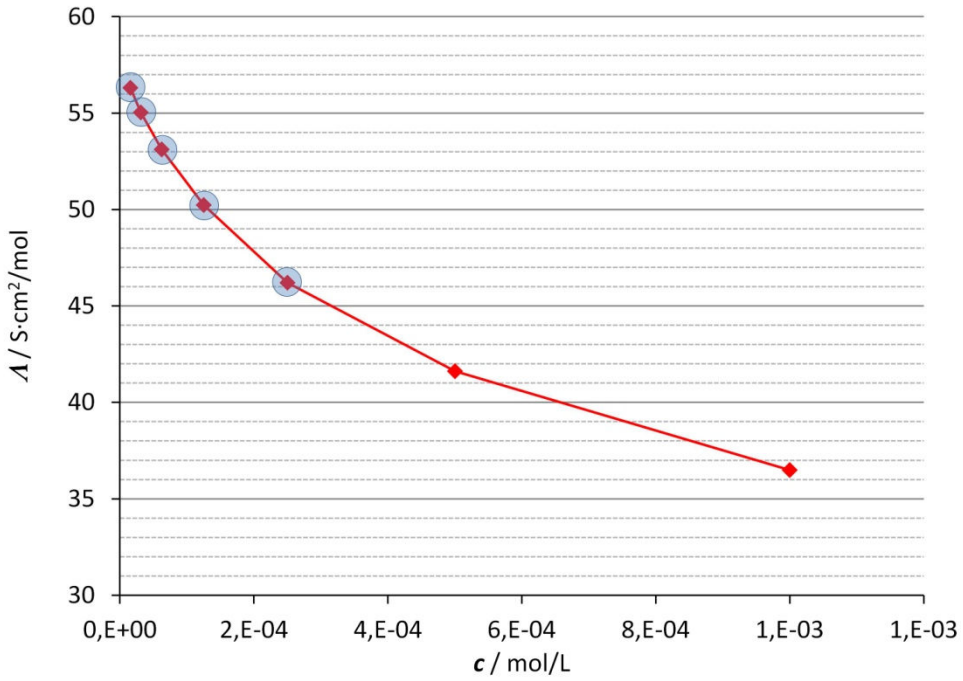

Figure 233: Molar conductivity of borate **41** in THF as a function of concentration

The inverse molar conductivities $1/\Lambda$ were then plotted as a function of conductivity σ (see Figure 234). Since the relation between $1/\Lambda$ and σ is best approaching a linear behaviour at the lowest concentrations (less interionic interactions), only those conductivity values determined at the five lowest concentrations ($c \leq 2.5 \cdot 10^{-4}$ mol/L; values marked with blue circles in Figure 233 and Figure 234) were considered in the linear regression.

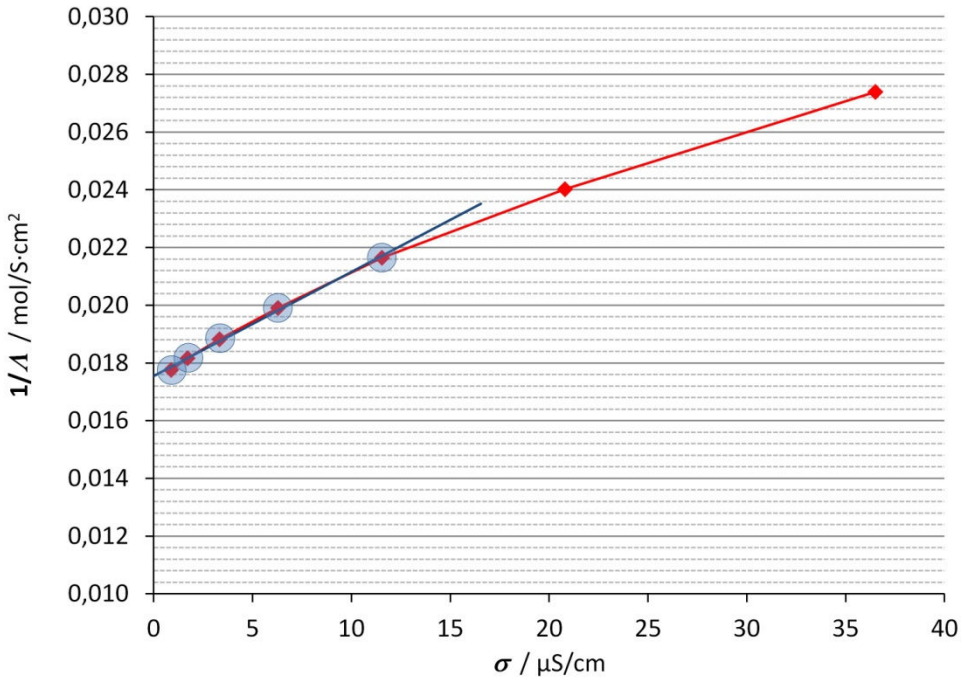

Figure 234: Estimation of the limiting molar conductivity $\boldsymbol{\Lambda_0}$ and the dissociation constant $\boldsymbol{K_d}$ of borate **41** in THF, as described in paragraph 1.3.2.4

Linear regression was performed to determine the limiting molar conductivity Λ_0 at infinite dilution from the line´s $1/\Lambda$ axis intercept, and the dissociation constant K_d from the line´s slope according to the *Ostwald* law of dilution (see equation (26), paragraph 1.3.2.4). Degrees of dissociation α were calculated as the ratio of Λ/Λ_0 (equation (24), paragraph 1.3.2.4). The results of all performed measurements, derived values and their standard errors are listed in the following Tables 3 to 10. Therein, a_0 denotes the axis intercept and a_1 the linear slope as derived by regression analysis.

THF	**93**				**94**				**14**				**41**			
	TBA^+ $[BPh_4]^-$				TBA^+ $[BPh^F_4]^-$				TBA^+ $[B\text{-}G1]^-$				TBA^+ $[\mathbf{B}\text{-}G1^F]^-$			
c	σ	Λ	$1/\Lambda$	α	σ	Λ	$1/\Lambda$	α	σ	Λ	$1/\Lambda$	α	σ	Λ	$1/\Lambda$	α
mol/L	µS/cm	S·cm²/mol	mol/ S·cm²		µS/cm	S·cm²/mol	mol/ S·cm²		µS/cm	S·cm²/mol	mol/ S·cm²		µS/cm	S·cm²/mol	mol/ S·cm²	
1.56E-05	1.09	69.76	0.0143	0.893	1.13	72.32	0.0138	0.972	0.80	51.20	0.0195	0.971	0.88	56.32	0.0178	0.988
3.13E-05	1.89	60.48	0.0165	0.774	2.13	68.16	0.0147	0.916	1.49	47.68	0.0210	0.905	1.72	55.04	0.0182	0.966
6.25E-05	3.23	51.68	0.0193	0.662	3.87	61.92	0.0161	0.832	2.75	44.00	0.0227	0.835	3.32	53.12	0.0188	0.932
1.25E-04	5.33	42.64	0.0235	0.546	6.93	55.44	0.0180	0.745	4.85	38.80	0.0258	0.736	6.28	50.24	0.0199	0.882
2.50E-04	8.63	34.52	0.0290	0.442	12.10	48.40	0.0207	0.651	8.46	33.84	0.0296	0.642	11.55	46.20	0.0216	0.811
5.00E-04	13.88	27.76	0.0360	0.355	20.70	41.40	0.0242	0.557	14.38	28.76	0.0348	0.546	20.81	41.62	0.0240	0.730
1.00E-03	21.90	21.90	0.0457	0.280	34.60	34.60	0.0289	0.465	24.40	24.40	0.0410	0.463	36.50	36.50	0.0274	0.640
			error				error				error				error	
	a_1	1.92E-03	8.40E-05		a_1	6.16E-04	3.97E-05		a_1	1.29E-03	7.71E-05		a_1	3.60E-04	1.18E-05	
	a_0	1.28E-02	4.08E-04		a_0	1.34E-02	2.60E-04		a_0	1.90E-02	3.54E-04		a_0	1.75E-02	7.26E-05	
	Λ_0	78.12	2.49	S·cm²/mol	Λ_0	74.38	1.44	S·cm²/mol	Λ_0	52.70	0.98	S·cm²/mol	Λ_0	56.99	0.24	S·cm²/mol
	K_d	8.55E-05	9.25E-06	mol/L	K_d	2.93E-04	3.04E-05	mol/L	K_d	2.79E-04	2.72E-05	mol/L	K_d	8.54E-04	3.52E-05	mol/L

Table 3: Measured conductivities and derived limiting molar conductivities $\boldsymbol{\Lambda_0}$, dissociation constants $\boldsymbol{K_d}$ and degrees of dissociation $\boldsymbol{\alpha}$ of borates in THF

THF	**53**				**56**				**62**				**59**			
	TBA^+ $[\mathbf{B}^F\text{-}G1]^-$				TBA^+ $[\mathbf{B}^F\text{-}G\mathbf{2}^2]^-$				TBA^+ $[\mathbf{B}^F\text{-}G\mathbf{2}^4]^-$				TBA^+ $[\mathbf{B}^F\text{-}G\mathbf{3}^{22}]^-$			
c	σ	Λ	$1/\Lambda$	α	σ	Λ	$1/\Lambda$	α	σ	Λ	$1/\Lambda$	α	σ	Λ	$1/\Lambda$	α
mol/L	µS/cm	S·cm²/mol	mol/ S·cm²		µS/cm	S·cm²/mol	mol/ S·cm²		µS/cm	S·cm²/mol	mol/ S·cm²		µS/cm	S·cm²/mol	mol/ S·cm²	
1.56E-05	0.79	50.56	0.0198	0.975	0.80	51.20	0.0195	0.994	0.73	46.72	0.0214	0.981	0.48	30.72	0.0326	0.975
3.13E-05	1.47	47.04	0.0213	0.907	1.48	47.36	0.0211	0.920	1.42	45.44	0.0220	0.955	0.92	29.44	0.0340	0.934
6.25E-05	2.67	42.72	0.0234	0.823	2.71	43.36	0.0231	0.842	2.72	43.52	0.0230	0.914	1.73	27.68	0.0361	0.878
1.25E-04	4.70	37.60	0.0266	0.725	4.92	39.36	0.0254	0.764	5.07	40.56	0.0247	0.852	3.15	25.20	0.0397	0.799
2.50E-04	8.25	33.00	0.0303	0.636	8.72	34.88	0.0287	0.677	9.15	36.60	0.0273	0.769	5.56	22.24	0.0450	0.705
5.00E-04	14.08	28.16	0.0355	0.543	15.08	30.16	0.0332	0.586	16.01	32.02	0.0312	0.673	9.60	19.20	0.0521	0.609
1.00E-03	23.60	23.60	0.0424	0.455	26.30	26.30	0.0380	0.511	27.60	27.60	0.0362	0.580	16.57	16.57	0.0604	0.526
			error				error				error				error	
	a_1	1.40E-03	1.11E-04		a_1	1.11E-03	1.09E-04		a_1	6.98E-04	1.58E-05		a_1	2.42E-03	7.92E-05	
	a_0	1.93E-02	4.98E-04		a_0	1.94E-02	5.14E-04		a_0	2.10E-02	7.73E-05		a_0	3.17E-02	2.37E-04	
	Λ_0	51.88	1.34	S·cm²/mol	Λ_0	51.49	1.36	S·cm²/mol	Λ_0	47.60	0.18	S·cm²/mol	Λ_0	31.52	0.24	S·cm²/mol
	K_d	2.66E-04	3.53E-05	mol/L	K_d	3.40E-04	5.20E-05	mol/L	K_d	6.32E-04	1.90E-05	mol/L	K_d	4.15E-04	1.98E-05	mol/L

Table 4: Measured conductivities and derived limiting molar conductivities $\boldsymbol{\Lambda_0}$, dissociation constants $\boldsymbol{K_d}$ and degrees of dissociation $\boldsymbol{\alpha}$ of borates in THF

THF	**65**				**68**				**69**				**70**			
	TBA^+ $[\mathbf{B}^{\mathbf{F}}\text{-}\mathbf{G3}^{24}]^-$				TBA^+ $[\mathbf{B}^{\mathbf{F}}\text{-}\mathbf{G1}(\mathbf{CF_3})_{32}]^-$				TBA^+ $[\mathbf{B}^{\mathbf{F}}\text{-}\mathbf{G2}^{2}(\mathbf{CF_3})_{64}]^-$				TBA^+ $[\mathbf{B}^{\mathbf{F}}\text{-}\mathbf{G3}^{22}(\mathbf{CF_3})_{128}]^-$			
c	σ	Λ	$1/\Lambda$	α	σ	Λ	$1/\Lambda$	α	σ	Λ	$1/\Lambda$	α	σ	Λ	$1/\Lambda$	α
mol/L	µS/cm	S·cm²/mol	mol/ S·cm²		µS/cm	S·cm²/mol	mol/ S·cm²		µS/cm	S·cm²/mol	mol/ S·cm²		µS/cm	S·cm²/mol	mol/ S·cm²	
1.56E-05	0.47	30.08	0.0332	0.994	0.68	43.52	0.0230	0.987	0.61	39.04	0.0256	0.996	0.70	44.80	0.0223	0.993
3.13E-05	0.92	29.44	0.0340	0.973	1.32	42.24	0.0237	0.958	1.19	38.08	0.0263	0.971	1.37	43.84	0.0228	0.971
6.25E-05	1.78	28.48	0.0351	0.941	2.55	40.80	0.0245	0.925	2.30	36.80	0.0272	0.939	2.61	41.76	0.0239	0.925
1.25E-04	3.39	27.12	0.0369	0.896	4.76	38.08	0.0263	0.863	4.38	35.04	0.0285	0.894	4.96	39.68	0.0252	0.879
2.50E-04	6.34	25.36	0.0394	0.838	8.70	34.80	0.0287	0.789	8.19	32.76	0.0305	0.836	9.19	36.76	0.0272	0.815
5.00E-04	11.52	23.04	0.0434	0.761	15.67	31.34	0.0319	0.711	15.32	30.64	0.0326	0.782	16.40	32.80	0.0305	0.727
1.00E-03	20.50	20.52	0.0487	0.678	27.30	27.30	0.0366	0.619	28.40	28.40	0.0352	0.725	29.00	29.00	0.0345	0.643
			error				error				error				error	
	a_1	1.04E-03	6.25E-05		a_1	7.10E-04	2.71E-05		a_1	6.33E-04	4.37E-05		a_1	5.68E-04	4.16E-05	
	a_0	3.30E-02	2.09E-04		a_0	2.27E-02	1.25E-04		a_0	2.55E-02	1.89E-04		a_0	2.22E-02	2.02E-04	
	Λ_0	30.26	0.19	S·cm²/mol	Λ_0	44.10	0.24	S·cm²/mol	Λ_0	39.20	0.29	S·cm²/mol	Λ_0	45.13	0.41	S·cm²/mol
	K_d	1.05E-03	7.69E-05	mol/L	K_d	7.24E-04	3.57E-05	mol/L	K_d	1.03E-03	8.67E-05	mol/L	K_d	8.65E-04	7.96E-05	mol/L

Table 5: Measured conductivities and derived limiting molar conductivities $\boldsymbol{\Lambda_0}$, dissociation constants $\boldsymbol{K_d}$ and degrees of dissociation $\boldsymbol{\alpha}$ of borates in THF

THF	**71**				**commercial**				**95**				**97**			
	TBA^+ $[\mathbf{B}^{\mathbf{F}}\text{-}\mathbf{G3}^{24}(\mathbf{CF_3})_{256}]^-$				$\mathbf{P}Ph_4^+$ $[\mathbf{B}Ph_4]^-$				$\mathbf{P}Ph_4^+$ $[\mathbf{B}Ph^{\mathbf{F}}{}_4]^-$				$\mathbf{P}Ph_4^+$ $[\mathbf{B}\text{-}\mathbf{G1}]^-$			
c	σ	Λ	$1/\Lambda$	α	σ	Λ	$1/\Lambda$	α	σ	Λ	$1/\Lambda$	α	σ	Λ	$1/\Lambda$	α
mol/L	µS/cm	S·cm²/mol	mol/ S·cm²		µS/cm	S·cm²/mol	mol/ S·cm²		µS/cm	S·cm²/mol	mol/ S·cm²		µS/cm	S·cm²/mol	mol/ S·cm²	
1.56E-05	0.32	20.48	0.0488	0.9942					1.15	73.60	0.0136	0.985	0.39	24.96	0.0401	0.965
3.13E-05	0.63	20.16	0.0496	0.9787	**Solubility too low in THF!**				2.13	68.16	0.0147	0.912	0.71	22.72	0.0440	0.878
6.25E-05	1.23	19.68	0.0508	0.9554					3.92	62.72	0.0159	0.839	1.27	20.32	0.0492	0.785
1.25E-04	2.37	18.96	0.0527	0.9204					7.10	56.80	0.0176	0.760	2.21	17.68	0.0566	0.683
2.50E-04	4.47	17.88	0.0559	0.8680					12.39	49.56	0.0202	0.663	3.79	15.16	0.0660	0.586
5.00E-04	8.40	16.80	0.0595	0.8156					21.60	43.20	0.0231	0.578	6.33	12.66	0.0790	0.489
1.00E-03	16.00	16.00	0.0625	0.7767					36.70	36.70	0.0272	0.491	10.31	10.31	0.0970	0.398
			error								error				error	
	a_1	1.68E-03	7.02E-05						a_1	5.65E-04	4.08E-05		a_1	7.48E-03	5.32E-04	
	a_0	4.85E-02	1.65E-04						a_0	1.34E-02	2.74E-04		a_0	3.86E-02	1.10E-03	
	Λ_0	20.60	0.07	S·cm²/mol					Λ_0	74.74	1.53	S·cm²/mol	Λ_0	25.88	0.74	S·cm²/mol
	K_d	1.40E-03	6.79E-05	mol/L					K_d	3.17E-04	3.60E-05	mol/L	K_d	2.00E-04	2.58E-05	mol/L

Table 6: Measured conductivities and derived limiting molar conductivities $\boldsymbol{\Lambda_0}$, dissociation constants $\boldsymbol{K_d}$ and degrees of dissociation $\boldsymbol{\alpha}$ of borates in THF

THF	**98**				**commercial**				**105** (trans)				**105** (cis)			
	PPh$_4^+$ [**B**$^{\mathbf{F}}$-G1]$^-$				TBA$^+$ **Br**$^-$				TBA$^+$ [**B**$^{\mathbf{F}}$-G(**azo**)G**2**]$^-$				TBA$^+$ [**B**$^{\mathbf{F}}$-G(**azo**)G**2**]$^-$			
c	σ	Λ	$1/\Lambda$	α	σ	Λ	$1/\Lambda$	α	σ	Λ	$1/\Lambda$	α	σ	Λ	$1/\Lambda$	α
mol/L	µS/cm	S·cm^2/mol	mol/ S·cm^2		µS/cm	S·cm^2/mol	mol/ S·cm^2		µS/cm	S·cm^2/mol	mol/ S·cm^2		µS/cm	S·cm^2/mol	mol/ S·cm^2	
1.56E-05	0.60	38.40	0.0260	0.977	0.12	7.68	0.1302	0.224	0.56	35.84	0.0279	0.996	0.65	41.60	0.0240	0.995
3.13E-05	1.13	36.16	0.0277	0.920	0.17	5.44	0.1838	0.159	1.05	33.60	0.0298	0.934	1.24	39.68	0.0252	0.949
6.25E-05	2.09	33.44	0.0299	0.851	0.24	3.84	0.2604	0.112	1.97	31.52	0.0317	0.876	2.36	37.76	0.0265	0.903
1.25E-04	3.77	30.16	0.0332	0.768	0.35	2.80	0.3571	0.082	3.61	28.88	0.0346	0.803	4.40	35.20	0.0284	0.842
2.50E-04	6.61	26.44	0.0378	0.673	0.51	2.04	0.4902	0.059	6.49	25.96	0.0385	0.721	8.00	32.00	0.0313	0.766
5.00E-04	11.27	22.54	0.0444	0.574	0.75	1.50	0.6667	0.044	11.25	22.50	0.0444	0.625	14.00	28.00	0.0357	0.670
1.00E-03	18.98	18.98	0.0527	0.483	1.14	1.14	0.8772	0.033	0.56	35.84	0.0279	0.996	0.65	41.60	0.0240	0.995
			error				error				error				error	
	a_1	1.92E-03	1.08E-04		a_1	9.18E-01	3.21E-02		a_1	1.72E-03	1.54E-04		a_1	9.47E-04	7.06E-05	
	a_0	2.55E-02	3.87E-04		a_0	2.92E-02	9.99E-03		a_0	2.78E-02	5.34E-04		a_0	2.39E-02	3.01E-04	
	Λ_0	39.29	0.60	S·cm^2/mol	Λ_0	34.30	11.75	S·cm^2/mol	Λ_0	35.98	0.69	S·cm^2/mol	Λ_0	41.80	0.53	S·cm^2/mol
	K_d	3.37E-04	2.93E-05	mol/L	K_d	9.26E-07	8.62E-07	mol/L	K_d	4.48E-04	5.77E-05	mol/L	K_d	6.05E-04	6.07E-05	mol/L

Table 7: Measured conductivities and derived limiting molar conductivities $\boldsymbol{\Lambda_0}$, dissociation constants $\boldsymbol{K_d}$ and degrees of dissociation $\boldsymbol{\alpha}$ of borates in THF

DCM	**53**				**commercial**				**95**				**97**			
	TBA$^+$ [**B**$^{\mathbf{F}}$-G1]$^-$				**P**Ph$_4^+$ [**B**Ph$_4$]$^-$				**P**Ph$_4^+$ [**B**Ph$^{\mathbf{F}}_4$]$^-$				**P**Ph$_4^+$ [**B**-G1]$^-$			
c	σ	Λ	$1/\Lambda$	α	σ	Λ	$1/\Lambda$	α	σ	Λ	$1/\Lambda$	α	σ	Λ	$1/\Lambda$	α
mol/L	µS/cm	S·cm^2/mol	mol/ S·cm^2		µS/cm	S·cm^2/mol	mol/ S·cm^2		µS/cm	S·cm^2/mol	mol/ S·cm^2		µS/cm	S·cm^2/mol	mol/ S·cm^2	
1.56E-05	1,23	78,72	0,0127	0,986	1,92	122,88	0,0081	1,000	1,47	94,08	0,0106	0,991	0,49	31,36	0,0319	0,986
3.13E-05	2,14	68,48	0,0146	0,858	3,30	105,60	0,0095	0,860	2,70	86,40	0,0116	0,910	0,95	30,4	0,0329	0,956
6.25E-05	3,79	60,64	0,0165	0,760	5,93	94,88	0,0105	0,772	4,87	77,92	0,0128	0,820	1,77	28,32	0,0353	0,890
1.25E-04	6,58	52,64	0,0190	0,659	10,41	83,28	0,0120	0,678	8,72	69,76	0,0143	0,734	3,3	26,4	0,0379	0,830
2.50E-04	11,33	45,32	0,0221	0,568	17,96	71,84	0,0139	0,585	15,38	61,52	0,0163	0,648	5,96	23,84	0,0419	0,750
5.00E-04	19,54	39,08	0,0256	0,490	30,70	61,40	0,0163	0,500	27,10	54,20	0,0185	0,571	10,59	21,18	0,0472	0,666
1.00E-03	33,6	33,60	0,0298	0,421	52,10	52,10	0,0192	0,424	45,80	45,80	0,0218	0,482	18,43	18,43	0,0543	0,579
			error				error				error				error	
	a_1	8,87E-04	9,75E-05		a_1	3,38E-04	4,06E-05		a_1	3,92E-04	4,07E-05		a_1	1,82E-03	1,30E-04	
	a_0	1,25E-02	6,04E-04		a_0	8,14E-03	3,98E-04		a_0	1,05E-02	3,38E-04		a_0	3,14E-02	4,15E-04	
	Λ_0	79,83	3,85	S·cm^2/mol	Λ_0	122,86	6,01	S·cm^2/mol	Λ_0	94,98	3,05	S·cm^2/mol	Λ_0	31,80	0,42	S·cm^2/mol
	K_d	1,77E-04	3,72E-05	mol/L	K_d	1,96E-04	4,35E-05	mol/L	K_d	2,83E-04	4,82E-05	mol/L	K_d	5,43E-04	5,35E-05	mol/L

Table 8: Measured conductivities and derived limiting molar conductivities $\boldsymbol{\Lambda_0}$, dissociation constants $\boldsymbol{K_d}$ and degrees of dissociation $\boldsymbol{\alpha}$ of borates in methylene chloride

DCM	98			
	PPh$_4^+$ [**B**$^{\mathbf{F}}$-G1]$^-$			
c	σ	Λ	$1/\Lambda$	α
mol/L	µS/cm	S·cm^2/mol	mol/ S·cm^2	
1.56E-05	0,79	50,56	0,0198	0,988
3.13E-05	1,49	47,68	0,0210	0,932
6.25E-05	2,78	44,48	0,0225	0,869
1.25E-04	5,07	40,56	0,0247	0,793
2.50E-04	9,04	36,16	0,0277	0,707
5.00E-04	15,8	31,6	0,0316	0,618
1.00E-03	27,6	27,6	0,0362	0,539
			error	
	a_1	9,30E-04	6,82E-05	
	a_0	1,95E-02	3,31E-04	
	Λ_0	51,17	0,87	S·cm^2/mol
	K_d	4,11E-04	4,43E-05	mol/L

Table 9: Measured conductivities and derived limiting molar conductivities $\boldsymbol{\Lambda_0}$, dissociation constants $\boldsymbol{K_\mathrm{d}}$ and degrees of dissociation $\boldsymbol{\alpha}$ of borate **98** in methylene chloride

$CHCl_3$	94				53				62				65			
	TBA$^+$ [**B**Ph$^{\mathbf{F}}_4$]$^-$				TBA$^+$ [**B**$^{\mathbf{F}}$-G1]$^-$				TBA$^+$ [**B**$^{\mathbf{F}}$-G**2**^{4}]$^-$				TBA$^+$ [**B**$^{\mathbf{F}}$-G**3**^{24}]$^-$			
c	σ	Λ	$1/\Lambda$	α	σ	Λ	$1/\Lambda$	α	σ	Λ	$1/\Lambda$	α	σ	Λ	$1/\Lambda$	α
mol/L	µS/cm	S·cm^2/mol	mol/ S·cm^2		µS/cm	S·cm^2/mol	mol/ S·cm^2		µS/cm	S·cm^2/mol	mol/ S·cm^2		µS/cm	S·cm^2/mol	mol/ S·cm^2	
1.56E-05	0,19	12,16	0,0822	0,358	0,08	5,12	0,1953	0,710	0,10	6,40	0,1563	0,791	0,03	1,92	0,5208	0,861
3.13E-05	0,25	8,00	0,1250	0,236	0,13	4,16	0,2404	0,577	0,16	5,12	0,1953	0,633	0,05	1,60	0,6250	0,717
6.25E-05	0,35	5,60	0,1786	0,165	0,20	3,20	0,3125	0,444	0,26	4,16	0,2404	0,514	0,08	1,28	0,7813	0,574
1.25E-04	0,52	4,16	0,2404	0,123	0,31	2,48	0,4032	0,344	0,41	3,28	0,3049	0,405	0,13	1,04	0,9615	0,466
2.50E-04	0,79	3,16	0,3165	0,093	0,48	1,92	0,5208	0,266	0,64	2,56	0,3906	0,316	0,21	0,84	1,1905	0,376
5.00E-04	1,20	2,40	0,4167	0,071	0,74	1,48	0,6757	0,205	0,98	1,96	0,5102	0,242	0,34	0,68	1,4706	0,305
1.00E-03	1,88	1,88	0,5319	0,055	1,16	1,16	0,8621	0,161	1,49	1,49	0,6711	0,184	0,56	0,56	1,7857	0,251
			error				error				error				error	
	a_1	3,79E-01	3,75E-02		a_1	8,16E-01	3,76E-02		a_1	4,26E-01	1,99E-02		a_1	3,68E+00	2,87E-01	
	a_0	2,95E-02	1,77E-02		a_0	1,39E-01	1,05E-02		a_0	1,24E-01	7,34E-03		a_0	4,48E-01	3,41E-02	
	Λ_0	33,92	20,40	S·cm^2/mol	Λ_0	7,21	0,55	S·cm^2/mol	Λ_0	8,09	0,48	S·cm^2/mol	Λ_0	2,23	0,17	S·cm^2/mol
	K_d	2,29E-06	7,61E-06	mol/L	K_d	2,36E-05	4,73E-06	mol/L	K_d	3,58E-05	5,99E-06	mol/L	K_d	5,46E-05	1,28E-05	mol/L

Table 10: Measured conductivities and derived limiting molar conductivities $\boldsymbol{\Lambda_0}$, dissociation constants $\boldsymbol{K_\mathrm{d}}$ and degrees of dissociation $\boldsymbol{\alpha}$ of borates in chloroform

$CHCl_3$	68				69				71			
	TBA^+ [B^F-G1(CF_3)$_{32}$]$^-$				TBA^+ [B^F-G**2**^{2}(CF_3)$_{64}$]$^-$				TBA^+ [B^F-G**3**^{24}(CF_3)$_{256}$]$^-$			
c	σ	Λ	$1/\Lambda$	α	σ	Λ	$1/\Lambda$	α	σ	Λ	$1/\Lambda$	α
mol/L	µS/cm	S·cm^2/mol	mol/ S·cm^2		µS/cm	S·cm^2/mol	mol/ S·cm^2		µS/cm	S·cm^2/mol	mol/ S·cm^2	
1.56E-05	0,34	21,76	0,0460	0,977	0,25	16,00	0,0625	0,654	0,29	18,56	0,0539	0,984
3.13E-05	0,61	19,52	0,0512	0,876	0,39	12,48	0,0801	0,511	0,57	18,24	0,0548	0,967
6.25E-05	1,09	17,44	0,0573	0,783	0,61	9,76	0,1025	0,399	1,10	17,60	0,0568	0,933
1.25E-04	1,92	15,36	0,0651	0,689	0,93	7,44	0,1344	0,304	2,06	16,48	0,0607	0,874
2.50E-04	3,29	13,16	0,0760	0,591	1,41	5,64	0,1773	0,231	3,80	15,20	0,0658	0,806
5.00E-04	5,80	11,60	0,0862	0,521	2,16	4,32	0,2315	0,177	6,94	13,88	0,0720	0,736
1.00E-03	10,1	10,10	0,0990	0,453	3,26	3,26	0,3067	0,133	12,50	12,5	0,0800	0,663
			error				error				error	
	a_1	9,82E-03	8,27E-04		a_1	9,81E-02	2,87E-03		a_1	3,43E-03	1,38E-04	
	a_0	4,49E-02	1,49E-03		a_0	4,09E-02	2,38E-03		a_0	5,30E-02	2,79E-04	
	Λ_0	22,28	0,74	S·cm^2/mol	Λ_0	24,45	1,42	S·cm^2/mol	Λ_0	18,86	0,10	S·cm^2/mol
	K_d	2,05E-04	3,12E-05	mol/L	K_d	1,71E-05	2,50E-06	mol/L	K_d	8,20E-04	4,17E-05	mol/L

Table 11: Measured conductivities and derived limiting molar conductivities $\boldsymbol{\Lambda_0}$, dissociation constants $\boldsymbol{K_d}$ and degrees of dissociation $\boldsymbol{\alpha}$ of borates in chloroform

Toluene	TBA^+ [B^F-G1]$^-$ (**53**)	
c	σ	Λ
mol/L	µS/cm	S·cm^2/mol
2,40E-03	0,02	0,008
3,20E-03	0,03	0,009
4,30E-03	0,06	0,014
5,70E-03	0,14	0,025
7,60E-03	0,27	0,036
1,01E-02	0,51	0,050
1,34E-02	0,98	0,073
1,79E-02	1,71	0,096
2,39E-02	2,79	0,117
3,19E-02	4,28	0,134
4,25E-02	6,15	0,145
5,67E-02	8,34	0,147
7,55E-02	10,55	0,140
1,01E-01	12,23	0,121
1,34E-01	12,27	0,091

Table 12: Measured conductivities of borate **53** in toluene

UV/Vis absorption spectra were recorded with a Varian Cary 4000 UV/Vis spectrometer (Varian Inc. Palo Alto, USA) using quartz cells with a path length of 0.2 cm. Fluorescence spectra were measured on a SPEX Fluorolog 2 spectrometer.

Field desorption (FD) mass spectrometry was performed on a VG Instruments ZAB 2-SE-FPD using 8 kV accelerating voltage. MALDI-TOF mass spectrometry was performed on a Bruker Reflex spectrometer. Samples for MALDI-TOF MS were prepared by mixing the analyte with dithranol as matrix in THF in a ratio of 1/250. Negatively charged ions were detected using the appropriate polarity of the field.

Crystals of compounds **12**, **52**, **93, 14**, **41, 101, 100, 99, 37, 102, 95** and **79** were grown by slow interdiffusion of a concentrated solution in methylene chloride into hexane. Crystals of **40** were grown by slow evaporation from a THF solution.

Crystal diffraction data were recorded using a Bruker AXS KCCD diffractometer with Mo Kα radiation at 120 K. Crystals of **41** and in particular of **14** turned out to be unstable under ambient conditions due to the loss of solvate molecules. Therefore crystals were isolated from the mother liquor in cooled Silicon oil (Riedel-de-Haën Perfluoroether 216) and mounted in sealed glass capillaries. Owing to the large amount of solvent molecules present in the structures of **14** and **41** the diffraction was limited to a θ_{max} of 27.5°. The crystal structures were solved by direct methods (Shelxs). Refinement was done by least-squares calculations on F with anisotropic temperature factors for all non-hydrogen atoms. The H atoms were included in the refinement with isotropic temperature factors in the riding mode. In the course of the structure solution of **41** large voids obviously containing disordered solvate molecules were detected in which no meaningful atomic parameters could be found. Their contributions (three hexane and four CH_2Cl_2 molecules, estimated by volume and electron count) were taken into account using the PLATON/SQUEEZE program.[263] The remaining solvate molecules could be resolved but show rather high adp's. In an attempt to crystallize compound **52**, crystals of the composition $(TBA^+)_2Cl^-B(C_8F_4H)_4^-$ were obtained and the structure of this crystal was determined. One of the tetrabutylammonium groups exhibited a disorder in one of ten butyl groups with occupancies of 0.65 and 0.35. These atoms were included in the refinement with distance, angle and adp constraints. The crystal structure of compound **94** is already known in literature.[264] However, X-ray structure determination was performed in order to confirm the purity and 1:1 composition of compound **94**. Projections of the structures and crystal data are shown in Figures 235 to 247.

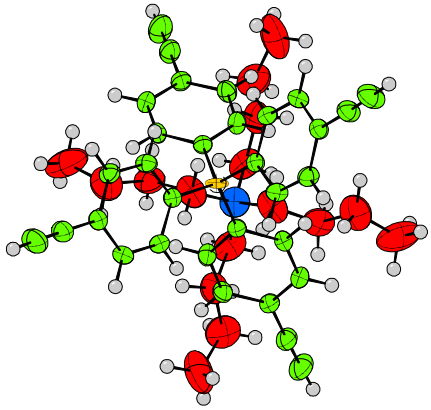

Figure 235: ORTEP view of crystal structure of compound **12**

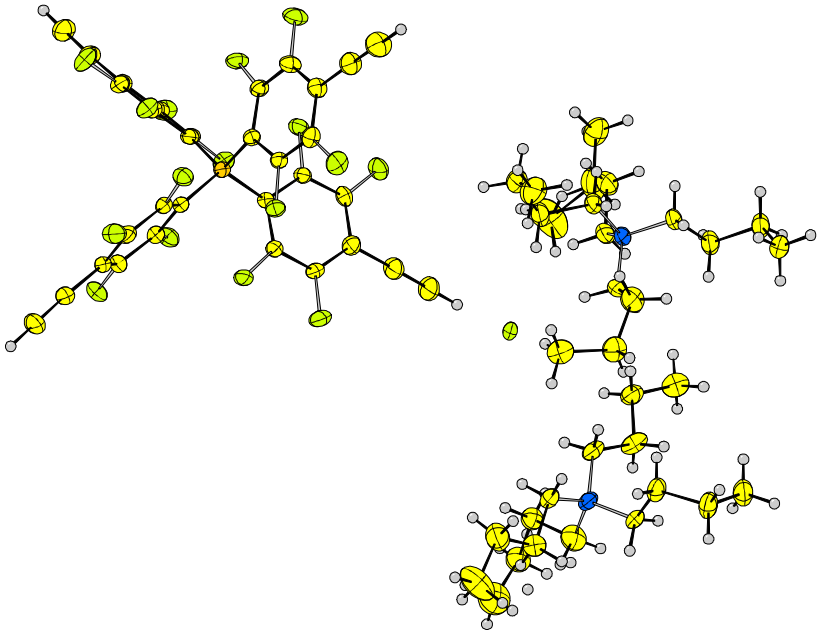

Figure 236: ORTEP view of crystal structure of mixed salt of compound **52** and $TBA^{+}Cl^{-}$

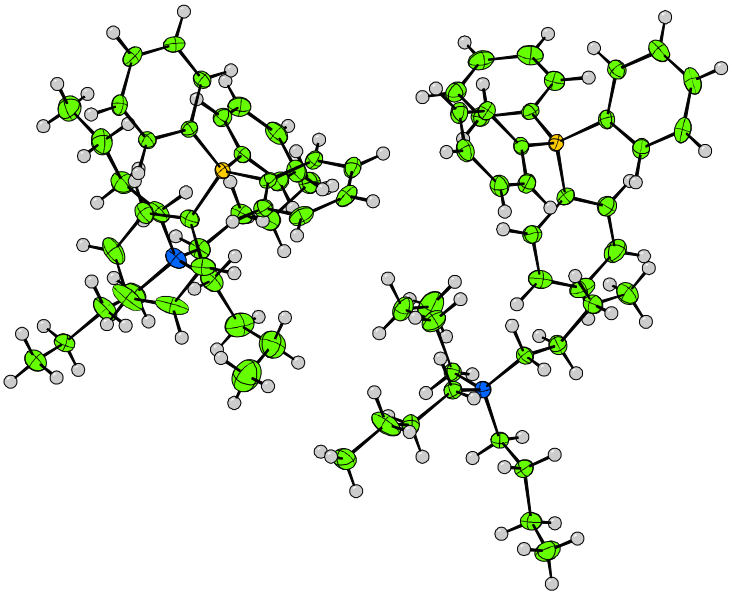

Figure 237: ORTEP view of crystal structure of compound **93**

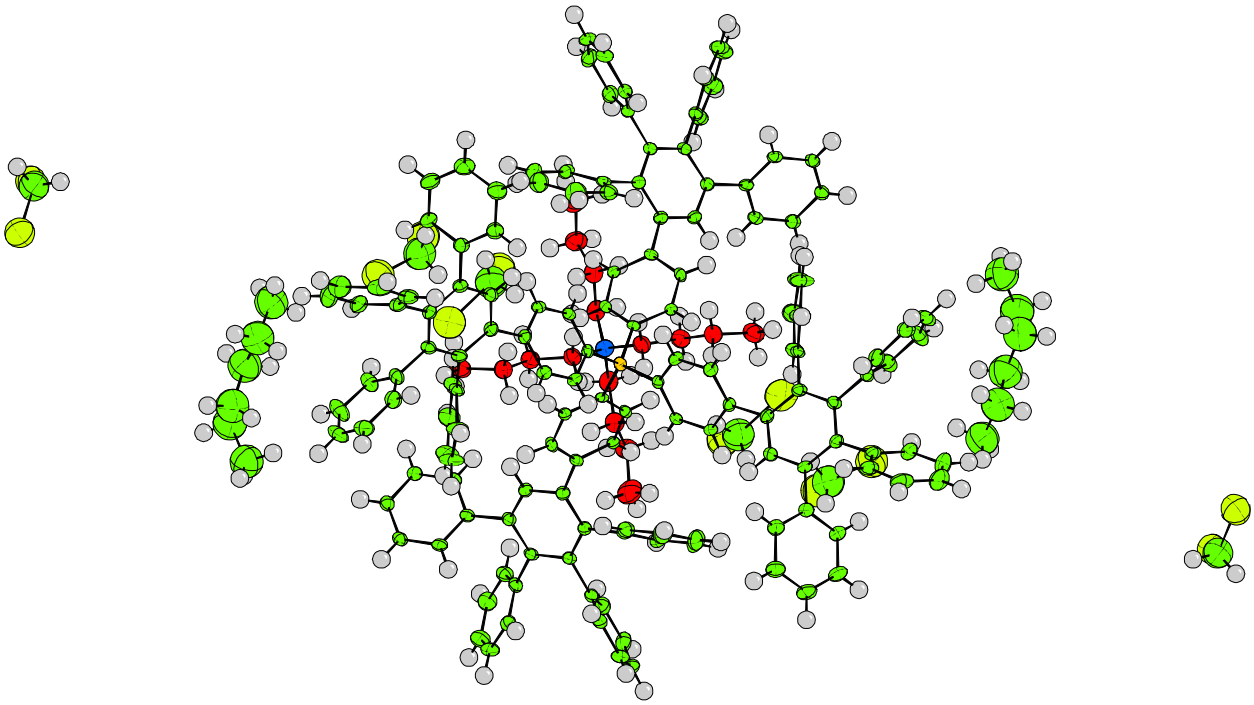

Figure 238: ORTEP view of crystal structure of compound **14**

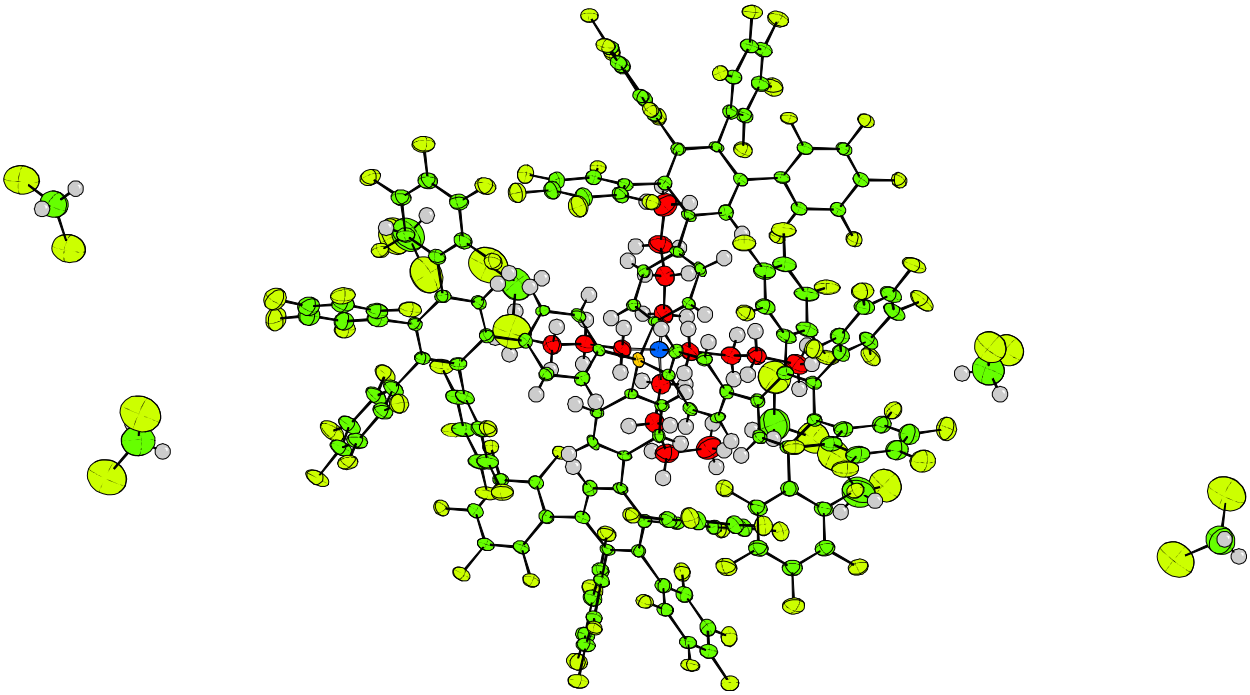

Figure 239: ORTEP view of crystal structure of compound **41**

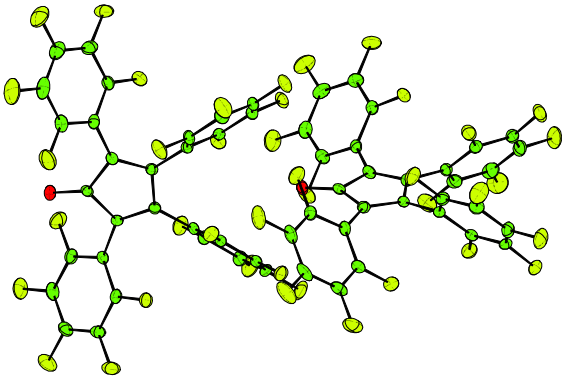

Figure 240: ORTEP view of crystal structure of compound **40**

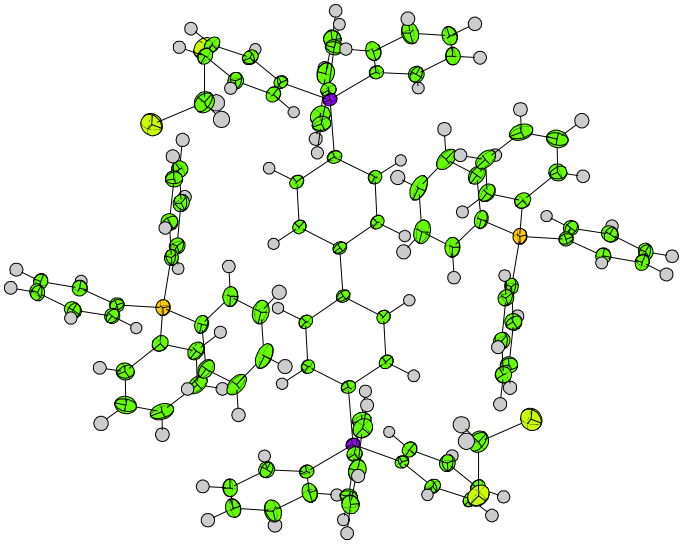

Figure 241: ORTEP view of crystal structure of compound **101**

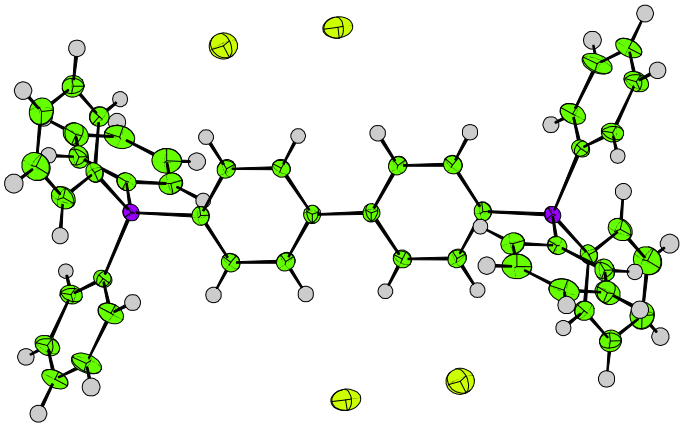

Figure 242: ORTEP view of crystal structure of compound **100**

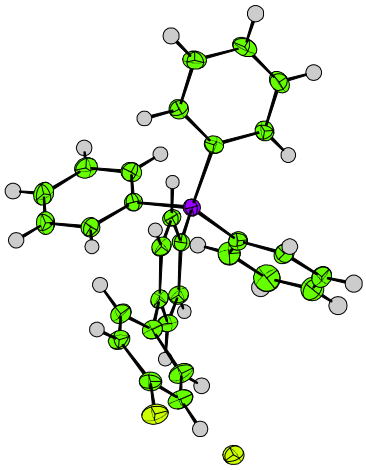

Figure 243: ORTEP view of crystal structure of compound **99**

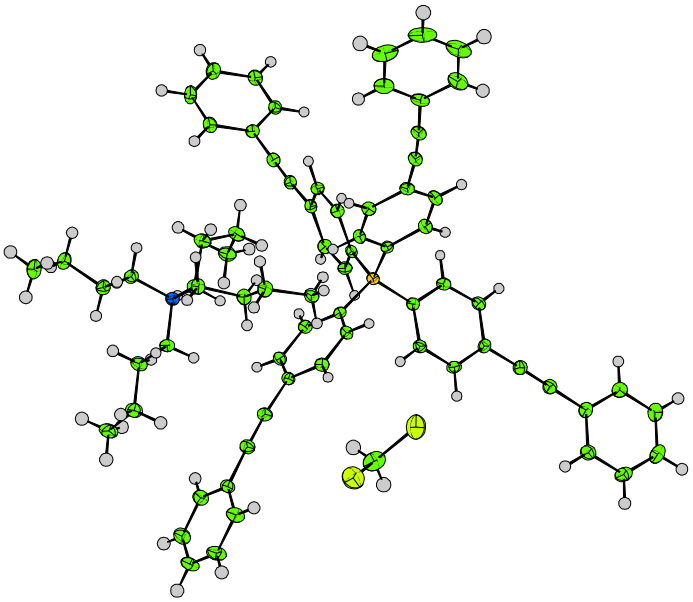

Figure 244: ORTEP view of crystal structure of compound **37**

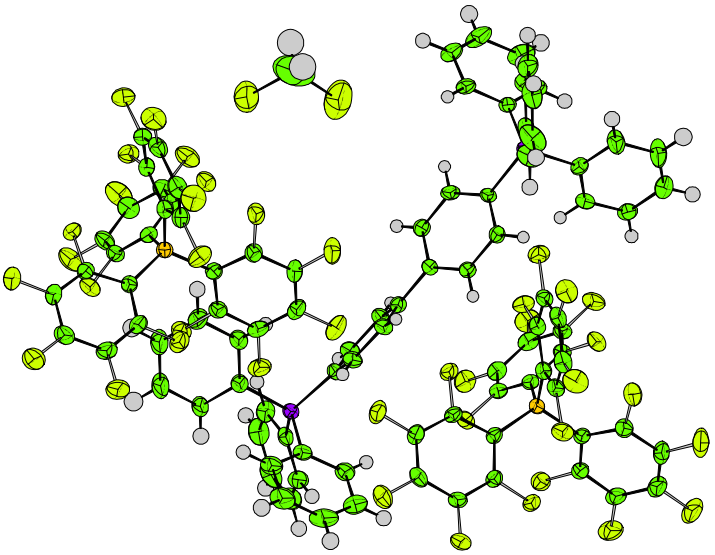

Figure 245: ORTEP view of crystal structure of compound **102**

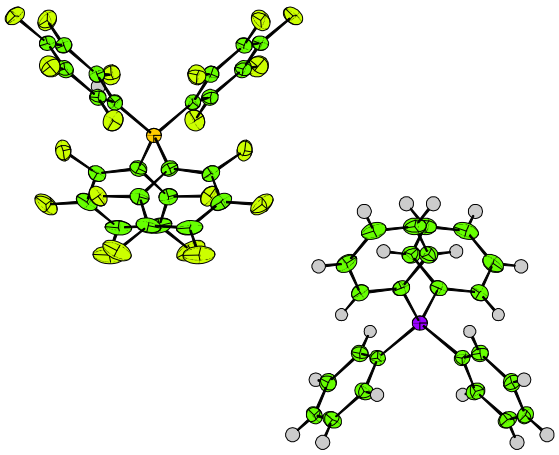

Figure 246: ORTEP view of crystal structure of compound **95**

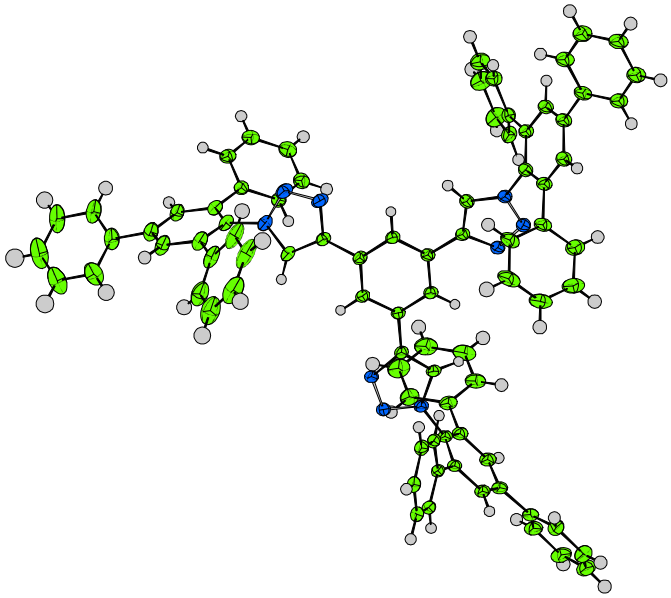

Figure 247: ORTEP view of crystal structure of compound **79**

Tables of crystallographic data:

compound	**12**	**52**	**93**	**94**
CCDC number	799999	800003	800002	MEBBAX
formula	$C_{48}H_{56}BN$	$C_{64}H_{76}BClF_{16}N_2$	$C_{40}H_{56}BN$	$C_{40}H_{36}BF_{20}N$
formula weight	657.78	1223.54	561.69	921.50
crystal system	tetragonal	monoclinic	triclinic	monoclinic
space group	P-42,c	Pc	P-1	Cc
color	colorless	colorless	colorless	colorless
shape	needles	prisms	needles	prisms
a (Å)	12.8820(5)	11.5818(2)	10.1603(2)	23.9489(8)
b (Å)	12.8820(5)	14.0456(3)	18.4262(4)	12.8161(5)
c (Å)	12.1790(2)	19.9942(4)	20.4923(4)	17.3557(5)
α (°)	90	90	69.9941(11)	90
β (°)	90	93.7836(12)	86.6684(12)	130.5617(13)
γ (°)	90	90	75.7475(9)	90
V (Å^3)	2021.1(1)	3245.4(2)	3492.6(2)	4046.9(5)
Z	8	2	4	4
ρ (g·cm^{-3})	1.081	1.251	1.07	1.512
R	0.0591	0.0452	0.0617	0.0364
R_W	0.0725	0.0555	0.0710	0.0383
T (K)	120	120	120	120

Table 13: Crystallographic data of compounds **12**, **52**, **93** and **94**

compound	**14**	**41**	**40**	**101**
CCDC number	800000	800001	800004	890830
formula	$C_{178}H_{176}Cl_{12}BN$	$C_{168}H_{72}F_{80}Cl_{16}BN$	$C_{58}F_{40}O$	$C_{49}H_{41}Cl_2BP$
formula weight	2765.56	4202.31	744.28	742.55
crystal system	monoclinic	triclinic	triclinic	triclinic
space group	P2/n	P-1	P-1	P-1
color	colorless	yellow	orange-red	colorless

shape	needles	needles	plates	prisms
a (Å)	20.6612(6)	21.3889(8)	11.3353(6)	9.9237(2)
b (Å)	12.3816(3)	14.8083(7)	15.1429(9)	12.6195(3)
c (Å)	30.6700(9)	33.5428(10)	15.3297(7)	15.7996(3)
α (°)	90	89.752(3)	80.574(5)	84.4236(10)
β (°)	103.0393(9)	107.915(4)	77.953(4)	88.7947(12)
γ (°)	90	89.972(4)	77.925(4)	85.7301(12)
V (Å^3)	7643.7(4)	10108.9(10)	2500.9(2)	1963.60(7)
Z	4	2	2	2
ρ (g·cm^{-3})	1.202	1.47	1.977	1.256
R	0.054	0.0739	0.0622	0.044
R_W	0.060	0.0842	0.0897	0.053
T (K)	120	120	120	120

Table 14: Crystallographic data of compounds **14**, **41**, **40** and **101**

compound	**100**	**99**	**37**	**102**
CCDC number	890831	890832	890833	890829
formula	$C_{24}H_{19}BrP$	$C_{30}H_{23}Br_2P$	$C_{73}H_{74}BCl_2N$	$C_{97}H_{40}B_2Cl_2F_{40}P_2$
formula weight	418.29	574.29	1047.11	2119.78
crystal system	triclinic	triclinic	triclinic	triclinic
space group	P-1	P-1	P-1	P-1
color	colorless	colorless	colorless	colorless
shape	prisms	needles	needles	prisms
a (Å)	9.2730(2)	9.8351(2)	12.7434(2)	16.6502(4)
b (Å)	10.5567(4)	10.1157(3)	13.4143(3)	17.1925(6)
c (Å)	12.3149(6)	13.5910(4)	17.8647(4)	17.9515(5)
α (°)	84.7365(17)	105.7365(16)	85.6864(9)	67.4032(13)
β (°)	78.272(2)	98.1206(17)	82.7611(12)	78.0100(16)
γ (°)	83.458(2)	99.4597(17)	77.3981(12)	84.1003(16)
V (Å^3)	1169.76(8)	1258.92(6)	2952.94(11)	4639.3(2)

Z	2	2	2	2
ρ (g·cm^{-3})	1.188	1.515	1.178	1.517
R	0.077	0.044	0.047	0.040
R_W	0.049	0.040	0.055	0.042
T (K)	120	120	120	120

Table 15: Crystallographic data of compounds **100**, **99**, **37** and **102**

compound	**95**	**79**
CCDC number	890834	890835
formula	$C_{48}H_{20}BF_{20}P$	$C_{85}H_{59}Cl_2N_9$
formula weight	1018.43	1277.37
crystal system	tetragonal	triclinic
space group	I-4	P-1
color	colorless	colorless
shape	needles	prisms
a (Å)	16.4616(5)	12.8600(3)
b (Å)	16.4616(5)	14.6180(3)
c (Å)	7.7426(2)	19.9820(4)
α (°)	90	103.4020(12)
β (°)	90	108.6650(12)
γ (°)	90	96.1170(13)
V (Å^3)	2098.12(11)	3394.67(13)
Z	2	2
ρ (g·cm^{-3})	1.612	1.250
R	0.029	0.062
R_W	0.034	0.067
T (K)	120	120

Table 16: Crystallographic data of compounds **95** and **79**

9.2 Syntheses

((4-Bromophenyl)ethynyl)triisopropylsilane Br-Ph-in-T*i*PS (**10**)

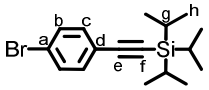

30.00 g (106.04 mmol) 1-bromo-4-iodobenzene, 2.78 g (10.60 mmol) PPh_3, 2.02 g (10.60 mmol) CuI and 3.72 g (5.30 mmol) $Pd(PPh_3)_2Cl_2$ were dissolved in a mixture of 200 mL triethylamine and 200 mL toluene. The mixture was cooled to 0 °C under argon. 20.31 g (24.98 mL, 111.35 mmol) T*i*PS-acetylene was added dropwise over 30 min, and the mixture was allowed to warm to room temperature over night. Water was added to the mixture and the organic phase was washed with saturated NH_4Cl (aq), 1 N HCl (aq), 10 % Na_2CO_3 (aq), and dried over $MgSO_4$. After evaporation of the solvent, the crude product was purified by column chromatography using hexane as eluent to yield 34.74 g (97%) of the pure compound as a colorless liquid.

R_f (hexane) = 0.80

^{1}H-NMR (300 MHz, $CDCl_3$, 298 K) δ 7.42 (d, $^3J_{HH}$ = 8.7 Hz, 2H, H^b), 7.33 (d, $^3J_{HH}$ = 8.7 Hz, 2H, H^c), 1.13 (m, 21H, H^g + H^h)

^{13}C-NMR (75 MHz, $CDCl_3$, 298 K) δ 133.42 (C^c), 131.41 (C^b), 122.50 (C^a), 122.46 (C^d), 105.87 (C^f), 91.99 (C^e), 18.63 (C^h), 11.27 (C^g)

FDMS (m/z): calcd. for $C_{17}H_{25}BrSi$: 338.1, found: 338.3 [M^+]

1-Bromo-4-(phenylethynyl)benzene (**35**)

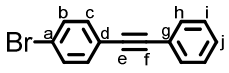

Synthesis according to literature procedure[61]

^{1}H-NMR (300 MHz, THF-d8, 298 K) δ 7.54 (d, *J* = 8.6 Hz, 2H, H^b), 7.51 – 7.48 (m, 2H, H^h) 7.42 (d, *J* = 8.6 Hz, 2H, H^c),7,37 – 7.32 (m, 3H, H^i + H^j)

^{13}C-NMR (75 MHz, THF-d8, 298 K) δ 134.08 (C^c), 132.73 (C^h), 132.48 (C^b), 129.55 (C^j), 129.44 (C^i), 124.12 (C^g), 123.56 (C^a), 123.38 (C^d), 91.43 (C^e), 89.09 (C^f)

FDMS (m/z): calcd. for $C_{14}H_9Br$: 257.1, found: 257.0

Triisopropyl((2,3,5,6-tetrafluorophenyl)ethynyl)silane (50)

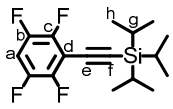

20.00 g (87.35 mmol) 3-bromo-1,2,4,5-tetrafluorobenzene, 2.29 g (8.73 mmol) PPh_3, 1.66 g (8.73 mmol) CuI and 3.07 g (4.37 mmol) $Pd(PPh_3)_2Cl_2$ were dissolved in a mixture of 150 mL triethylamine and 150 mL toluene. The mixture was heated to 80 °C under argon. 23.90 g (29.39 mL, 131.02 mmol) T*i*PS-acetylene was added dropwise and the mixture was stirred at 80 °C over night. Water was added to the mixture and the organic phase was washed with sat. NH_4Cl (aq), 1 N HCl(aq), 10% Na_2CO_3 (aq), and dried over $MgSO_4$. After evaporation of the solvent, the crude product was purified by column chromatography using hexane as eluent to yield 27.03 g (94%) of the pure compound as a colorless liquid.

R_f (hexane) = 0.77

^{1}H-NMR (300 MHz, THF-d8, 298 K) δ 7.51 (tt, $^3J_{HF}$ = 10.3 Hz, $^4J_{HF}$ = 7.5 Hz, 1H, H^a), 1.17 (m, 21H, H^g + H^h)

^{13}C-NMR (126 MHz, THF-d8, 298 K) δ 148.19 (dddd, $^1J_{CF}$ = 251.6 Hz, $^2J_{CF}$ = 14.8 Hz, $^3J_{CF}$ = 3.8 Hz, $^4J_{CF}$ = 3.3 Hz, C^c), 146.90 (dddd, $^1J_{CF}$ = 247.0 Hz, $^2J_{CF}$ = 13.4 Hz, $^3J_{CF}$ = 11.1 Hz, $^4J_{CF}$ = 4.3 Hz, C^b), 107.91 (t, $^2J_{CF}$ = 23.5 Hz, C^a), 106.72 (t, $^4J_{CF}$ = 3.9 Hz, C^f), 105.74 (tt, $^2J_{CF}$ = 18.2 Hz, $^3J_{CF}$ = 2.7 Hz, C^d), 91.65 (t, $^3J_{CF}$ = 3.9 Hz, C^e), 18.93 (C^h), 12.06 (C^g)

^{19}F-NMR (471 MHz, THF-d8, 298 K) δ -140.49 (m), -142.73 (m)

FDMS (m/z): calcd. for $C_{17}H_{22}F_4Si$: 330.1, found: 330.1 [M^+]

1,2-Bis(perfluorophenyl)ethyne (39)

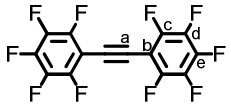

Analog procedure to *Stille* coupling for electron poor aromatics[199]

0.217 g (0.83 mmol) PPh_3, 0.158 g (0.83 mmol) CuI, 2.51 g (16.55 mmol) CsF, 0.290 g (0.41 mmol) $Pd(PPh_3)_2Cl_2$ and 6.131 g (24.82 mmol, 3.095 mL) 1-bromo-2,3,4,5,6-pentafluorobenzene were dissolved in 300 mL anhydrous DMF. 5.000 g (4.36 mL, 8.27 mmol) 1,2-bis(tributylstannyl)ethyne were added dropwise over 30 min, and the stirred mixture was heated to

45 °C over night. Triethylamine (5%) was added and the mixture was filtered over silica. After removal of the solvent in vacuo the crude product was purified by column chromatography using hexane as eluent to yield 2.211 g (75%) of the pure compound as colorless crystalline needles.

^{19}F-NMR (471 MHz, THF-d8, 298 K) δ -135.23 (d, $^{3}J_{FF}$ = 16.9 Hz, 4F, F^{c}), -150.15 (t, $^{3}J_{FF}$ = 20.7 Hz, 2F, F^{e}), -161.42 (m, 4F, F^{d})

^{13}C-NMR (126 MHz, THF-d8, 298 K) δ 148.46 (d, $^{1}J_{CF}$ = 253.6 Hz, 4C, C^{c}), 143.91 (d, $^{1}J_{CF}$ = 253.6 Hz, 2C, C^{e}), 139.05 (d, $^{1}J_{CF}$ = 253.6 Hz, 4C, C^{d}), 99.39 (2C, C^{b}), 85.49 (2C, C^{a})

FDMS (m/z): calcd. for $C_{14}F_{10}$: 358.0, found: 358.0 [M^{+}]

2,3,4,5-Tetrakis(perfluorophenyl)cyclopenta-2,4-dienone Cp-on^{F} (**40**)

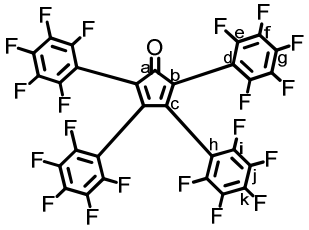

Synthesis from 1,2-Bis(perfluorophenyl)ethyne **39** according to literature procedure[39]

^{19}F-NMR (471 MHz, THF-d8, 298 K) δ -136.45 (d, $^{3}J_{FF}$ = 16.8 Hz, 4F, F^{e}), -136.67 (d, $^{3}J_{FF}$ = 16.8 Hz, 4F, F^{i}),-147.09 (t, $^{3}J_{FF}$ = 20.8 Hz, 2F, F^{g}), -149.27 (t, $^{3}J_{FF}$ = 20.8 Hz, 2F, F^{k}), -157.92 (m, 4F, F^{f}), -159.59 (m, 4F, F^{j})

^{13}C-NMR (126 MHz, THF-d8, 298 K, ^{19}F-decoupled) δ 189.36 (C^{a}), 146.44 (*C*), 145.74 (*C*-F), 144.46 (*C*-F), 144.08 (*C*-F, C^{para}), 143.64 (*C*-F, C^{para}), 139.21 (*C*-F), 139.15 (*C*-F), 123.64 (*C*), 107.14 (*C*), 105.01 (*C*)

FDMS (m/z): calcd. for $C_{29}F_{20}O$: 744.0, found: 744.2 [M^{+}]

XRD: red plates, triclinic, P-1

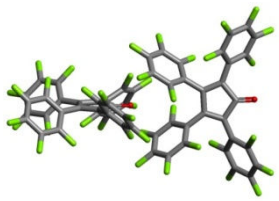

Tetrabutylammonium tetraphenylborate $TBA^+ BPh_4^-$ **(93)**

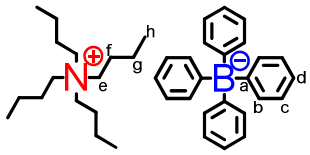

To a solution of 3.000 g (8.766 mmol) sodium tetraphenylborate in 10 mL THF was added an excess of about 6.2 g (19.3 mmol) tetrabutylammonium bromide. The solution was stirred for 10 min at room temperature and then filtered over silica. After removal of the solvent in vacuo, a crystalline white solid was obtained. The crude product was dissolved in methylene chloride and filtered over silica. After removal of the solvent in vacuo, the colorless solid was dissolved in methylene chloride, precipitated in hexane, filtered and dried to afford 4.711 g (8.387 mmol, 96%) of the pure compound as colorless crystalline needles.

^{1}H-NMR (700 MHz, THF-d8, 298 K) δ 7.29 (m, 8H, H^b), 6.87 (t, $^3J_{HH}$ = 7.4 Hz, 8H, H^c), 6.72 (t, $^3J_{HH}$ = 7.1 Hz, 4H, H^d), 2.92 (m, 8H, H^e), 1.48 (m, 8H, H^f), 1.29 (m, 8H, H^g), 0.95 (t, $^3J_{HH}$ = 7.2 Hz, 12H, H^h)

^{13}C-NMR (75 MHz, THF-d8, 298 K) δ 165.36 (q, $^1J_{BC}$ = 49.4 Hz, C^a), 137.39 (C^b), 125.97 (q, $^3J_{BC}$ = 2.7 Hz, C^c), 122.13 (C^d), 59.26 (C^e), 24.68 (C^f), 20.64 (C^g), 14.11 (C^h)

^{11}B-NMR (225 MHz, THF-d8, 298 K) δ -5.51

MALDI-TOF (m/z): calcd. for $C_{24}H_{20}B^-$: 319.2, found: 319.0 [M^-]

XRD: colorless needles, triclinic, P-1

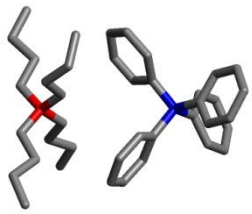

Tetrabutylammonium tetrakis(perfluorophenyl)borate $TBA^+ BPh^F_4{}^-$ **(94)**

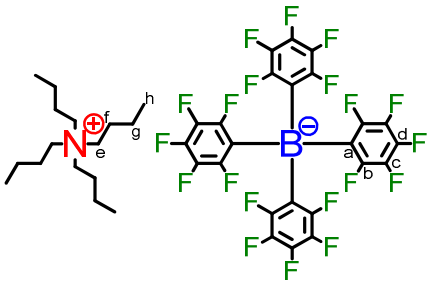

To a solution of 3.000 g (3.596 mmol) lithium tetrakis(perfluorophenyl)borate dietherate in 10 mL THF was added an excess of about 2.5 g (7.9 mmol) tetrabutylammonium bromide. The solution was stirred for 10 min at room temperature and then filtered over silica. After removal of the solvent in vacuo, a viscous oil was obtained which slowly crystallized. The crude product was dissolved in methylene chloride and filtered over silica. After removal of the solvent in vacuo, the colorless solid was dissolved in methylene chloride, precipitated in hexane, filtered and dried to afford 3.121 g (3.387 mmol, 94%) of the pure product as a colorless crystalline powder.

^{1}H-NMR (500 MHz, THF-d8, 298 K) δ 3.38 (m, 8H, H^e), 1.71 (m, 8H, H^f), 1.41 (m, 8H, H^g), 1.00 (t, $^3J_{HH}$ = 7.4 Hz, 12H, H^h)

^{13}C-NMR: borate signals not resolved due to C-F coupling

^{19}F-NMR (471 MHz, THF-d8, 298 K) δ -132.72 (m, 8F, F^b), -164.93 (t, $^3J_{FF}$ = 20.2 Hz, 4F, F^d), -168.43 (m, 8F, F^c)

^{11}B-NMR (225 MHz, THF-d8, 298 K) δ -15.54

MALDI-TOF (m/z): calcd. for $C_{24}BF_{20}^-$: 679.0, found: 678.9 [M^-]

XRD: colorless prisms, monoclinic, Cc

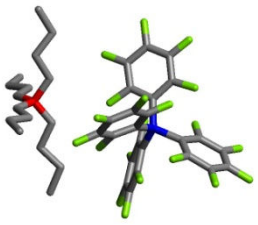

Tetraphenylphosphonium tetrakis(perfluorophenyl)borate $PPh_4^+ BPh^F_4^-$ **(95)**

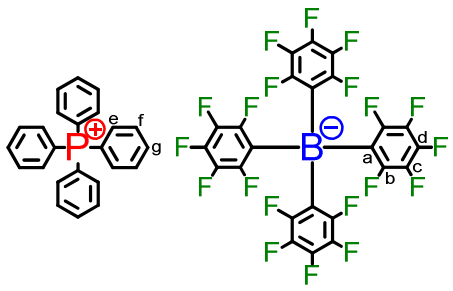

To a solution of 1.5 g (1.8 mmol) lithium tetrakis(perfluorophenyl)borate dietherate in 25 mL DCM was added an excess of about 1.6 g (3.8 mmol) tetraphenylphosphonium bromide. The solution was stirred for 10 min at room temperature and then filtered over silica. Upon addition of hexane to the DCM solution, transparent crystal needles of up to several centimetre length formed immediately. The needles were filtered off and dried to afford 1.778 g (1.746 mmol, 97%) of the pure product as a colorless crystalline powder.

^{1}H-NMR (300 MHz, CD_2Cl_2, 298 K) δ 7.90 (td, $^{3}J_{HH}$ = 7.5 Hz, $^{5}J_{PH}$ = 1.9 Hz, 4H, H^g), 7.72 (td, $^{3}J_{HH}$ = 7.9 Hz, $^{4}J_{PH}$ = 3.7 Hz, 8H, H^f), 7.60 (dd, $^{3}J_{PH}$ = 12.9 Hz, $^{3}J_{HH}$ = 8.1 Hz, 8H, H^e)

^{13}C-NMR (75 MHz, CD_2Cl_2, 298 K) δ 136.35 (d, $^{4}J_{PC}$ = 3.1 Hz, *C*-H, C^g), 134.97 (d, $^{3}J_{PC}$ = 10.3 Hz, *C*-H, C^f), 131.18 (d, $^{2}J_{PC}$ = 13.0 Hz, *C*-H, C^e), 118.15 (d, $^{1}J_{PC}$ = 89.6 Hz, *C*); signals of borate anion not resolved due to C-F coupling

^{19}F-NMR (471 MHz, CD_2Cl_2, 298 K) δ -133.72 (s, 8F, F^b), -164.35 (t, $^{3}J_{FF}$ = 20.4 Hz, 4F, F^d), -168.19 (t, $^{3}J_{FF}$ = 16.89 Hz, 8F, F^c)

^{11}B-NMR (160 MHz, CD_2Cl_2, 298 K) δ -16.66

^{31}P-NMR (202 MHz, CD_2Cl_2, 298 K) δ 23.35

XRD: colorless needles, tetragonal, I-4

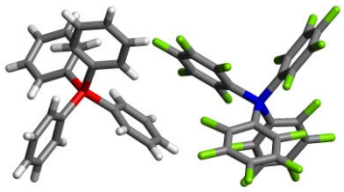

Lithium tetrakis(4-((triisopropylsilyl)ethynyl)phenyl)borate $Li^+ [B(Ph\text{-}in\text{-}T\mathit{i}PS)_4]^-$ **(11)**

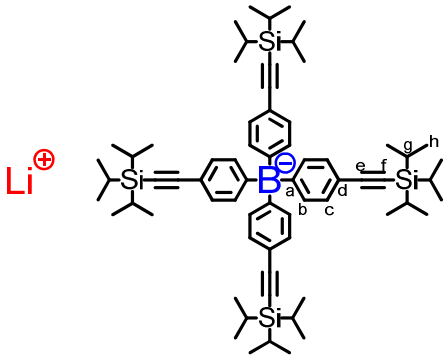

5.00 g (14.82 mmol) ((4-Bromophenyl)ethinyl)triisopropylsilane **10** were dissolved in 20 mL anhydrous diethyl ether under argon. The solution was cooled to -78 °C and one equivalent *n*-Butyllithium (9.26 mL of a 1.6 M solution in hexane) was added dropwise. After one hour 0.25 equivalents BCl_3 (3.71 mL of a 1 M solution in heptane) were slowly added. The mixture was allowed to warm to room temperature over night, whereupon a white suspension was obtained. After removal of the solvent in vacuo, the white precipitate was dispersed in methylene chloride, precipitated in hexane, filtered, washed with hexane and dried to afford 1.78 g (46%) of the pure compound as a white powder.

^{1}H-NMR (300 MHz, THF-d8, 298 K) δ 7.19 (dq, $^3J_{HH}$ = 7.9 Hz, $^3J_{BH}$ = 2.6 Hz, 8H, H^b), 7.05 (d, $^3J_{HH}$ = 7.9 Hz, 8H, H^c), 1.12 (m, 84H, H^g + H^h)

^{13}C-NMR (126 MHz, THF-d8, 298 K) δ 166.41 (q, $^1J_{BC}$ = 49.4 Hz, 80.1% ^{11}B, C^a), 166.41 (sept, $^1J_{BC}$ = 16.5 Hz, 19.9% ^{10}B, C^a), 136.69 (C^b), 130.19 (q, $^3J_{BC}$ = 2.8 Hz, C^c), 117.22 (C^d), 112.32 (C^f), 85.84 (C^e), 19.33 (C^h), 12.58 (C^g)

^{11}B-NMR (160 MHz, THF-d8, 298 K) δ -6.28

MALDI-TOF (m/z): calcd. for $C_{68}H_{100}BSi_4^-$: 1039.7, found: 1039.3 [M^-]

Tetrabutylammonium tetrakis(4-ethynylphenyl)borate $TBA^+ [B(Ph\text{-}in)_4]^-$ **(12)**

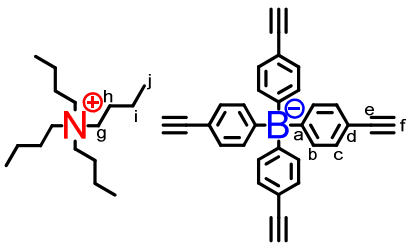

To a solution of 1.00 g (0.95 mmol) $Li^+[B(Ph\text{-}in\text{-}TiPS)_4]^-$ **11** in THF (100 mL) was added dropwise a solution of tetrabutylammonium fluoride (1.60 g, 5.73 mmol) in THF (50 mL). The mixture was stirred for 2 h at room temperature. The mixture was extracted 6 times with concentrated aqueous solution of sodium chloride and dried over $MgSO_4$. Upon removal of the solvent in vacuo, a crystalline precipitate was formed which was washed 3 times with cold methylene chloride. Recrystallization from methylene chloride/hexane afforded 511 mg (81%) of the pure compound as colorless crystalline needles.

^{1}H-NMR (300 MHz, THF-d8, 298 K) δ 7.20 (dq, $^3J_{HH}$ = 7.9 Hz, $^3J_{BH}$ = 2.7 Hz, 8H, H^b), 7.06 (d, $^3J_{HH}$ = 7.9 Hz, 8H, H^c), 3.10 (s, 4H, H^f), 3.04 (m, 8H, H^g), 1.55 (m, 8H, H^h), 1.32 (m, 8H, H^i), 0.96 (t, $^3J_{HH}$ = 7.4 Hz, 12H, H^j)

^{13}C-NMR (75 MHz, THF-d8, 298 K) δ 166.02 (q, $^1J_{BC}$ = 49.4 Hz, 80.1% ^{11}B, C^a), 166.02 (sept, $^1J_{BC}$ = 16.6 Hz, 19.9% ^{10}B, C^a), 136.82 (C^b), 130.18 (q, $^3J_{BC}$ = 2.8 Hz, C^c), 116.53 (C^d), 87.14 (C^e), 75.35 (C^f), 59.37 (C^g), 24.64 (C^h), 20.71 (C^i), 14.10 (C^j)

^{11}B-NMR (160 MHz, THF-d8, 298 K) δ -6.50

MALDI-TOF (m/z): calcd. for $C_{32}H_{20}B^-$: 415.2, found: 415.1 [M^-]

XRD: colorless needles, orthorhombic, Ccc2

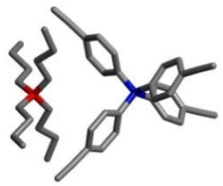

Tetrabutlyammonium tetrakis(4-(G1)phenyl)borate $TBA^+[B\text{-}G1]^-$ **(14)**

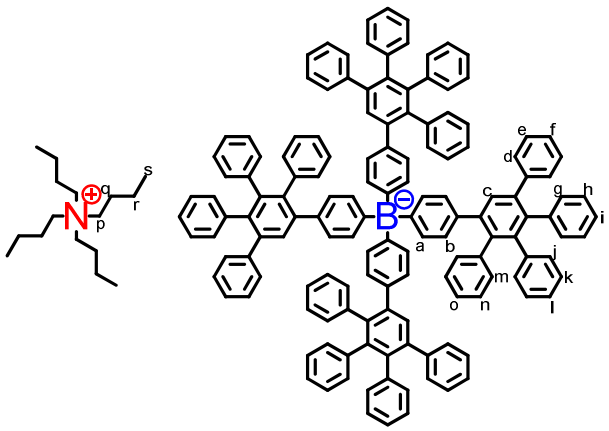

100 mg (0.15 mmol) of $TBA^+B(Ph\text{-}in)_4^-$ **12** and 263 mg (0.68 mmol) tetraphenylcyclopentadienone were dissolved in diglyme (5 mL) in a microwave tube. The argon bubbled mixture was stirred at 160 °C for 12 h. After cooling to room temperature, the mixture was purified by column chromatography using firstly a 10:1 mixture of hexane and ethyl acetate and then THF as eluent. After removal of the solvent in vacuo, the product was dissolved in methylene chloride, precipitated in hexane, filtered and dried to afford 194 mg (0.093 mmol, 62%) pure compound as a colorless powder.

^{1}H-NMR (700 MHz, THF-d8, 298 K) δ 7.52 (s, 4H, H^c), 7.14 (d, $^3J_{HH}$ = 7.1 Hz, 8H, H^d), 7.08 (t, $^3J_{HH}$ = 7.4 Hz, 8H, H^e), 7.03 (t, $^3J_{HH}$ = 7.3 Hz, 4H, H^f), 6.90 (m, 8H, H^a), 6.86 – 6.74 (m, 60H, H^g – H^o), 6.66 (d, $^3J_{HH}$ = 8.1 Hz, 8H, H^b), 2.99 (m, 8H, H^p), 1.50 (m, 8H, H^q), 1.26 (m, 8H, H^r), 0.90 (t, $^3J_{HH}$ = 7.4 Hz, 12H, H^s)

^{13}C-NMR (176 MHz, THF-d8, 298 K) δ 163.45 (q, $^1J_{BC}$ = 49.6 Hz), 144.92, 143.83, 142.49, 142.36, 142.08, 141.95, 140.75, 138.93, 136.73 (C^a), 135.41, 132.85 (C^{ortho}), 132.86 (C^{ortho}), 132.87 (C^{ortho}), 132.45 (C^c), 131.07 (C^d), 128.24 (C^e), 127.72 (C^b), 127.58 (C^{meta}), 127.49 (C^{meta}), 127.28 (C^{meta}), 126.67 (C^f), 126.06 (C^{para}), 126.00 (C^{para}), 125.79 (C^{para}), 59.60 (C^p), 24.76 (C^q), 20.65 (C^r), 13.99 (C^s)

^{11}B-NMR (160 MHz, THF-d8, 298 K) δ -6.95

DOSY-NMR (700 MHz, THF-d8, 298 K) D_{borate} = 4.47·10^{-10} m^{2}s^{-1}; r_H = 0.98 nm

MALDI-TOF (m/z): calcd. for $C_{144}H_{100}B^-$: 1840.8, found: 1840.8 [M^-]

XRD: colorless needles, monoclinic, P2/n

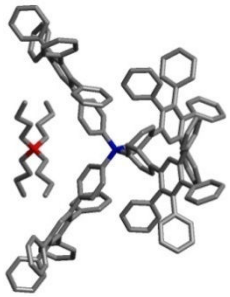

Tetrabutlyammonium tetrakis(4-(perfluoro-G1)phenyl)borate $TBA^+ [B\text{-}G1^F]^-$ **(41)**

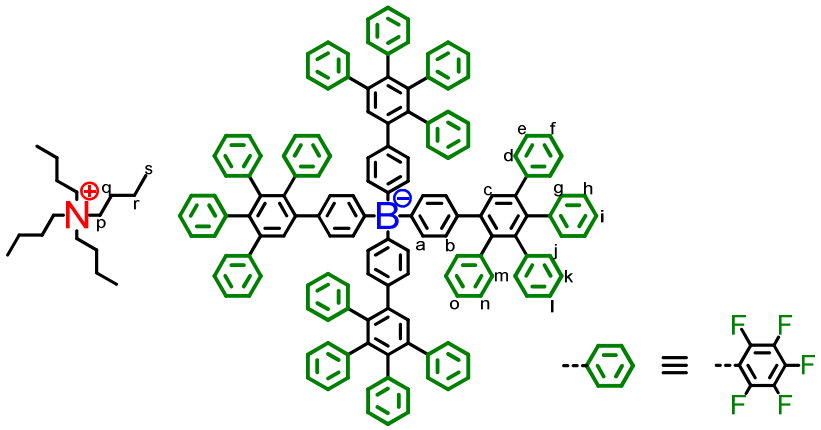

50 mg (0.076 mmol) of $TBA^+B(Ph\text{-}in)_4^-$ **12** and 255 mg (0.342 mmol) perfluorinated tetracyclone **40** were dissolved in diglyme (10 mL) in a microwave tube. The argon bubbled mixture was stirred at 155 °C for 16 h. After cooling to room temperature, the mixture was purified by column chromatography using firstly a 10:1 mixture of hexane and ethyl acetate and then THF as eluent. After removal of the solvent in vacuum, the crude product was dissolved in methylene chloride, precipitated in hexane, filtered and dried to afford 164 mg (0.047 mmol, 61%) pure compound as a yellow powder.

^{1}H-NMR (500 MHz, THF-d8, 298 K) δ 7.98 (s, 4H, H^c), 6.98 (m, 8H, H^a), 6.77 (d, $^3J_{HH}$ = 8.0 Hz, 8H, H^b), 3.24 (m, 8H, H^p), 1.68 (m, 8H, H^q), 1.40 (m, 8H, H^r), 1.00 (t, $^3J_{HH}$ = 7.4 Hz, 12H, H^s)

^{13}C-NMR (176 MHz, THF-d8, 298 K) δ 165.28 (q, $^1J_{BC}$ = 49.0 Hz), 150.30, 146.25 (m), 144.28 (m), 143.65 (m), 141.67 (m), 139.46 (m), 137.49 (m), 136.83 (C^a), 136.07 (C^c), 132.62, 131.17, 130.88, 130.36, 127.64, 126.33 (C^b), 114.18 (m), 112.87 (m), 59.41 (C^p), 24.65 (C^q), 20.73 (C^r), 14.01 (C^s)

^{19}F-NMR (471 MHz, THF-d8, 298 K) δ -137.45 (8F, F^{ortho}), -138.36 (8F, F^{ortho}), -138.53 (8F, F^{ortho}), -139.53 (8F, F^{ortho}), -151.61 (t, $^3J_{FF}$ = 20.5 Hz, 8F, F^{para}), -153.41 (t, $^3J_{FF}$ = 20.5 Hz, 4F, F^{para}), -153.45 (t, $^3J_{FF}$ = 20.5 Hz, 4F, F^{para}), -161.20 (m, 8F, F^{meta}), -161.31 (m, 8F, F^{meta}), -161.70 (m, 8F, F^{meta}), -162.32 (m, 8F, F^{meta})

^{11}B-NMR (160 MHz, THF-d8) δ -4.91

DOSY-NMR (700 MHz, THF-d8, 298 K) D_{borate} = 4.07·10^{-10} m^{2}s^{-1}; r_H = 1.07 nm

MALDI-TOF (m/z): calcd. for $C_{144}H_{20}BF_{80}^-$: 3280.0, found: 3280.2 [M$^-$]

XRD: yellow needles, triclinic, P-1

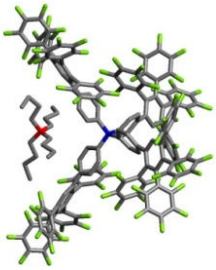

Lithium tetrakis(4-(phenylethynyl)phenyl)borate $Li^+ [B(Ph\text{-}in\text{-}Ph)_4]^-$ **(36)**

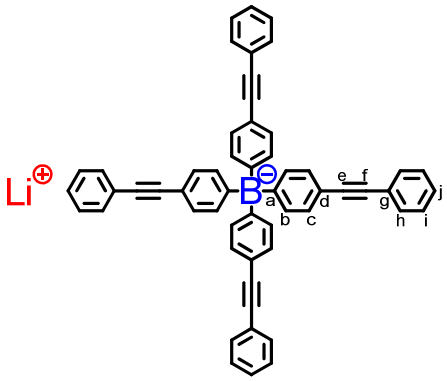

1.00 g (3.89 mmol) 1-bromo-4-(phenylethynyl)benzol **35** was dissolved in 20 mL anhydrous diethyl ether under argon. The solution was cooled to -78 °C and one equivalent *n*-Butyllithium (2.43 mL of a 1.6 M solution in hexane) was added dropwise. After 1 h 0.25 equivalents BCl_3 (0.97 mL of a 1 M solution in heptane) were slowly added. The mixture was allowed to warm to room temperature over night, whereby a white suspension was obtained. After removal of the solvent in vacuo, the white precipitate was dispersed in methylene chloride, precipitated in hexane, filtered and washed with hexane to afford 350 mg (0.48 mmol, 50%) of the crude product as a colorless and hygroscopic precipitate.

^{1}H-NMR (300 MHz, THF-d8, 298 K) δ 7.43 (d, $^3J_{HH}$ = 7.2 Hz, 8H, H^h), 7.34 – 7.19 (m, 20H, H^b + H^i + H^j), 7.11 (d, $^3J_{HH}$ = 7.9 Hz, 8H, H^c)

^{13}C-NMR (75 MHz, THF-d8, 298 K) δ 165.99 (q, $^1J_{BC}$ = 49.4 Hz, C^a), 136.78 (C^b), 132.04 (C^h), 129.52 (q, $^3J_{BC}$ = 2.8 Hz, C^c), 129.03 (C^i), 127.95 (C^j), 125.77 (C^g), 117.00 (C^d), 93.23 (C^e), 87.09 (C^f)

MALDI-TOF (m/z): calcd. for $C_{56}H_{36}B^-$: 719.3, 719.3

Tetrabutylammonium tetrakis(4-(phenylethynyl)phenyl)borate TBA^+ $[B(Ph\text{-}in\text{-}Ph)_4]^-$ **(37)**

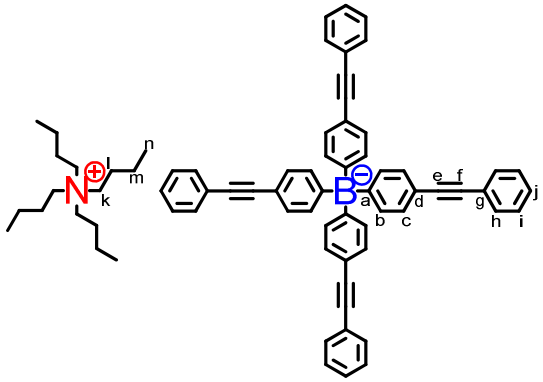

350 mg (about 0.48 mmol) of crude Li^+ $[B(Ph\text{-}in\text{-}Ph)_4]^-$ **36** was dissolved in 100 mL THF. An excess of tetrabutylammonium chloride (about 270 mg, 0.97 mmol) was added and the solution was stirred for 2 h at room temperature. After washing 6 times with a concentrated aqueous solution of sodium chloride, the solution was filtered over silica and the solvent removed under vacuum. The remainder was dissolved in methylene chloride, precipitated in hexane, filtered and dried to afford 431 mg (0.45 mmol, 93%) of the product as a colorless powder.

^{1}H-NMR (500 MHz, THF-d8, 298 K) δ 7.43 (d, $^3J_{HH}$ = 7.2 Hz, 8H, H^h), 7.32 (dq, $^3J_{HH}$ = 7.9 Hz, $^3J_{BH}$ = 2.5 Hz, 8H, H^b), 7.27 (t, $^3J_{HH}$ = 7.3 Hz, 8H, H^i), 7.21 (t, $^3J_{HH}$ = 7.3 Hz, 4H, H^j), 7.16 (d, $^3J_{HH}$ = 7.9 Hz, 8H, H^c), 2.98 (m, 8H, H^k), 1.52 (m, 8H, H^l), 1.30 (m, 8H, H^m), 0.94 (t, $^3J_{HH}$ = 7.3 Hz, 12H, H^n)

^{13}C-NMR (75 MHz, THF-d8, 298 K) δ 166.17 (q, $^1J_{BC}$ = 49.5 Hz, C^a), 137.04 (C^b), 132.21 (C^h), 129.84 (q, $^3J_{BC}$ = 2.8 Hz, C^c), 129.15 (C^i), 128.17 (C^j), 125.94 (C^g), 117.29 (C^d), 93.37 (C^e or C^f), 87.50 (C^e or C^f), 59.34 (C^k), 24.63 (C^l), 20.71 (C^m), 14.12 (C^n)

^{11}B-NMR (160 MHz, THF-d8, 298 K) δ -8.02

MALDI-TOF (m/z): calcd. for $C_{56}H_{36}B^-$: 719.3, found: 719.3

XRD: colorless needles, triclinic, P-1

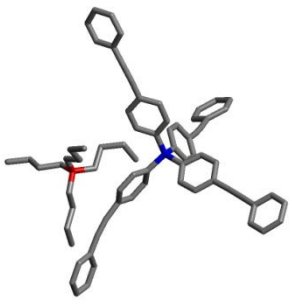

Tetrabutlyammonium tetrakis(4-((bis(triisopropylsilylethynyl))G1)phenyl)borate TBA^+ [B-G1(in-T*i*PS)$_8$]$^-$ (**18**)

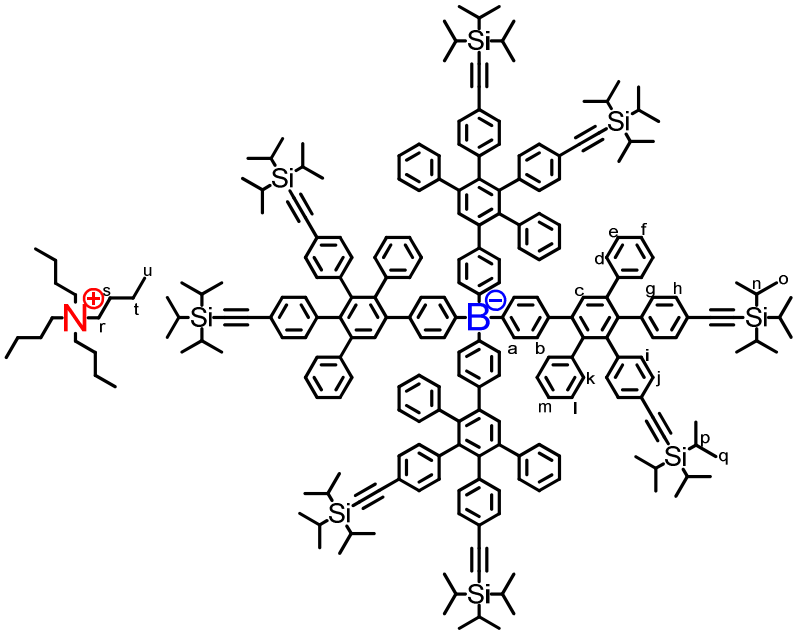

150 mg (0.23 mmol) of borate core **12** and 765 mg (1.03 mmol) AB_2 building block **1** were dissolved in diglyme (15 mL) in a microwave tube. The argon bubbled mixture was stirred at 160 °C for 12 h. After cooling to room temperature, the mixture was purified by column chromatography using firstly a 4:1 mixture of hexane and ethyl acetate and then THF as eluent. After removal of the solvent in vacuum and drying in high vacuum over night, 362 mg (0.103 mmol, 45%) of the compound were obtained as a pale beige powder.

^{1}H-NMR (700 MHz, THF-d8, 298 K) δ 7.51 (s, 4H, H^c), 7.14 (d, $^3J_{HH}$ = 7.2 Hz, 8H, H^d), 7.11 (t, $^3J_{HH}$ = 7.5 Hz, 8H, H^e), 7.06 (t, $^3J_{HH}$ = 7.2 Hz, 4H, H^f), 7.01 (d, $^3J_{HH}$ = 8.2 Hz, 8H, H^g), 6.96 (d, $^3J_{HH}$ = 8.2 Hz, 8H, H^i), 6.89 (m, 8H, H^a), 6.85 – 6.82 (m, 12H, H^k + H^m), 6.82 (d, $^3J_{HH}$ = 8.2 Hz, 8H, H^h), 6.81 – 6.78 (m, 8H, H^l), 6.78 (d, $^3J_{HH}$ = 8.2 Hz, 8H, H^j), 6.63 (d, $^3J_{HH}$ = 7.9 Hz, 8H, H^b), 3.04 (m, 8H, H^r), 1.54 (m, 8H, H^s), 1.30 (m, 8H, H^t), 1,10 (m, 168H, H^n + H^o + H^p + H^q), 0.92 (t, $^3J_{HH}$ = 7.4 Hz, 12H, H^u)

^{13}C-NMR (75 MHz, THF-d8, 298 K) δ 163.38 (q, $^1J_{BC}$ = 49.5 Hz), 145.42, 143.32, 142.91, 142.45, 141.45, 141.40, 141.22, 140.63, 137.78, 136.68 (C^a), 135.04, 133.04 (C^c), 132.81 (C^h), 132.77 (C^j), 132.72 (C^l), 131.63 (C^g), 131.36 (C^i), 130.99 (C^d), 128.50 (C^e), 127.72 (C^k), 127.56 (C^b), 127.01 (C^f), 126.35 (C^m), 121.39 (*C*-C≡C-Si), 121.14 (*C*-C≡C-Si), 109.12 (C-C≡*C*-Si), 109.05 (C-C≡*C*-Si), 89.96 (C-*C*≡C-Si), 89.74 (C-*C*≡C-Si), 59.33 (C^r), 24.65 (C^s), 20.70 (C^t), 19.22 (C^o + C^q), 14.09 (C^u), 12.44 (C^n + C^p)

^{11}B-NMR (160 MHz, THF-d8, 298 K) δ -7.20

MALDI-TOF (m/z): calcd. for $C_{232}H_{260}BSi_8^-$: 3283.9, found: 3285.0

Tetrabutlyammonium tetrakis(4-((bis(ethynyl))G1)phenyl)borate (20) $TBA^+ [B\text{-}G1(in)_8]^-$

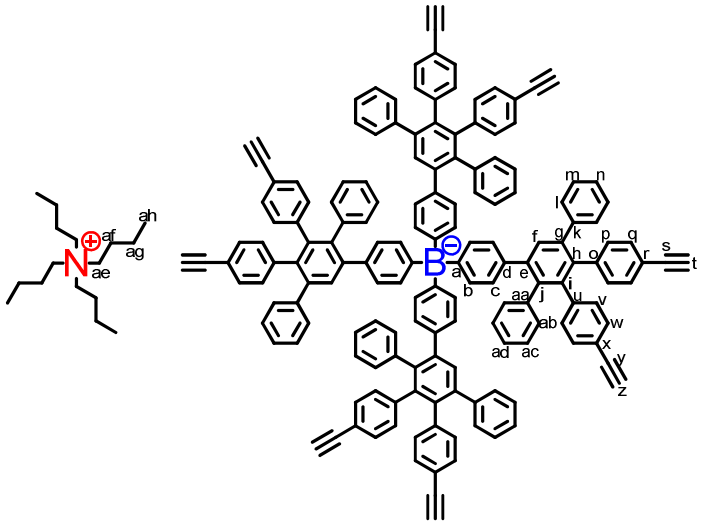

To a solution of 159 mg (0.045 mmol) $TBA^+[B\text{-}G1(in\text{-}T\mathit{i}PS)_8]^-$ **18** in THF (25 mL) was added dropwise a solution of tetrabutylammonium fluoride (126 mg, 0.451 mmol) in THF (15 mL). The mixture was stirred for 2 h at room temperature. After washing 3 times with a concentrated aqueous solution of sodium chloride, the solution was filtered over silica and the solvent removed under vacuum. The remainder was dissolved in methylene chloride, precipitated in hexane, filtered and dried to afford 92 mg (0.040 mmol, 90%) of the product as a colorless powder.

^{1}H-NMR (700 MHz, THF-d8, 298 K) δ 7.55 (s, 4H, H^f), 7.13 (m, 16H, H^l + H^m), 7.08 (m, 4H, H^n), 7.02 (d, $^3J_{HH}$ = 8.2 Hz, 8H, H^p), 6.96 (d, $^3J_{HH}$ = 8.2 Hz, 8H, H^v), 6.89 (m, 8H, H^b), 6.87 – 6.84 (m, 12H, H^{ab} + H^{ad}), 6.82 (d, $^3J_{HH}$ = 8.2 Hz, 8H, H^q), 6.81 – 6.78 (m, 8H, H^{ac}), 6.77 (d, $^3J_{HH}$ = 8.2 Hz, 8H, H^w), 6.64 (d, $^3J_{HH}$ = 8.0 Hz, 8H, H^c), 3.37 (s, 4H, C≡C-*H*), 3.33 (s, 4H, C≡C-*H*), 3.08 (m, 8H, H^{ae}), 1.56 (m, 8H, H^{af}), 1.30 (m, 8H, H^{ag}), 0.93 (t, $^3J_{HH}$ = 7.4 Hz, 12H, H^{ah})

^{13}C-NMR (176 MHz, THF-d8, 298 K) δ 163.35 (q, $^1J_{BC}$ = 49.4 Hz, C^a), 145.33 (C^d), 143.14 (C^g), 142.91 (C^u), 142.44 (C^o), 141.40 (C^{aa}), 141.31 (C^k), 141.25 (C^i), 140.51 (C^j), 137.78 (C^h), 136.66 (*C*H, C^b), 135.01 (C^e), 132.94 (*C*H, C^f), 132.82 (*C*H, C^q), 132.79 (*C*H, C^w), 132.71 (*C*H, C^{ac}), 131.58 (*C*H, C^p), 131.29 (*C*H, C^v), 130.97 (*C*H, C^l), 128.50 (*C*H, C^m), 127.69 (*C*H, C^{ab}), 127.55 (*C*H, C^c), 127.01 (*C*H, C^n), 126.29 (*C*H, C^{ad}), 120.66 (C^r), 120.38 (C^x), 84.69 (C^s), 84.62 (C^y), 78.56 (C^t), 78.34 (C^z), 59.28 (C^{ae}), 24.61 (C^{af}), 20.67 (C^{ag}), 14.10 (C^{ah})

^{11}B-NMR (160 MHz, THF-d8, 298 K) δ -7.07

MALDI-TOF (m/z): calcd. for $C_{160}H_{100}B^-$: 2032.8, found: 2033.4

Tetrabutlyammonium tetrakis(4-((tetrakis(triisopropylsilylethynyl))G1)phenyl)borate

TBA^+ $[B\text{-}G1(in\text{-}T\mathit{i}PS)_{16}]^-$ (**19**)

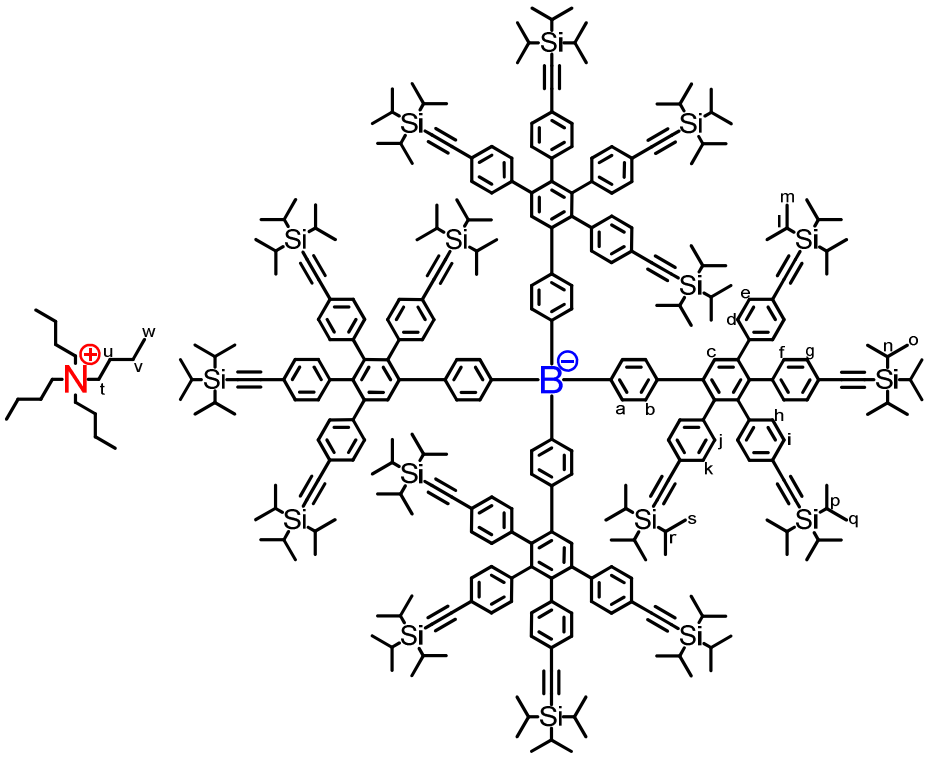

150 mg (0.23 mmol) of $TBA^+B(Ph\text{-}in)_4^-$ **12** and 1.135 g (1.03 mmol) AB_4 building block **2** were dissolved in diglyme (15 mL) in a microwave tube. The argon bubbled mixture was stirred at 160 °C for 12 h. After cooling to room temperature, the mixture was purified by column chromatography using firstly a 10:1 mixture of hexane and ethyl acetate and then THF as eluent. After removal of the solvent in vacuum and drying in high vacuum over night, 143 mg (0.028 mmol, 13%) of the compound were obtained as a pale yellow solid.

^{1}H-NMR (700 MHz, THF-d8, 298 K) δ 7.53 (s, 4H, H^c), 7.24 (d, $^3J_{HH}$ = 8.3 Hz, 8H, H^d), 7.13 (d, $^3J_{HH}$ = 8.3 Hz, 8H, H^e), 7.06 (d, $^3J_{HH}$ = 8.3 Hz, 4H, H^j), 7.00 (d, $^3J_{HH}$ = 8.3 Hz, 8H, H^f), 6.99 (d, $^3J_{HH}$ = 8.3 Hz, 8H, H^h), 6.96 (m, 8H, H^a), 6.82 (d, $^3J_{HH}$ = 8.3 Hz, 8H, H^k), 6.78 (d, $^3J_{HH}$ = 8.3 Hz, 8H, H^g), 6.76 (d, $^3J_{HH}$ = 8.3 Hz, 8H, H^i), 6.67 (d, $^3J_{HH}$ = 8.0 Hz, 8H, H^b), 3.13 (m, 8H, H^t), 1.61 (m, 8H, H^u), 1.35 (m, 8H, H^v), 1.14 – 1.08 (m, 336H, T*i*PS, H^l - H^r), 0.97 (t, $^3J_{HH}$ = 7.4 Hz, 12H, H^w)

^{13}C-NMR (75 MHz, THF-d8, 298 K) δ 163.74 (q, $^1J_{BC}$ = 49.4 Hz), 145.83, 143.57, 142.57, 142.18, 141.99, 141.18, 140.58, 140.10, 137.70, 136.83 (C^a), 134.75, 133.35 (C^c), 132.74 (C^f + C^h

+ C^{j}), 132.29 (C^{d}), 131.85 (C^{e}), 131.54 (C^{g} + C^{i}), 131.08 (C^{k}), 127.64 (C^{b}), 122.22 (*C*-C≡C-Si), 121.67 (*C*-C≡C-Si), 121.43 (*C*-C≡C-Si), 121.32 (*C*-C≡C-Si), 109.42 (C-C≡*C*-Si), 109.05 (C-C≡*C*-Si), 108.94 (2C, C-C≡*C*-Si), 90.51 (C-*C*≡C-Si), 90.23 (C-*C*≡C-Si), 90.00 (C-*C*≡C-Si), 89.51 (C-*C*≡C-Si), 59.41 (C^{t}), 24.65 (C^{u}), 20.74 (C^{v}), 19.41 + 19.25 + 19.23 (1:1:2, C^{m} + C^{o} + C^{q} + C^{s}), 14.10 (C^{w}), 12.45 (C^{l} + C^{n} + C^{p} + C^{r})

^{11}B-NMR (160 MHz, THF-d8, 298 K) δ -7.01

MALDI-TOF (m/z): calcd. for $C_{320}H_{420}BSi_{16}^{-}$: 4725.9, found: 4726.6

Tetrabutlyammonium tetrakis(4-((tetrakis(ethynyl))G1)phenyl)borate (21) TBA^{+} $[B\text{-}G1(in)_{16}]^{-}$

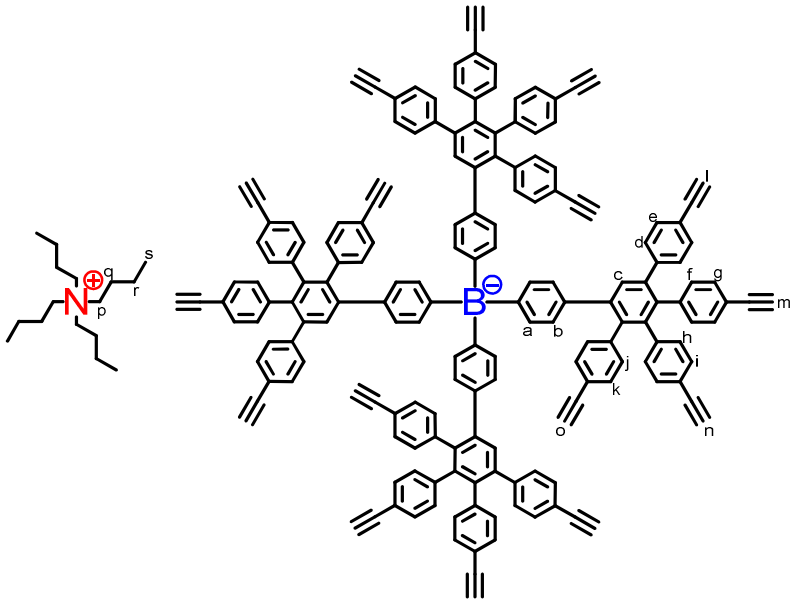

To a solution of 143 mg (0.028 mmol) $TBA^{+}[B\text{-}G1(in\text{-}T\mathit{i}PS)_{16}]^{-}$ **19** in THF (25 mL) was added dropwise a solution of tetrabutylammonium fluoride (161 mg, 0.460 mmol) in THF (15 mL). The mixture was stirred for 2 h at room temperature. After washing 3 times with a concentrated aqueous solution of sodium chloride, the solution was filtered over silica and the solvent removed under vacuum. The remainder was dissolved in methylene chloride, precipitated in hexane, filtered and dried to afford 62 mg (0.025 mmol, 87%) of the product as a pale yellow powder.

^{1}H-NMR (300 MHz, THF-d8, 298 K) δ 7.61 (s, 4H, H^{c}), 7.26 (d, $^{3}J_{HH}$ = 8.4 Hz, 8H, H^{d}), 7.14 (d, $^{3}J_{HH}$ = 8.3 Hz, 8H, H^{e}), 7.06 (d, $^{3}J_{HH}$ = 8.3 Hz, 4H, H^{j}), 7.00 (d, $^{3}J_{HH}$ = 8.3 Hz, 8H, H^{f}), 6.99 (d, $^{3}J_{HH}$ = 8.3 Hz, 8H, H^{h}), 6.96 (m, 8H, H^{a}), 6.82 (d, $^{3}J_{HH}$ = 8.3 Hz, 8H, H^{k}), 6.78 (d, $^{3}J_{HH}$ = 8.4 Hz, 8H, H^{g}), 6.77 (d, $^{3}J_{HH}$ = 8.3 Hz, 8H, H^{i}), 6.71 (d, $^{3}J_{HH}$ = 8.1 Hz, 8H, H^{b}), 3.47 (s, 4H,

C≡C-*H*), 3.39 (s, 4H, C≡C-*H*), 3.35 (s, 4H, C≡C-*H*), 3.12 (m, 8H, H^p), 2.79 (s, 4H, C≡C-*H*, H^o), 1.58 (m, 8H, H^q), 0.94 (t, $^3J_{HH}$ = 7.3 Hz, 12H, H^s)

^{13}C-NMR (75 MHz, THF-d8, 298 K) δ 163.61 (q, $^1J_{BC}$ = 49.5 Hz), 145.54, 143.57, 142.42, 142.16, 141.99, 141.27, 140.69, 140.08, 137.80, 136.80 (C^a), 134.75, 133.02 (C^c), 132.79 (*C*-H), 132.72 (*C*-H), 132.58 (*C*-H),, 132.30 (*C*-H), 131.78 (*C*-H), 131.49 (*C*-H), 131.04 (*C*-H), 130.87 (*C*-H), 127.75 (C^b), 121.53 (*C*-C≡C-H), 120.99 (*C*-C≡C-H), 120.72 (*C*-C≡C-H), 120.54 (*C*-C≡C-H), 85.04 (C-*C*≡C-H), 84.59 (C-*C*≡C-H), 84.53 (C-*C*≡C-H), 84.40 (C-*C*≡C-H), 79.02 (C-C≡*C*-H), 78.71 (C-C≡*C*-H), 78.50 (C-C≡*C*-H), 77.92 (C-C≡*C*-H), 59.36 (C^p), 24.64 (C^q), 20.70 (C^r), 14.11 (C^s)

MALDI-TOF (m/z): calcd. for $C_{176}H_{100}B^-$: 2224.8, found: 2224.5

Lithium tetrakis(2,3,5,6-tetrafluoro-4-((triisopropylsilyl)ethynyl)phenyl)borate Li^+ [$B(Ph^F$-in-T*i*PS$)_4]^-$ **(51)**

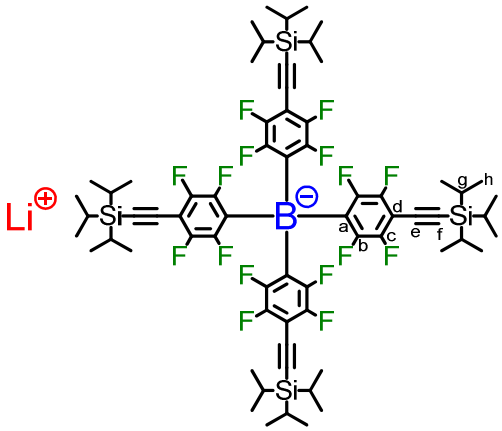

5.00 g (15.13 mmol) triisopropyl((2,3,5,6-tetrafluorophenyl)ethynyl)silane **50** were dissolved in 20 mL anhydrous diethyl ether under argon. The solution was cooled to -78 °C and one equivalent *n*-Butyllithium (9.46 mL of a 1.6 M solution in hexane) was added dropwise. After one hour 0.25 equivalents BCl_3 (3.78 mL of a 1 M solution in heptane) were slowly added. The mixture was allowed to warm to room temperature over night, whereupon a white suspension was obtained. After removal of the solvent in vacuo, the white precipitate was dissolved in methylene chloride and precipitated in hexane two times. The precipitate was filtered, washed with hexane and dried to afford 2.616 g (52%) of the pure compound as a white powder.

^{1}H-NMR (500 MHz, $C_2D_2Cl_4$, 298 K) δ 1.08 (m, 84H, H^g + H^h)

^{13}C-NMR: not resolved due to C-F coupling

^{19}F-NMR (471 MHz, $C_2D_2Cl_4$, 298 K) δ -133.06 (s, 8F, F^b), -141.04 (s, 8F, F^c)

^{11}B-NMR (160 MHz, $C_2D_2Cl_4$, 298 K) δ -15.94

MALDI-TOF (m/z): calcd. for $C_{68}H_{84}BF_{16}Si_4^-$: 1327.6, found: 1327.7 [M^-]

Tetrabutylammonium tetrakis(4-ethynyl-2,3,5,6-tetrafluorophenyl)borate $TBA^+ [B(Ph^F\text{-in})_4]^-$ **(52)**

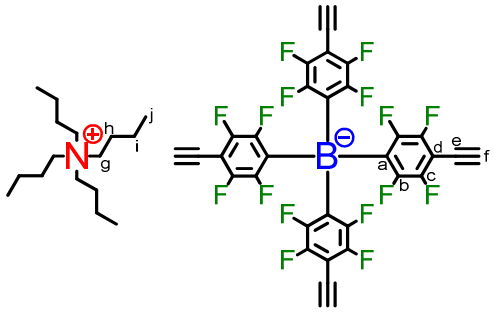

To a solution of 1,500 g (1.123 mmol) $Li^+[B(Ph^F\text{-in-T}i\text{PS})_4]^-$ **51** in THF (50 mL) was added dropwise a solution of tetrabutylammonium fluoride (1.882 g, 6.739 mmol) in THF (50 mL). The mixture was stirred for 2 h at room temperature. After washing 3 times with a concentrated aqueous solution of sodium chloride, the THF solution was filtered over silica and the solvent removed under vacuum. The remainder was dissolved in methylene chloride, filtered over silica, precipitated in hexane two times and dried to afford 981 mg (0.802 mmol, 71%) of the pure compound as a colorless solid.

^{1}H-NMR (500 MHz, THF-d8, 298 K) δ 4.03 (s, 4H, H^f), 3.21 (m, 8H, H^g), 1.66 (m, 8H, H^h), 1.37 (m, 8H, H^i), 0.95 (t, $^3J_{HH}$ = 7.3 Hz, 12H, H^j)

^{13}C-NMR (126 MHz, THF-d8, 298 K) δ 149.24 (d, $^1J_{CF}$ = 244.1 Hz, C^b), 147.34 (d, $^1J_{CF}$ = 244.1 Hz, C^c), 133.87 (n.r., C^a), 99.60 (t, $^2J_{CF}$ = 17.7 Hz, C^d), 89.23 (s, C^f), 71.16 (s, C^e), 59.41 (C^g), 24.60 (C^h), 20.66 (C^i), 13.97 (C^j)

^{19}F-NMR (471 MHz, THF-d8, 298 K) δ -130.43 (s, 8F, F^b), -140.90 (s, 8F, F^c)

^{11}B-NMR (225 MHz, $C_2D_2Cl_4$, 298 K) δ -15.95

MALDI-TOF (m/z): calcd. for $C_{32}H_4BF_{16}^-$: 703.0, found: 703.1 [M^-]

XRD: $(TBA^+)_2Cl^-(B(Ph^F\text{-in})_4)^-$ colorless needles, monoclinic, Pc

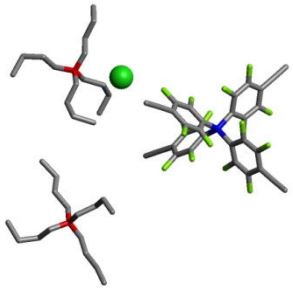

Tetrabutlyammonium tetrakis(2,3,5,6-tetrafluoro-4-(G1)phenyl)borate (53) $TBA^+ [B^F\text{-}G1]^-$

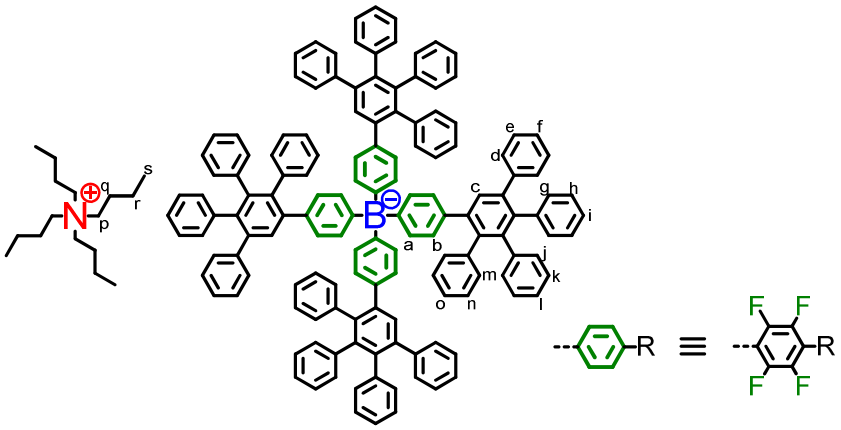

100 mg (0.106 mmol) of $TBA^+B(Ph^F\text{-}in)_4^-$ **52** and 183 mg (0.476 mmol) tetraphenylcyclopentadienone were dissolved in diglyme (15 mL) in a microwave tube. The argon bubbled mixture was stirred at 170 °C for 16 h. After cooling to room temperature, the mixture was purified by column chromatography using firstly a 4:1 mixture of hexane and ethyl acetate and then THF as eluent. After removal of the solvent, the crude product was dissolved in methylene chloride, precipitated in hexane, filtered and dried in vacuum to afford 221 mg (0.093 mmol, 88%) pure compound as a beige powder.

^{1}H-NMR (500 MHz, THF-d8, **298 K**) δ 7.54 – 7.44 (≥12 s, 4H, H^c), 7.22 – 7.01 (m, 20H, H^d + H^e + H^f), 6.97 – 6.57 (m, 60H, H^g – H^o), 3.19 (m, 6.24H, H^p), 2.98 (m, 1.76H, H^p), 1.63 (m, 8H, H^q), 1.36 (m, 8H, H^r), 0.97 (t, $^3J_{HH}$ = 7.4 Hz, 9.36H, H^s), 0.94 (t, $^3J_{HH}$ = 7.4 Hz, 2.64H, H^s)

^{1}H-NMR (500 MHz, $C_2D_2Cl_4$, **413 K**) δ 7.41 (s, 4H, H^c), 7.16 (d, $^3J_{HH}$ = 7.7 Hz, 8H, H^d), 7.09 (t, $^3J_{HH}$ = 7.2 Hz, 8H, H^e), 7.06 (t, $^3J_{HH}$ = 7.2 Hz, 4H, H^f), 6.89 – 6.73 (m, 60H, H^g – H^o), 2.89 (m, 8H, H^p), 1.46 (m, 8H, H^q), 1.28 (m, 8H, H^r), 0.88 (t, $^3J_{HH}$ = 7.4 Hz, 12H, H^s)

^{13}C-NMR (176 MHz, $C_2D_2Cl_4$, 298 K) δ 149.05, 147.71, 143.28, 141.68, 140.57, 140.45, 140.31, 140.08, 139.29, 132.21 (C^c), 131.83, 130.55, 130.31 (C^d), 128.78, 127.81 (C^e), 127.20,

127.01, 126.89, 126.46 (C^f), 126.12, 125.81, 125.51, 115.84, 59.00 + 53.86 (C^p), 25.79 + 23.83 (C^q), 19.82 + 19.78 (C^r), 13.71 + 13.62 (C^s)

^{19}F-NMR (471 MHz, THF-d8, 298 K) δ -132.13 – -134.03 (m, 8F, F^a), -146.50 – -147.91 (m, 8F, F^b)

^{11}B-NMR (160 MHz, THF-d8, 298 K) δ -16.64

DOSY-NMR (700 MHz, THF-d8, 298 K) D_{borate} = 4.17·10^{-10} m^{2}s^{-1}; r_H = 1.05 nm

MALDI-TOF (m/z): calcd. for $C_{144}H_{84}BF_{16}^-$: 2128.6, found: 2128.0 [M$^-$]

Tetrabutlyammonium tetrakis(2,3,5,6-tetrafluoro-4-((bis(triisopropylsilylethynyl))G1)phenyl)-borate TBA^+ $[B^F\text{-}G1(in\text{-}T\mathit{i}PS)_8]^-$ **(54)**

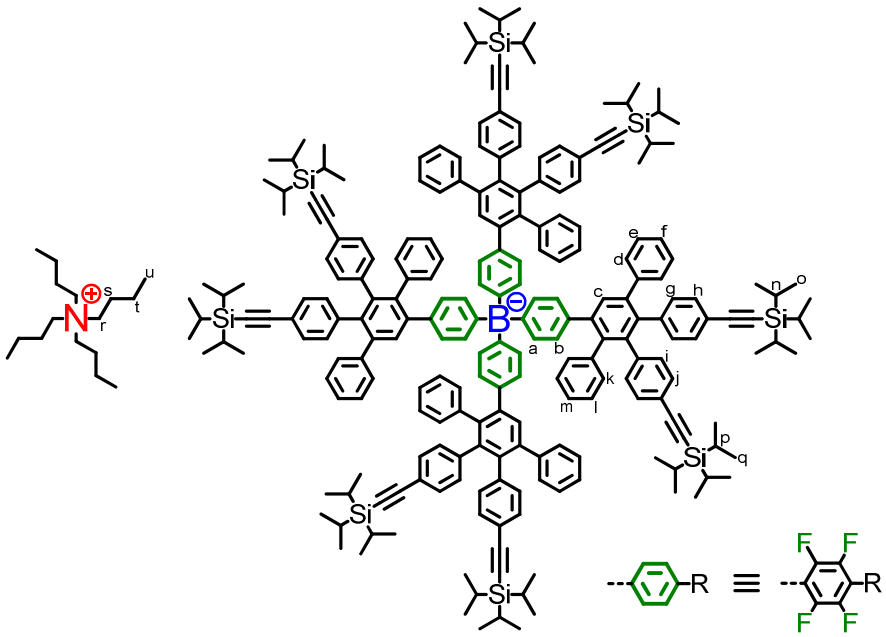

100 mg (0.106 mmol) of $TBA^+B(Ph^F\text{-}in)_4^-$ **52** and 355 mg (0.476 mmol) AB_2 building block **1** were dissolved in diglyme (15 mL) in a microwave tube. The argon bubbled mixture was stirred at 170 °C for 16 h. After cooling to room temperature, the mixture was purified by column chromatography using firstly a 10:1 mixture of hexane and ethyl acetate and then THF as eluent. The solvent was removed in vacuum to afford 366 mg (0.096 mmol, 91%) of the compound as an orange solid.

^{1}H-NMR (300 MHz, THF-d8, 298 K) δ 7.55 – 7.44 (≥11 s, 4H, H^c), 7.23 – 6.57 (72H, H^d – H^m), 3.18 (m, 4.48H, H^r), 3.10 (m, 3.52H, H^r), 1.63 (m, 8H, H^s), 1.36 (m, 8H, H^t), 1.11 (m, 168H, H^n – H^q), 0.97 (t, $^3J_{HH}$ = 7.4 Hz, 6.72H, H^u), 0.95 (t, $^3J_{HH}$ = 7.4 Hz, 5.28H, H^u)

^{13}C-NMR (75 MHz, THF-d8, 298 K) δ 141.61, 132.58, 131.59, 131.36, 130.86, 128.45, 127.77, 127.18, 121.61, 121.35, 108.77, 108.46, 90.07, 89.85, 59.31 (C^r), 24.49 (C^s), 20.58 (C^t), 19.09 (C^o + C^q), 13.94 (C^u), 12.30 (C^n + C^p)

^{19}F-NMR (471 MHz, THF-d8, 298 K) δ -130.76 – -133.03 (m, 8F, F^a), -144.95 – -146.81 (m, 8F, F^b)

^{11}B-NMR (225 MHz, THF-d8, 298 K) δ -15.62

MALDI-TOF (m/z): calcd. for $C_{232}H_{244}BF_{16}Si_8^-$: 3570.7, found: 3570.9 [M^-]

Tetrabutlyammonium tetrakis(2,3,5,6-tetrafluoro-4-((bis(ethynyl))G1)phenyl)borate

TBA^+ $[B^F\text{-}G1(in)_8]^-$ (**55**)

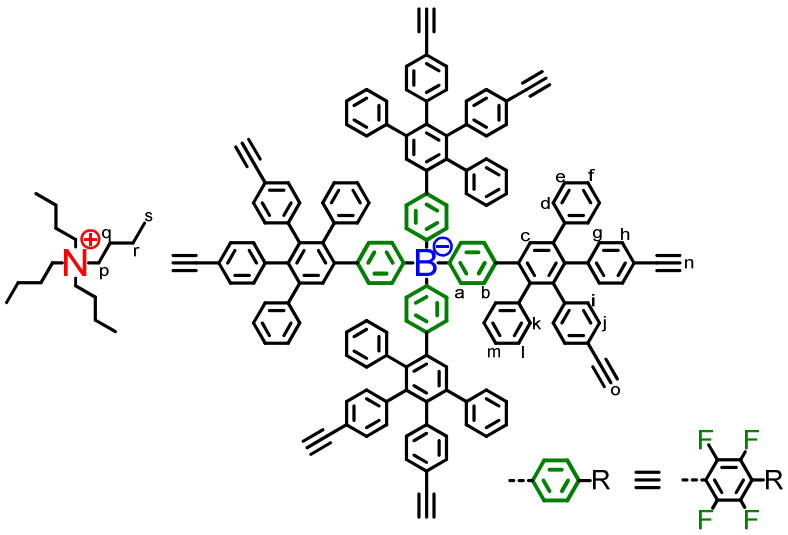

To a solution of 200 mg (0.052 mmol) $TBA^+[B^F\text{-}G1(in\text{-}T\mathit{i}PS)_8]^-$ **54** in THF (25 mL) was added dropwise a solution of tetrabutylammonium fluoride (1.464 g, 0.524 mmol) in THF (25 mL). The mixture was stirred for 2 h at room temperature. After washing 3 times with a concentrated aqueous solution of sodium chloride, the solution was filtered over silica and the solvent removed under vacuum. The remainder was dissolved in methylene chloride, precipitated in hexane, filtered and dried to afford 124 mg (0.048 mmol, 92%) of the product as colorless powder.

^{1}H-NMR (500 MHz, $C_2D_2Cl_4$, **413 K**) δ 7.47 (s, 4H, H^c), 7.16 (m, 20H, H^d + H^e + H^f), 7.09 (d, $^3J_{HH}$ = 7.7 Hz, 8H, H^g), 7.03 (d, $^3J_{HH}$ = 7.3 Hz, 8H, H^i), 7.00 – 6.62 (m, 20H, H^k + H^l + H^m), 6.85 (d, $^3J_{HH}$ = 6.6 Hz, 8H, H^h), 6.80 (d, $^3J_{HH}$ = 6.6 Hz, 8H, H^j), 2.97 (s, 4H, C≡C-*H*), 2.94 (s, 4H, C≡C-*H*), 2.92 (m, 8H, H^p), 1.49 (m, 8H, H^q), 1.31 (m, 8H, H^r), 0.92 (t, $^3J_{HH}$ = 7.3 Hz, 12H, H^s)

^{13}C-NMR (176 MHz, THF-d8, **298 K**) δ 149.96, 148.66, 144.03, 143.07, 142.79, 142.74, 142.46, 142.37, 142.06, 141.83, 141.70, 141.50, 141.42, 140.41, 140.35, 140.27, 139.91, 139.79, 132.77, 131.67, 131.12, 131.01, 128.57, 127.28, 120.99, 120.74, 115.91, 84.58, 78.63, 78.61, 78.49, 78.41, 59.40 (C^p), 24.62 (C^q), 20.70 (C^r), 14.05 (C^s)

^{13}C-NMR (126 MHz, $C_2D_2Cl_4$, **413 K**) δ 149.61, 147.65, 142.21, 141.53, 141.21, 140.96, 140.86, 140.73, 139.63, 138.89, 132.22, 131.67, 131.01, 130.76, 130.11, 129.83, 127.76, 127.02, 126.61, 119.93, 119.65, 115.38, 84.58, 84.51, 77.05, 76.88, 59.90 (C^p), 24.13 (C^q), 19.69 (C^r), 13.15 (C^s)

^{19}F-NMR (471 MHz, THF-d8, 298 K) δ -130.70 – -132.73 (m, 8F, F^a), -145.05 – -146.68 (m, 8F, F^b)

^{11}B-NMR (225 MHz, THF-d8, 298 K) δ -15.64

MALDI-TOF (m/z): calcd. for $C_{160}H_{84}BF_{16}^-$: 2320.6, found: 2320.9 [M^-]

Tetrabutlyammonium tetrakis(2,3,5,6-tetrafluoro-4-(G2^2)phenyl)borate (56) TBA^+ $[B^F\text{-}G2^2]^-$

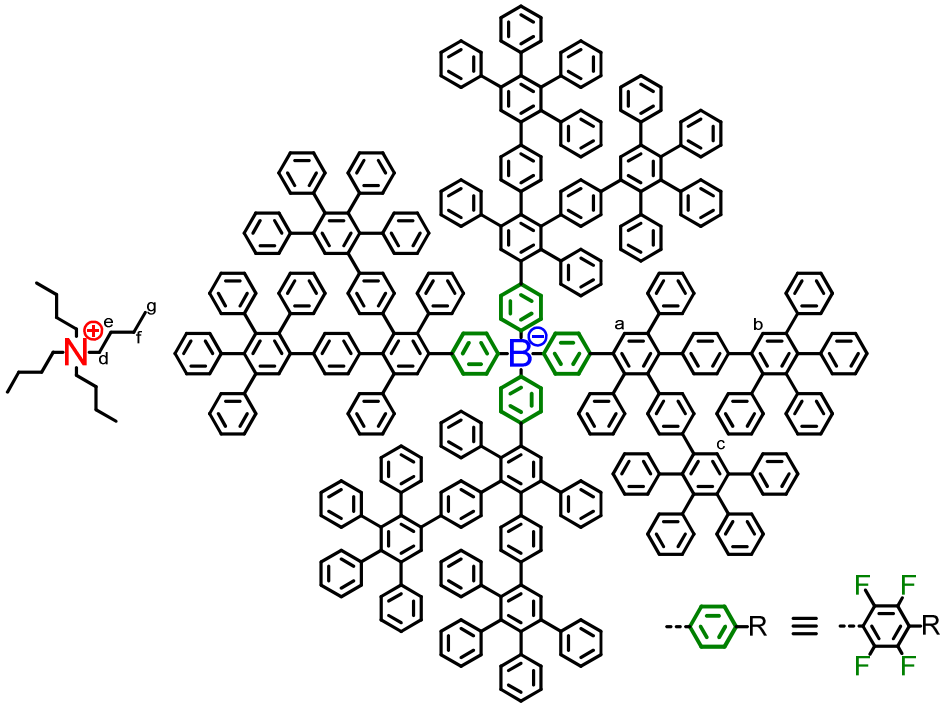

50 mg (0.020 mmol) of $TBA^+[B^F\text{-}G1(in)_8]^-$ **55** and 75 mg (0.195 mmol) tetraphenylcyclopentadienone were dissolved in diglyme (5 mL) in a microwave tube. The argon bubbled mixture was stirred at 170 °C for 16 h. After cooling to room temperature, the mixture was purified by column chromatography using firstly a 10:1 mixture of hexane and ethyl acetate and then

THF as eluent. After removal of the solvent in vacuum, the crude product was dissolved in methylene chloride, precipitated in hexane, filtered and dried to afford 71 mg (0.013 mmol, 67%) pure compound as a colorless powder.

^{1}H-NMR (700 MHz, THF-d8, **298 K**) δ 7.51 – 7.39 (≥16 s, 12H, H^a + H^b + H^c), 7.20 – 7.02 (m, 60H), 7.00 – 6.44 (m, 172H), 3.33 (m, 2.96H, H^d), 3.18 (m, 5.04H, H^d), 1.62 (m, 8H, H^e), 1.35 (m, 8H, H^f), 0.96 (t, $^{3}J_{HH}$ = 7.4 Hz, 4.44H, H^g), 0.95 (t, $^{3}J_{HH}$ = 7.4 Hz, 7.56H, H^g)

^{1}H-NMR (500 MHz, $C_2D_2Cl_4$, **413 K**) δ 7.43 (s, 4H), 7.38 (s, 8H), 7.19 – 7.03 (m, 60H), 6.93 – 6.50 (m, 172H), 2.89 (m, 8H, H^d), 1.45 (m, 8H, H^e), 1.28 (m, 8H, H^f), 0.88 (t, $^{3}J_{HH}$ = 7.2 Hz, 12H, H^g)

^{13}C-NMR (126 MHz, THF-d8, 298 K) δ 143.08, 142.86, 141.96, 141.72, 141.66, 141.40, 141.25, 141.20, 140.31, 132.73, 132.63, 132.39, 132.07, 130.91, 129.69, 128.44, 127.87, 127.76, 127.47, 127.03, 126.63, 126.36, 126.14, 59.36 (C^d), 24.58 (C^e), 20.78 + 20.67 (C^f), 14.21 + 14.06 (C^g)

^{19}F-NMR (471 MHz, THF-d8, 298 K) δ -130.26 – -132.29 (m, 8F, F^a), -144.75 – -146.29 (m, 8F, F^b)

^{11}B-NMR (160 MHz, THF-d8, 298 K) δ -14.78

DOSY-NMR (700 MHz, THF-d8, 298 K) D_{borate} = $2.75 \cdot 10^{-10}$ m^2s^{-1}; r_H = 1.58 nm

MALDI-TOF (m/z): calcd. for $C_{384}H_{244}BF_{16}^-$: 5172.9, found: 5172.1 [M^-]

Tetrabutlyammonium tetrakis(2,3,5,6-tetrafluoro-4-((tetrakis(triisopropylsilylethynyl))G1)-phenyl)borate TBA^+ $[B^F\text{-}G1(in\text{-}T\mathit{i}PS)_{16}]^-$ **(60)**

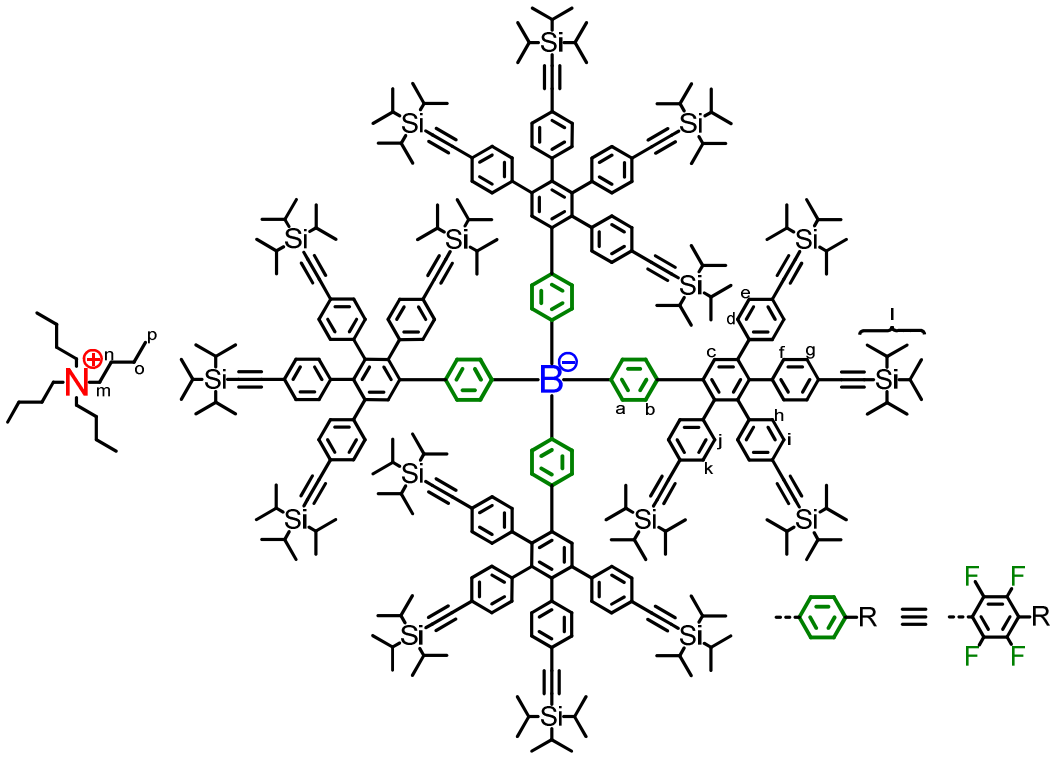

100 mg (0.106 mmol) of $TBA^+B(Ph^F\text{-}in)_4^-$ **52** and 526 mg (0.476 mmol) AB_4 building block **2** were dissolved in diglyme (15 mL) in a microwave tube. The argon bubbled mixture was stirred at 170 °C for 16 h. After cooling to room temperature, the mixture was purified by column chromatography using firstly a 10:1 mixture of hexane and ethyl acetate and then THF as eluent. The solvent was removed in vacuum to afford 362 mg (0.069 mmol, 65%) of the compound as an orange solid.

^{1}H-NMR (300 MHz, THF-d8, 298 K): δ 7.58 – 7.45 (≥5 s, 4H, H^c), 7.32 – 6.64 (m, 64H, H^d – H^k), 3.13 (m, 8H, H^m), 1.65 (m, 8H, H^n), 1.36 (m, 8H, H^o), 1.16 – 1.06 (m, 336H, H^l), 0.98 (t, $^3J_{HH}$ = 7.4 Hz, H^p)

^{13}C-NMR (75 MHz, THF-d8, 298 K) δ 142.76, 141.50, 141.05, 140.45, 140.11, 132.62, 132.33, 131.91, 131.66, 131.09, 122.73, 122.52, 122.06, 121.81, 108.81, 90.75, 90.51, 90.29, 59.44 (C^m), 24.64 (C^n), 20.73 (C^o), 19.23, 14.07 (C^p), 12.45

^{19}F-NMR (471 MHz, THF-d8, 298 K) δ -130.67 – -136.48 (m, 8F, F^a), -146.01 – -148.21 (m, 8F, F^b)

^{11}B-NMR (225 MHz, THF-d8, 298 K) δ -14.62

MALDI-TOF (m/z): calcd. for $C_{320}H_{404}BF_{16}Si_{16}^-$: 5013.8, found: 5014.3 [M^-]

Tetrabutlyammonium tetrakis(2,3,5,6-tetrafluoro-4-((tetrakis(ethynyl))G1)phenyl)borate

TBA^+ $[B^F\text{-}G1(in)_{16}]^-$ (**61**)

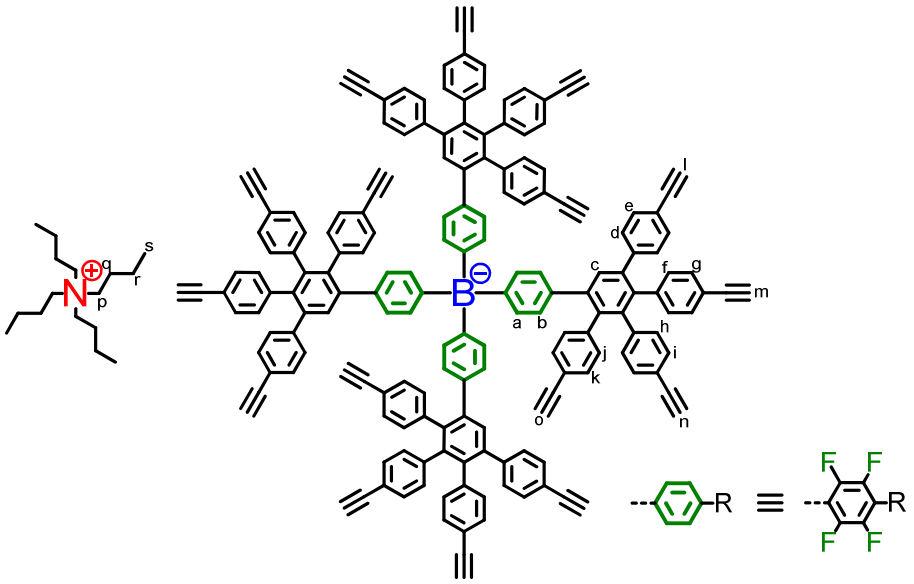

To a solution of 200 mg (0.038 mmol) $TBA^+[B^F\text{-}G1(in\text{-}T\mathit{i}PS)_{16}]^-$ **60** in THF (25 mL) was added dropwise a solution of tetrabutylammonium fluoride (2.125 g, 0.761 mmol) in THF (25 mL). The mixture was stirred for 2 h at room temperature. After washing 3 times with a concentrated aqueous solution of sodium chloride, the solution was filtered over silica and the solvent removed under vacuum. The remainder was dissolved in methylene chloride, precipitated in hexane, filtered and dried to afford 92 mg (0.033 mmol, 88%) of the product as colorless powder.

^{1}H-NMR (300 MHz, THF-d8, 298 K) δ 7.66 – 7.50 (≥5 s, 4H, H^c), 7.30 – 6.64 (m, 64H, H^d – H^k), 3.46 (s, 4H, C≡C-*H*), 3.40 (s, 4H, C≡C-*H*), 3.36 (s, 4H, C≡C-*H*), 3.18 (m, 8H, H^p), 3.00 (s, 4H, C≡C-*H*), 1.62 (m, 8H, H^q), 1.34 (m, 8H, H^r), 0.95 (t, $^3J_{HH}$ = 7.4 Hz, 12H, H^s)

^{13}C-NMR (75 MHz, THF-d8, 298 K) δ 142.64, 142.41, 142.17, 141.72, 141.41, 141.04, 140.37, 132.62, 132.30, 131.86, 131.60, 131.14, 130.35, 126.67, 121.76, 121.32, 121.04, 84.46, 84.42, 78.89, 59.41 (C^p), 24.61 (C^q), 20.69 (C^r), 14.07(C^s)

^{19}F-NMR (471 MHz, THF-d8, 298 K) δ -129.56 – -132.69 (m, 8F, F^a), -144.31 – -146.42 (m, 8F, F^b)

^{11}B-NMR (225 MHz, THF-d8, 298 K) δ -15.49

MALDI-TOF (m/z): calcd. for $C_{176}H_{84}BF_{16}^-$: 2513.7, found: 2510.5 [M^-]

Tetrabutlyammonium tetrakis(2,3,5,6-tetrafluoro-4-(G2^4)phenyl)borate (62) $TBA^+ [B^F\text{-}G2^4]^-$

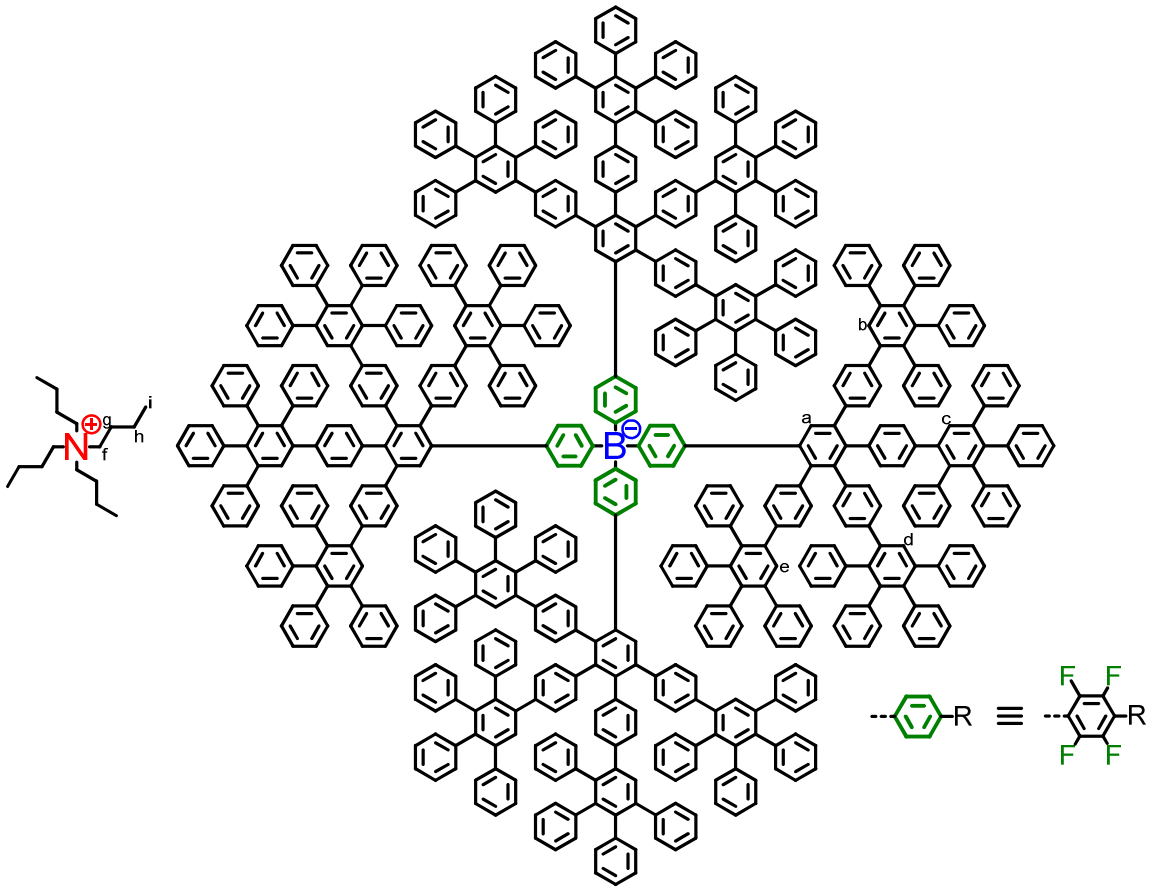

50 mg (0.018 mmol) of $TBA^+[B^F\text{-}G1(in)_{16}]^-$ **61** and 140 mg (0.363 mmol) tetracyclone were dissolved in diglyme (5 mL) in a microwave tube. The argon bubbled mixture was stirred at 170 °C for 16 h. After cooling to room temperature, the mixture was purified by column chromatography using firstly a 10:1 mixture of hexane and ethyl acetate and then THF as eluent. After removal of the solvent in vacuum, the crude product was dissolved in methylene chloride, precipitated in hexane, filtered and dried to afford 103 mg (0.012 mmol, 67%) pure compound as a colorless powder.

^{1}H-NMR (700 MHz, THF-d8, 298 K) δ 7.56 – 7.44 (≥5 s, 20H, H^a – H^e), 7.20 – 6.29 (m, 384H), 3.20 (m, 5.12H, H^f), 3.06 (m, 2.88H, H^f), 1.64 (m, 8H, H^g), 1.36 (m, 8H, H^h), 0.96 (t, $^3J_{HH}$ = 7.4 Hz, 7.68H, H^i), 0.93 (t, $^3J_{HH}$ = 7.4 Hz, 4.32H, H^i)

^{13}C-NMR (75 MHz, THF-d8, 298 K) δ 143.09, 142.86, 142.10, 141.89, 141.81, 141.51, 141.21, 140.23, 139.49, 132.70, 132.17, 130.96, 129.84, 128.48, 127.76, 127.48, 127.03, 126.66, 126.37, 126.15, 59.43 (C^f), 24.63 (C^g), 20.70 (C^h), 14.08 (C^i)

^{19}F-NMR (471 MHz, THF-d8, 298 K) δ -128.40 (s, 0.57F), -129.74 (s, 6.85F), -133.52 (s, 0.57F), -143.43 (s, 6.85F), -144.19 (s, 0.57F), -145.31 (s, 0.57F)

^{11}B-NMR (160 MHz, THF-d8, 298 K) δ -16.63

DOSY-NMR (700 MHz, THF-d8, 298 K) D_{borate} = 2.00·10^{-10} m^{2}s^{-1}; r_H = 2.18 nm

MALDI-TOF (m/z): calcd. for $C_{624}H_{404}BF_{16}^-$: 8213.2, found: 8213.0 [M$^-$]

Tetrabutlyammonium tetrakis(2,3,5,6-tetrafluoro-4-((tetrakis(triisopropylsilylethynyl))G2^2)-phenyl)borate TBA$^+$ [B^F-G2(in-T*i*PS)$_{16}$]$^-$ (**57**)

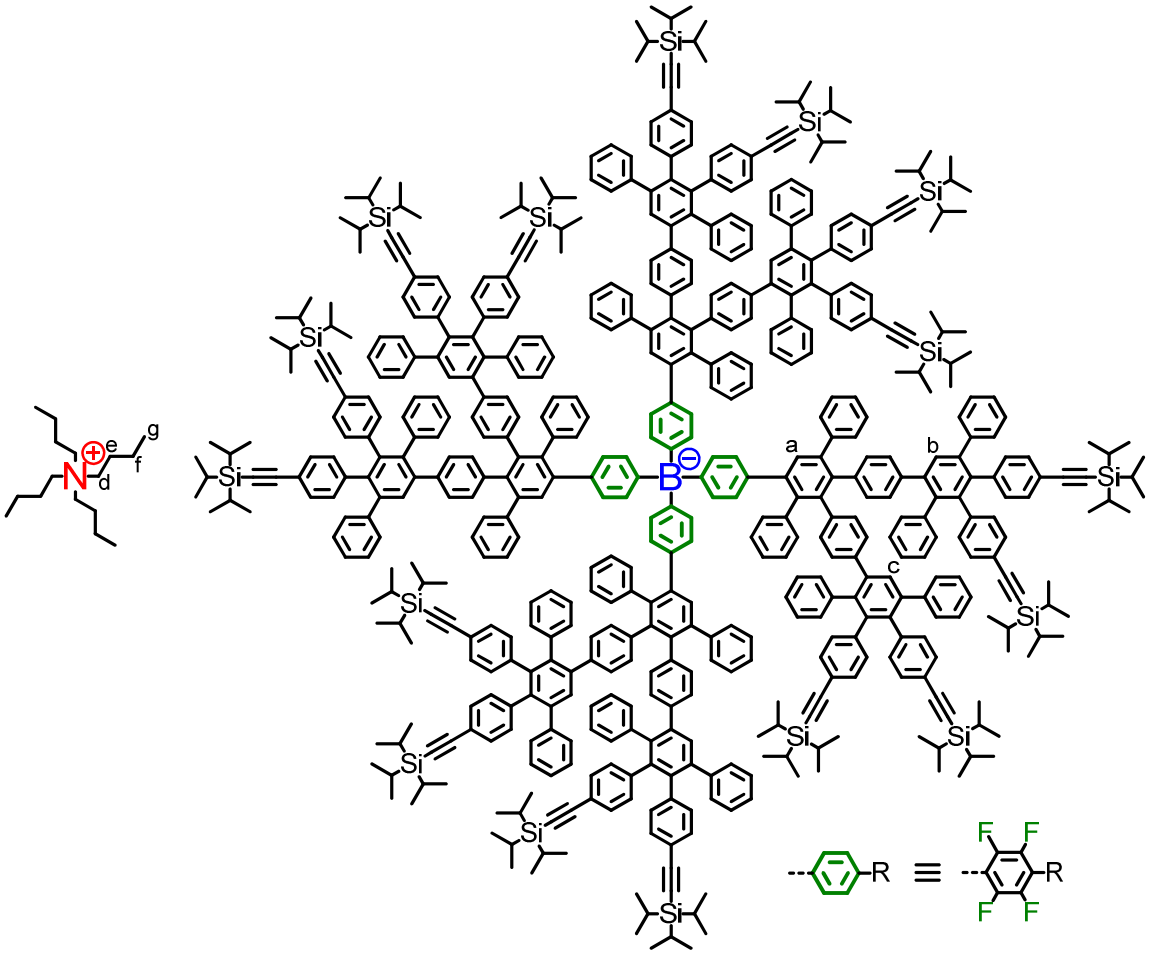

40 mg (0.016 mmol) of TBA$^+$[B^F-G1(in)$_8$]$^-$ **55** and 116 mg (0.156 mmol) AB$_2$ building block **1** were dissolved in diglyme (5 mL) in a microwave tube. The argon bubbled mixture was stirred at 170 °C for 16 h. After cooling to room temperature, the mixture was purified by column chromatography using firstly a 10:1 mixture of hexane and ethyl acetate and then THF as eluent. The

solvent was removed in vacuum to afford 75 mg (0.009 mmol, 58%) of the compound as a yellow solid.

^{1}H-NMR (300 MHz, THF-d8, 298 K) δ 7.52 – 7.32 (≥5 s, 12H, H^{a} – H^{c}), 7.19 – 6.42 (m, 216H), 3.17 (m, 8H, H^{d}), 1.62 (m, 8H, H^{e}), 1.33 (m, 8H, H^{f}), 1.10 (m, 336H, T*i*PS), 0.95 (t, $^{3}J_{HH}$ = 7.3 Hz, 12H, H^{g})

^{13}C-NMR (75 MHz, THF-d8, 298 K) δ 142.72, 142.13, 141.74, 140.83, 140.33, 139.60, 139.28, 132.59, 131.71, 131.45, 131.15, 130.83, 129.62, 128.65, 128.07, 127.38, 126.98, 121.75, 121.52, 108.83, 108.57, 90.30, 90.15, 59.35 (C^{d}), 24.59 (C^{e}), 20.67(C^{f}), 19.21, 14.05 (C^{g}), 12.42

^{19}F-NMR (471 MHz, THF-d8, 298 K) δ -131.84 – -134.23 (m, 8F), -146.33 – -148.20 (m, 8F)

^{11}B-NMR (225 MHz, THF-d8, 298 K) δ -17.51

MALDI-TOF (m/z): calcd. for $C_{560}H_{564}BF_{16}Si_{16}^{-}$: 8054.0, found: 8053.4 [M^{-}]

Tetrabutlyammonium tetrakis(2,3,5,6-tetrafluoro-4-((tetrakis(ethynyl))G2^{2})phenyl)borate

TBA^{+} [B^{F}-G2(in)$_{16}$]$^{-}$ (**58**)

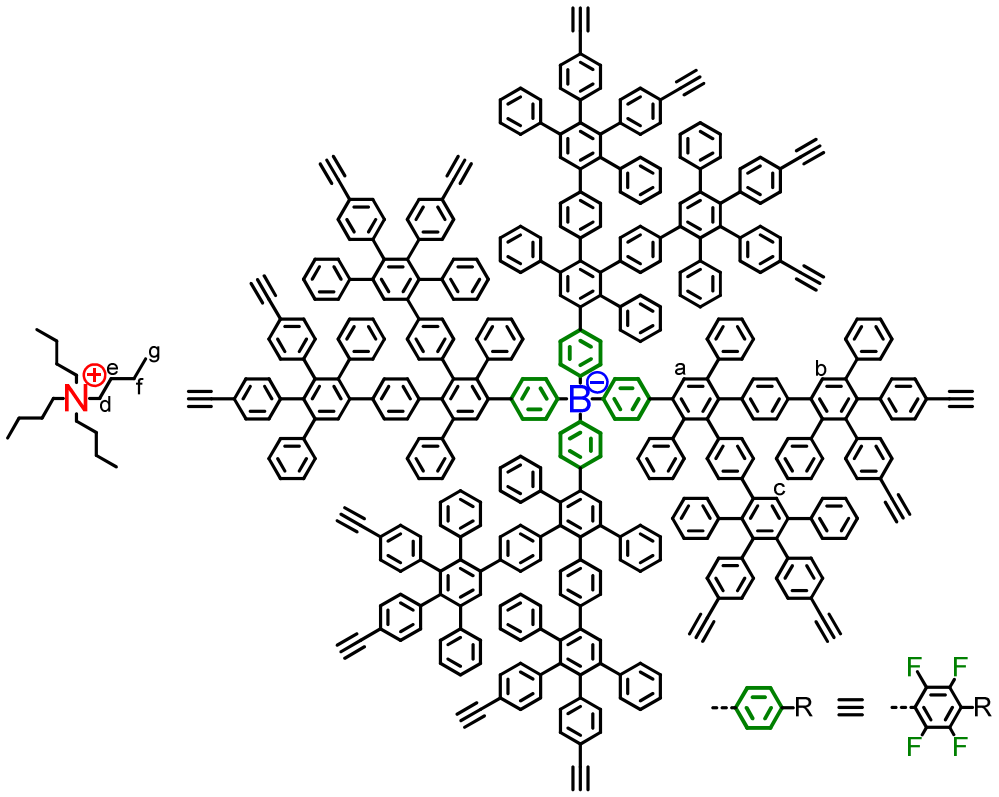

To a solution of 75 mg (0.009 mmol) TBA^{+}[B^{F}-G2(in-T*i*PS)$_{16}$]$^{-}$ **57** in THF (15 mL) was added dropwise a solution of tetrabutylammonium fluoride (51 mg, 0.181 mmol) in THF (5 mL). The

mixture was stirred for 2 h at room temperature. After washing 3 times with a concentrated aqueous solution of sodium chloride, the solution was filtered over silica and the solvent removed under vacuum. The remainder was dissolved in methylene chloride, precipitated in hexane, filtered and dried to afford 40 mg (0.007 mmol, 76%) of the product as a colorless powder.

^{1}H-NMR (300 MHz, THF-d8, 298 K) δ 7.51 – 7.39 (≥6 s, 12H, H^{a} – H^{c}), 7.19 – 6.43 (m, 216H), 3.39 (s, 4H, C≡C-*H*), 3.38 (s, 4H, C≡C-*H*), 3.36 (s, 4H, C≡C-*H*), 3.35 (s, 4H, C≡C-*H*), 3.18 (m, 8H, H^{d}), 1.62 (m, 8H, H^{e}), 1.33 (m, 8H, H^{f}), 0.95 (t, $^{3}J_{HH}$ = 7.3 Hz, 12H, H^{g})

^{13}C-NMR (75 MHz, THF-d8, 298 K) δ 142.59, 142.05, 141.77, 140.68, 140.31, 139.36, 132.63, 132.40, 131.67, 131.39, 131.14, 130.83, 128.65, 128.07, 127.36, 126.99, 121.02, 120.76, 84.49, 78.74, 78.63, 59.40 (C^{d}), 24.59 (C^{e}), 20.67 (C^{f}), 14.05 (C^{g})

^{19}F-NMR (471 MHz, THF-d8, 298 K) δ -130.27 – -132.32 (m, 8F), -144.55 – -146.32 (m, 8F)

^{11}B-NMR (225 MHz, THF-d8, 298 K) δ -17.52

MALDI-TOF (m/z): calcd. for $C_{416}H_{244}BF_{16}^{-}$: 5556.9, found: 5558.1 [M^{-}]

Tetrabutlyammonium tetrakis(2,3,5,6-tetrafluoro-4-(G3^{22})phenyl)borate $TBA^+ [B^F\text{-}G3^{22}]^-$ **(59)**

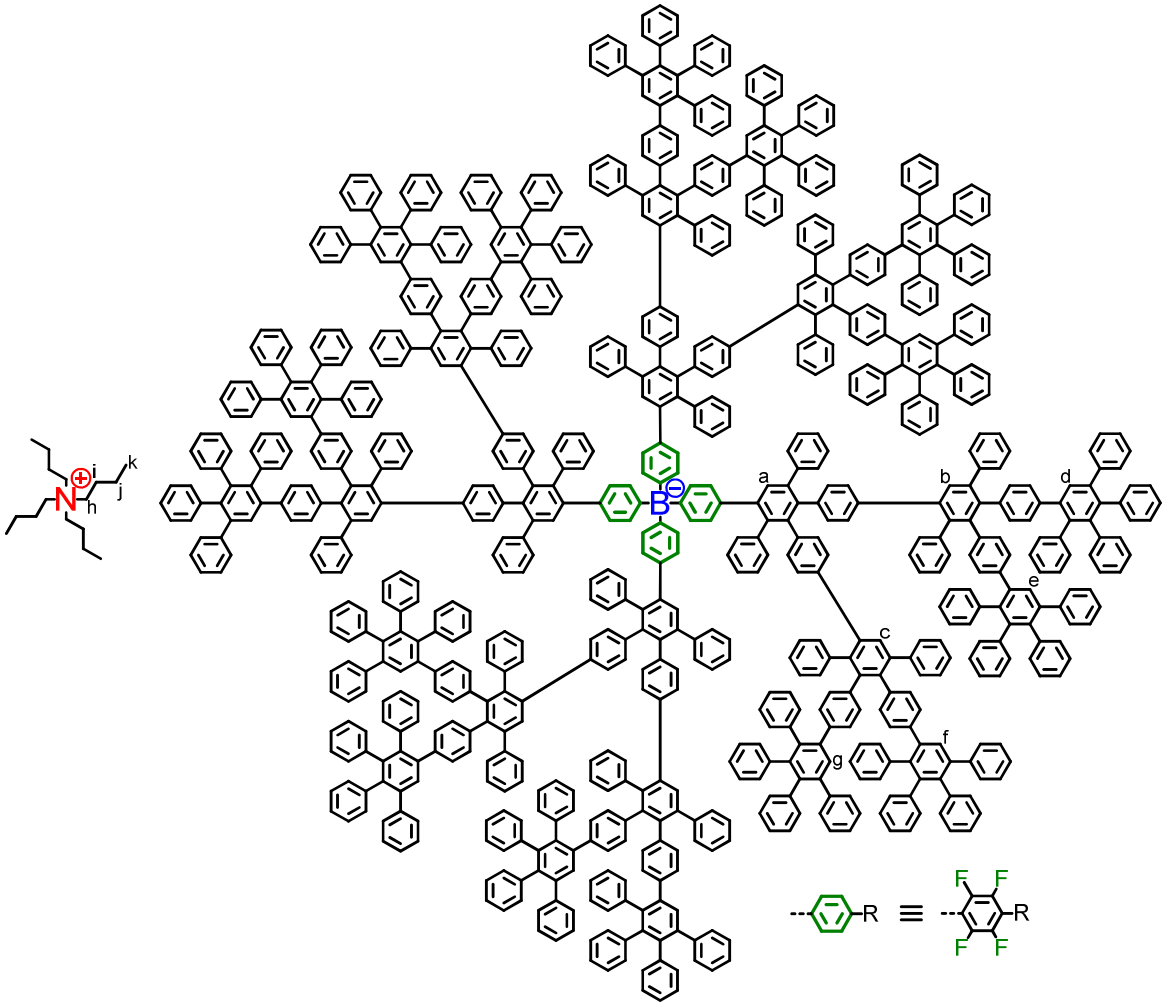

40 mg (0.007 mmol) of $TBA^+[B^F\text{-}G2(in)_{16}]^-$ **58** and 53 mg (0.138 mmol) tetracyclone were dissolved in diglyme (5 mL) in a microwave tube. The argon bubbled mixture was stirred at 170 °C for 16 h. After cooling to room temperature, the mixture was purified by column chromatography using firstly a 10:1 mixture of hexane and ethyl acetate and then THF as eluent. After removal of the solvent in vacuum, the crude product was dissolved in methylene chloride, precipitated in hexane, filtered and dried to afford 38 mg (0.003 mmol, 48%) of the compound as a colorless powder.

^{1}H-NMR (700 MHz, THF-d8, 298 K) δ 7.61 – 6.40 (m, 564H), 3.17 (m, 8H, H^h), 1.62 (m, 8H, H^i), 1.34 (m, 8H, H^j), 0.95 (t, $^3J_{HH}$ = 7.4 Hz, 12H, H^k)

^{13}C-NMR (176 MHz, THF-d8, 298 K) δ 143.05, 142.89, 141.94, 141.70, 141.37, 141.23, 140.30, 139.85, 139.54, 139.20, 132.61, 132.28, 132.10, 131.00, 130.88, 129.65, 129.38, 128.47,

127.88, 127.77, 127.48, 127.06, 126.59, 126.40, 126.16, 59.39 (C^h), 24.59 (C^i), 20.68 (C^j), 14.58 (C^k)

^{19}F-NMR (471 MHz, THF-d8, 298 K) δ -129.53 – -132.25 (m, 8F), -144.74 – -146.99 (m, 8F)

^{11}B-NMR (225 MHz, THF-d8, 298 K) δ -18.52

DOSY-NMR (700 MHz, THF-d8, 298 K) D_{borate} = 1.95·10^{-10} m^{2}s^{-1}; r_H = 2.23 nm

MALDI-TOF (m/z): calcd. for $C_{864}H_{564}BF_{16}^-$: 11260.4, found: 11266.8 [M$^-$]

Tetrabutlyammonium tetrakis(2,3,5,6-tetrafluoro-4-((octakis(triisopropylsilylethynyl))G2^2)-phenyl)borate TBA^+ $[B^F\text{-}G2(in\text{-}T\mathit{i}PS)_{32}]^-$ (**63**)

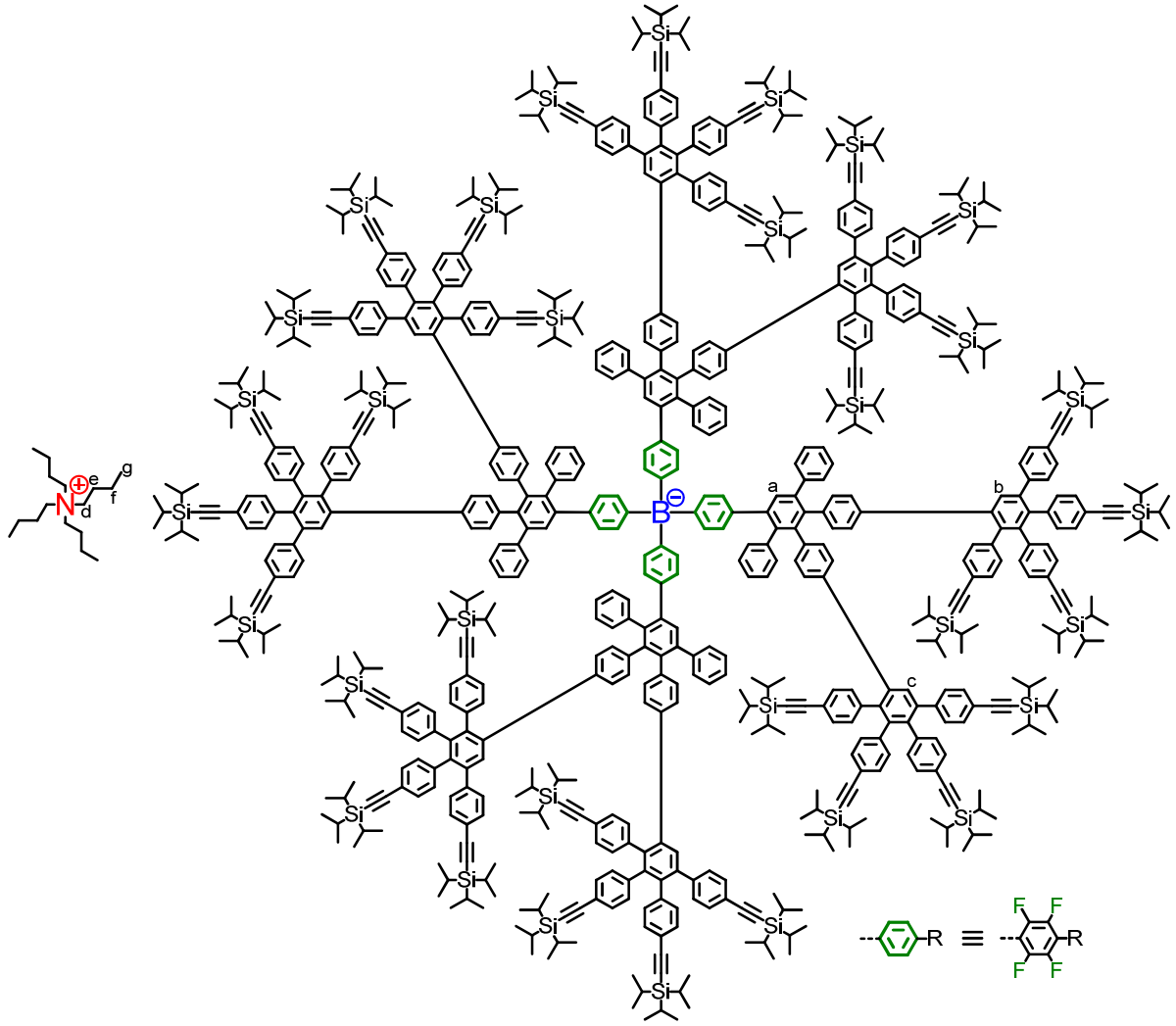

40 mg (0.016 mmol) of $TBA^+[B^F\text{-}G1(in)_8]^-$ **55** and 173 mg (0.156 mmol) AB_4 building block **2** were dissolved in diglyme (5 mL) in a microwave tube. The argon bubbled mixture was stirred at 170 °C for 16 h. After cooling to room temperature, the mixture was purified by column chromatography using firstly a 10:1 mixture of hexane and ethyl acetate and then THF as eluent. The solvent was removed in vacuum to afford 92 mg (0.008 mmol, 53%) of the compound as a yellow solid.

^{1}H-NMR (300 MHz, THF-d8, 298 K) δ 7.57 – 6.49 (m, 212H), 3.17 (m, 8H, H^d), 1.61 (m, 8H, H^e), 1.32 (m, 8H, H^f), 1.11 (m, 672H, T*i*PS), 0.95 (t, $^3J_{HH}$ = 7.3 Hz, 12H, H^g)

^{13}C-NMR (75 MHz, THF-d8, 298 K) δ 142.92, 141.97, 141.63, 141.59, 141.36, 141.27, 140.13, 140.01, 139.81, 139.29, 132.45, 131.91, 131.66, 131.02, 130.84, 129.37, 128.44, 122.67, 122.07, 121.95, 121.84, 108.71, 90.94, 90.80, 90.63, 90.45, 59.42 (C^d), 24.60 (C^e), 20.67 (C^f), 19.22, 14.06 (C^g), 12.44

^{19}F-NMR (471 MHz, THF-d8, 298 K) δ -131.91 – -134.23 (m, 8F), -146.11 – -148.21 (m, 8F)

^{11}B-NMR (225 MHz, THF-d8, 298 K) δ -17.46

MALDI-TOF (m/z): calcd. for $C_{736}H_{884}BF_{16}Si_{32}^-$: 10944.2, found: 10948.7 [M^-]

Tetrabutlyammonium tetrakis(2,3,5,6-tetrafluoro-4-((octakis(ethynyl))G2²)phenyl)borate

TBA^+ $[B^F\text{-}G2(in)_{32}]^-$ (**64**)

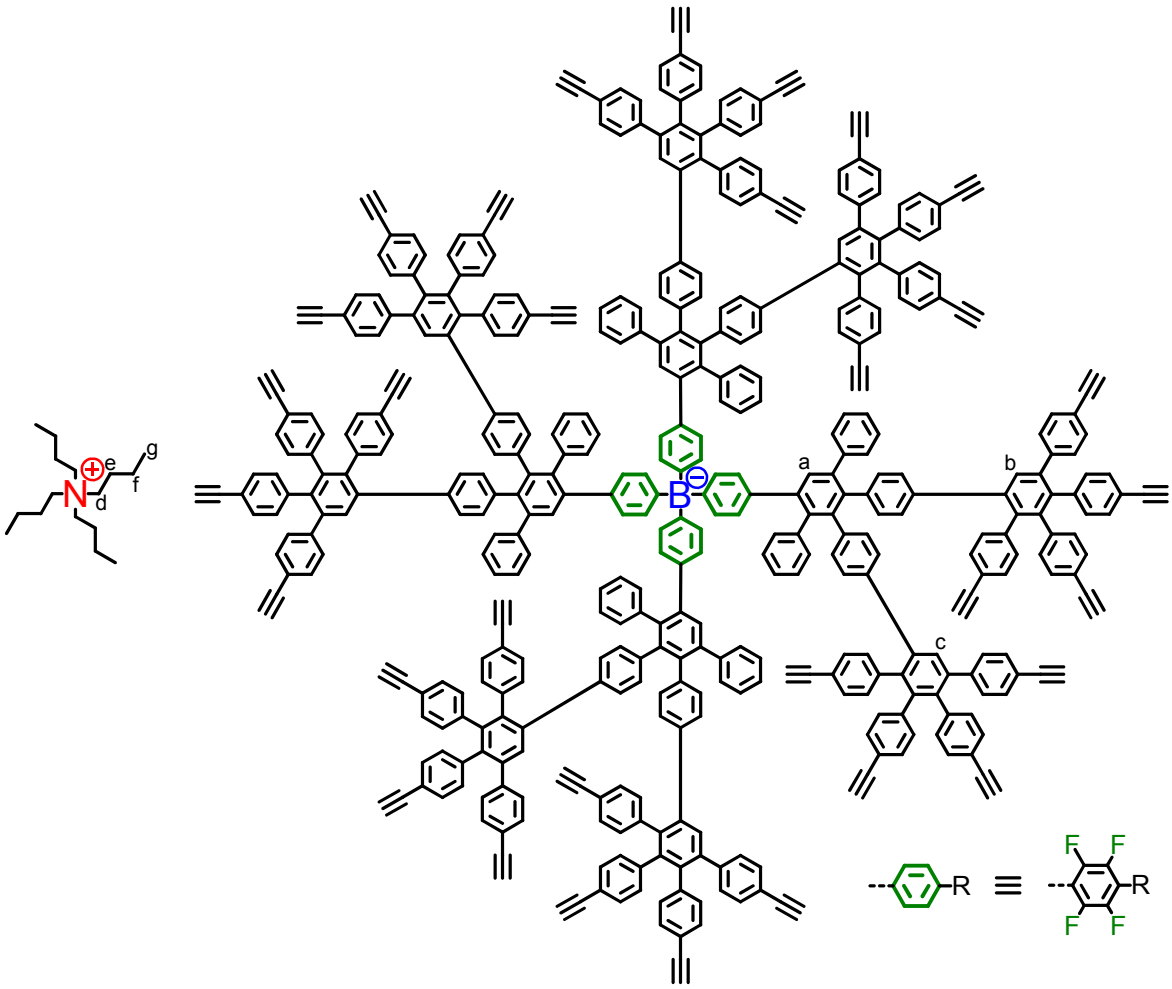

To a solution of 92 mg (0.008 mmol) $TBA^+[B^F\text{-}G2(in\text{-}T\mathit{i}PS)_{32}]^-$ **63** in THF (15 mL) was added dropwise a solution of tetrabutylammonium fluoride (92 mg, 0.329 mmol) in THF (5 mL). The mixture was stirred for 2 h at room temperature. After washing 3 times with a concentrated aqueous solution of sodium chloride, the solution was filtered over silica and the solvent removed under vacuum. The remainder was dissolved in methylene chloride, precipitated in hexane, filtered and dried to afford 42 mg (0.007 mmol, 83%) of the product as a colorless powder.

^{1}H-NMR (300 MHz, THF-d8, 298 K) δ 7.53 – 6.49 (m, 212H), 3.41 – 3.37 (m, 32H, C≡C-*H*), 3.17 (m, 8H, H^d), 1.62 (m, 8H, H^e), 1.33 (m, 8H, H^f), 0.95 (t, $^3J_{HH}$ = 7.7 Hz, 12H, H^g)

^{13}C-NMR (75 MHz, THF-d8, 298 K) δ 142.89, 142.30, 142.02, 141.95, 141.66, 141.32, 139.92, 139.39, 132.82, 132.59, 132.53, 132.36, 131.86, 131.60, 131.12, 130.92, 130.59, 129.51, 128.45, 126.07, 121.91, 121.35, 121.12, 84.40, 84.29, 79.38, 79.12, 78.86, 59.40 (C^d), 24.60 (C^e), 20.69 (C^f), 14.06 (C^g)

^{19}F-NMR (471 MHz, THF-d8, 298 K) δ -130.42 – -132.36 (m, 8F), -144.59 – -146.34 (m, 8F)

^{11}B-NMR (225 MHz, THF-d8, 298 K) δ -17.48

MALDI-TOF (m/z): calcd. for $C_{448}H_{244}BF_{16}^-$: 5940.9, found: 5942.9 [M^-]

Tetrabutlyammonium tetrakis(2,3,5,6-tetrafluoro-4-(G3^{24})phenyl)borate $TBA^+ [B^F\text{-}G3^{24}]^-$ **(65)**

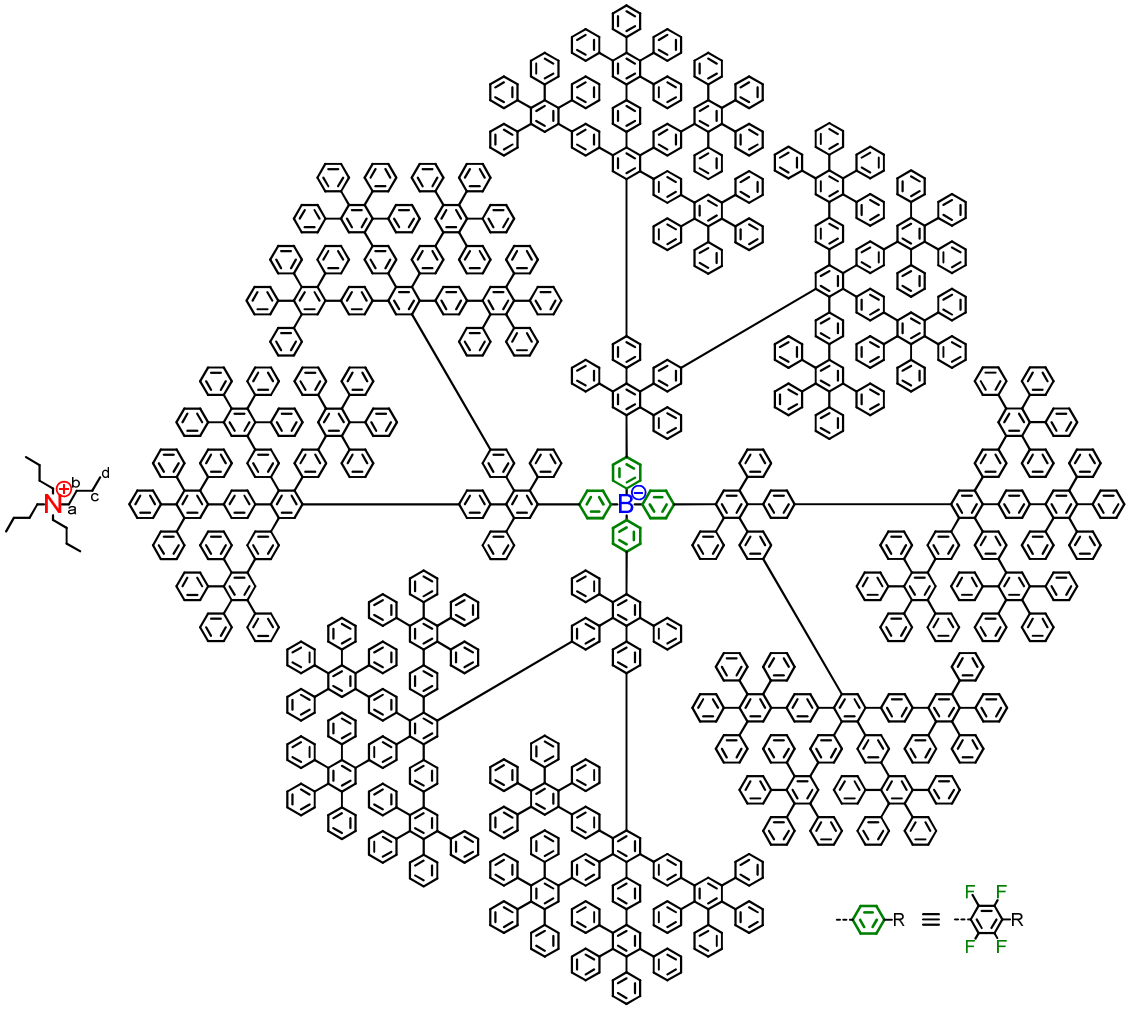

42 mg (0.007 mmol) of $TBA^+[B^F\text{-}G2(in)_{32}]^-$ **64** and 104 mg (0.272 mmol) tetracyclone were dissolved in diglyme (5 mL) in a microwave tube. The argon bubbled mixture was stirred at 170 °C for 16 h. After cooling to room temperature, the mixture was purified by column chromatography using firstly a 10:1 mixture of hexane and ethyl acetate and then THF as eluent. After removal of the solvent in vacuum, the crude product was dissolved in methylene chloride, precipitated in hexane, filtered and dried to afford 36 mg (0.002 mmol, 30%) of the compound as a colorless powder.

^{1}H-NMR (700 MHz, THF-d8, 298 K) δ 7.6 – 6.2 (m, 884H), 3.18 (m, 8H, H^{a}), 1.62 (m, 8H, H^{b}), 1.33 (m, 8H, H^{c}), 0.96 (t, $^{3}J_{HH}$ = 7.5 Hz, 12H, H^{d})

^{13}C-NMR (75 MHz, THF-d8, 298 K) δ 142.92, 141.71, 141.41, 140.29, 139.65, 138.87, 132.64, 130.94, 128.54, 127.80, 127.53, 127.06, 126.21, 59.39, 24.59, 20.68, 14.58

^{19}F-NMR (471 MHz, THF-d8, 298 K) δ -127.88 – -132.09 (m, 8F), -143.74 – -146.46 (m, 8F)

^{11}B-NMR (160 MHz, THF-d8, 298 K) δ -14.67

DOSY-NMR (700 MHz, THF-d8, 298 K) D_{borate} = 1.45·10^{-10} m^{2}s^{-1}; r_{H} = 3.01 nm

MALDI-TOF (m/z): calcd. for $C_{1344}H_{884}BF_{16}^{-}$: 17348.0, found: 17343.9 [M^{-}]

Tris-(**b**enzyl**t**riazolylmethyl)**a**mine (TBTA) (**28**)

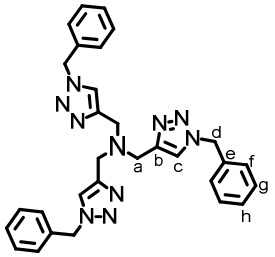

Synthesis according to literature procedure[195]

^{1}H-NMR (300 MHz, THF-d8, 298 K) δ 7.66 (s, 3H, H^{c}), 7.40 – 7.23 (n.r., 15H, H^{f} + H^{g} + H^{h}), 5.50 (s, 6H, H^{d}), 3.68 (s, 6H, H^{a})

^{13}C-NMR (75 MHz, CD_2Cl_2, 298 K) δ 144.86 (*C*, C^{b}), 135.85 (*C*, C^{e}), 129.53 (*C*-H, C^{g}), 129.04 (*C*-H, C^{h}), 128.47 (*C*-H, C^{f}), 124.28 (*C*-H, C^{c}), 54.52 (*C*, C^{d}), 47.72 (*C*, C^{a})

MALDI-TOF (m/z): calcd. for $C_{30}H_{30}N_{10}$+Cu^{+}: 593.2, found: 593.3

4-Methyl-3,5-bis((triisopropylsilyl)ethynyl)aniline (**73**)

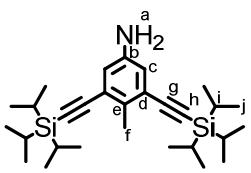

15.00 g (56.61 mmol) 3,5-dibromo-4-methylaniline, 2,97 g (11.32 mmol) PPh_3, 2.16 g (11.32 mmol) CuI and 3.97 g (5.66 mmol) $Pd(PPh_3)_2Cl_2$ were dissolved in a mixture of 140 mL triethylamine and 150 mL toluene. The mixture was heated to 80 °C under argon. 21.68 g (26.67 mL, 118.89 mmol) T*i*PS-acetylene was added dropwise (orange suspension turns black) and the mixture was stirred at 80 °C over night. Water was added to the mixture and the organic phase was washed with sat. NH_4Cl (aq), 1 N HCl(aq), 10% Na_2CO_3 (aq), and dried over $MgSO_4$. After evaporation of the solvent, the crude product was purified by column chromatography using firstly hexane and then a 10:1 mixture of petrol ether and ethyl acetate as eluent to yield 22.71 g (86%) of the pure compound as a viscous yellow oil.

R_f (PE/EtOAc = 10/1) = 0.65

^{1}H-NMR (300 MHz, THF-d8, 298 K) δ 6.72 (s, 2H, H^c), 4.46 (s, 2H, H^a), 2.47 (s, 3H, H^f), 1.16 (m, 42H, H^i + H^j)

^{13}C-NMR (75 MHz, THF-d8, 298 K) δ 146.95 (*C*, C^b), 131.34 (*C*, C^e), 124.76 (*C*, C^d), 119.66 (*C*-H, C^c), 107.88 (*C*, C^g), 93.38 (*C*, C^h), 19.30 (*C*H_3, C^j), 18.84 (*C*H_3, C^f), 12.45 (*C*-H, C^i)

FDMS (m/z): calcd. for $C_{29}H_{49}NSi_2$: 467.3, found: 467.4

((5-Azido-2-methyl-1,3-phenylene)bis(ethyne-2,1-diyl))bis(triisopropylsilane) (74)

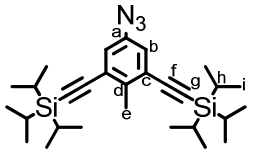

1.320 g (2.824 mmol) **73** were dissolved in a mixture of acetonitrile and THF (9:1) in an open flask. The mixture was cooled to 0 °C. 0.874 g (8.473 mmol, 1.01 mL) *tert*-butyl nitrite and 0.814 g (7.061 mmol, 0.93 mL) trimethylsilyl azide (release of N_2!) were added dropwise and the solution was allowed to warm to room temperature. Two liquid phases were obtained, which were homogenized by addition of THF. The orange solution was adsorbed on silica and purified by column chromatography using hexane as eluent to yield 1,289 g (92%) of the pure product as a viscous yellow oil.

R_f (hexane) = 0.50

^{1}H-NMR (300 MHz, THF-d8, 298 K) δ 7.12 (s, 2H, H^b), 2.61 (s, 3H, H^e), 1.17 (m, 42H, H^h + H^i)

^{13}C-NMR (75 MHz, THF-d8, 298 K) δ 140.35 (*C*, C^{a}), 138.88 (*C*, C^{d}), 126.14 (*C*, C^{c}), 123.66 (*C*-H, C^{b}), 105.69 (*C*, C^{f}), 96.89 (*C*, C^{g}), 19.56 (*C*H$_3$, C^{e}), 19.25 (*C*H$_3$, C^{i}), 12.40 (*C*-H, C^{h})

FDMS (m/z): calcd. for $C_{29}H_{47}N_3Si_2$: 493.3, found: 492.8

2'-Azido-5'-phenyl-1,1':3',1''-terphenyl (25)

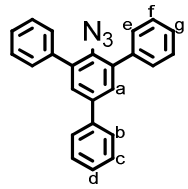

2.000 g (6.223 mmol) 5'-phenyl-[1,1':3',1''-terphenyl]-2'-amine **24** were dissolved in a mixture of acetonitrile and THF (5:1) in an open flask. The mixture was cooled to 0 °C. 1.925 g (18.668 mmol, 2.22 mL) *tert*-butyl nitrite and 1.792 g (15.556 mmol, 2.05 mL) trimethylsilyl azide (release of N_2!) were added dropwise and the solution was allowed to warm to room temperature. The solution was adsorbed on silica and purified by column chromatography using a 4:1 mixture of hexane and ethyl acetate as eluent to yield 2.108 g (98%) of the pure product as a viscous yellow oil.

R_f (hexane/EtOAc = 4/1) = 0.80

^{1}H-NMR (300 MHz, THF-d8, 298 K) δ 7.69 (d, $^{3}J_{HH}$ = 7.2 Hz, 2H, H^{b}), 7.61 (s, 2H, H^{a}), 7.58 (d, $^{3}J_{HH}$ = 7.0 Hz, 4H, H^{e}), 7.49 – 7.29 (m, 9H, H^{c} + H^{d} + H^{f} + H^{g})

^{13}C-NMR (75 MHz, THF-d8, 298 K) δ 140.94 (*C*), 139.84 (*C*), 139.71 (*C*), 138.28 (*C*), 134.91 (*C*), 130.46 (*C*-H, C^{f}), 129.91 (*C*-H), 129.78 (*C*-H), 129.31 (*C*-H, C^{e}), 128.65 (*C*-H), 128.49 (*C*-H, C^{d}), 127.89 (*C*-H)

FDMS (m/z): calcd. for $C_{24}H_{17}N_3$: 347.1, found: 346.7

Tetrakis(4-(1-(5'-phenyl-[1,1':3',1''-terphenyl]-2'-yl)-1H-1,2,3-triazol-4-yl)phenyl)methane

Td-c1(Ph(Ph)$_3$)$_4$ (**84**)

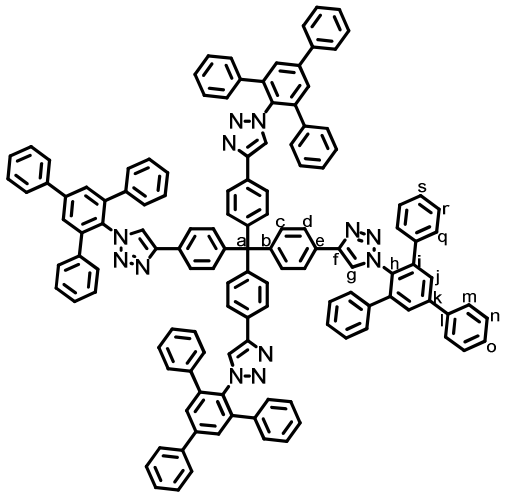

10 mg (0.024 mmol) ethynyl functionalized tetraphenylmethane core **83** and 67 mg (0.192 mmol) bulky azide **25** were dissolved in THF. To the solution were added 5 mg (0.024 mmol) sodium ascorbate, 6 mg (0.012 mmol) TBTA, 0.5 mL triethylamine and 3 mg (0.012 mmol) $CuSO_4 \cdot 5H_2O$. The solution was stirred at room temperature for 16 h, whereupon a yellow-white suspension was obtained. The suspension was purified by column chromatography using firstly a 4:1 mixture of hexane and ethyl acetate and then methylene chloride as eluent to yield 0.017 g (40%) of the compound as a white solid.

^{1}H-NMR (700 MHz, CD_2Cl_2, 298 K) δ 7.79 (s, 8H, H^j), 7.75 (d, $^3J_{HH}$ = 7.7 Hz, 8H, H^m), 7.51 (t, $^3J_{HH}$ = 7.5 Hz, 8H, H^n), 7.49 (s, 4H, H^g), 7.49 (d, $^3J_{HH}$ = 8.4 Hz, 8H, H^c), 7.44 (t, $^3J_{HH}$ = 7.4 Hz, 4H, H^o), 7.28 (m, 24H, H^q + H^s), 7.24 (d, $^3J_{HH}$ = 8.4 Hz, 8H, H^d), 7.23 (m, 16H, H^r)

^{13}C-NMR (75 MHz, CD_2Cl_2, 298 K) δ 146.98 (*C*), 146.87 (*C*), 143.63 (*C*), 141.10 (*C*), 140.00 (*C*), 138.41 (*C*), 132.53 (*C*), 131.52 (*C*-H, C^d), 129.61 (*C*-H, C^n), 129.37 (*C*-H, C^j), 128.98 (*C*-H, C^r), 128.87 (*C*-H, C^o + C^q), 128.64 (*C*), 128.37 (*C*-H, C^s), 127.86 (*C*-H, C^m), 125.59 (*C*-H, C^c), 123.74 (*C*-H, C^g)

FDMS (m/z): calcd. for $C_{129}H_{88}N_{12}$: 1805.7, found: no signal due to UV laser induced decomposition.

Tetrakis(4-(1-(4-methyl-3,5-bis((triisopropylsilyl)ethynyl)phenyl)-1H-1,2,3-triazol-4-yl)-phenyl)methane Td-c1(in-T*i*PS)$_8$ (**85**)

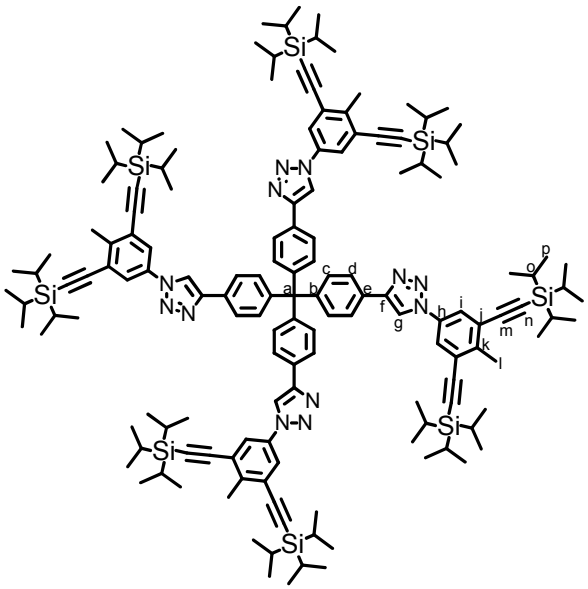

117 mg (0.281 mmol) ethynyl functionalized tetraphenylmethane core **83** and 1.110 g (2.247 mmol) of AB_2 azide **74** were dissolved in THF. To the solution were added 56 mg (0.281 mmol) sodium ascorbate, 75 mg (0.140 mmol) TBTA, 3 mL triethylamine and 35 mg (0.140 mmol) $CuSO_4{\cdot}5H_2O$. The solution was stirred at room temperature for 16 h. After adsorption to silica, the solution was purified by column chromatography using firstly hexane and then a mixture of hexane and ethyl acetate (10:1) as eluent to yield 578 mg (88%) of the product as a colorless solid.

R_f (hexane/EtOAc = 10/1) = 0.72

^{1}H-NMR (300 MHz, THF-d8, 298 K) δ 8.93 (s, 4H, H^g), 8.00 (s, 8H, H^i), 7.93 (d, $^3J_{HH}$ = 8.5 Hz, 8H, H^c), 7.48 (d, $^3J_{HH}$ = 8.5 Hz, 8H, H^d), 2.71 (s, 12H, H^l), 1.19 (m, 168H, H^o + H^p)

^{13}C-NMR (75 MHz, THF-d8, 298 K) δ 148.67 (*C*), 147.53 (*C*), 143.52 (*C*), 136.19 (*C*), 132.35 (*C*-H, C^d), 129.89 (*C*), 125.93 (*C*), 125.90 (*C*-H, C^c), 124.16 (*C*-H, C^i), 119.13 (*C*-H, C^g), 105.36 (*C*, C^n), 97.47 (*C*, C^m), 19.75 (*C*H$_3$, C^l), 19.12 (*C*H$_3$, C^p), 12.28 (*C*-H, C^o)

MALDI-TOF (m/z): calcd. for $C_{149}H_{208}N_{12}Si_8$: 2390.5, found: 2393.4 (and fragments from UV-induced decomposition)

Tetrakis(4-(1-(3,5-diethynyl-4-methylphenyl)-1H-1,2,3-triazol-4-yl)phenyl)methane

Td-c1(in)$_8$ (**86**)

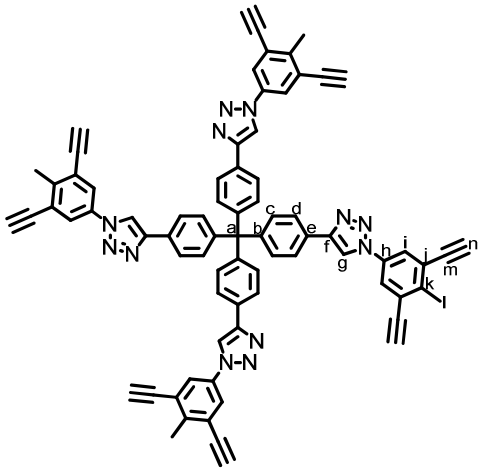

To a solution of 238 mg (0.102 mmol) **85** in THF (50 mL) was added dropwise a solution of tetrabutylammonium fluoride (273 mg, 0.978 mmol) in THF (10 mL). The mixture was stirred for 2 h at room temperature. After washing 3 times with a concentrated aqueous solution of sodium chloride, the solution was filtered over silica and the solvent removed under vacuum to afford 44 mg (0.039mmol, 38%) of the product as a beige-white powder.

R_f (hexane/EtOAc = 10/1) = 0.00

^{1}H-NMR (300 MHz, THF-d8, 298 K) δ 8.90 (s, 4H, H^g), 8.05 (s, 8H, H^i), 7.93 (d, $^3J_{HH}$ = 8.5 Hz, 8H, H^c), 7.47 (d, $^3J_{HH}$ = 8.5 Hz, 8H, H^d), 4.03 (s, 8H, H^n), 2.63 (s, 12H, H^l)

^{13}C-NMR (75 MHz, THF-d8, 298 K) δ 148.83 (*C*), 147.66 (*C*), 143.59 (*C*), 136.32 (*C*), 132.54 (*C*-H, C^d), 129.99 (*C*), 125.99 (*C*), 125.37 (*C*-H, C^c), 124.55 (*C*-H, C^i), 118.98 (*C*-H, C^g), 85.08 (C^n), 81.80 (C^m), 19.10 (C^l)

MALDI-TOF (m/z): calcd. for $C_{77}H_{48}N_{12}$: 1140.4, found: no signal due to UV laser induced decomposition.

Tetrakis(4-(1-(4-methyl-3,5-bis(1-phenyl-1H-1,2,3-triazol-4-yl)phenyl)-1H-1,2,3-triazol-4-yl)phenyl)methane Td-c2(Ph)$_8$ (**87**)

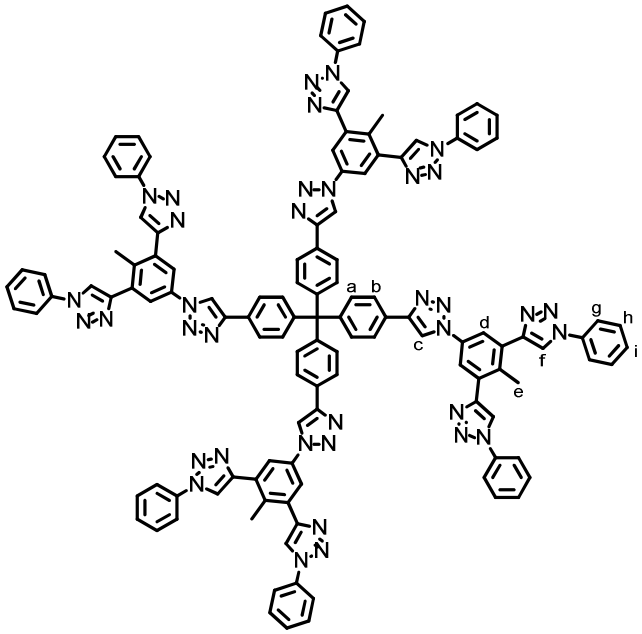

20 mg (0.018 mmol) of ethynyl functionalized compound **86** and 33 mg (0.280 mmol) of phenyl azide **75** were dissolved in THF. To the solution were added 7 mg (0.035 mmol) sodium ascorbate, 9 mg (0.018 mmol) TBTA, 0.5 mL triethylamine and 9 mg (0.018 mmol) $CuSO_4 \cdot 5H_2O$. The solution was stirred at room temperature for 15 h. The obtained suspension was exposed to ultrassonic sound and filtered. The remaining solid was washed firstly with a mixture of hexane and ethyl acetate (4:1) and then acetonitrile, whereupon the solid was transferred into THF for dissolution. After 2 h, the obtained solution was filtered over cotton fibers and the solvent removed in vacuum to yield 8 mg (0.004 mmol, 23%) of the compound as a white solid.

^{1}H-NMR (500 MHz, THF-d8, 298 K) δ 9.00 (s, 4H, H^c), 8.83 (s, 8H, H^f), 8.37 (s, 8H, H^d), 7.98 (d, $^3J_{HH}$ = 7.7 Hz, 16H, H^g), 7.97 (d, $^3J_{HH}$ = 8.1 Hz, 8H, H^a), 7.58 (t, $^3J_{HH}$ = 7.7 Hz, 16H, H^h), 7.50 (d, $^3J_{HH}$ = 8.1 Hz, 8H, H^b), 7.45 (t, $^3J_{HH}$ = 7.4 Hz, 8H, H^i), 2.79 (s, 12H, H^e)

^{13}C-NMR (126 MHz, THF-d8, 298 K) δ 149.19 (*C*), 148.07 (*C*), 147.72 (*C*), 142.92 (*C*), 137.75 (*C*), 134.44 (*C*), 132.49 (*C*-H, C^b), 130.72 (*C*-H, C^h), 129.41 (*C*-H, C^i), 126.07 (*C*-H, C^a), 122.36 (*C*-H, C^f), 121.20 (*C*-H, C^d), 121.15 (*C*-H, C^g), 119.16 (*C*-H, C^c), 19.03 (*C*-H, C^e)

MALDI-TOF (m/z): calcd. for $C_{125}H_{88}N_{36}$: 2093.8, found: no signal due to UV laser induced decomposition.

Td-c2(Ph(Ph)$_3$)$_8$ (**88**)

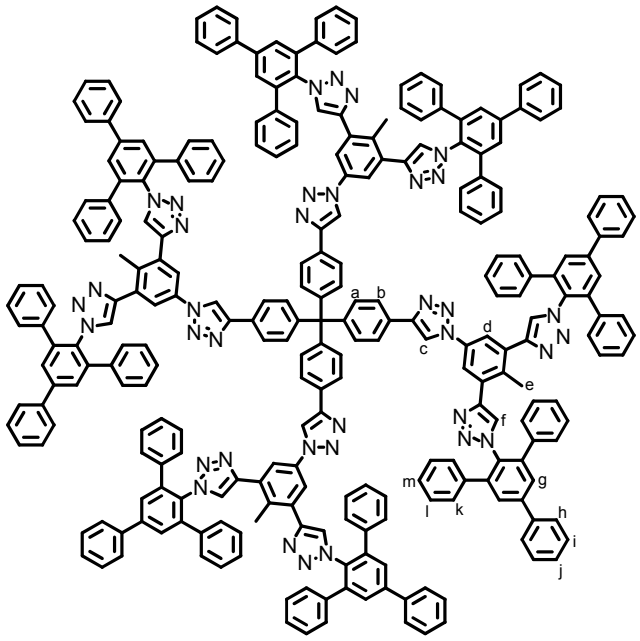

50 mg (0.044 mmol) of ethynyl functionalized compound **86** and 244 mg (0.701 mmol) of azide **25** were dissolved in THF. To the solution were added 17 mg (0.088 mmol) sodium ascorbate, 23 mg (0.044 mmol) TBTA, 1 mL triethylamine and 11 mg (0.044 mmol) $CuSO_4 \cdot 5H_2O$. The solution was stirred at room temperature for 16 h. The yellow solution was purified by column chromatography using firstly a mixture of hexane and ethyl acetate (4:1) and then THF as eluent. After removal of the solvent in vacuum, the crude product was dissolved in methylene chloride, precipitated in hexane, filtered, dried, dissolved in chloroform and purified by recycling GPC to afford 88 mg (0.022 mmol, 51%) of the compound as a colorless powder.

^{1}H-NMR (700 MHz, CD_2Cl_2, 298 K) δ 8.30 (s, 4H, H^c), 7.91 (d, $^3J_{HH}$ = 8.5 Hz, 8H, H^a), 7.85 (s, 8H, H^d), 7.83 (s, 16H, H^g), 7.76 (d, $^3J_{HH}$ = 7.3 Hz, 16H, H^h), 7.53 (d, $^3J_{HH}$ = 8.5 Hz, 8H, H^b), 7.52 (t, $^3J_{HH}$ = 7.7 Hz, 16H, H^i), 7.46 (s, 8H, H^f), 7.45 (t, $^3J_{HH}$ = 7.4 Hz, 8H, H^j), 7.35 – 7.31 (m, 48H, H^k + H^m), 7.28 – 7.25 (m, 32H, H^l), 1.71 (s, 12H, H^e)

^{13}C-NMR (176 MHz, CD_2Cl_2, 298 K) δ 148.29 (*C*), 147.22 (*C*), 145.76 (*C*), 143.77 (*C*), 141.08 (*C*), 139.94 (*C*), 138.44 (*C*), 135.34 (*C*), 135.29 (*C*), 133.22 (*C*), 132.45 (*C*), 132.13 (*C*-H, C^b), 129.62 (*C*-H, C^i), 129.33 (*C*-H, C^g), 129.01 (*C*-H, C^k), 128.97 (*C*-H, C^l), 128.90 (*C*-H, C^j), 128.45 (*C*-H, C^m), 127.87 (*C*-H, C^h), 127.13 (*C*-H, C^f), 125.78 (*C*-H, C^a), 121.17 (*C*-H, C^d), 118.47 (*C*-H, C^c), 18.37 (*C*H$_3$, C^e)

MALDI-TOF (m/z): calcd. for $C_{269}H_{184}N_{36}$: 3919.6, found: no signal due to UV laser induced decomposition.

Tetrakis(4-(1-(3,5-bis(1-(3,5- bis((triisopropylsilyl)ethynyl)-4-methylphenyl)-1H-1,2,3-triazol-4-yl)-4-methylphenyl)-1H-1,2,3-triazol-4-yl)phenyl)methane Td-c2(in-T*i*PS)$_{16}$ (**89**)

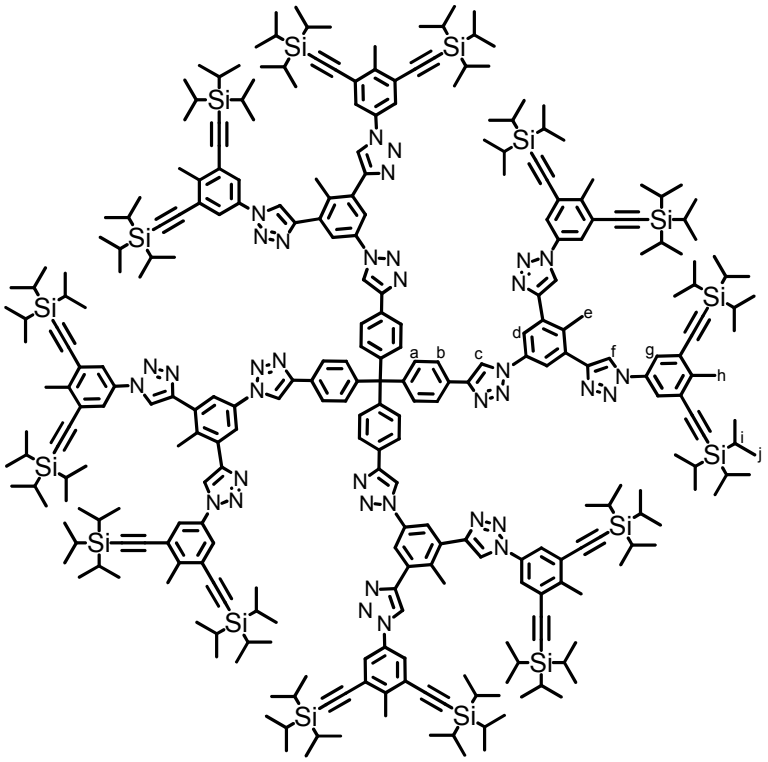

117 mg (0.103 mmol) ethynyl functionalized compound **86** and 810 mg (1.640 mmol) of AB_2 azide **74** were dissolved in THF. To the solution were added 41 mg (0.205 mmol) sodium ascorbate, 41 mg (0.205mmol) TBTA, 3 mL triethylamine and 26 mg (0.103 mmol) $CuSO_4 \cdot 5H_2O$. The solution was stirred at room temperature for 16 h and the product purified by column chromatography using firstly a mixture of hexane and ethyl acetate (1:1) and then THF as eluent. After evaporation of the solvent in vacuum, the raw product was dissolved in chloroform and purified by recycling GPC to yield 294 mg (0.058 mmol, 56%) of the product as a transparent, orange solid.

^{1}H-NMR (700 MHz, CD_2Cl_2, 298 K) δ 8.49 (s, 4H, H^c), 8.36 (s, 8H, H^f), 8.31 (s, 8H, H^d), 7.95 (d, $^3J_{HH}$ = 8.4 Hz, 8H, H^a), 7.92 (s, 16H, H^g), 7.55 (d, $^3J_{HH}$ = 8.4 Hz, 8H, H^b), 2.75 (s, 12H, H^e), 2.73 (s, 24H, H^h), 1.18 (n.r., 336H, H^i + H^j)

^{13}C-NMR (176 MHz, CD_2Cl_2, 298 K) δ 148.51 (*C*), 147.41 (*C*), 147.30 (*C*), 144.29 (*C*), 135.77 (*C*), 135.52 (*C*), 134.99 (*C*), 133.46 (*C*), 132.18 (*C*-H, C^b), 128.91 (*C*), 126.00 (*C*), 125.87 (*C*-H, C^a), 124.27 (*C*-H, C^g), 121.65 (*C*-H, C^f), 121.49 (*C*-H, C^d), 118.49 (*C*-H, C^c), 104.41 (*C*, *C*≡C-Si), 98.07 (*C*, C≡*C*-Si), 19.82 (*C*H$_3$, C^h), 19.45 (*C*H$_3$, C^e), 19.05 (*C*-H, C^j), 11.86 (*C*-H, C^i)

FDMS (m/z): calcd. for $C_{309}H_{424}N_{36}Si_{16}$: 5091.1, found: no signal due to UV laser induced decomposition.

Tetrakis(4-(1-(3,5-bis(1-(3,5-diethynyl-4-methylphenyl)-1H-1,2,3-triazol-4-yl)-4-methylphenyl)-1H-1,2,3-triazol-4-yl)phenyl)methane Td-c2(in)$_{16}$ (**90**)

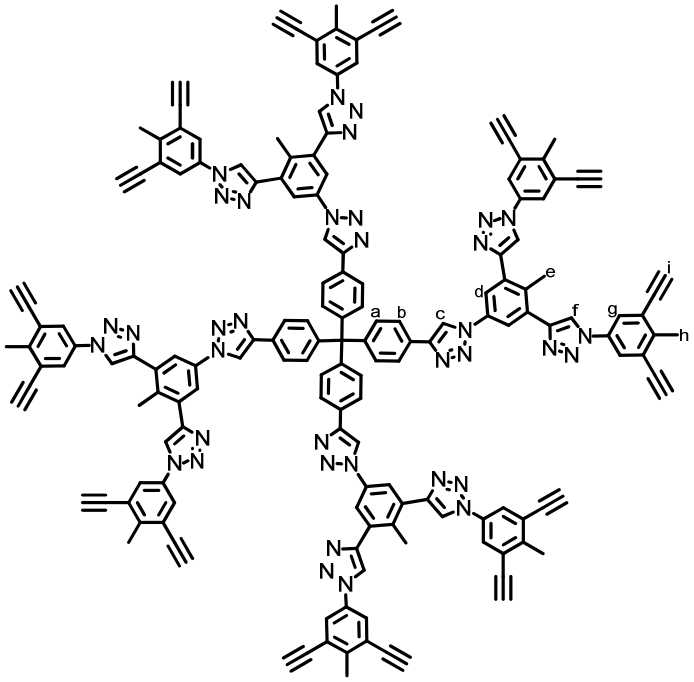

To a solution of 142 mg (0.028 mmol) **89** in THF (50 mL) was added dropwise a solution of tetrabutylammonium fluoride (140 mg, 0.502 mmol) in THF (10 mL). The mixture was stirred for 15 minutes at room temperature, whereupon a slightly turbid solution was obtained. The solution was filtered over silica, and the silica was rinsed with tetrahydrofuran several times. After removal of the solvent under vacuum, the solid remainder was further purified by means of extraction of impurities using methylene chloride (since the product was found to be largely insoluble in methylene chloride). After filtration of the remaining precipitate, the filter residue was redissolved in tetrahydrofuran an the solvent removed in vacuum to afford 18 mg (0.007 mmol, 25%) of the product as a colorless solid.

^{1}H-NMR (300 MHz, THF-d8, 298 K) δ 8.96 (s, 4H, H^{c}), 8.89 (s, 8H, H^{f}), 8.33 (s, 8H, H^{d}), 8.07 (s, 16H, H^{g}), 7.97 (d, $^{3}J_{HH}$ = 8.4 Hz, 8H, H^{a}), 7.50 (d, $^{3}J_{HH}$ = 8.4 Hz, 8H, H^{b}), 4.03 (s, 16H, H^{i}), 2.78 (s, 12H, H^{e}), 2.63 (s, 24H, H^{h})

^{13}C-NMR (75 MHz, THF-d8, 298 K) δ 148.81 (*C*), 148.18 (*C*), 147.65 (*C*), 143.80 (*C*), 136.40 (*C*), 136.13 (*C*), 135.43 (*C*), 134.09 (*C*), 132.50 (*C*-H, C^{b}), 130.05 (*C*), 126.11 (*C*-H, C^{a}), 125.40

(*C*), 124.71 (*C*-H, C^g), 122.37 (*C*-H, C^f), 121.10 (*C*-H, C^d), 119.08 (*C*-H, C^c), 85.17 (*C*-H, C^i), 81.81 (*C*, *C*≡C-H), 19.28 (CH_3, C^e), 19.18 (CH_3, C^h)

FDMS (m/z): calcd. for $C_{165}H_{104}N_{36}$: 2590.0, found: no signal due to UV laser induced decomposition.

Td-c3(Ph(Ph)$_3$)$_{16}$ (**91**)

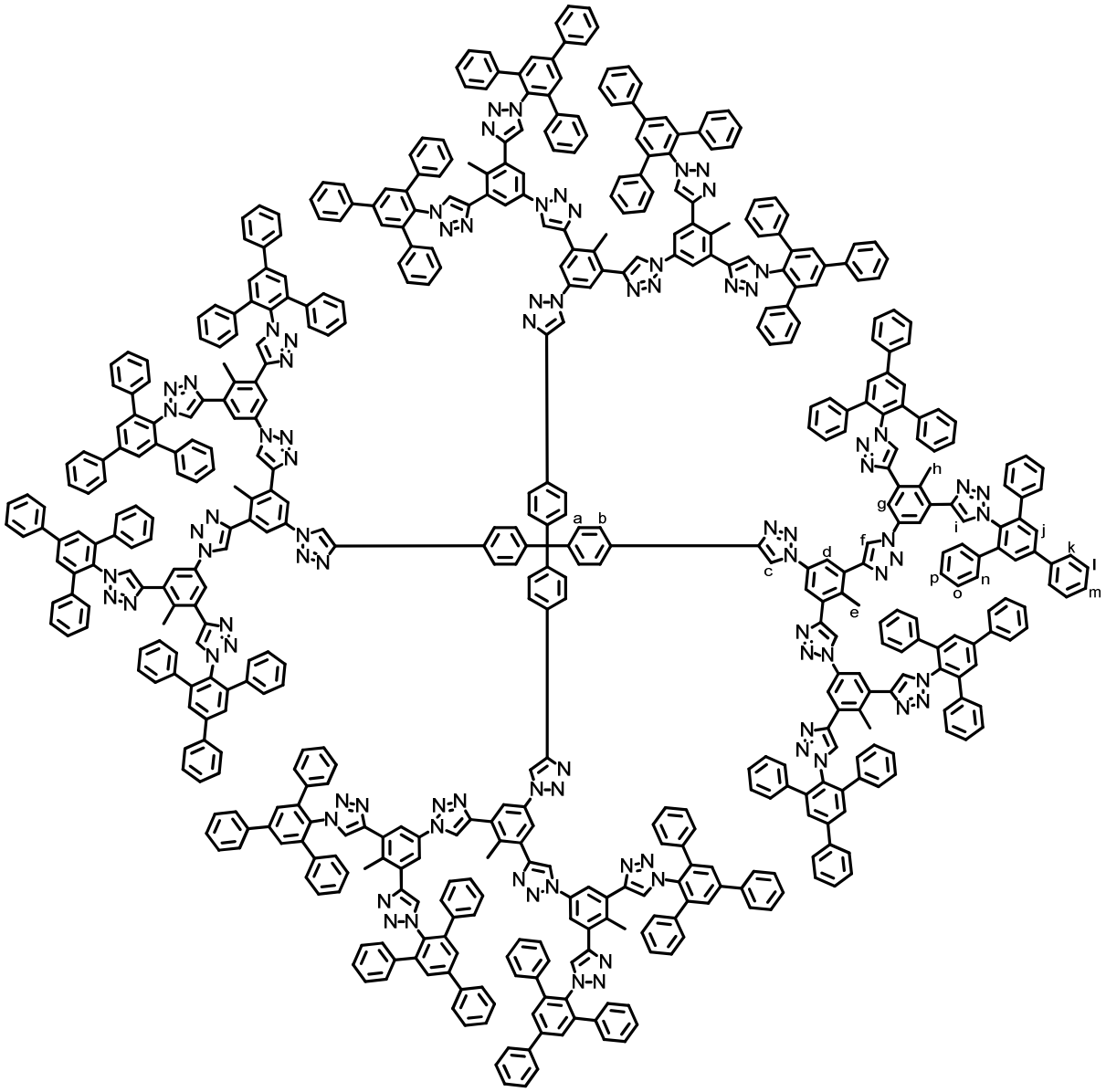

14 mg (0.005 mmol) of ethynyl functionalized compound **90** and 60 mg (0.173mmol) of azide **25** were dissolved in THF. To the solution were added 6 mg (0.011 mmol) TBTA, 0.5 mL triethylamine and 4 mg (0.011 mmol) $Cu(MeCN)_4PF_6$. The solution was stirred at room temperature for

16 h and then filtered over silica using firstly a mixture of hexane and ethyl acetate (4:1) and then THF as eluent. After removal of the solvent in vacuum, the crude product was dissolved in chloroform and purified by recycling GPC to afford 0.8 mg (0.098 μmol, 2%) of the product as a colorless powder.

^{1}H-NMR (300 MHz, THF-d8, 298 K) δ 8.99 (s, 4H, H^{c}), 8.82 (s, 8H, H^{f}), 8.33 (s, 8H, H^{d}), 8.02 (d, $^{3}J_{HH}$ = 8.4 Hz, 8H, H^{a}), 8.01 (s, 16H, H^{g}), 7.84 (s, 32H, H^{j}), 7.82 (s, 16H, H^{i}), 7.80 (d, $^{3}J_{HH}$ = 7.6 Hz, 32H, H^{k}), 7.56 (d, $^{3}J_{HH}$ = 8.4 Hz, 8H, H^{b}), 7.45 (t, $^{3}J_{HH}$ = 7.5 Hz, 32H, H^{l}), 7.36 (t, $^{3}J_{HH}$ = 7.4 Hz, 16H, H^{m}), 7.30 – 7.20 (n.r., 160H, H^{n} + H^{o} + H^{p}), 2.80 (s, 12H, H^{e}), 1.77 (s, 24H, H^{h})

FDMS (m/z): calcd. for $C_{549}H_{376}N_{84}$: 8148.2, found: no signal due to UV laser induced decomposition.

1,3,5-Tris((triisopropylsilyl)ethynyl)benzene Tp(in-T*i*PS)$_3$ (**77**)

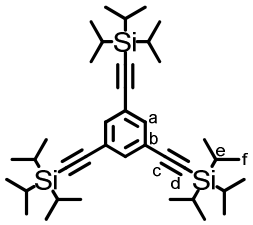

Synthesis according to literature procedure[114]

^{1}H-NMR (300 MHz, THF-d8, 298 K) δ 7.49 (s, 3H, H^{a}), 1.15 (s, 63H, H^{e} + H^{f})

^{13}C-NMR (75 MHz, THF-d8, 298 K) δ 135.84 (*C*-H, C^{a}), 125.16 (*C*, C^{b}), 106.26 (*C*, C^{d}), 92.99 (*C*, C^{c}), 19.19 (*C*-H, C^{f}), 12.38 (*C*-H, C^{e})

1-(1-(5'-Phenyl-[1,1':3',1''-terphenyl]-2'-yl)-1H-1,2,3-triazol-4-yl)-3,5-bis(1-(5'-phenyl-[1,1':3',1''-terphenyl]-4'-yl)-1H-1,2,3-triazol-4-yl)benzene Tp-c1(Ph(Ph)$_3$)$_3$ (**79**)

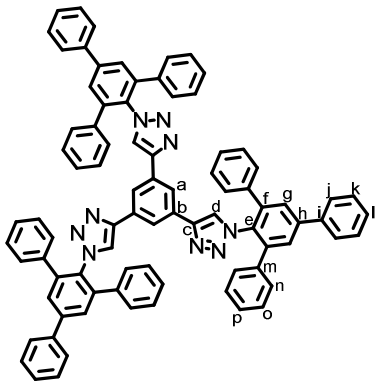

10 mg (0.067 mmol) of 1,3,5-triethynylbenzene **78** and 139 mg (0.400 mmol) of azide **25** were dissolved in THF. To the solution were added 10 mg (0.051 mmol) sodium ascorbate, 13 mg (0.025 mmol) TBTA, 0.5 mL triethylamine and 6 mg (0.025 mmol) $CuSO_4 \cdot 5H_2O$. The solution was stirred at room temperature for 16 h and then purified by column chromatography using firstly a mixture of hexane and ethyl acetate (4:1) and then THF as eluent. After removal of the solvent in vacuum, the crude product was dissolved in methylene chloride, precipitated in hexane, filtered, dried, dissolved in chloroform and purified by recycling GPC to afford 50 mg (0.042 mmol, 63%) of the compound as a colorless powder.

^{1}H-NMR (300 MHz, THF-d8, 298 K) δ 8.02 (s, 3H, H^a), 7.95 (s, 3H, H^d), 7.83 (s, 6H, H^g), 7.82 (d, $^3J_{HH}$ = 7.4 Hz, 6H, H^j), 7.48 (t, $^3J_{HH}$ = 7.4 Hz, 6H, H^k), 7.39 (t, $^3J_{HH}$ = 7.3 Hz, 3H, H^l), 7.28 – 7.14 (n.r., 30H, H^n + H^o + H^p)

^{13}C-NMR (75 MHz, THF-d8, 298 K) δ 147.25 (*C*, C^c), 144.01 (*C*), 142.10 (*C*, C^m), 140.69 (*C*), 139.22 (*C*, C^e), 133.61 (*C*), 132.85 (*C*), 129.93 (*C*-H, C^k), 129.57 (*C*-H, C^g + C^o), 129.10 (*C*-H, C^l + C^n), 128.59 (*C*-H, C^p), 128.31 (*C*-H, C^j), 125.01 (*C*-H, C^a), 122.35 (*C*-H, C^d)

FDMS (m/z): calcd. for $C_{84}H_{57}N_9$: 1191.5, found: no signal due to UV laser induced decomposition.

XRD: colorless prisms, triclinic, P-1

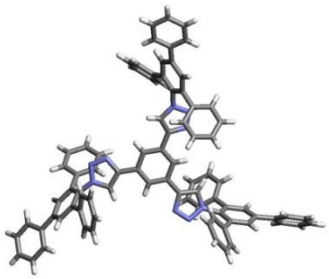

1,3,5-Tris(1-(4-methyl-3,5-bis((triisopropylsilyl)ethynyl)phenyl)-1H-1,2,3-triazol-4-yl)benzene

Tp-c1(in-T*i*PS)$_6$ (**80**)

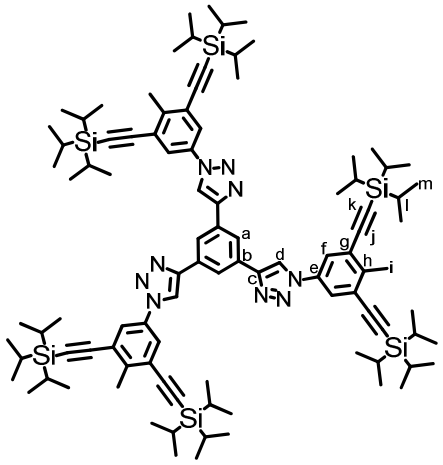

50 mg (0.333 mmol) 1,3,5-triethynylbenzene **78** and 0.987 g (1.998 mmol) of AB_2 azide **74** were dissolved in THF. To the solution were added 50 mg (0.253 mmol) sodium ascorbate, 67 mg (0.127 mmol) TBTA, 2 mL triethylamine and 32 mg (0.127 mmol) $CuSO_4 \cdot 5H_2O$. The solution was stirred at room temperature for 15 h. After adsorption to silica, the solution was purified by column chromatography using firstly hexane and then mixtures of hexane and ethyl acetate (10:1 to 4:1; consumption of large amounts of solvent) as eluent to yield 490 mg (90%) of the product as a colorless solid.

^{1}H-NMR (300 MHz, THF-d8, 298 K) δ 9.27 (s, 3H, H^d), 8.63 (s, 3H, H^a), 8.10 (s, 6H, H^f), 2.74 (s, 9H, H^i), 1.21 (s, 126H, H^l + H^m)

^{13}C-NMR (75 MHz, THF-d8, 298 K) δ 148.70 (*C*, C^c), 143.78 (*C*), 136.33 (*C*), 133.38 (*C*), 126.13 (*C*, C^g), 124.25 (*C*-H, C^f), 123.15 (*C*-H, C^a), 120.10 (*C*-H, C^d), 105.51 (*C*, C^j), 97.60 (*C*, C^k), 19.91 (*C*H$_3$, C^i), 19.27 (*C*H$_3$, C^m), 12.43 (*C*-H, C^l)

MALDI-TOF (m/z): calcd. for $C_{99}H_{147}N_9Si_6$: 1631.0, found: 1633.5

1,3,5-Tris(1-(3,5-diethynyl-4-methylphenyl)-1H-1,2,3-triazol-4-yl)benzene Tp-c1(in)$_6$ (**81**)

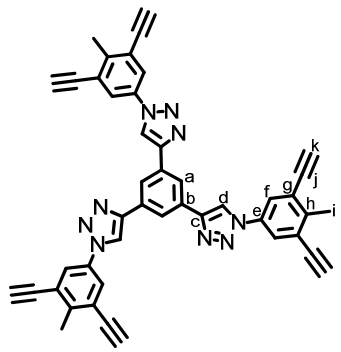

To a solution of 200 mg (0.123 mmol) **80** in THF (50 mL) was added dropwise a solution of tetrabutylammonium fluoride (240 mg, 0.858 mmol) in THF (10 mL). The mixture was stirred for 2 h at room temperature and then filtered over silica. After removal of the solvent under vacuum, the solid remainder was dispersed in methylene chloride, filtered, washed with methylene chloride and dried to afford 66 mg (0.095 mmol, 78%) of the compound as a colorless powder.

^{1}H-NMR (300 MHz, THF-d8, 298 K) δ 9.22 (s, 3H, H^d), 8.63 (s, 3H, H^a), 8.16 (s, 6H, H^f), 4.06 (s, 6H, H^k), 2.66 (s, 9H, H^i)

^{13}C-NMR (176 MHz, THF-d8, 298 K) δ 148.82 (*C*), 143.72 (*C*), 136.38 (*C*), 133.38 (*C*), 125.50 (*C*, C^g), 124.70 (*C*-H, C^f), 123.28 (*C*-H, C^a), 119.79 (*C*-H, C^d), 84.83 (C^j), 81.87 (C^k), 19.08 (*C*H$_3$, C^i)

MALDI-TOF (m/z): calcd. for $C_{45}H_{27}N_9$: 693.2, found: no signal due to UV laser induced decomposition.

1-(1-(4-methyl-3,5-bis(1-(5'-phenyl-[1,1':3',1''-terphenyl]-2'-yl)-1H-1,2,3-triazol-4-yl)phenyl)-1H-1,2,3-triazol-4-yl)-3-(1-(4-methyl-3,5-bis(1-(5'-phenyl-[1,1':3',1''-terphenyl]-4'-yl)-1H-1,2,3-triazol-4-yl)phenyl)-1H-1,2,3-triazol-4-yl)-5-(1-(4-methyl-3-(1-(5'-phenyl-[1,1':3',1''-terphenyl]-2'-yl)-1H-1,2,3-triazol-4-yl)-5-(1-(5'-phenyl-[1,1':3',1''-terphenyl]-4'-yl)-1H-1,2,3-triazol-4-yl)phenyl)-1H-1,2,3-triazol-4-yl)benzene Tp-c2(Ph(Ph)$_3$)$_6$ (**82**)

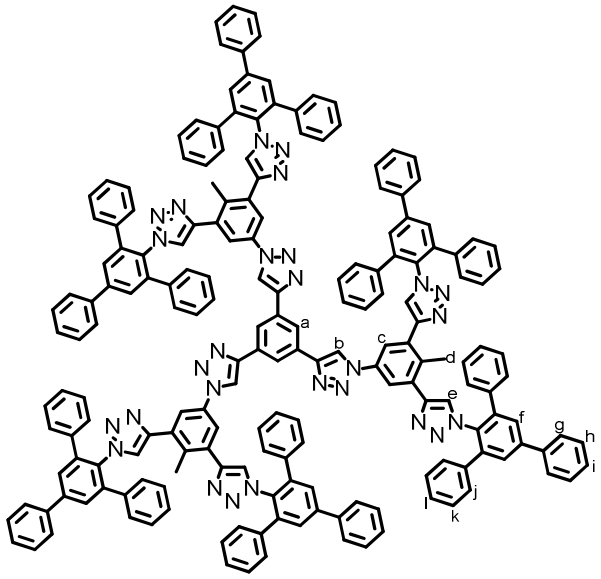

40 mg (0.058 mmol) of ethynyl functionalized compound **80** and 240 mg (0.692 mmol) of azide **25** were dissolved in THF. To the solution were added 17 mg (0.088 mmol) sodium ascorbate, 23 mg (0.044 mmol) TBTA, 1 mL triethylamine and 11 mg (0.044 mmol) $CuSO_4 \cdot 5H_2O$. The solution was stirred at room temperature for 16 h and then purified by column chromatography using firstly a mixture of hexane and ethyl acetate (4:1) and then THF as eluent. After removal of the solvent in vacuum, the crude product was dissolved in THF, precipitated in hexane, filtered, dried, dissolved in chloroform and purified by recycling GPC to afford 68 mg (0.024 mmol, 42%) of the compound as a colorless powder.

^{1}H-NMR (700 MHz, THF-d8, 298 K) δ 9.11 (s, 3H, H^b), 8.67 (s, 3H, H^a), 8.05 (s, 6H, H^c), 7.88 (s, 12H, H^f), 7.86 (s, 6H, H^e), 7.83 (d, $^3J_{HH}$ = 8.1 Hz, 12H, H^g), 7.49 (t, $^3J_{HH}$ = 7.7 Hz, 12H, H^h), 7.40 (t, $^3J_{HH}$ = 7.3 Hz, 3H, H^i), 7.33 – 7.28 (n.r., 60H, H^j + H^k + H^l), 1.87 (s, 9H, H^d)

^{13}C-NMR (126 MHz, THF-d8, 298 K) δ 146.33 (*C*), 144.16 (*C*), 142.12 (*C*), 140.68 (*C*), 139.28 (*C*), 137.06 (*C*), 133.58 (*C*), 129.97 (*C*-H), 129.71 (*C*-H), 129.66 (*C*-H), 129.55 (*C*-H), 129.25 (*C*-H), 129.10 (*C*-H), 128.95 (*C*-H), 128.79 (*C*-H), 128.33 (*C*-H), 18.11(*C*H$_3$)

MALDI-TOF (m/z): calcd. for $C_{189}H_{129}N_{27}Si_6$: 2778.1, found: no signal due to UV laser induced decomposition.

Tp-cG2 (**92**)

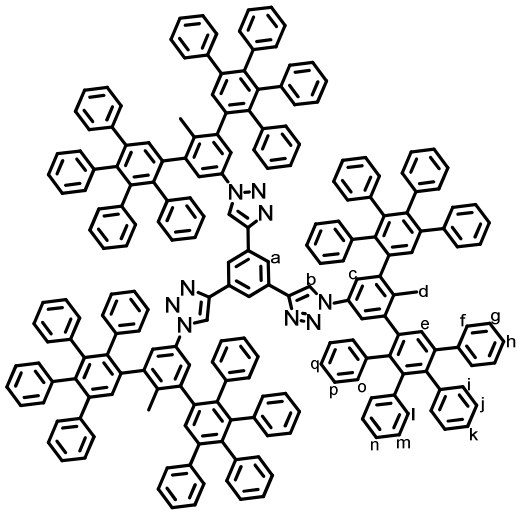

22 mg (0.019 mmol) of ethynyl functionalized compound **81** and 89 mg (0.231 mmol) tetraphenylcyclopentadienone were dispersed in *o*-xylene (5 mL) in a microwave tube. The argon bubbled mixture was stirred at 160 °C for 14 h. After cooling to room temperature, the mixture was purified by column chromatography using firstly a 10:1 mixture of hexane and ethyl acetate and then methylene chloride as eluent. After removal of the solvent in vacuo, the product was dissolved in methylene chloride, precipitated in hexane, filtered and dried to afford 44 mg (0.055 mmol, 81%) of the pure compound as a colorless powder.

In NMR measurements, two local conformations A and B could be discerned (see paragraph 3.3.3 for details):

^{1}H-NMR (700 MHz, THF-d8, 298 K) δ 8.84 – 8.81 (≥3s, 3H, conf. B, H^{b}), 8.56 – 8.53 (≥3s, 3H, conf. A, H^{b}), 8.52 – 8.41 (≥8s, 3H + 3H, conf. A + B, H^{a}), 7.72 (≥3s, 6H, conf. B, H^{c}), 7.57 (≥3s, 6H, conf. A, H^{c}), 7.46 (≥3s, 6H, conf. A, H^{e}), 7.16 – 7.05 (n.r., 30H + 30H, conf. A + B, H^{f} + H^{g} + H^{h}), 7.11 (≥3s, 6H, conf. B, H^{e}), 6.98 (s, conf. B), 6.95 – 6.77 (n.r., conf. A + B, polyphenylenes), 6.61 (s, conf. A), 2.23 (s, 9H, conf. A, H^{d}), 1.92 (s, 9H, conf. B, H^{d})

^{13}C-NMR (176 MHz, THF-d8, 298 K) δ 148.31 (*C*), 148.18 (*C*), 144.39 (*C*), 144.37 (*C*), 143.23 (*C*), 142.94 (*C*), 142.87 (*C*), 142.75 (*C*), 141.88 (*C*), 141.79 (*C*), 141.48 (*C*), 141.41 (*C*), 141.17 (*C*), 141.13 (*C*), 141.07 (*C*), 140.98 (*C*), 140.93 (*C*), 140.82 (*C*), 140.74 (*C*), 135.15 (*C*), 135.01 (*C*), 134.60 (*C*), 134.52 (*C*), 133.40 (*C*), 133.32 (*C*), 132.68 (*C*-H), 132.64 (*C*-H), 132.54 (*C*-H), 132.49 (*C*-H), 132.39 (*C*-H), 131.92 (*C*-H), 130.98 (*C*-H), 130.92 (*C*-H), 128.52 (*C*-H), 128.49 (*C*-H), 127.97 (*C*-H), 127.88 (*C*-H), 127.77 (*C*-H), 127.69 (*C*-H), 127.62 (*C*-H), 127.58 (*C*-H), 127.55 (*C*-H), 127.22 (*C*-H), 127.18 (*C*-H), 126.84 (*C*-H), 126.79 (*C*-H), 126.57 (*C*-H), 126.34 (*C*-H), 126.27 (*C*-H), 121.69 (*C*-H), 121.53 (*C*-H), 19.77 (*C*H_3), 19.30 (*C*H_3)

MALDI-TOF (m/z): calcd. for $C_{213}H_{147}N_9$: 2832.5, found: 2833.5 (+decomposition due to UV laser irradiation: $-N_2$, $-2N_2$, $-3N_2$)

Tetrabutylammonium bis(4-(1-(5'-phenyl-[1,1':3',1''-terphenyl]-2'-yl)-1H-1,2,3-triazol-4-yl)-phenyl)bis(4-(1-(5'-phenyl-[1,1':3',1''-terphenyl]-4'-yl)-1H-1,2,3-triazol-4-yl)phenyl)borate

TBA^+ $(B\text{-}c1(Ph(Ph)_3)_4)^-$ **(29)**

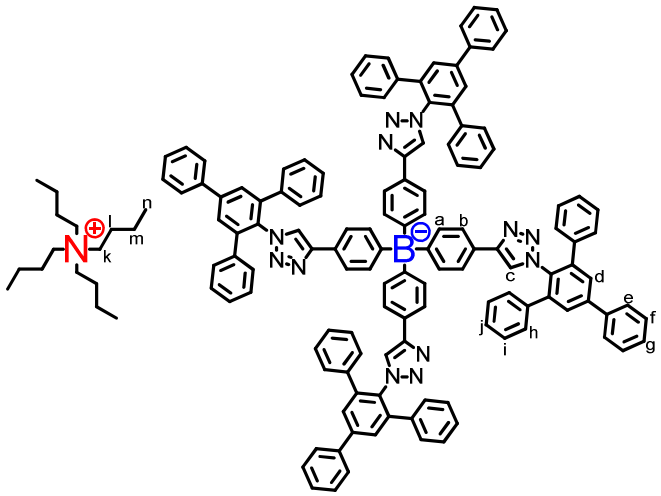

50 mg (0.076 mmol) of borate core **12** and 211 mg (0.608 mmol) of azide **25** were dissolved in THF. To the solution were added 15 mg (0.076 mmol) sodium ascorbate, 20 mg (0.038 mmol) TBTA, 1 mL triethylamine and 9 mg (0.038 mmol) $CuSO_4 \cdot 5H_2O$. The solution was stirred at room temperature for 14 h, whereupon a turbid white suspension was obtained. The suspension was purified by column chromatography using firstly a 10:1 mixture of hexane and ethyl acetate and then THF as eluent to yield 33 mg (21%) of the compound as a white solid.

^{1}H-NMR (700 MHz, CD_2Cl_2, 298 K) δ 7.78 (s, 8H, H^d), 7.75 (d, $^3J_{HH}$ = 8.1 Hz, 8H, H^e), 7.51 (t, $^3J_{HH}$ = 7.7 Hz, 8H, H^f), 7.43 (t, $^3J_{HH}$ = 7.5 Hz, 4H, H^g), 7.43 (s, 4H, H^c), 7.33 (n.r., 8H, H^a), 7.28 (m, 24H, H^h + H^j), 7.24 (d, $^3J_{HH}$ = 7.8 Hz, 8H, H^b), 7.22 (m, 16H, H^i), 2.95 (m, 8H, H^k), 1.58 (m, 8H, H^l), 1.29 (m, 8H, H^m), 0.93 (t, $^3J_{HH}$ = 7.4 Hz, 12H, H^n)

^{13}C-NMR (75 MHz, CD_2Cl_2, 298 K) δ 149.36 (*C*), 143.35 (*C*), 141.07 (*C*), 140.15 (*C*), 138.56 (*C*), 136.39 (*C*H, C^b), 132.87 (*C*), 129.57 (*C*H, C^f), 129.30 (*C*H, C^d), 128.98 (*C*H, C^g), 128.91 (*C*H, C^i), 128.85 (*C*H, C^h), 128.31 (*C*H, C^j), 127.86 (*C*H, C^e), 124.46 (*C*), 124.00 (*C*H, C^a), 122.98 (*C*H, C^c), 59.45 (C^k), 24.32 (C^l), 20.20 (C^m), 13.91 (C^n)

MALDI-TOF (m/z): calcd. for $C_{128}H_{88}BN_{12}$: 1804.7, found: 1804.5 (additional fragmentation caused by UV laser irradiation)

Tetrabutlyammonium tetrakis(2,3,5,6-tetrafluoro-4-(G1(Ph(CF$_3$)$_2$)$_{16}$)phenyl)borate TBA^+ $[B^F\text{-}G1(CF_3)_{32}]^-$ **(68)**

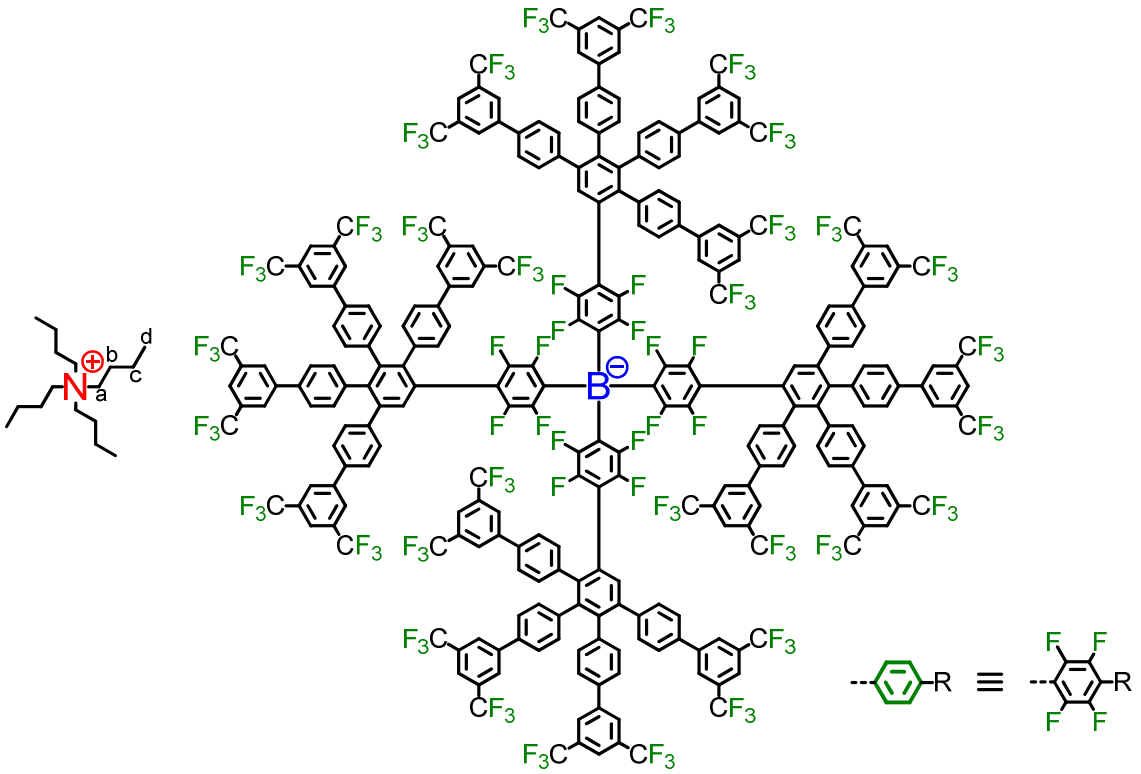

20 mg (0.021 mmol) of $TBA^+B(Ph^F\text{-}in)_4^-$ **52** and 117 mg (0.095 mmol) of tetracyclone **47** were dissolved in *o*-xylene (15 mL) in a microwave tube. The argon bubbled mixture was stirred at 160 °C for 16 h. After cooling to room temperature, the mixture was purified by column chromatography using firstly a 10:1 mixture of hexane and ethyl acetate and then methylene chloride as eluent. After removal of the solvent, the crude product was dissolved in methylene chloride, precipitated in petrol ether, filtered and dried in vacuum to afford 36 mg (0.006 mmol, 30%) pure product as a beige powder.

^{1}H-NMR (500 MHz, THF-d8, 298 K) δ 8.32 – 6.74 (n.r., 116H), 3.25 (m, 5.92H, H^a), 3.14 (m, 2.08H, H^a), 1.69 (m, 8H, H^b), 1.41 (m, 8H, H^c), 1.02 (t, $^3J_{HH}$ = 7.3 Hz, 8.88H, H^d), 0.99 (t, $^3J_{HH}$ = 7.5 Hz, 3.12H, H^d)

^{13}C-NMR (126 MHz, THF-d8, 298 K) δ 144.21, 143.81, 142.32, 135.77, 133.76 (*C*-H), 133.00, 131.93 (*C*-H), 128.48 (*C*-H), 128.15 (*C*-H), 127.79 (*C*-H), 127.12 (*C*-H), 126.84 (*C*-H), 126.59 (*C*-H), 123.62, 59.41 (*C*H$_2$, C^a), 24.65 (*C*H$_2$, C^b), 20.75 (*C*H$_2$, C^c), 14.05 (*C*H$_3$, C^d)

^{19}F-NMR (471 MHz, THF-d8, 298 K) δ -63.23 – -63.84 (n.r., 96F, C*F*$_3$), -131.13 – -135.78 (n.r., 8F), -145.59 – -149.46 (n.r., 8F)

^{11}B-NMR (160 MHz, THF-d8, 298 K) δ -16.62

MALDI-TOF (m/z): calcd. for $C_{272}H_{116}BF_{112}^-$: 5521.7, found: 5521.7 [M^-]

Tetrabutlyammonium tetrakis(2,3,5,6-tetrafluoro-4-(G2(Ph(CF$_3$)$_2$)$_{32}$)phenyl)borate TBA^+ [B^F-G2$(CF_3)_{64}]^-$ **(69)**

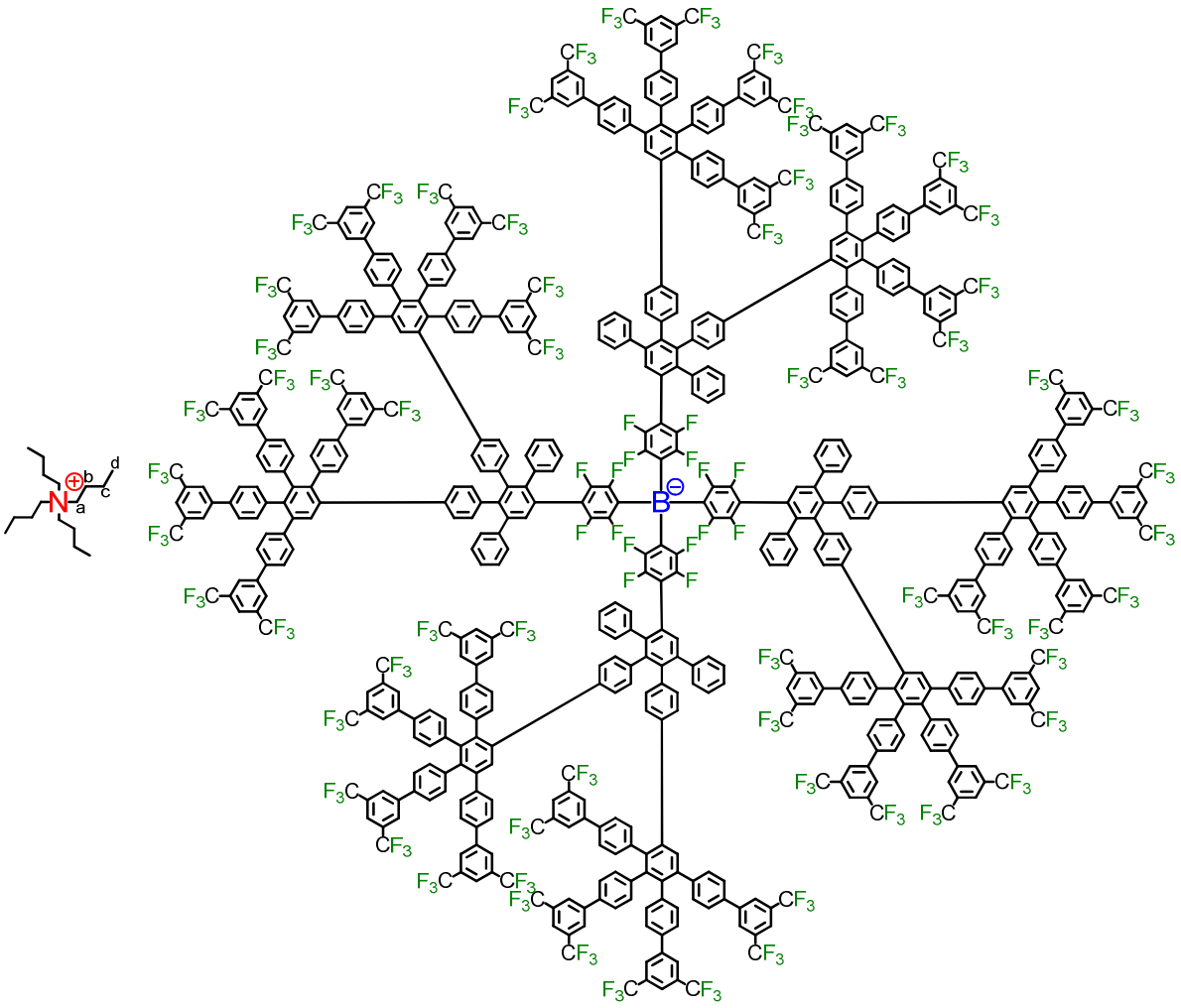

40 mg (0.016 mmol) of $TBA^+(B^F\text{-}G1(in)_8)^-$ **55** and 192 mg (0.156 mmol) of tetracyclone **47** were dissolved in *o*-xylene (15 mL) in a microwave tube. The argon bubbled mixture was stirred at 160 °C for 16 h. After cooling to room temperature, the mixture was purified by column chromatography using firstly a 10:1 mixture of hexane and ethyl acetate and then methylene chloride as eluent. After removal of the solvent, the crude product was dissolved in methylene chloride, precipitated in petrol ether, filtered and dried in vacuum to afford 127 mg (0.010 mmol, 67%) pure compound as a beige powder.

^{1}H-NMR (500 MHz, THF-d8, 298 K) δ 8.21 – 6.57 (n.r., 308H), 3.24 (m, 8H, H^a), 1.68 (m, 8H, H^b), 1.40 (m, 8H, H^c), 1.01 (t, $^3J_{HH}$ = 7.4 Hz, 12H, H^d)

^{13}C-NMR (126 MHz, THF-d8, 298 K) δ 143.94, 143.64, 143.43, 142.42, 142.02, 141.62, 140.11, 137.11, 136.21, 133.60 (*C*-H), 133.07, 132.81, 131.85 (*C*-H), 131.10, 129.60, 128.08 (*C*-H), 127.73 (*C*-H), 126.92 (*C*-H), 126.62 (*C*-H), 125.76, 123.60, 121.74 (*C*-H), 59.40 (*C*H$_2$, C^a), 24.64 (*C*H$_2$, C^b), 20.73 (*C*H$_2$, C^c), 14.05 (*C*H$_3$, C^d)

^{19}F-NMR (471 MHz, THF-d8, 298 K) δ -63.44 – -63.92 (n.r., 192F, C*F*$_3$), -132.18 – -134.04 (n.r., 8F), -146.27 – -148.67 (n.r., 8F)

^{11}B-NMR (160 MHz, THF-d8, 298 K) δ -16.73

MALDI-TOF (m/z): calcd. for $C_{640}H_{308}BF_{208}^-$: 11956.1, found: 11962.4 [M$^-$]

Tetrabutlyammonium tetrakis(2,3,5,6-tetrafluoro-4-(G3^{22}(Ph(CF$_3$)$_2$)$_{64}$)phenyl)borate TBA$^+$ [B^F-G3^{22}(CF$_3$)$_{128}$]$^-$ (**70**)

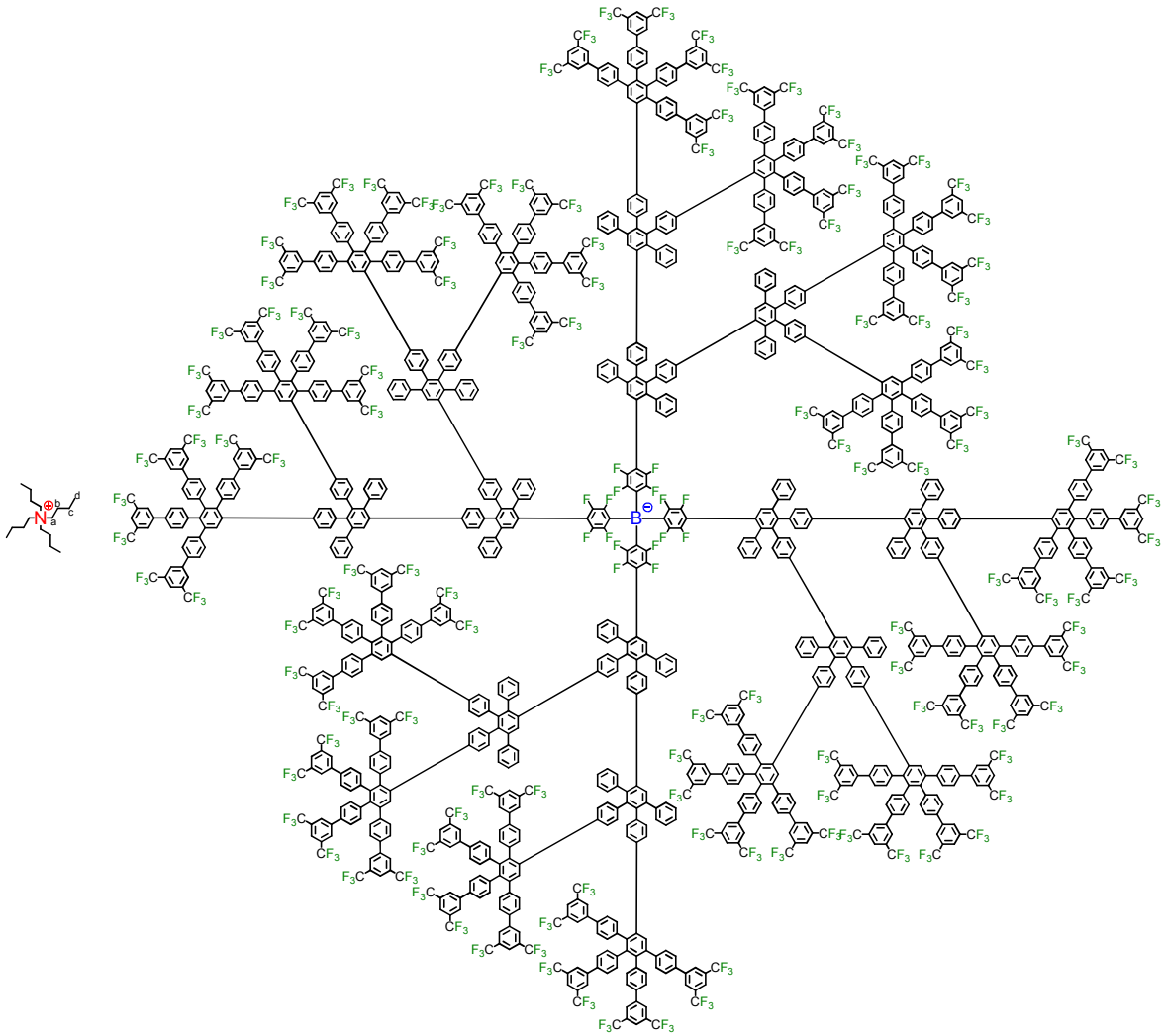

25 mg (0.004 mmol) of $TBA^+(B^F\text{-}G2(in)_{16})^-$ **58** and 106 mg (0.086 mmol) of tetracyclone **47** were dissolved in *o*-xylene (15 mL) in a microwave tube. The argon bubbled mixture was stirred at 160 °C for 16 h. After cooling to room temperature, the mixture was purified by column chromatography using firstly a 10:1 mixture of hexane and ethyl acetate and then methylene chloride as eluent. After removal of the solvent, the crude product was dissolved in methylene chloride, precipitated in petrol ether, filtered and dried in vacuum to afford 53 mg (0.002 mmol, 49%) pure compound as a beige powder.

^{1}H-NMR (300 MHz, THF-d8, 298 K) δ 8.29 – 6.33 (n.r., 692H), 3.24 (m, 8H, H^a), 1.68 (m, 8H, H^b), 1.40 (m, 8H, H^c), 1.01 (t, $^3J_{HH}$ = 7.3 Hz, 12H, H^d)

^{13}C-NMR (75 MHz, THF-d8, 298 K) δ 143.96, 143.85, 143.59, 143.38, 142.95, 142.41, 141.90, 141.57, 140.30, 139.95, 139.75, 139.39, 137.14, 136.31, 136.09, 133.54 (*C*-H), 133.26, 132.83, 132.53 (*C*-H), 131.81 (*C*-H), 130.08, 128.37 (*C*-H), 127.99 (*C*-H), 127.73 (*C*-H), 126.94 (*C*-H), 126.62 (*C*-H), 126.47, 122.86, 121.79 (*C*-H), 119.24, 59.45 (CH_2, C^a), 24.66 (CH_2, C^b), 20.74 (CH_2, C^c), 14.04 (CH_3, C^d)

^{19}F-NMR (471 MHz, THF-d8, 298 K) δ -61.33 – -62.38 (n.r., 384F, CF_3), -131.04 (n.r., 8F), -145.58 (n.r., 8F)

^{11}B-NMR (160 MHz, THF-d8, 298 K) δ -14.80

MALDI-TOF (m/z): calcd. for $C_{1376}H_{692}BF_{400}^-$: 24833.8, found: 24820.1 [M^-]

Tetrabutlyammonium tetrakis(2,3,5,6-tetrafluoro-4-(G3(Ph(CF_3)$_2$)$_{128}$)phenyl)borate TBA^+ [B^F-$G3^{24}$ $(CF_3)_{256}$]$^-$ **(71)**

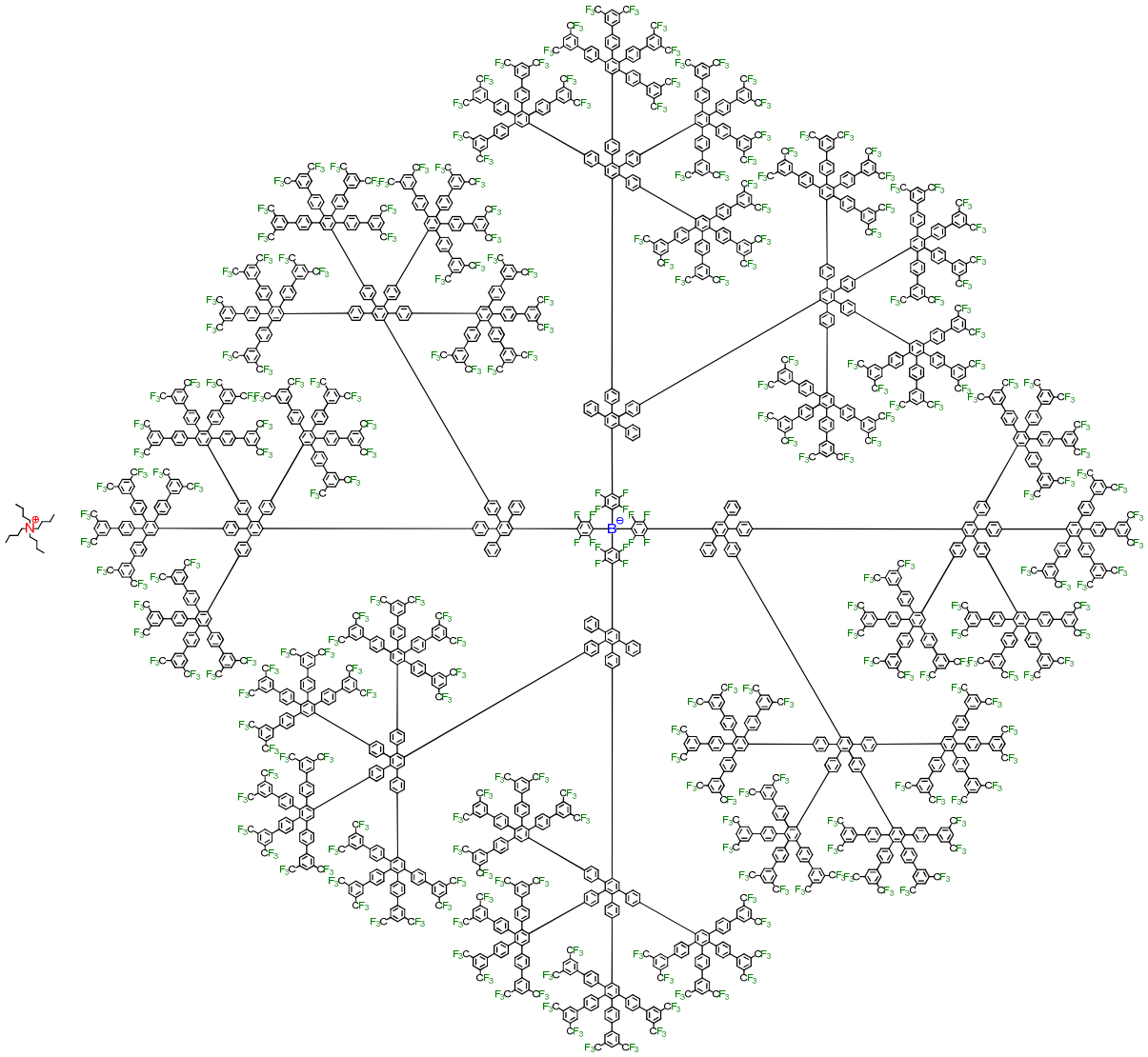

25 mg (0.004 mmol) of $TBA^+(B^F\text{-}G2(in)_{32})^-$ **64** and 199 mg (0.162 mmol) of tetracyclone **47** were dissolved in *o*-xylene (15 mL) in a microwave tube. The argon bubbled mixture was stirred at 170 °C for 336 h. After cooling to room temperature, the mixture was purified by column chromatography using firstly a 10:1 mixture of hexane and ethyl acetate and then methylene chloride as eluent. After removal of the solvent, the crude product was dissolved in methylene chloride, precipitated in petrol ether, filtered and dried in vacuum to afford 69 mg (0.002 mmol, 38% if it were complete) of not completely converted product as a beige powder.

MALDI-TOF (m/z): calcd. for $C_{2368}H_{1140}BF_{784}^-$: 44495.8, found: 44417.2 [M^-] (and additional signals from incompletely converted species; see Figure 113 in paragraph 2.3.5.2)

1,3-Di(2,3,4,5,6-pentadeuterophenyl)propan-2-one (104)

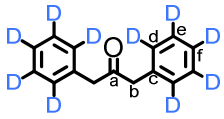

4.800 g (27.262 mmol) deuterated benzylbromide, 0.186 g (0.818 mmol) *N*,*N*,*N*-triethylbenzenaminium chloride and 2.777 g (14.176 mmol, 1.92 mL) iron pentacarbonyl were dissolved in methylene chloride. 6.623 g (118 mmol) potassium hydroxide dissolved in 5 mL water were added and the obtained two-phase system was stirred for 12 h under reflux. After cooling to room temperature, 1 M HCl (aq) was added and the organic phase was washed several times with 1 M HCl (aq). The dark organic phase was adsorbed on silica and the product was purified by means of column chromatography using hexane as eluent to yield 2.097 g (9.518 mmol, 70%) of the product as colorless crystals with a melting point around room temperature.

R_f (Hexane/EtOAc = 4/1) = 0.63

^{1}H-NMR (300 MHz, THF-d8, 298 K) δ 3.70 (s, 4H, H^b)

^{2}H-NMR (77 MHz, THF, 298 K) δ 6.87 – 6.46 (n.r.)

^{13}C-NMR (75 MHz, THF-d8, 298 K) δ 204.54 (C^a), 135.74 (C^c), 130.11 (t, $^1J_{CD}$ = 24.2 Hz, C^d), 128.80 (t, $^1J_{CD}$ = 24.2 Hz, C^e), 127.04 (t, $^1J_{CD}$ = 24.2 Hz, C^f), 49.48 (C^b)

FDMS (m/z): calcd. for $C_{15}H_4D_{10}O$: 220.2, found: 221.2

Perdeuterated 2,3,4,5-tetraphenylcyclopenta-2,4-dienone Cp-on^D **(105)**

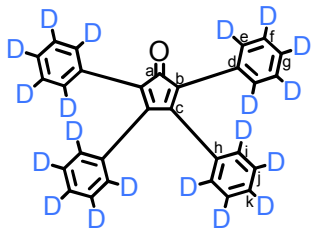

0.883 g (4.008 mmol) deuterated benzil and 0.883 g (4.008 mmol) deuterated diphenylacetone **104** were dissolved in 5 mL ethanol and heated to 80 °C. 0.225 g (4.008 mmol) potassium hydroxide dissolved in 1 mL ethanol were added and the resulting dark mixture was stirred at 80 °C for 15 min. After cooling, the mixture was filtered over silica, using additional methylene chloride as eluent. After evaporation of the solvent in vacuum, the crude product was purified by column

chromatography using a 3:1 mixture of petrol ether and methylene chloride as eluent to yield 1.348 g (3.332 mmol, 83%) of the product as dark violet crystals.

R_f (Hexane/EtOAc = 4/1) = 0.73

^{2}H-NMR (77 MHz, THF-d8, 298 K) δ 7.22 (n.r., 12D), 6.99 (n.r., 8D)

^{13}C-NMR (176 MHz, THF-d8, 298 K) δ 200.41 (C^a), 155.49 (C^c), 134.36 (C^d), 131.97 (C^h), 130.74 (t, $^1J_{CD}$ = 24.2 Hz, C^e), 129.93 (t, $^1J_{CD}$ = 24.2 Hz, C^i), 128.85 (t, $^1J_{CD}$ = 23.9 Hz, C^k), 128.47 (t, $^1J_{CD}$ = 24.2 Hz, C^f), 128.24 (t, $^1J_{CD}$ = 24.2 Hz, C^j), 127.71 (t, $^1J_{CD}$ = 23.9 Hz, C^g), 126.16 (C^b)

FDMS (m/z): calcd. for $C_{29}D_{20}O$: 404.3, found: 406.0

Tetrabutlyammonium tetrakis(4-(deutero-G1)phenyl)borate $TBA^+ [B\text{-}G1^D]^-$ **(106)**

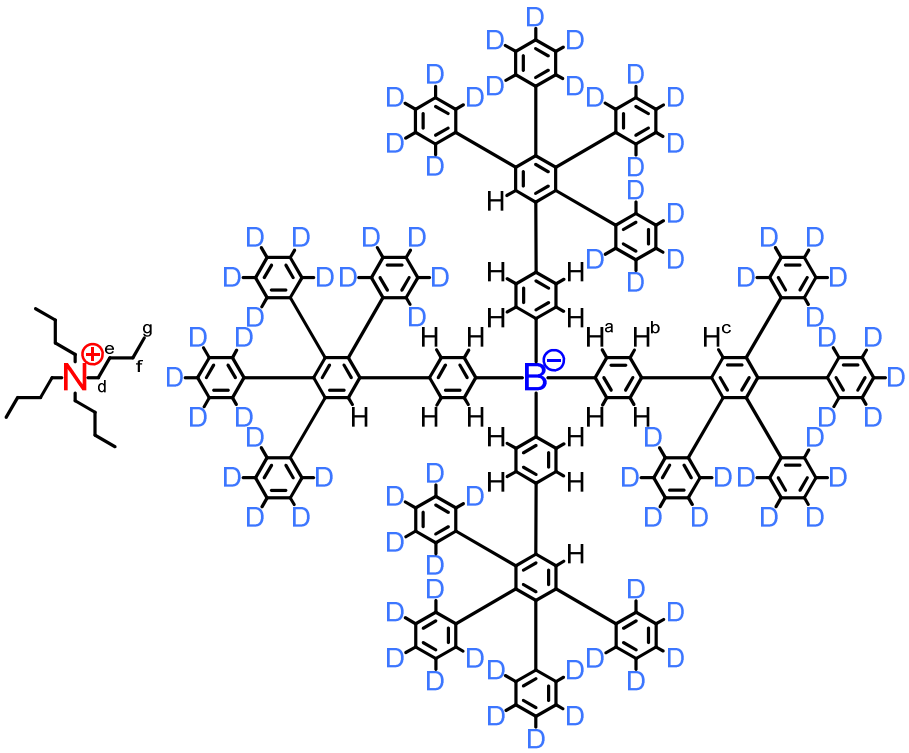

100 mg (0.15 mmol) of $TBA^+B(Ph\text{-}in)_4^-$ **12** and 277 mg (0.68 mmol) deuterated tetracyclone **105** were dissolved in diglyme (5 mL) in a microwave tube. The argon bubbled mixture was stirred at 155 °C for 12 h. After cooling to room temperature, the mixture was purified by column chromatography using firstly a 4:1 mixture of hexane and ethyl acetate and then THF as eluent. After removal of the solvent in vacuo, the product was dissolved in methylene chloride, precipitated in hexane, filtered and dried to afford 183 mg (0.085 mmol, 56%) pure compound as a pale yellow powder.

^{1}H-NMR (700 MHz, THF-d8, 298 K) δ 7.53 (s, 4H, H^{c}), 6.90 (m, 8H, H^{a}), 6.67 (d, $^{3}J_{HH}$ = 7.8 Hz, 8H, H^{b}), 2.97 (m, 8H, H^{d}), 1.49 (m, 8H, H^{e}), 1.25 (m, 8H, H^{f}), 0.89 (t, $^{3}J_{HH}$ = 7.3 Hz, 12H, H^{g})

^{2}H-NMR (77 MHz, THF-d8, 298 K) δ 6.97

^{13}C-NMR (176 MHz, THF-d8, 298 K) δ 163.24 (q, $^{1}J_{BC}$ = 49.3 Hz, *C*), 144.85 (*C*), 143.49 (*C*), 142.23 (*C*), 141.80 (*C*), 141.66 (*C*), 141.17 (*C*), 140.55 (*C*), 138.79 (*C*), 136.69 (*C*-H, C^{a}), 135.37 (*C*), 132.52 (*C*-H, C^{c}), 132.36 (n.r., *C*-D), 130.60 (n.r., *C*-D), 127.79 (n.r., *C*-D), 127.66 (*C*-H, C^{b}), 127.00 (n.r., *C*-D), 126.17 (n.r., *C*-D), 125.45 (n.r., *C*-D), 59.23 (*C*H$_2$, C^{d}), 24.62 (*C*H$_2$, C^{e}), 20.66 (*C*H$_2$, C^{f}), 14.11 (*C*H$_3$, C^{g})

^{11}B-NMR (225 MHz, THF-d8, 298 K) δ -7.33

MALDI-TOF (m/z): calcd. for $C_{144}H_{20}D_{80}B^-$: 1921.3, found: 1921.3 [M$^-$]

Tetrabutlyammonium tetrakis(2,3,5,6-tetrafluoro-4-(deutero-G1)phenyl)borate TBA$^+$ [B^F-G1^D]$^-$ (**107**)

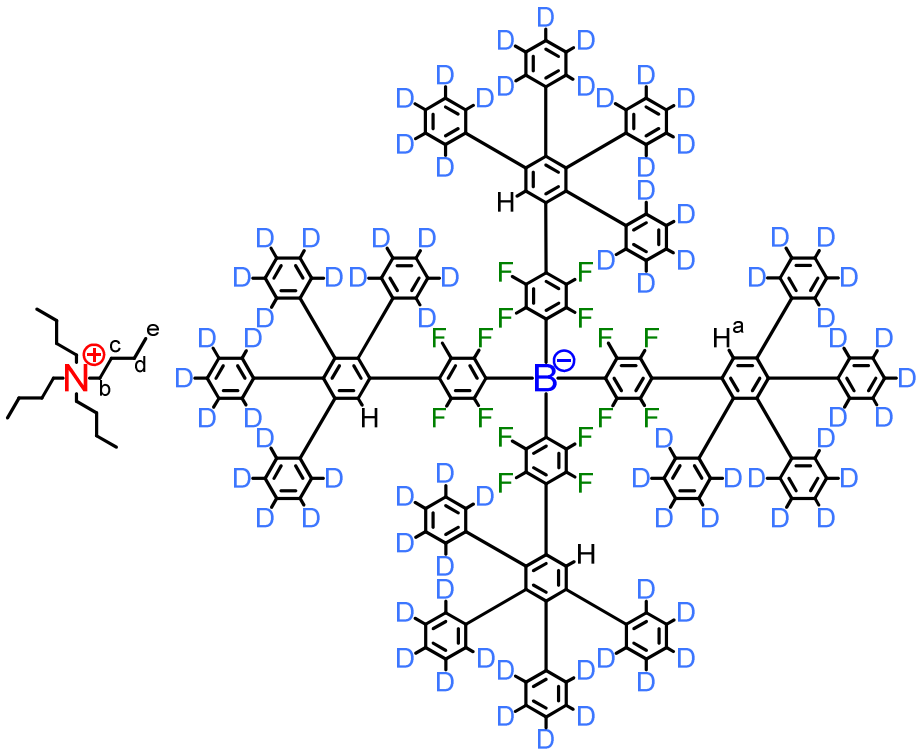

120 mg (0.127 mmol) of TBA$^+$B(Ph^F-in)$_4^-$ **52** and 231 mg (0.571 mmol) deuterated tetracyclone **105** were dissolved in diglyme (5 mL) in a microwave tube. The argon bubbled mixture was stirred at 155 °C for 16 h. After cooling to room temperature, the mixture was purified by column

chromatography using firstly a 4:1 mixture of hexane and ethyl acetate and then THF as eluent. After removal of the solvent in vacuo, the product was dissolved in methylene chloride, filtered over silica, concentrated in vacuo, precipitated in hexane, filtered and dried to afford 221 mg (0.090 mmol, 71%) pure compound as a pale yellow powder.

^{1}H-NMR (500 MHz, THF-d8, 298 K) δ 7.54 – 7.44 (≥12 s, 4H, H^{a}), 3.14 (m, 8H, H^{b}), 1.59 (m, 8H, H^{c}), 1.32 (m, 8H, H^{d}), 0.93 (t, $^{3}J_{HH}$ = 7.3 Hz, 12H, H^{e})

^{2}H-NMR (77 MHz, THF-d8, 298 K) δ 7.07

^{13}C-NMR (126 MHz, THF-d8, 298 K) δ 150.26, 148.43, 144.49, 143.08–142.34 (n.r.), 141.62–141.08 (n.r.), 140.20–140.01 (n.r.), 133.21-132.69 (≥8 s, *C*-H, C^{a}), 132.25, 130.60, 127.87, 127.06, 126.47, 125.91, 125.65, 116.29, 59.36 (*C*H$_2$, C^{b}), 24.56 (*C*H$_2$, C^{c}), 20.64 (*C*H$_2$, C^{d}), 14.05 (*C*H$_3$, C^{e})

^{19}F-NMR (471 MHz, THF-d8, 298 K) δ -130.31 – -132.72 (m, 8F), -144.81 – -146.46 (m, 8F)

^{11}B-NMR (160 MHz, THF-d8, 298 K) δ -14.75

MALDI-TOF (m/z): calcd. for $C_{144}H_4D_{80}BF_{16}^-$: 2209.2, found: 2209.0 [M$^-$]

Tetrabutlyammonium tetrakis(2,3,5,6-tetrafluoro-4-(^{D}G1)phenyl)borate (109) TBA$^+$ [B^{F}-^{D}G1]$^-$

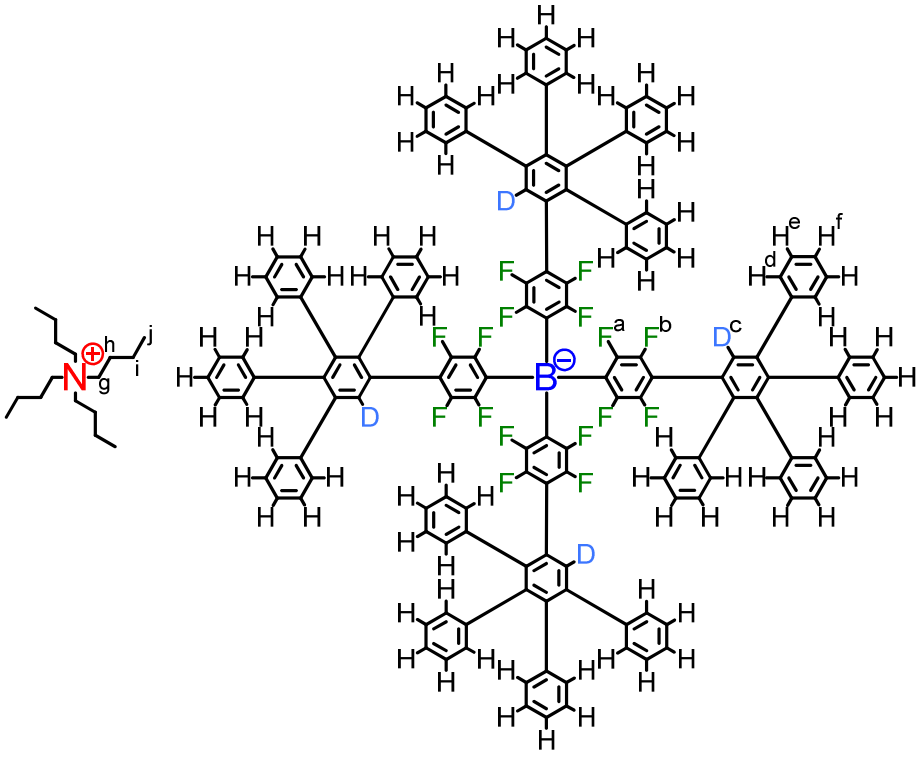

50 mg (0.053 mmol) of freshly prepared, partly deuterated $TBA^+B(Ph^F\text{-in-}D)_4^-$ **52** and 91 mg (0.237 mmol) tetracyclone were dissolved in *o*-xylene (5 mL) in a microwave tube. The argon bubbled mixture was stirred at 155 °C for 16 h. After cooling to room temperature, the mixture was purified by column chromatography using firstly a 10:1 mixture of hexane and ethyl acetate and then THF as eluent. After removal of the solvent in vacuo, the product was dissolved in methylene chloride, precipitated in hexane, filtered and dried to afford 90 mg (0.038 mmol, 72%) of the product as a pale yellow powder.

^{1}H-NMR (300 MHz, THF-d8, 298 K) δ 7.54 – 7.44 (≥12 s, 1.92H/2.08D, H^c), 7.22 – 7.01 (m, 20H, H^d + H^e + H^f), 6.95 – 6.59 (m, 60H), 3.18 (m, 8H, H^g), 1.63 (m, 8H, H^h), 1.35 (m, 8H, H^i), 0.96 (t, $^3J_{HH}$ = 7.3 Hz, 12H, H^j)

^{2}H-NMR (77 MHz, THF-d8, 298 K) δ 7.63

^{13}C-NMR (126 MHz, THF-d8, 298 K) δ 142.86, 141.63, 141.43, 140.35, 132.75 (*C*-H), 132.58 (*C*-H), 131.07 (*C*-H), 130.89 (*C*-H), 128.38 (*C*-H), 126.97 (*C*-H), 126.39 (*C*-H), 126.19 (*C*-H), 59.42 (CH_2, C^g), 24.62 (CH_2, C^h), 20.70 (CH_2, C^i), 14.05 (CH_3, C^j)

^{19}F-NMR (471 MHz, THF-d8, 298 K) δ -130.49 – -132.25 (m, 8F, F^a), -144.79 – -146.16 (m, 8F, F^b)

^{11}B-NMR (160 MHz, THF-d8, 298 K) δ -14.76

MALDI-TOF (m/z): calcd. for $C_{144}H_{80}D_4BF_{16}^-$: 2132.7, found: 2131.3 [M^-]

1,2-bis(3,5-bis(trifluoromethyl)phenyl)ethyne (42)

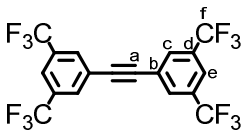

Analoge procedure to *Stille* coupling for electron poor aromatics[199]

0.434 g (1.655 mmol) PPh_3, 0.315 g (1.655 mmol) CuI, 5.028 g (33.100 mmol) CsF, 0.581 g (0.827 mmol) $Pd(PPh_3)_2Cl_2$ and 14.547 g (49.650 mmol, 8.53 mL) 1-bromo-3,5-bis(trifluoromethyl)benzene were dissolved in 500 mL anhydrous DMF. 10.000 g (8.72 mL, 16.550 mmol) 1,2-bis(tributylstannyl)ethyne were added dropwise over 30 min, and the stirred mixture was heated to 45 °C over night. Triethylamine (5%) was added and the mixture was filtered over silica. After removal of the solvent in vacuo the crude product was purified by column chromatography using hexane as eluent to yield 3.906 g (52%) of the pure compound as colorless crystals.

R_f (Hexane) = 0.73

^{1}H-NMR (300 MHz, THF-d8, 298 K) δ 8.23 (s, 4H, H^c), 8.12 (s, 2H, H^e)

^{13}C-NMR (75 MHz, THF-d8, 298 K) δ 133.16 (q, $^2J_{CF}$ = 33.8 Hz, *C*, C^d), 133.09 (q, $^3J_{CF}$ = 3.3 Hz, *C*H, C^c), 125.70 (s, C^b), 124.28 (q, $^1J_{CF}$ = 272.7 Hz, *C*, C^f), 123.86 (sept, $^3J_{CF}$ = 3.8 Hz, *C*H, C^e), 90.23 (s, C^a)

^{19}F-NMR (471 MHz, THF-d8, 298 K) δ -62.08 (s, 12F)

FDMS (m/z): calcd. for $C_{18}H_6O_{12}$: 450.0, found: 449.5 (detection difficult!)

Dicobalt hexacarbonyl complex of 42 (43)

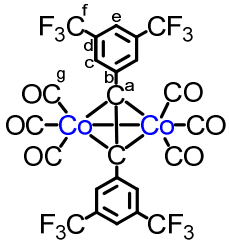

182 mg (0.404 mmol) of 1,2-bis(3,5-bis(trifluoromethyl)phenyl)ethyne **42** were dissolved in *o*-xylene (5 mL) in a microwave tube. After several times of degassing the solution under argon, about 138 mg (0.404 mmol) of dicobalt octacarbonyl were added and the mixture stirred at room temperature for 14 h. The mixture was then heated to 140 °C for 24 h (initial goal: formation of tetracyclone; failed). After removal of the solvent in vacuo, the remainder was dissolved in methylene chloride and filtered over aluminum oxide, evaporated and dried under vacuum to yield 280 mg (0.377 mmol, 93%) **43** as a dark red solid.

R_f (Hexane) = 0.36

^{1}H-NMR (300 MHz, CD_2Cl_2, 298 K) δ 7.93 (s, 4H, H^c), 7.91 (s, 2H, H^e)

^{13}C-NMR (176 MHz, CD_2Cl_2, 298 K) δ 141.73 (*C*, C^b), 133.29 (q, $^2J_{CF}$ = 33.5 Hz, *C*, C^d), 129.12 (q, $^3J_{CF}$ = 2.8 Hz, *C*H, C^c), 123.56 (q, $^1J_{CF}$ = 272.7 Hz, *C*, C^f), 122.31 (sept, $^3J_{CF}$ = 3.4 Hz, *C*H, C^e), 87.33 (s, *C*, C^a), carbonyl-C (C^g) expected at negative chemical shifts which were not measured!

FDMS (m/z): calcd. for $C_{24}H_{12}Co_2F_{12}O_6$: 741.9, found: 739.3

(5-bromo-1,3-phenylene)bis(ethyne-2,1-diyl)bis(triisopropylsilane) (33)

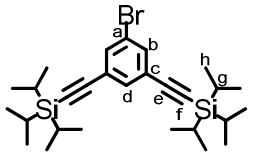

Synthesis according to literature procedure[61]

^{1}H-NMR (300 MHz, THF-d8, 298 K) δ 7.61 (d, $^{4}J_{HH}$ = 1.4 Hz, 2H, H^{b}), 7.48 (t, $^{4}J_{HH}$ = 1.4 Hz, 1H, H^{d}), 1.15 (n.r., 42H, H^{g} + H^{h})

^{13}C-NMR (75 MHz, THF-d8, 298 K) δ 135.65 (*C*H, C^{b}), 134.53 (*C*H, C^{d}), 126.48 (C^{c}), 122.79 (C^{a}), 105.67 (C^{f}), 93.89 (C^{e}), 19.16 (*C*H, C^{h}), 12.36 (*C*H, C^{g})

FDMS (m/z): calcd. for $C_{28}H_{45}BrSi_2$: 518.2, found: 518.8

1-bromo-4-ethynylbenzene (15)

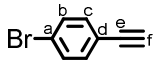

To a solution of 1.00 g (2.96 mmol) ((4-Bromophenyl)ethynyl)triisopropylsilane **10** in 100 mL THF was added dropwise a solution of tetrabutylammonium fluoride (0.99 g, 3.56 mmol) in 40 mL THF. The mixture was stirred for 2 h at room temperature. The mixture was extracted three times with concentrated aqueous solution of sodium chloride and dried over $MgSO_4$. After removal of the solvent in vacuo, the raw product was purified by column chromatography using hexane as eluent to afford 515 mg (96%) of the pure product as a colorless solid.

^{1}H-NMR (300 MHz, THF-d8, 298 K) δ 7.51 (d, $^{3}J_{HH}$ = 8.6 Hz, 2H, H^{b}), 7.36 (d, $^{3}J_{HH}$ = 8.6 Hz, 2H, H^{c}), 3.65 (s, 1H, H^{f})

^{13}C-NMR (75 MHz, THF-d8, 298 K) δ 134.60 (*C*H, C^{c}), 132.68 (*C*H, C^{b}), 123.75 (C^{a}), 122.80 (C^{d}), 83.30 (C^{e}), 80.34 (C^{f})

4-Bromo-3',4',5'-triphenyl-1,1':2',1''-terphenyl (16)

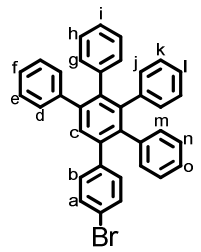

150 mg (0.829 mmol) of 1-bromo-4-ethynylbenzene **15** and 382 mg (0.994 mmol) tetraphenylcyclopentadienone were dissolved in *o*-xylene (5 mL) in a microwave tube. The mixture was heated to 160 °C for 12 h. After cooling to room temperature, the product had formed a white precipitate from which the remaining solution was decanted off. The precipitate was suspended in methanol, filtered and dried to afford 409 mg (0,761 mmol, 92%) of the product as a white powder.

R_f (Hexane) = 0.03

^{1}H-NMR (300 MHz, CD_2Cl_2, 298 K) δ 7.50 (s, 1H, H^c), 7.30 (d, $^3J_{HH}$ = 8.5 Hz, 2H, H^a), 7.17 (s, 5H, H^d + H^e + H^f), 7.06 (d, $^3J_{HH}$ = 8.5 Hz, 2H, H^b), 6.99 – 6.82 (n.r., 15H, H^g – H^o)

^{13}C-NMR (75 MHz, CD_2Cl_2, 298 K) δ 142.55 (*C*), 142.26 (*C*), 141.53 (*C*), 141.44 (*C*), 140.92 (*C*), 140.62 (*C*), 140.43 (*C*), 140.30 (*C*), 140.07 (*C*), 139.84 (*C*), 132.23 (*C*-H), 132.05 (*C*-H), 131.99 (*C*-H), 131.55 (*C*-H), 131.26 (*C*-H), 130.48 (*C*-H), 128.18 (*C*H), 127.62 (*C*-H), 127.45 (*C*-H), 127.17 (*C*-H), 126.92 (*C*-H), 126.40 (*C*-H), 126.25 (*C*-H), 125.98 (*C*-H), 121.04 (*C*)

MALDI-TOF (m/z): calcd. for $C_{36}H_{25}Br$: 536.1, found: 535.8

Cp-on(G1)$_2$ (**23**)

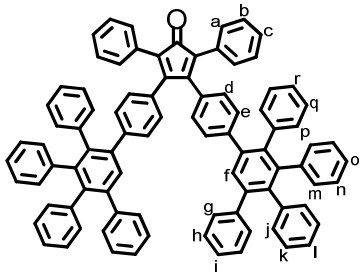

Synthesis according to literature procedure[191]

^{1}H-NMR (300 MHz, CD_2Cl_2, 298 K) δ 7.50 (s, 2H, H^f), 7.27 – 7.12 (n.r., 20H, H^a + H^b + H^c + H^g + H^h + H^i), 6.95 (d, $^{3}J_{HH}$ = 8.4 Hz, 4H, H^e), 6.95 – 6.79 (n.r., 30H, H^j – H^r), 6.65 (d, $^{3}J_{HH}$ = 8.4 Hz, 4H, H^d)

^{13}C-NMR (75 MHz, CD_2Cl_2, 298 K) δ 200.57 (*C*, carbonyl-C), 154.66 (*C*, β-carbonyl-C), 142.74 (*C*), 142.31 (*C*), 142.27 (*C*), 141.38 (*C*), 140.94 (*C*), 140.81 (*C*), 140.62 (*C*), 140.44 (*C*), 140.18 (*C*), 139.81 (*C*), 132.08 (*C*H), 132.02 (*C*H), 131.97 (*C*H), 131.55 (*C*), 131.37 (*C*H), 131.27 (*C*), 130.67 (*C*H), 130.45 (*C*H), 129.96 (*C*H), 129.42 (*C*H), 128.51 (*C*H), 128.12 (*C*H), 127.86 (*C*H), 127.36 (*C*H), 127.10 (*C*H), 126.86 (*C*H), 126.35 (*C*H), 126.17 (*C*H), 125.91 (*C*H), 125.80 (*C*)

Lithium tetrakis(2,3,5,6-tetrafluoro-4-(G1)phenyl)borate $Li^+ [B^F\text{-}G1]^-$ **(96)**

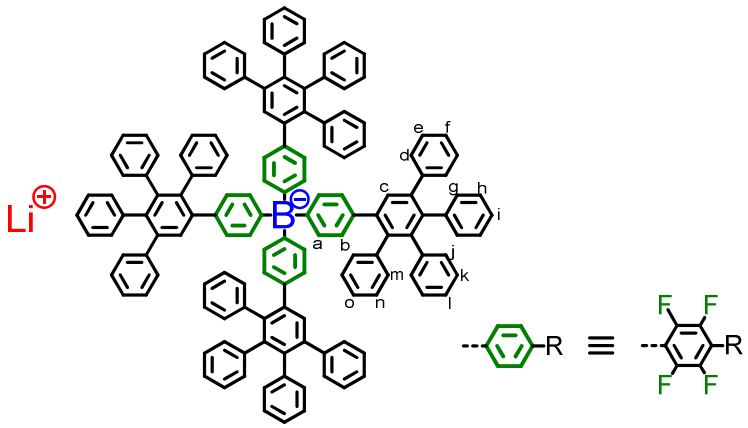

256 mg (0.108 mmol) of $TBA^+ (B^F\text{-}G1)_4^-$ **53** were dissolved in 15 mL anhydrous THF under argon. The solution was cooled to -78 °C, an excess of *n*-BuLi (0.2 mL of a 1.6 M solution in hexane; about 0.324 mmol) was added and the solution was allowed to warm to room temperature. After 3 h at room temperature, an excess of water was added. Methylene chloride was added and the organic phase was separated. After evaporation of the solvent in vacuum, the orange remainder was dissolvend in methylene chloride, precipitated in hexane, filtered and dried to afford 176 mg (0.095 mmol, 90%) of the product as a beige powder.

^{1}H-NMR (700 MHz, THF-d8, 298 K) δ 7.55 – 7.44 (≥13 s, 4H, H^c), 7.22 – 7.02 (m, 20H, H^d + H^e + H^f), 6.96 – 6.57 (m, 60H, H^g – H^o)

^{7}Li-NMR (194 MHz, THF-d8, 298 K) δ -0.74

^{13}C-NMR (75 MHz, THF-d8, 298 K) δ 145.24, 142.88, 141.44, 140.35, 132.74, 131.07, 128.35, 127.72, 127.46, 126.93, 126.35, 126.14

^{19}F-NMR (471 MHz, THF-d8, 298 K) δ -132.79 – -134.57 (m, 8F, F^a), -147.19 – -148.79 (m, 8F, F^b)

^{11}B-NMR (160 MHz, THF-d8, 298 K) δ -16.66

DOSY-NMR (194 MHz, THF-d8, 298 K) $D_{lithium}$ = 3.16·10^{-10} m^{2}s^{-1}; r_H = 1.34 nm (due to THF solvation shell!)

Tetraphenylphosphonium tetrakis(4-(G1)phenyl)borate PPh_4^+ [B-G1]$^-$ **(97)**

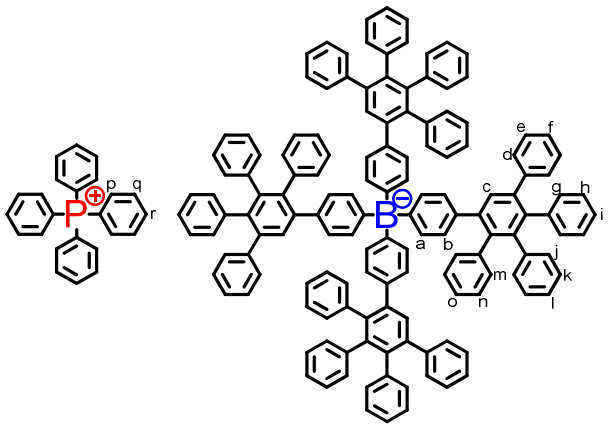

About 90 mg (0.049 mmol) of Li^+B-G1$^-$ and about 400 mg (0.954 mmol) of tetraphenylphosphonium bromide were dissolved in a 3:1 mixture of methylene chloride and THF. The mixture was filtered over silica using methylene chloride as eluent. After evaporation of the solvent in vacuum, the solid remainder was redissolved in methylene chloride, precipitated in hexane, filtered and dried to afford 96 mg (0.044 mmol, about 91%) pure product as a colorless powder.

^{1}H-NMR (500 MHz, THF-d8, 298 K) δ 7.76 (t, $^3J_{HH}$ =7.8 Hz, 4H, H^r), 7.56 (n.r., 16H, H^p + H^q), 7.45 (s, 4H, H^c), 7.10 (d, $^3J_{HH}$ = 6.6 Hz, 8H, H^d), 7.05 (t, $^3J_{HH}$ = 7.1 Hz, 8H, H^e), 7.02 (t, $^3J_{HH}$ = 7.0 Hz, 4H, H^f), 6.86 – 6.74 (m, 60H, H^a + H^g–H^o), 6.58 (d, $^3J_{HH}$ = 7.9 Hz, 8H, H^b)

^{13}C-NMR (126 MHz, THF-d8, 298 K) δ 163.27 (q, $^1J_{BC}$ = 49.5 Hz, *C*-B), 144.90 (*C*), 143.65 (*C*), 142.41 (*C*), 142.18 (*C*), 141.98 (*C*), 141.87 (*C*), 141.19 (*C*), 140.50 (*C*), 138.71 (*C*), 136.68(*C*-H, C^a), 136.55 (d, $^4J_{PC}$ = 2.7 Hz, *C*-H, C^r), 135.67 (d, $^3J_{PC}$ = 10.4 Hz, *C*-H, C^q), 135.29 (*C*), 132.80 (*C*-H, C^g + C^j + C^m), 132.69 (*C*-H, C^c), 131.57 (d, $^2J_{PC}$ = 12.9 Hz, *C*-H, C^p), 131.05 (*C*-H, C^d), 128.30 (*C*-H, C^e), 127.67 (*C*-H, C^{meta}), 127.58 (*C*-H, C^b), 127.51 (*C*-H, C^{meta}), 127.36 (*C*-H, C^{meta}), 126.68 (*C*-H, C^f), 126.08 (*C*-H, C^{para}), 125.99 (*C*-H, C^{para}), 125.81 (*C*-H, C^{para}), 119.06 (d, $^1J_{PC}$ = 89.3 Hz, *C*)

^{11}B-NMR (160 MHz, THF-d8, 298 K) δ -5.46

^{31}P-NMR (202 MHz, THF-d8, 298 K) δ 24.76

Tetraphenylphosphonium tetrakis(2,3,5,6-tetrafluoro-4-(G1)phenyl)borate PPh_4^+ $[B^F\text{-}G1]^-$ **(98)**

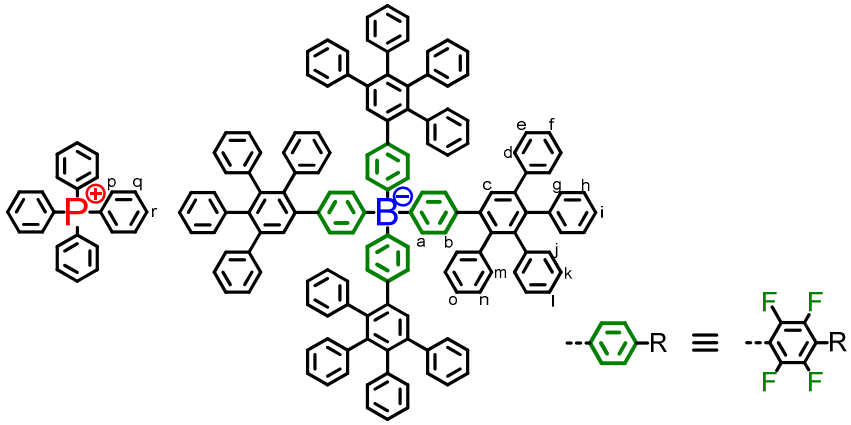

About 33 mg (0.018 mmol) of $Li^+B^F\text{-}G1^-$ **96** and about 200 mg (0.477 mmol) of tetraphenylphosphonium bromide were dissolved in a 3:1 mixture of methylene chloride and THF. The mixture was filtered over silica using methylene chloride as eluent. After evaporation of the solvent in vacuum, the solid remainder was redissolved in methylene chloride, precipitated in hexane, filtered and dried to afford 41 mg (0.017 mmol, about 93%) pure product as a colorless powder.

^{1}H-NMR (700 MHz, CD_2Cl_2, 298 K) δ 7.86 (t, $^3J_{HH}$ = 7.5 Hz, 4H, H^r), 7.66 (td, $^3J_{HH}$ = 7.8 Hz, $^4J_{PH}$ = 3.4 Hz, 8H, H^q), 7.54 (dd, $^3J_{PH}$ = 12.9 Hz, $^3J_{HH}$ = 7.8 Hz, 8H, H^p), 7.50 – 7.36 (≥10 s, 4H, H^c), 7.22 – 7.10 (m, 20H, H^d + H^e + H^f), 7.03 – 7.62 (m, 60H, H^g – H^o)

^{13}C-NMR (176 MHz, CD_2Cl_2, 298 K) δ 142.35 (*C*), 142.10 (*C*), 142.01 (*C*), 141.93 (*C*), 141.10 (*C*), 140.99 (*C*), 140.88 (*C*), 140.65 (*C*), 139.70 (*C*), 136.30 (d, $^4J_{PC}$ = 2.7 Hz, *C*-H, C^r), 134.92 (d, $^3J_{PC}$ = 10.4 Hz, *C*-H, C^q), 132.10 (*C*-H), 131.14 (d, $^2J_{PC}$ = 12.9 Hz, *C*-H, C^p), 130.58 (*C*-H), 130.55 (*C*-H), 130.51 (*C*-H), 129.49 (*C*-H), 128.09 (*C*-H), 128.04 (*C*-H), 127.38 (*C*-H), 127.11 (*C*-H), 126.77 (*C*-H), 126.68 (*C*-H), 126.17 (*C*-H), 125.95 (*C*-H), 118.03 (d, $^1J_{PC}$ = 89.8 Hz, *C*), 115.86 (*C*)

^{19}F-NMR (471 MHz, CD_2Cl_2, 298 K) δ -133.86 – -135.16 (m, 8F, F^a), -146.59 – -147.46 (m, 8F, F^b)

^{11}B-NMR (225 MHz, CD_2Cl_2, 298 K) δ -16.73

^{31}P-NMR (283 MHz, CD_2Cl_2, 298 K) δ 23.25

(4'-bromo-[1,1'-biphenyl]-4-yl)triphenylphosphonium bromide $Ph_3P(PhPh\text{-}Br)^+ Br^-$

(99)

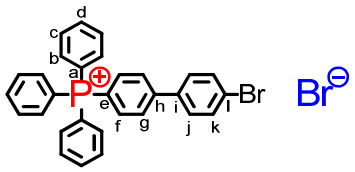

Synthesis according to literature procedure[220]

^{1}H-NMR (700 MHz, CD_2Cl_2, 298 K) δ 7.98 (dd, $^3J_{HH}$ = 8.4 Hz, $^4J_{PH}$ = 3.0 Hz, 2H, H^g), 7.95 (t, $^3J_{HH}$ = 7.6 Hz, 3H, H^d), 7.80 (td, $^3J_{HH}$ = 8.0 Hz, $^4J_{PH}$ = 3.6 Hz, 6H, H^c), 7.73 (dd, $^3J_{PH}$ = 12.7 Hz, $^3J_{HH}$ = 8.4 Hz, 2H, H^f), 7.68 (dd, $^3J_{PH}$ = 13.1 Hz, $^3J_{HH}$ = 7.5 Hz, 6H, H^b), 7.66 (d, $^3J_{HH}$ = 8.5 Hz, 2H, H^k), 7.62 (d, $^3J_{HH}$ = 8.5 Hz, 2H, H^j)

^{13}C-NMR (176 MHz, CD_2Cl_2, 298 K) δ 147.49 (d, $^4J_{PC}$ = 3.1 Hz, *C*, C^h), 137.67 (d, $^5J_{PC}$ = 1.3 Hz, *C*, C^j), 136.26 (d, $^4J_{PC}$ = 3.1 Hz, *C*-H, C^d), 135.61 (d, $^3J_{PC}$ = 10.6 Hz, *C*-H, C^g), 134.95 (d, $^3J_{PC}$ = 10.3 Hz, *C*-H, C^c),132.90 (*C*, C^j), 131.18 (d, $^2J_{PC}$ = 12.9 Hz, *C*-H, C^b), 129.61 (*C*, C^k), 129.34 (d, $^2J_{PC}$ = 13.4 Hz, *C*-H, C^f), 124.25 (*C*, C^l), 118.02 (d, $^1J_{PC}$ = 89.9 Hz, *C*, C^a), 115.97 (d, $^1J_{PC}$ = 91.1 Hz, *C*, C^e)

^{31}P-NMR (284 MHz, CD_2Cl_2, 298 K) δ 23.02

MALDI-TOF (m/z): calcd. for $C_{30}H_{23}BrP^+$: 493.1, found: 493.0 [M^+]

XRD: colorless needles, triclinic, P-1

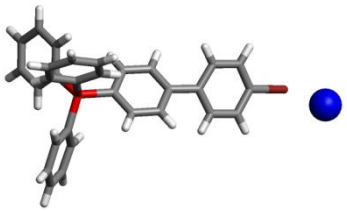

[1,1'-biphenyl]-4,4'-diylbis(triphenylphosphonium) bromide $[Ph_3P(PhPh)PPh_3]^{2+} Br^-Br^-$

(100)

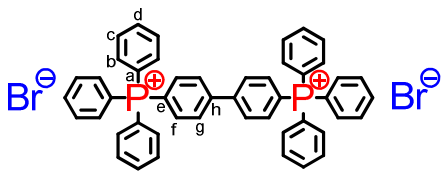

1.500 g (2.612 mmol) of phosphonium salt **99**, 1.370 g (5.224 mmol) PPh_3 and about 0.571 g (2.612 mmol) $NiBr_2$ were vigorously pestled, filled into a teflon container, put into an autoclave and heated to 200 °C for 5 h. The obtained dark-green solid was loosened with a metal spatula, dispersed in water and extracted several times with diethylether (removal of excess PPh_3 and phosphinoxide). The product was then extracted into methylene chloride, precipitated in THF, filtered, dried and recrystallized from a mixture of methylene chloride and THF to afford 1.890 g (86%) of the product as a white powder.

^{1}H-NMR (700 MHz, CD_2Cl_2, 298 K) δ 8.32 (dd, $^3J_{HH}$ = 8.5 Hz, $^4J_{PH}$ = 3.0 Hz, 4H, H^g), 7.93 (t, $^3J_{HH}$ = 7.5 Hz, 6H, H^d), 7.85 (dd, $^3J_{PH}$ = 12.7 Hz, $^3J_{HH}$ = 8.5 Hz, 4H, H^f), 7.79 (td, $^3J_{HH}$ = 7.9 Hz, $^4J_{PH}$ = 3.5 Hz, 12H, H^c), 7.69 (dd, $^3J_{PH}$ = 13.1 Hz, $^3J_{HH}$ = 7.4 Hz, 12H, H^b)

^{13}C-NMR (176 MHz, CD_2Cl_2, 298 K) δ 145.89 (*C*, C^h), 136.26 (*C*-H, C^d), 135.97 (d, $^3J_{PC}$ = 10.3 Hz, *C*-H, C^g), 135.15 (d, $^3J_{PC}$ = 10.6 Hz, *C*-H, C^c), 131.23 (d, $^2J_{PC}$ = 13.0 Hz, *C*-H, C^b), 130.58 (d, $^2J_{PC}$ = 13.3 Hz, *C*-H, C^f), 118.31 (d, $^1J_{PC}$ = 90.3 Hz, *C*, C^e), 118.14 (d, $^1J_{PC}$ = 89.6 Hz, *C*, C^a)

^{31}P-NMR (284 MHz, CD_2Cl_2, 298 K) δ 23.05

MALDI-TOF (m/z): calcd. for $C_{48}H_{38}P_2^{2+}$: 338.1, found: 339.5 [M^{2+}] (+fragmentation)

XRD: colorless prisms, triclinic, P-1

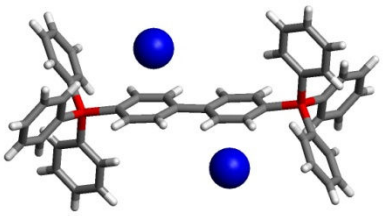

[1,1'-biphenyl]-4,4'-diylbis(triphenylphosphonium) tetraphenylborate $[Ph_3P(PhPh)PPh_3]^{2+}\ BPh_4^-\ BPh_4^-$ (**101**)

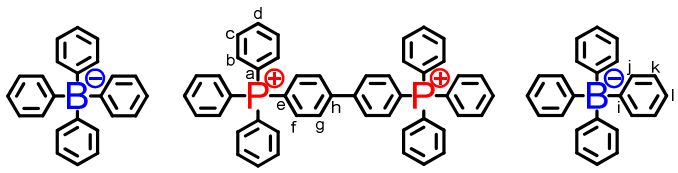

To a solution of 191 mg (0.228 mmol) diphosphonium salt **100** in a 1:1 mixture of methylene chloride and THF were added 71 mg (0.207 mmol) sodium tetraphenylborate. The solution was stirred for 10 min at room temperature and the solvent removed in vacuum. The solid remainder

was redissolved in methylene chloride and the solution filtered over silica. Upon addition of hexane to the DCM solution, 245 mg (0.186 mmol, 90%) of the product started crystallizing as a colorless solid.

^{1}H-NMR (700 MHz, CD_2Cl_2, 298 K) δ 7.90 (t, $^{3}J_{HH}$ = 7.2 Hz, 6H, H^{d}), 7.69 (td, $^{3}J_{HH}$ = 7.9 Hz, $^{4}J_{PH}$ = 3.6 Hz, 12H, H^{c}), 7.59 (dd, $^{3}J_{HH}$ = 8.4 Hz, $^{4}J_{PH}$ = 3.0 Hz, 4H, H^{g}), 7.55 (dd, $^{3}J_{PH}$ = 13.1 Hz, $^{3}J_{HH}$ = 7.5 Hz, 12H, H^{b}), 7.47 (dd, $^{3}J_{PH}$ = 12.7 Hz, $^{3}J_{HH}$ = 8.4 Hz, 4H, H^{f}), 7.22 (n.r., 16H, H^{j}), 6.86 (t, $^{3}J_{HH}$ = 7.4 Hz, 16H, H^{k}), 6.73 (t, $^{3}J_{HH}$ = 7.2 Hz, 8H, H^{l})

^{13}C-NMR (176 MHz, CD_2Cl_2, 298 K) δ 164.55 (q, $^{1}J_{BC}$ = 49.2 Hz, *C*, C^{i}), 145.66 (*C*, C^{h}), 136.50 (*C*-H, C^{j}), 136.40 (*C*-H, C^{d}), 135.69 (d, $^{3}J_{PC}$ = 10.7 Hz, *C*-H, C^{g}), 134.98 (d, $^{3}J_{PC}$ = 10.3 Hz, *C*-H, C^{c}), 131.26 (d, $^{2}J_{PC}$ = 13.1 Hz, *C*-H, C^{b}), 130.14 (d, $^{2}J_{PC}$ = 13.2 Hz, *C*-H, C^{f}), 126.09 (*C*-H, C^{k}), 122.26 (*C*-H, C^{l}), 118.22 (d, $^{1}J_{PC}$ = 90.4 Hz, *C*, C^{e}), 117.85 (d, $^{1}J_{PC}$ = 89.4 Hz, *C*, C^{a})

^{11}B-NMR (225 MHz, CD_2Cl_2, 298 K) δ -6.64

^{31}P-NMR (283 MHz, CD_2Cl_2, 298 K) δ 23.09

XRD: colorless prisms, triclinic, P-1

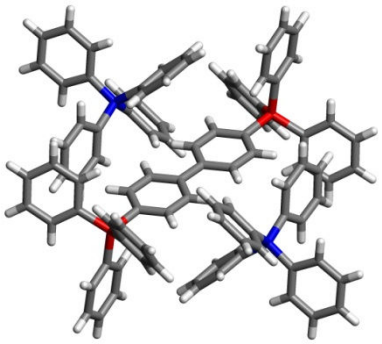

[1,1'-biphenyl]-4,4'-diylbis(triphenylphosphonium) tetrakis(perfluorophenyl)borate

$[Ph_3P(PhPh)PPh_3]^{2+}$ $BPh^{F}_{4}{}^{-}$ $BPh^{F}_{4}{}^{-}$ (**102**)

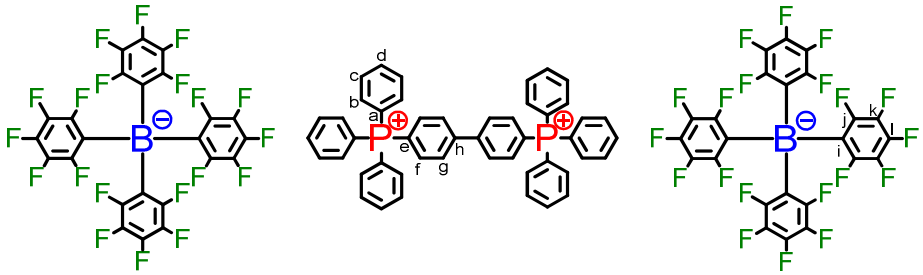

To a solution of 221 mg (0.264 mmol) diphosphonium salt **100** in methylene chloride were added 200 mg (0.240 mmol) lithium tetrakis(perfluorophenyl)borate dietherate. The solution was stirred

for 10 min at room temperature and then filtered directly over silica. After addition of hexane to the DCM solution and gradual evaporation of solvent, 401 mg (0.197 mmol, 82%) of the product crystallized as a colorless solid.

^{1}H-NMR (700 MHz, CD_2Cl_2, 298 K) δ 7.91 (t, $^{3}J_{HH}$ = 7.6 Hz, 6H, H^{d}), 7.87 (dd, $^{3}J_{HH}$ = 8.5 Hz, $^{4}J_{PH}$ = 3.0 Hz, 4H, H^{g}), 7.72 (td, $^{3}J_{HH}$ = 8.0 Hz, $^{4}J_{PH}$ = 3.7 Hz, 12H, H^{c}), 7.71 (dd, $^{3}J_{PH}$ = 12.6 Hz, $^{3}J_{HH}$ = 8.5 Hz, 4H, H^{f}), 7.63 (dd, $^{3}J_{PH}$ = 13.1 Hz, $^{3}J_{HH}$ = 7.4 Hz, 12H, H^{b})

^{13}C-NMR (75 MHz, CD_2Cl_2, 298 K) δ 150.37 (*C*), 147.12 (*C*), 145.84 (*C*, C^{h}), 140.44 (*C*), 138.47 (*C*), 137.16 (*C*), 136.47 (d, $^{4}J_{PC}$ = 3.0 Hz, *C*-H, C^{d}), 135.76 (d, $^{3}J_{PC}$ = 10.7 Hz, *C*-H, C^{g}), 134.96 (d, $^{3}J_{PC}$ = 10.4 Hz, *C*-H, C^{c}), 131.24 (d, $^{2}J_{PC}$ = 13.0 Hz, *C*-H, C^{b}), 129.78 (d, $^{2}J_{PC}$ = 13.3 Hz, *C*-H, C^{f}), 119.06 (d, $^{1}J_{PC}$ = 90.4 Hz, *C*, C^{e}), 117.85 (d, $^{1}J_{PC}$ = 89.9 Hz, *C*, C^{a})

^{19}F-NMR (471 MHz, CD_2Cl_2, 298 K) δ -133.02 (s, 16F, F^{j}), -163.49 (t, $^{3}J_{FF}$ = 20.3 Hz, 8F, F^{l}), -167.34 (m, 16F, F^{k})

^{11}B-NMR (160 MHz, CD_2Cl_2, 298 K) δ -16.70

^{31}P-NMR (283 MHz, CD_2Cl_2, 298 K) δ 23.32

XRD: colorless prisms, triclinic, P-1

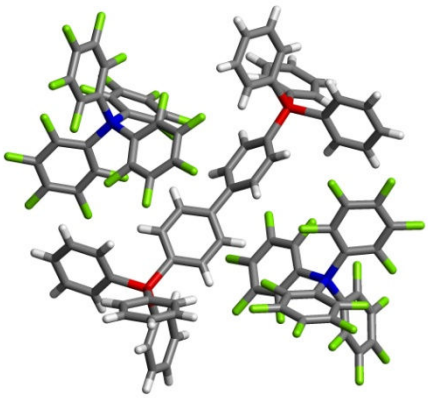

2,5-diphenyl-3,4-bis(4'-((*E*)-(4-((triisopropylsilyl)ethynyl)phenyl)diazenyl)-[1,1'-biphenyl]-4-yl)cyclopenta-2,4-dienone Cp-on(azo-in-T*i*PS)$_2$ (**111**)

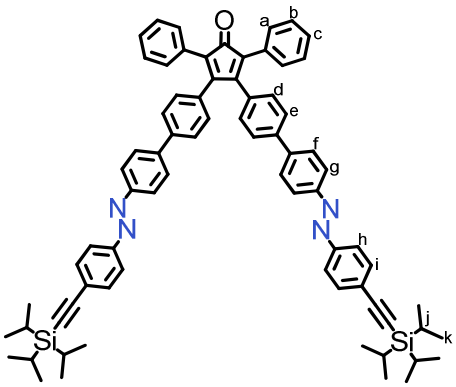

0.460 g (0.494 mmol) of azobenzene functionalized benzil **110** and 0.104 g (0.494 mmol) 1,3-diphenylpropan-2-one were dispersed in 5 mL ethanol, dissolved in 40 mL THF and heated to reflux. 0.128 g (494 mmol; 1 M in methanol) tetrabutylammonium were added and the mixture was stirred for 10 min. After cooling to room temperature, the mixture was filtered over silica using methylene chloride as eluent. After evaporation of the solvent in vacuum, the crude product was purified by means of gel permeation chromatography using methylene chloride as eluent to yield 0.271 g (0.245 mmol, 50%) of the product (which also contained about 20% of the according hydroxytetracyclone **122**, see paragraph 7.2) as a dark red solid.

^{1}H-NMR (300 MHz, THF-d8, 298 K) δ 8.00 (d, $^{3}J_{HH}$ = 8.6 Hz, 4H, H^{g}), 7.91 (d, $^{3}J_{HH}$ = 8.6 Hz, 4H, H^{h}), 7.87 (d, $^{3}J_{HH}$ = 8.7 Hz, 4H, H^{f}), 7.69 (d, $^{3}J_{HH}$ = 8.5 Hz, 4H, H^{e}), 7.63 (d, $^{3}J_{HH}$ = 8.6 Hz, 4H, H^{i}), 7.32 – 7.20 (n.r., 10H, H^{a} + H^{b} + H^{c}), 7.15 (d, $^{3}J_{HH}$ = 8.4 Hz, 4H, H^{d}), 1.18 (m, 42H, H^{j} + H^{k})

^{13}C-NMR (75 MHz, THF-d8, 298 K) δ 200.04 (*C*=O), 154.75 (*C*), 153.19 (*C*), 153.06 (*C*), 143.94 (*C*), 140.79 (*C*), 134.29 (*C*), 133.87 (*C*-H), 132.22 (*C*), 131.34 (*C*-H), 131.29 (*C*-H), 128.92 (*C*-H), 128.48 (*C*-H), 128.41 (*C*-H), 127.54 (*C*-H), 127.15 (*C*), 126.82 (*C*), 124.53 (*C*-H), 123.84 (*C*-H), 108.15 (C≡*C*-Si), 94.00 (*C*≡C-Si), 19.23 (*C*-H, C^{j}), 12.44 (*C*H$_3$, C^{k})

FDMS (m/z): calcd. for $C_{75}H_{76}N_4OSi_2$: 1104.6, found: 1106.3, 1122.3 (+OH)

Tetrabutlyammonium tetrakis(2,3,5,6-tetrafluoro-4-((bis(triisopropylsilylethynylazobenzene))-G1)phenyl)borate TBA^+ $[B^F\text{-G1(azo-in-T}i\text{PS)}_8]^-$ (**113**)

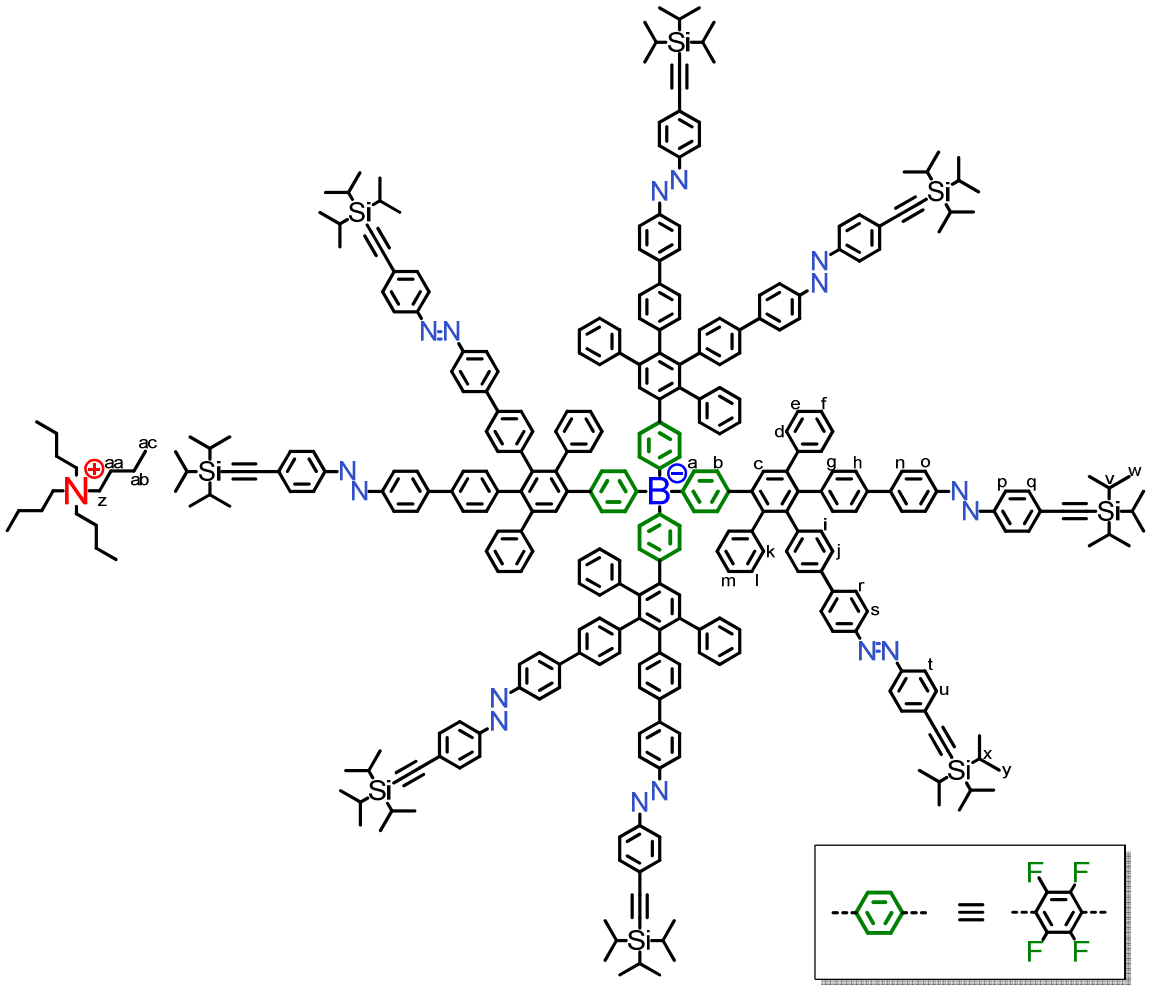

14 mg (0.015 mmol) of $TBA^+[B(Ph^F\text{-in})_4]^-$ **52** and 98 mg (0.089 mmol) azo-AB_2 building block **111** were dissolved in *o*-xylene (15 mL) in a microwave tube. The argon bubbled mixture was stirred at 155 °C for 40 h. After cooling to room temperature, the mixture was purified by column chromatography using firstly a 10:1 mixture of hexane and ethyl acetate and then methylene chloride as eluent. The solvent was removed in vacuum to afford 27.9 mg (0.005 mmol, 36%) of the compound as a red-orange solid.

^{1}H-NMR (700 MHz, THF-d8, 298 K) δ 7.93 – 7.86 (n.r., 32H, H^o + H^p + H^s + H^t), 7.75 – 7.68 (n.r., 16H, H^n + H^r), 7.65 – 7.54 (≥6 s, 4H, H^c), 7.62 – 7.59 (n.r., 16H, H^q + H^u), 7.45 – 6.68 (n.r., 72H), 3.19 (m, 4.80H, H^z), 3.11 (m, 3.20H, H^z), 1.64 (m, 8H, H^{aa}), 1.37 (m, 8H, H^{ab}), 1.17 (m, 168H, H^v + H^w + H^x + H^y), 0.98 (t, $^3J_{HH}$ = 7.4 Hz, 7.20H, H^{ac}), 0.96 (t, $^3J_{HH}$ = 7.4 Hz, 4.80H, H^{ac})

^{13}C-NMR (75 MHz, THF-d8, 298 K) δ 153.24 (*C*), 152.62 (*C*), 144.80 (*C*), 144.70 (*C*), 143.02 (*C*), 142.88 (*C*), 142.77 (*C*), 141.88 (*C*), 141.77 (*C*), 141.50 (*C*), 140.71 (*C*), 140.31 (*C*), 137.80 (*C*), 137.61 (*C*), 133.80 (*C*-H), 133.55 (*C*-H), 131.15 (*C*-H), 128.56 (*C*-H), 128.20 (*C*-H), 126.87 (*C*), 126.49 (*C*-H), 126.27 (*C*-H), 124.34 (*C*-H), 123.77 (*C*-H), 108.24 (C≡*C*-Si), 93.71 (*C*≡C-Si), 59.43 (CH_2, C^z), 24.63 (CH_2, C^{aa}), 20.86 (CH_2, C^{ab}), 19.23 (CH_3, C^w + C^y), 14.06 (CH_3, C^{ac}), 12.44 (*C*-H, C^x + C^v)

^{19}F-NMR (471 MHz, THF-d8, 298 K) δ -130.61 – -133.09 (m, 8F, F^a), -144.70 – -146.63 (m, 8F, F^b)

^{11}B-NMR (160 MHz, THF-d8, 298 K) δ -14.61

MALDI-TOF (m/z): calcd. for $C_{328}H_{308}BF_{16}N_{16}Si_8^-$: 5013.3, found: 5014.4 [M^-]

Tetrabutlyammonium tetrakis(2,3,5,6-tetrafluoro-4-((bis(ethynylazobenzene))G1)phenyl)-borate TBA^+ $[B^F\text{-G1(azo-in)}_8]^-$ (**114**)

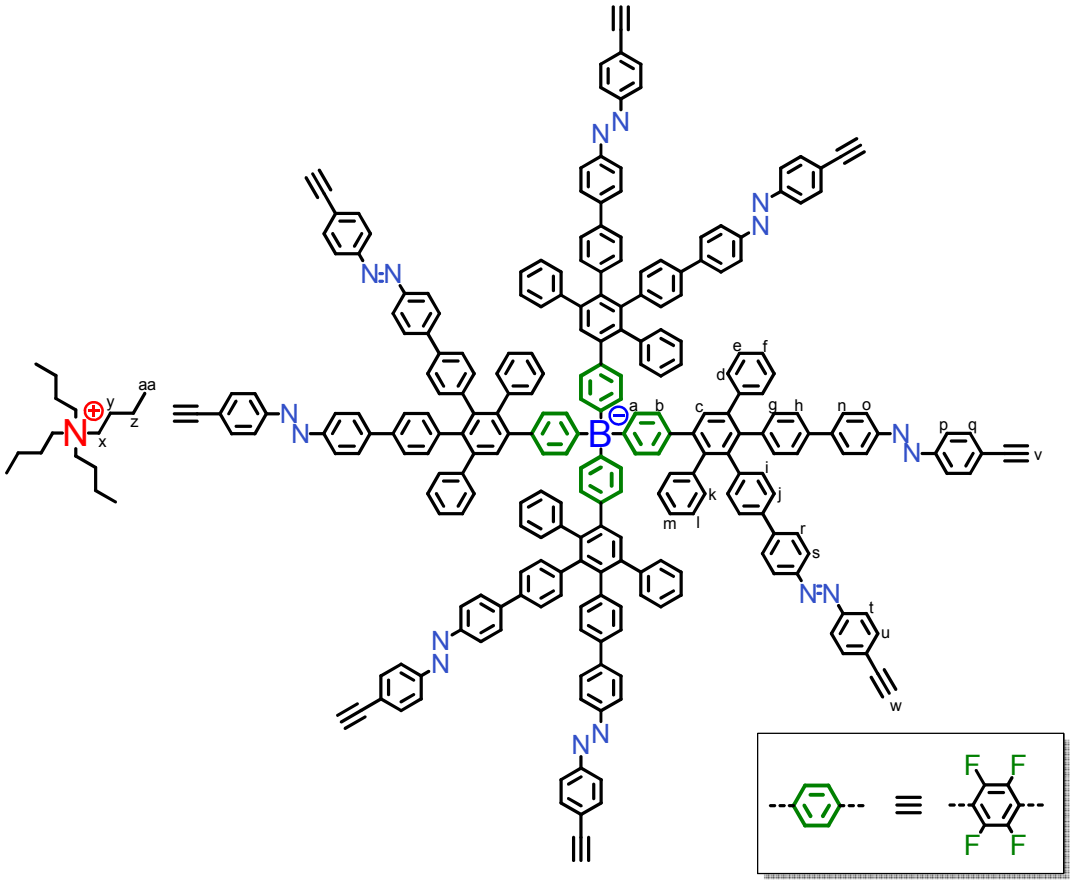

To a solution of 27.9 mg (0.005 mmol) $TBA^+[B^F\text{-G1(azo-in-T}i\text{PS)}_8]^-$ **113** in THF (25 mL) was added dropwise a solution of tetrabutylammonium fluoride (15 mg, 0.053 mmol) in THF (5 mL).

The mixture was stirred for 2 h at room temperature. The solution was filtered over silica and the solvent removed under vacuum. The orange remainder was dissolved in methylene chloride and precipitated in hexane two times. The precipitate was filtered and dried to afford 18 mg (0.004 mmol, 84%) of the product as an orange powder.

^{1}H-NMR (700 MHz, THF-d8, 298 K) δ 7.93 – 7.86 (n.r., 32H, H^{o} + H^{p} + H^{s} + H^{t}), 7.75 – 7.68 (n.r., 16H, H^{n} + H^{r}), 7.65 – 7.55 (≥7 s, 4H, H^{c}), 7.62 – 7.58 (n.r., 16H, H^{q} + H^{u}), 7.45 – 6.68 (n.r., 72H), 3.75 (s, 4H, C≡C-*H*), 3.74 (s, 4H, C≡C-*H*), 3.19 (m, 8H, H^{x}), 1.64 (m, 8H, H^{y}), 1.37 (m, 8H, H^{z}), 0.98 (t, $^{3}J_{HH}$ = 7.4 Hz, 12H, H^{aa})

^{13}C-NMR (176 MHz, THF-d8, 298 K) δ 153.33, 152.59, 144.78, 144.73, 143.30, 142.99, 142.85, 142.78, 141.88, 141.78, 141.50, 140.70, 140.29, 140.18, 137.77, 137.55, 133.84 (*C*-H), 133.55 (*C*-H), 133.41 (*C*-H), 131.17 (*C*-H), 131.04 (*C*-H), 128.56 (*C*-H), 128.21 (*C*-H), 127.92 (*C*-H), 127.69 (*C*-H), 127.60 (*C*-H), 127.21 (*C*-H), 126.48 (*C*-H), 126.29 (*C*-H), 126.15, 124.34 (*C*-H), 123.79 (*C*-H), 116.12, 84.07 (*C*≡C-H), 81.45 (C≡*C*-H), 59.38 (CH_2, C^{x}), 24.61 (CH_2, C^{y}), 20.71 (CH_2, C^{z}), 14.07 (CH_3, C^{aa})

^{19}F-NMR (471 MHz, THF-d8, 298 K) δ -130.51 – -132.63 (m, 8F, F^{a}), -145.19 – -146.97 (m, 8F, F^{b})

^{11}B-NMR (160 MHz, THF-d8, 298 K) δ -14.59

MALDI-TOF (m/z): calcd. for $C_{256}H_{148}BF_{16}N_{16}^{-}$: 3762.2, found: 3762.2 [M^{-}]

Tetrabutlyammonium tetrakis(2,3,5,6-tetrafluoro-4-(G2)phenyl)borate TBA^+ $[B^F$-G(azo)G2$]^-$ (**115**)

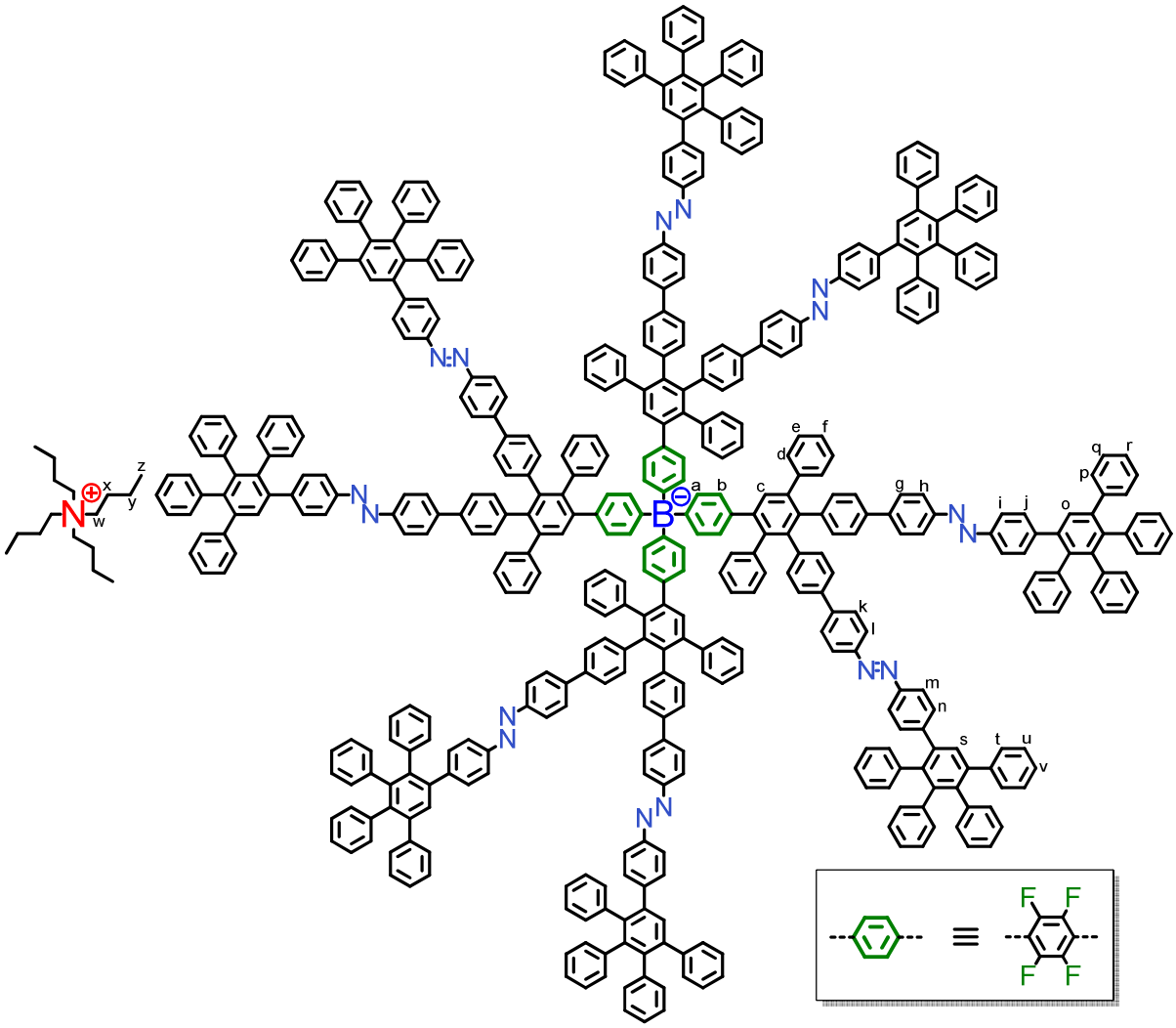

10 mg (0.003 mmol) of $TBA^+[B^F$-G1(azo-in)$_8]^-$ **114** and 10 mg (0.025 mmol) tetraphenylcyclopentadienone were dissolved in *o*-xylene (5 mL) in a microwave tube. The argon bubbled mixture was stirred at 155 °C for 12 h. After cooling to room temperature, the mixture was purified by column chromatography using firstly a 10:1 mixture of hexane and ethyl acetate and then methylene chloride as eluent. After removal of the solvent in vacuum, 10 mg (0.001 mmol, 58%) of the compound were obtained as an orange powder.

^{1}H-NMR (700 MHz, THF-d8, 298 K) δ 7.87 – 7.72 (n.r., 16H, H^h + H^l), 7.72 – 7.64 (n.r., 32H, H^i + H^m + H^g + H^k), 7.64 – 7.53 (≥8 s, 4H, H^c), 7.60 (s, 8H, H^o + H^s), 7.42 – 6.59 (248H), 3.21 (m, 8H, H^w), 1.65 (m, 8H, H^x), 1.38 (m, 8H, H^y), 0.99 (t, $^3J_{HH}$ = 7.4 Hz, 12H, H^z)

^{13}C-NMR (176 MHz, THF-d8, 298 K) δ 152.66, 152.00, 145.93, 144.23, 143.14, 142.89, 142.77, 142.18, 141.87, 141.64, 141.46, 141.36, 141.19, 141.13, 141.06, 140.94, 140.73, 140.50, 140.28, 137.84, 137.64, 133.51, 132.56, 132.54, 132.16, 131.72, 131.12, 130.91, 128.54, 128.12, 128.07, 127.87, 127.59, 127.19, 126.80, 126.55, 126.42, 126.30, 126.23, 124.13, 124.10, 123.15, 60.64 (*C*H$_2$, C^w), 59.37 (*C*H$_2$, C^w), 24.61 (*C*H$_2$, C^x), 20.77 (*C*H$_2$, C^y), 20.71 (*C*H$_2$, C^y), 14.71 (*C*H$_3$, C^z), 14.07 (*C*H$_3$, C^z)

^{19}F-NMR (471 MHz, THF-d8, 298 K) δ -131.11 – -132.79 (m, 8F, F^a), -145.81 – -146.95 (m, 8F, F^b)

^{11}B-NMR (160 MHz, THF-d8, 298 K) δ -16.58

MALDI-TOF (m/z): calcd. for $C_{480}H_{308}BF_{16}N_{16}^-$: 6613.5, found: 6613.5 [M$^-$]

10 Literature

(1) Tomalia, D. A.; Naylor, A. M.; Goddard, W. A. *Angewandte Chemie International Edition in English* **1990**, *29*, 138.

(2) Tomalia, D. A.; Naylor, A. M.; Goddard, W. A. *Angewandte Chemie* **1990**, *102*, 119.

(3) Buhleier, E.; Wehner, W.; Vögtle, F. *Synthesis* **1978**, 155.

(4) Newkome, G. R.; Yao, Z.; Baker, G. R.; Gupta, V. K. *The Journal of Organic Chemistry* **1985**, *50*, 2003.

(5) Tomalia, D. A.; Baker, H.; Dewald, J.; Hall, M.; Kallos, G.; Martin, S.; Roeck, J.; Ryder, J.; Smith, P. *Macromolecules* **1986**, *19*, 2466.

(6) Hawker, C.; Frechet, J. M. J. *Journal of the Chemical Society, Chemical Communications* **1990**, 1010.

(7) Miller, T. M.; Neenan, T. X. *Chemistry of Materials* **1990**, *2*, 346.

(8) Miller, T. M.; Neenan, T. X.; Zayas, R.; Bair, H. E. *Journal of the American Chemical Society* **1992**, *114*, 1018.

(9) Xu, Z.; Moore, J. S. *Angewandte Chemie International Edition in English* **1993**, *32*, 246.

(10) Moore, J. S.; Xu, Z. *Macromolecules* **1991**, *24*, 5893.

(11) Morgenroth, F.; Reuther, E.; Müllen, K. *Angew. Chem. Int. Ed. Engl.* **1997**, *36*, 631.

(12) de Gennes, P. G.; Hervet, H. *J. Physique Lett.* **1983**, *44*, 351.

(13) Lescanec, R. L.; Muthukumar, M. *Macromolecules* **1990**, *23*, 2280.

(14) Ballauff, M.; Likos, C. N. *Angewandte Chemie International Edition* **2004**, *43*, 2998.

(15) Likos, C. N.; Schmidt, M.; Löwen, H.; Ballauff, M.; Pötschke, D.; Lindner, P. *Macromolecules* **2001**, *34*, 2914.

(16) Rosenfeldt, S.; Dingenouts, N.; Pötschke, D.; Ballauff, M.; Berresheim, A. J.; Müllen, K.; Lindner, P.; Saalwächter, K. *Journal of Luminescence* **2005**, *111*, 225.

(17) Andreitchenko, E. V.; Clark, C. G.; Bauer, R. E.; Lieser, G.; Müllen, K. *Angewandte Chemie International Edition* **2005**, *44*, 6348.

(18) Bosman, A. W.; Janssen, H. M.; Meijer, E. W. *Chemical Reviews* **1999**, *99*, 1665.

(19) Jansen, J. F. G. A.; de Brabander-van den Berg, E. M. M.; Meijer, E. W. *Science* **1994**, *266*, 1226.

(20) Cram, D. J.; Cram, J. M. *Container Molecules and Their Guests*; The Royal Society of Chemistry: Cambridge, 1997.

(21) Stone, D. L.; Smith, D. K.; McGrail, P. T. *Journal of the American Chemical Society* **2002**, *124*, 856.

(22) Waybright, S. M.; McAlpine, K.; Laskoski, M.; Smith, M. D.; Bunz, U. H. F. *Journal of the American Chemical Society* **2002**, *124*, 8661.

(23) Vögtle, F.; Plevoets, M.; Nieger, M.; Azzellini, G. C.; Credi, A.; De Cola, L.; De Marchis, V.; Venturi, M.; Balzani, V. *Journal of the American Chemical Society* **1999**, *121*, 6290.

(24) Qin, T.; Ding, J.; Wang, L.; Baumgarten, M.; Zhou, G.; Müllen, K. *Journal of the American Chemical Society* **2009**, *131*, 14329.

(25) Bernhardt, S.; Kastler, M.; Enkelmann, V.; Baumgarten, M.; Müllen, K. *Chemistry – A European Journal* **2006**, *12*, 6117.

(26) Issberner, J.; Vögtle, F.; Cola, L. D.; Balzani, V. *Chemistry – A European Journal* **1997**, *3*, 706.

(27) Bernhardt, S.; Baumgarten, M.; Müllen, K. *European Journal of Organic Chemistry* **2006**, *2006*, 2523.

(28) Vögtle, F.; Richardt, G.; Werner, N. *Dendritische Moleküle; Konzepte, Synthesen, Eigenschaften, Anwendungen*; 1st ed.; B. G. Teubner Verlag: Wiesbaden, 2007.

(29) Iwasawa, T.; Tokunaga, M.; Obora, Y.; Tsuji, Y. *Journal of the American Chemical Society* **2004**, *126*, 6554.

(30) Tsuji, Y.; Fujihara, T. *Inorganic Chemistry* **2007**, *46*, 1895.

(31) Komano, T.; Iwasawa, T.; Tokunaga, M.; Obora, Y.; Tsuji, Y. *Organic Letters* **2005**, *7*, 4677.

(32) Hovestad, N. J.; Eggeling, E. B.; Heidbüchel, H. J.; Jastrzebski, J. T. B. H.; Kragl, U.; Keim, W.; Vogt, D.; van Koten, G. *Angewandte Chemie International Edition* **1999**, *38*, 1655.

(33) de Groot, D.; C. de Wilde, J.; J. van Haaren, R.; N. H. Reek, J.; C. J. Kamer, P.; W. N. M. van Leeuwen, P.; B. Eggeling, E.; Vogt, D.; Kooijman, H.; L. Spek, A.; W. van der Made, A. *Chemical Communications* **1999**, 1623.

(34) Albrecht, M.; Hovestad, N. J.; Boersma, J.; van Koten, G. *Chemistry – A European Journal* **2001**, *7*, 1289.

(35) Bauer, R. E.; Clark, J. C. G.; Müllen, K. *New Journal of Chemistry* **2007**, *31*, 1275.

(36) Dhanikula, R. S.; Hildgen, P. *Bioconjugate Chemistry* **2005**, *17*, 29.

(37) Lubczyk, D.; Siering, C.; Lörgen, J.; Shifrina, Z. B.; Müllen, K.; Waldvogel, S. R. *Sensors and Actuators B: Chemical* **2010**, *143*, 561.

(38) Baars, M.; Meijer, E. In *Dendrimers II*; Vögtle, F., Ed.; Springer Berlin / Heidelberg: 2000; Vol. 210, p 131.

(39) Bauer, R.; Liu, D.; Ver Heyen, A.; De Schryver, F.; De Feyter, S.; Müllen, K. *Macromolecules* **2007**, *40*, 4753.

(40) Schmelzeisen, M.; Zhao, Y.; Klapper, M.; Müllen, K.; Kreiter, M. *ACS Nano* **2010**, *4*, 3309.

(41) Jevprasesphant, R.; Penny, J.; Jalal, R.; Attwood, D.; McKeown, N. B.; D'Emanuele, A. *International Journal of Pharmaceutics* **2003**, *252*, 263.

(42) Jevprasesphant, R.; Penny, J.; Attwood, D.; McKeown, N. B.; D'Emanuele, A. *Pharmaceutical Research* **2003**, *20*, 1543.

(43) Thomas, T. P.; Patri, A. K.; Myc, A.; Myaing, M. T.; Ye, J. Y.; Norris, T. B.; Baker, J. R. *Biomacromolecules* **2004**, *5*, 2269.

(44) Shukla, R.; Thomas, T. P.; Peters, J. L.; Desai, A. M.; Kukowska-Latallo, J.; Patri, A. K.; Kotlyar, A.; Baker, J. R. *Bioconjugate Chemistry* **2006**, *17*, 1109.

(45) Devadoss, C.; Bharathi, P.; Moore, J. S. *Journal of the American Chemical Society* **1996**, *118*, 9635.

(46) Weil, T.; Reuther, E.; Müllen, K. *Angewandte Chemie* **2002**, *114*, 1980.

(47) Gilat, S. L.; Adronov, A.; Fréchet, J. M. J. *Angewandte Chemie International Edition* **1999**, *38*, 1422.

(48) Weil, T.; Reuther, E.; Beer, C.; Müllen, K. *Chemistry – A European Journal* **2004**, *10*, 1398.

(49) Archut, A.; Azzellini, G. C.; Balzani, V.; De Cola, L.; Vögtle, F. *Journal of the American Chemical Society* **1998**, *120*, 12187.

(50) Puntoriero, F.; Ceroni, P.; Balzani, V.; Bergamini, G.; Vögtle, F. *Journal of the American Chemical Society* **2007**, *129*, 10714.

(51) Nguyen, T.-T.-T.; Türp, D.; Wang, D.; Nölscher, B.; Laquai, F. d. r.; Müllen, K. *Journal of the American Chemical Society* **2011**, *133*, 11194.

(52) Türp, D.; Nguyen, T.-T.-T.; Baumgarten, M.; Müllen, K. *New Journal of Chemistry* **2012**, *36*, 282.

(53) Dilthey, W.; Schommer, W.; Trösken, O. *Berichte der deutschen chemischen Gesellschaft (A and B Series)* **1933**, *66*, 1627.

(54) Dilthey, W.; Hurtig, G. *Berichte der deutschen chemischen Gesellschaft (A and B Series)* **1934**, *67*, 2004.

(55) Dilthey, W.; Hurtig, G. *Berichte der deutschen chemischen Gesellschaft (A and B Series)* **1934**, *67*, 495.

(56) Dilthey, W.; Schommer, W.; Höschen, W.; Die-richs, H. *Berichte der deutschen chemischen Gesellschaft (A and B Series)* **1935**, *68*, 1159.

(57) Dilthey, W.; Henkels, S.; Schaefer, A. *Berichte der deutschen chemischen Gesellschaft (A and B Series)* **1938**, *71*, 974.

(58) Hanack, M.; Massa, F. *Tetrahedron Letters* **1977**, *18*, 661.

(59) Morgenroth, F. *Chemical Communications* **1998**, 1139.

(60) Berresheim, A. J.; Müller, M.; Müllen, K. *Chemical Reviews* **1999**, *99*, 1747.

(61) Sonogashira, K.; Tohda, Y.; Hagihara, N. *Tetrahedron Letters* **1975**, *16*, 4467.

(62) Morgenroth, F.; Kübel, C.; Müller, M.; Wiesler, U. M.; Berresheim, A. J.; Wagner, M.; Müllen, K. *Carbon* **1998**, *36*, 833.

(63) GerstnerEd *Nat Phys* **2010**, *6*, 836.

(64) Tomović, Ž.; Watson, M. D.; Müllen, K. *Angewandte Chemie International Edition* **2004**, *43*, 755.

(65) Müller, M.; Kübel, C.; Müllen, K. *Chemistry – A European Journal* **1998**, *4*, 2099.

(66) Clark, C. G.; Wenzel, R. J.; Andreitchenko, E. V.; Steffen, W.; Zenobi, R.; Müllen, K. *Journal of the American Chemical Society* **2007**, *129*, 3292.

(67) Vanhee, S.; Rulkens, R.; Lehmann, U.; Rosenauer, C.; Schulze, M.; Köhler, W.; Wegner, G. *Macromolecules* **1996**, *29*, 5136.

(68) Petekidis, G.; Vlassopoulos, D.; Galda, P.; Rehahn, M.; Ballauff, M. *Macromolecules* **1996**, *29*, 8948.

(69) Harre, K.; Wegner, G. *Polymer* **2006**, *47*, 7312.

(70) Fuckel, B.; Hinze, G.; Diezemann, G.; Nolde, F.; Müllen, K.; Gauss, J.; Basche, T. *The Journal of Chemical Physics* **2006**, *125*, 144903.

(71) Zhang, H.; Grim, P. C. M.; Foubert, P.; Vosch, T.; Vanoppen, P.; Wiesler, U. M.; Berresheim, A. J.; Müllen, K.; De Schryver, F. C. *Langmuir* **2000**, *16*, 9009.

(72) Wind, M.; Wiesler, U. M.; Saalwächter, K.; Müllen, K.; Spiess, H. W. *Advanced Materials* **2001**, *13*, 752.

(73) Wind, M.; Saalwächter, K.; Wiesler, U. M.; Müllen, K.; Spiess, H. W. *Macromolecules* **2002**, *35*, 10071.

(74) Weil, T.; Vosch, T.; Hofkens, J.; Peneva, K.; Müllen, K. *Angewandte Chemie International Edition* **2010**, *49*, 9068.

(75) Qu, J.; Pschirer, N. G.; Liu, D.; Stefan, A.; De Schryver, F. C.; Müllen, K. *Chemistry – A European Journal* **2004**, *10*, 528.

(76) Qu, J.; Zhang, J.; Grimsdale, A. C.; Müllen, K.; Jaiser, F.; Yang, X.; Neher, D. *Macromolecules* **2004**, *37*, 8297.

(77) Herrmann, A.; Weil, T.; Sinigersky, V.; Wiesler, U.-M.; Vosch, T.; Hofkens, J.; De Schryver, F. C.; Müllen, K. *Chemistry – A European Journal* **2001**, *7*, 4844.

(78) Jaiser, F.; Neher, D.; Meisel, A.; Nothofer, H.-G.; Miteva, T.; Herrmann, A.; Müllen, K.; Scherf, U. *The Journal of Chemical Physics* **2008**, *129*, 114901.

(79) Murov, S. L.; Carmichael, I.; Hug, G. L. *Handbook of Photochemistry*; 1st ed.; CRC Press: New York, 1993.

(80) Castanheira, E. M. S.; Martinho, J. M. G. *Chemical Physics Letters* **1991**, *185*, 319.

(81) Kimura, M.; Sakaguchi, A.; Ohta, K.; Hanabusa, K.; Shirai, H.; Kobayashi, N. *Inorganic Chemistry* **2003**, *42*, 2821.

(82) Qin, T.; Zhou, G.; Scheiber, H.; Bauer, R. E.; Baumgarten, M.; Anson, C. E.; List, E. J. W.; Müllen, K. *Angewandte Chemie* **2008**, *120*, 8416.

(83) Qin, T.; Zhou, G.; Scheiber, H.; Bauer, R. E.; Baumgarten, M.; Anson, C. E.; List, E. J. W.; Müllen, K. *Angewandte Chemie International Edition* **2008**, *47*, 8292.

(84) Qin, T.; Wiedemair, W.; Nau, S.; Trattnig, R.; Sax, S.; Winkler, S.; Vollmer, A.; Koch, N.; Baumgarten, M.; List, E. J. W.; Müllen, K. *Journal of the American Chemical Society* **2011**, *133*, 1301.

(85) Wiesler, U.-M.; Weil, T.; Müllen, K. In *Dendrimers III*; Vögtle, F., Ed.; Springer Berlin / Heidelberg: 2001; Vol. 212, p 1.

(86) Avouris, P.; Chen, Z.; Perebeinos, V. *Nat Nano* **2007**, *2*, 605.

(87) Pang, S.; Tsao, H. N.; Feng, X.; Müllen, K. *Advanced Materials* **2009**, *21*, 3488.

(88) Bai, J.; Zhong, X.; Jiang, S.; Huang, Y.; Duan, X. *Nat Nano* **2010**, *5*, 190.

(89) Liao, L.; Bai, J.; Lin, Y.-C.; Qu, Y.; Huang, Y.; Duan, X. *Advanced Materials* **2010**, *22*, 1941.

(90) Jang, S.; Jang, H.; Lee, Y.; Suh, D.; Baik, S.; Hong, B. H.; Ahn, J.-H. *Nanotechnology* **2010**, *21*, 425201.

(91) Jang, S.; et al. *Nanotechnology* **2010**, *21*, 425201.

(92) Simpson, C. D.; Wu, J.; Watson, M. D.; Müllen, K. *Journal of Materials Chemistry* **2004**, *14*, 494.

(93) Wu, J.; Pisula, W.; Müllen, K. *Chemical Reviews* **2007**, *107*, 718.

(94) Stabel, A.; Herwig, P.; Müllen, K.; Rabe, J. P. *Angewandte Chemie International Edition in English* **1995**, *34*, 1609.

(95) Ito, S.; Wehmeier, M.; Brand, J. D.; Kübel, C.; Epsch, R.; Rabe, J. P.; Müllen, K. *Chemistry – A European Journal* **2000**, *6*, 4327.

(96) Simpson, C. D.; Mattersteig, G.; Martin, K.; Gherghel, L.; Bauer, R. E.; Räder, H. J.; Müllen, K. *Journal of the American Chemical Society* **2004**, *126*, 3139.

(97) Gibson, J.; Holohan, M.; Riley, H. L. *Journal of the Chemical Society* **1946**, 456.

(98) Shen, X.; Ho, D. M.; Pascal, R. A. *Organic Letters* **2003**, *5*, 369.

(99) Shen, X.; Ho, D. M.; Pascal, R. A. *Journal of the American Chemical Society* **2004**, *126*, 5798.

(100) Wasserfallen, D.; Mattersteig, G.; Enkelmann, V.; Müllen, K. *Tetrahedron* **2006**, *62*, 5417.

(101) Song, Q.; Lebeis, C. W.; Shen, X.; Ho, D. M.; Pascal, R. A. *Journal of the American Chemical Society* **2005**, *127*, 13732.

(102) Liu, D.; Zhang, H.; Grim, P. C. M.; De Feyter, S.; Wiesler, U. M.; Berresheim, A. J.; Müllen, K.; De Schryver, F. C. *Langmuir* **2002**, *18*, 2385.

(103) Liu, D.; De Feyter, S.; Grim, P. C. M.; Vosch, T.; Grebel-Koehler, D.; Wiesler, U. M.; Berresheim, A. J.; Müllen, K.; De Schryver, F. C. *Langmuir* **2002**, *18*, 8223.

(104) Heyen, A. J. J. V.; Buron, C. C.; Tianshi, Q.; Bauer, R.; Jonas, A. M.; Müllen, K.; De Schryver, F. C.; De Feyter, S. *Small* **2008**, *4*, 1160.

(105) Liu, D.; Feyter, S. D.; Cotlet, M.; Wiesler, U.-M.; Weil, T.; Herrmann, A.; Müllen, K.; De Schryver, F. C. *Macromolecules* **2003**, *36*, 8489.

(106) Loi, S.; Wiesler, U.-M.; Butt, H.-J.; Müllen, K. *Chemical Communications* **2000**, 1169.

(107) Loi, S.; Wiesler, U.-M.; Butt, H.-J.; Müllen, K. *Macromolecules* **2001**, *34*, 3661.

(108) Loi, S.; Butt, H.-J.; Hampel, C.; Bauer, R.; Wiesler, U.-M.; Müllen, K. *Langmuir* **2002**, *18*, 2398.

(109) Yin, M.; Bauer, R.; Klapper, M.; Müllen, K. *Macromolecular Chemistry and Physics* **2007**, *208*, 1646.

(110) Yin, M.; Cheng, Y.; Liu, M.; Gutmann, J. S.; Müllen, K. *Angewandte Chemie International Edition* **2008**, *47*, 8400.

(111) Yin, M.; Cheng, Y.; Liu, M.; Gutmann, J. S.; Müllen, K. *Angewandte Chemie* **2008**, *120*, 8528.

(112) Marek, T.; Süvegh, K.; Vértes, A.; Ernst, A.; Bauer, R.; Weil, T.; Wiesler, U.; Klapper, M.; Müllen, K. *Radiation Physics and Chemistry* **2003**, *67*, 325.

(113) Bauer, R. E.; Enkelmann, V.; Wiesler, U. M.; Berresheim, A. J.; Müllen, K. *Chemistry – A European Journal* **2002**, *8*, 3858.

(114) Wiesler, U.-M., Johannes Gutenberg Universität

2000.

(115) Köhn, F.; Hofkens, J.; Wiesler, U.-M.; Cotlet, M.; van der Auweraer, M.; Müllen, K.; De Schryver, F. C. *Chemistry – A European Journal* **2001**, *7*, 4126.

(116) Sakamoto, J.; Müllen, K. *Organic Letters* **2004**, *6*, 4277.

(117) Gardner, J. W.; Yinon, J. *Electronic Noses & Sensors for the Detection of Explosives*

Kluwer Academic Publishers, 2003.

(118) Shifrina, Z. B.; Rajadurai, M. S.; Firsova, N. V.; Bronstein, L. M.; Huang, X.; Rusanov, A. L.; Muellen, K. *Macromolecules* **2005**, *38*, 9920.

(119) Schlupp, M.; Weil, T.; Berresheim, A. J.; Wiesler, U. M.; Bargon, J.; Müllen, K. *Angewandte Chemie International Edition* **2001**, *40*, 4011.

(120) Lévy, É. *Dictionnaire de Physique*; Presses universitaires de France: Paris, 1988.

(121) Born, M. *Verhandl. deut. phys. Ges.* **1918**, *20*, 202.

(122) Born, M. *Verhandl. deut. phys. Ges.* **1919**, *21*, 13.

(123) Born, M.; Landé, A. *Ber. Preuß. Akad. Wiss. Berlin* **1918**, *Nr. 45*, 1048.

(124) Kapustinskii, A. F. *Quarterly Reviews, Chemical Society* **1956**, *10*, 283.

(125) Jenkins, H. D. B.; Roobottom, H. K.; Passmore, J.; Glasser, L. *Inorganic Chemistry* **1999**, *38*, 3609.

(126) Krossing, I.; Raabe, I. *Angewandte Chemie International Edition* **2004**, *43*, 2066.

(127) Izutsu, K. *Electrochemistry in Nonaqueous Solutions*; WILEY-VCH: Weinheim, 2002.

(128) Kortüm, G. *Lehrbuch der Elektrochemie*; 5th ed.; Verlag Chemie GmbH: Weinheim, 1972.

(129) Bjerrum; Wynne-Jones, W. F. K.; Onsager; Fowler; Bronsted *Transactions of the Faraday Society* **1927**, *23*, 432.

(130) Strauss, S. H. *Chemical Reviews* **1993**, *93*, 927.

(131) Rosenthal, M. R. *Journal of Chemical Education* **1973**, *50*, 331.

(132) Beck, W.; Suenkel, K. *Chemical Reviews* **1988**, *88*, 1405.

(133) Trapp, N.; Krossing, I. *Nachrichten aus der Chemie* **2009**, *57*, 632.

(134) Krossing, I.; Reisinger, A. *Coordination Chemistry Reviews* **2006**, *250*, 2721.

(135) Reisinger, A.; Trapp, N.; Krossing, I.; Altmannshofer, S.; Herz, V.; Presnitz, M.; Scherer, W. *Angewandte Chemie* **2007**, *119*, 8445.

(136) Mercier, H. P. A.; Moran, M. D.; Schrobilgen, G. J.; Steinberg, C.; Suontamo, R. J. *Journal of the American Chemical Society* **2004**, *126*, 5533.

(137) Sarazin, Y.; Hughes, D. L.; Kaltsoyannis, N.; Wright, J. A.; Bochmann, M. *Journal of the American Chemical Society* **2007**, *129*, 881.

(138) Fang, M.; Wilson, S. R.; Suslick, K. S. *Journal of the American Chemical Society* **2008**, *130*, 1134.

(139) Ewart, S. W.; Sarsfield, M. J.; Williams, E. F.; Baird, M. C. *Journal of Organometallic Chemistry* **1999**, *579*, 106.

(140) Li, Y.; Cokoja, M.; Kühn, F. E. *Coordination Chemistry Reviews* **2011**, *255*, 1541.

(141) Chen, E. Y.-X.; Marks, T. J. *Chemical Reviews* **2000**, *100*, 1391.

(142) Chen, M.-C.; Roberts, J. A. S.; Seyam, A. M.; Li, L.; Zuccaccia, C.; Stahl, N. G.; Marks, T. J. *Organometallics* **2006**, *25*, 2833.

(143) Roberts, J. A. S.; Chen, M.-C.; Seyam, A. M.; Li, L.; Zuccaccia, C.; Stahl, N. G.; Marks, T. J. *Journal of the American Chemical Society* **2007**, *129*, 12713.

(144) Zhang, Y.; Ning, Y.; Caporaso, L.; Cavallo, L.; Chen, E. Y. X. *Journal of the American Chemical Society* **2010**, *132*, 2695.

(145) Moss, S.; King, B. T.; de Meijere, A.; Kozhushkov, S. I.; Eaton, P. E.; Michl, J. *Organic Letters* **2001**, *3*, 2375.

(146) Barbarich, T. J.; Handy, S. T.; Miller, S. M.; Anderson, O. P.; Grieco, P. A.; Strauss, S. H. *Organometallics* **1996**, *15*, 3776.

(147) Anderson, L. L.; Arnold, J.; Bergman, R. G. *Journal of the American Chemical Society* **2005**, *127*, 14542.

(148) Patmore, N. J.; Hague, C.; Cotgreave, J. H.; Mahon, M. F.; Frost, C. G.; Weller, A. S. *Chemistry - A European Journal* **2002**, *8*, 2088.

(149) LeSuer, R. J.; Geiger, W. E. *Angewandte Chemie International Edition* **2000**, *39*, 248.

(150) Barrière, F.; Camire, N.; Geiger, W. E.; Mueller-Westerhoff, U. T.; Sanders, R. *Journal of the American Chemical Society* **2002**, *124*, 7262.

(151) Camire, N.; Nafady, A.; Geiger, W. E. *Journal of the American Chemical Society* **2002**, *124*, 7260.

(152) Camire, N.; Mueller-Westerhoff, U. T.; Geiger, W. E. *Journal of Organometallic Chemistry* **2001**, *637-639*, 823.

(153) Stewart, M. P.; Paradee, L. M.; Raabe, I.; Trapp, N.; Slattery, J. S.; Krossing, I.; Geiger, W. E. *Journal of Fluorine Chemistry*, *In Press, Corrected Proof*.

(154) Raabe, I.; Wagner, K.; Guttsche, K.; Wang, M.; Grätzel, M.; Santiso-Quiñones, G.; Krossing, I. *Chemistry - A European Journal* **2009**, *15*, 1966.

(155) Stewart, M. P.; Paradee, L. M.; Raabe, I.; Trapp, N.; Slattery, J. S.; Krossing, I.; Geiger, W. E. *Journal of Fluorine Chemistry* **2010**, *131*, 1091.

(156) Barrière, F.; Geiger, W. E. *Journal of the American Chemical Society* **2006**, *128*, 3980.

(157) Geiger, W. E.; Barrière, F. d. r. *Accounts of Chemical Research* **2010**, *43*, 1030.

(158) Kita, F.; Sakata, H.; Sinomoto, S.; Kawakami, A.; Kamizori, H.; Sonoda, T.; Nagashima, H.; Nie, J.; Pavlenko, N. V.; Yagupolskii, Y. L. *Journal of Power Sources* **2000**, *90*, 27.

(159) S. H. Strauss, B. G. N., B. P. Fauber *WO 00/53611* **2000**.

(160) Armand, M.; Johansson, P. *Journal of Power Sources* **2008**, *178*, 821.

(161) Nolan, B. G.; Tsujioka, S.; Strauss, S. H. In *Fluorinated Materials for Energy Conversion*; Tsuyoshi, N., Henri, G., Eds.; Elsevier Science: Amsterdam, 2005, p 195.

(162) Bösmann, A.; Franciò, G.; Janssen, E.; Solinas, M.; Leitner, W.; Wasserscheid, P. *Angewandte Chemie International Edition* **2001**, *40*, 2697.

(163) Larsen, A. S.; Holbrey, J. D.; Tham, F. S.; Reed, C. A. *Journal of the American Chemical Society* **2000**, *122*, 7264.

(164) Bejan, D.; Ignat'ev, N.; Willner, H. *Journal of Fluorine Chemistry* **2010**, *131*, 325.

(165) Timofte, T.; Pitula, S.; Mudring, A.-V. *Inorganic Chemistry* **2007**, *46*, 10938.

(166) Jelínek, T.; Plešek, J.; Heřmánek, S.; Štíbr, B. *Collection of Czechoslovak Chemical Communications* **1986**, *51*, 819.

(167) Reed, C. A. *Accounts of Chemical Research* **1998**, *31*, 133.

(168) Tsang, C.-W.; Yang, Q.; Sze, E. T.-P.; Mak, T. C. W.; Chan, D. T. W.; Xie, Z. *Inorganic Chemistry* **2000**, *39*, 5851.

(169) Xie, Z.; Tsang, C.-W.; Sze, E. T.-P.; Yang, Q.; Chan, D. T. W.; Mak, T. C. W. *Inorganic Chemistry* **1998**, *37*, 6444.

(170) King, B. T.; Janoušek, Z.; Grüner, B.; Trammell, M.; Noll, B. C.; Michl, J. *Journal of the American Chemical Society* **1996**, *118*, 3313.

(171) King, B. T.; Michl, J. *Journal of the American Chemical Society* **2000**, *122*, 10255.

(172) Ivanova, S. M.; Ivanov, S. V.; Miller, S. M.; Anderson, O. P.; Solntsev, K. A.; Strauss, S. H. *Inorganic Chemistry* **1999**, *38*, 3756.

(173) Ivanov, S. V.; Rockwell, J. J.; Polyakov, O. G.; Gaudinski, C. M.; Anderson, O. P.; Solntsev, K. A.; Strauss, S. H. *Journal of the American Chemical Society* **1998**, *120*, 4224.

(174) Sun, Y.; Metz, M. V.; Stern, C. L.; Marks, T. J. *Organometallics* **2000**, *19*, 1625.

(175) Metz, M. V.; Sun, Y.; Stern, C. L.; Marks, T. J. *Organometallics* **2002**, *21*, 3691.

(176) Krossing, I. *Chemistry – A European Journal* **2001**, *7*, 490.

(177) Seppelt, K. *Angewandte Chemie International Edition in English* **1993**, *32*, 1025.

(178) Kobayashi, H.; Sonoda, T.; Iwamoto, H. *Chemistry Letters* **1982**, 1185.

(179) Iwamoto, H.; Sonoda, T.; Kobayashi, H. *Tetrahedron Letters* **1983**, *24*, 4703.

(180) Iwamoto, H.; Sonoda, T.; Kobayashi, H. *Journal of Fluorine Chemistry* **1984**, *24*, 535.

(181) Kobayashi, H. *Journal of Fluorine Chemistry* **2000**, *105*, 201.

(182) van den Broeke, J.; Deelman, B.-J.; van Koten, G. *Tetrahedron Letters* **2001**, *42*, 8085.

(183) Fujiki, K.; Ichikawa, J.; Kobayashi, H.; Sonoda, A.; Sonoda, T. *Journal of Fluorine Chemistry* **2000**, *102*, 293.

(184) Kaul, F. A. R.; Puchta, G. T.; Schneider, H.; Grosche, M.; Mihalios, D.; Herrmann, W. A. *Journal of Organometallic Chemistry* **2001**, *621*, 177.

(185) Jia, L.; Yang, X.; Stern, C. L.; Marks, T. J. *Organometallics* **1997**, *16*, 842.

(186) Jia, L.; Yang, X.; Ishihara, A.; Marks, T. J. *Organometallics* **1995**, *14*, 3135.

(187) Rodriguez, G.; Brant, P. *Organometallics* **2001**, *20*, 2417.

(188) Hesp, K. D.; Stradiotto, M. *Journal of the American Chemical Society* **2010**, null.

(189) Li, Y.; Diebl, B.; Raith, A.; Kühn, F. E. *Tetrahedron Letters* **2008**, *49*, 5954.

(190) Li, Y.; Cokoja, M.; Kühn, F. E. *Coordination Chemistry Reviews*, *In Press, Accepted Manuscript*.

(191) Wiesler, U.-M.; Müllen, K. *Chemical Communications* **1999**, 2293.

(192) Huisgen, R. *Proceedings of the Chemical Society* **1961**, 357.

(193) Kolb, H. C.; Finn, M. G.; Sharpless, K. B. *Angewandte Chemie International Edition* **2001**, *40*, 2004.

(194) Barral, K.; Moorhouse, A. D.; Moses, J. E. *Organic Letters* **2007**, *9*, 1809.

(195) Chan, T. R.; Hilgraf, R.; Sharpless, K. B.; Fokin, V. V. *Organic Letters* **2004**, *6*, 2853.

(196) Donnelly, P. S.; Zanatta, S. D.; Zammit, S. C.; White, J. M.; Williams, S. J. *Chemical Communications* **2008**, 2459.

(197) Birchall, J. M.; Bowden, F. L.; Haszeldine, R. N.; Lever, A. B. P. *Journal of the Chemical Society [Section] A: Inorganic, Physical, Theoretical* **1967**, 747.

(198) Gastinger, R. G.; Tokas, E. F.; Rausch, M. D. *The Journal of Organic Chemistry* **1978**, *43*, 159.

(199) Mee, S. P. H.; Lee, V.; Baldwin, J. E. *Angewandte Chemie International Edition* **2004**, *43*, 1132.

(200) Ren, W.; Xia, Y.; Ji, S.-J.; Zhang, Y.; Wan, X.; Zhao, J. *Organic Letters* **2009**, *11*, 1841.

(201) Nishida, H.; Takada, N.; Yoshimura, M.; Sonoda, T.; Kobayashi, H. *Bulletin of the Chemical Society of Japan* **1984**, *57*, 2600.

(202) Bonnesen, P. V.; Puckett, C. L.; Honeychuck, R. V.; Hersh, W. H. *Journal of the American Chemical Society* **1989**, *111*, 6070.

(203) Camponovo, J.; Ruiz, J.; Cloutet, E.; Astruc, D. *Chemistry – A European Journal* **2009**, *15*, 2990.

(204) Ornelas, C.; Ruiz Aranzaes, J.; Cloutet, E.; Alves, S.; Astruc, D. *Angewandte Chemie* **2007**, *119*, 890.

(205) Wook Lee, J.; Kim, B.-K. *Bulletin of the Korean Chemical Society* **2005**, *26*, 658.

(206) Lee, J. W.; Kim, J. H.; Kim, B.-K.; Kim, J. H.; Shin, W. S.; Jin, S.-H. *Tetrahedron* **2006**, *62*, 9193.

(207) Wu, P.; Malkoch, M.; Hunt, J. N.; Vestberg, R.; Kaltgrad, E.; Finn, M. G.; Fokin, V. V.; Sharpless, K. B.; Hawker, C. J. *Chemical Communications* **2005**, 5775.

(208) Wu, P.; Feldman, A. K.; Nugent, A. K.; Hawker, C. J.; Scheel, A.; Voit, B.; Pyun, J.; Fréchet, J. M. J.; Sharpless, K. B.; Fokin, V. V. *Angewandte Chemie International Edition* **2004**, *43*, 3928.

(209) Antoni, P.; Nystrom, D.; Hawker, C. J.; Hult, A.; Malkoch, M. *Chemical Communications* **2007**, 2249.

(210) Killops, K. L.; Campos, L. M.; Hawker, C. J. *Journal of the American Chemical Society* **2008**, *130*, 5062.

(211) Rosen, B. M.; Lligadas, G.; Hahn, C.; Percec, V. *Journal of Polymer Science Part A: Polymer Chemistry* **2009**, *47*, 3931.

(212) Becer, C. R.; Hoogenboom, R.; Schubert, U. S. *Angewandte Chemie International Edition* **2009**, *48*, 4900.

(213) Hoyle, C. E.; Bowman, C. N. *Angewandte Chemie International Edition* **2010**, *49*, 1540.

(214) Binder, W. H.; Kluger, C. *Current Organic Chemistry* **2006**, *10*, 1791.

(215) Plietzsch, O.; Schilling, C. I.; Tolev, M.; Nieger, M.; Richert, C.; Muller, T.; Brase, S. *Organic & Biomolecular Chemistry* **2009**, *7*, 4734.

(216) Katritzky, A. R.; Wang, Z.; Tsikolia, M.; Hall, C. D.; Carman, M. *Tetrahedron Letters* **2006**, *47*, 7653.

(217) Kürti, L.; Czakó, B. *Strategic Applications of Named Reactions in Organic Synthesis*; Elsevier Academic Press: Burlington, 2005.

(218) Bach, R. D.; Bair, K. W.; Andrzejewski, D. *Journal of the American Chemical Society* **1972**, *94*, 8608.

(219) Sekine, A.; Ohshima, T.; Shibasaki, M. *Tetrahedron* **2002**, *58*, 75.

(220) Marcoux, D.; Charette, A. B. *The Journal of Organic Chemistry* **2007**, *73*, 590.

(221) Horner, L.; Mummenthey, G.; Moser, H.; Beck, P. *Chemische Berichte* **1966**, *99*, 2782.

(222) Friebolin, H. *Ein- und zweidimensionale NMR-Spektroskopie*; Wiley-VCH: Weinheim, 2006.

(223) Lloyd, M. A.; Brock, C. P. *Acta Crystallographica Section B* **1997**, *53*, 773.

(224) Patrick, C. R.; Prosser, G. S. *Nature* **1960**, *187*, 1021.

(225) West, A. P.; Mecozzi, S.; Dougherty, D. A. *Journal of Physical Organic Chemistry* **1997**, *10*, 347.

(226) Lorenzo, S.; Lewis, G. R.; Dance, I. *New Journal of Chemistry* **2000**, *24*, 295.

(227) Desiraju, G. R. *Angewandte Chemie International Edition in English* **1995**, *34*, 2311.

(228) Dunitz, J. D.; Gavezzotti, A.; Schweizer, W. B. *Helvetica Chimica Acta* **2003**, *86*, 4073.

(229) Babudri, F.; Farinola, G. M.; Naso, F.; Ragni, R. *Chemical Communications* **2007**, 1003.

(230) Kasai, K. *Chemistry Letters* **2006**, *35*, 54.

(231) Coates, G. W.; Dunn, A. R.; Henling, L. M.; Dougherty, D. A.; Grubbs, R. H. *Angewandte Chemie International Edition in English* **1997**, *36*, 248.

(232) El-azizi, Y.; Schmitzer, A.; Collins, S. K. *Angewandte Chemie International Edition* **2006**, *45*, 968.

(233) Zaporojtchenko, V.; Strunskus, T.; Zargarani, D.; Herges, R.; Faupel, F. *Nanotechnology* **2010** *21*, 465201.

(234) Li, Y.; Jia, X.; Gao, M.; He, H.; Kuang, G.; Wei, Y. *J.Polym. Sci. Polym. Chem.* **2010**, *48*, 551.

(235) Tomasulo, M.; Deniz, E.; Benelli, T.; Sortino, S.; Raymo, F. M. *Adv. Func. Mater.* **2009**, *19*, 3956.

(236) Klajn, R.; Wesson, P. J.; Bishop, K. J. M.; Grzybowski, B. A. *Angew. Chem. Int. Ed.* **2009**, *48*, 7035.

(237) Sugiura, S.; Sumaru, K.; Ohi, K.; Hiroki, K.; Takagi, T.; Kanamori, T. *Sensor. Actuatt. A-Phys.* **2007**, *140*, 176.

(238) Kimura, K. S., Hidefumi; Nakamura, Takateru *J. NanoSci. Nanotech.* **2006**, *6*, 1741.

(239) Yu, Y.; Nakano, M.; Ikeda, T. *Nature* **2003**, *425*, 145.

(240) Yasuda, S.; Nakamura, T.; Matsumoto, M.; Shigekawa, H. *J. Am. Chem. Soc.* **2003**, *125*, 16430.

(241) Shimoboji, T.; Larenas, E.; Fowler, T.; Kulkarni, S.; Hoffman, A. S.; Stayton, P. S. *Proc. Natl. Acad. Sci. U. S. A.* **2002**, *99*, 16592.

(242) Ichimura, K.; Oh, S.-K.; Nakagawa, M. *Science* **2000**, *288*, 1624.

(243) Khan, I. M. H., J. S. *Field Responsive Polymers. Electroresponsive, Photoresponsive, and Responsive Polymers in Chemistry and Biology*; Oxford University Press Oxford, U.K., 1999.

(244) Moore, J. S. *Acc. Chem. Res.* **1997**, *30*, 402.

(245) Trie, M. *Pure & Appl.Chem.* **1990**, *62*, 1495.

(246) Burakowska, E.; Zimmerman, S. C.; Haag, R. *Small* **2009**, *5*, 2199.

(247) Hartley, G. S. *Nature* **1937**, *140*, 281.

(248) Deloncle, R.; Caminade, A.-M. *J. PhotoChem. Photobiol. C. Photochem. Rev.* **2010**, *11*, 25.

(249) Puntoriero, F.; Bergamini, G.; Ceroni, P.; Balzani, V.; Vagtle, F. *New J. Chem.* **2008**, *32*, 401.

(250) Liao, L.-X.; Stellacci, F.; McGrath, D. V. *J. Am. Chem. Soc.* **2004**, *126*, 2181.

(251) Weener, J. W.; Meijer, E. W. *Adv. Mater.* **2000**, *12*, 741.

(252) Tsuda, K.; Dol; Gensch, T.; Hofkens, J.; Latterini, L.; Weener; Meijer; De, S. *J. Am. Chem. Soc.* **2000**, *122*, 3445.

(253) Li, S.; McGrath, D. V. *J. Am. Chem. Soc.* **2000**, *122*, 6795.

(254) Junge, D. M.; McGrath, D. V. *J. Am. Chem. Soc.* **1999**, *121*, 4912.

(255) M. Junge, D.; V. McGrath, D. *Chem. Commun.* **1997**, 857.

(256) Shen, X.; Liu, H.; Li, Y.; Liu, S. *Macromolecules* **2008**, *41*, 2421.

(257) Morgenroth, F.; Kubel, C.; Müllen, K. *J. Mater. Chem.* **1997**, *7*, 1207.

(258) Türp, D.; Nguyen, T.-T.-T.; Baumgarten, M.; Müllen, K. *New Journal of Chemistry* **2012**.

(259) Grebel-Koehler, D.; Liu, D.; De Feyter, S.; Enkelmann, V.; Weil, T.; Engels, C.; Samyn, C.; Müllen, K.; De Schryver, F. C. *Macromolecules* **2003**, *36*, 578.

(260) Türp, D.; Wagner, M.; Enkelmann, V.; Müllen, K. *Angewandte Chemie International Edition* **2011**, *50*, 4962.

(261) Mpoukouvalas, K.; Türp, D.; Wagner, M.; Müllen, K.; Butt, H.-J. r.; Floudas, G. *The Journal of Physical Chemistry B* **2011**, *115*, 5801.

(262) Einstein, A. *Annalen der Physik* **1905**, *17*, 549

(263) van der Sluis, P.; Spek, A. L. *Acta Crystallographica Section A* **1990**, *46*, 194.

(264) Schodel, F.; Lerner, H.-W.; Bru Roig, M.; Bolte, M. *Acta Crystallographica Section E* **2006**, *62*, o372.

11 List of Publications

Konstantinos Mpoukouvalas, David Türp, Manfred Wagner, Klaus Müllen, Hans-Jürgen Butt, George Floudas, "Dissociation and Charge Transport in Salts of Dendronized Ions in Solvents of Low Polarity" *The Journal of Physical Chemistry B* **2011**, *115*, 5801.

David Türp, Manfred Wagner, Volker Enkelmann, Klaus Müllen, "Synthesis of Nanometer-Sized, Rigid and Hydrophobic Anions", *Angewandte Chemie International Edition* **2011**, *50*, 4962.

Thi-Thanh-TamNguyen, David Türp, Dapeng Wang, Belinda Nölscher, Frédéric Laquai, Klaus Müllen, "A Fluorescent, Shape-Persistent Dendritic Host with Photoswitchable Guest Encapsulation and Intramolecular Energy Transfer", *Journal of the American Chemical Society* **2011**, *133*, 11194.

David Türp, Thi-Thanh-Tam Nguyen, Martin Baumgarten, Klaus Müllen, "Uniquely versatile: nano-site defined materials based on polyphenylene dendrimers", *New Journal of Chemistry* **2012**, *36*, 282.

Thi-Thanh-Tam Nguyen, David Türp, Klaus Müllen, "Photoswitchable Conductivity in a Dendronized Salt" (to be submitted).